NUREG/CR–5960

Steam Explosions: Fundamentals and Energetic Behavior

Prepared by
T. G. Theofanous, W. W. Yuen, S. Angelini, X. Chen
W. H. Amarasooriya, S. Medhekar

Center for Risk Studies and Safety
Department of Chemical and Nuclear Engineering
University of California at Santa Barbara

Prepared for
U.S. Nuclear Regulatory Commission

AVAILABILITY NOTICE

Availability of Reference Materials Cited in NRC Publications

Most documents cited in NRC publications will be available from one of the following sources:

1. The NRC Public Document Room, 2120 L Street, NW., Lower Level, Washington, DC 20555-0001

2. The Superintendent of Documents, U.S. Government Printing Office, Mail Stop SSOP, Washington, DC 20402-9328

3. The National Technical Information Service, Springfield, VA 22161

Although the listing that follows represents the majority of documents cited in NRC publications, it is not intended to be exhaustive.

Referenced documents available for inspection and copying for a fee from the NRC Public Document Room include NRC correspondence and internal NRC memoranda; NRC bulletins, circulars, information notices, inspection and investigation notices; licensee event reports; vendor reports and correspondence; Commission papers; and applicant and licensee documents and correspondence.

The following documents in the NUREG series are available for purchase from the GPO Sales Program: formal NRC staff and contractor reports, NRC-sponsored conference proceedings, international agreement reports, grant publications, and NRC booklets and brochures. Also available are regulatory guides, NRC regulations in the *Code of Federal Regulations*, and *Nuclear Regulatory Commission Issuances*.

Documents available from the National Technical Information Service include NUREG-series reports and technical reports prepared by other Federal agencies and reports prepared by the Atomic Energy Commission, forerunner agency to the Nuclear Regulatory Commission.

Documents available from public and special technical libraries include all open literature items, such as books, journal articles, and transactions. *Federal Register* notices, Federal and State legislation, and congressional reports can usually be obtained from these libraries.

Documents such as theses, dissertations, foreign reports and translations, and non-NRC conference proceedings are available for purchase from the organization sponsoring the publication cited.

Single copies of NRC draft reports are available free, to the extent of supply, upon written request to the Office of Administration, Distribution and Mail Services Section, U.S. Nuclear Regulatory Commission, Washington, DC 20555-0001.

Copies of industry codes and standards used in a substantive manner in the NRC regulatory process are maintained at the NRC Library, 7920 Norfolk Avenue, Bethesda, Maryland, for use by the public. Codes and standards are usually copyrighted and may be purchased from the originating organization or, if they are American National Standards, from the American National Standards Institute, 1430 Broadway, New York, NY 10018.

DISCLAIMER NOTICE

NUREG/CR-5960

Steam Explosions: Fundamentals and Energetic Behavior

Prepared by
T. G. Theofanous, W. W. Yuen, S. Angelini, X. Chen
W. H. Amarasooriya, S. Medhekar

Center for Risk Studies and Safety
Department of Chemical and Nuclear Engineering
University of California at Santa Barbara

Prepared for
U.S. Nuclear Regulatory Commission

AVAILABILITY NOTICE

Availability of Reference Materials Cited in NRC Publications

Most documents cited in NRC publications will be available from one of the following sources:

1. The NRC Public Document Room, 2120 L Street, NW., Lower Level, Washington, DC 20555-0001
2. The Superintendent of Documents, U.S. Government Printing Office, Mail Stop SSOP, Washington, DC 20402-9328
3. The National Technical Information Service, Springfield, VA 22161

Although the listing that follows represents the majority of documents cited in NRC publications, it is not intended to be exhaustive.

Referenced documents available for inspection and copying for a fee from the NRC Public Document Room include NRC correspondence and internal NRC memoranda; NRC bulletins, circulars, information notices, inspection and investigation notices; licensee event reports; vendor reports and correspondence; Commission papers; and applicant and licensee documents and correspondence.

The following documents in the NUREG series are available for purchase from the GPO Sales Program: formal NRC staff and contractor reports, NRC-sponsored conference proceedings, international agreement reports, grant publications, and NRC booklets and brochures. Also available are regulatory guides, NRC regulations in the *Code of Federal Regulations*, and *Nuclear Regulatory Commission Issuances*.

Documents available from the National Technical Information Service include NUREG-series reports and technical reports prepared by other Federal agencies and reports prepared by the Atomic Energy Commission, forerunner agency to the Nuclear Regulatory Commission.

Documents available from public and special technical libraries include all open literature items, such as books, journal articles, and transactions. *Federal Register* notices, Federal and State legislation, and congressional reports can usually be obtained from these libraries.

Documents such as theses, dissertations, foreign reports and translations, and non-NRC conference proceedings are available for purchase from the organization sponsoring the publication cited.

Single copies of NRC draft reports are available free, to the extent of supply, upon written request to the Office of Administration, Distribution and Mail Services Section, U.S. Nuclear Regulatory Commission, Washington, DC 20555-0001.

Copies of industry codes and standards used in a substantive manner in the NRC regulatory process are maintained at the NRC Library, 7920 Norfolk Avenue, Bethesda, Maryland, for use by the public. Codes and standards are usually copyrighted and may be purchased from the originating organization or, if they are American National Standards, from the American National Standards Institute, 1430 Broadway, New York, NY 10018.

DISCLAIMER NOTICE

NUREG/CR–5960

Steam Explosions: Fundamentals and Energetic Behavior

Manuscript Completed: December 1993
Date Published: January 1994

Prepared by
T. G. Theofanous, W. W. Yuen, S. Angelini, X. Chen
W. H. Amarasooriya, S. Medhekar

Department of Chemical and Nuclear Engineering
Center for Risk Studies and Safety
University of California
Santa Barbara, CA 93106

Prepared for
Division of Systems Research
Office of Nuclear Regulatory Research
U.S. Nuclear Regulatory Commission
Washington, DC 20555–0001
NRC FIN L1173

Abstract

This report presents the results of a multifaceted research effort in the field of steam explosions. The scope ranges from the fundamentals to assessing the energetics in applications relevant to Severe Accidents in Light Water Reactors. The consideration of fundamentals is built around two key ideas: the water depletion phenomenon during premixing and the microinteractions, including fragmentation kinetics, during propagation. The application to reactor conditions includes consideration of in-vessel steam explosions in PWRs and ex-vessel explosions in all five containment designs in current plants (in the USA). The report is structured in three parts, dealing with premixing, propagation, and energetics, respectively.

Table of Contents

Acknowledgments

This work was supported by the U.S. Nuclear Regulatory Commission under Contract No. 04-89-082. The cooperation and support of our project manager, Dr. F. Eltawila, is gratefully acknowledged.

Introduction and Overview

This report presents the results of a multifaceted research effort in the field of steam explosions. As the title indicates the scope ranges from the fundamentals to assessing the energetics in applications relevant to LWR severe accidents. The consideration of fundamentals is built around two key ideas: the water depletion phenomenon during premixing, and the microinteractions, including fragmentation kinetics, during propagation. The application to reactor conditions includes consideration of in-vessel steam explosions (in PWRs only, since BWRs with their massive lower plenum structures are not vulnerable to energetically significant explosions), and ex-vessel steam explosions in all five containment designs in current use (in the USA). Accordingly, the report is structured in three parts, dealing with premixing, propagation, and energetics, in that order.

The water depletion phenomenon refers to the formation of a very high void fraction region in the major central portion of large scale melt pours in water. This "steam bubble" is due to the high heat transfer rates and associated high steaming that "drive" the water out while at the same time it is being vaporized. The significance of this phenomenon is that large quantities of melt cannot coexist with water in a coarsely mixed configuration, a condition necessary to achieve an efficient thermal interaction. This allows putting bounding limits on interacting masses from arbitrarily large pours, and thus it has served as a central element of the argument against the α-mode containment failure in the past (Theofanous et al., 1987; Steam Explosions Review Group, 1985). This is important because then, and this remains true now, late phase core melt progression uncertainties do not allow a rigorous argument to be made against massive molten corium dumps into the lower plenum.

Given that all previous assessments of premixing limitations due to the water depletion phenomenon have been analytically based, the present work sought to fulfill the need for experimental verification. The body of Part I describes this work, including the experimental facility, MAGICO, a new diagnostic tool [the FLUTE, invented as a part of this work for measuring the local water content within the transient, multiphase, multidimensional premixing zone], the data obtained, and comparisons with predictions from our computer code PM-ALPHA. Details on supporting parts in the main theme are provided in the appendices. All data obtained (mixing front advancement, zone-averaged void fraction transients, and local void fraction transients) are documented together with PM-ALPHA predictions in Appendices I.B and I.C. The formulation of the PM-ALPHA code has been published previously; however, it is summarized in Appendix I.A also, for convenience. Details on the FLUTE, its calibration, and its theoretical basis can be found in Appendices I.E and I.F. Some detailed aspects of the multiphase interaction, as observed experimentally, are discussed in conjunction with PM-ALPHA results in Appendix I.D. Finally, some scaling considerations that went into the design of the MAGICO are given in Appendix I.G.

While convenient energetic limits can be put on the basis of the water depletion phenomenon described above, the assessment of potential for lower head failure, and of adjoining structures (i.e., pedestal wall) from ex-vessel explosions, require consideration of the explosion escalation and pressure wave propagation dynamics. The fundamental issues in carrying out such a task are the fragmentation kinetics of the coarsely-mixed melt drops in the so-called "reaction zone" immediately behind the pressure wave, and the associated micromixing and thermal interaction of the resulting fragments with the coolant in the immediate vicinity. In the past the fragmentation issue has been approached mainly through hydrodynamically-driven instabilities, and the

micromixing issue only macroscopically. Furthermore, experimentally produced and characterized detonation events have been rather tentative, and rather inadequate to provide a test bed for assessment, or even guidance, of propagation models.

In this portion of the work the primary focus is on producing experimental data of fragmentation, and micromixing, under conditions precisely relevant to propagating steam explosions. This is accomplished in a hydrodynamic shock tube, the SIGMA facility, in which molten drops (at various temperatures) falling through water in film boiling, are subjected to pressure pulses (of magnitude and duration appropriate for the various stages of escalation) and observed. The observations, besides high speed movies, include quantitative, flash X-ray, radiography that reveal not only the rates but also the morphology of fragmentation (i.e., micromixing). These data are used to test our propagation code (ESPROSE), and to distinguish between the hydrodynamic and thermally-driven fragmentation mechanisms. The code is then applied to experimentally-observed interactions in the KROTOS facility in ISPRA. The body of Part II describes this work, while supporting material is provided in the appendices. In particular, details of the SIGMA facility and of the ESPROSE simulations of SIGMA runs are given in Appendices II.B and II.C, respectively. The formulation of ESPROSE has been published previously, but it is summarized, for convenience, in Appendix I.A also.

Finally, the consideration of steam explosion energetics in reactor accident situations is given in Part III. In-vessel and ex-vessel scenarios are treated in Section III.1 and III.2, respectively. For in-vessel explosions we reexamine the Theofanous et al. (1987) quantification in light of the results of this work and of a recently-published comparative study between the PM-ALPHA and CHYMES codes by Fletcher (1992). In Appendix III.A we take this comparison to a conclusive further step, and also we present illustrative propagation calculations, triggered from realistic (as calculated by PM-ALPHA) premixtures, to assess the potential for lower head failure. For the ex-vessel explosions our approach is to consider the specifics of melt release scenarios, and contact modes, as dictated by the geometry of each one of the five containment designs in existence in the US. We conclude that in no case are there significant energetic events, and with the exception of the Mark III (Grand Gulf) deeply flooded cavity condition, this is in agreement with the results of NUREG-1150. For Mark III this study (the 1150) left the issue open, and to help add additional perspective to the scenarios considerations offered here we also provide certain illustrative (in the sense that they are unrealistically pessimistic) calculations of pedestal loading as predicted by PM-ALPHA/ESPROSE.

References

1. Steam Explosion Review Group (1985) "A Review of Current Understanding of the Potential for Containment Failure Arising from In-Vessel Steam Explosions," NUREG-1116, U.S. Nuclear Regulatory Commission.

2. Theofanous, T.G., B. Najafi and E. Rumble (1987) "An Assessment of Steam-Explosion-Induced Containment Failure. Part I: Probabilistic Aspects," *Nuclear Science and Engineering*, **97**, 259-281 (1987).

PART I: MULTIPHASE TRANSIENTS IN THE PREMIXING OF STEAM EXPLOSIONS

Table of Contents

Figures

Page

Tables

I.1 Introduction

Essentially all practically relevant steam explosions occur in the pouring mode of contact. Large, energetic explosions can only evolve from (or propagate through) "adequately" dispersed states created in this pouring/mixing process. In analogy with chemical explosions these states are referred to as "premixtures." A premixture is characterized by the spatial distribution of the "reactants," the "hot" and "cold" liquids (alternatively referred to as "fuel" and "coolant") and a third thermally "inert" component, the "vapor." The role of this third component is dual: first, it introduces compressibility which has a dissipative effect on triggering, escalation and propagation of an explosion; second, it implies depletion of liquid coolant (the "working" fluid) and thus reduced energetics even if an explosion were to occur. This latter aspect was first recognized by Henry and Fauske (1981), and it was a key ingredient in the quantification of steam-explosion-induced containment failure by Theofanous et al. (1987). These initial predictions were made with a transient, two-dimensional, two-fluid model, i.e., with the assumption that the vapor and liquid coolant behave as a homogeneous-equilibrium mixture. In subsequent work (Amarasooriya and Theofanous, 1991) this assumption was relaxed by the use of a three-fluid model, which produced similarly-depleted (in water) premixtures. Clearly, it is important that these predictions are confirmed experimentally.

This experimentally-oriented effort consists of three parts. The first is to examine the interface transfer laws (the so-called "closure" relations) in three-phase systems, with the one phase in film boiling. Initial results have been reported by Liu et al. (1992). The second effort is to examine the integral aspects of the premixing process with emphasis on the performance of the three-fluid modelling approach. For this purpose we use an already particulated hot mass (particles of a given size) instead of a liquid, and seek to characterize in detail the spatial-temporal evolution of the three-phase mixing zone created when these particles are dumped (as a cloud) into a liquid coolant pool. This is the subject of this work. Finally, the third effort is to test the prediction in experiments, run with molten "fuel" thus including the "fuel" break-up phenomenon during premixing. It is expected that the FARO experiments at the European Joint Research Center (ISPRA) and the ALPHA experiments at the Japan Atomic Energy Research Institute (Tokai) will provide data adequate for this purpose. It should be mentioned, however, that, by its very nature, the breakup process can only be indirectly inferred from these experiments (i.e., vapor production rates), and it is expected to remain uncertain in its details—nevertheless, its effect on the water-depletion phenomenon, and thus on energetics, can be bounded by parametric evaluations.

I.2 Experimental Facilities

The basic concept of the experiment (called MAGICO) is illustrated in Figure I.1. Tens-of-kilograms quantities of mm-size steel balls are heated to a uniform high (up to 1000 °C) temperature, then transferred into an intermediate container equipped with a dumper mechanism, and within a few seconds are released into a pool of saturated water in a lower-plenum-like geometry. The intent is to match (except for the breakup) the water-depletion regimes of the reactor in a 1/8- and 1/4-scale geometries, and numerical simulations (PM-ALPHA) are used for this purpose (see Appendix I.G). The major experimental parameters are: particle size, particle temperature, pour diameter, particle entry velocity and pool depth. Pool depths of 25 and 50 cm correspond to 1/8- and 1/4-scale simulation, respectively. In addition, in future work we intend to vary the particle cloud density and the lower plenum geometry (by including internal structures). In the following we provide some details of the experimental equipment and the measurement techniques.

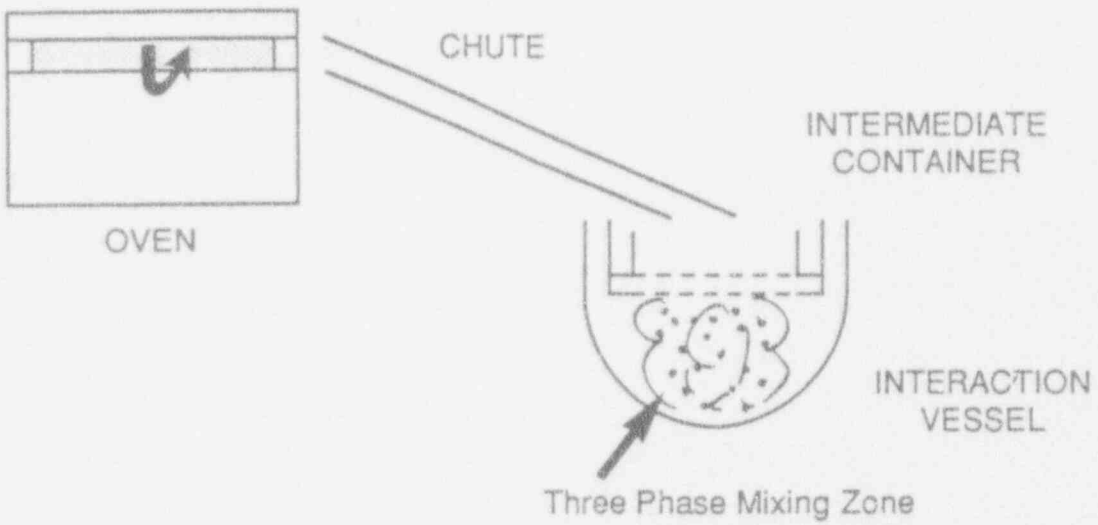

Figure I.1 Schematic of the MAGICO experiment.

For this experiment the oven cavity was equipped with a ceramic cylinder (1.67 m long, 8.2 cm in diameter) that could be loaded, plugged at both ends, and rotated during heating to prevent the steel balls from sticking together at high temperatures. The rotation also helped obtain temperature uniformity. Integrity of the ceramic cylinder requires that heat-up be regulated closely at less than 150 °C per hour—13 hours are required for a 1000 °C run, including cooldown. When the desired temperature level is reached, the one end of the cylinder is unplugged, and the whole oven is tilted so that by gravity flow the balls are transferred to the intermediate container (this process lasts about 2 min.). The intermediate container (21 cm in diameter) is equipped with several thermocouples located such as to allow a good characterization of the initial temperature of the particulate at the moment it is released. Both the nominal (initially in the oven) temperature and this, actual, temperature are recorded, and typically they differ by less than 100 °C. Sudden and uniform release is achieved by a solenoid-operated air-cylinder operation that, by a slight movement, aligns the holes of two perforated plates that make up the bottom of the intermediate container. In the present set-up, the holes are 1.1 cm in diameter,

placed on a square 1.27 cm pitch. In future tests this pitch will be varied to obtain different cloud densities. The maximum pour diameter is 20 cm.

The lower plenum scale model (the interaction vessel) was fabricated from steel and is equipped with an observation window. Preliminary tests indicated that the behavior is quite similar to that obtained in a plain rectangular vessel (406 mm on the side, with a height of 355 mm), and the use of such (made of tempered glass) was made, henceforth, to allow easy and complete visualization. The whole experimental setup is shown in Figure I.2. Not discernible are the FLUTE components (see next section) as they are located just behind the interaction vessel. Not shown is the data acquisition system which is located in another room.

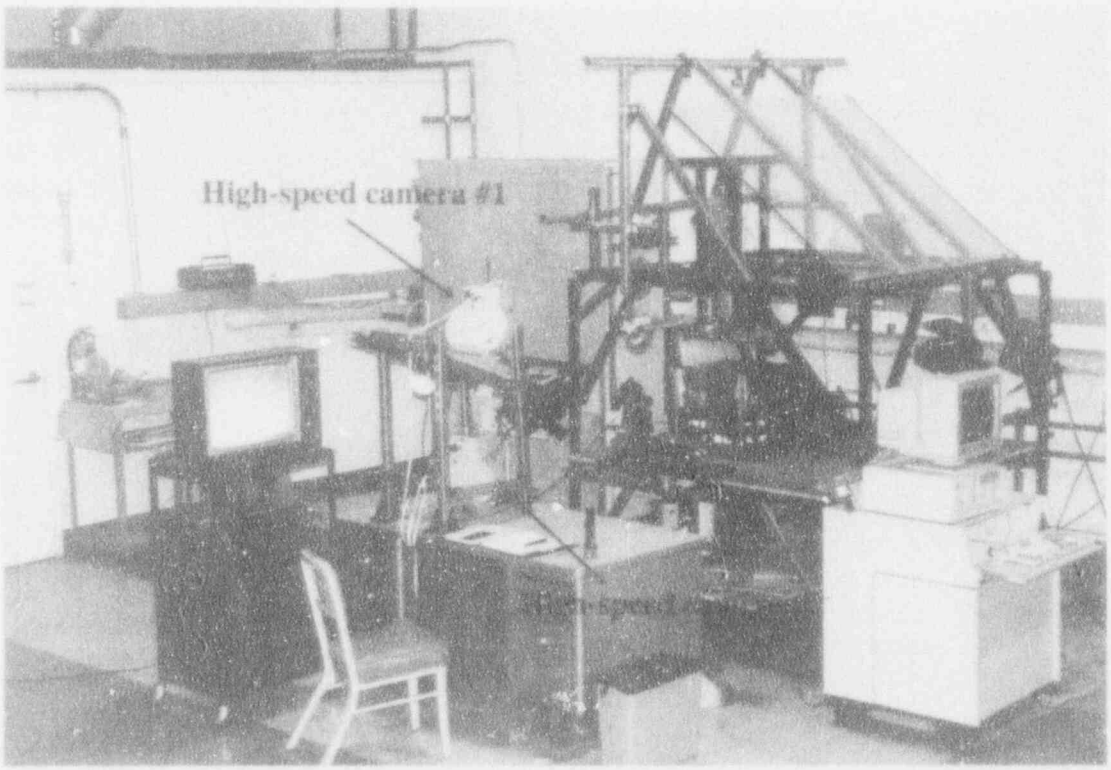

Figure I.2 An overall view of the MAGICO experimental setup.

I.3 Measurement Techniques

As mentioned above, the key measurement in these experiments is the space–time evolution of the liquid fractions, in the two-dimensional evolving mixing zone, during the short (less than 1 second) transient. [An indication of what is involved is given in Figure I.3]. Such measurements were made at the global level (averages over the whole mixing zone), as well as at the local level (on a sample volume of $\sim$ 1/4 cm^3 at several locations within the mixing zone). The presence of hot particles introduced a different sort of difficulty for each of these two measurement approaches—correspondingly they were susceptible to different kinds of limitations. This made them complimentary to each other, specifically with regards to the portion of the transient (earlier vs. later) best suited to each. Each measurement is discussed further below.

Since the melt volume fraction in the mixing zone is less than 2% (this is estimated from the pour area and the particle delivery rate, and is consistent with the results of PM-ALPHA calculations) the liquid (water) volume fraction in it can be deduced from measurements of the zone-averaged void fraction. By mass continuity this can be related to the apparent increase in volume of the surrounding liquid which, in turn, can be obtained from the observed level rise. Such data were obtained throughout the transient by closeup high speed movies (camera #1 in Figure I.2). In addition, the whole interaction vessel, and especially the whole free liquid surface, were observed with high speed camera #2. Void fraction data were reduced in two different ways. One referred the measured void volume to the whole mixing zone volume, while the other made use of the whole volume under the pour area (a cylinder with a cross section the same as that of the pour area and a height equal to the instantaneous height of the liquid in the interaction vessel). The first will be referred to as "mixing-zone-averaged" void fraction, while the latter as "pool-height-averaged" void fraction. Clearly, the two should agree when the melt-front just touches the pool bottom and begins to accumulate on it. As seen in Figure I.3, the mixing zone maintains the cross section of the pour area, thus for the "mixing-zone-averaged" void fraction the mixing zone front only needs to be tracked. The error in estimating the water position is ± 1 mm, thus the "pool-height-averaged" void fraction data involve an absolute error of $\pm 2\%$. The "mixing-zone-averaged" void fraction measurement uncertainty is primarily impacted by properly following the mixing zone front. It is estimated that this was done to within ± 1 cm, which translates to a rather significant error initially, decreasing gradually to about $\pm 10\%$ (relative error) near the end. Errors due to air entrained with the particles are negligible. At still later times, the interface breaks up in the manner illustrated by the third snapshot in Figure I.3. This often happens at around the time the mixing-zone front reaches the pool bottom, but sometimes earlier also. Clearly, this marks the end of the time period for this sort of data.

From a practical standpoint, this is also the time period of interest for steam explosion energetics—if an explosion has not been triggered up to this point, it should be at the point of impact, rather than at any later time. Still, it is interesting to follow the void fraction transient for somewhat longer time. The local void fraction measurement besides providing the local structure is complementary to the volume-averaged one also in this respect.

Even though less than 2% by volume , the presence of the hot, solid particles present serious difficulty in the measurement of local liquid (void) fractions. [For example, particle interference and count statistics in such fast transients become prohibitive for the widely used γ-attenuation techniques. Even selective attenuation using 2 gamma energies led to a stiff system of equations

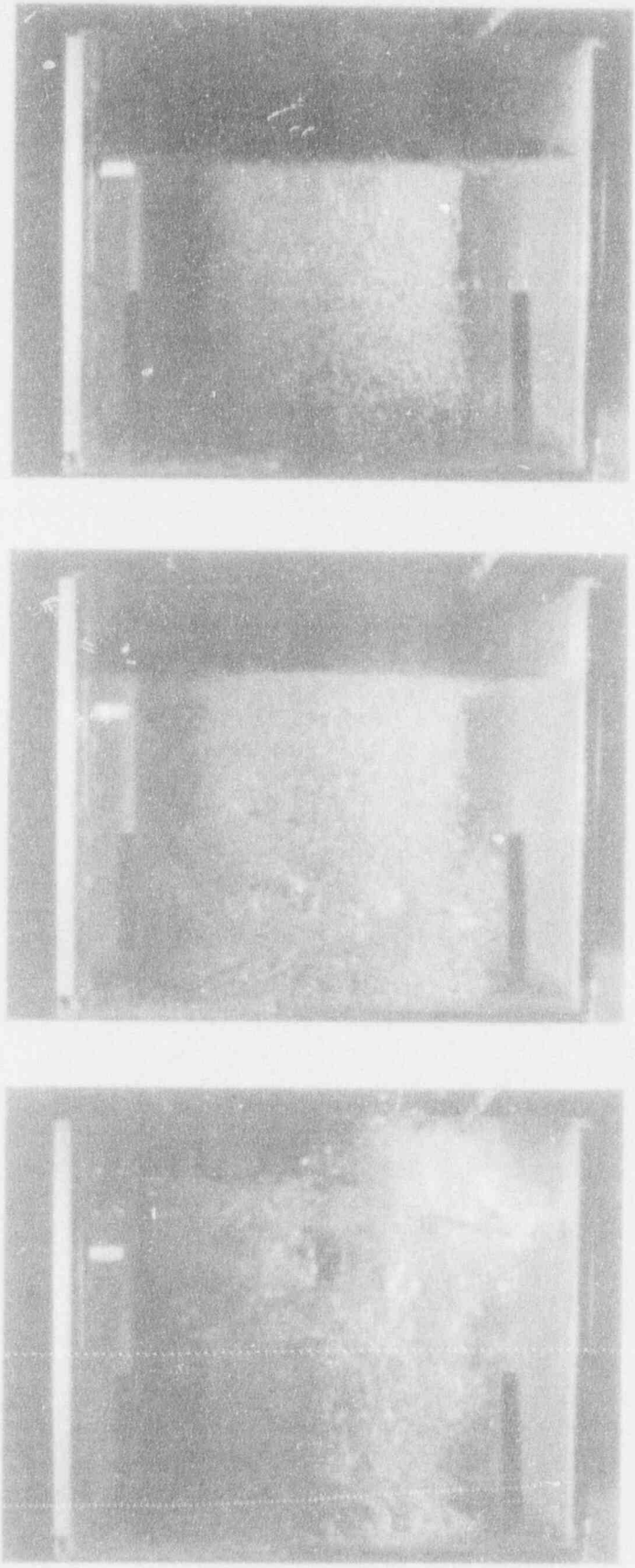

Figure I.3 Snapshots of a typical premixing transient in MAGICO. The times are 0.27, 0.57, and .87 seconds.

and did not appear to be very promising.] A new instrument, FLUTE, had to be invented for this purpose (see Appendices I.E and I.F). The principle of this measurement can be explained with the help of Figure I.4. The idea is to measure the intensity of fluorescent light emitted from a local fluid region, activated by ultraviolet radiation (a dye, fluorescein, dissolved in the liquid being the active ingredient). The size of the measurement volume is controlled by the distance L between the fibers (the acceptance angle θ_ℓ is 29°). Because the fibers are very fine (1 mm in diameter) their presence provides hardly any disturbance to the flow. For this application (because of the hot, solid particles) the fibers are protected by very fine steel tubing, and they also need to be securely supported, as illustrated in Figure I.5. The supports are made to offer minimal cross-sectional exposure in the main flow direction, and we believe that the disturbance introduced by their presence is insignificant. The data rate is limited only by the capability of the data acquisition system. In the present configuration, this is 8 kHz, but an upgrade to 80 kHz is readily possible.

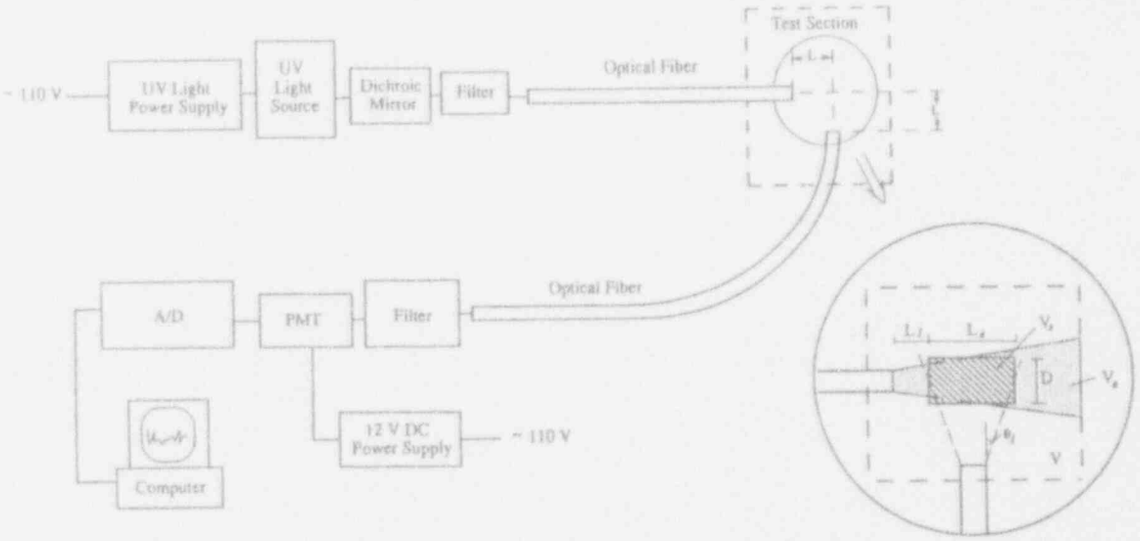

Figure I.4 Schematic illustration of FLUTE. The measurement volume is V_s.

This instrument offers a unique capability, in general, for the measurement of local, essentially instantaneous, liquid volume fractions in highly transient, multidimensional, dispersed two phase flows. In the present application, the solid particles introduce some additional consideration with regard to the choice of fiber spacing (L in Figure I.4). Particle interference with both the emitting and receiving light beams increases with L. From numerical simulations (Monte Carlo type) we find that for $L = 4$ mm, a melt volume fraction of 2%, and very low void fractions, this interference leads to a *maximum* absolute error in void fraction of about 10%. That is, for real void fractions of ~10%, the FLUTE reading may be as high as 20%. However, as the void fraction increases, diminishing portions of the particle interference are attributable to the quantity of liquid "shadowed" and thus the *absolute* error decreases. As a consequence, we expect that the relative error at void fractions over 30% to be under 10%. On the other hand, as this interference effect is diminished by reducing L, liquid "trapping" between the fibers can lead to errors. We call this fiber interference; it tends to produce erroneously higher values of liquid fraction. From experiments, we found this error to be significant for $L = 1$ or 2 mm. Thus, the measurements with $L = 4$ or 5 mm are considered to be the reliable ones.

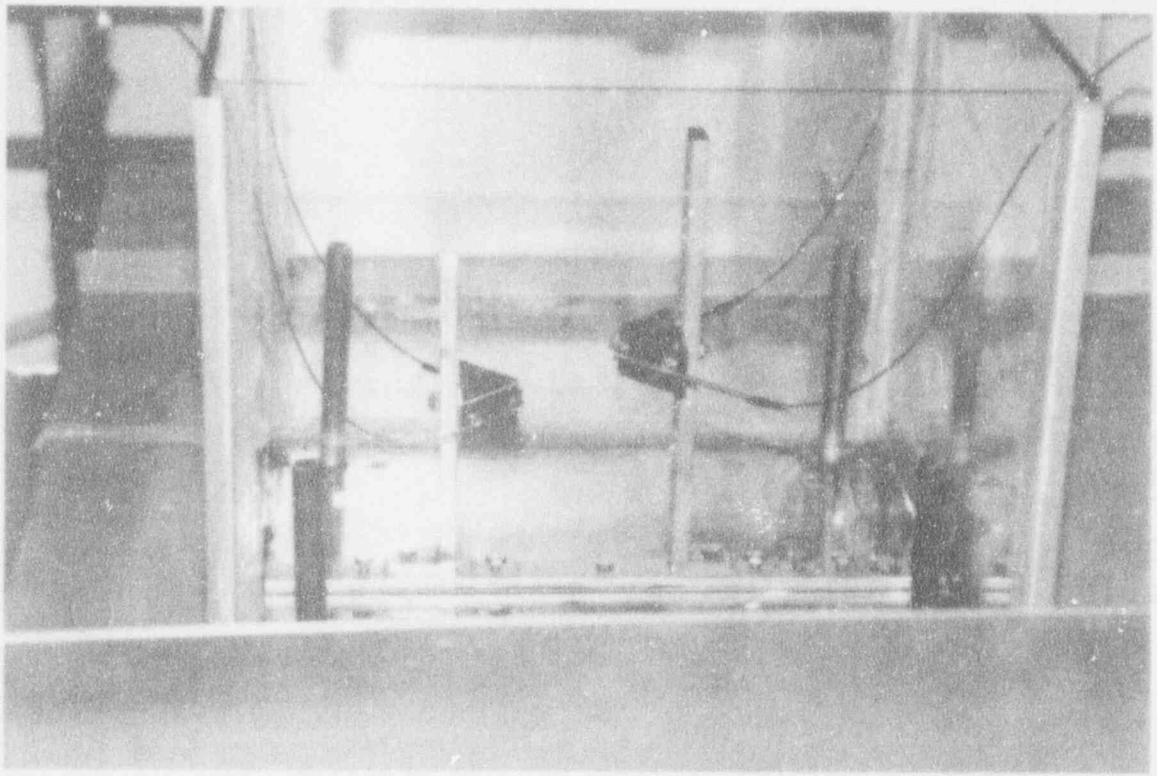

Figure I.5 The FLUTE fibers and supports for two simultaneous measurement locations in the interaction vessel.

Recognizing the novelty of these measurements (with FLUTE) and the desirability, therefore, of an independent verification, significant additional efforts were devoted to this purpose. This goal was finally met using a pattern recognition approach on flash X-ray images of the mixing zone taken at selected times during the transient. Through careful experimental configurations and precise calibrations, we could determine 2D chordal-averaged void fraction distributions (in the plane of the film) over a significant fraction of the image found to be free of particle interference. The results were in substantial agreement with the FLUTE measurements and PM-ALPHA predictions, as described in section I.5.

I.4 Experimental Results and Interpretations

The runs with high speed movies were carried out as a separate series. Run numbers and respective experimental conditions have been listed in Tables I.1 through I.3. From Tables I.1 and I.2 it can be seen that nominal particle temperatures varied in the 600 to 1000 °C range (the particle temperatures quoted in this table are those measured in the intermediate vessel just prior to the initiation of the pour); the rest of the experimental matrix covered variations in pour diameter, pool depth, and freefall distance. The freefall distance refers to the distance between the particle release point and the pool surface—this variation creates different particle velocities at the point of pool entry. In the FLUTE runs (Table I.3) the main effect studied was the fiber spacing, but other variations included were particle temperature and measurement position.

Table I.1 Experimental Matrix for Runs with Global Liquid Fraction Measurement
(1.5 mm chrome-alloy AISI-52100 particles)

Run #	Oven Temperature (°C)	Particle Temperature (°C)	Pool Depth (cm)	Freefall Distance (cm)	Pour Diameter (cm)
101	600	560	25	15	20
102	800	750	25	15	20
103	1000	880	25	15	20
104	600	550	15	15	20
105	600	580	15	25	20
106	800	720	15	15	20
107	600	560	25	5	20
108	1000	800	15	15	20
109	1000	860	15	25	20
111	800	760	15	25	20
112	800	760	25	5	20
113	600	550	25	15	12
114	800	760	25	15	12
115	600	550	15	15	12
116	800	780	15	15	12
904	600	550	50	15	20
905	800	750	50	15	20

In all runs the water was at saturation—it was brought to a boil by 4 immersion heaters located at the corners of the interaction vessel (these heaters are visible in Figure I.3).

In the following, the experimental results are presented in conjunction with predictions using the PM-ALPHA code. The three-fluid formulation used in this code and the set of constitutive laws in it have been completely specified previously (Amarasooriya and Theofanous, 1991); a

Table I.2 Experimental Matrix for Runs with Global Liquid Fraction Measurement
(2.4 mm stainless steel SS316 particles)

Run #	Oven Temperature (°C)	Particle Temperature (°C)	Pool Depth (cm)	Freefall Distance (cm)	Pour Diameter (cm)
701	600	550	25	15	20
702	800	750	25	15	20
703	600	550	15	15	20
704	800	750	15	15	20
705	600	550	25	15	12
706	800	750	25	15	12
901	600	550	50	15	20
902	800	750	50	15	20

Table I.3 Experimental Matrix for Runs with Local Liquid Fraction Measurement
(2.4 mm stainless steel particles, 25 cm pool depth, 20 cm pour diameter, and freefall distance 15 cm, except runs 204 and 401, set at 5 and 3 cm, respectively)

Run #	Oven Temperature (°C)	FLUTE Position #1			FLUTE Position #2		
		H* (cm)	R† (cm)	L (mm)	H* (cm)	R† (cm)	L (mm)
204	800	17.5	0.0	5	19	2.5	5
209	600	20	3.4	4	16.5	3.4	4
210	600	20	3.4	4	16.5	3.4	4
211	800	20	3.4	4	16.5	3.4	4
301	600	20	3.4	4	19	3.4	4
302	600	20	3.4	4	19	3.4	4
303	600	20	3.4	4	19	3.4	4
304	600	20	3.4	4	19	3.4	4
305	600	20	3.4	6	19	3.4	2
401	600	20	3.4	2	19	3.4	2
402	600	20	3.4	2	19	3.4	2
403	600	20	3.4	1	19	3.4	1
404	600	20	2.5	1	19	2.5	1
406	600	9.5	3.4	5	8.8	3.4	5
407	600	20	3.4	5	19	3.4	5
408	800	20	3.4	4	19	3.4	4
603	600	20	3.4	4	19	3.4	4
604	600	20	3.4	4	19	3.4	4

*Height from vessel bottom.
†Radial distance from centerline.

summary including an improvement made on the phase change model are provided in Appendix I.A. The predictions are made on this basis. The flow field (which includes the freefall space) was discretized by 2.5 cm (axial) by 2 cm (radial) nodes, in axisymmetric cylindrical geometry (the radial dimension was chosen to represent the interaction vessel cross-sectional area). The particle velocity at the point of release (inlet to the flow fields) was obtained from the high speed movies as 72 cm/s, and it was found to be independent of the quantity of material in the intermediate vessel (presumably the particle's sliding against each other as they enter the holes in the bottom of the intermediate vessel controls the release rate). The particle volume fraction in the same location was found from the volumetric release rate of particles to be 1.87% and 2% for the 2.4 and 1.5 mm balls, respectively. In the calculations, the two-phase zone front lagged the particle front by about 3 nodes. To check for numerical diffusion we implemented also a Langrangian treatment, as a side to the main calculation, and the results were found to be in good agreement with both the calculated Eulerian particle front and the particle front motion obtained from the movies.

From such numerical simulations, the two experimentally deduced void fraction transients were computed for the conditions of each experimental run—these are the "predictions" shown with the experimental data in what follows. Details of the calculated evolution of the mixing zone, the void fraction distributions in it, the related flow fields, and other salient features of the interaction may be found in Appendix I.D. Note that the qualitative features are similar to those of Figure I.3, although maybe somewhat more pronounced.

Mixing-zone-averaged and pool-height-averaged results from 25 runs in the 100-, 700-, and 900-series are shown in Appendix I.B. As may be seen in Table I.1, these illustrations cover the effects of particle temperature, pool depth, freefall distance, and pour diameter. The mixing zone average results extend roughly up to the time that the zone front reaches the pool bottom. The calculation shows an initial rapid increase and an eventual leveling off in the void fraction as the pool bottom is approached. This is because at higher void fractions steam is able to vent off the top (see Appendix I.D), there is less water "feeding" the mixing zone at its front, and heat transfer (and vaporization) degrade because of increase in void fraction. Note that the radiation component of the heat transfer at these particle temperatures is not as strong as what would be expected for the very high temperature fuel in reactor situations. In general, these trends are born out by the experimental data, with the only notable exception, possibly, the case of runs 113, 114, 115 and 116. In these runs the pour area was ~1/3 that of the other runs. Turning next to the pool-height-averaged void fractions, which also are shown in these figures, we note that the numerical results show initially a rapid rise, but peak and "level off" within a short time after the particles begin to accumulate at the pool bottom. An oscillatory structure, of varying amplitude, on this "level" part is also observed. The experimental data are seen to reveal clearly this early rising trend, but unfortunately they stop short of the peak—as explained earlier, this sort of measurement is not possible after the pool surface begins to break up. This is where the local measurements are very helpful, and they are discussed next.

At 8 kHz, FLUTE provides essentially instantaneous readings of the local liquid fraction—because the sampling volume is so small, the signal often shows either 100% liquid or 100% vapor. These readings were time-averaged over 10, 20, 50 and 100 millisecond time intervals while "sliding" on the time axis. The results for all runs with measurement positions at 2 different depths (see Table I.3) are shown in Appendix I.C. An additional reduction was performed by ensemble averaging the so-smoothed results from 9 different runs (2 equivalent FLUTE positions in 7 of these runs), and these results are shown in Figure I.6. The FLUTE readings show the

first arrival of the hot particles by the interference signals already discussed in section I.3. Synchronization between the experimental and predicted traces is accomplished by establishing coincidence of this instance to the arrival of the hot particles at the measurement location in the calculation. We see in the measurements a rather complicated structure, but the general trends are consistent with the predictions. This is particularly evident in the multi-run, or ensemble, average as indicated in Figure I.6. More specifically, in the calculation we observe an initial rapid rise when the two-phase front reaches the measuring location, a more moderate increase for a period of time well past the particle arrival time at the pool bottom and a short and sharp peak followed by a rather marked fall. In the experimental data, the initial rapid rise is somewhat marred by the particle interference; however, it is still quite evident. Note that this early period is well covered by the global void fraction data discussed earlier. More clear is the intermediate period of moderate rise. As noted already, in this range of high void fractions the interference error is reduced drastically, and this is very important because we thus have measurements in the region for which the global void fraction measurements were not possible. It is also very interesting to note that in the overlapping region there appears to be good consistency between these two measurements. Finally, at the very end of the transients shown, the data do not exhibit as pronounced a fall-off as found in the prediction; indeed, even discerning such a fall-off in the data is rather subjective.

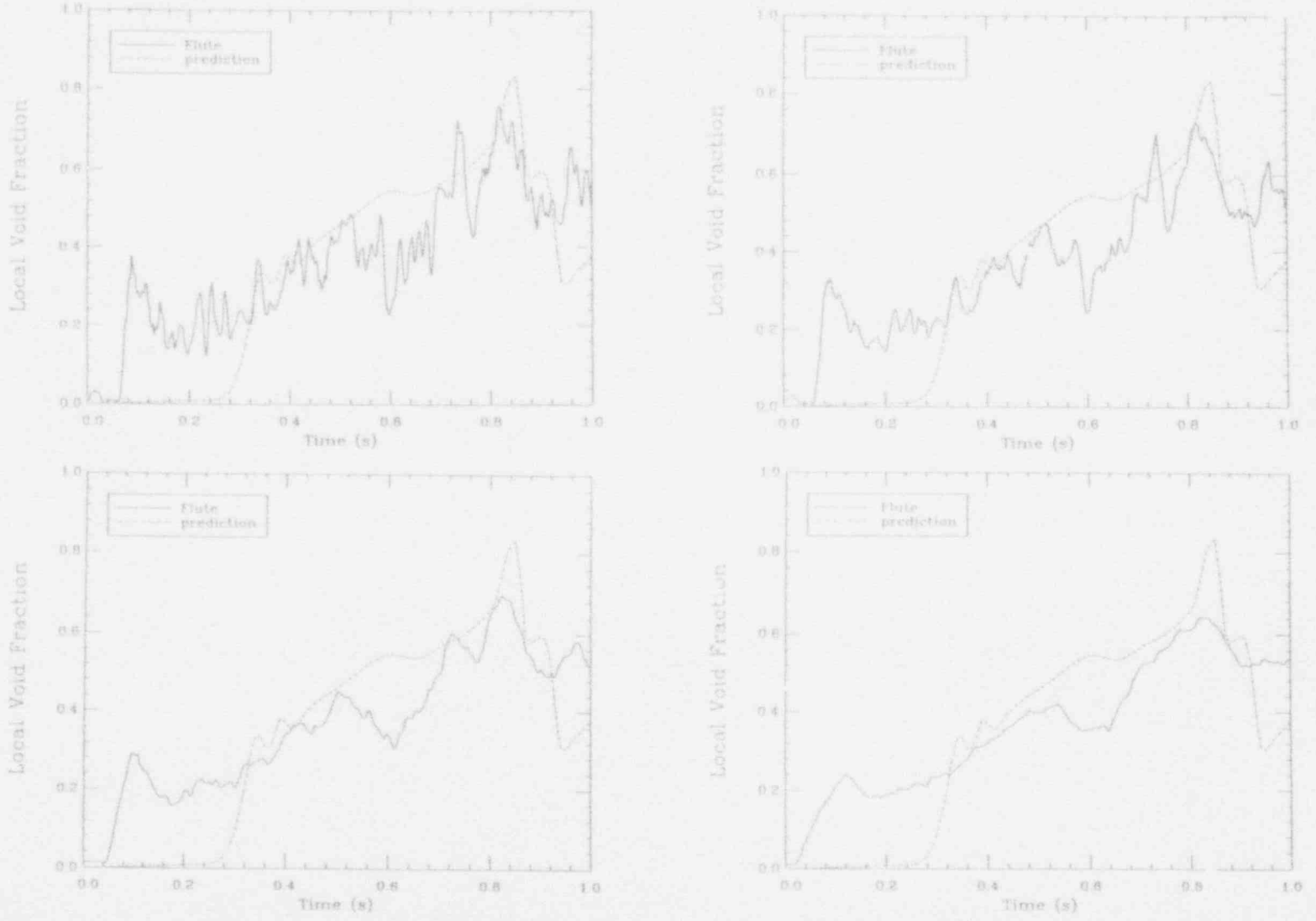

Figure I.6 The local void fraction transient obtained by averaging the time-smoothed signals (obtained as in the figures of Appendix I.C).

I.5 Independent Verification of FLUTE Measurements

The reason for creating the FLUTE is that our efforts in using absorbing radiation to image the whole mixing zone during the design phase of MAGICO did not yield promising results. The working concept in this effort was to make use of two different γ- and X-ray energies and the differences in attenuation between the water and the material of the balls so as to simultaneously measure both. Although in principle this approach is fine, in practice, it results in a stiff system of equations that yield large error amplification in the solution, and thus it was abandoned.

We returned to it after the completion of the first phase of the experimental program in MAGICO that made use of FLUTE. The reapproach appeared hopeful, basically because actual experience with MAGICO indicated that the particle volume fractions in the mixing zone are in the 2 to 3% range, thus creating the possibility of "seeing" through limited (sporadic) areas of this zone without ball interference. Numerical experiments attempting to recreate realization of the particle cloud and the optical paths through it revealed that this was indeed the case. These experiments also provided guidance on how to optimize the orientation of the X-ray shot and the source-to-object distance, taking advantage of the hole pattern in the dumper plate.

In actual implementation, we used a flash of "soft" X rays timed at the desired instant within the premixing transient in MAGICO. The image is recorded on a 13 x 18 cm film positioned to cover the region of interest in the mixing zone. By changing the timing of the flash and the film position, we can map out a premixing transient in any temporal and spatial detail desired—this is possible because of the excellent reproducibility of the MAGICO runs, as already demonstrated by the FLUTE measurements and the high-speed movies. We have limited our goal here to the independent check of the FLUTE results, and only a few runs are adequate for this purpose. In the process of developing the quantitative aspects of this technique, we have made quite a few runs that successively appeared more and more promising. A great deal of the success depends on establishing adequate safeguards and procedures to ensure that the image obtained can be directly related to a calibration image obtained with a known stepwise variation of void in the optical path. Besides, we confirmed that the effect of X-ray scattering from the steel balls (they are not present, clearly, in the calibration shot) is negligible. At this time, the technique is well-developed, and we have one run in the MAGICO series (the 1000-series) to discuss here. Rather than carry out the many special FLUTE runs needed to cover the information on the X rays, our approach is to use PM-ALPHA as the means of comparison; the PM-ALPHA interpretations are the ultimate purpose in any case.

This MAGICO test, #1005, was run with the 2.4-mm steel balls at 600 °C poured into a 25-cm-deep pool of saturated water from a height of 21 cm. The X-ray shot was timed at 0.52 s after initiation of the pour, which corresponds to just about when the particle front hits the pool bottom. The X-ray image obtained is shown in Figure I.7. It is noteworthy that individual balls are recognizable, even when they partly overlap, and we believe with a pattern recognition technique, we will have, from such shots, the particle number densities as well. Also in this figure, small areas where balls are completely absent are clearly distinguishable, and it is in these areas that with the application of the water/void calibration curve we can obtain the chordal-average void fractions.

The "reading" and analysis of these films was done on 6 x 6 cm film segments in order to obtain the high resolution required—this gave a pixel size of 0.12 mm. These readings were analyzed in groups of 20 pixels. For each such group, an average value of void (and hence of void fraction) was obtained by using the calibration curve and a criterion excluding readings indicating the presence of spheres. Moreover, to ensure that readings too close to the sphere boundaries were excluded, we used as an additional criterion that the fraction of unaffected readings within a group was above some value—otherwise, the space associated with the particular group of (20) pixels was taken to be interfered by the presence of steel. The data analysis was repeated with f values of this fraction set to 25, 50, and 75%, with very consistent results, indicating absence of the boundary-type influence being addressed by this operation.

The results from film segments covering the region $19 < z < 25$ cm (i.e., a 6-cm slice of the pool top; z is measured from the pool bottom) over two radial segments, $-1.5 < r < 5.5$) cm and $5.5 < r < 11.5$ cm presented here. Spatial void fraction maps (using the 50% criteria discussed above) are shown in Figures I.8 and I.9 for the above two radial regions, respectively. The blank spaces in these maps indicate regions of ball interference. Immediately, we can notice that these results indicate void fractions in the general range measured by FLUTE. In a more detailed examination, we have plotted these results against PM-ALPHA predictions for four different radial computational cells (at $r = 1$, 3, 5, and 7 cm) at three axial positions ($z = 18.75$, 21.25, and 23.75 cm), as shown in Figures I.10. In these figures, the PM-ALPHA results were obtained by an appropriate chordal-average equivalent to projecting the cylindrically-symmetric void fraction distribution, as effected by the X ray on the film. The X-ray results were obtained from the spatial maps by averaging all measured values within the cell being considered. The agreement is quite remarkable in all cases. It is also interesting to note that the "water flux reversal" phenomenon discussed in Appendix I.D is quite evident in Figure I.10b; the insurge of water causes a precipitous drop of void fraction at the outer edges of the mixing zone. The X ray happened to be taken just prior to this time.

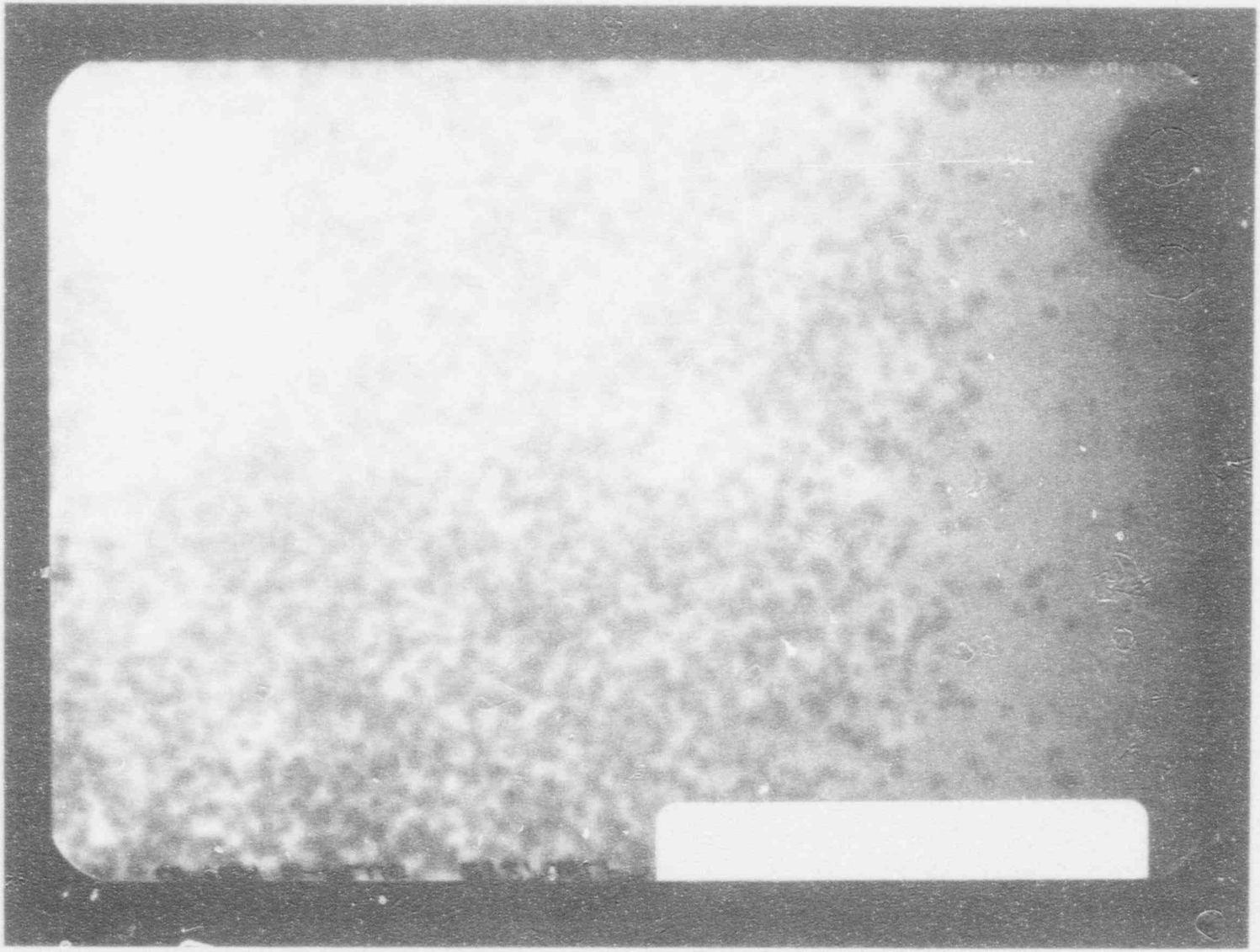

Figure I.7 Print of the X-ray film taken in Run #1005.

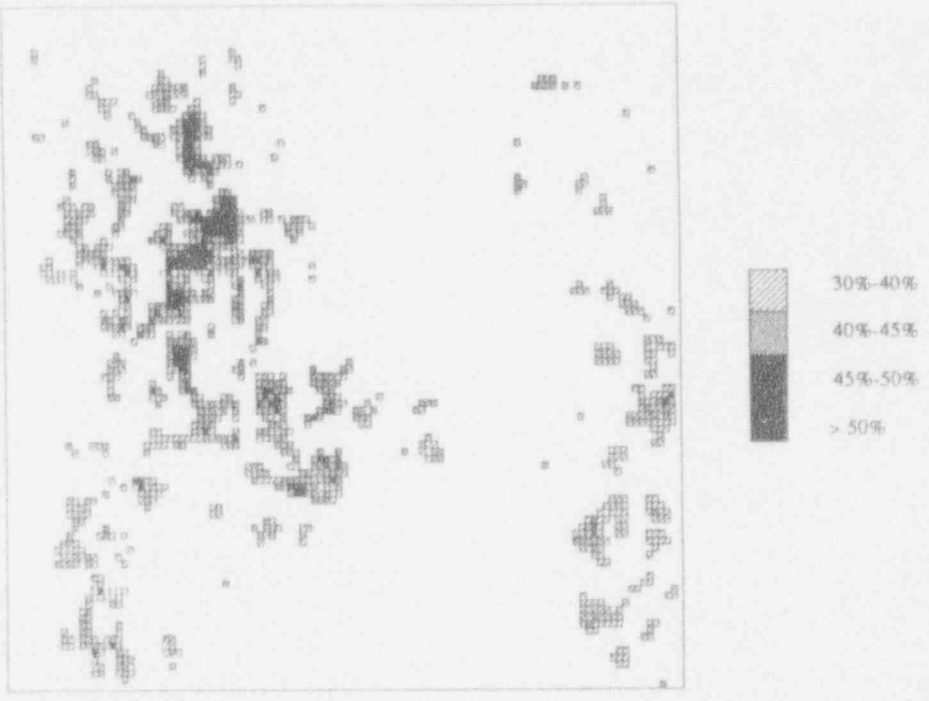

Figure I.8 Void fraction distribution obtained from X-ray analysis of run #1005. The region covered is $-1.5 < r < 5.5$ cm and $19 < z < 25$ cm.

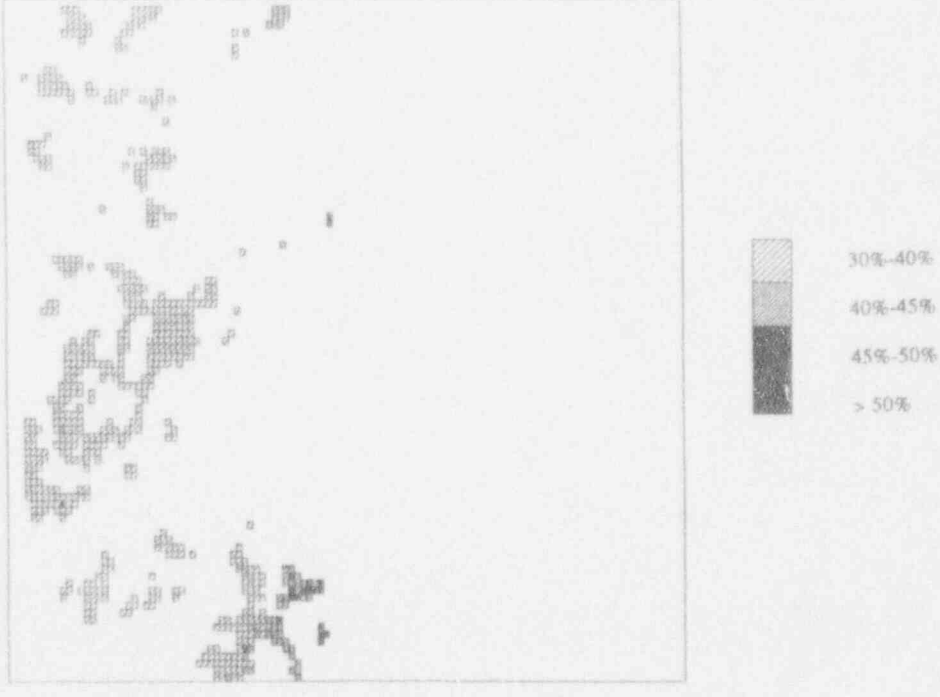

Figure I.9 Void fraction distribution obtained from X-ray analysis of run #1005. The region covered is $5.5 < r < 11.5$ cm and $19 < z < 25$ cm.

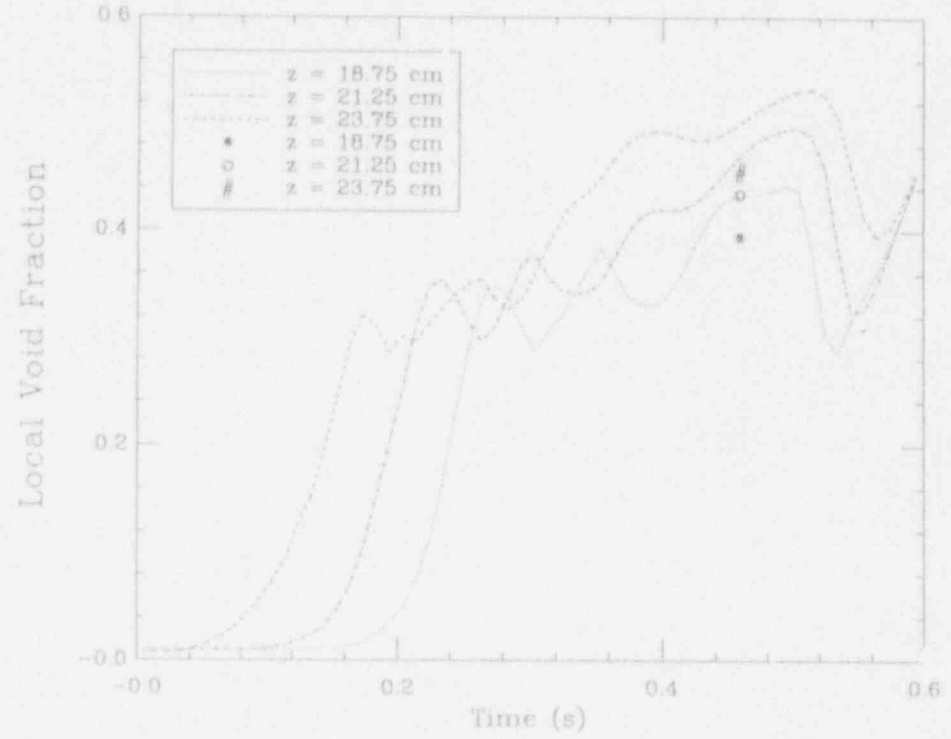

Figure I.10a Comparison between prediction and X-ray measurement for run #1005 for cell centered at $r = 1$ cm and three different heights.

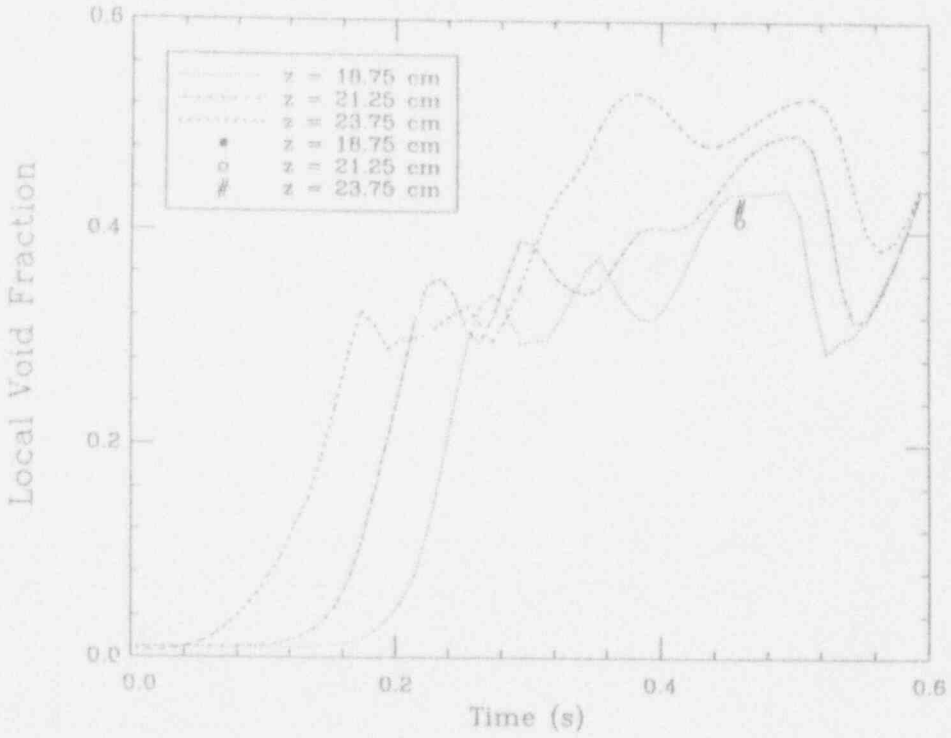

Figure I.10b Comparison between prediction and X-ray measurement for run #1005 for cell centered at $r = 3$ cm and three different heights.

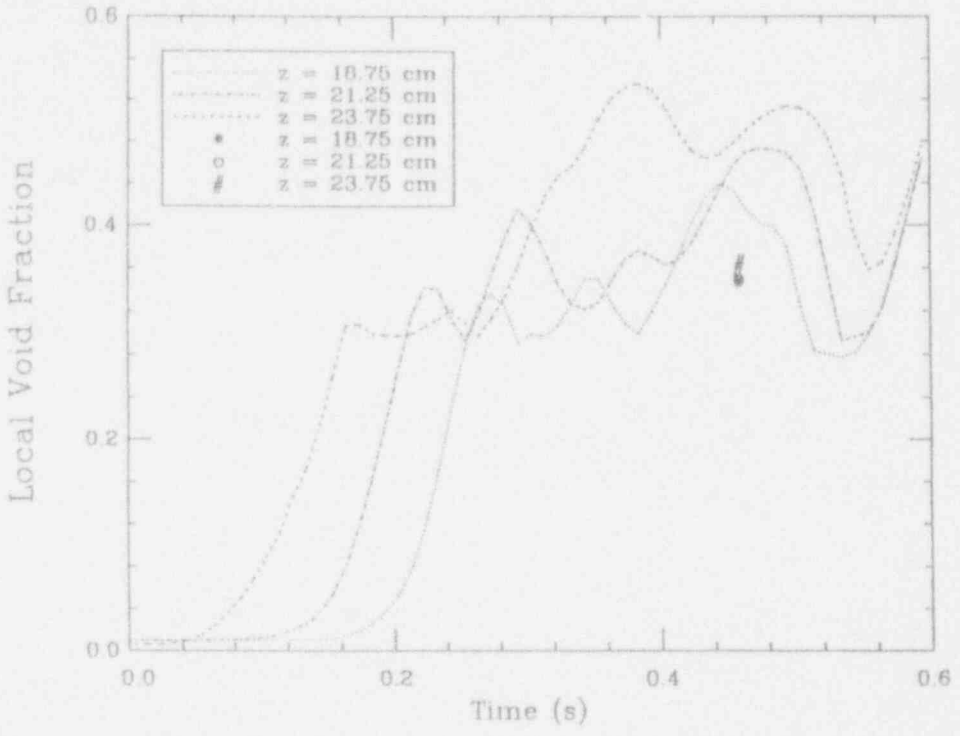

Figure I.10c Comparison between prediction and X-ray measurement for run #1005 for cell centered at $r = 5$ cm and three different heights.

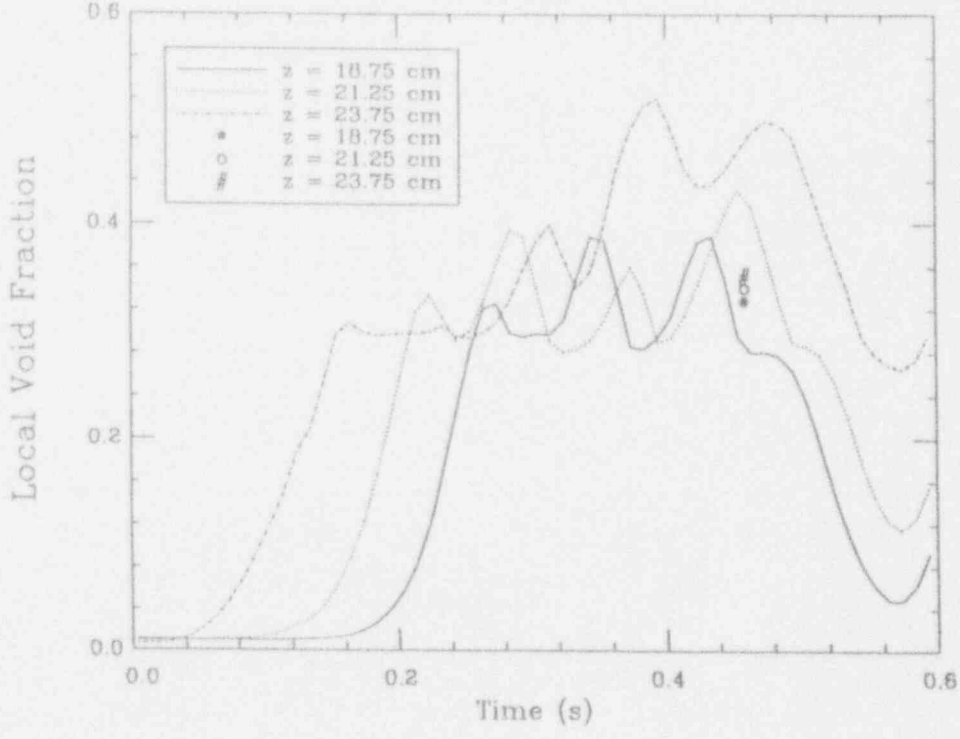

Figure I.10d Comparison between prediction and X-ray measurement for run #1005 for cell centered at $r = 7$ cm and three different heights.

I.6 Conclusions

An experimental facility and related experimental techniques have been demonstrated to provide a viable vehicle for the study of the extremely complex multiphase zone created by the interaction of a hot particulated phase poured into a volatile liquid. All indications are that the process is dominated by heat transfer and the resulting vapor production, in general, is not sensitive to details of the phenomenology. Comparison with predictions made by using the PM-ALPHA code are very encouraging.

I.7 References

1. Amarasooriya, W.H. and T.G. Theofanous (1991) "Premixing of Steam Explosions: A Three-Fluid Model," *Nuclear Engineering and Design* **126**, 23-39.

2. Henry, R.E. and H. K. Fauske (1981) "Required Initial Conditions for Energetic Steam Explosions," *Fuel-Coolant Interactions, HTD-V19*, American Society of Mechanical Engineers.

3. Liu, C., T.G. Theofanous and W. Yuen (1992) "Film Boiling from Spheres in Single- and Two-Phase Flow," 1992 National Heat Transfer Conference, San Diego, August 9–12.

4. Theofanous, T.G., B. Najafi and E. Rumble (1987) "An Assessment of Steam-Explosion-Induced Containment Failure. Part I: Probabilistic Aspects," *Nuclear Science and Engineering*, **97**, 259-281.

APPENDIX A

FORMULATION OF THE PM-ALPHA MODEL

Appendix A: Formulation of the PM-ALPHA Model

A.1 Conservation Equations

There are three separate phases: namely, coolant vapor, coolant liquid, and fuel (melt) drops. They will be referred to as gas, liquid, and fuel, respectively. Each phase is represented by one flow field with its own local concentration and temperature. Thus, we have three continuity equations, three momentum equations, and three energy equations. In the usual manner, the fields are allowed to exchange energy and momentum with each other, but only the steam and water fields are allowed to exchange mass. With the definition of the macroscopic density of phase i,

$$\rho_i' = \theta_i \rho_i \qquad \text{for} \quad i = g, \ell, \text{ and } f, \tag{A.1}$$

and the compatibility condition,

$$\theta_g + \theta_\ell + \theta_f = 1, \tag{A.2}$$

these equations can be interpreted rather directly (Ishii, 1975).

• Continuity Equations.

Gas:

$$\frac{\partial \rho_g'}{\partial t} + \nabla \cdot (\rho_g' \mathbf{u}_g) = J \tag{A.3}$$

Liquid:

$$\frac{\partial \rho_\ell'}{\partial t} + \nabla \cdot (\rho_\ell' \mathbf{u}_\ell) = -J \tag{A.4}$$

Fuel:

$$\frac{\partial \rho_f'}{\partial t} + \nabla \cdot (\rho_f' \mathbf{u}_f) = 0 \tag{A.5}$$

• Momentum Equations.

Gas:

$$\begin{aligned} \frac{\partial}{\partial t}(\rho_g' \mathbf{u}_g) + \nabla \cdot (\rho_g' \mathbf{u}_g \mathbf{u}_g) = &- \theta_g \nabla p - F_{g\ell}(\mathbf{u}_g - \mathbf{u}_\ell) - F_{gf}(\mathbf{u}_g - \mathbf{u}_f) \\ &+ J(H[J]\mathbf{u}_\ell + H[-J]\mathbf{u}_g) + \rho_g' \mathbf{g} \end{aligned} \tag{A.6}$$

Liquid:

$$\begin{aligned} \frac{\partial}{\partial t}(\rho_\ell' \mathbf{u}_\ell) + \nabla \cdot (\rho_\ell' \mathbf{u}_\ell \mathbf{u}_\ell) = &- \theta_\ell \nabla p + F_{g\ell}(\mathbf{u}_g - \mathbf{u}_\ell) - F_{\ell f}(\mathbf{u}_\ell - \mathbf{u}_f) \\ &- J(H[J]\mathbf{u}_\ell + H[-J]\mathbf{u}_g) + \rho_\ell' \mathbf{g} \end{aligned} \tag{A.7}$$

Fuel:

$$\frac{\partial}{\partial t}(\rho'_f \mathbf{u}_f) + \nabla \cdot (\rho'_f \mathbf{u}_f \mathbf{u}_f) = -\theta_f \nabla p + F_{gf}(\mathbf{u}_g - \mathbf{u}_f) + F_{\ell f}(\mathbf{u}_\ell - \mathbf{u}_f) + \rho'_f \mathbf{g} \qquad (A.8)$$

• Energy Equations.

Gas:

$$\frac{\partial}{\partial t}(\rho'_g I_g) + \nabla \cdot (\rho'_g I_g \mathbf{u}_g) = -p\left[\frac{\partial \theta_g}{\partial t} + \nabla \cdot (\theta_g \mathbf{u}_g)\right] + J(H[J]h_\ell + H[-J]h_g) - R_{gs}(T_g - T_s) + \dot{Q}_{fg} \qquad (A.9)$$

Liquid:

$$\frac{\partial}{\partial t}(\rho'_\ell I_\ell) + \nabla \cdot (\rho'_\ell I_\ell \mathbf{u}_\ell) = -p\left[\frac{\partial \theta_\ell}{\partial t} + \nabla \cdot (\theta_\ell \mathbf{u}_\ell)\right] - J(H[J]h_\ell + H[-J]h_g) - R_{\ell s}(T_\ell - T_s) + \dot{Q}_{f\ell} \qquad (A.10)$$

Fuel:

$$\frac{\partial}{\partial t}(\rho'_f I_f) + \nabla \cdot (\rho'_f I_f \mathbf{u}_f) = -\dot{Q}_{fg} - \dot{Q}_{f\ell} \qquad (A.11)$$

In the above equations $H[J]$ is the Heavyside step function that becomes unity for positive values of the argument and zero otherwise, and J is given by

$$J = \frac{1}{h_g - h_\ell}\left[R_{gs}(T_g - T_s) + R_{\ell s}(T_\ell - T_s)\right]$$

It should be pointed out that diffusive transport **within** each field (shear stresses and conduction) has been ignored in the above formulation. Indeed, resolution of the shear layers would impose quite more extensive demands on the computation in both nodalization and the physics of turbulence processes responsible for such transport. Although this is certainly an area for further improvement, we doubt that it will materially change the results for the particular process quantified here.

A.2 The Exchange Laws

The interfacial exchanges of mass, momentum and energy are clearly regime dependent, and uncertainties remain even for two-phase flows. For now, our approach aims to incorporate first-order physics that account for the major flow and heat transfer regimes as identified by simple criteria of fuel volume fraction, θ_f, and gas void fraction, α, i.e., $\alpha = \theta_g/(\theta_g + \theta_\ell)$. The flow regimes are shown in Figure A.1. For $\theta_f < 0.3$ we consider the fuel particles immersed in a two-phase gas-liquid flow, whose own flow regimes are defined by the value of the void fraction: $\alpha \leq 0.3$ (Bubbly), $0.3 < \alpha < 0.7$ (Churn-Turbulent), and $\alpha \geq 0.7$ (Droplet). For $\theta_f \geq 0.3$, as the fuel particles are densely packed, we considered a flow of gas and liquid through a porous bed of fuel particles.

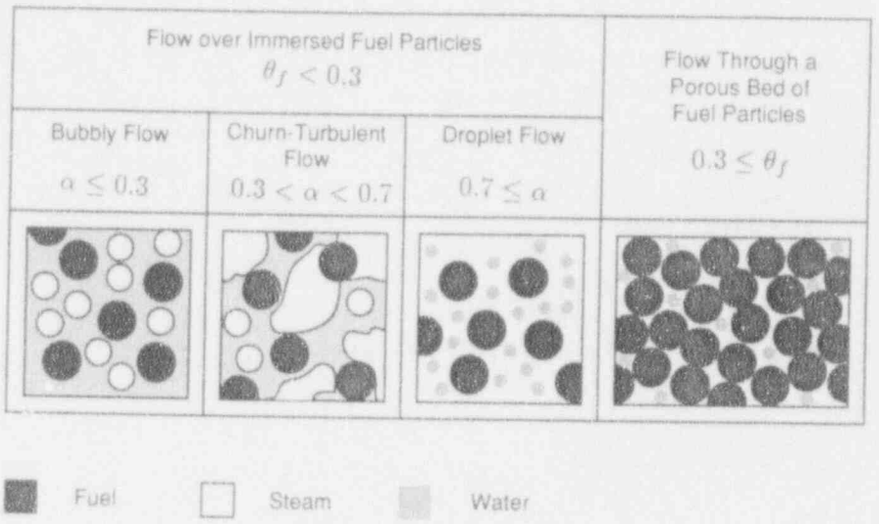

Figure A.1. Schematic diagram of flow regimes considered in characterizing interface transfers.

We use the exchange laws available for two-phase systems after making suitable modifications to account for, as a first approximation, the effect of a third phase. In calculating interfacial momentum exchange, one needs to know the projected area concentration of the dispersed phase. Also, in calculating interfacial heat exchange, one needs to know the interfacial area concentration. In a two-phase system, these area concentrations can be estimated from the length scale and the volume fraction of the dispersed phase. However, the presence of a third phase reduces the area concentration as the third phase must also share the same area. Therefore, we modify the area concentration, by a factor, ϕ_{ij}; ϕ_{ij} representing the effect of the phase k on the area concentration of phase i for its interaction with phase j. This is calculated from the respective volume fractions as

$$\phi_{ij} = \frac{\theta_j}{\theta_j + \theta_k}. \qquad (A.12)$$

Note that with this definition ϕ_{ij} lies between 0 and 1.

A.2.1 Interfacial Momentum Coupling

The interfacial momentum coupling is primarily due to drag. For the bubbly flow regime ($\alpha < 0.3$) we have also included the added mass effect as given by Wallis (1969)

$$F_a = \frac{\theta_g}{3 - \theta_g} \rho_\ell \frac{1}{| \mathbf{u}_g - \mathbf{u}_\ell |} \left| \frac{\partial}{\partial t} (\mathbf{u}_g - \mathbf{u}_\ell) \right| \qquad (A.13)$$

For $\theta_f < 0.3$ the drag force is based on Ishii and Zuber (1979). Specifically,

$$F_{ij} = \frac{3}{4} \theta_i \phi_{ij} \rho_j \frac{C_{Dij}}{\ell_i} | \mathbf{u}_i - \mathbf{u}_j | \qquad (A.14)$$

where suffices i and j refer to dispersed and continuous phases, respectively. The drag coefficient for churn flow ($0.3 < \alpha < 0.7$) is defined by:

$$i = g,\ j = \ell,\ C_{Dij} = \frac{8}{3}(1-\alpha)^2 \text{ and } \ell_i = 4\left\{\frac{g\Delta\rho}{\gamma}\right\}^{-1/2} \tag{A.15}$$

For dispersed flow we have:

$$C_{Dij} = \frac{2}{3}\ell_i \left\{\frac{g\Delta\rho}{\gamma}\right\}^{1/2} \left\{\frac{1+17.67(f(\alpha_i))^{6/7}}{18.67 f(\alpha_i)}\right\}^2 \tag{A.16}$$

where

$$i = g, \quad j = \ell, \quad \alpha \le 0.3 \qquad f(\alpha_i) = (1-\alpha)^{1.5} \tag{A.17}$$

$$i = \ell, \quad j = g, \quad \alpha > 0.7 \qquad f(\alpha_i) = \alpha^3 \tag{A.18}$$

$$i = f, \quad j = g, \ell, \quad f(\alpha_i) = (1-\theta_f)^{1.5} \tag{A.19}$$

and ℓ_i is obtained from

$$\frac{\rho_j \mid \mathbf{u}_\ell - \mathbf{u}_g \mid^2 \ell_i}{\gamma} = \text{We}_{cr} \begin{cases} 8 & \text{for } i = g \\ 12 & \text{for } i = \ell \end{cases} \tag{A.20}$$

For the "dense fuel regime" ($\theta_f > 0.3$) we use laminar and turbulent permeabilities (Sissom and Pitts, 1972).

$$F_{if} = F_{if}^{\ell} + F_{if}^{t} \qquad i = g, \ell \tag{A.21}$$

where

$$F_{if}^{\ell} = \begin{cases} 150\frac{\theta_i \theta_f^2}{(1-\theta_f)^3}\frac{\mu_i}{\ell_f^2} & \text{for } \text{Re}_i' < 1000 \\ 0 & \text{for } \text{Re}_i' \ge 1000 \end{cases} \tag{A.22}$$

and

$$F_{if}^{t} = \begin{cases} 1.75\frac{\theta_i \theta_f}{(1-\theta_f)^3}\frac{\rho_i' \mid \mathbf{u}_i - \mathbf{u}_f \mid}{\ell_f} & \text{for } \text{Re}_i' > 10 \\ 0 & \text{for } \text{Re}_i' \le 10, \end{cases} \tag{A.23}$$

$$\text{Re}_i' = \theta_f \frac{\rho_i' \ell_f \mid \mathbf{u}_i - \mathbf{u}_f \mid}{\mu_i} \tag{A.24}$$

It is noted, however, that this regime is of very limited relevance to computations of practical interest.

A.2.2 Interfacial Heat Transfer and Phase Change

The distinction of the fuel-to-coolant heat transfer mechanisms is made again on the basis of the flow regimes. The key distinction is whether or not there is sufficient water in the coolant phase to completely engulf the fuel particles, thus a gas void fraction criterion is used.

For $\alpha < 0.7$, heat transfer to liquid is estimated by superposition of radiation and film boiling heat fluxes. That is,

$$\dot{Q}_{f\ell} = n_f(h_r + h_c)\pi\ell_f^2\phi_{f\ell}(T_f - T_\ell) \tag{A.25}$$

where

$$n_f = \frac{6\theta_f}{\pi\ell_f^3}, \qquad h_r = \sigma E_f \frac{T_f^4 - T_\ell^4}{T_f - T_\ell} \tag{A.26, A.27}$$

and (Witte, 1968; Liu et al., 1992)

$$h_c = 2.98\left\{\frac{\rho_g k_g[h_{fg} + 0.68c_{pg}(T_f - T_\ell)]}{\ell_f(T_f - T_\ell)} \mid \mathbf{u}_f - \mathbf{u}_\ell \mid\right\}^{\frac{1}{2}} \tag{A.28}$$

The emissivity value $E_f = 0.7$ is selected for the calculations of typical interest. Heat transfer from fuel to gas in this regime need not be accounted for separately.

For $\alpha > 0.7$, we assume a vapor-continuous regime in which heat is transferred to liquid drops by irradiation and to the gas by convection. The gas is allowed to superheat and convect heat to the liquid drops which boil at saturation. Thus:

$$\dot{Q}_{f\ell} = \min(n_\ell\pi\ell_\ell^2, n_f\pi\ell_f^2)\,\sigma E_f E_\ell(T_f^4 - T_\ell^4) \tag{A.29}$$

and

$$\dot{Q}_{fg} = n_f\phi_{fg}\pi\ell_f^2 h_c'(T_f - T_g) \tag{A.30}$$

where $n_\ell = 6\theta_\ell/\pi\ell_\ell^3$ and h_c' is given by Bird et al. (1960):

for $\theta_f < 0.3$

$$h_c' = \frac{k_g}{\ell_f}\left\{2 + 0.6\mathrm{Re}_g^{1/2}\mathrm{Pr}_g^{1/3}\right\} \tag{A.31}$$

where

$$\mathrm{Re}_g = \frac{\rho_g \mid \mathbf{u}_g - \mathbf{u}_f \mid \ell_f}{\mu_g} \tag{A.32}$$

and for $\theta_f \geq 0.3$

$$h_c' = 0.91 c_{pf} \rho_g' \mid \mathbf{u}_g - \mathbf{u}_f \mid \mathrm{Re}_g''^{-0.51} \mathrm{Pr}_g^{-2/3} \text{ for } \mathrm{Re}_g'' \leq 50 \tag{A.33}$$

$$h_c' = 0.61 c_{pf} \rho_g' \mid \mathbf{u}_g - \mathbf{u}_f \mid \mathrm{Re}_g''^{-0.41} \mathrm{Pr}_g^{-2/3} \text{ for } \mathrm{Re}_g'' > 50 \tag{A.34}$$

where

$$\mathrm{Re}_g'' = \frac{\rho_g' \ell_f \mid \mathbf{u}_g - \mathbf{u}_f \mid}{6\theta_f \mu_g} \tag{A.35}$$

The factor E_ℓ in Eq. (A.29) was introduced to empirically degrade the radiation heat transfer to liquid by the portion that could not be absorbed. For reactor calculations we typically use $E_\ell = 0.3$ to conservatively bias the predictions.

Similarly, for vapor-to-liquid heat transfer we have:

For $\alpha < 0.7$, with vapor as the dispersed phase

$$R_{\ell s} = c_\ell n \phi_{g\ell} \pi \ell_g^2 \frac{k_\ell}{g_g} \left\{ 2 + 0.6 \ \mathrm{Re}^{1/2} \mathrm{Pr}_\ell^{1/3} \right\} \tag{A.36}$$

$$R_{gs} = 2 n_g \phi_{g\ell} \pi \ell_g^2 \frac{k_g}{\ell_g}$$

while for $\alpha > 0.7$, with liquid (drops) as the dispersed phase

$$R_{gs} = n_\ell \phi_{\ell g} \pi \ell_\ell^2 \frac{k_g}{\ell_\ell} \left\{ 2 + 0.6 \ \mathrm{Re}^{1/2} \mathrm{Pr}_g^{1/3} \right\} \tag{A.37}$$

$$R_{\ell s} = 2 c_\ell \eta_\ell \phi_{\ell g} \pi \ell_\ell^2 \frac{k_\ell}{\ell_\ell}$$

In the above the coefficient c_ℓ was introduced as a way to control the liquid superheat in cases where these simplified formulations for heat transfer coefficients are not deemed adequate.

A.3 Nomenclature

C_D	drag coefficient
c_t	control coefficient
c_p	specific heat at constant pressure
E_f	emissivity of fuel particles
E_ℓ	absorptivity of water droplets
F	factor for interficial momentum exchange
g	acceleration of gravity
H	Heaviside step function
h	heat transfer coefficient; specific enthalpy
h_{fg}	enthalpy of evaporation
I	specific internal energy
J	phase change rate per unit volume
k	thermal conductivity
ℓ	length scale
n	number of particles (or drops) per unit volume
Pr	Prandtl number
p	pressure
Q	rate of heat transfer per unit volume
R	heat transfer coefficient between the phase (liquid or vapor) and interface
Re	Reynolds number
T	temperature
t	time
u	velocity vector
We_{cr}	critical Weber number for bubble/drop breakup

Greek

α	void fraction of vapor (per unit volume of coolant)
γ	surface tension between vapor and liquid; specific heat ratio
θ	volume fraction (per unit volume of total mixture)
μ	viscosity
ρ	microscopic density
ρ'	macroscopic density
σ	Stefan–Boltzmann coefficient
ϕ_{ij}	area concentration factor, defined in eq. (A.12)

Subscripts

a	added-mass effect
c	convection
f	fuel
g	gas (steam)
ℓ	liquid (water)
r	radiation
s	saturation

Superscripts

ℓ	laminar flow
t	turbulent flow

A.4 References

1. Bird, R.B., W.E. Stewart and E.N. Lightfoot (1960) *Transport Phenomena*, Wiley, New York.
2. Ishii, M. (1975) "Thermo-Fluid Dynamic Theory of Two-Phase Flow," Eyrolles.
3. Ishii, M. and N. Zuber (1979) "Drag Coefficient and Relative Velocity in Bubbly, Droplet or Particulate Flows," *AIChE J.* **5**, 843.
4. Liu, C., T.G. Theofanous and W. Yuen (1992) "Film Boiling from Spheres in Single- and Two-Phase Flow," 1992 National Heat Transfer Conference, San Diego, August 9–12, 1992.
5. Sissom, L.E. and D.R. Pitts (1972) *Elements of Transport Phenomena*, McGraw-Hill, New York.
6. Wallis, G.B. (1969) *One-dimensional Two-phase Flow*, McGraw-Hill, Inc., New York.
7. Witte, L.C. (1968) *Ind. Eng. Chem. Fundamentals* **7**, 517.

APPENDIX B

FRONT ADVANCEMENT AND GLOBAL VOID FRACTION TRANSIENTS IN MAGICO

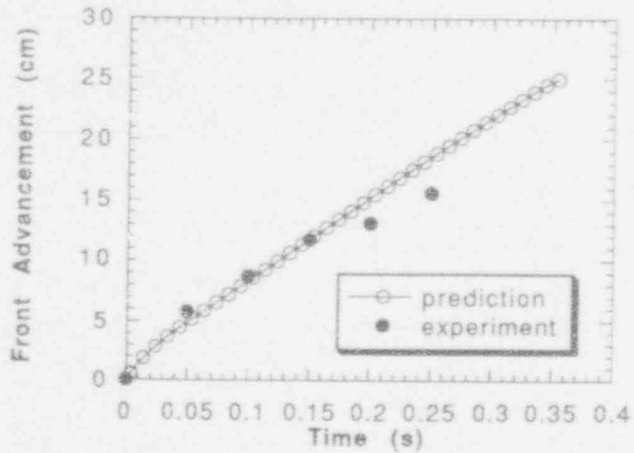

Figure I.B.1. The advancement of the front of hot particles for Run #101.

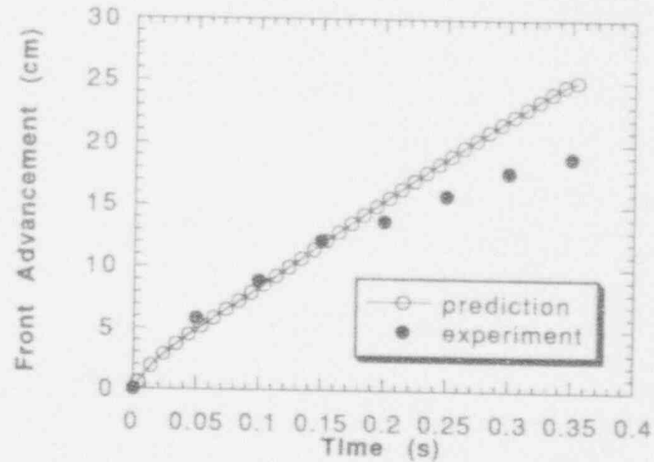

Figure I.B.2. The advancement of the front of hot particles for Run #102.

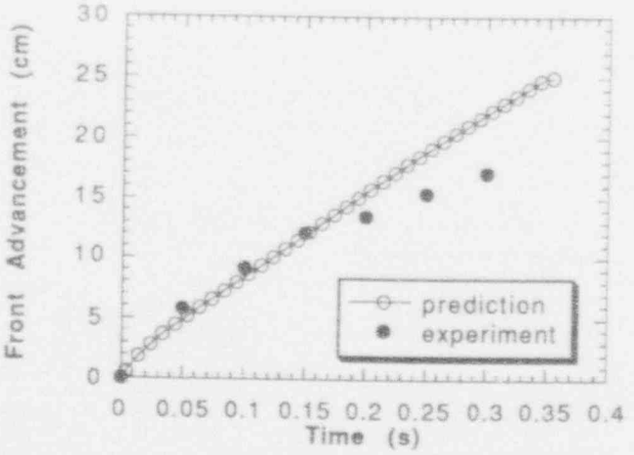

Figure I.B.3. The advancement of the front of hot particles for Run #103.

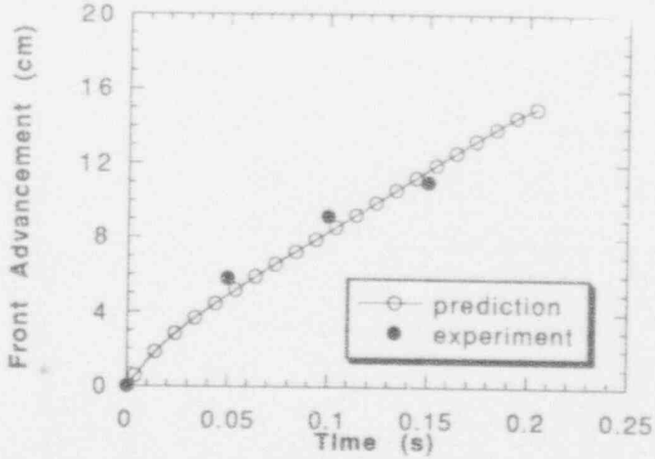

Figure I.B.4. The advancement of the front of hot particles for Run #104.

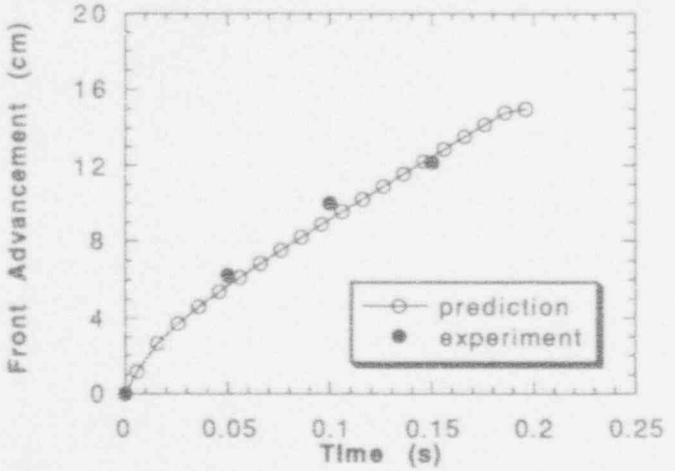

Figure I.B.5. The advancement of the front of hot particles for Run #105.

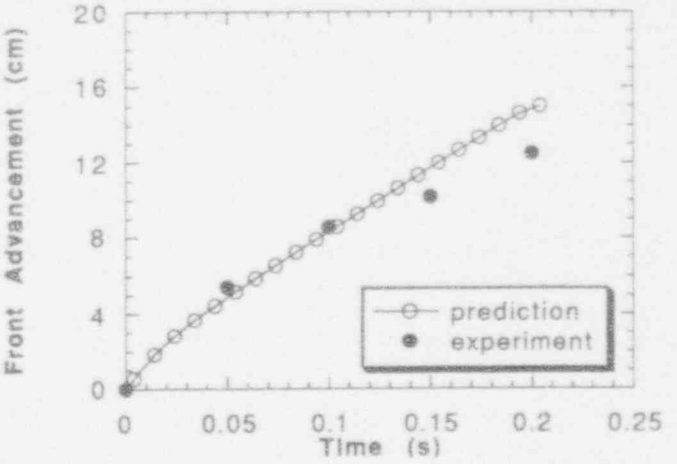

Figure I.B.6. The advancement of the front of hot particles for Run #106.

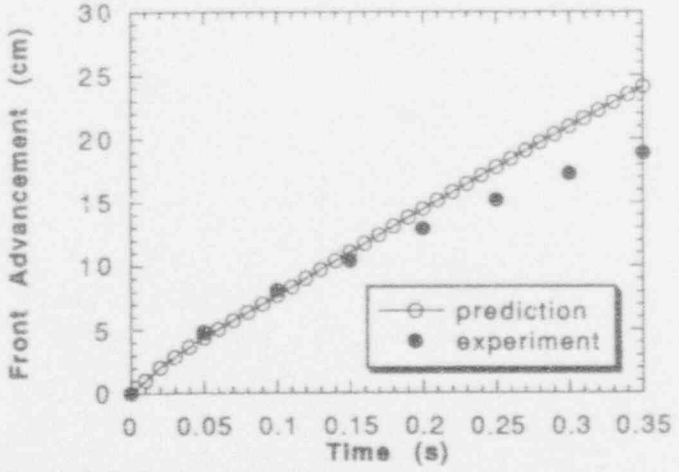

Figure I.B.7. The advancement of the front of hot particles for Run #107.

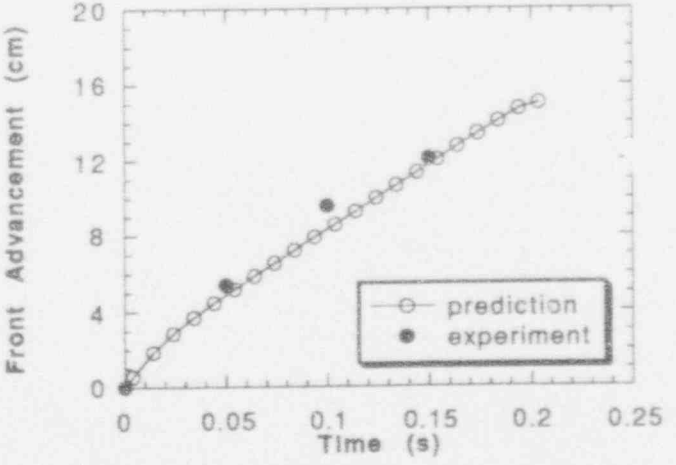

Figure I.B.8. The advancement of the front of hot particles for Run #108.

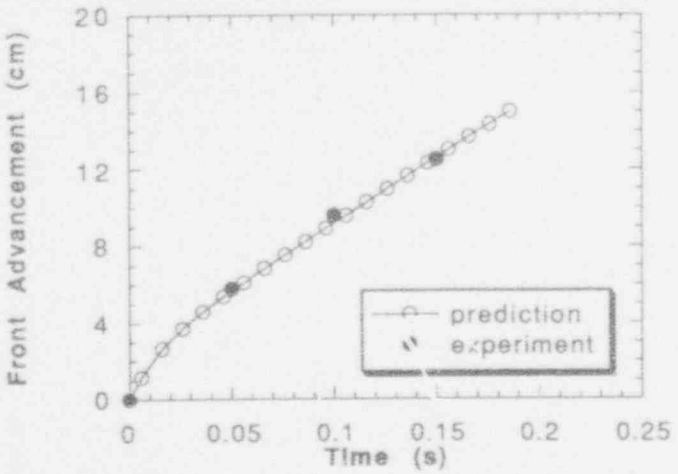

Figure I.B.9. The advancement of the front of hot particles for Run #109.

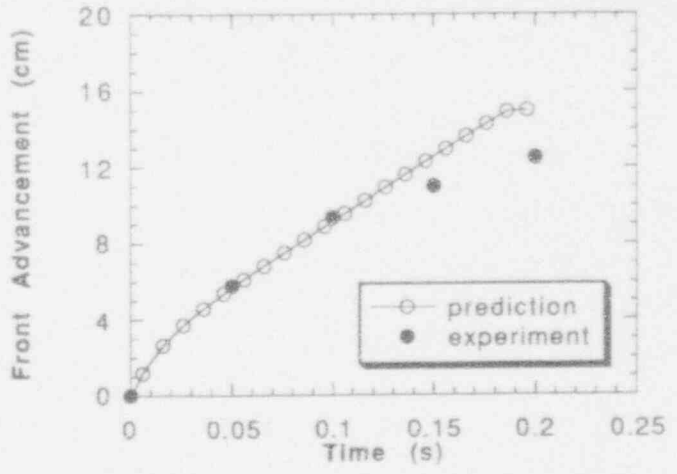

Figure I.B.10. The advancement of the front of hot particles for Run #111.

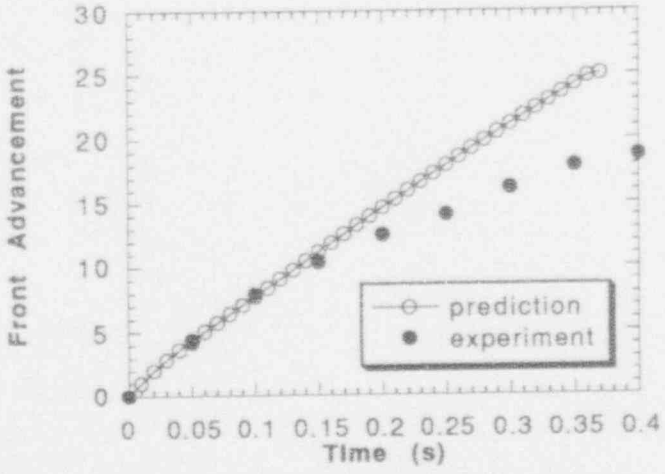

Figure I.B.11. The advancement of the front of hot particles for Run #112.

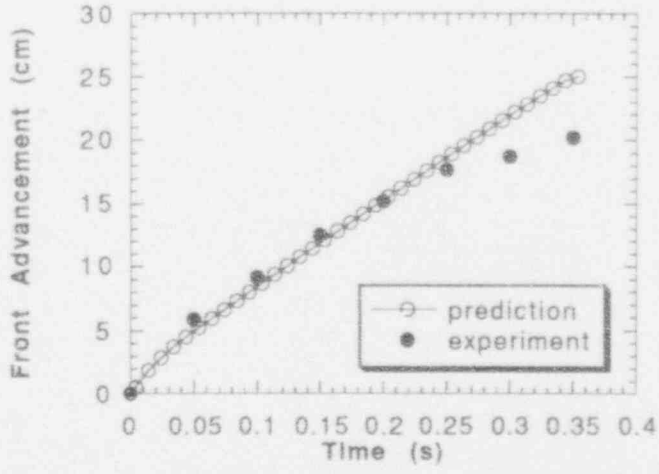

Figure I.B.12. The advancement of the front of hot particles for Run #113.

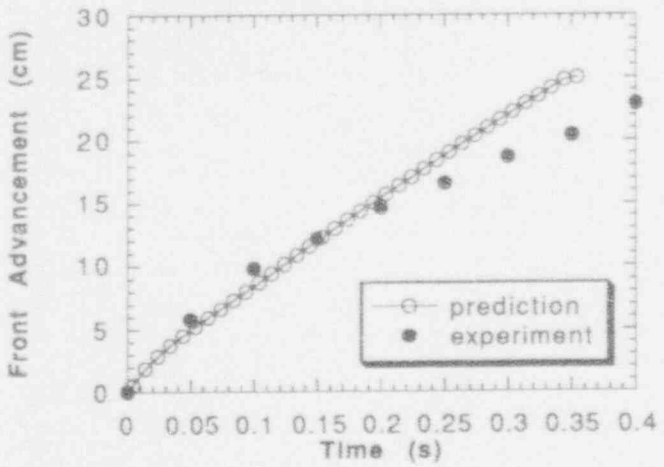

Figure I.B.13. The advancement of the front of hot particles for Run #114.

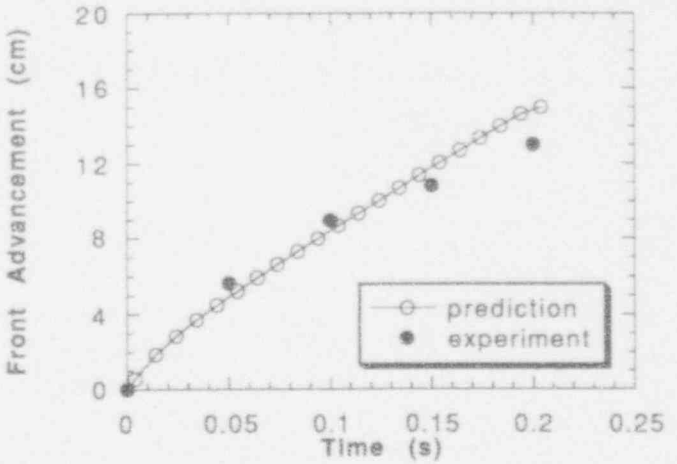

Figure I B.14. The advancement of the front of hot particles for Run #115.

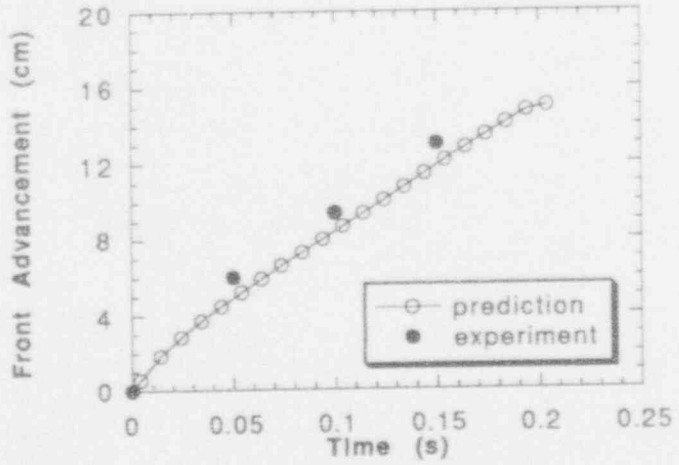

Figure I.B.15. The advancement of the front of hot particles for Run #116.

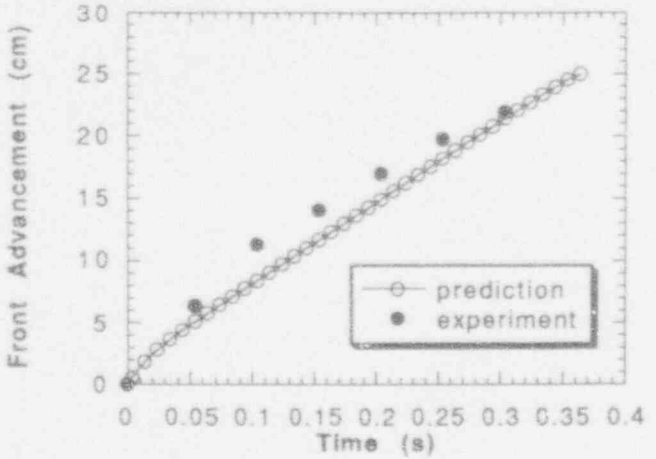

Figure I.B.16. The advancement of the front of hot particles for Run #701.

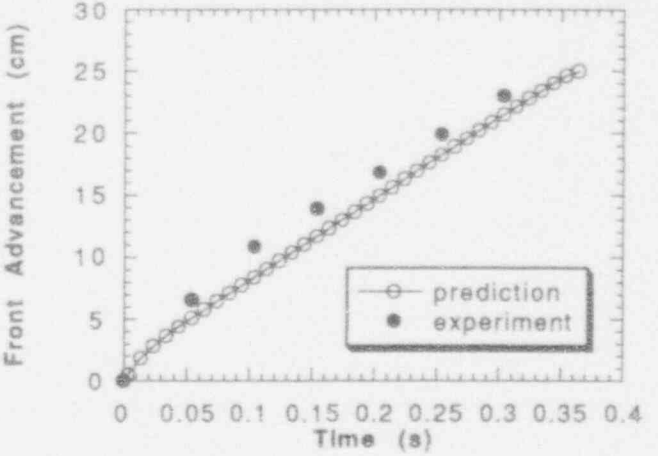

Figure I.B.17. The advancement of the front of hot particles for Run #702.

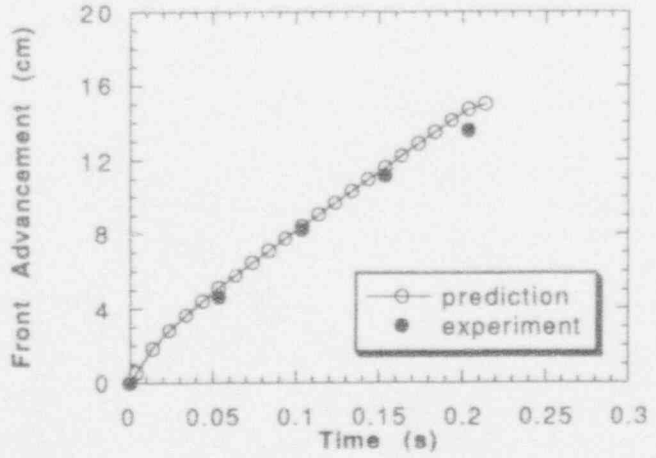

Figure I.B.18. The advancement of the front of hot particles for Run #703.

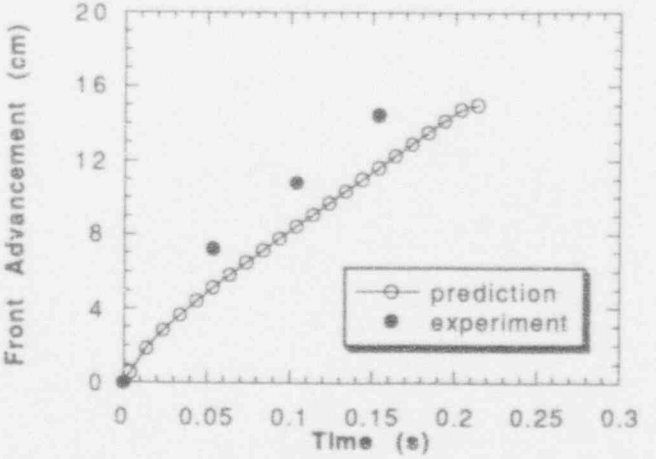

Figure I.B.19. The advancement of the front of hot particles for Run #704.

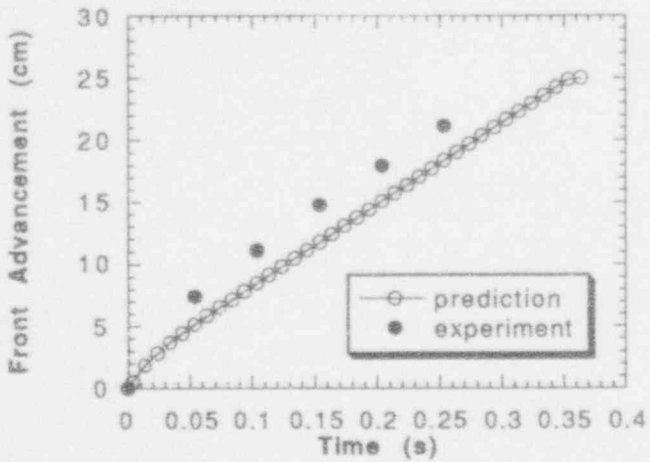

Figure I.B.20. The advancement of the front of hot particles for Run #705.

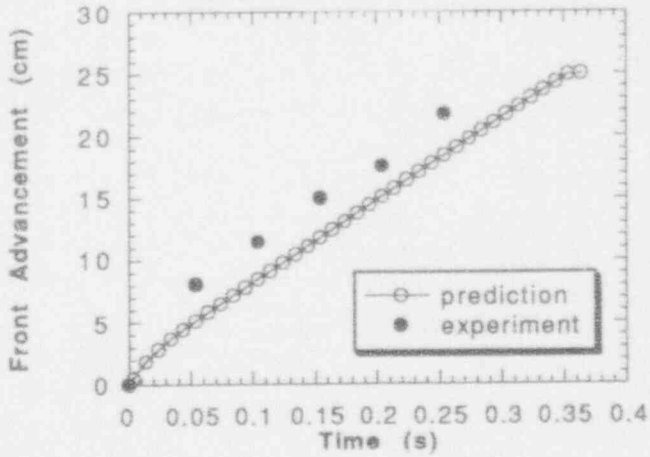

Figure I.B.21. The advancement of the front of hot particles for Run #706.

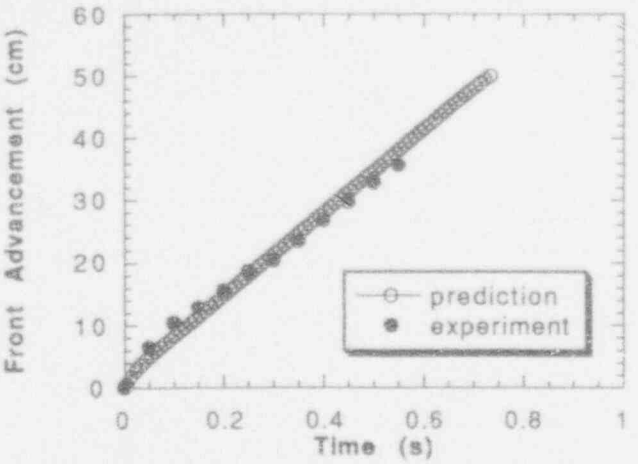

Figure I.B.22. The advancement of the front of hot particles for Run #901.

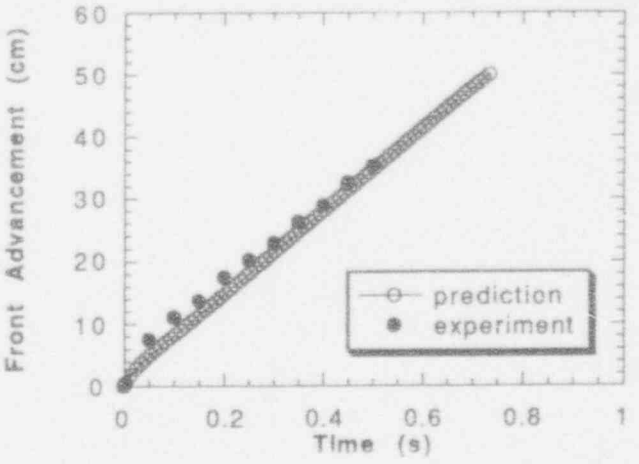

Figure I.B.23. The advancement of the front of hot particles for Run #902.

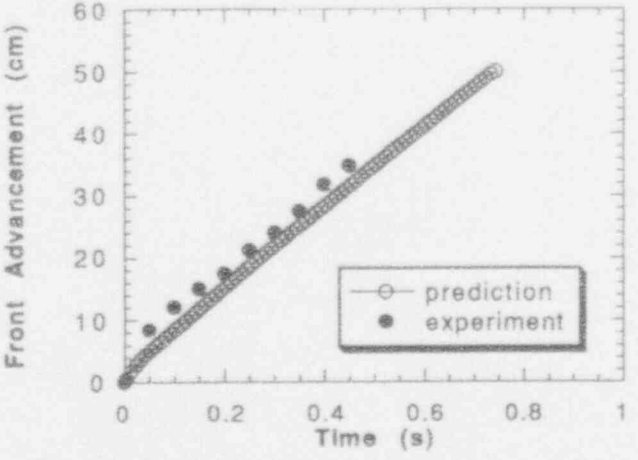

Figure I.B.24. The advancement of the front of hot particles for Run #904.

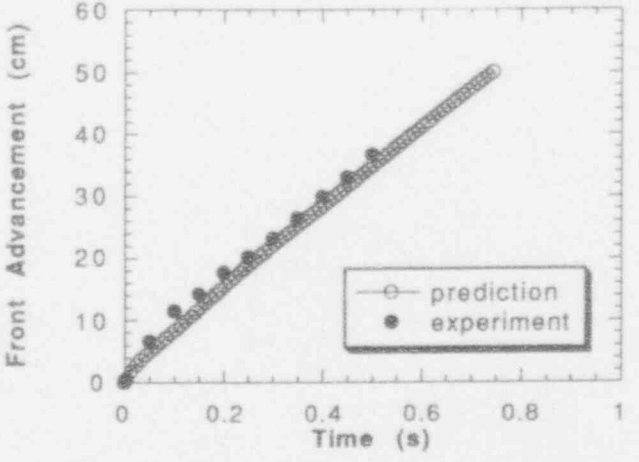

Figure I.B.25. The advancement of the front of hot particles for Run #905.

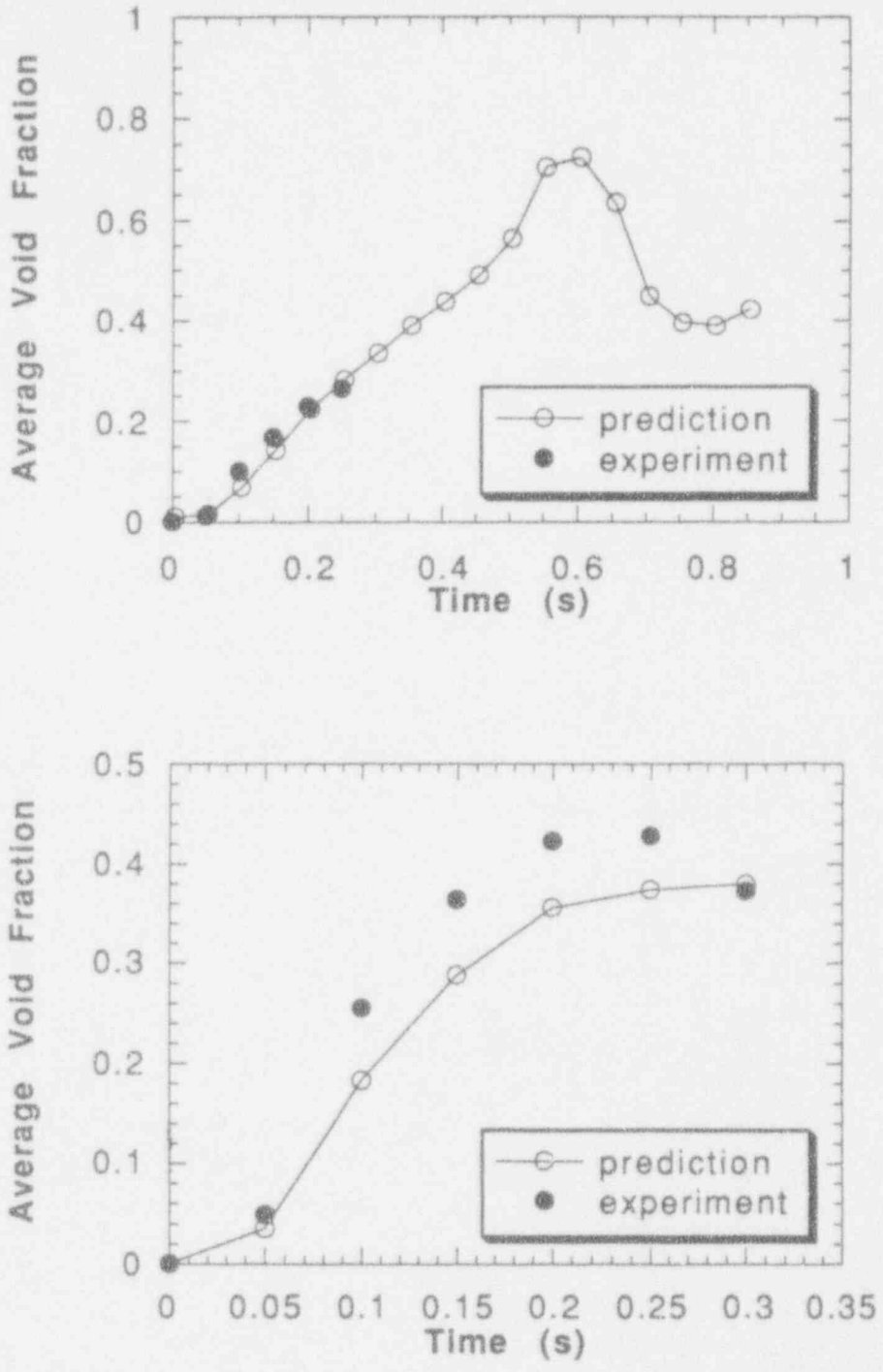

Figure I.B.26. The pool-depth-average (top) and mixing-zone-average (bottom) void fraction transients for Run #101.

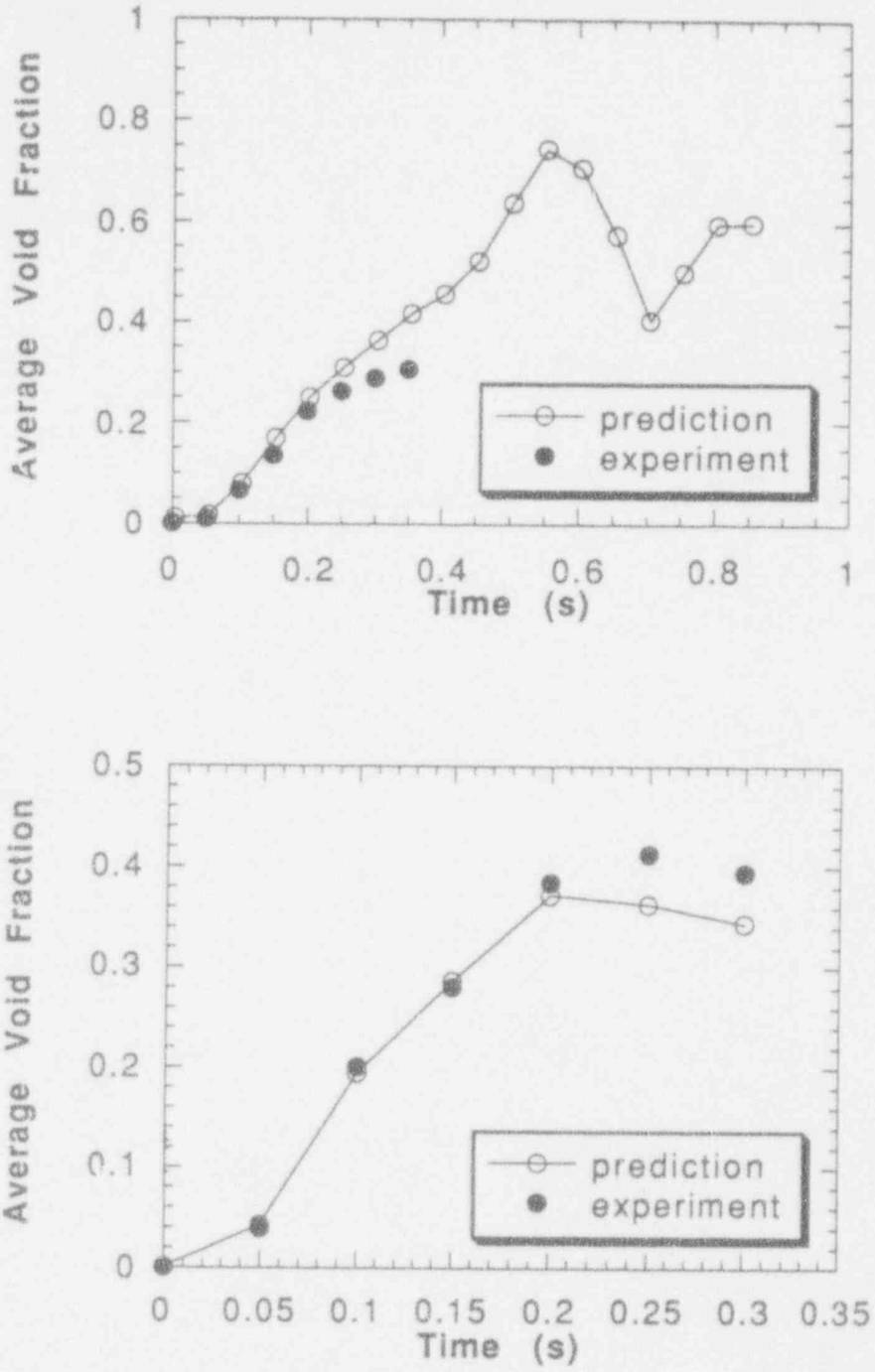

Figure I.B.27. The pool-depth-average (top) and mixing-zone-average (bottom) void fraction transients for Run #102.

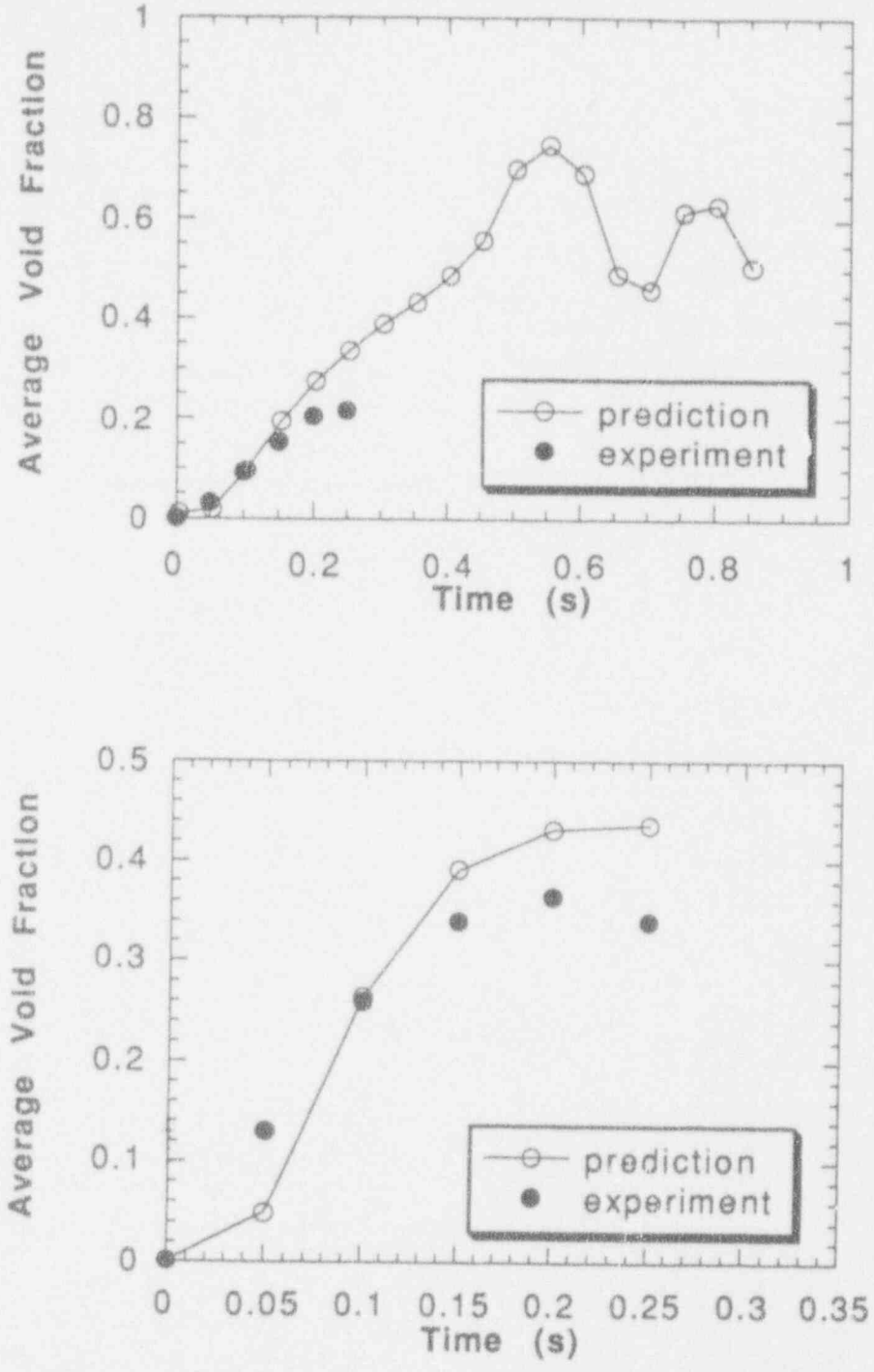

Figure I.B.28. The pool-depth-average (top) and mixing-zone-average (bottom) void fraction transients for Run #103.

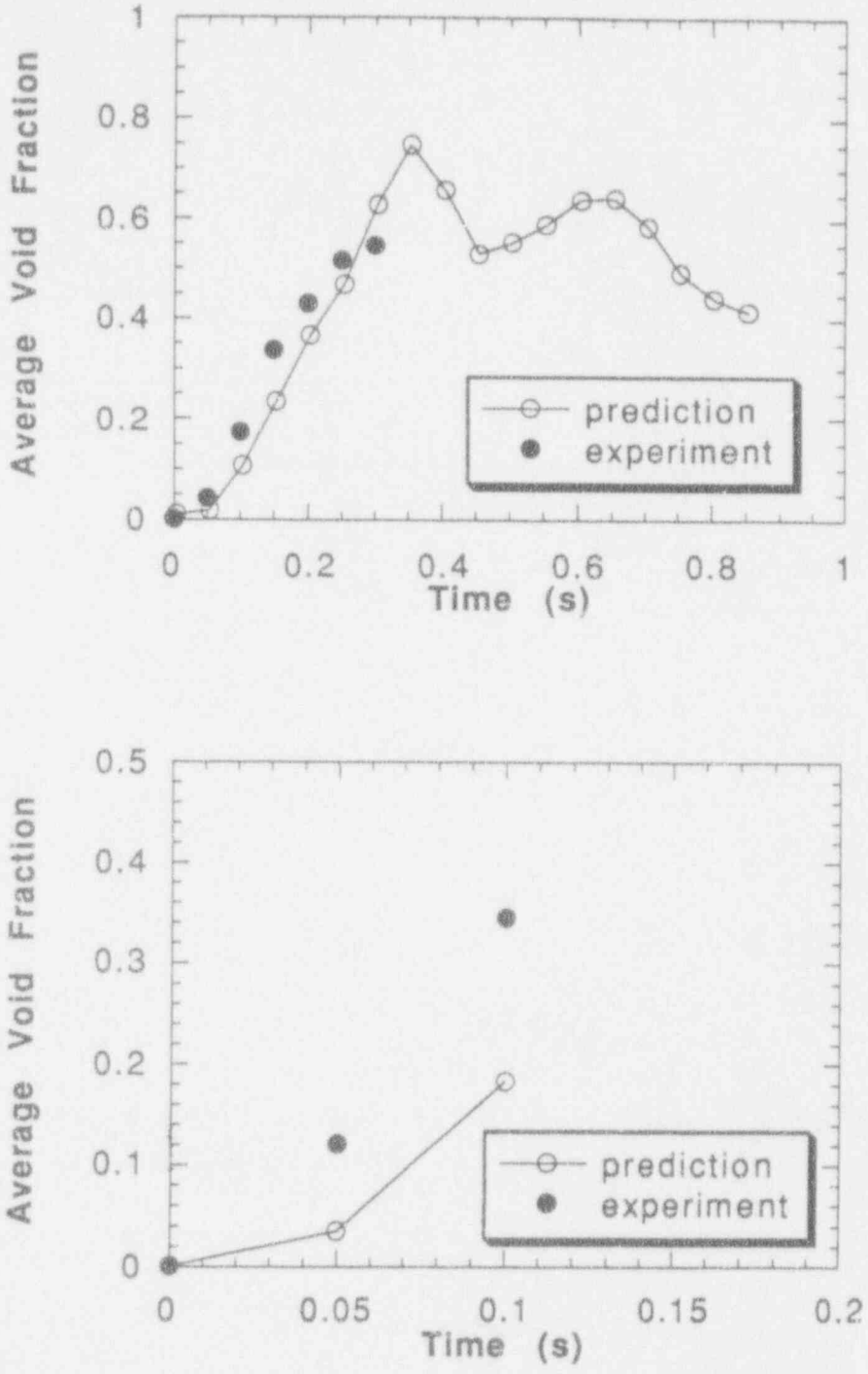

Figure I.B.29. The pool-depth-average (top) and mixing-zone-average (bottom) void fraction transients for Run #104.

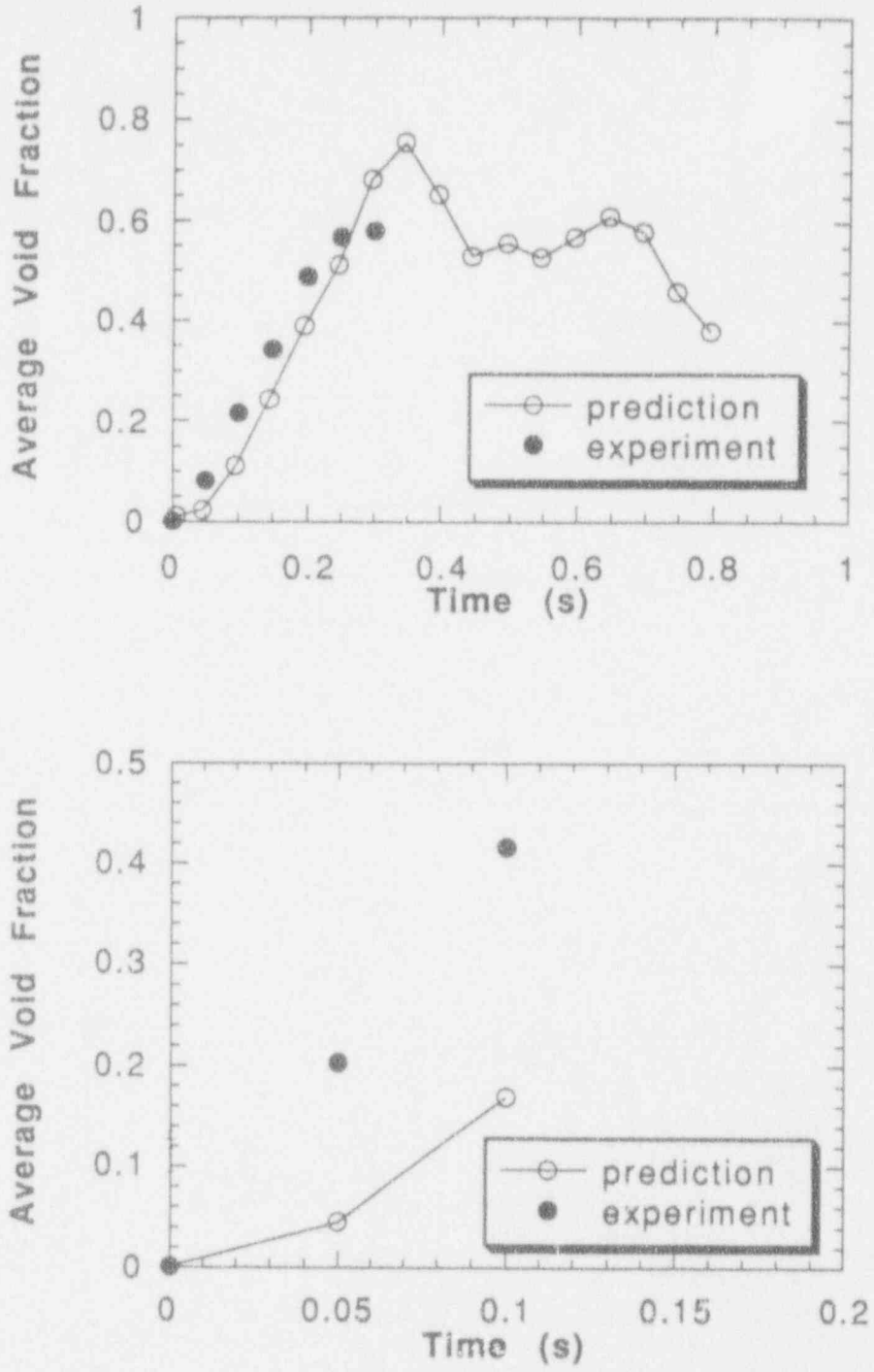

Figure I.B.30. The pool-depth-average (top) and mixing-zone-average (bottom) void fraction transients for Run #105.

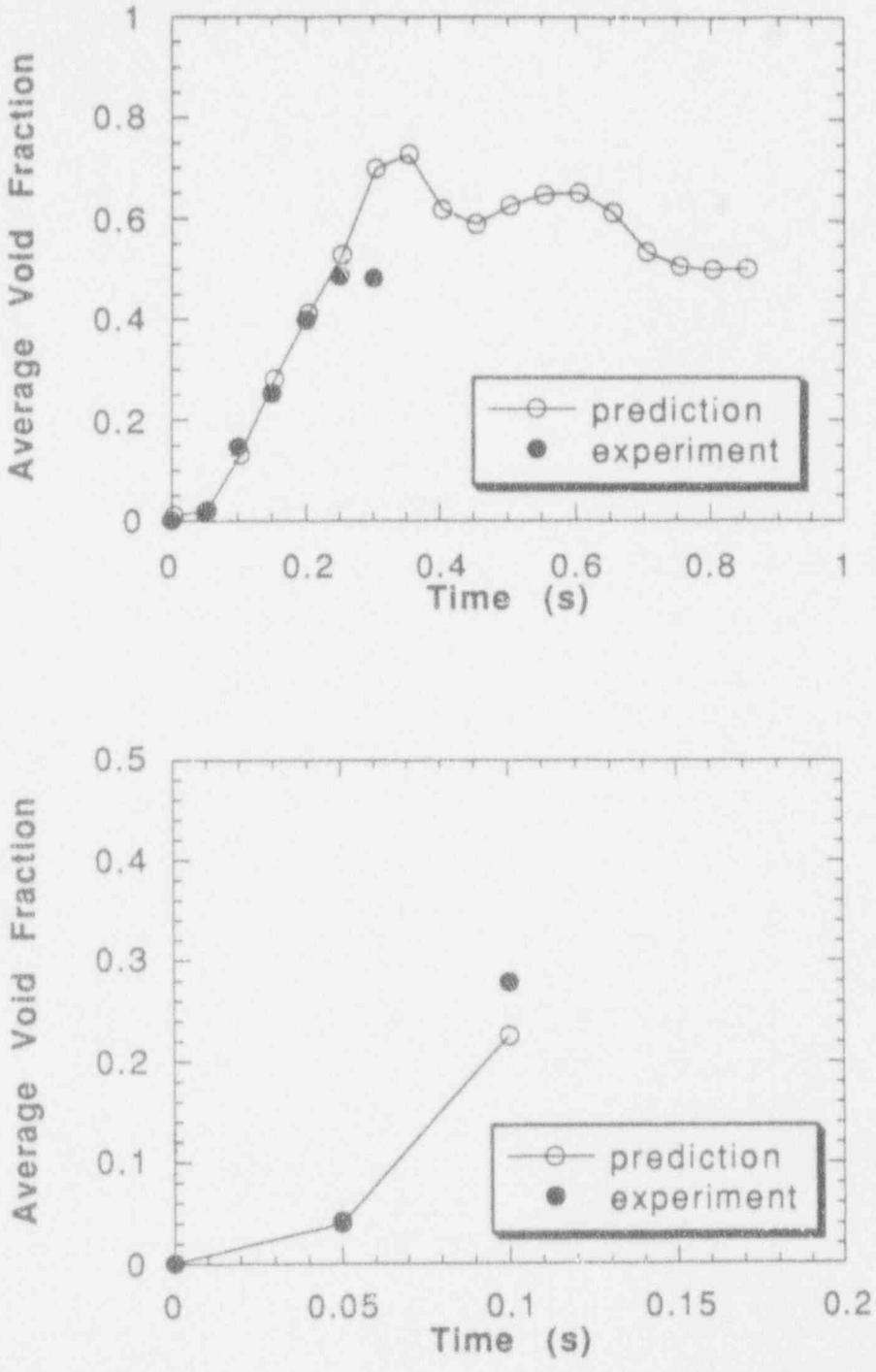

Figure I.B.31. The pool-depth-average (top) and mixing-zone-average (bottom) void fraction transients for Run #106.

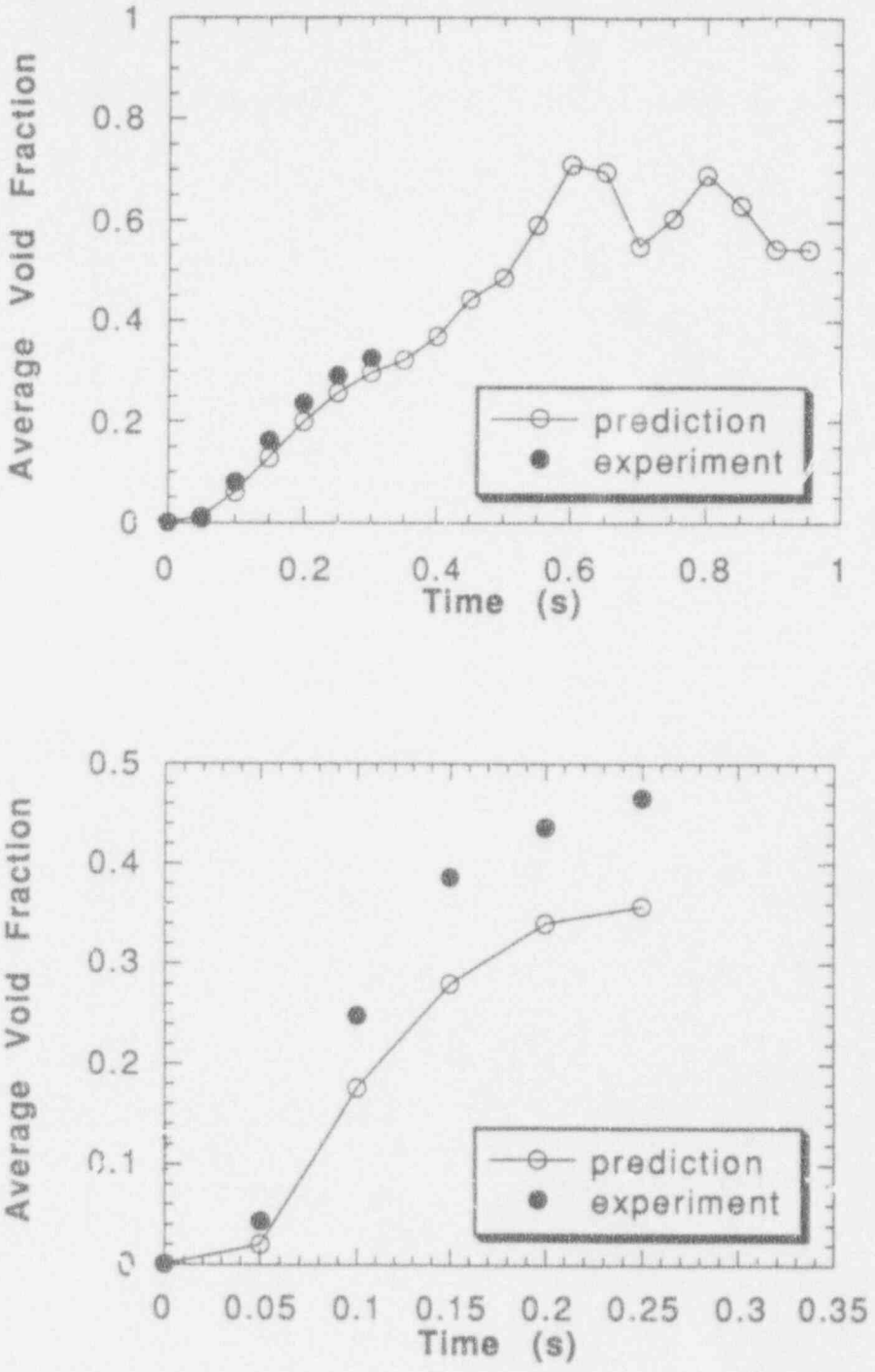

Figure I.B.32. The pool-depth-average (top) and mixing-zone-average (bottom) void fraction transients for Run #107.

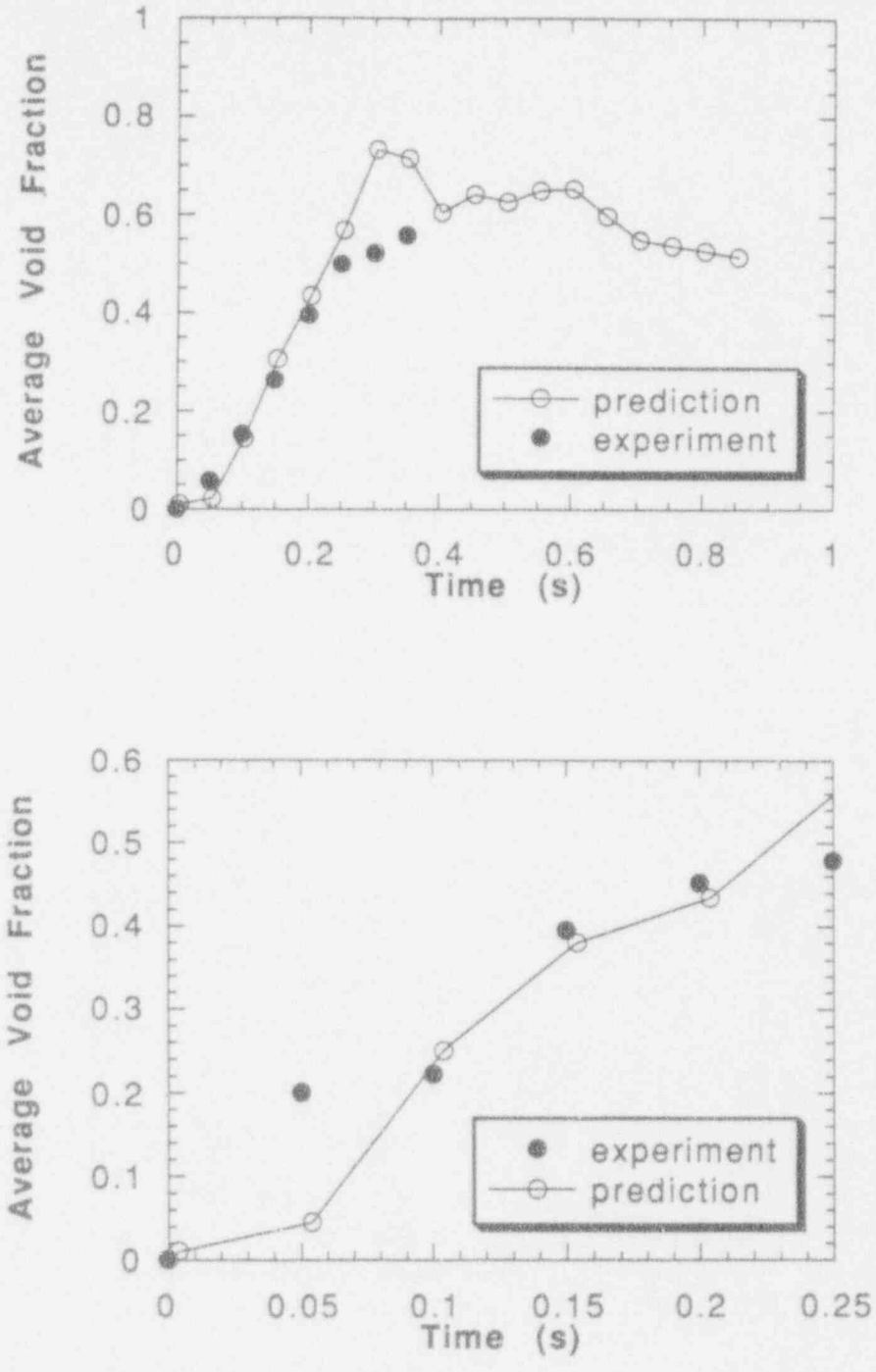

Figure I.B.33. The pool-depth-average (top) and mixing-zone-average (bottom) void fraction transients for Run #108.

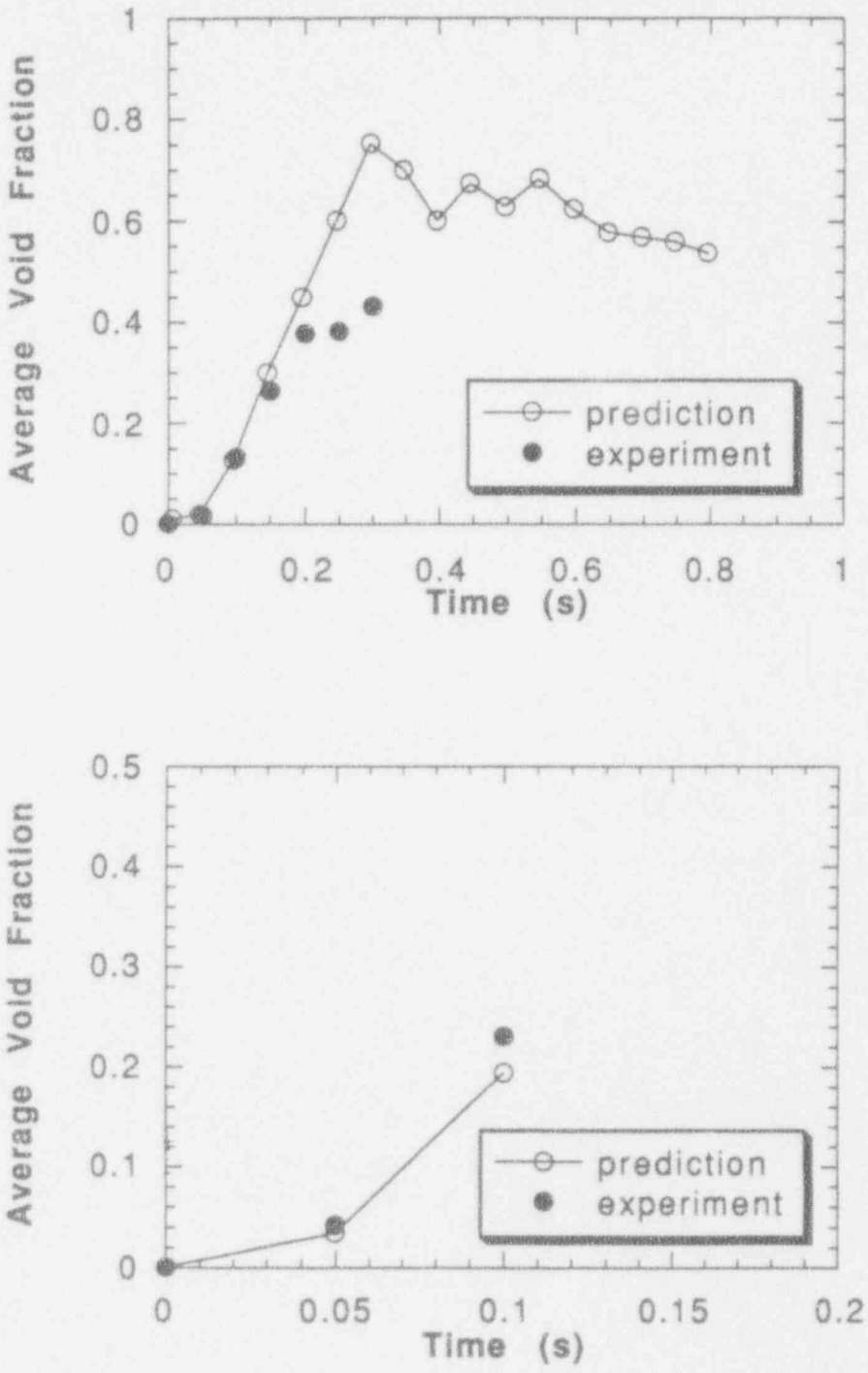

Figure I.B.34. The pool-depth-average (top) and mixing-zone-average (bottom) void fraction transients for Run #109.

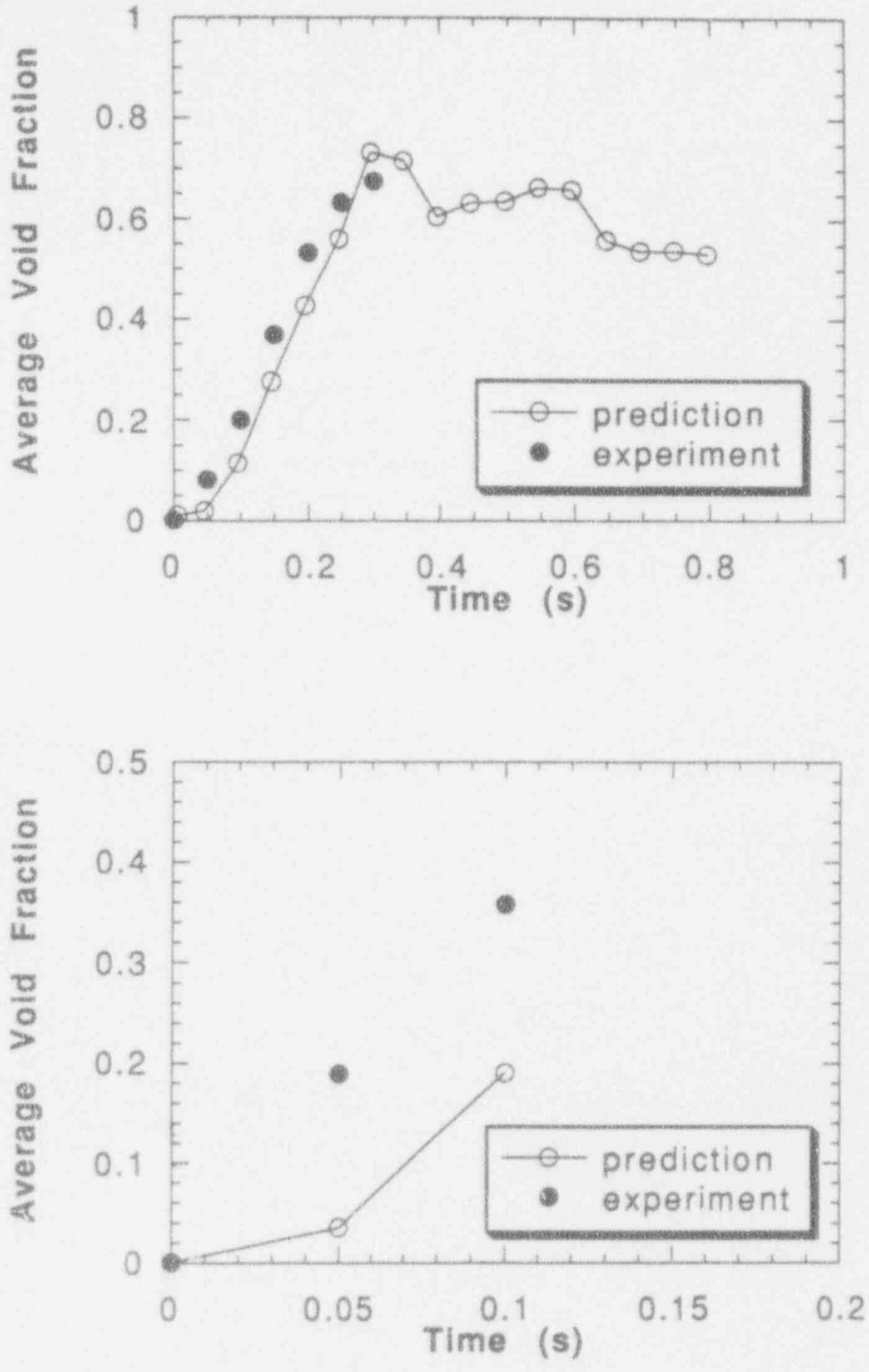

Figure I.B.35. The pool-depth-average (top) and mixing-zone-average (bottom) void fraction transients for Run #111.

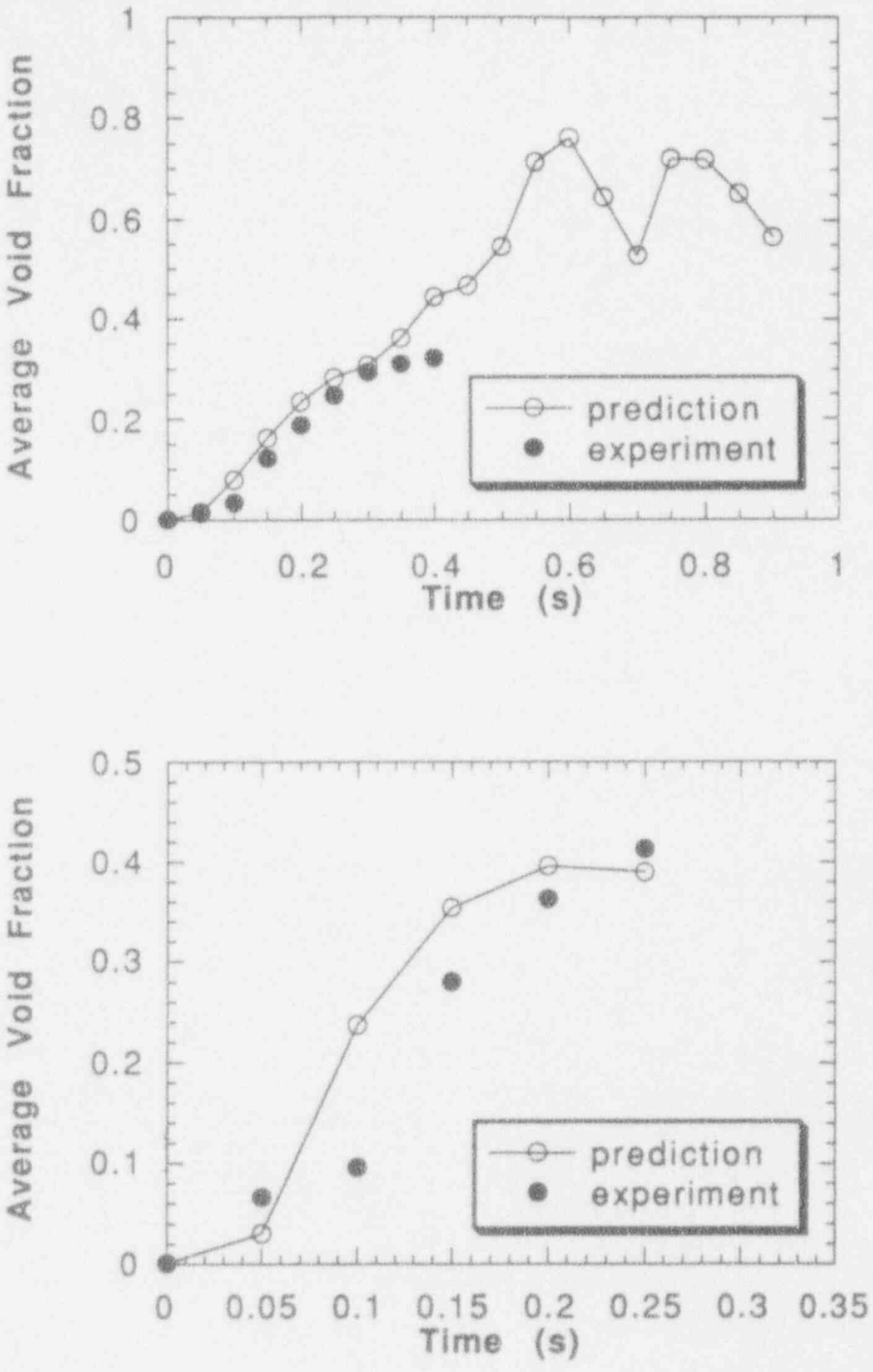

Figure I.B.36. The pool-depth-average (top) and mixing-zone-average (bottom) void fraction transients for Run #112.

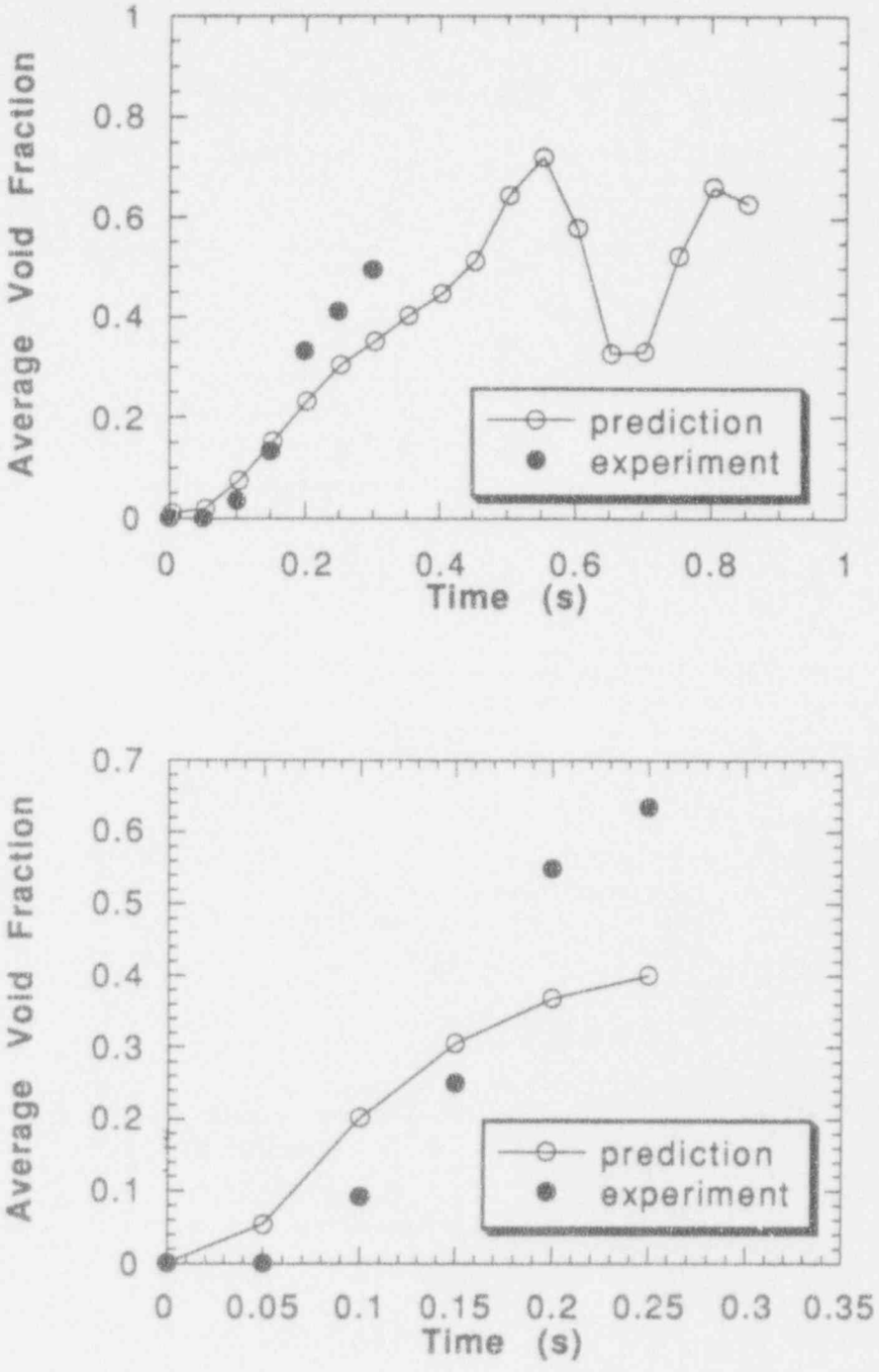

Figure I.B.37. The pool-depth-average (top) and mixing-zone-average (bottom) void fraction transients for Run #113.

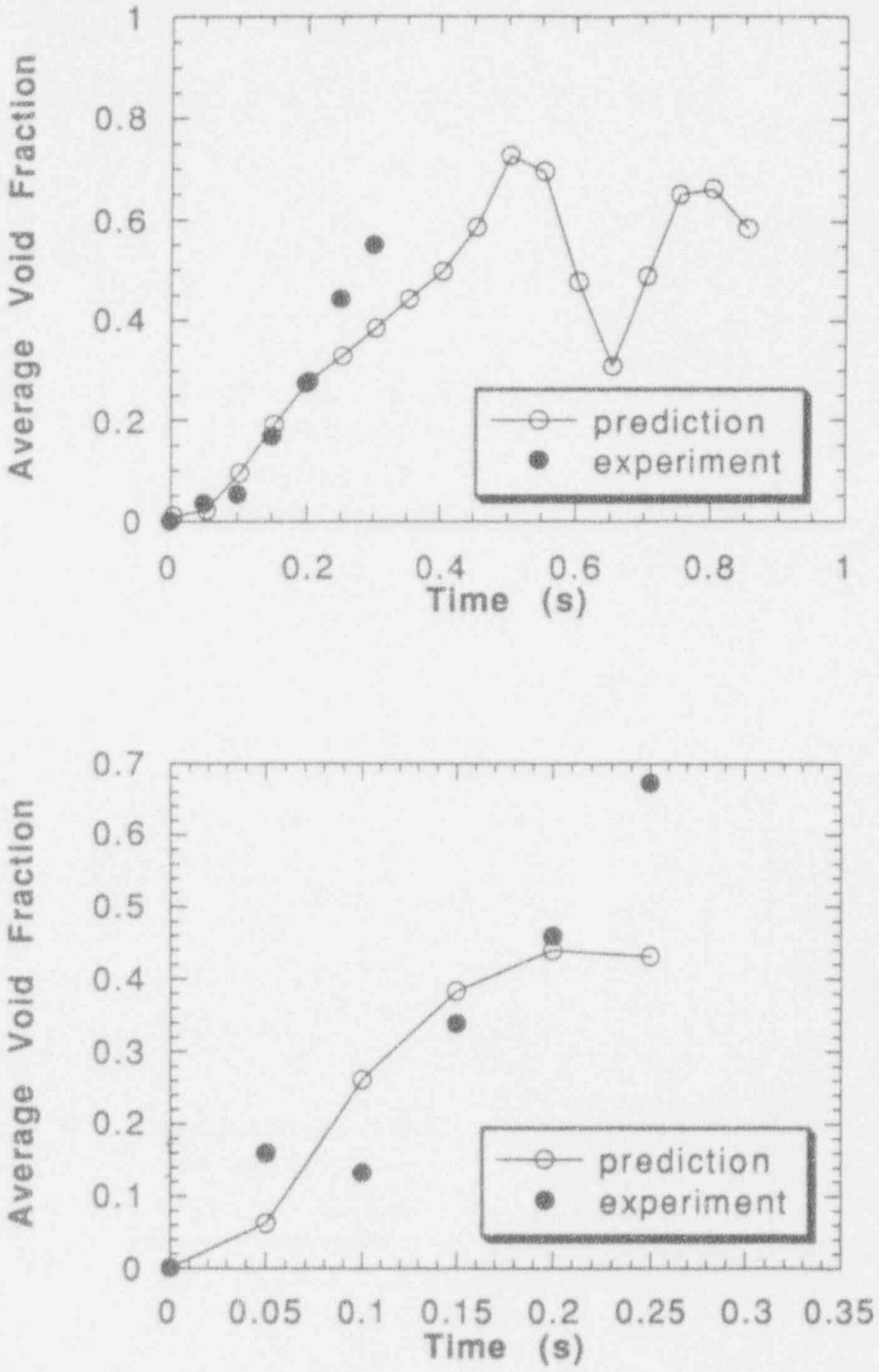

Figure I.B.38. The pool-depth-average (top) and mixing-zone-average (bottom) void fraction transients for Run #114.

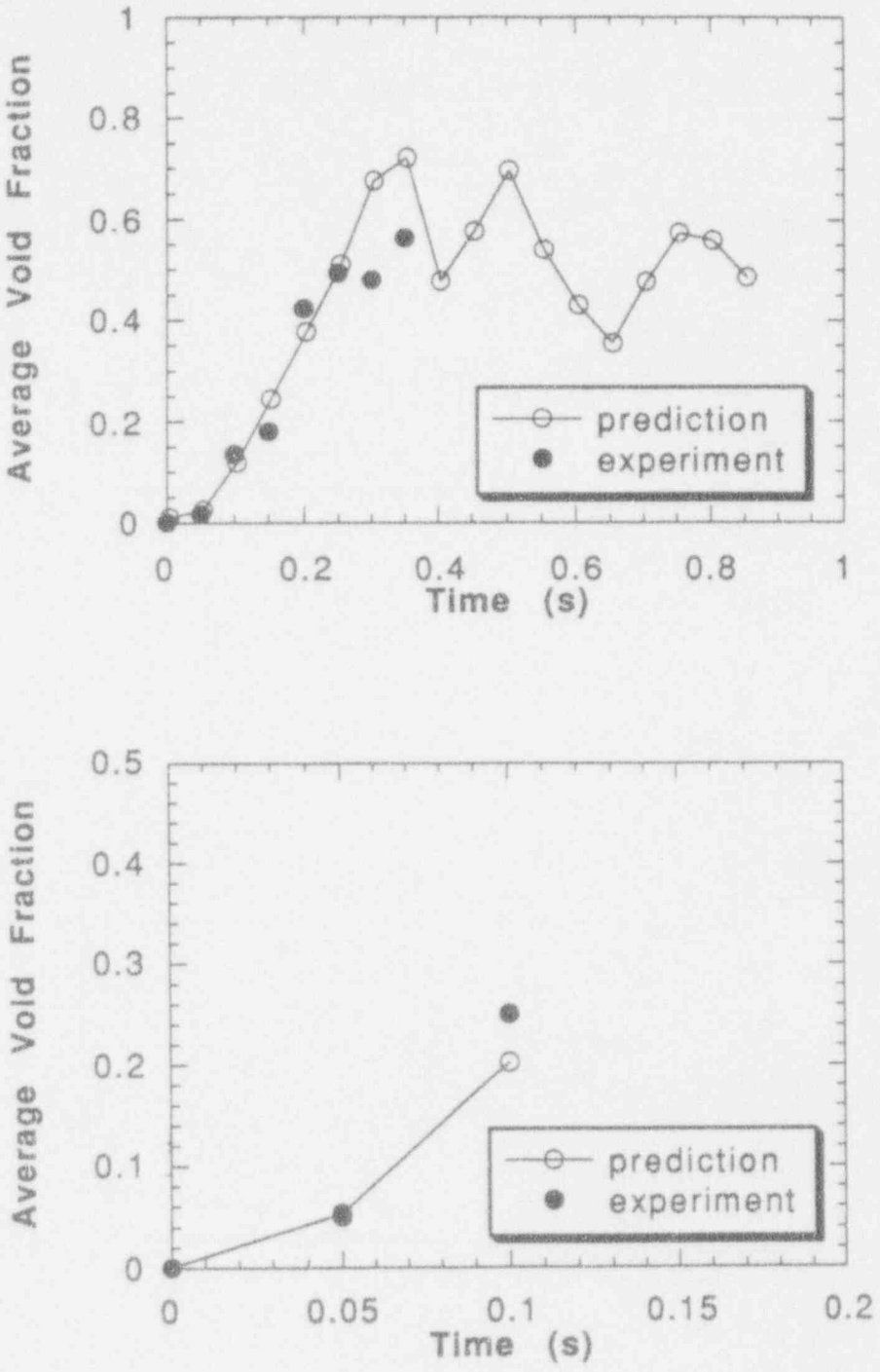

Figure I.B.39. The pool-depth-average (top) and mixing-zone-average (bottom) void fraction transients for Run #115.

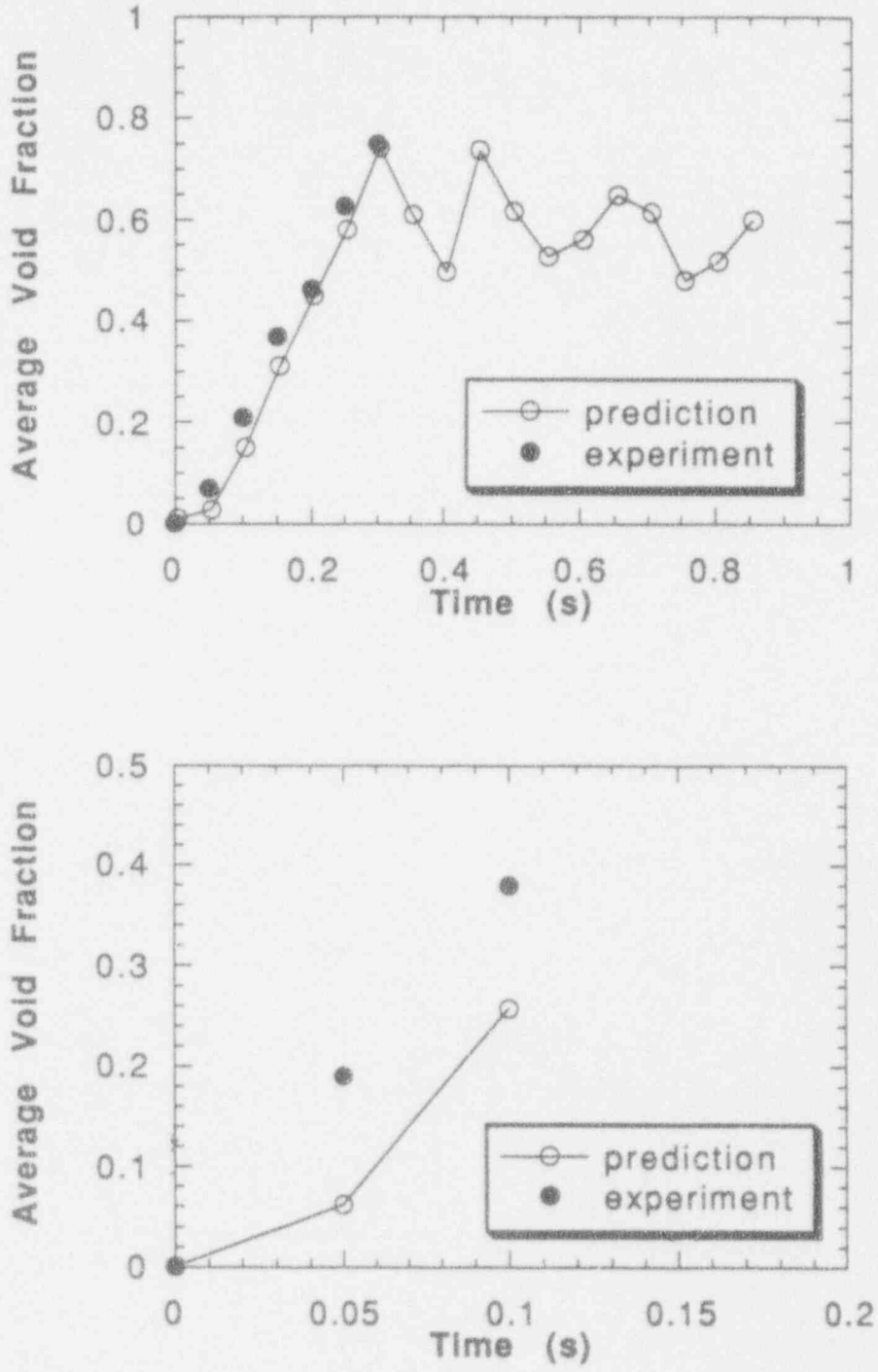

Figure I.B.40. The pool-depth-average (top) and mixing-zone-average (bottom) void fraction transients for Run #116.

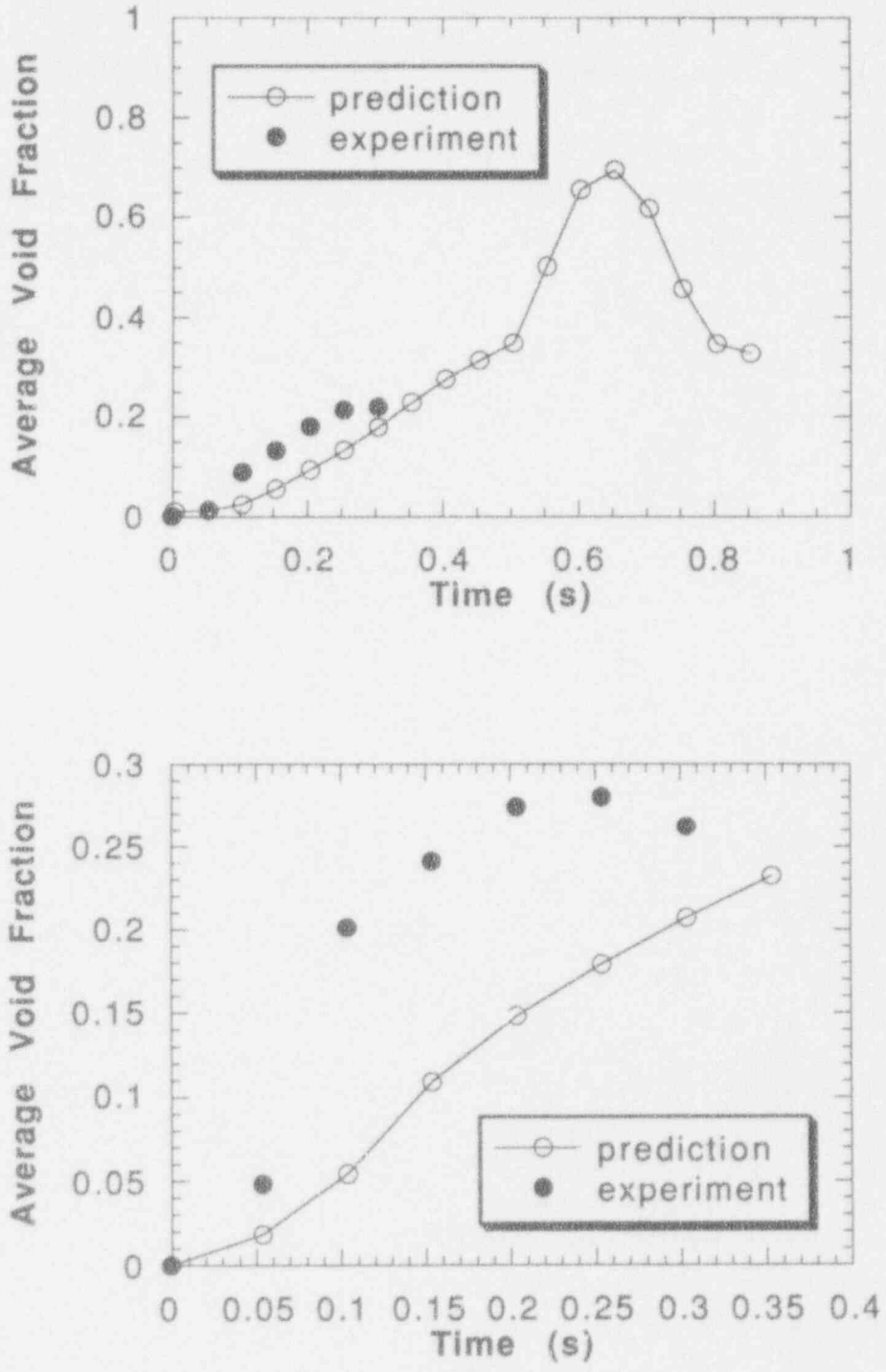

Figure I.B.41. The pool-depth-average (top) and mixing-zone-average (bottom) void fraction transients fc Run #701.

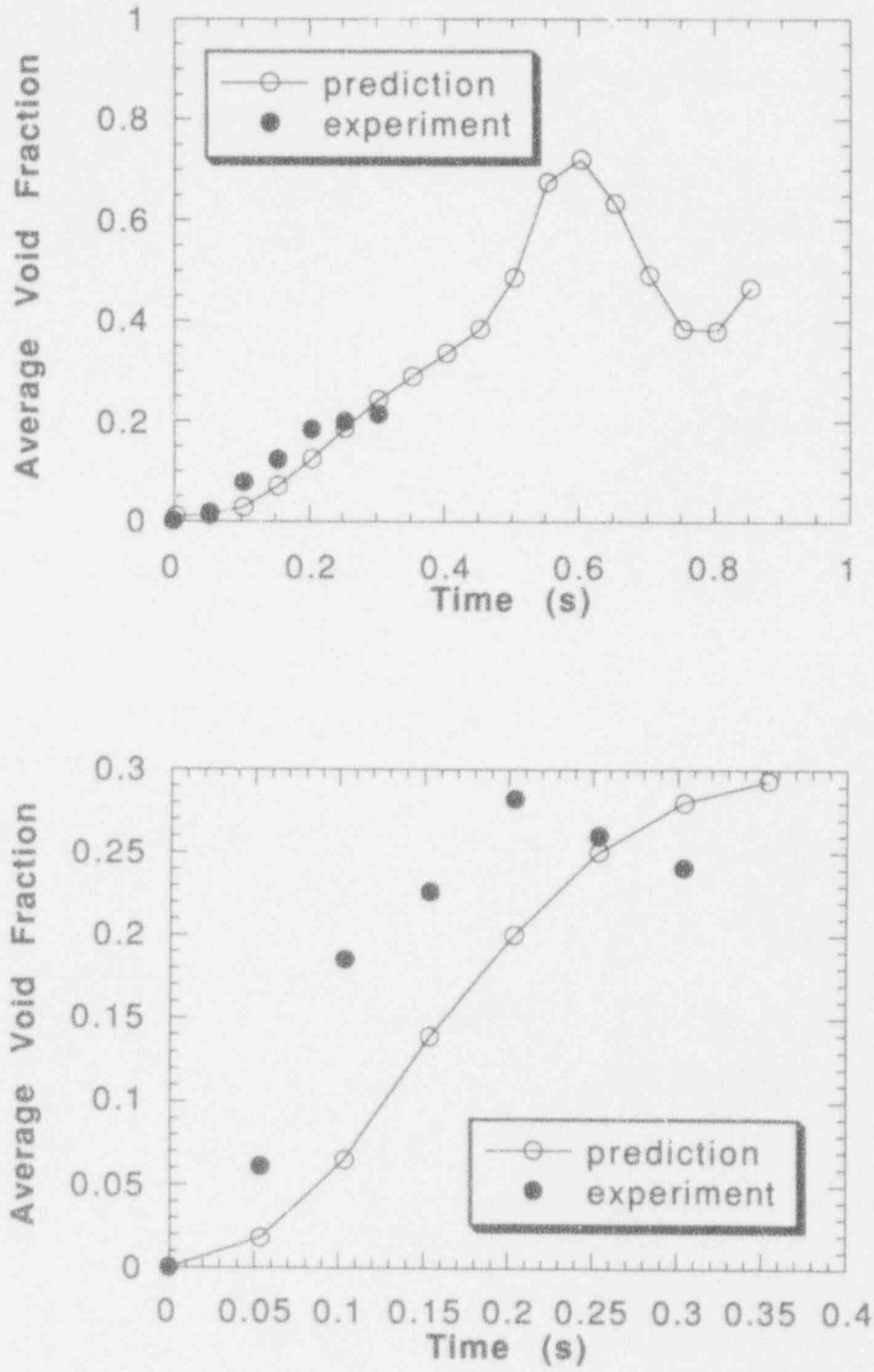

Figure I.B.42. The pool-depth-average (top) and mixing-zone-average (bottom) void fraction transients for Run #702.

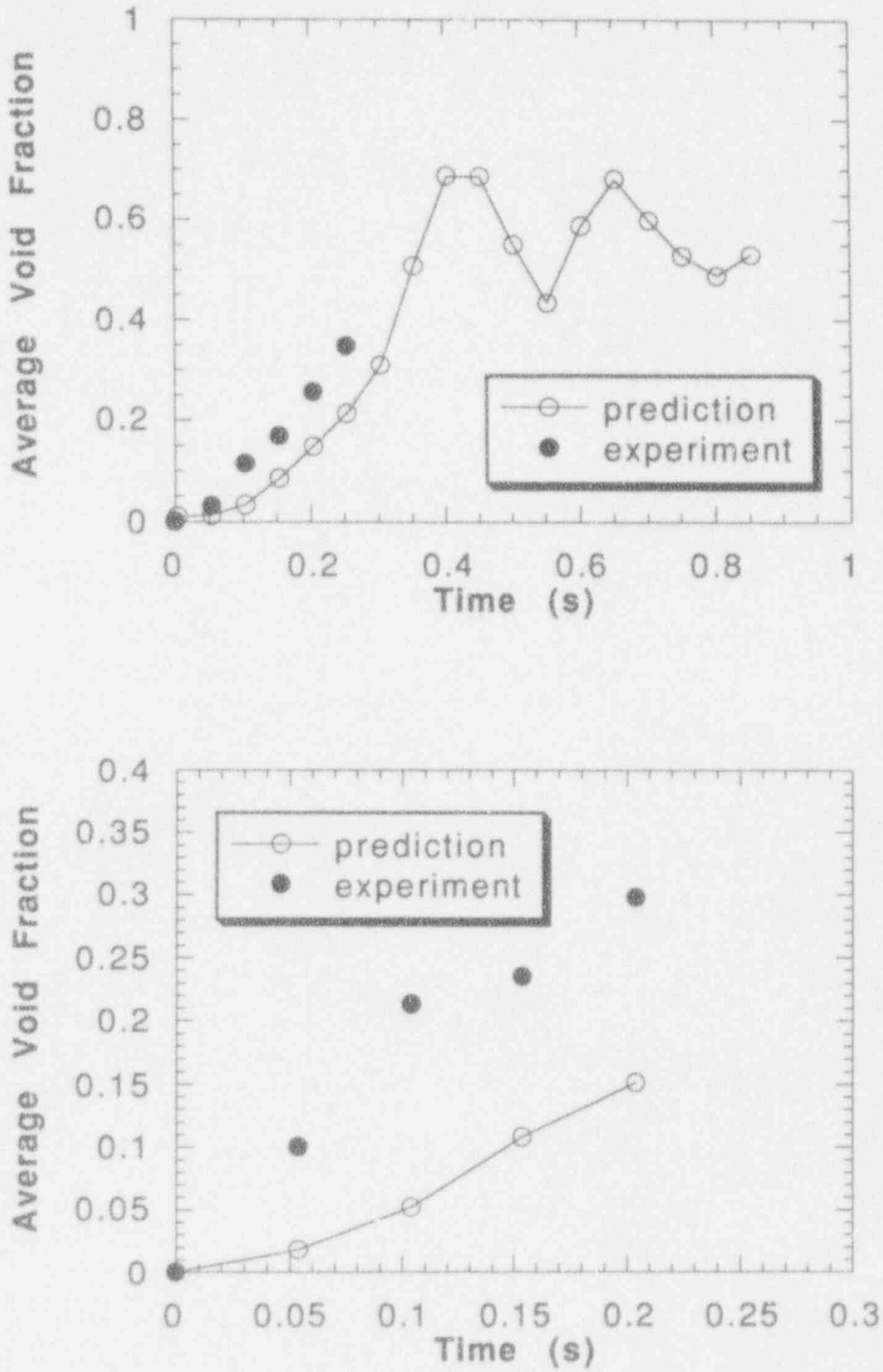

Figure I.B.43. The pool-depth-average (top) and mixing-zone-average (bottom) void fraction transients for Run #703.

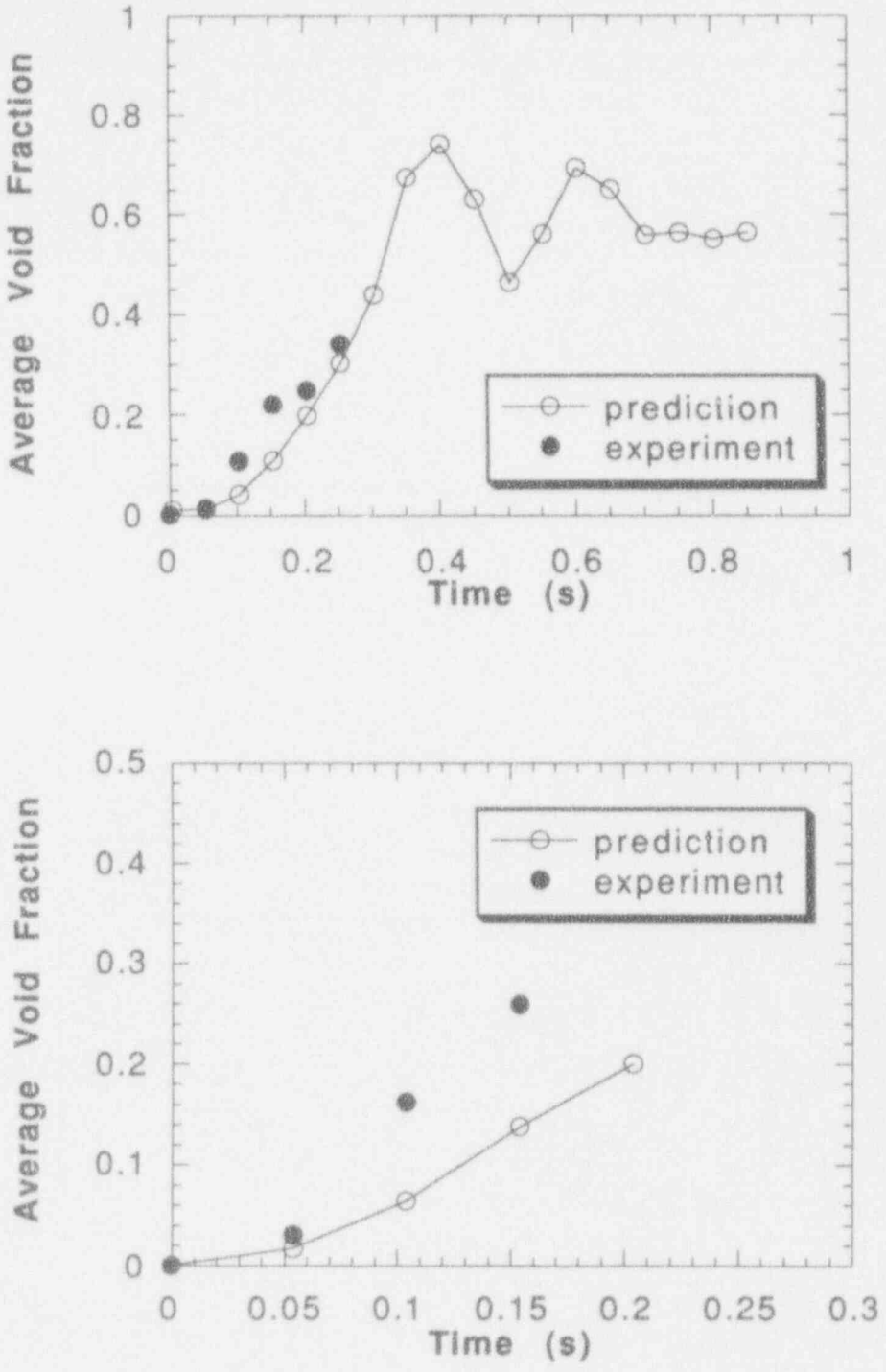

Figure I.B.44. The pool-depth-average (top) and mixing-zone-average (bottom) void fraction transients for Run #704.

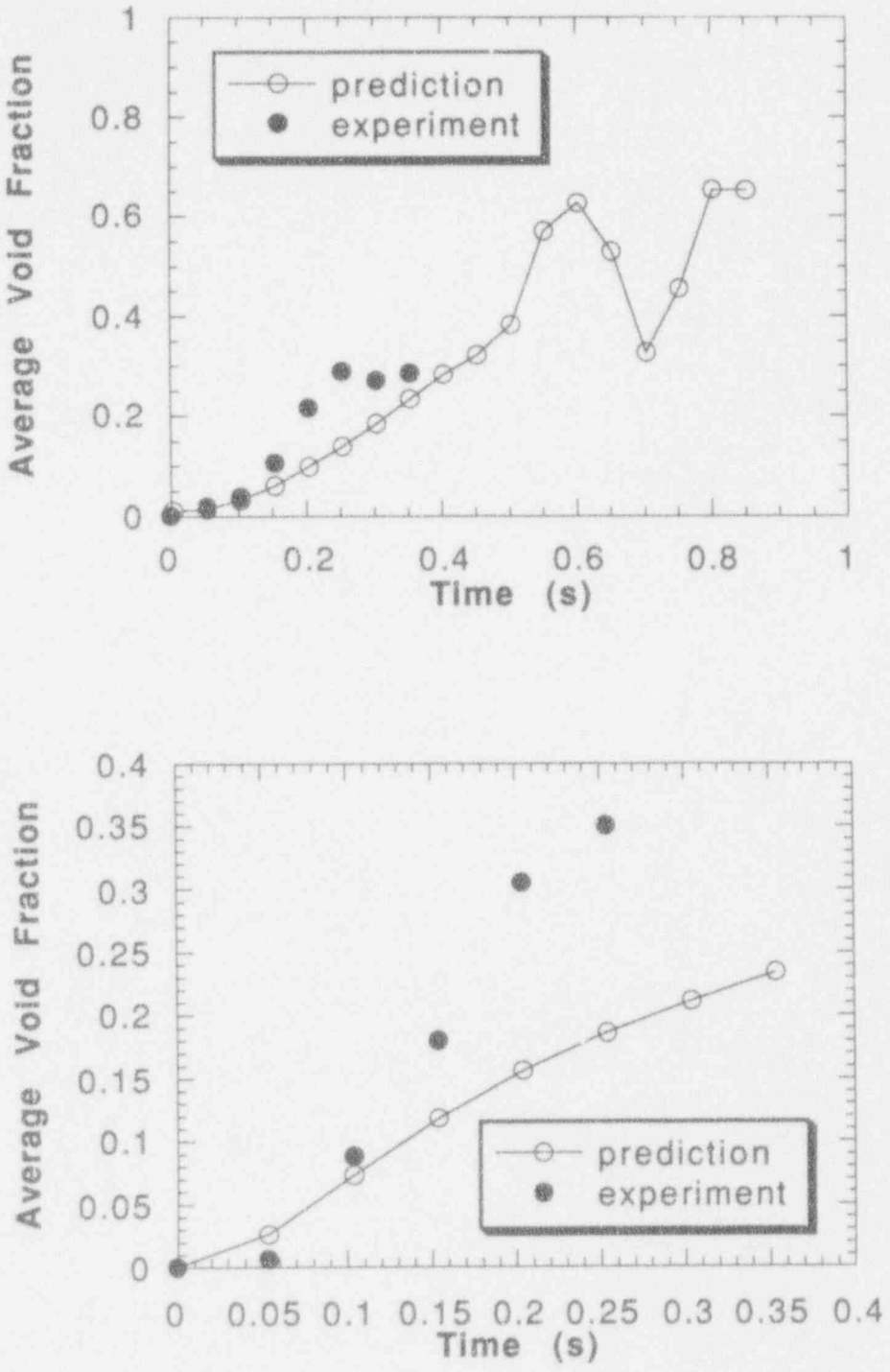

Figure I.B.45. The pool-depth-average (top) and mixing-zone-average (bottom) void fraction transients for Run #705.

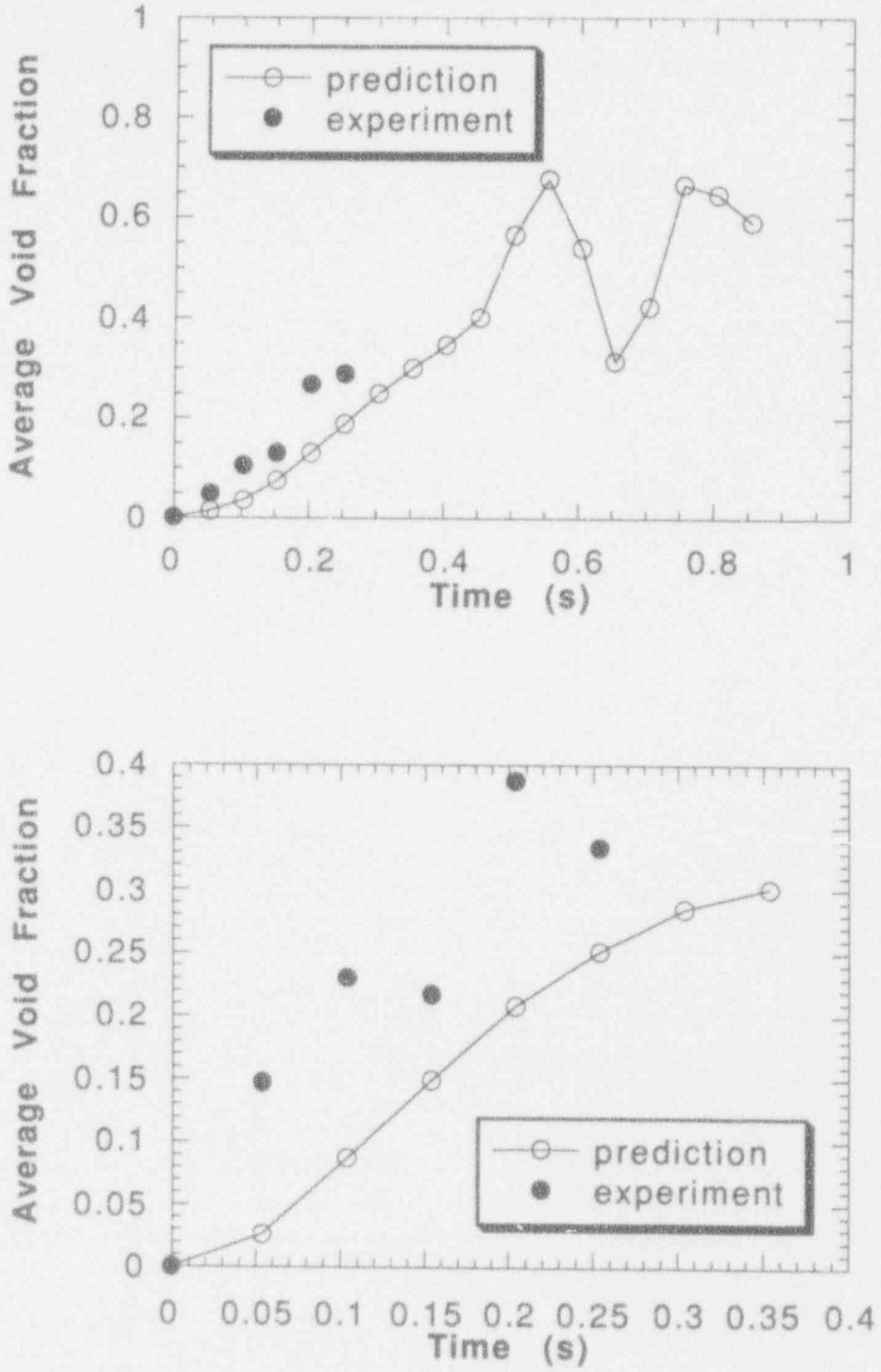

Figure I.B.46. The pool-depth-average (top) and mixing-zone-average (bottom) void fraction transients for Run #706.

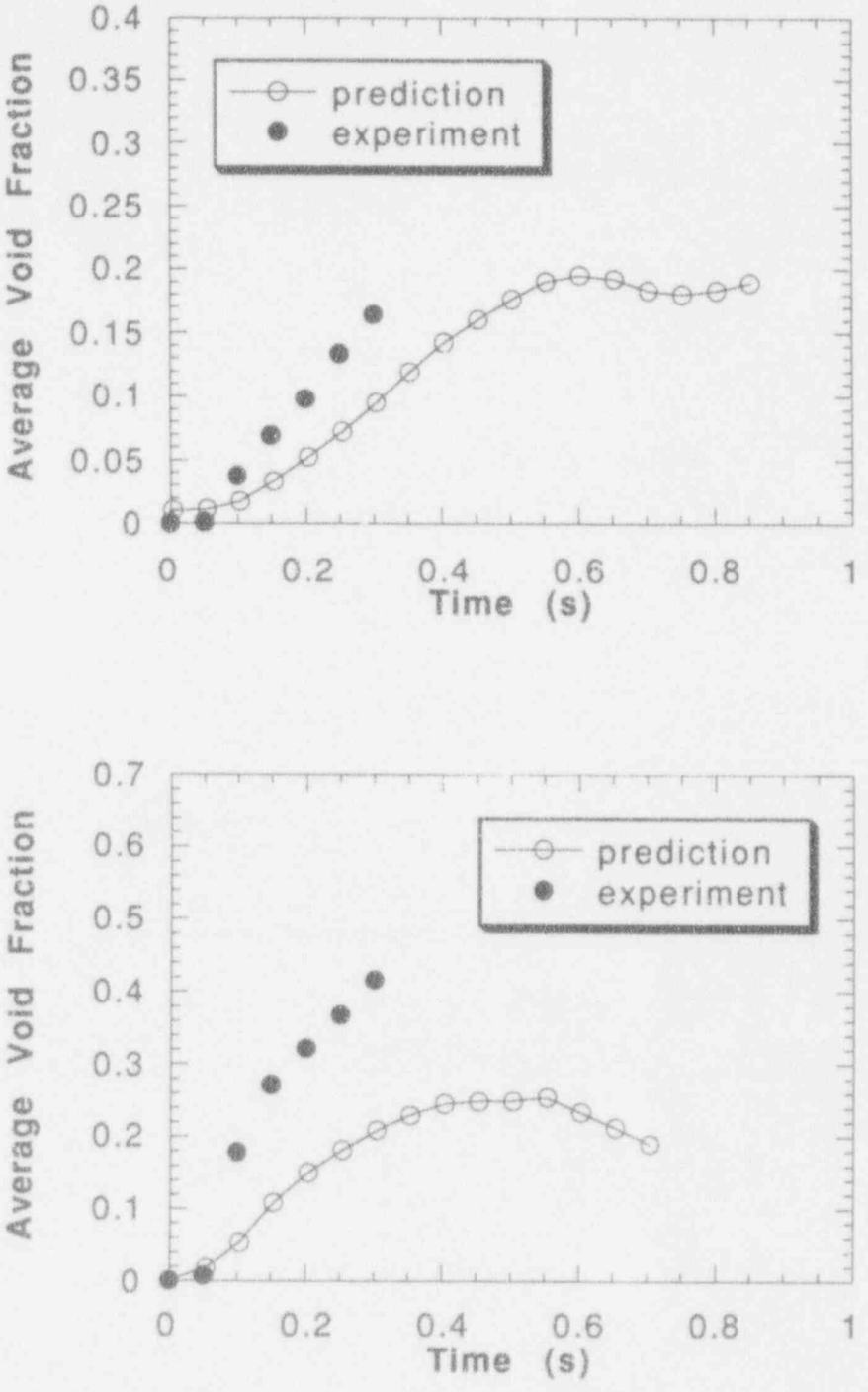

Figure I.B.47. The pool-depth-average (top) and mixing-zone-average (bottom) void fraction transients for Run #901.

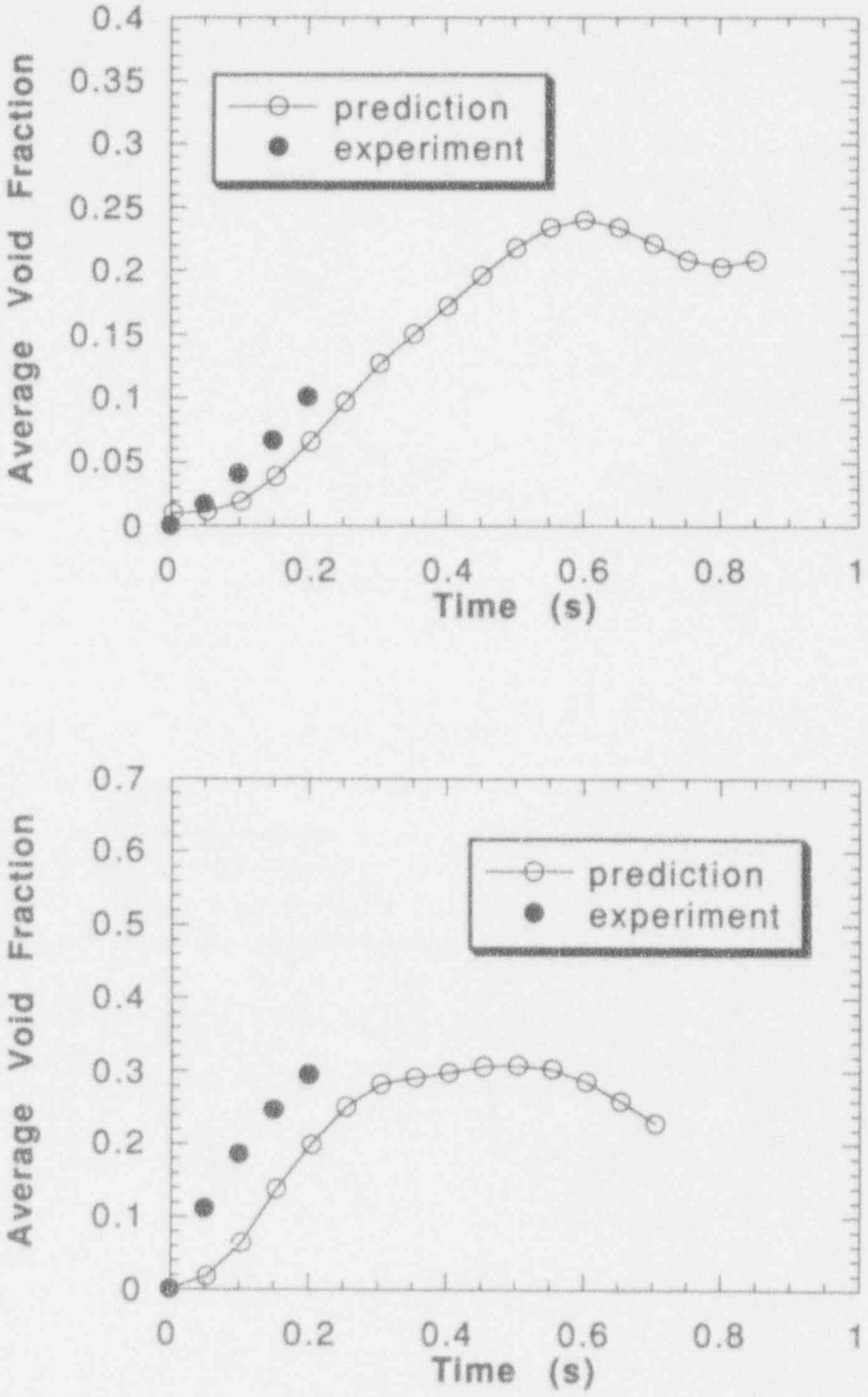

Figure I.B.48. The pool-depth-average (top) and mixing-zone-average (bottom) void fraction transients for Run #902.

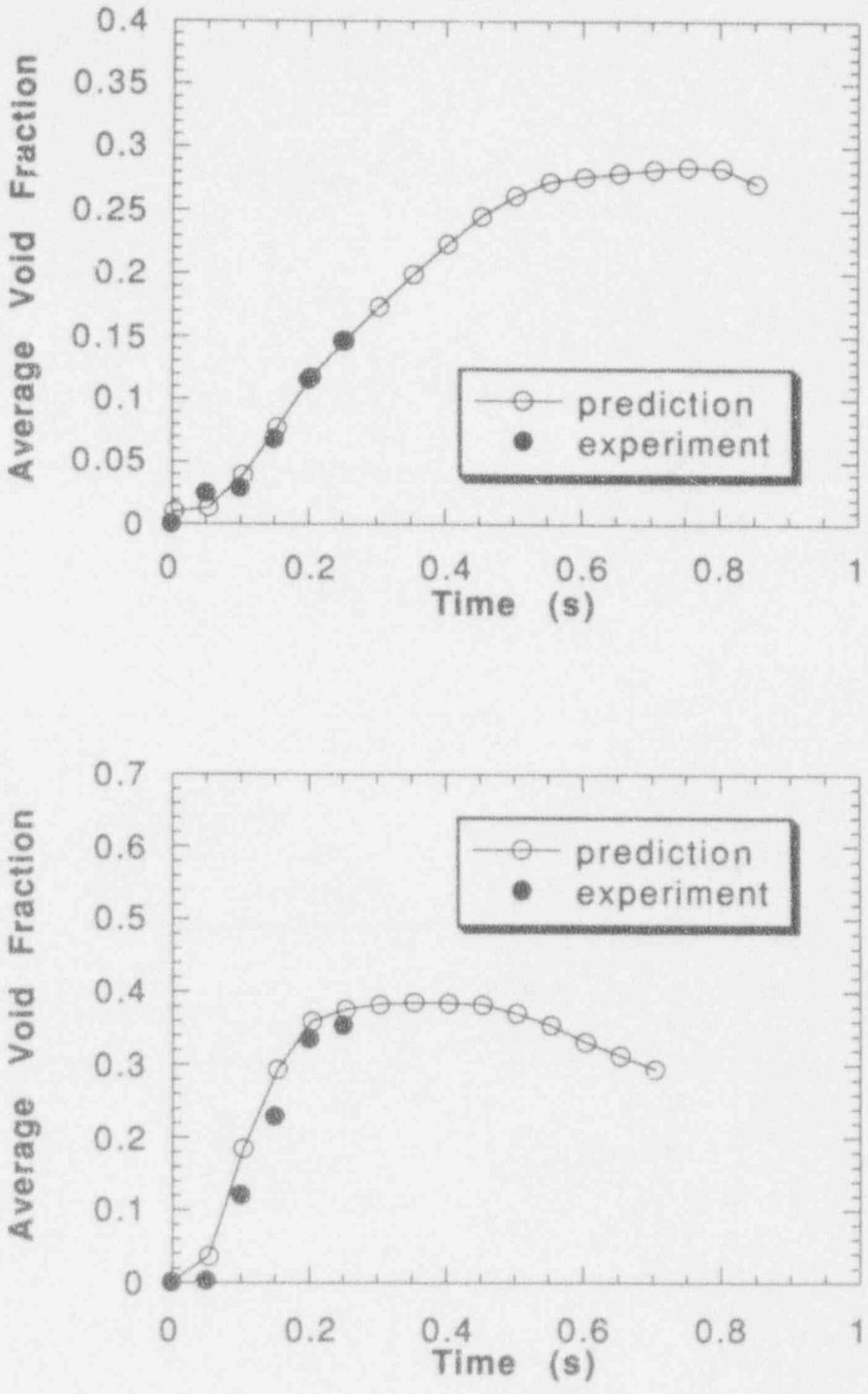

Figure I.B.49. The pool-depth-average (top) and mixing-zone-average (bottom) void fraction transients for Run #904.

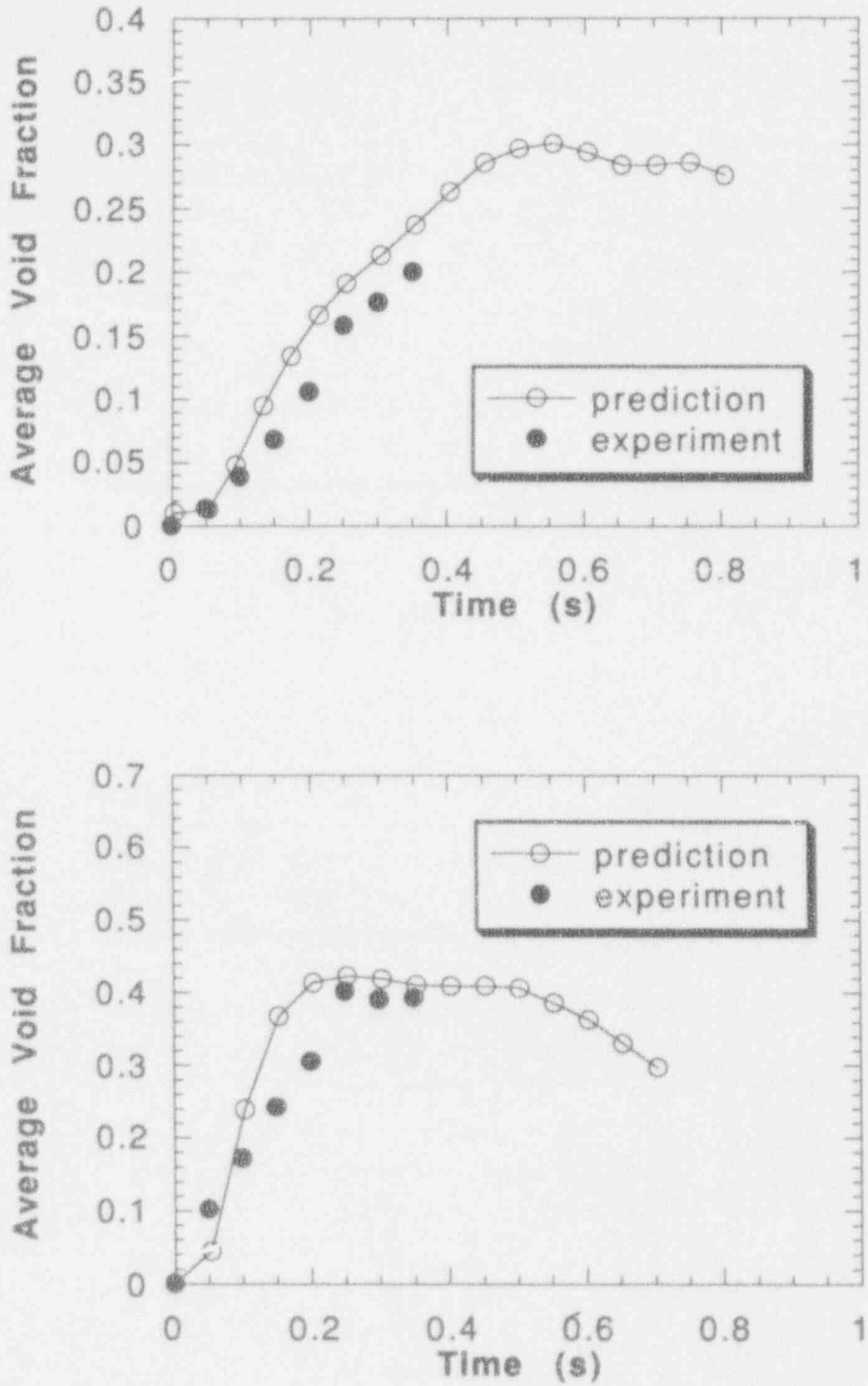

Figure I.B.50. The pool-depth-average (top) and mixing-zone-average (bottom) void fraction transients for Run #905.

APPENDIX C

LOCAL VOID FRACTION TRANSIENTS IN MAGICO

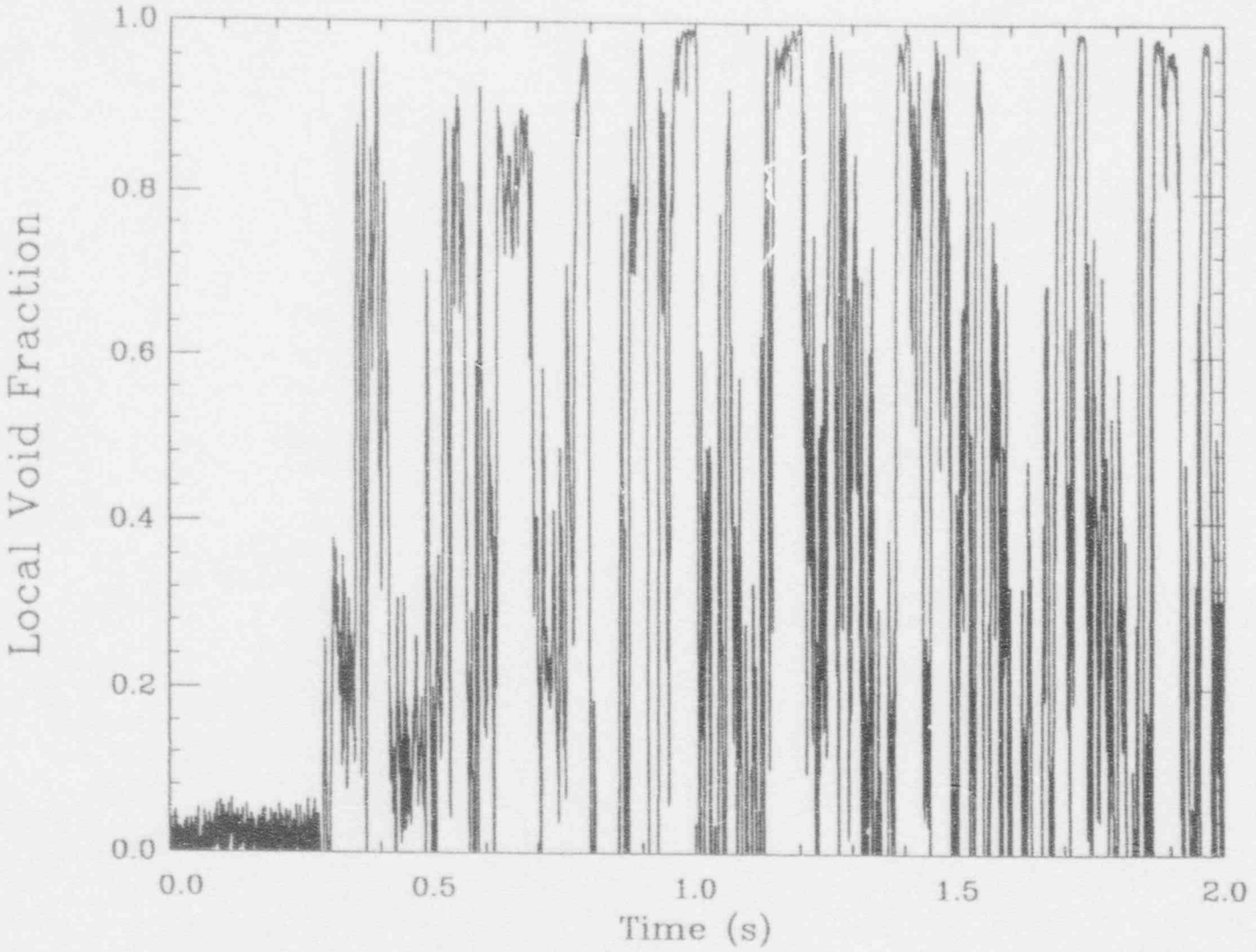

Figure I.C.1. The FLUTE signal for Run #204, position #1 (sampling rate 8 kHz).

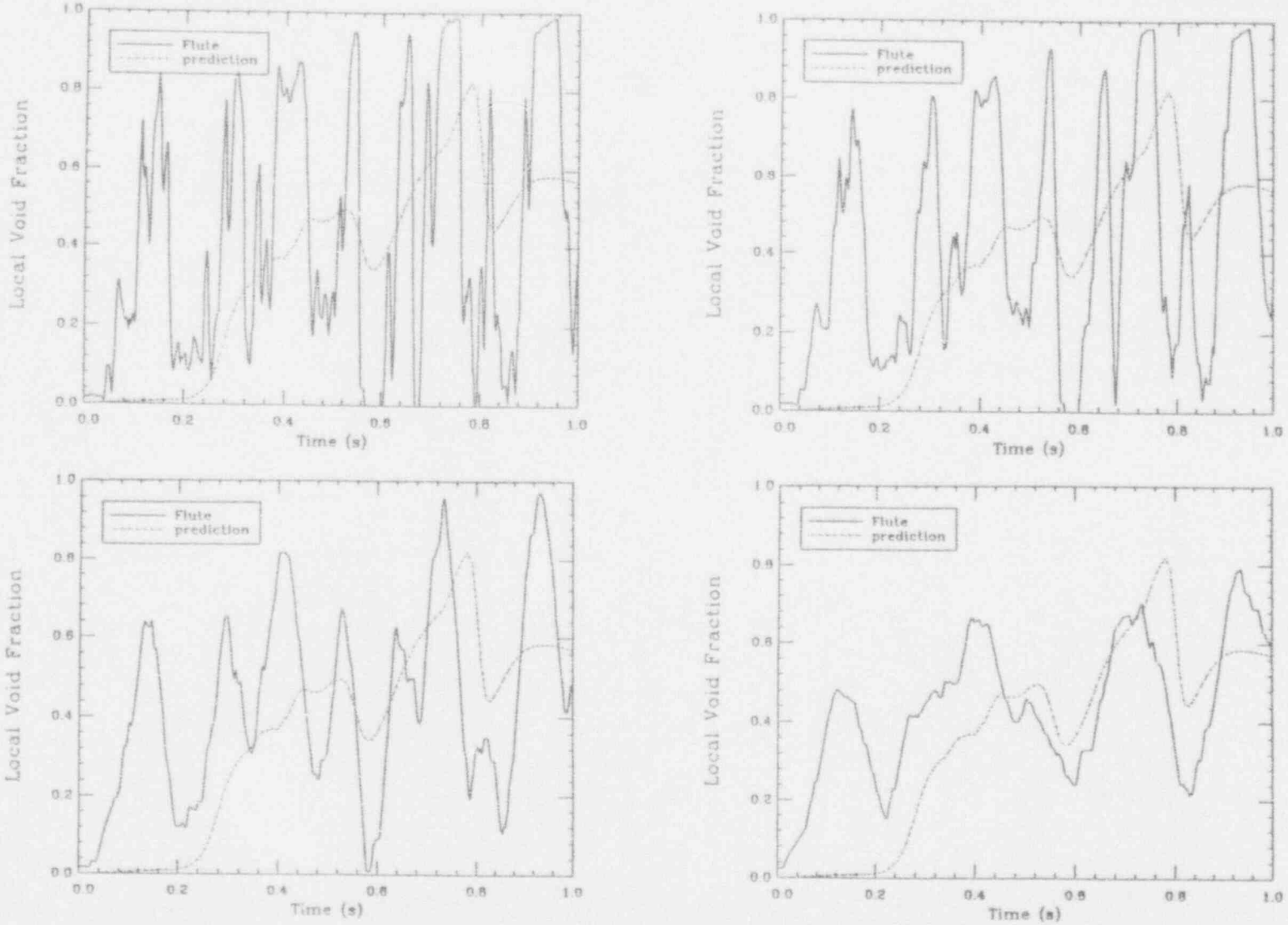

Figure I.C.2. The local void fraction transient for Run #204, position #1 as deduced by 10 (top left) 20 (top right) 50 (bottom left) and 100 (bottom right) millisecond time-averaging of the 8 kHz FLUTE signal.

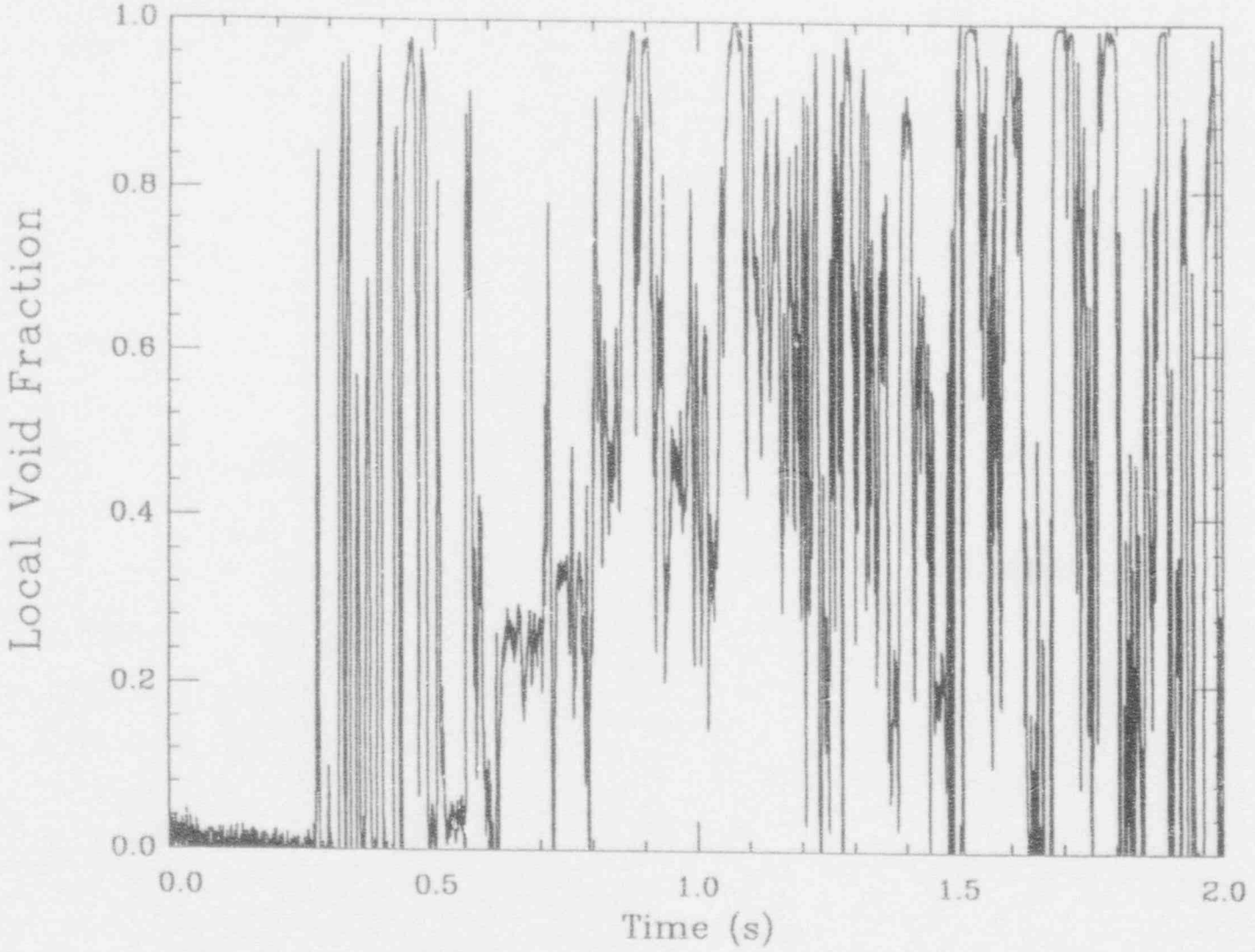

Figure I.C.3. The FLUTE signal for Run #204, position #2 (sampling rate 8 kHz).

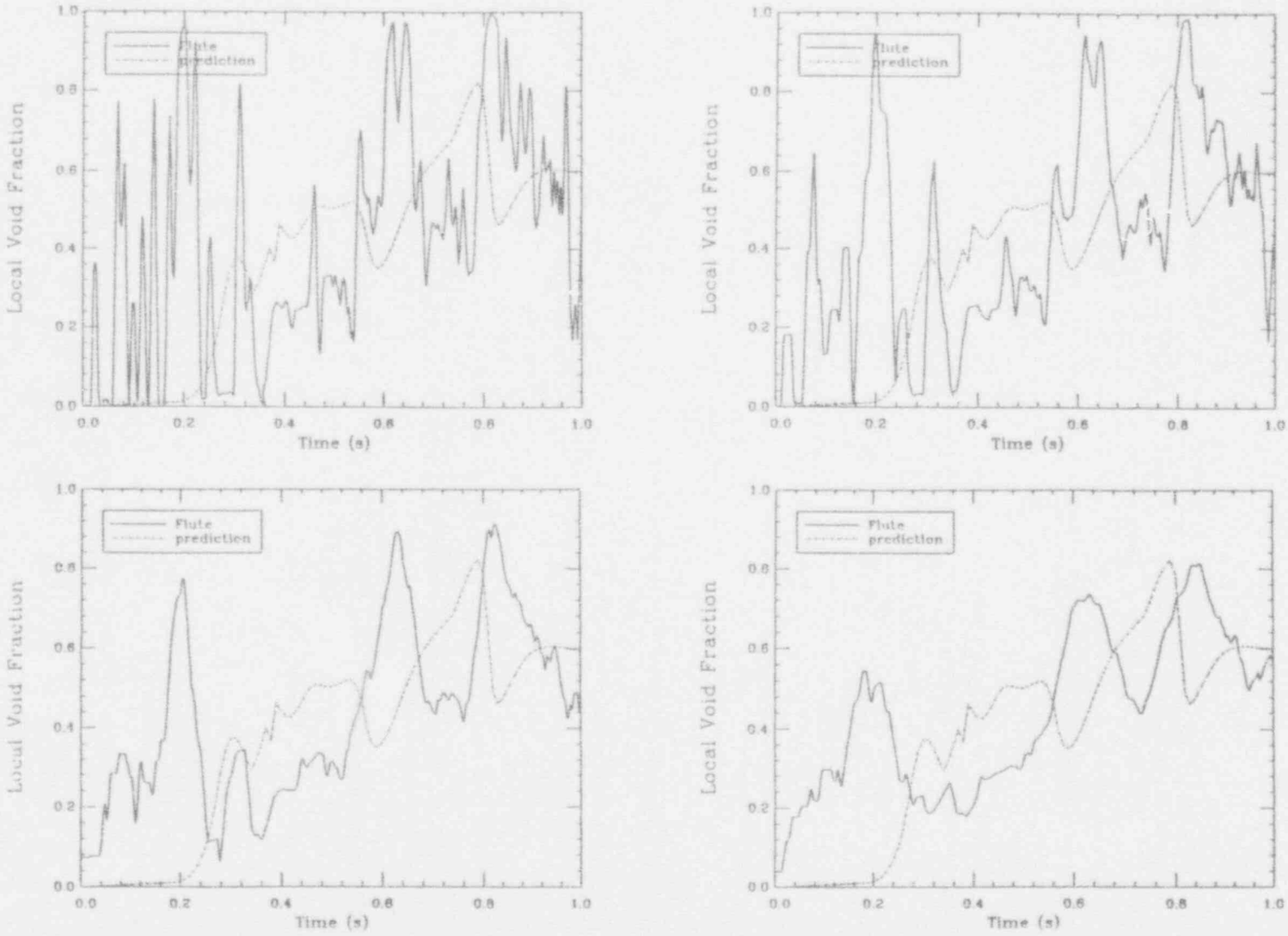

Figure I.C.4. The local void fraction transient for Run #204, position #2 as deduced by 10 (top left) 20 (top right) 50 (bottom left) and 100 (bottom right) millisecond time-averaging of the 8 kHz FLUTE signal.

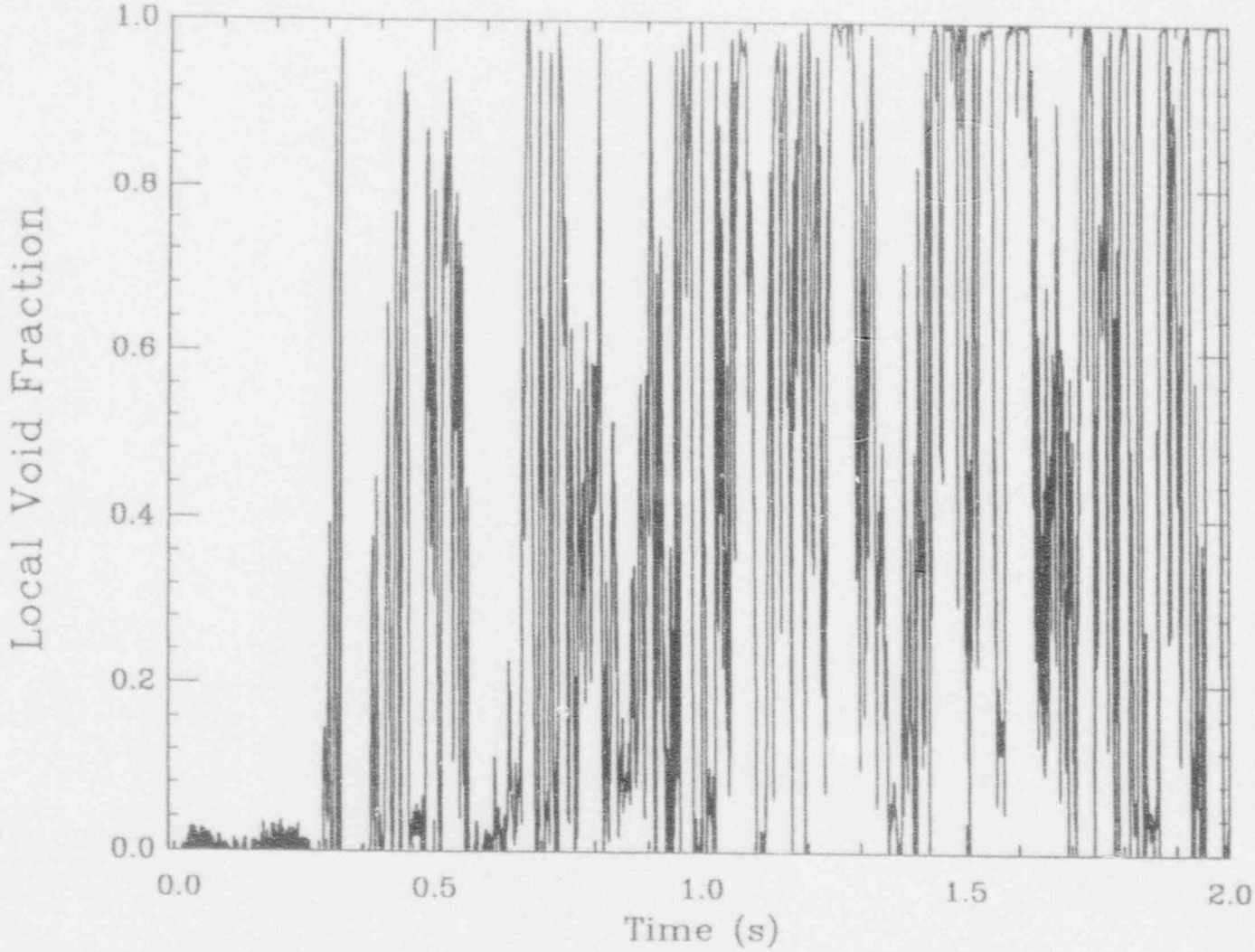

Figure I.C.5. The FLUTE signal for Run #209, position #1 (sampling rate 8 kHz).

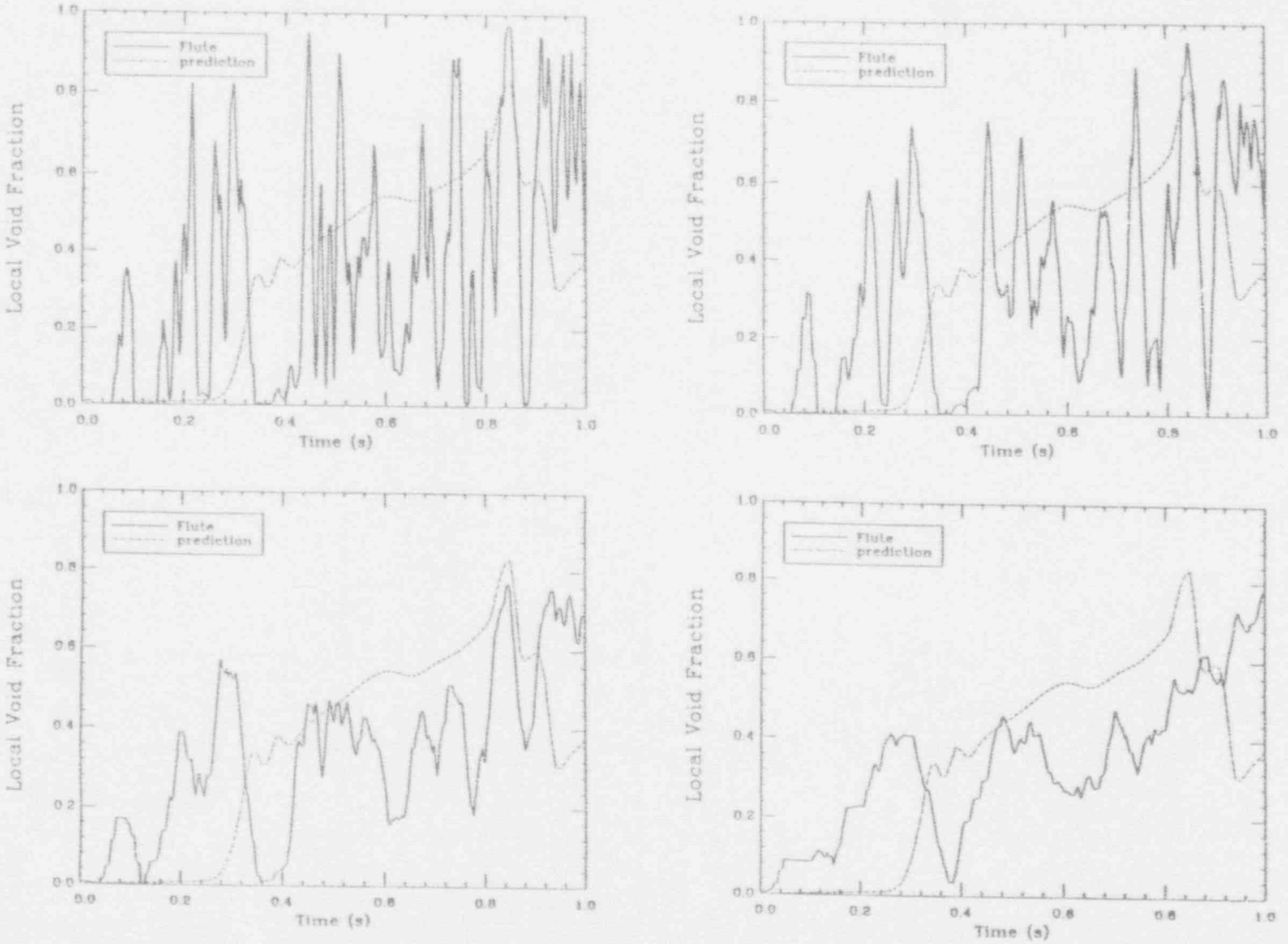

Figure I.C.6. The local void fraction transient for Run #209, position #1 as deduced by 10 (top left) 20 (top right) 50 (bottom left) and 100 (bottom right) millisecond time-averaging of the 8 kHz FLUTE signal.

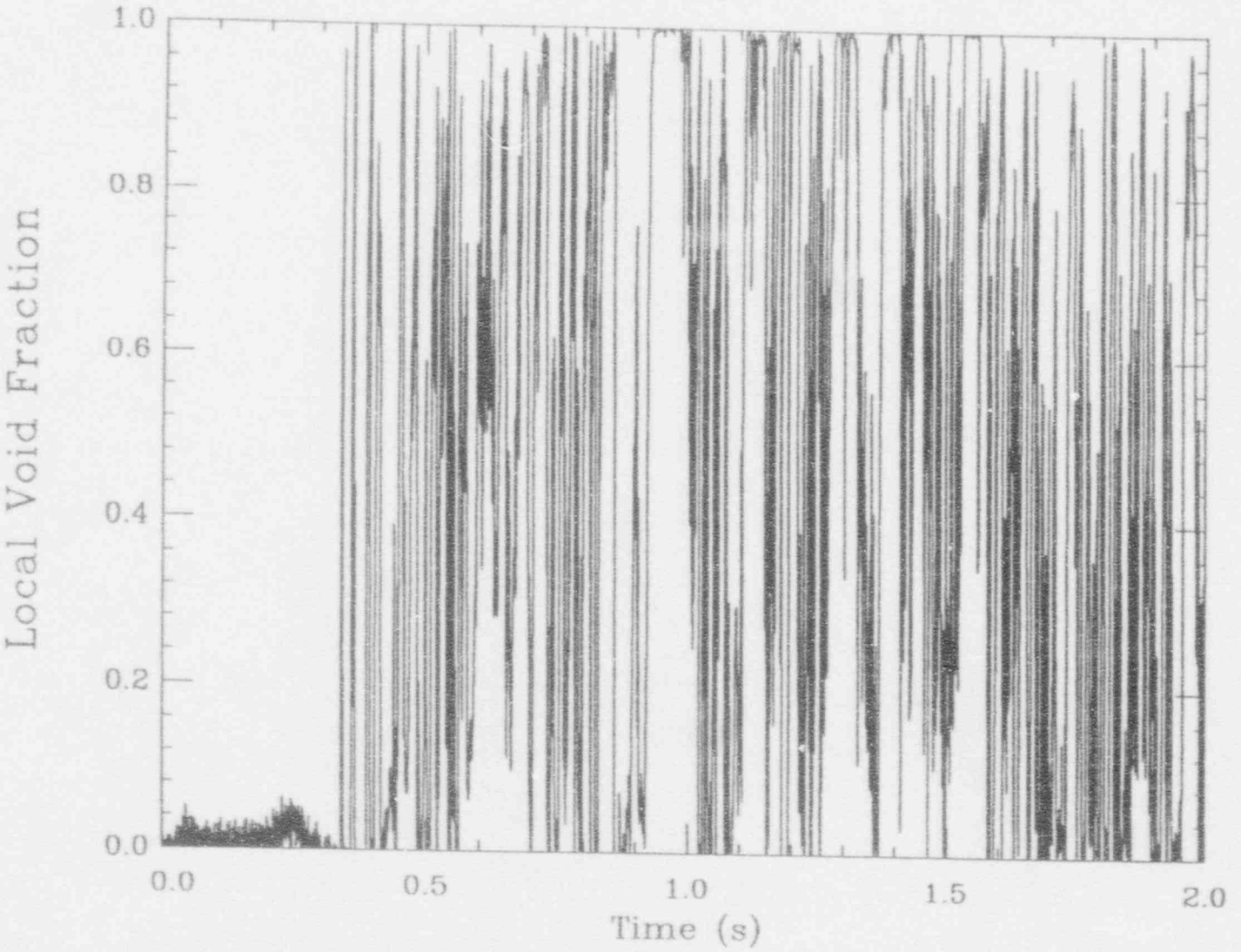

Figure I.C.7. The FLUTE signal for Run #209, position #2 (sampling rate 8 kHz).

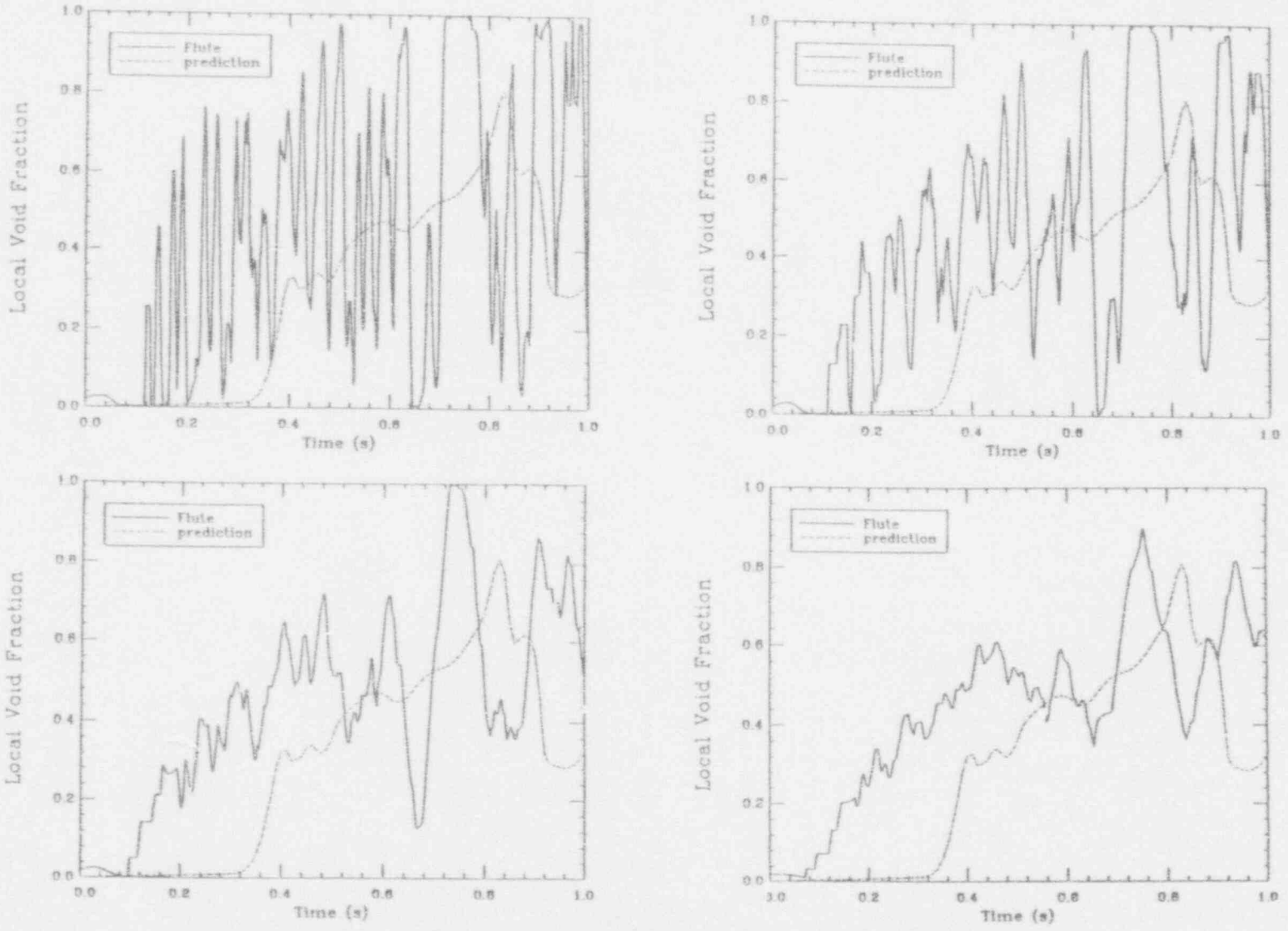

Figure I.C.8. The local void fraction transient for Run #209, position #2 as deduced by 10 (top left) 20 (top right) 50 (bottom left) and 100 (bottom right) millisecond time-averaging of the 8 kHz FLUTE signal.

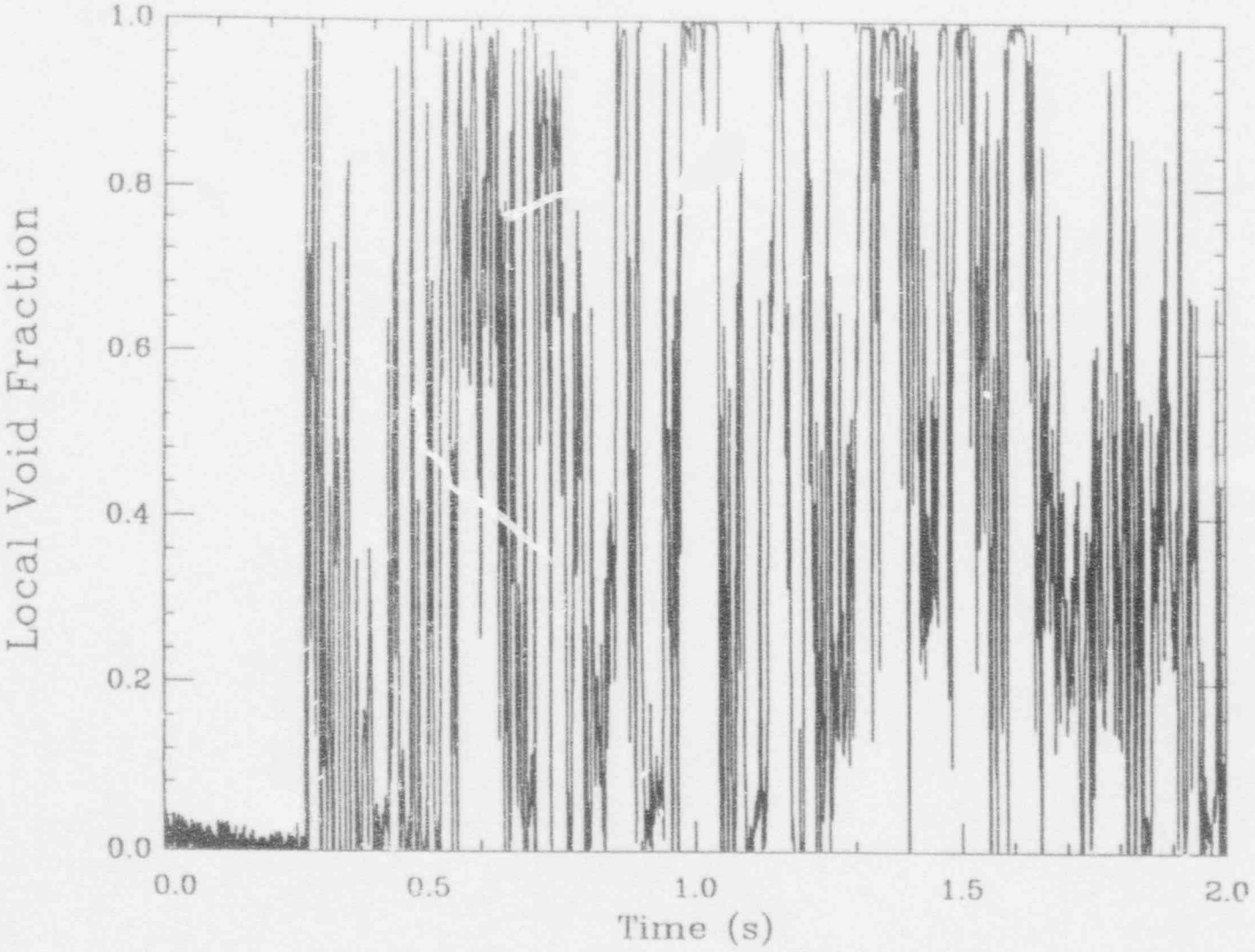

Figure I.C.9. The FLUTE signal for Run #210, position #1 (sampling rate 8 kHz).

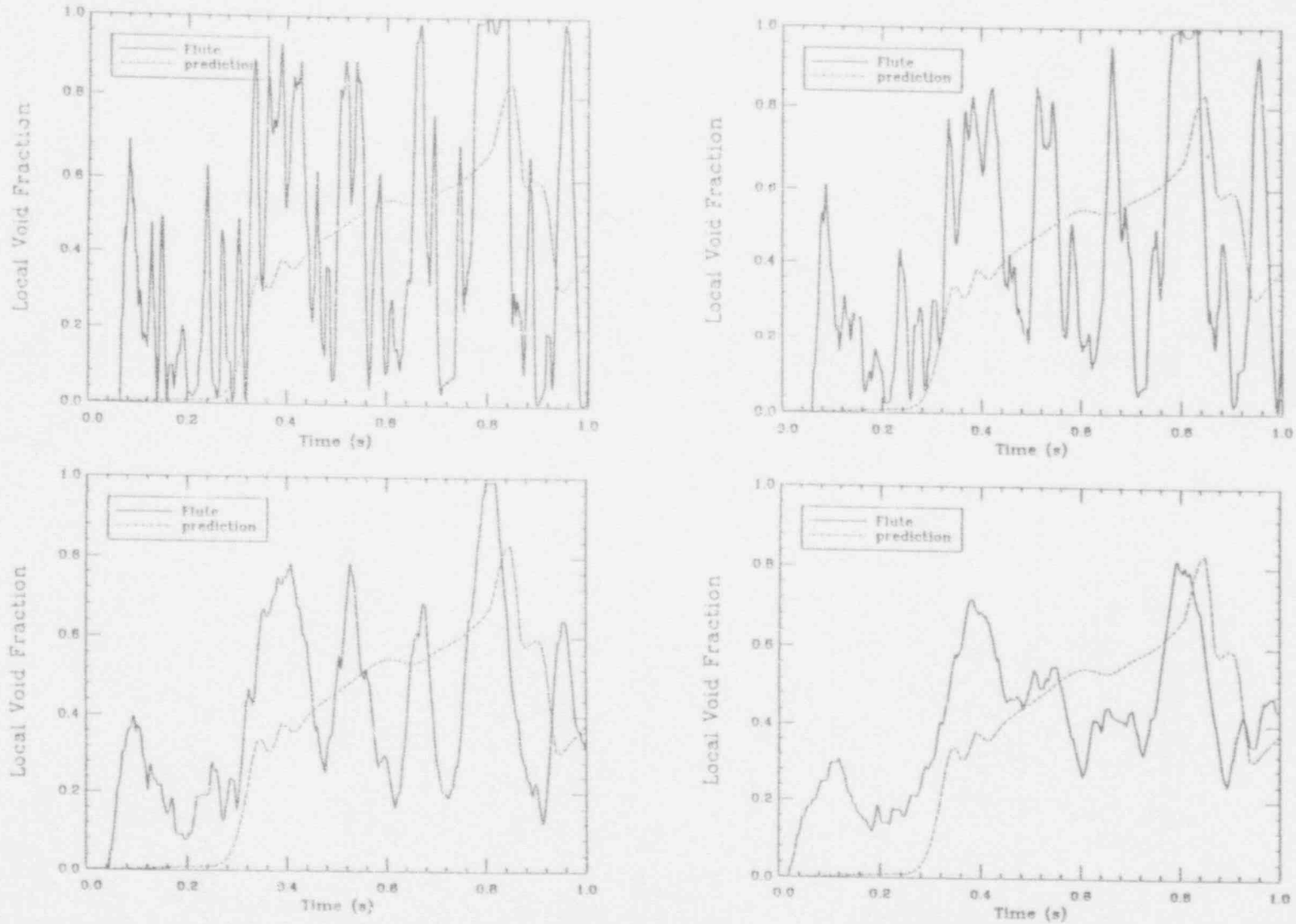

Figure I.C.10. The local void fraction transient for Run #210, position #1 as deduced by 10 (top left) 20 (top right) 50 (bottom left) and 100 (bottom right) millisecond time-averaging of the 8 kHz FLUTE signal.

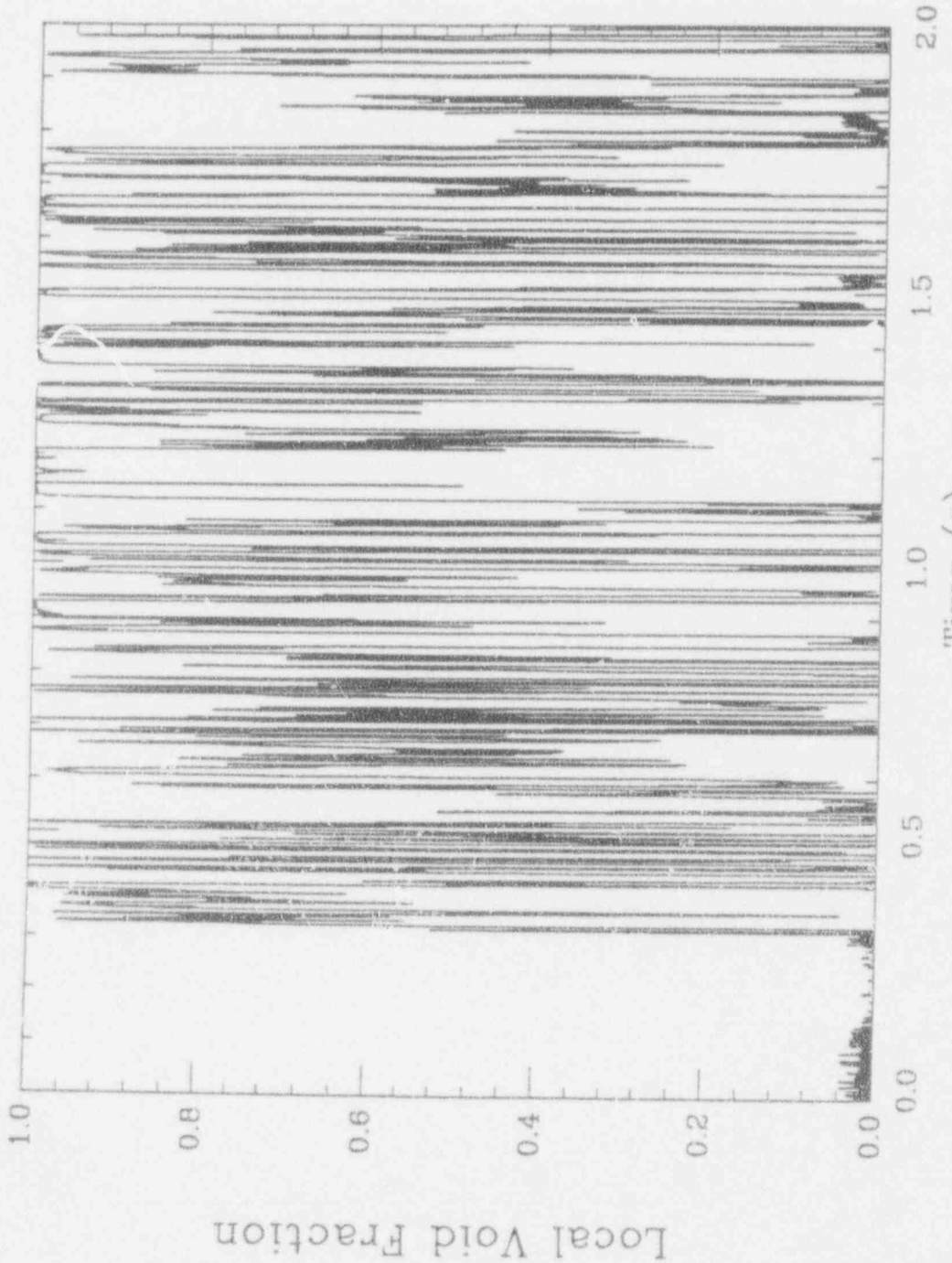

Figure I.C.11. The FLUTE signal for Run #210, position #2 (sampling rate 8 kHz).

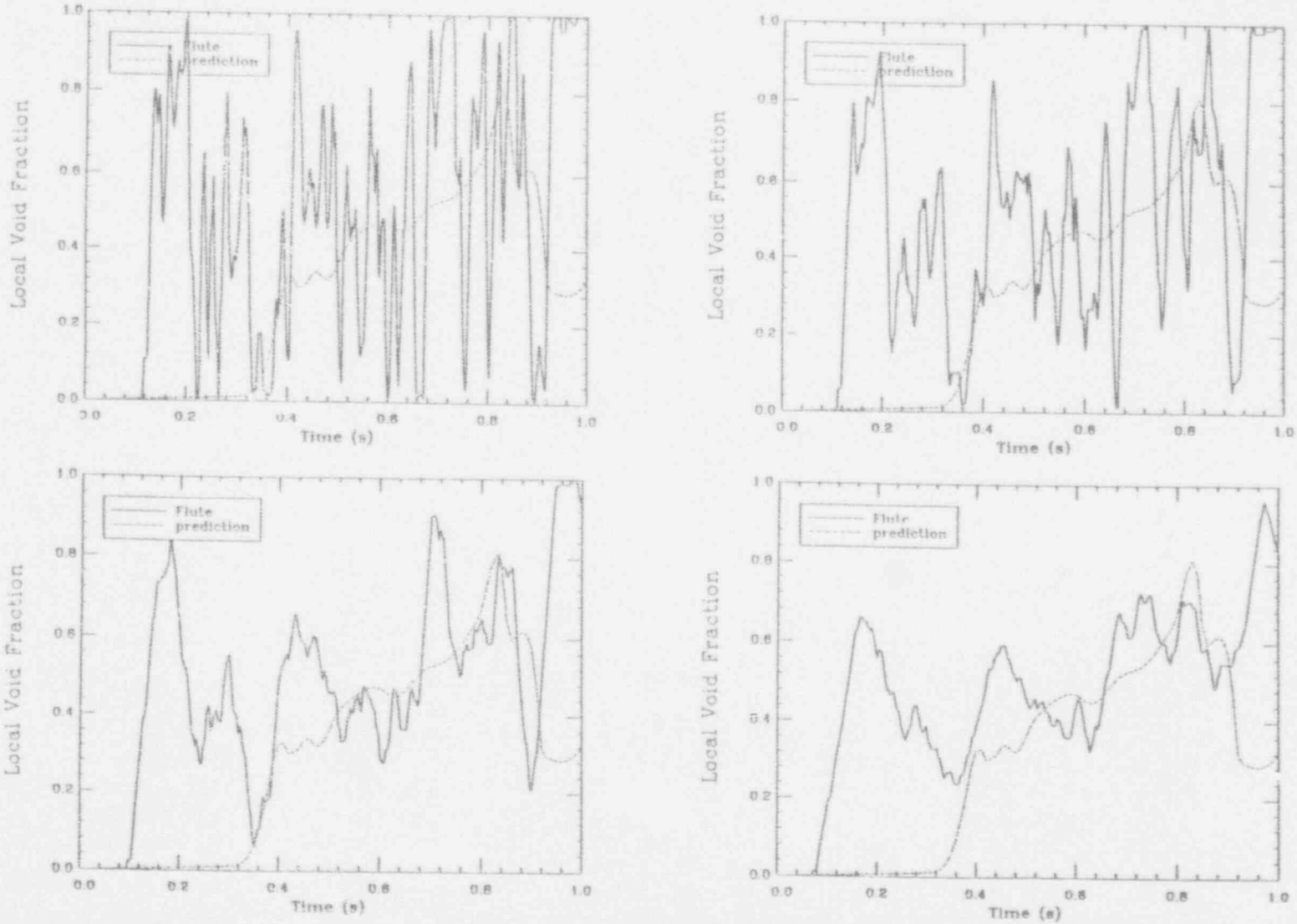

Figure I.C.12. The local void fraction transient for Run #210, position #2 as deduced by 10 (top left) 20 (top right) 50 (bottom left) and 100 (bottom right) millisecond time-averaging of the 8 kHz FLUTE signal.

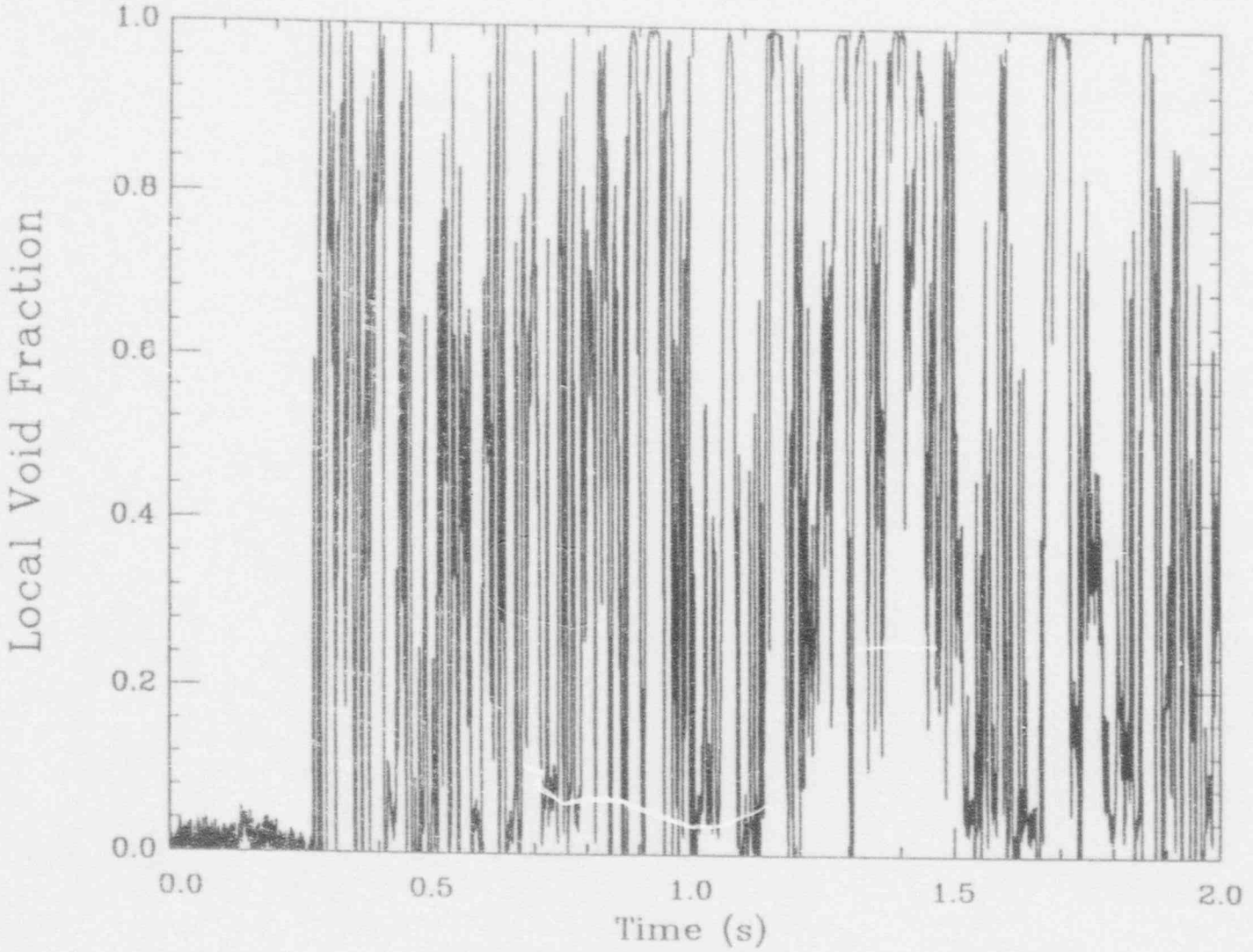

Figure I.C.13. The FLUTE signal for Run #211, position #1 (sampling rate 8 kHz).

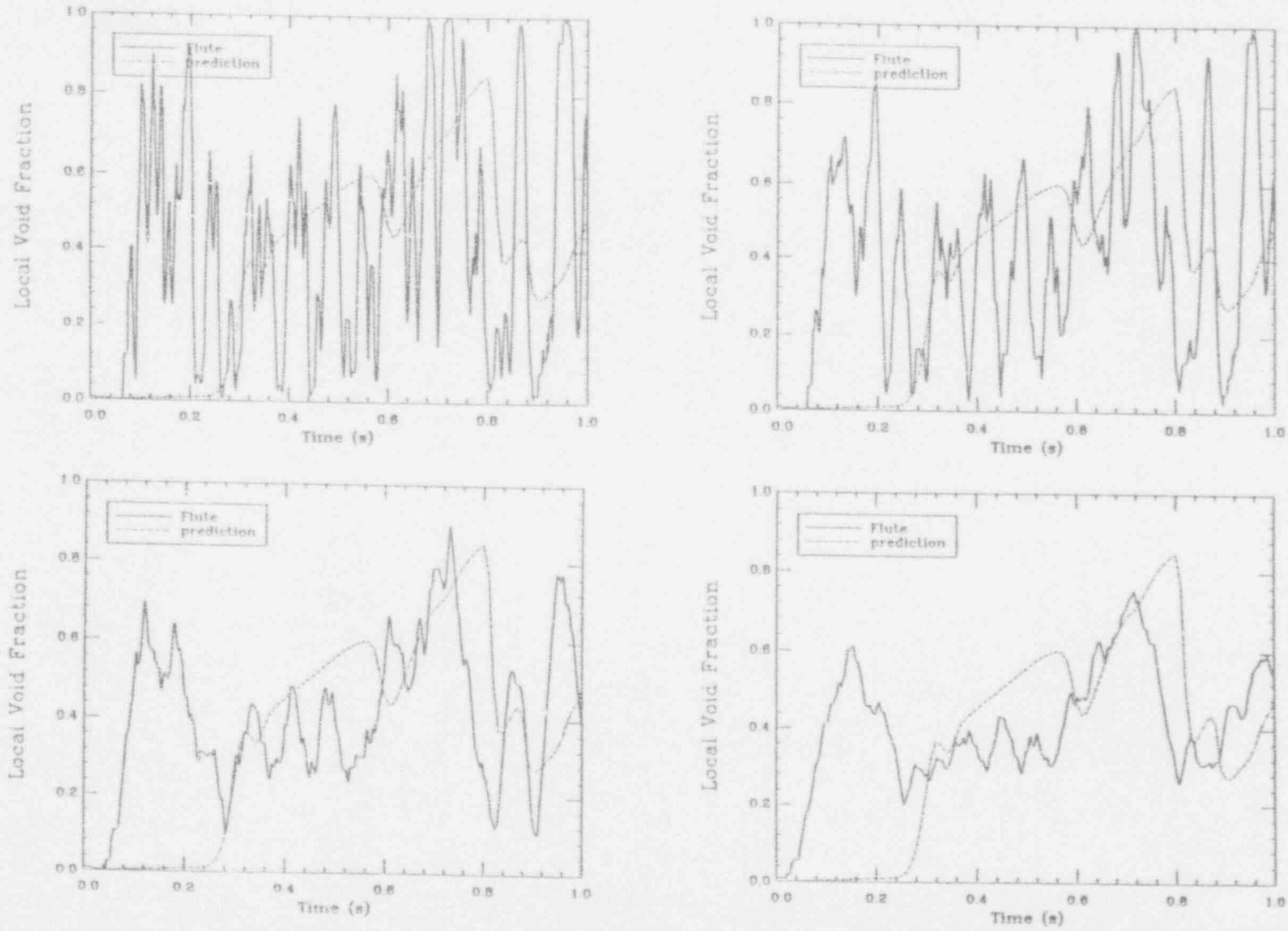

Figure I.C.14. The local void fraction transient for Run #211, position #1 as deduced by 10 (top left) 20 (top right) 50 (bottom left) and 100 (bottom right) millisecond time-averaging of the 8 kHz FLUTE signal.

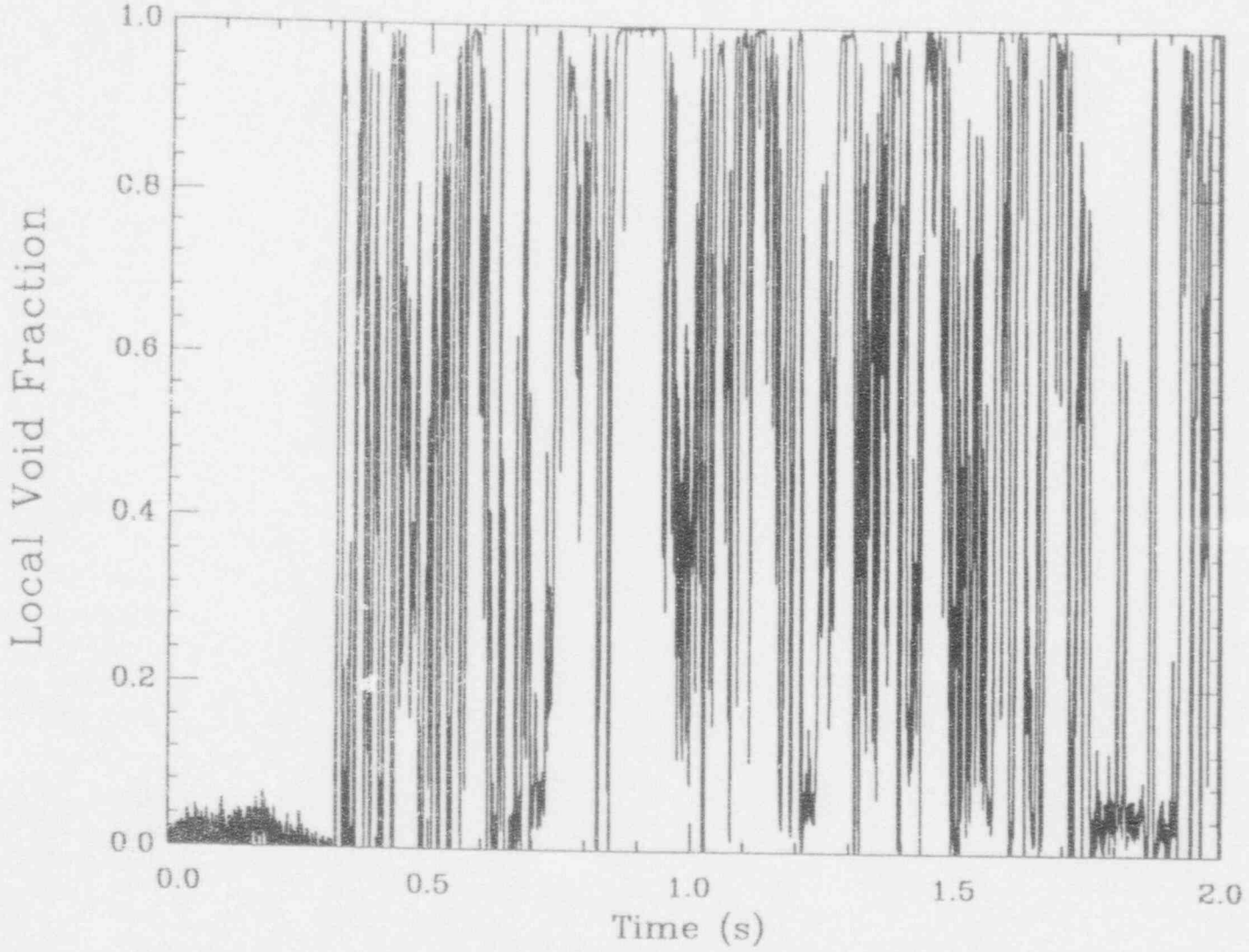

Figure I.C.15. The FLUTE signal for Run #211, position #2 (sampling rate 8 kHz).

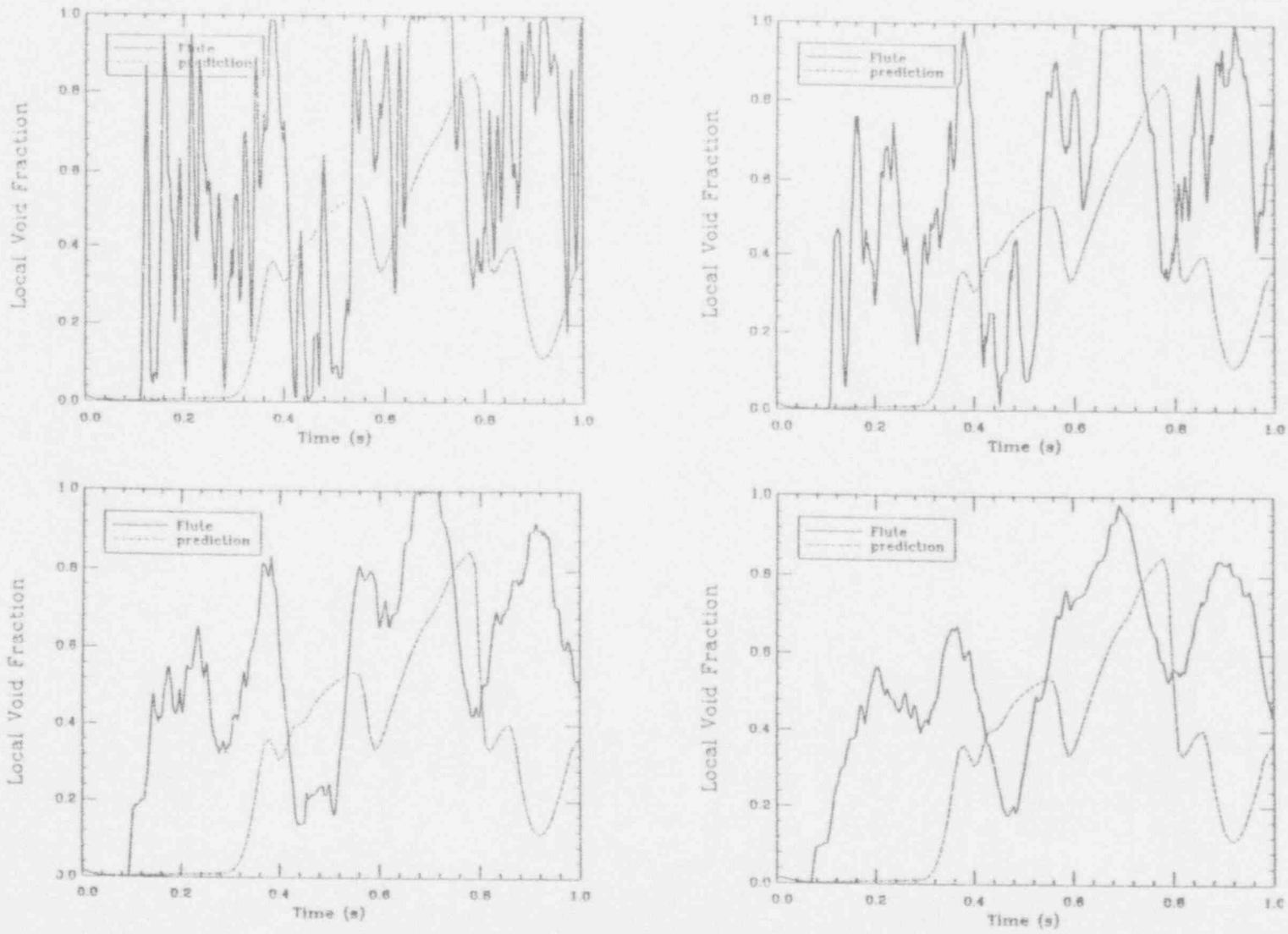

Figure I.C.16. The local void fraction transient for Run #211, position #2 as deduced by 10 (top left) 20 (top right) 50 (bottom left) and 100 (bottom right) millisecond time-averaging of the 8 kHz FLUTE signal.

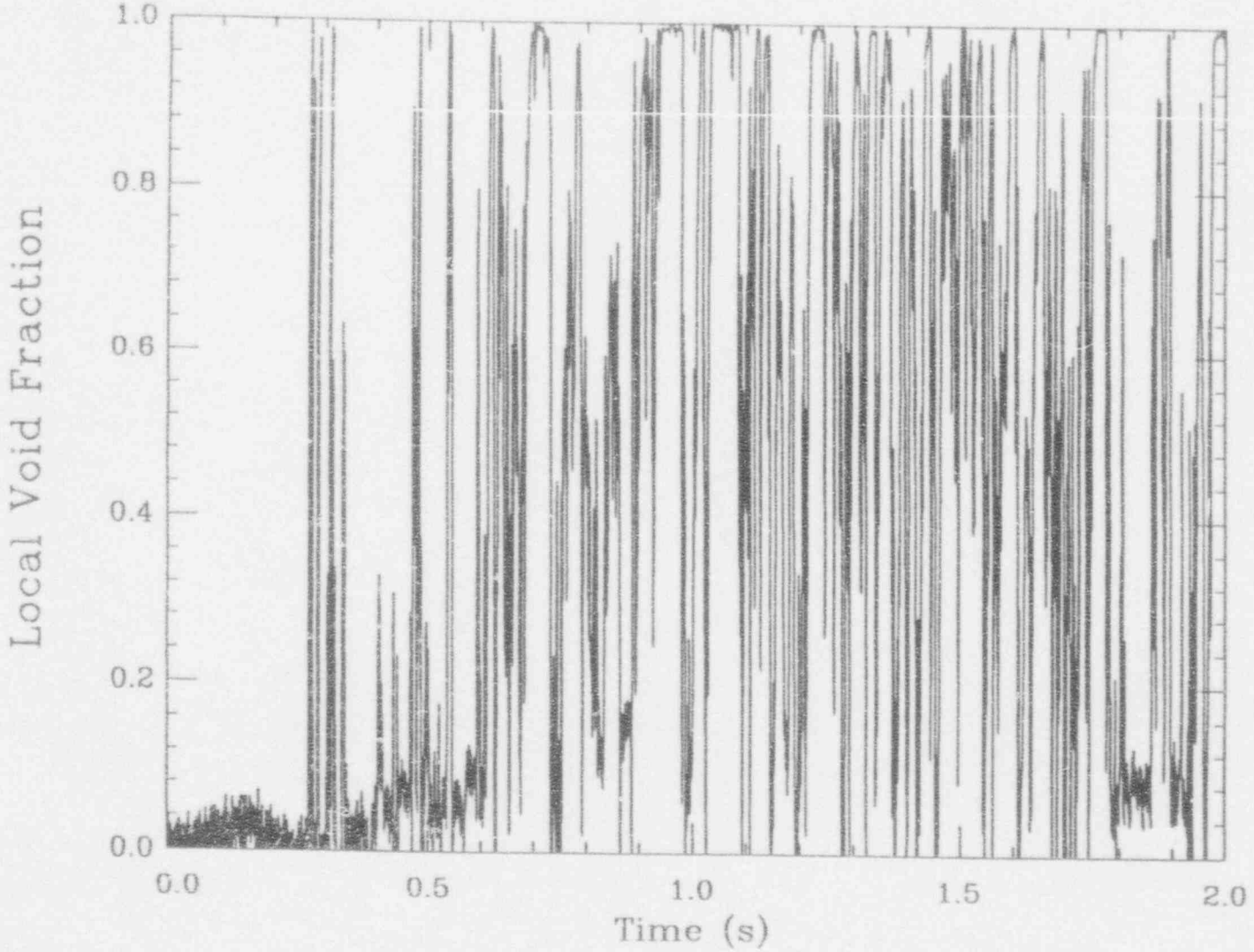

Figure I.C.17. The FLUTE signal for Run #301, position #1 (sampling rate 8 kHz).

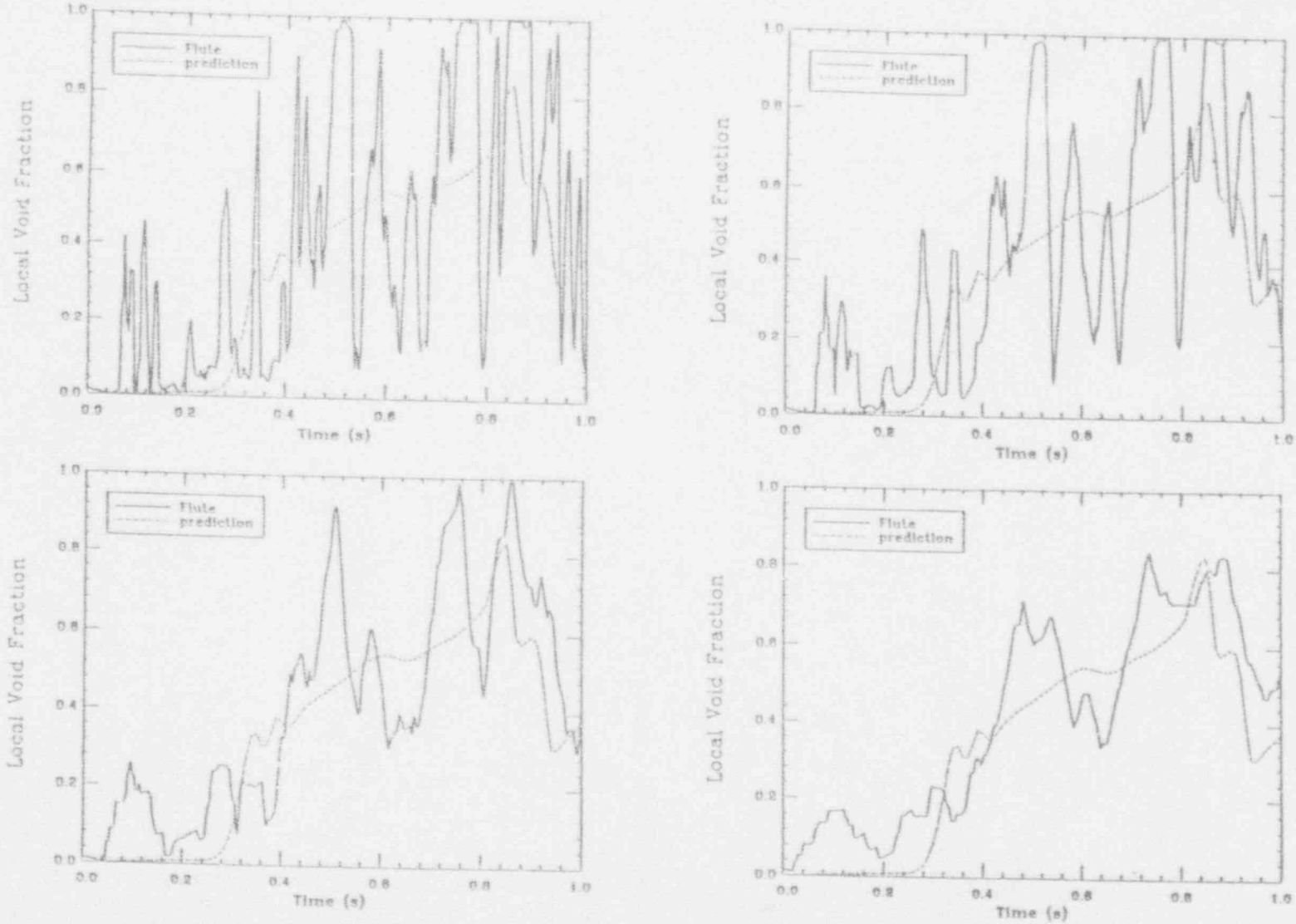

Figure I.C.18. The local void fraction transient for Run #301, position #1 as deduced by 10 (top left) 20 (top right) 50 (bottom left) and 100 (bottom right) millisecond time-averaging of the 8 kHz FLUTE signal.

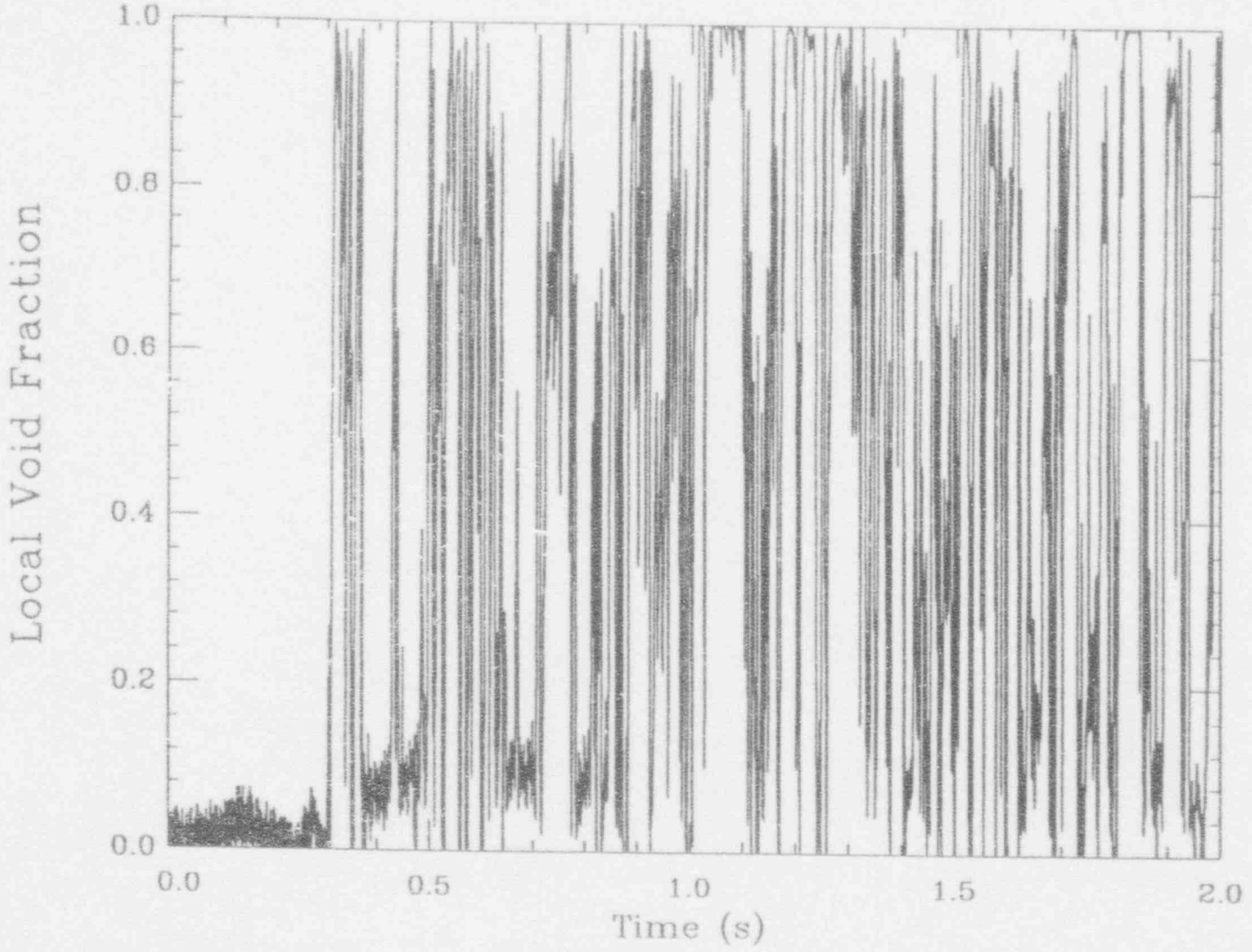

Figure I.C.19. The FLUTE signal for Run #301, position #2 (sampling rate 8 kHz).

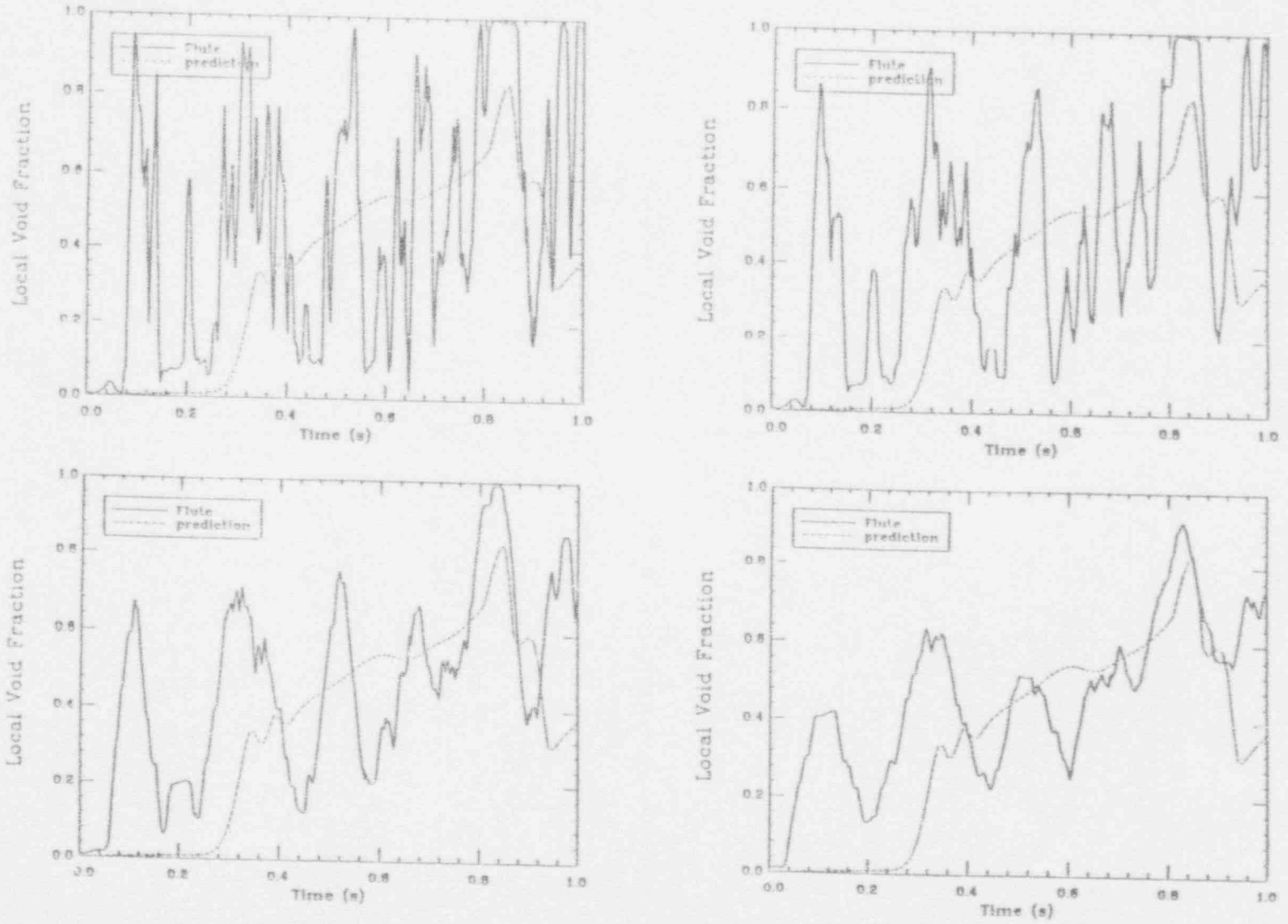

Figure I.C.20. The local void fraction transient for Run #301, position #2 as deduced by 10 (top left) 20 (top right) 50 (bottom left) and 100 (bottom right) ms second time-averaging of the 8 kHz FLUTE signal.

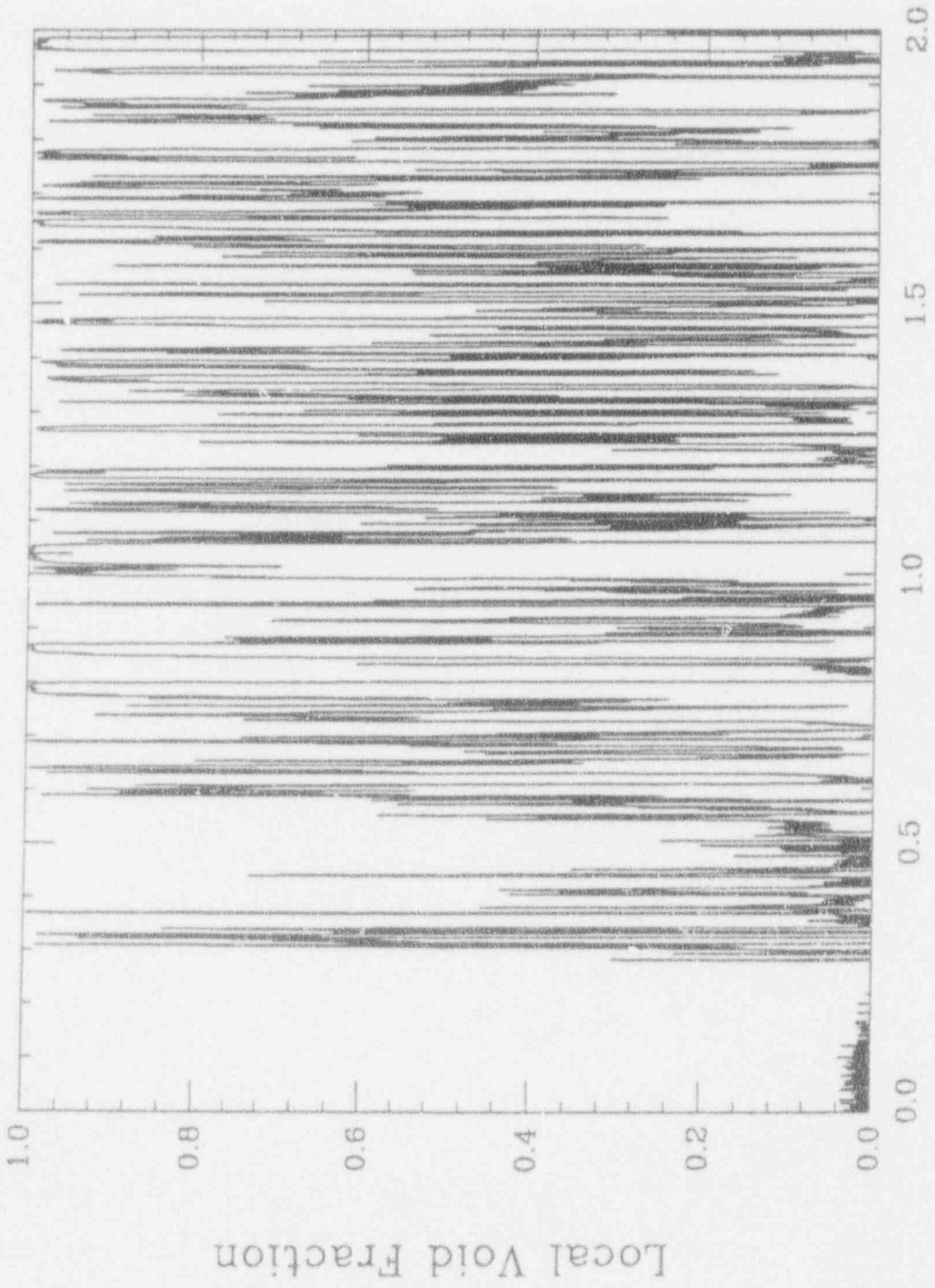

Figure I.C.21. The FLUTE signal for Run #302, position #1 (sampling rate 8 kHz).

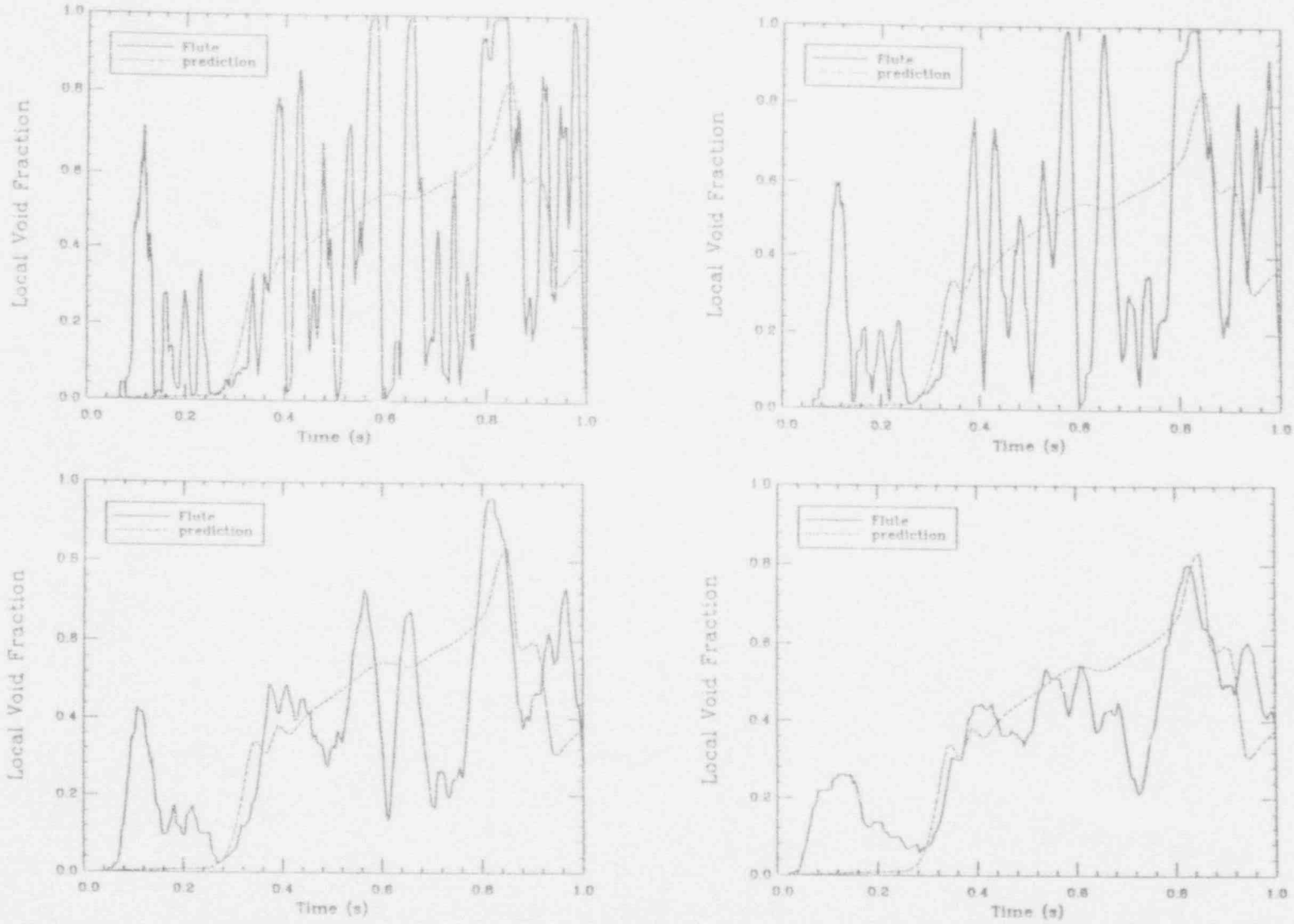

Figure I.C.22. The local void fraction transient for Run #302, position #1 as deduced by 10 (top left) 20 (top right) 50 (bottom left) and 100 (bottom right) millisecond time-averaging of the 8 kHz FLUTE signal.

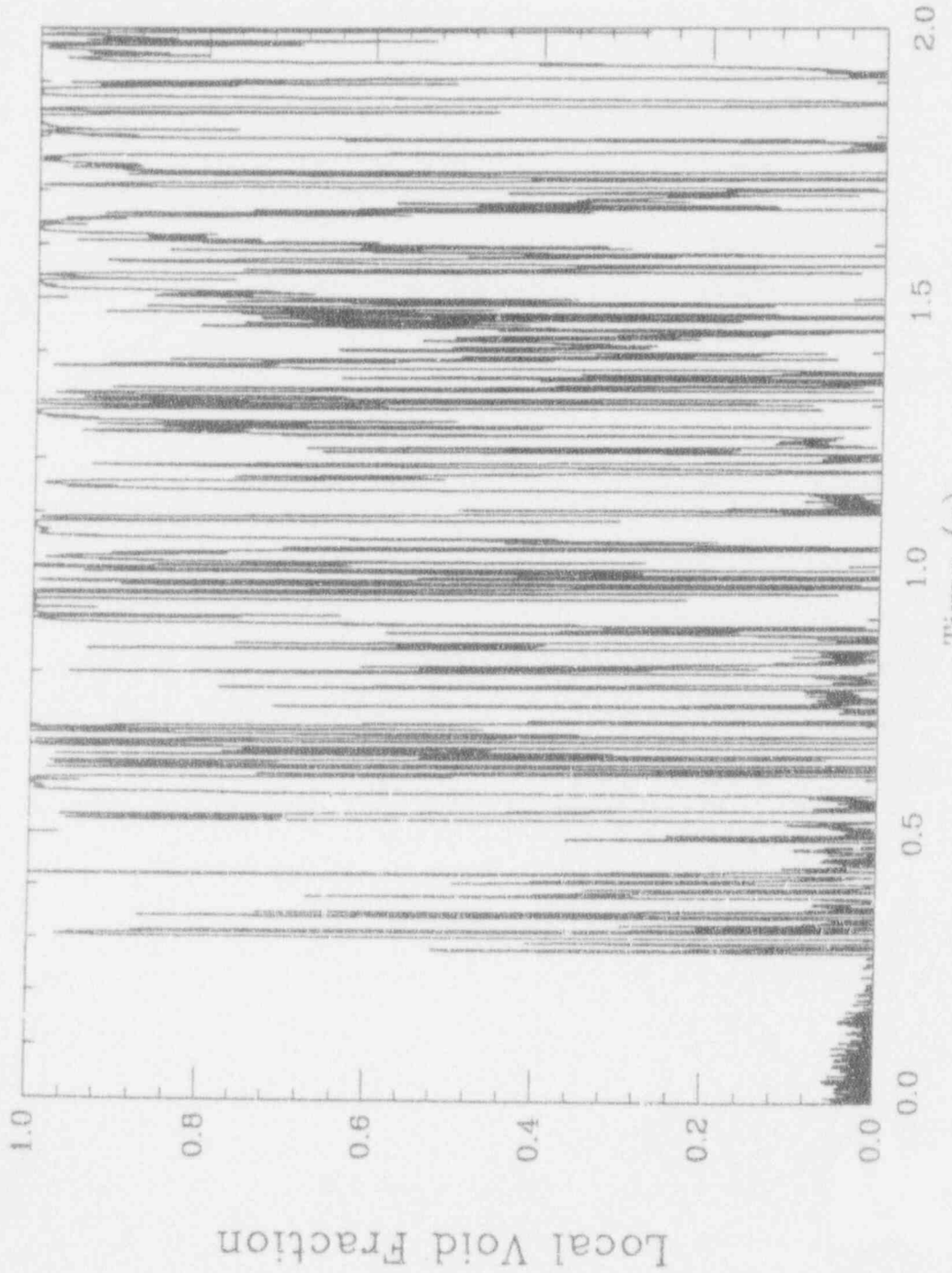

Figure I.C.23. The FLUTE signal for Run #302, position #2 (sampling rate 8 kHz).

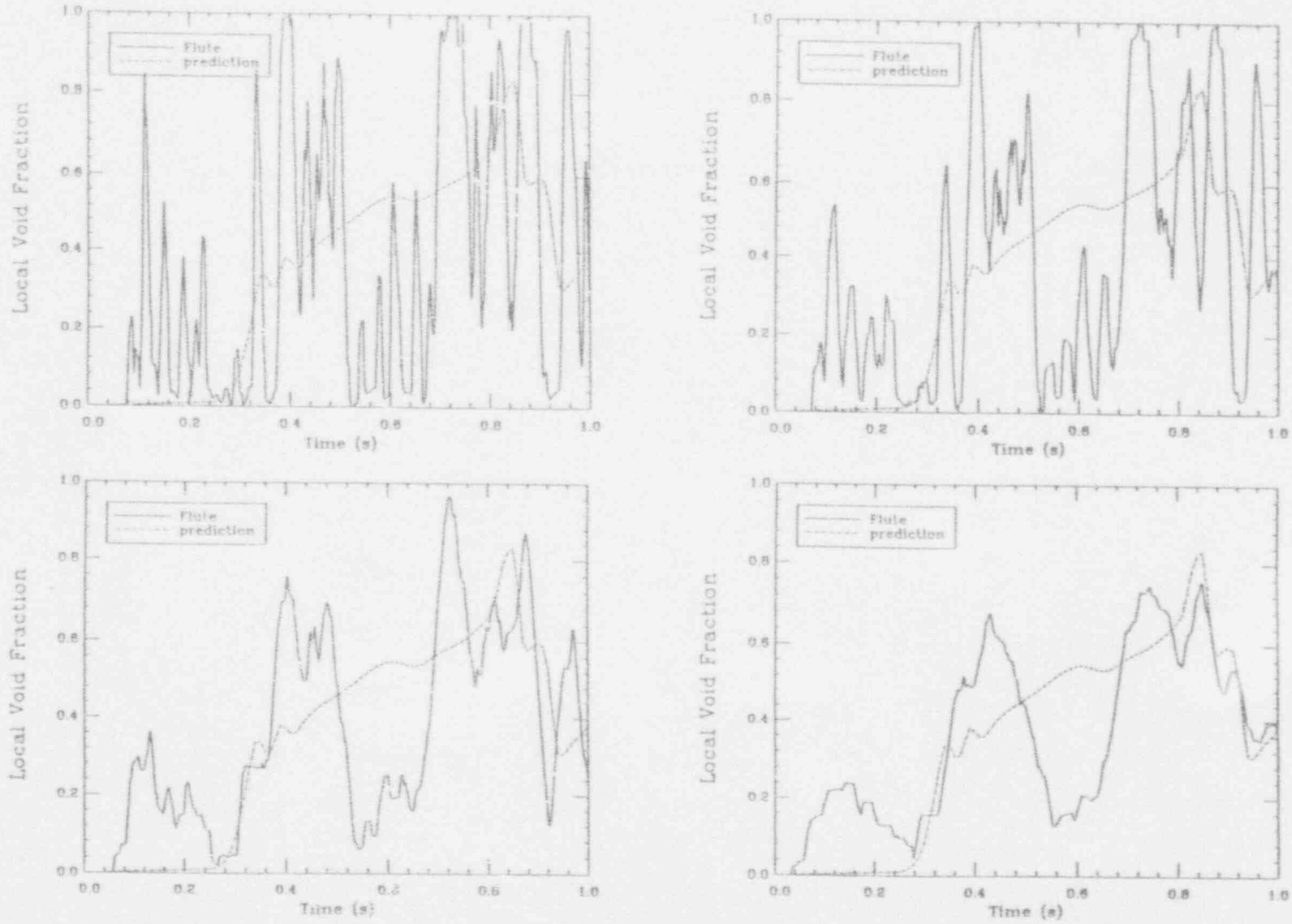

Figure I.C.24. The local void fraction transient for Run #302, position #2 as deduced by 10 (top left) 20 (top right) 50 (bottom left) and 100 (bottom right) millisecond time-averaging of the 8 kHz FLUTE signal.

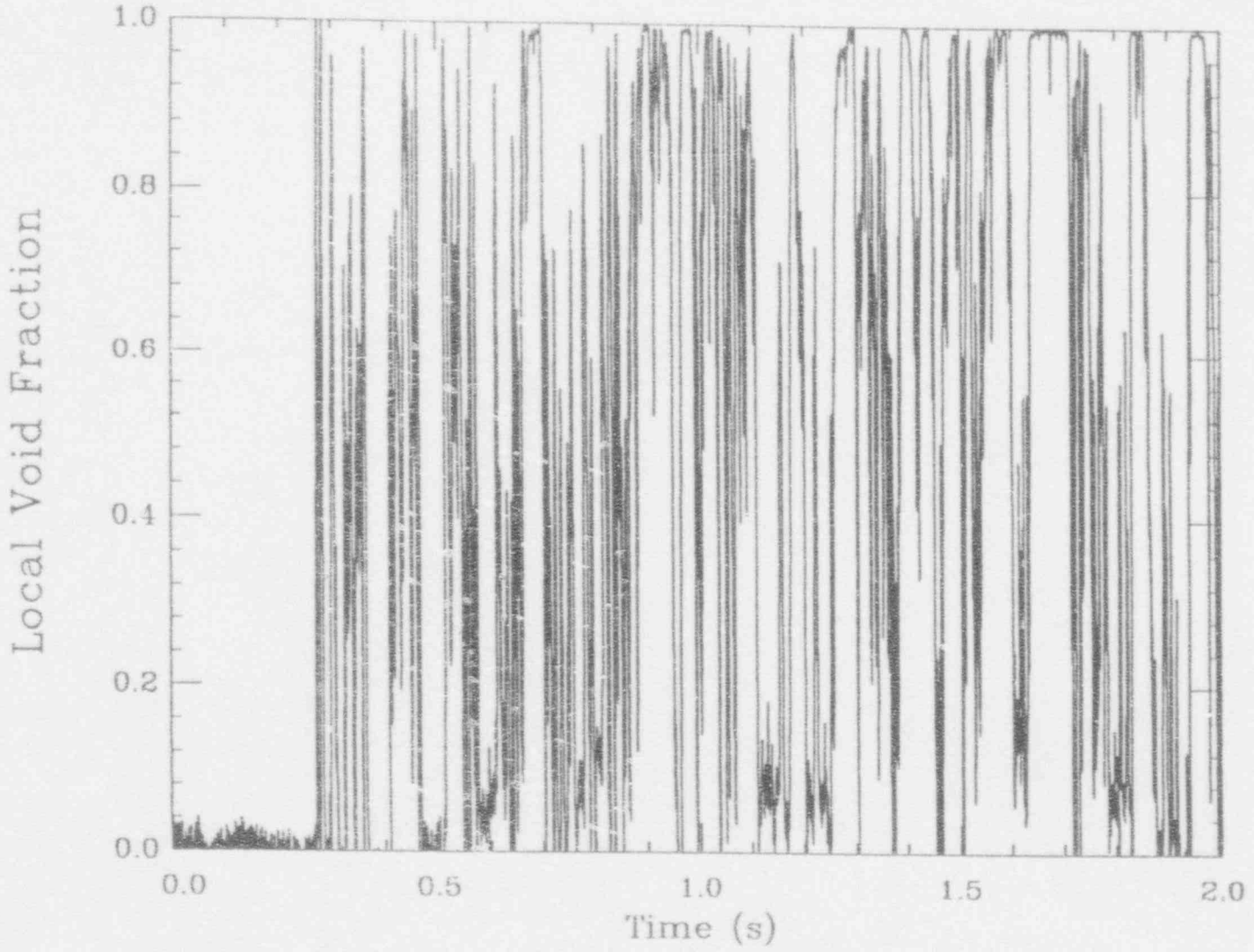

Figure I.C.25. The FLUTE signal for Run #303, position #1 (sampling rate 8 kHz).

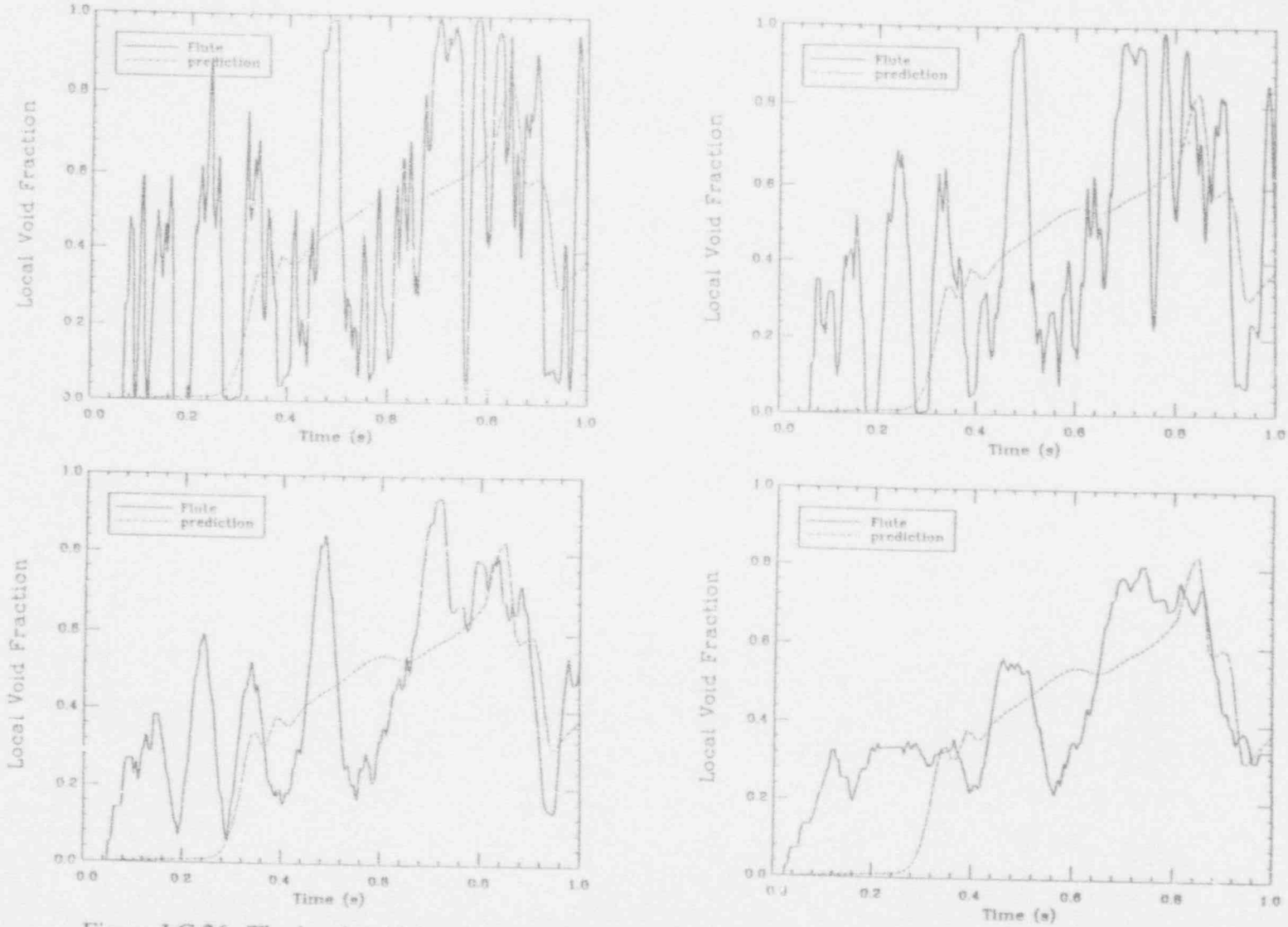

Figure I.C.26. The local void fraction transient for Run #303, position #1 as deduced by 10 (top left) 20 (top right) 50 (bottom left) and 100 (bottom right) millisecond time-averaging of the 8 kHz FLUTE signal.

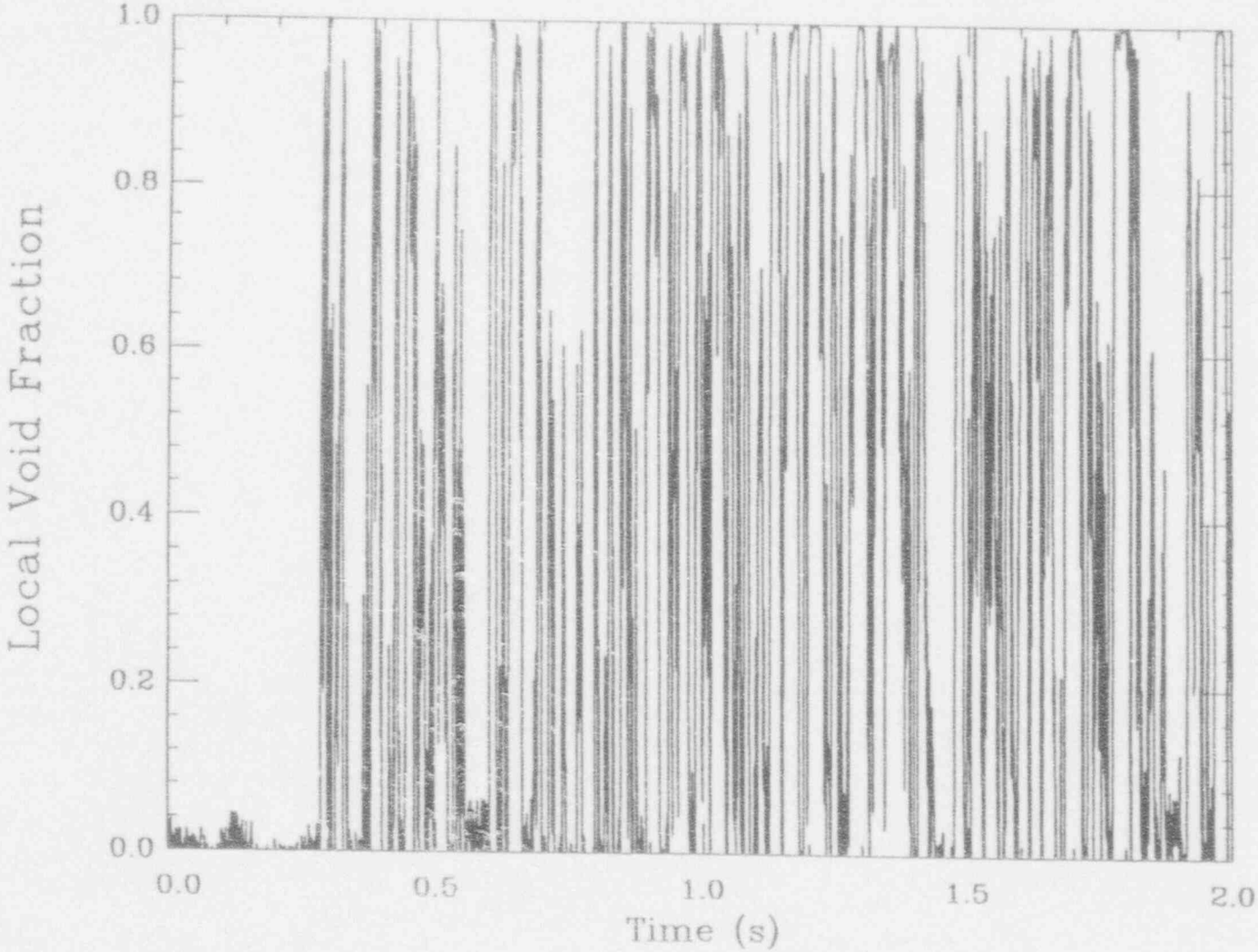

Figure I.C.27. The FLUTE signal for Run #303, position #2 (sampling rate 8 kHz).

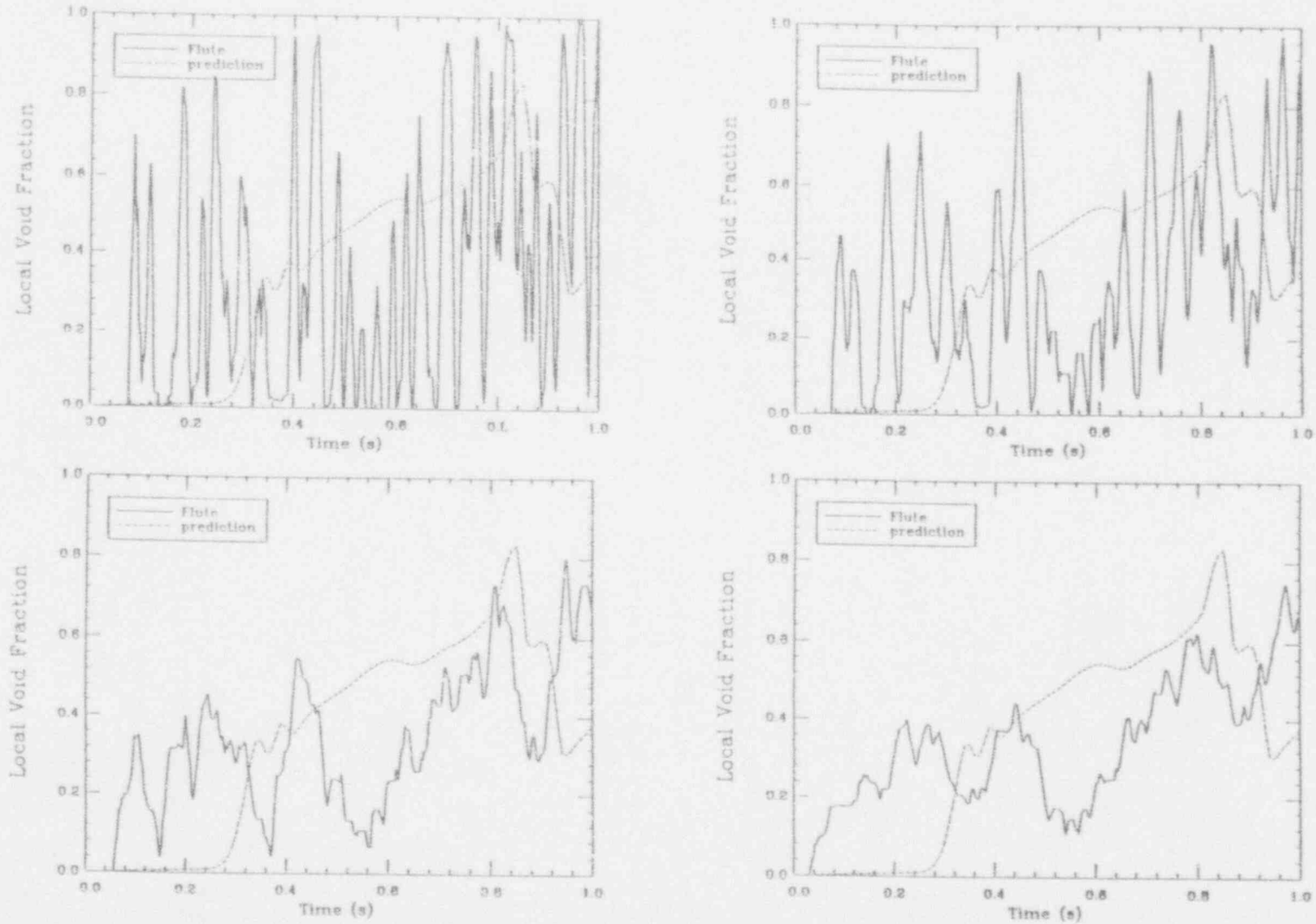

Figure I.C.28. The local void fraction transient for Run #303, position #2 as deduced by 10 (top left) 20 (top right) 50 (bottom left) and 100 (bottom right) millisecond time-averaging of the 8 kHz FLUTE signal.

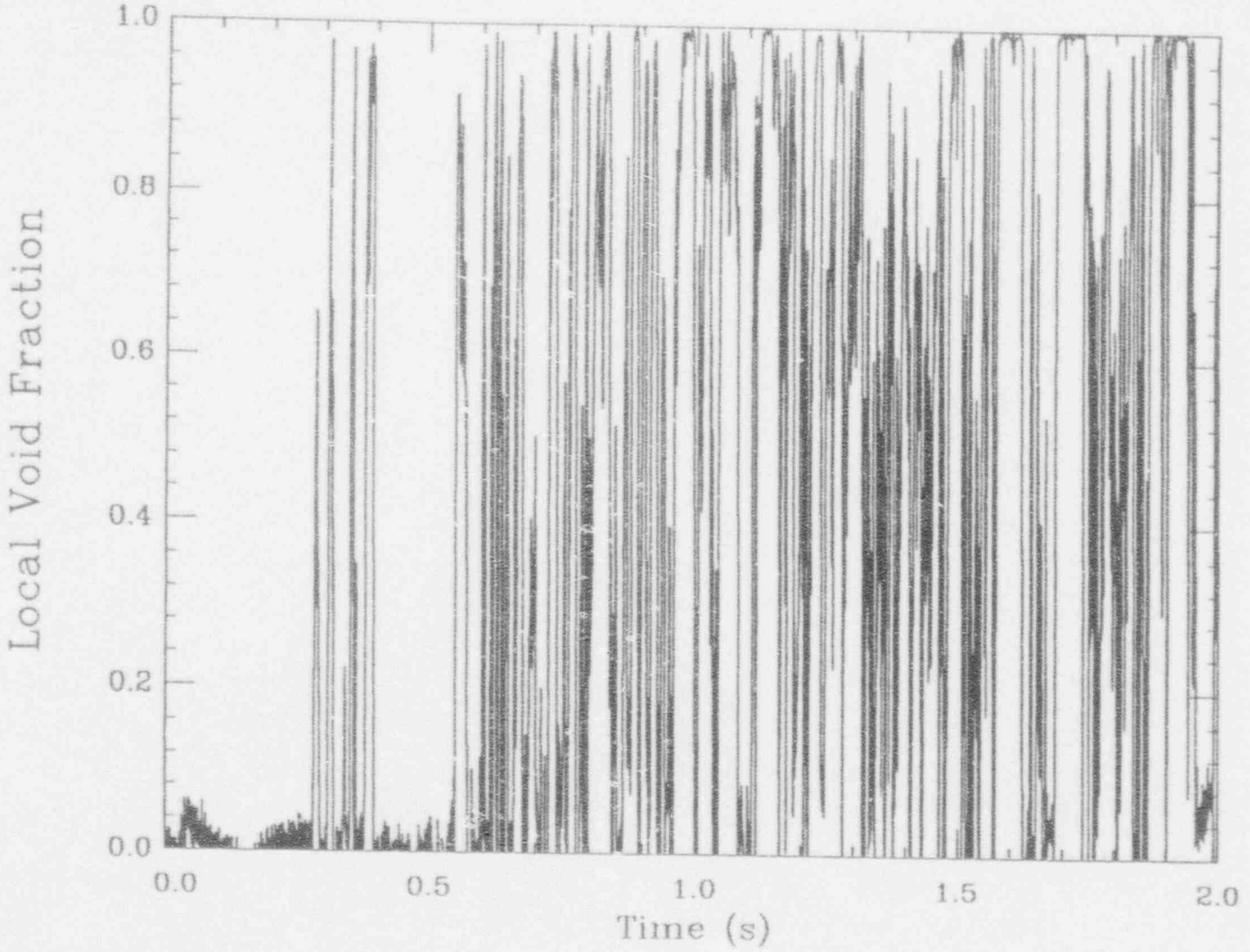

Figure I.C.29. The FLUTE signal for Run #304, position #1 (sampling rate 8 kHz).

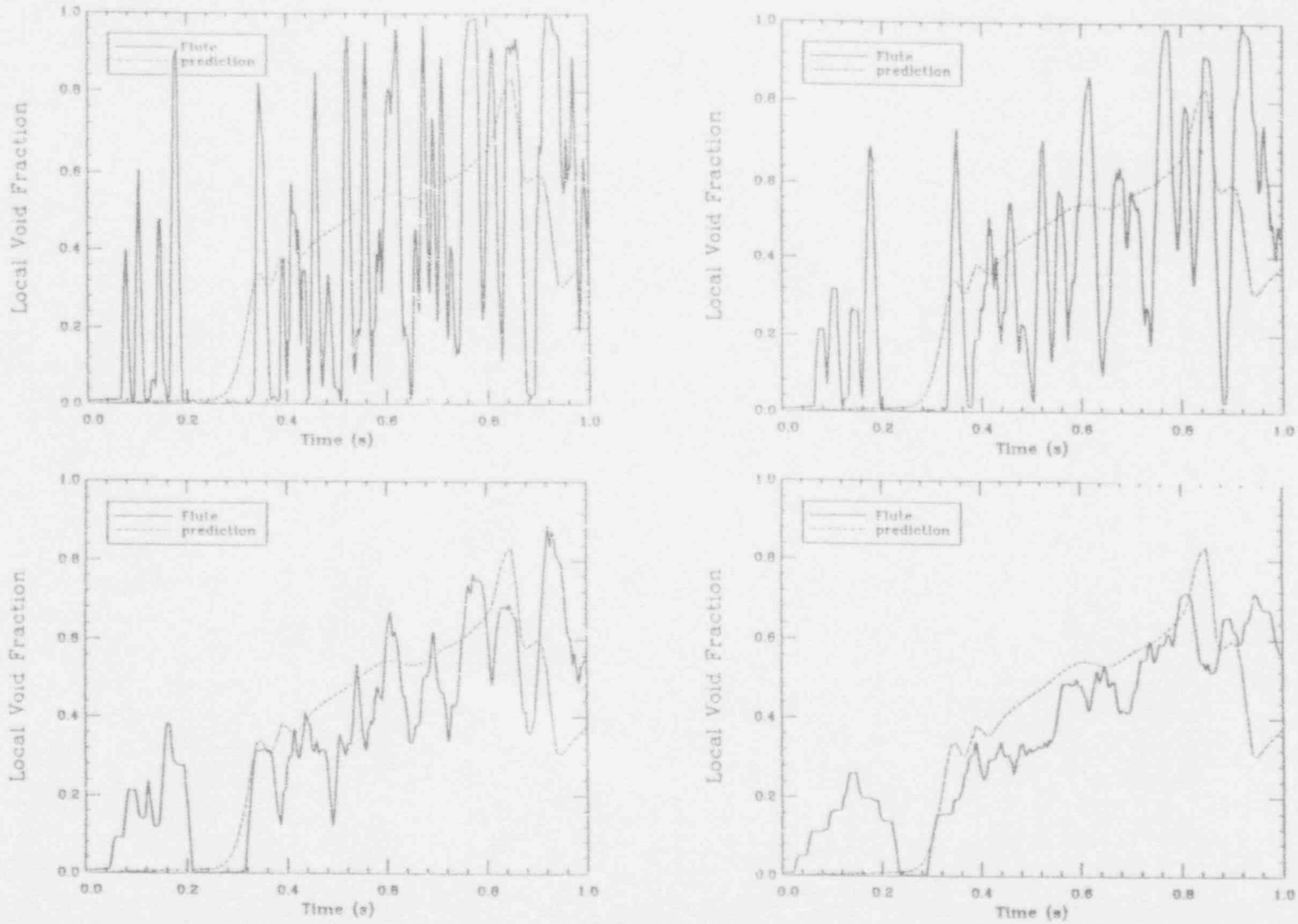

Figure I.C.30. The local void fraction transient for Run #304, position #1 as deduced by 10 (top left) 20 (top right) 50 (bottom left) and 100 (bottom right) millisecond time-averaging of the 8 kHz FLUTE signal.

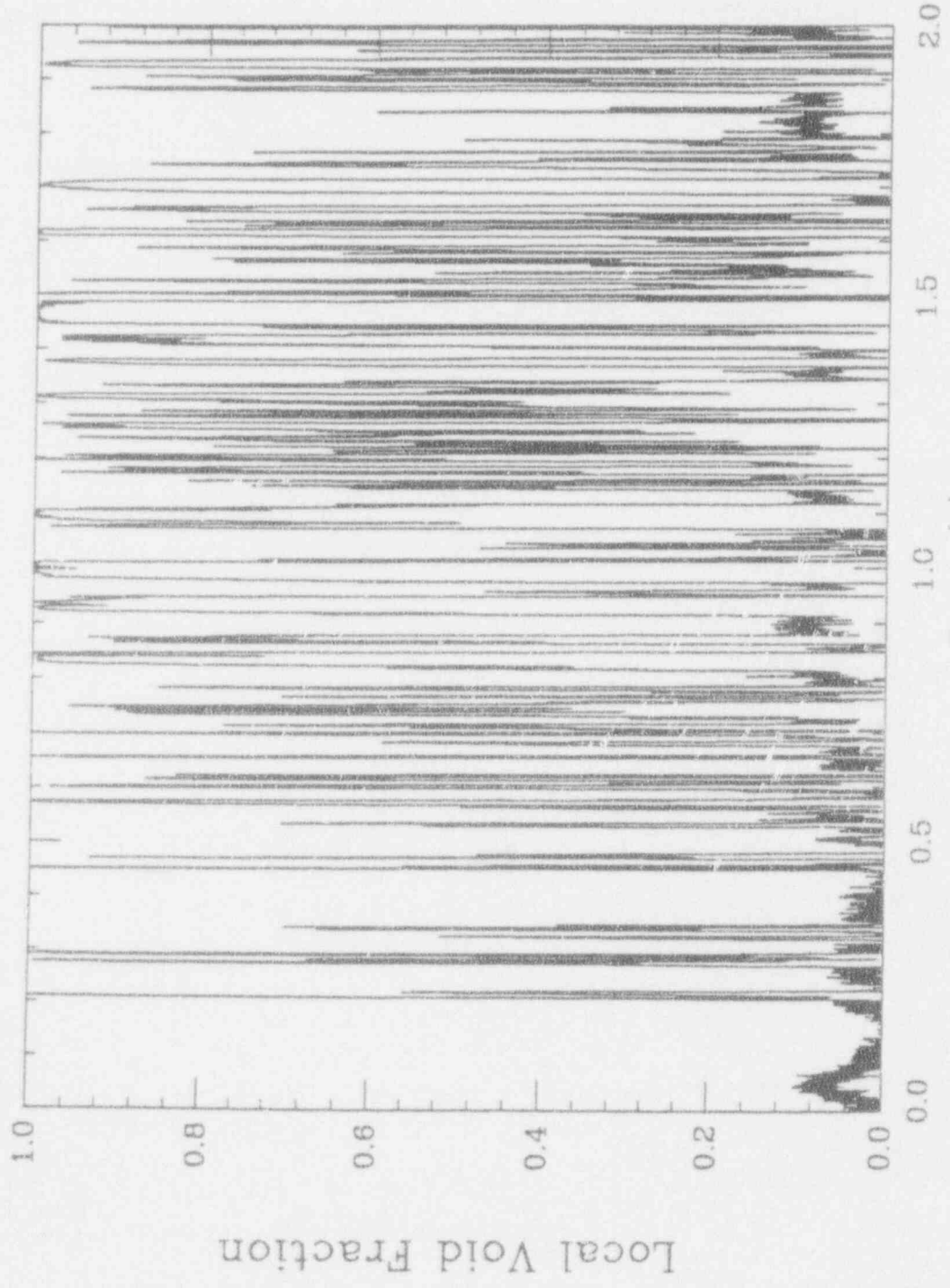

Figure I.C.31. The FLUTE signal for Run #304, position #2 (sampling rate 8 kHz).

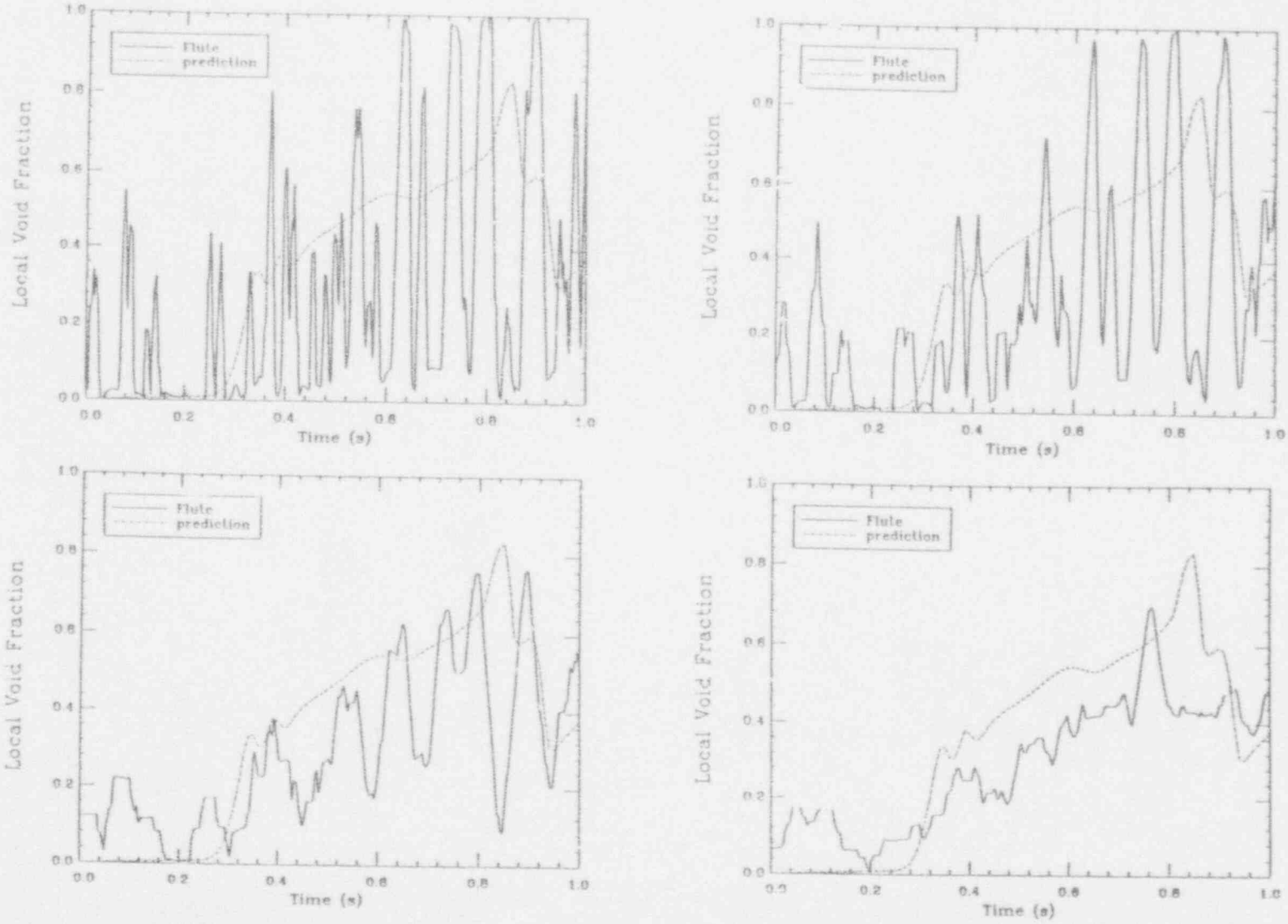

Figure I.C.32. The local void fraction transient for Run #304, position #2 as deduced by 10 (top left) 20 (top right) 50 (bottom left) and 100 (bottom right) millisecond time-averaging of the 8 kHz FLUTE signal.

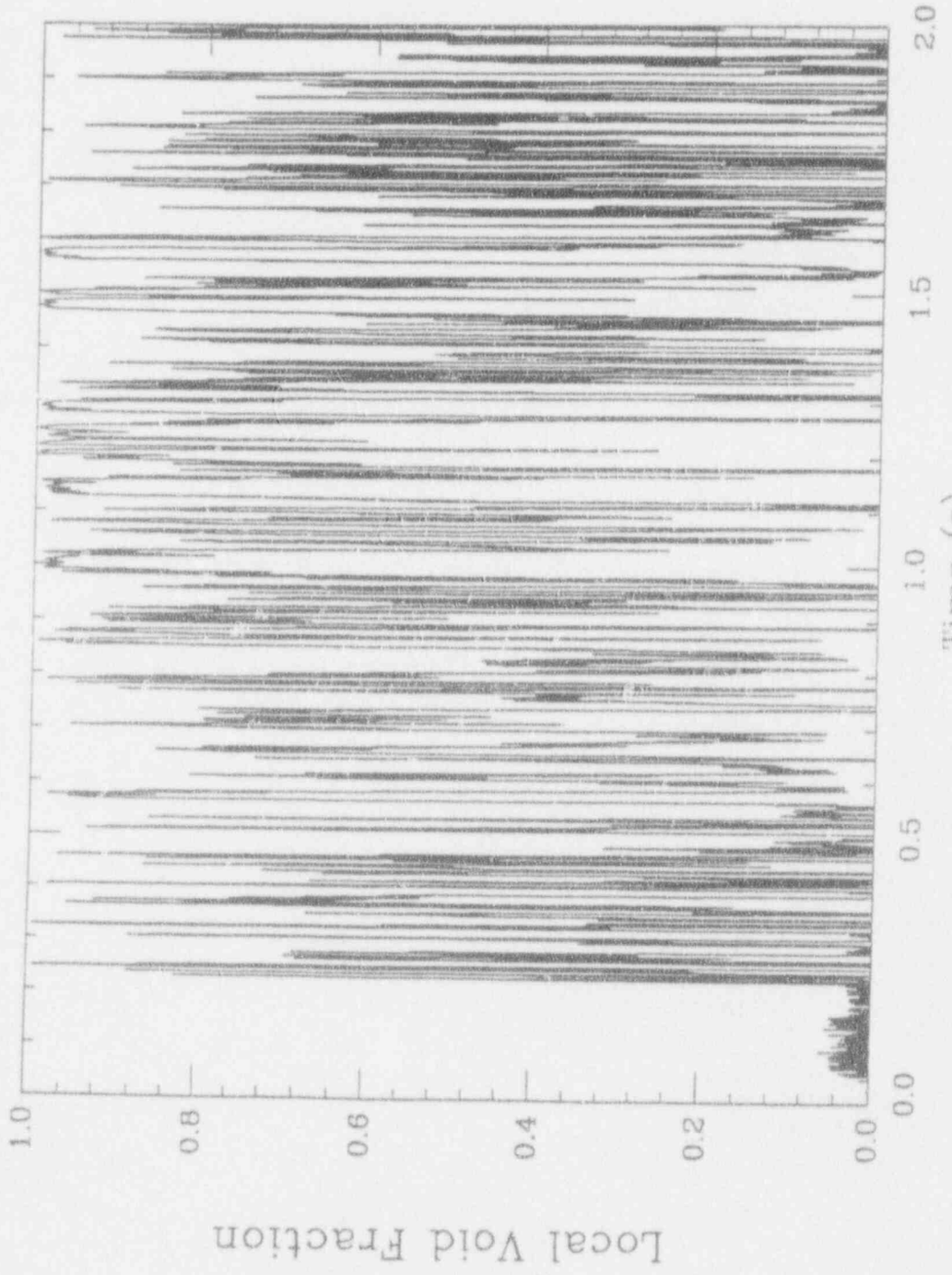

Figure I.C.33. The FLUTE signal for Run #305, position #1 (sampling rate 8 kHz).

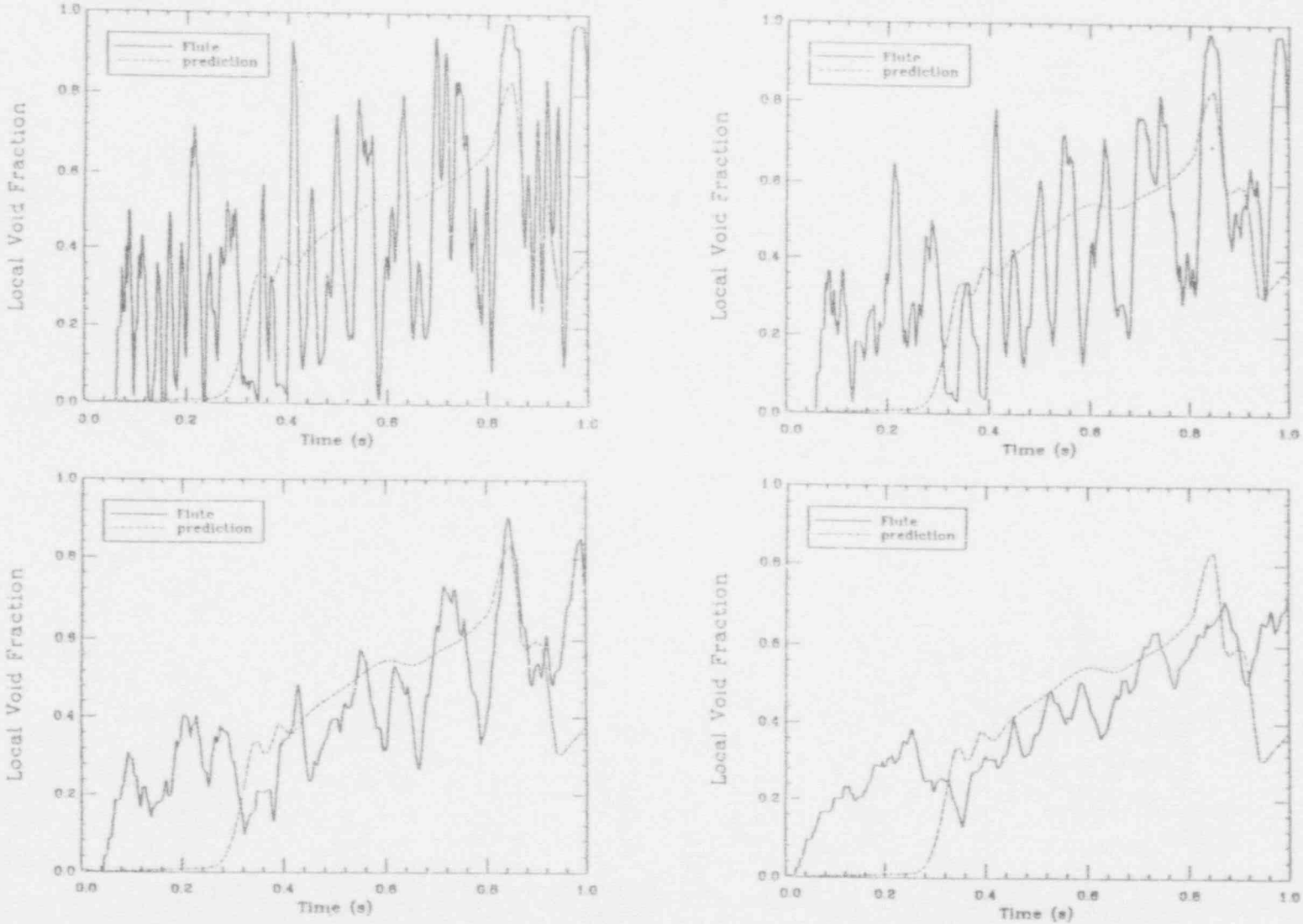

Figure I.C.34. The local void fraction transient for Run #305, position #1 as deduced by 10 (top left) 20 (top right) 50 (bottom left) and 100 (bottom right) millisecond time-averaging of the 8 kHz FLUTE signal.

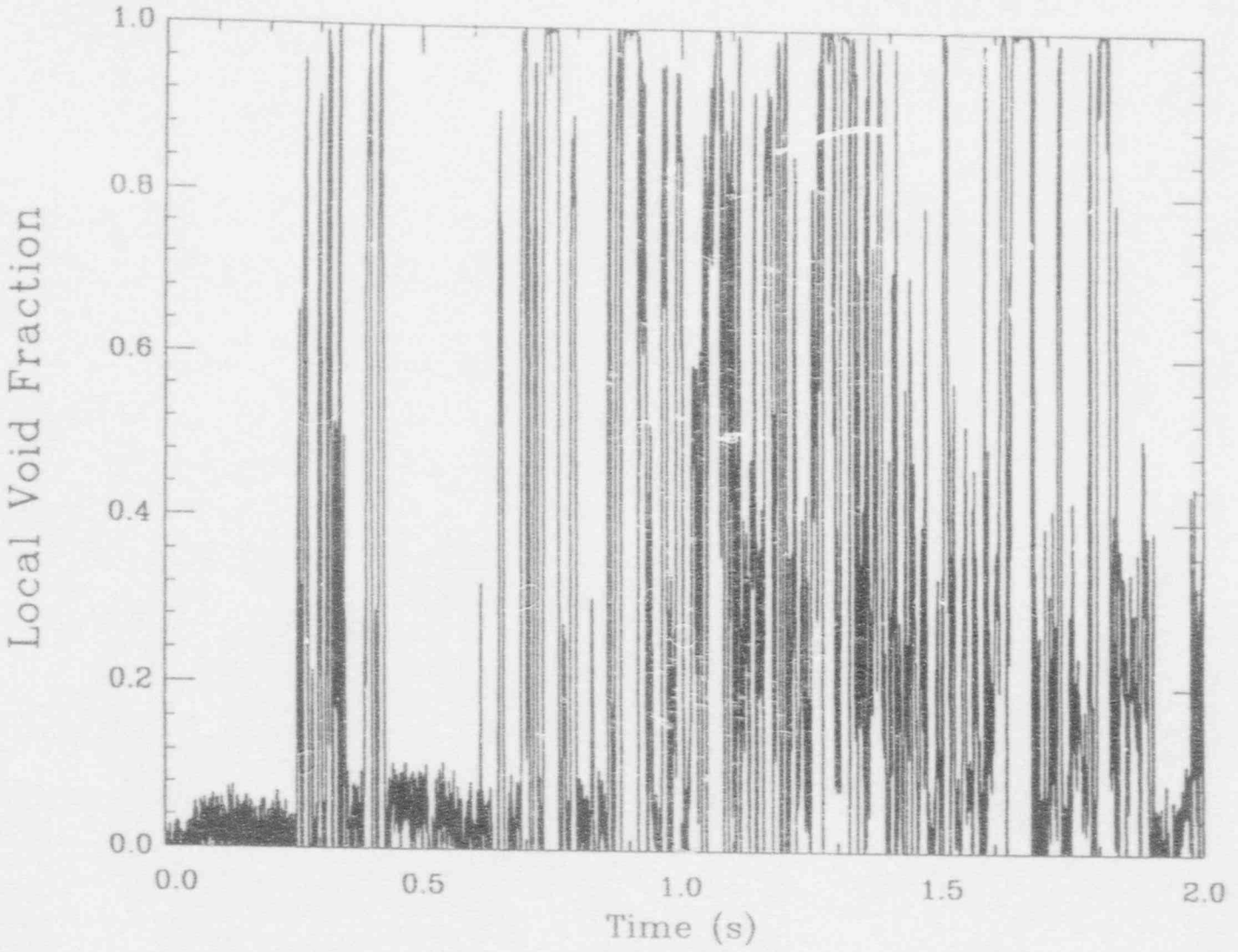

Figure I.C.35. The FLUTE signal for Run #305, position #2 (sampling rate 8 kHz).

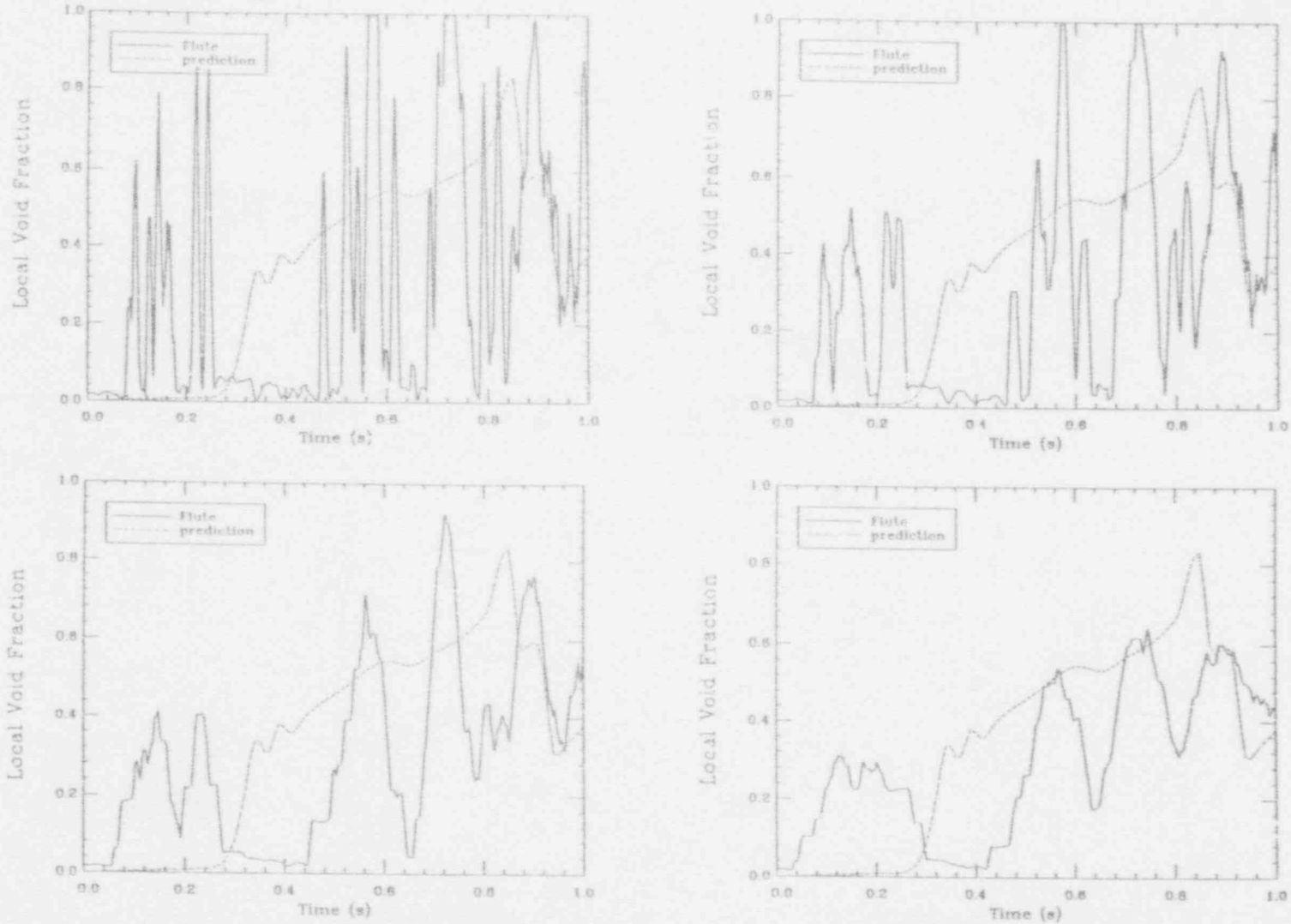

Figure I.C.36. The local void fraction transient for Run #305, position #2 as deduced by 10 (top left) 20 (top right) 50 (bottom left) and 100 (bottom right) millisecond time-averaging of the 8 kHz FLUTE signal.

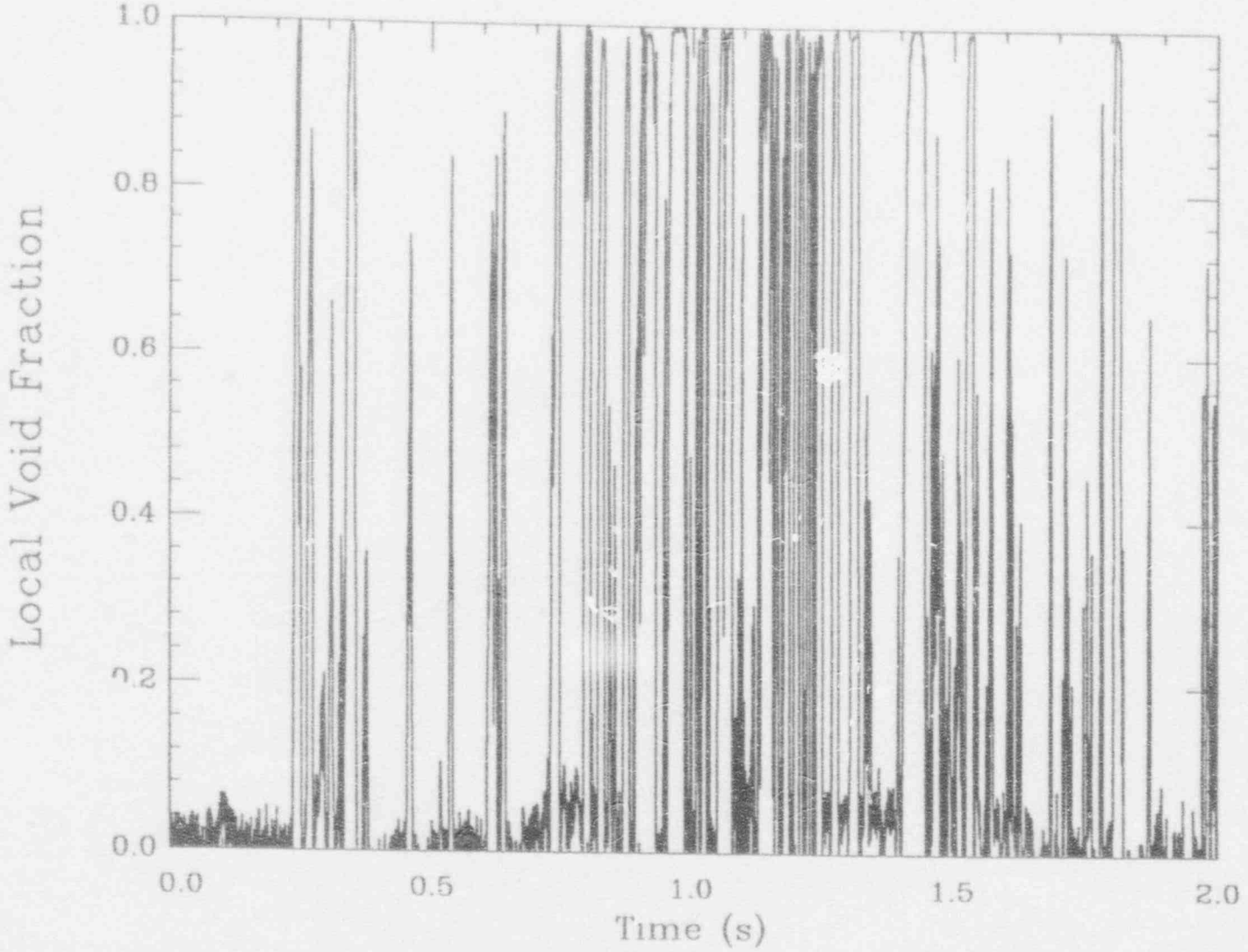

Figure I.C.37. The FLUTE signal for Run #401, position #1 (sampling rate 8 kHz).

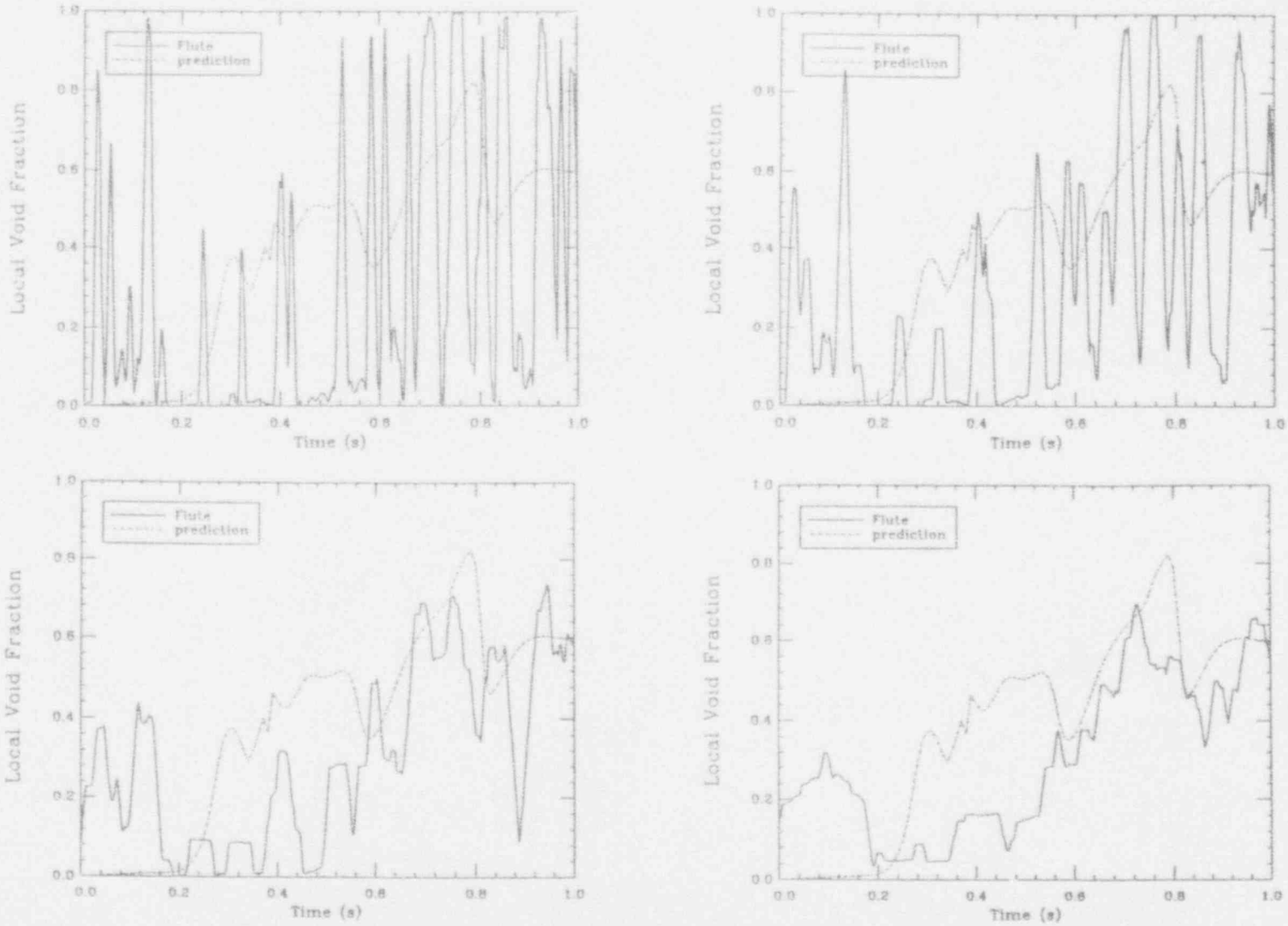

Figure I.C.38. The local void fraction transient for Run #401, position #1 as deduced by 10 (top left) 20 (top right) 50 (bottom left) and 100 (bottom right) millisecond time-averaging of the 8 kHz FLUTE signal.

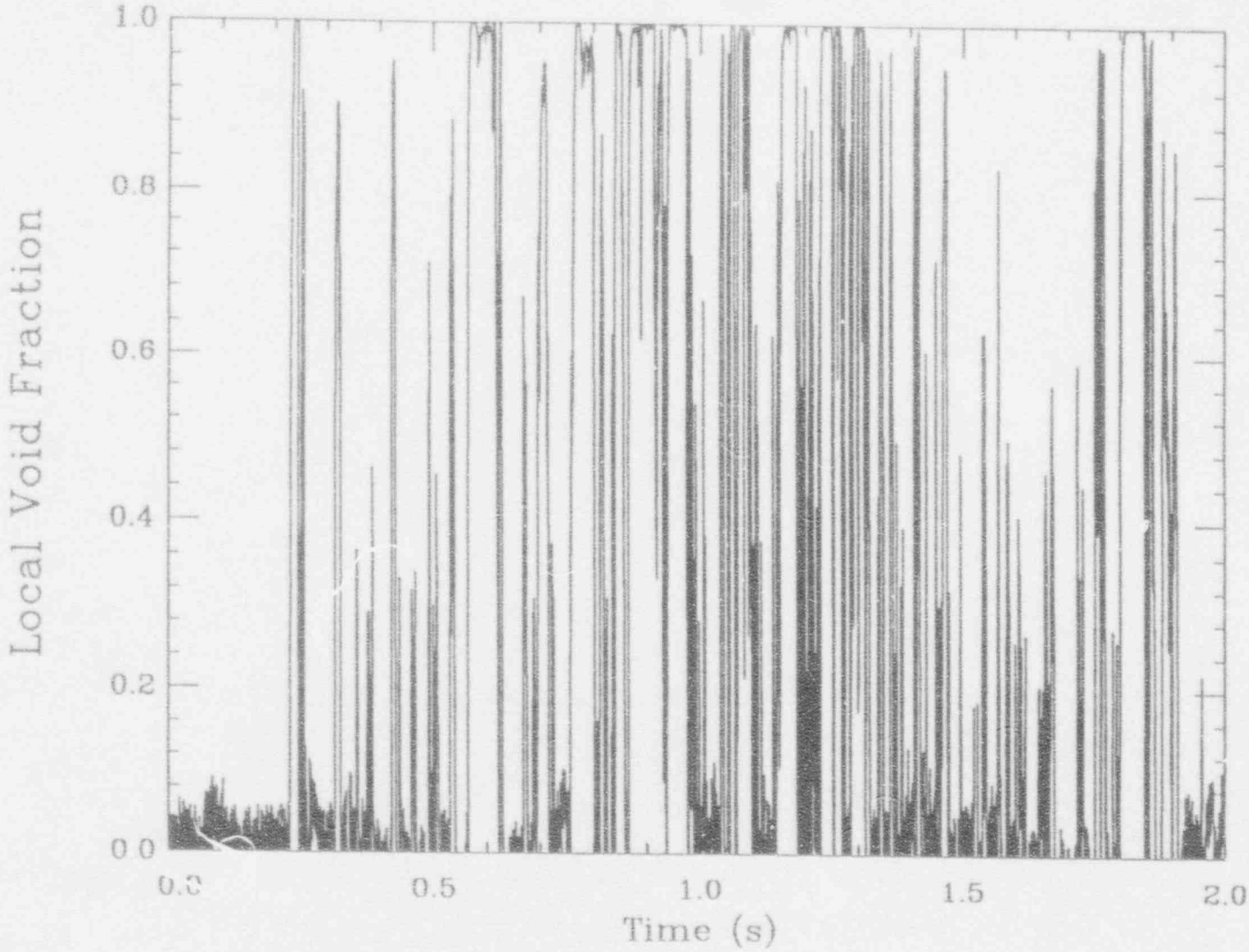

Figure I.C.39. The FLUTE signal for Run #401, position #2 (sampling rate 8 kHz).

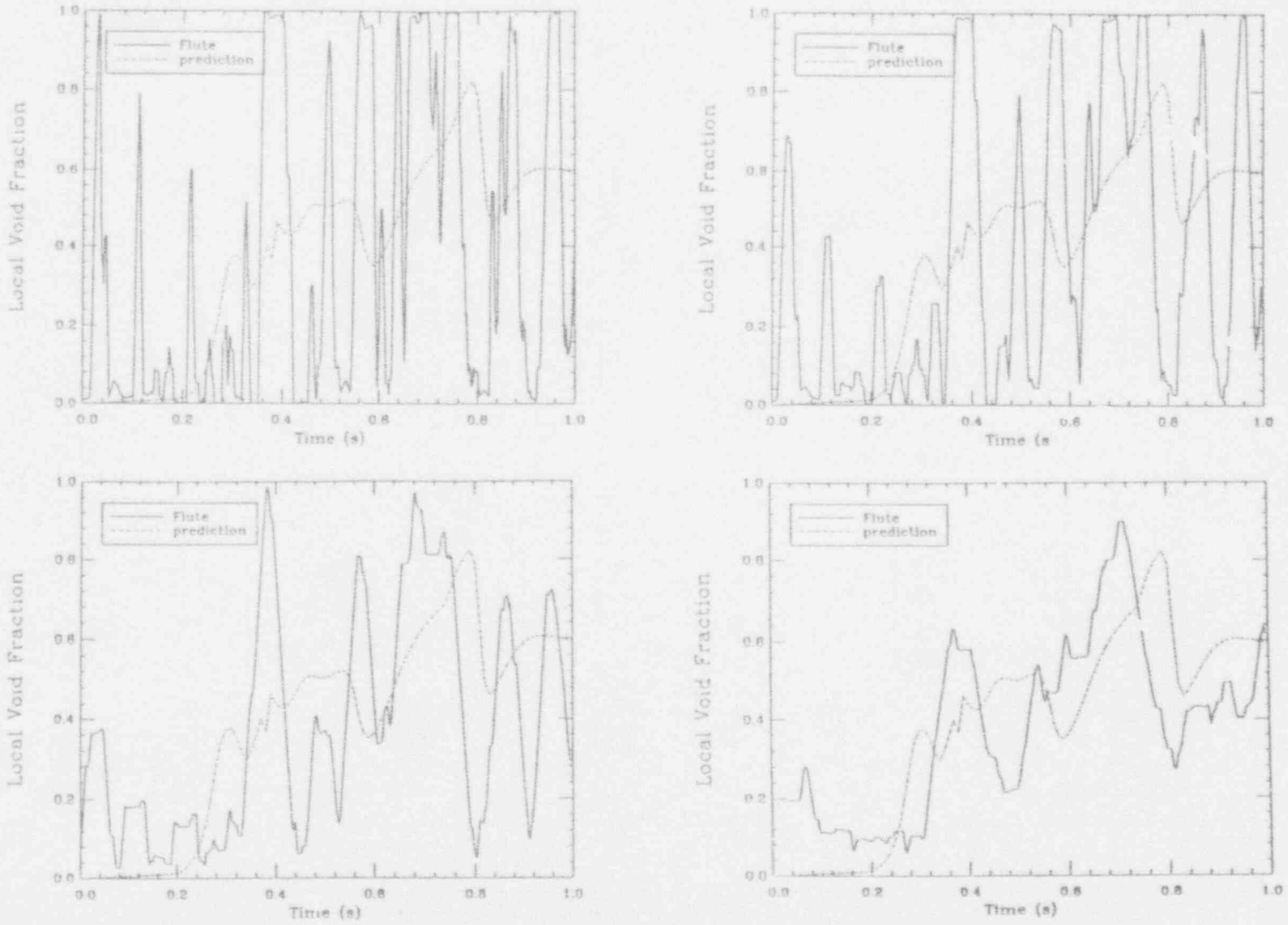

Figure I.C.40. The local void fraction transient for Run #401, position #2 as deduced by 10 (top left) 20 (top right) 50 (bottom left) and 100 (bottom right) millisecond time averaging of the 8 kHz FLUTE signal.

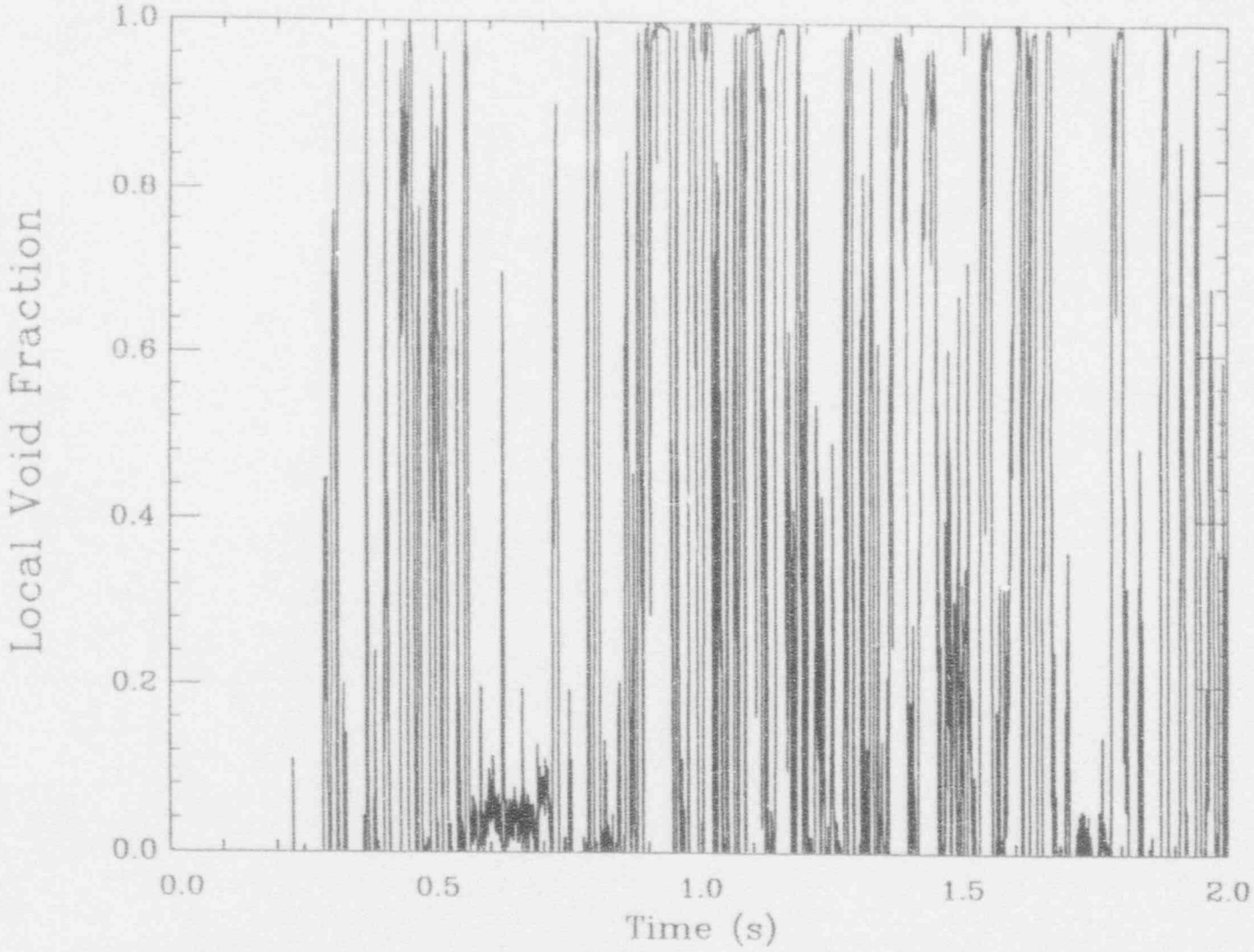

Figure I.C.41. The FLUTE signal for Run #402, position #1 (sampling rate 8 kHz).

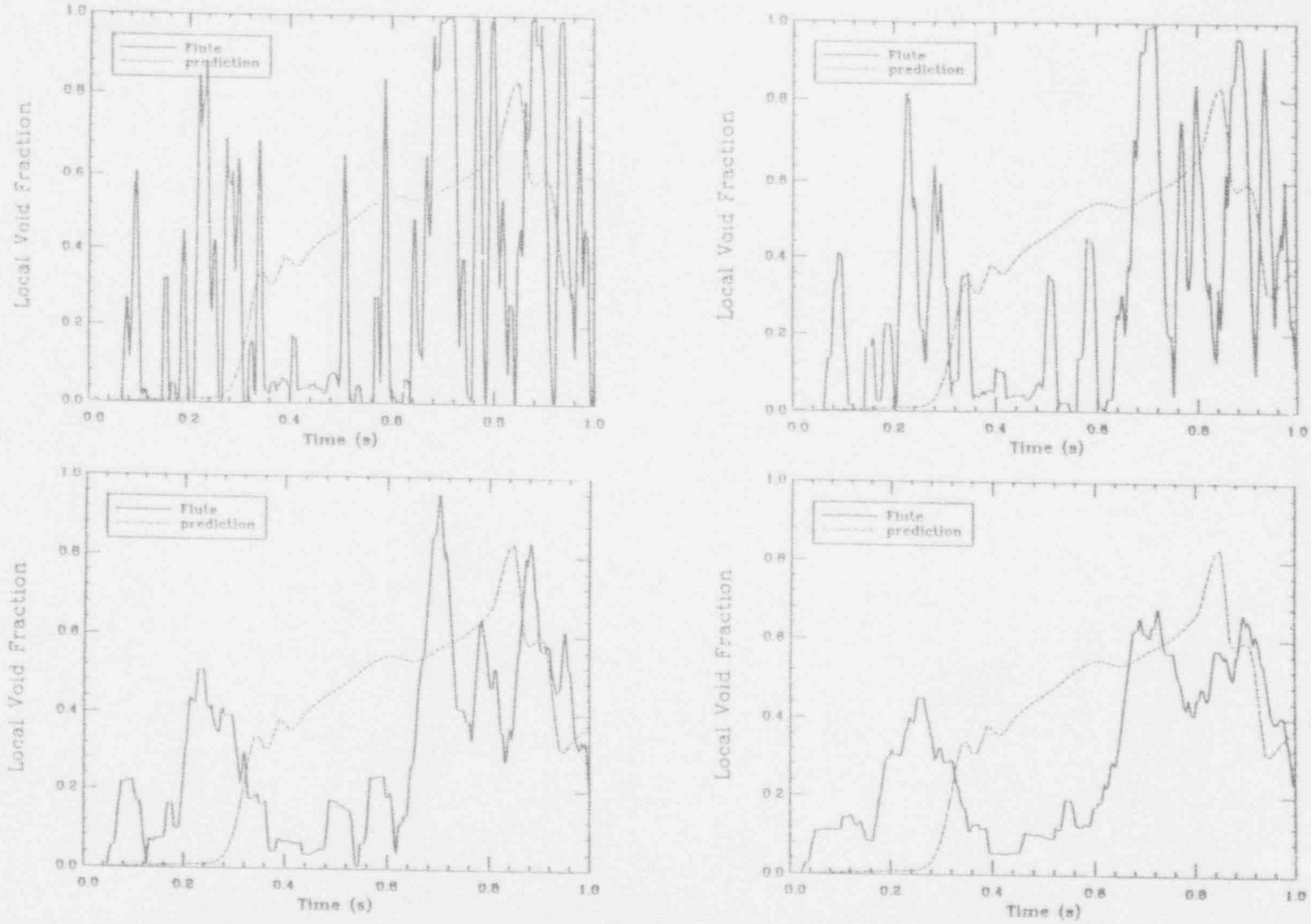

Figure I.C.42. The local void fraction transient for Run #402, position #1 as deduced by 10 (top left) 20 (top right) 50 (bottom left) and 100 (bottom right) millisecond time-averaging of the 8 kHz FLUTE signal.

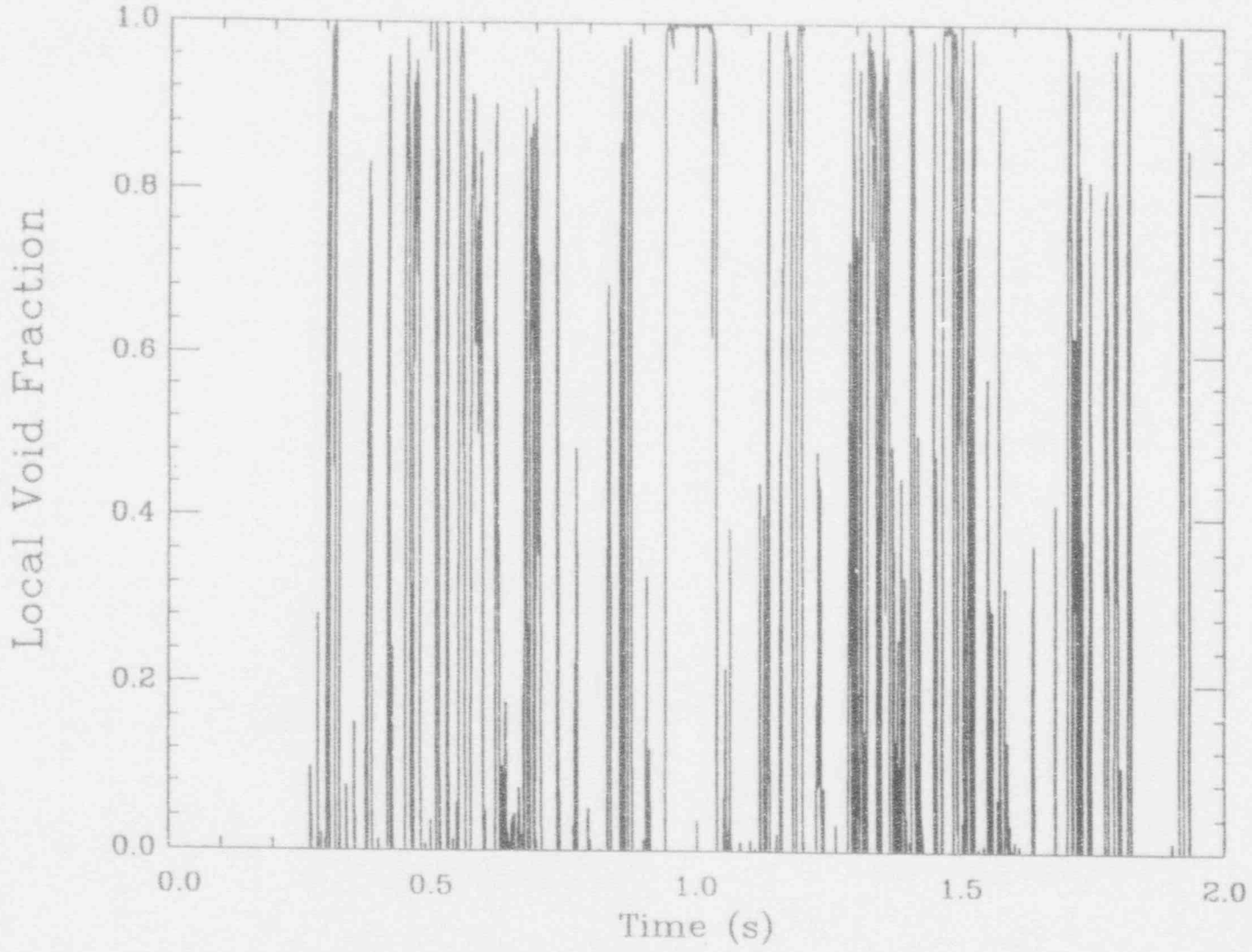

Figure I.C.43. The FLUTE signal for Run #402, position #2 (sampling rate 8 kHz).

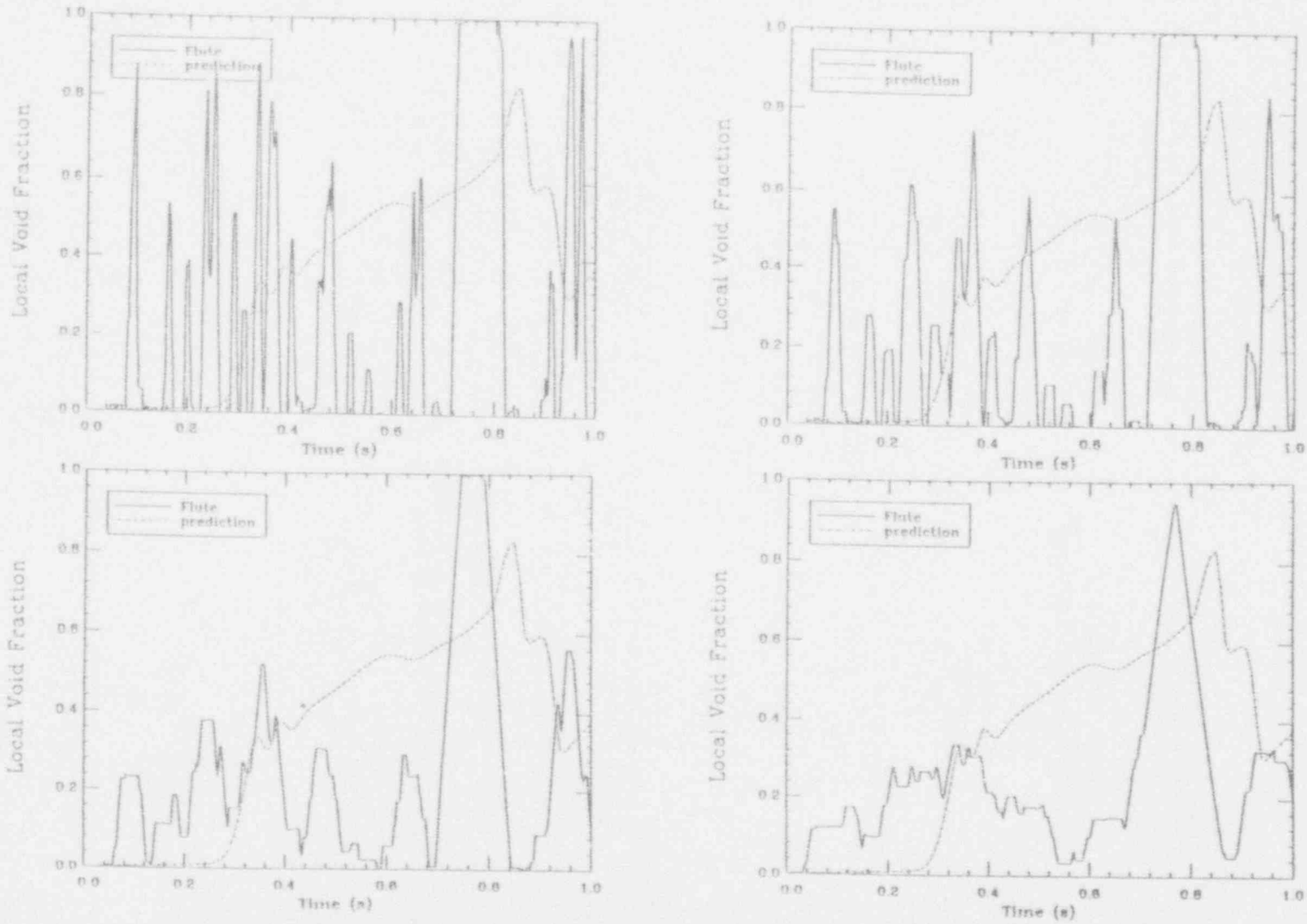

Figure I.C.44. The local void fraction transient for Run #402, position #2 as deduced by 10 (top left) 20 (top right) 50 (bottom left) and 100 (bottom right) millisecond time-averaging of the 8 kHz FLUTE signal.

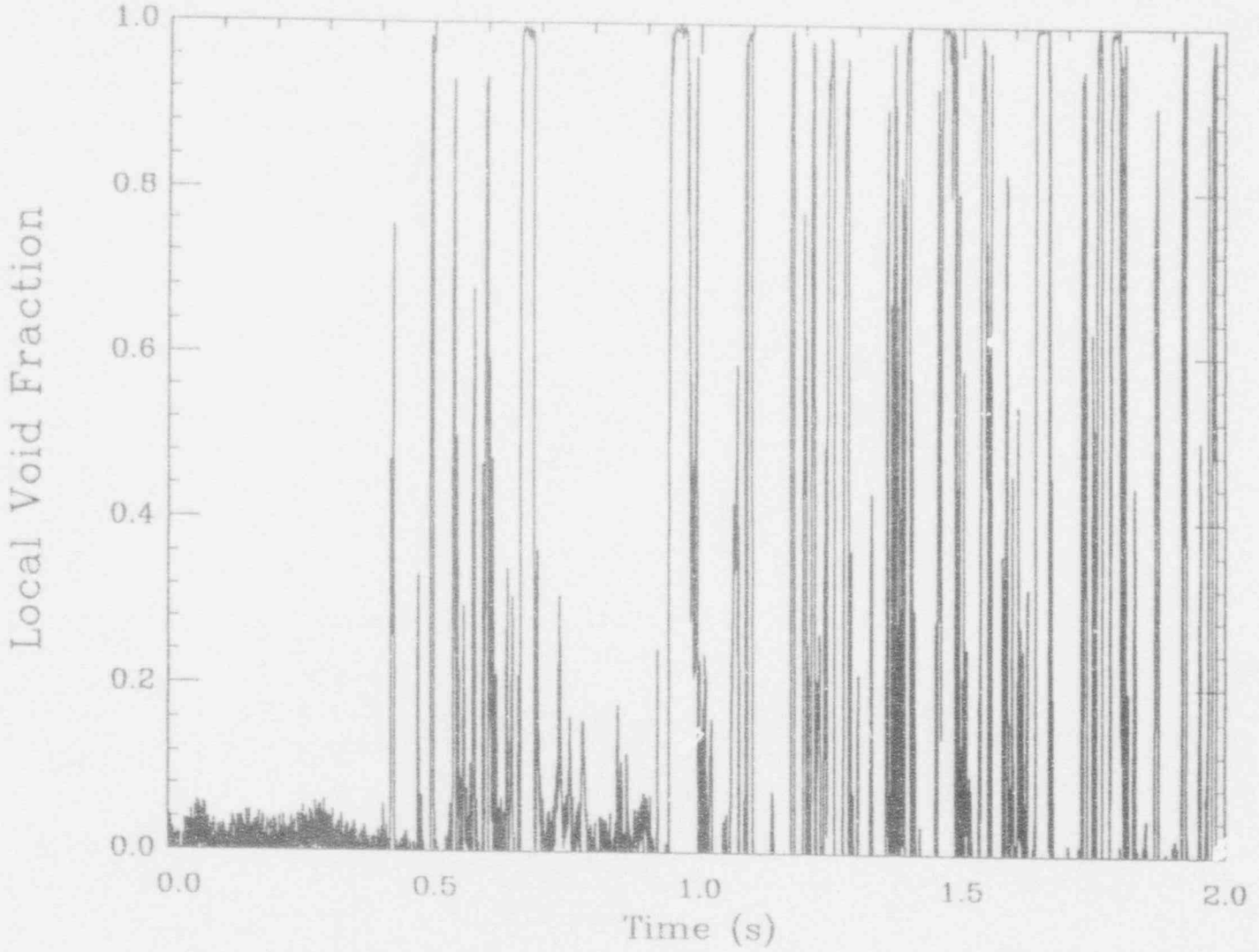

Figure I.C.45. The FLUTE signal for Run #403, position #1 (sampling rate 8 kHz).

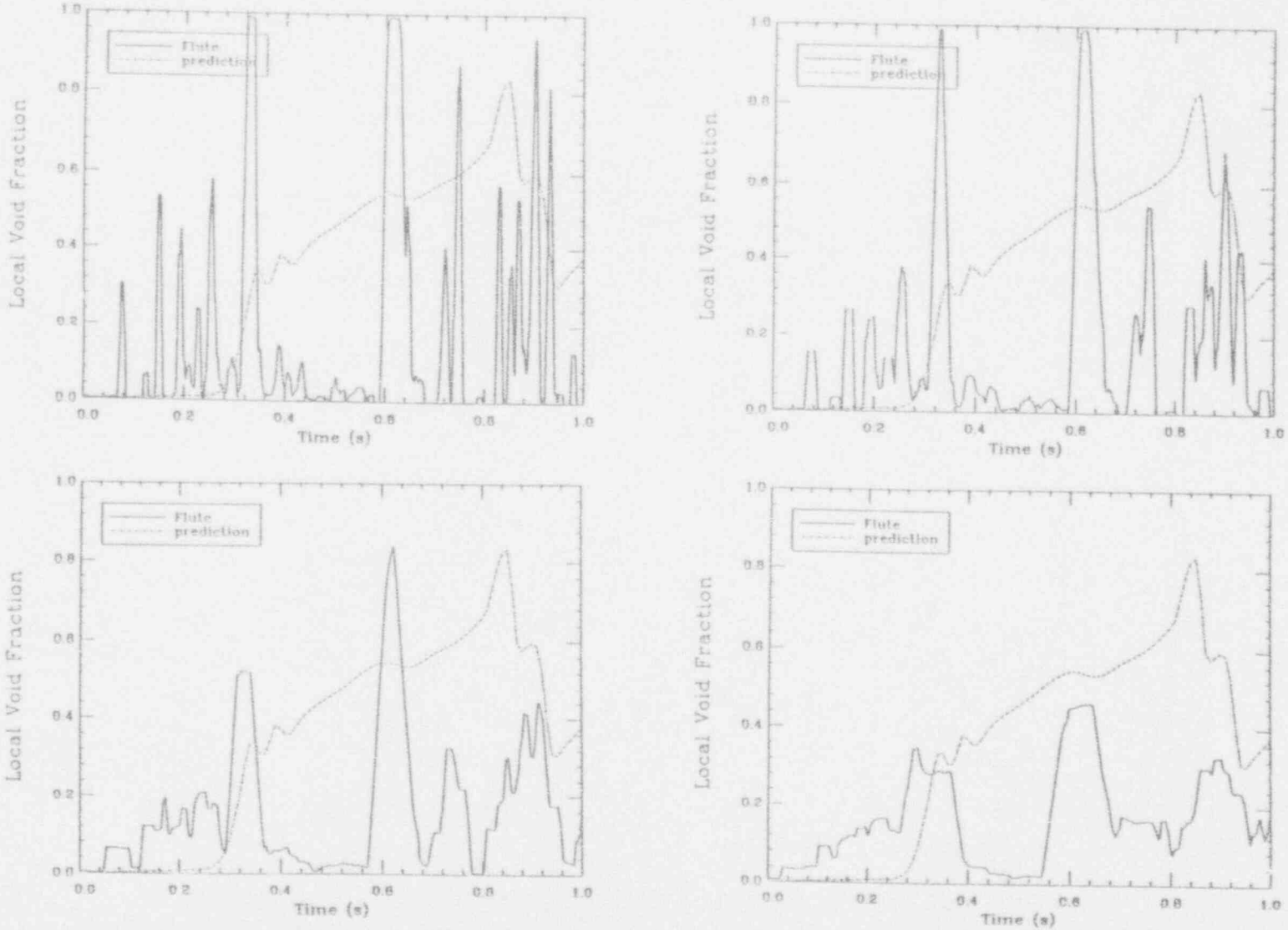

Figure I.C.46. The local void fraction transient for Run #403, position #1 as deduced by 10 (top left) 20 (top right) 50 (bottom left) and 100 (bottom right) millisecond time-averaging of the 8 kHz FLUTE signal.

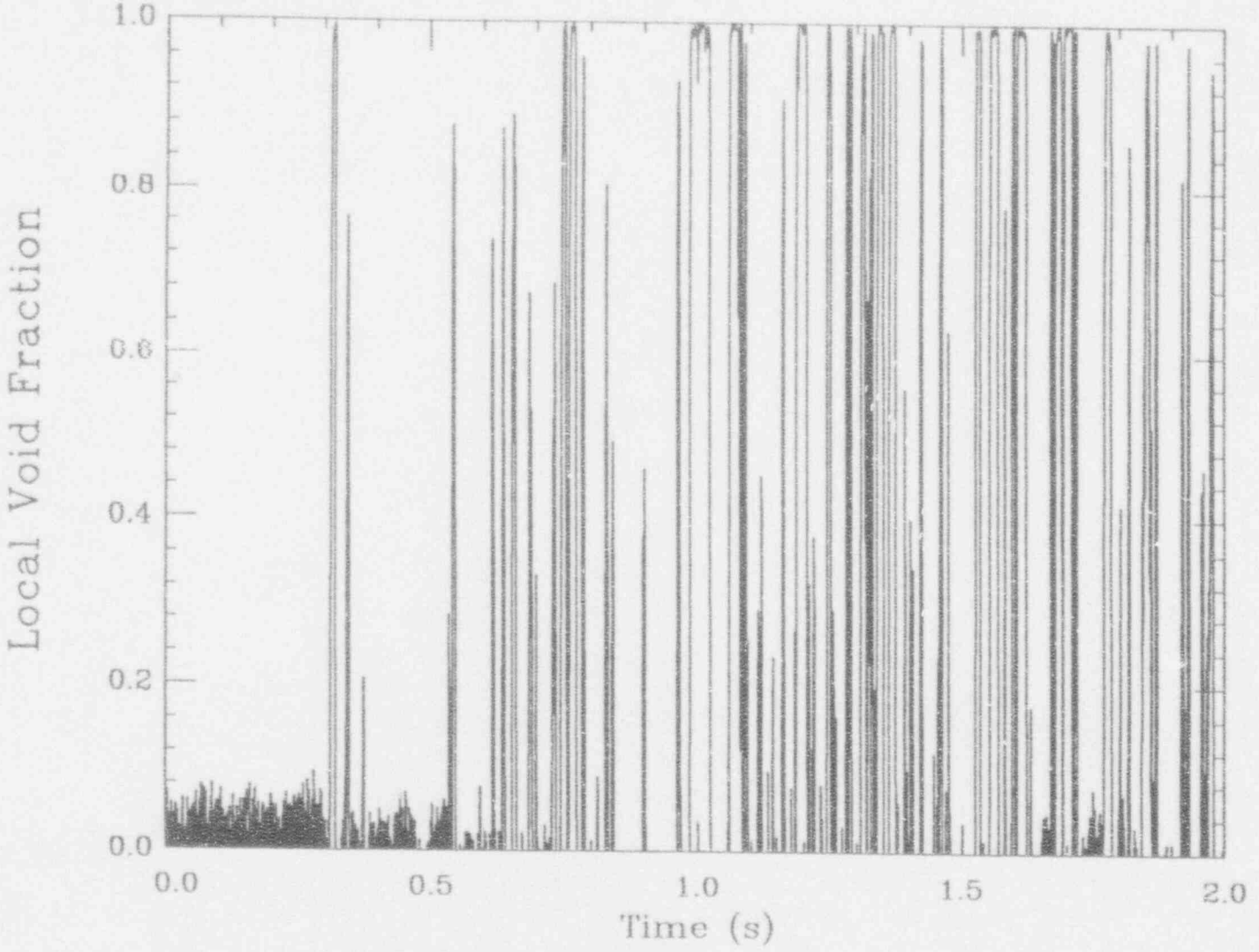

Figure I.C.47. The FLUTE signal for Run #403, position #2 (sampling rate 8 kHz).

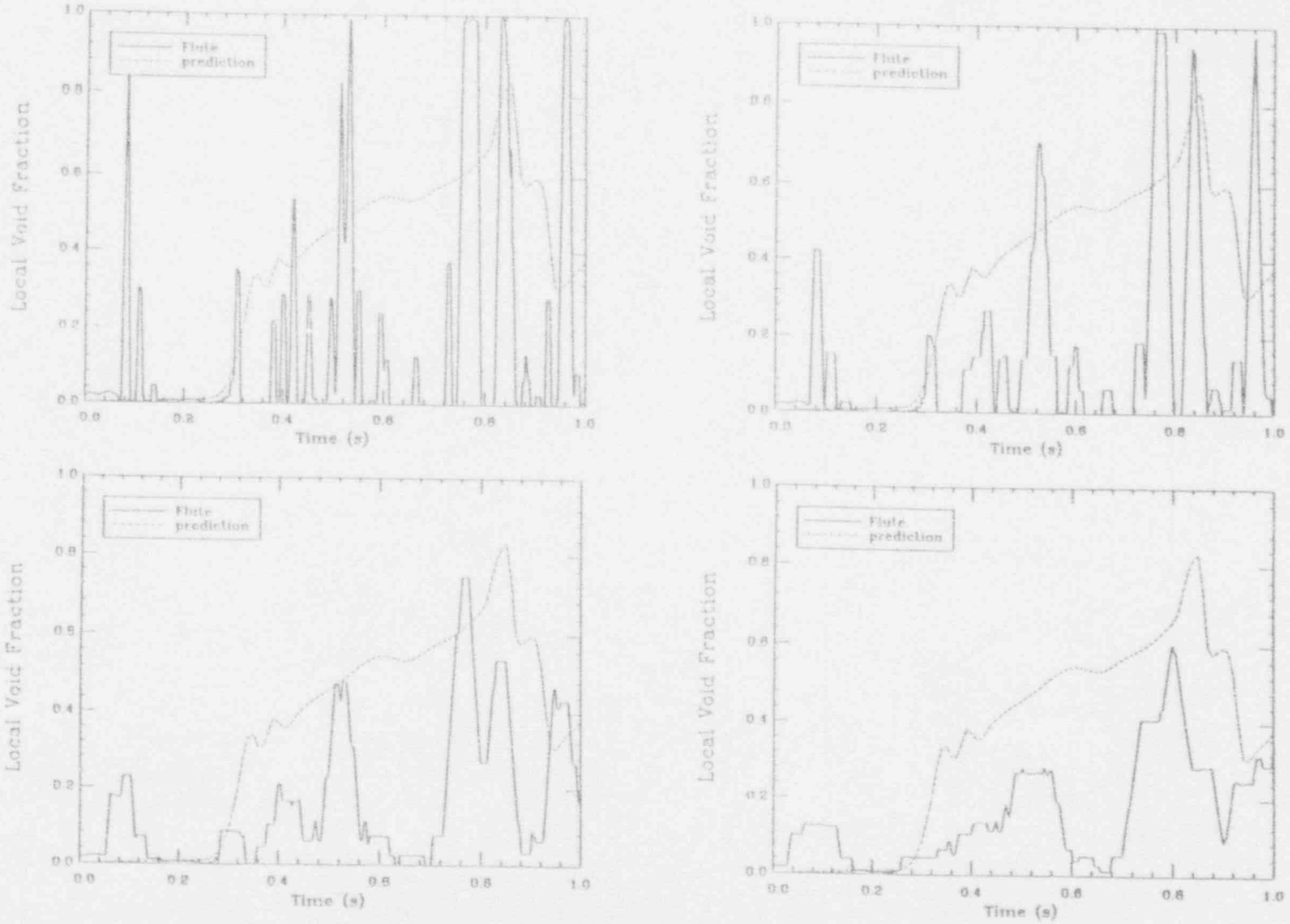

Figure I.C.48. The local void fraction transient for Run #403, position #2 as deduced by 10 (top left) 20 (top right) 50 (bottom left) and 100 (bottom right) millisecond time-averaging of the 8 kHz FLUTE signal.

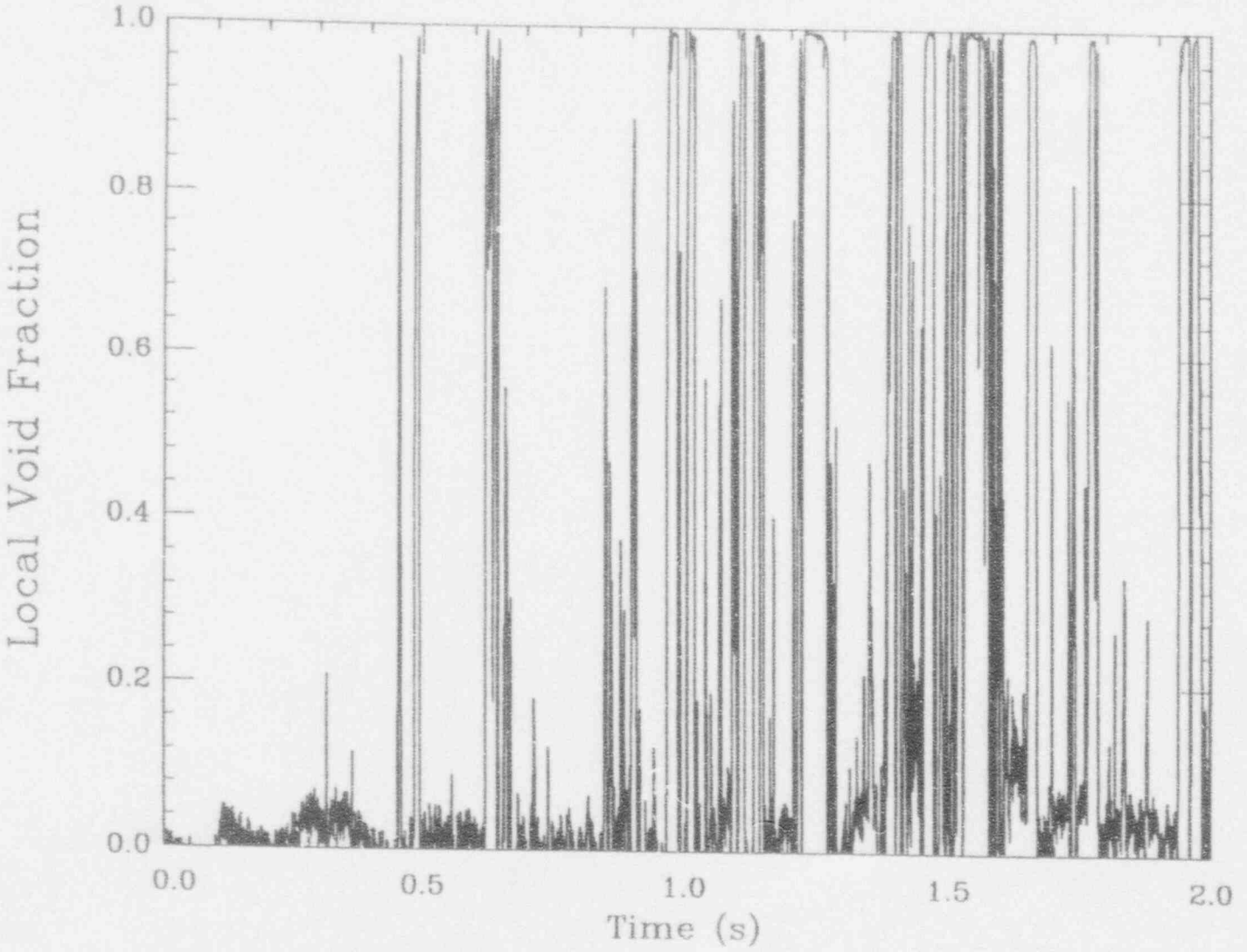

Figure I.C.49. The FLUTE signal for Run #404, position #1 (sampling rate 8 kHz).

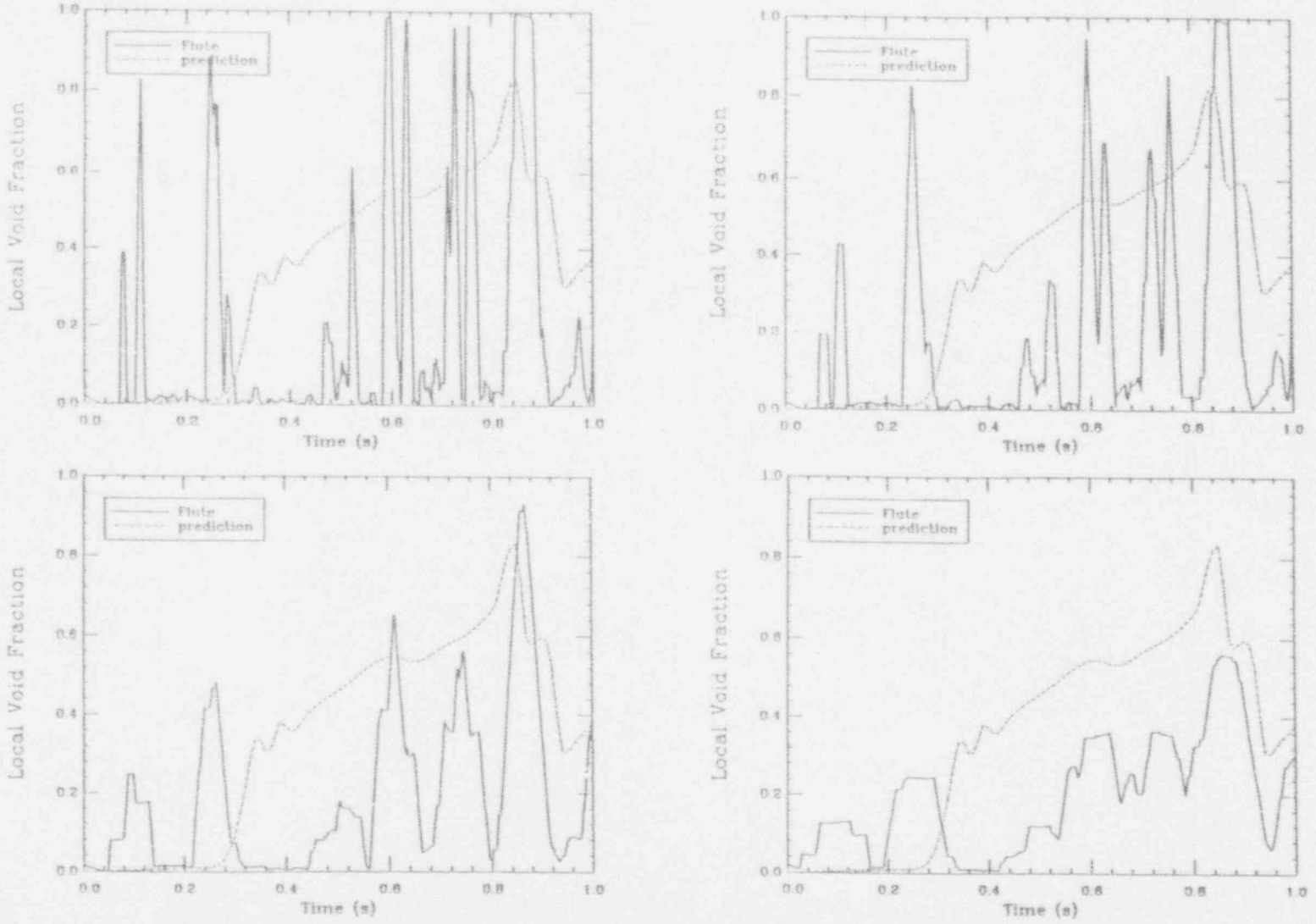

Figure I.C.50. The local void fraction transient for Run #404, position #1 as deduced by 10 (top left) 20 (top right) 50 (bottom left) and 100 (bottom right) millisecond time-averaging of the 8 kHz FLUTE signal.

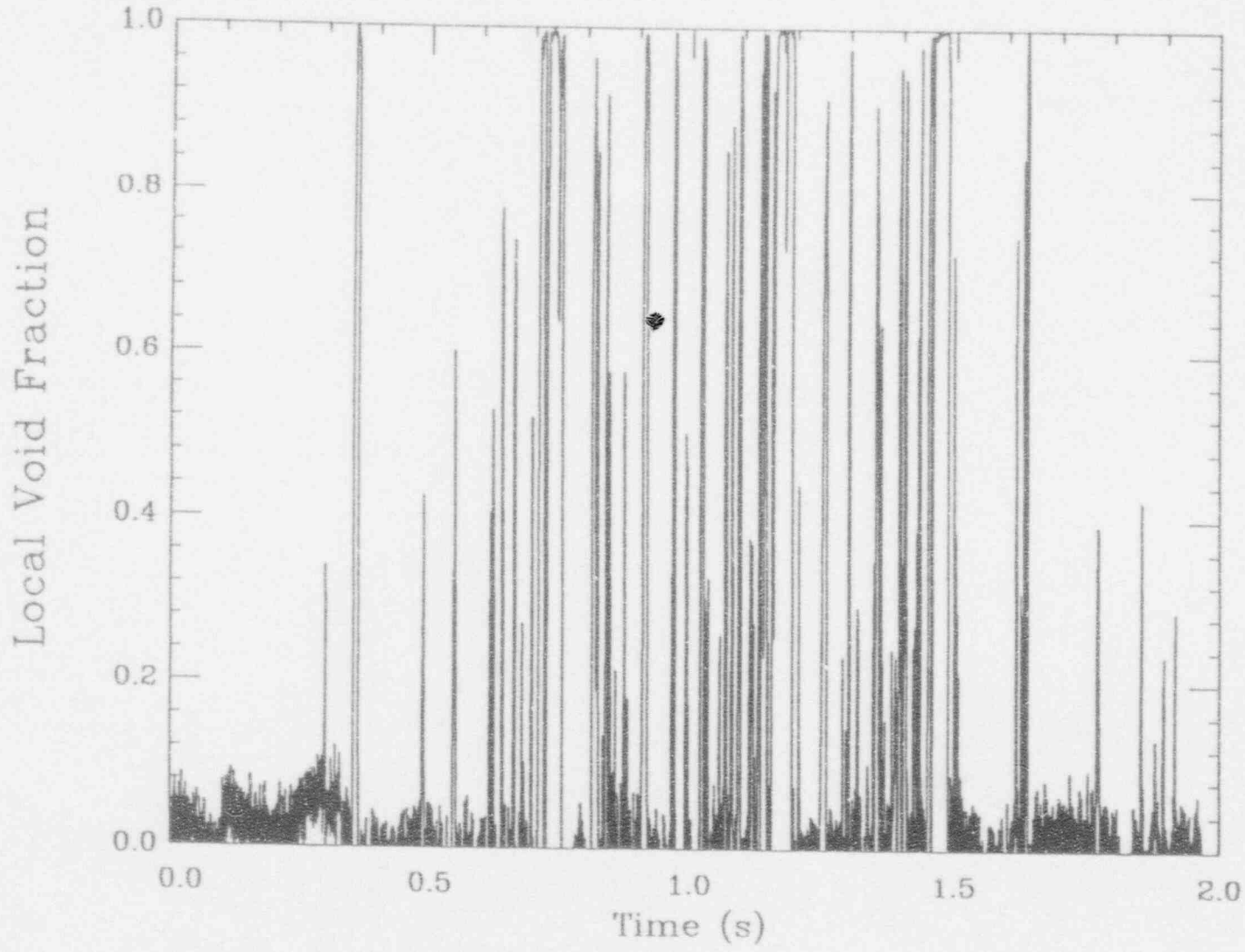

Figure I.C.51. The FLUTE signal for Run #404, position #2 (sampling rate 8 kHz).

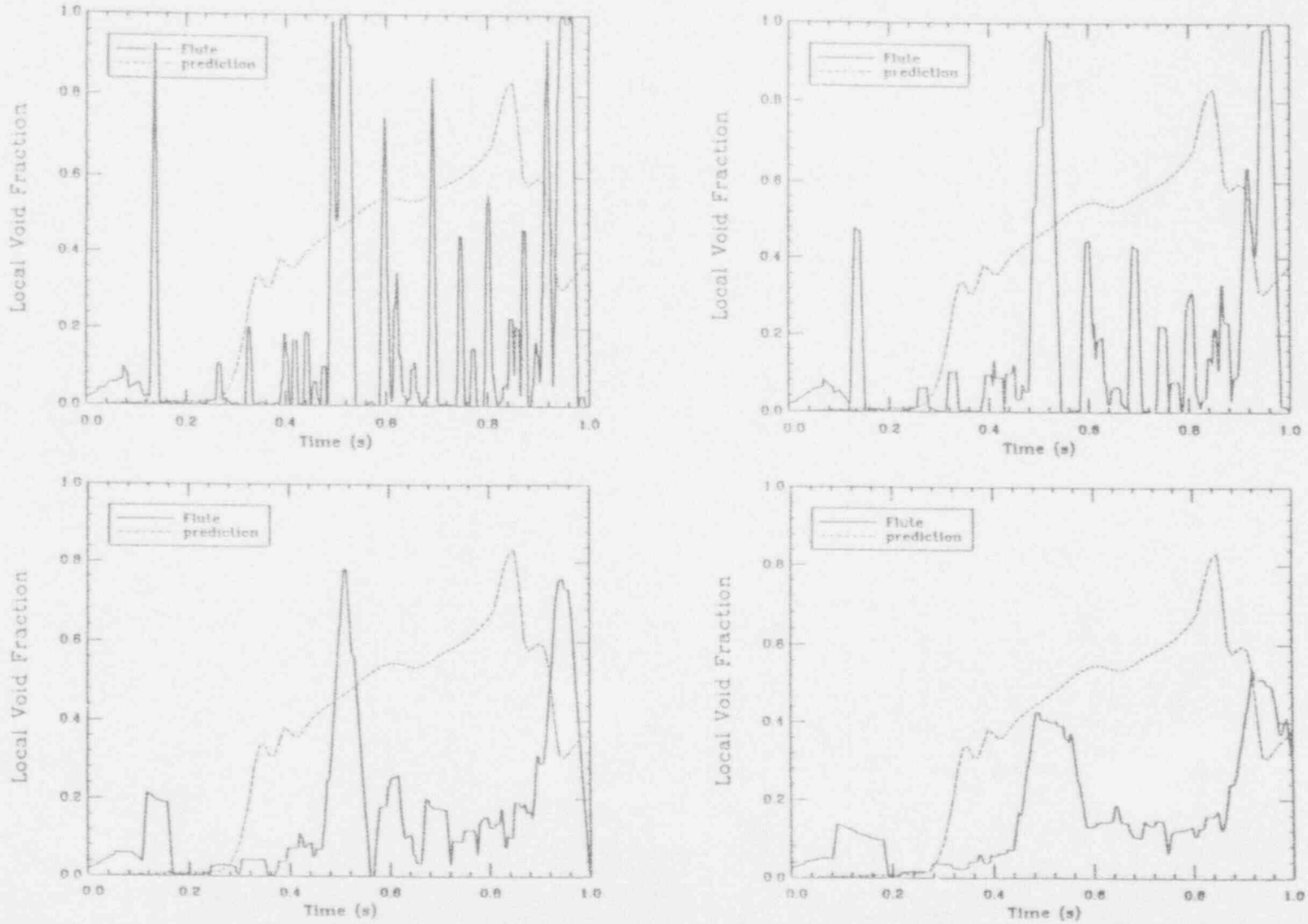

Figure I.C.52. The local void fraction transient for Run #404, position #2 as deduced by 10 (top left) 20 (top right) 50 (bottom left) and 100 (bottom right) millisecond time-averaging of the 8 kHz FLUTE signal.

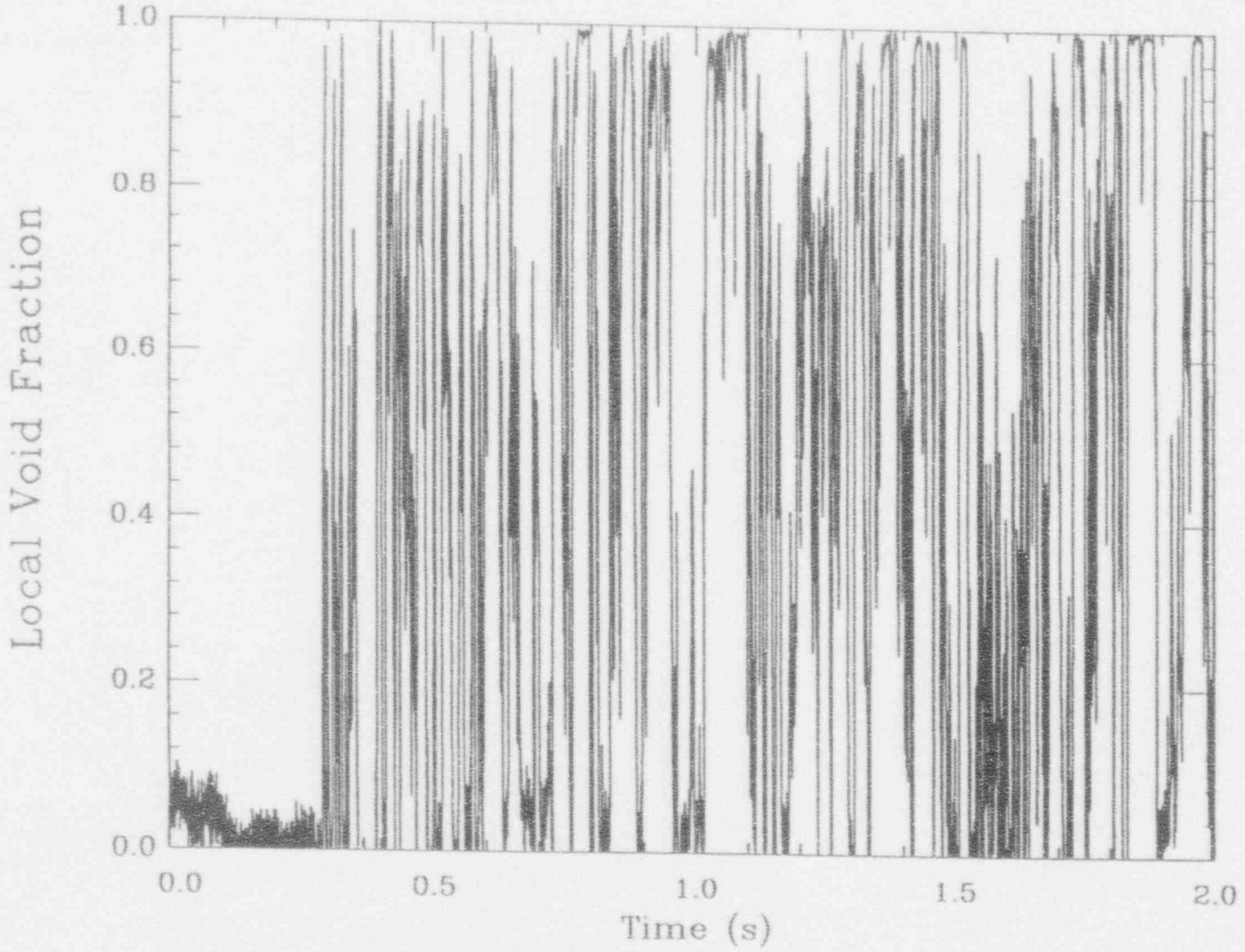

Figure I.C.53. The FLUTE signal for Run #406, position #1 (sampling rate 8 kHz).

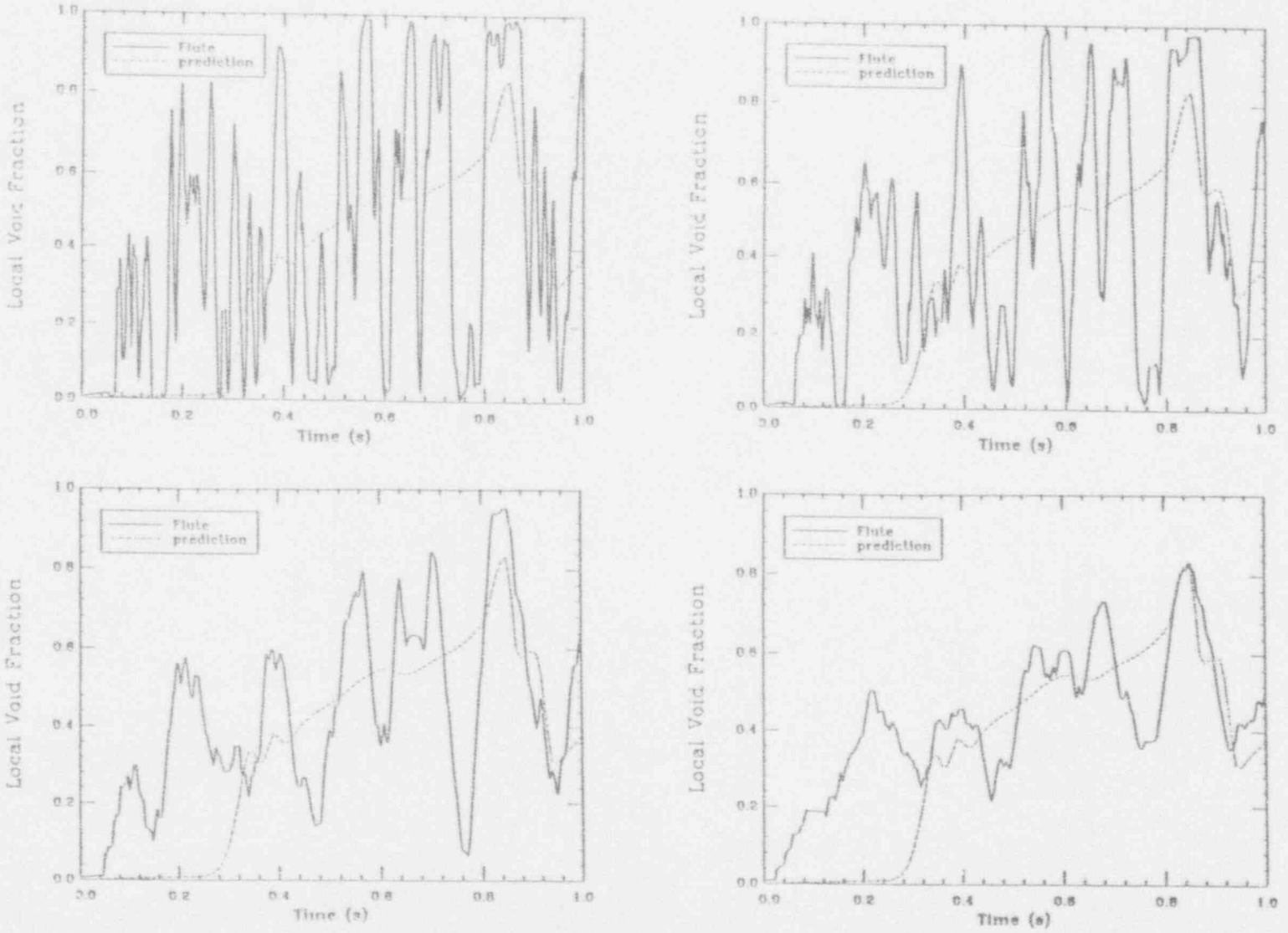

Figure I.C.54. The local void fraction transient for Run #406, position #1 as deduced by 10 (top left) 20 (top right) 50 (bottom left) and 100 (bottom right) millisecond time-averaging of the 8 kHz FLUTE signal.

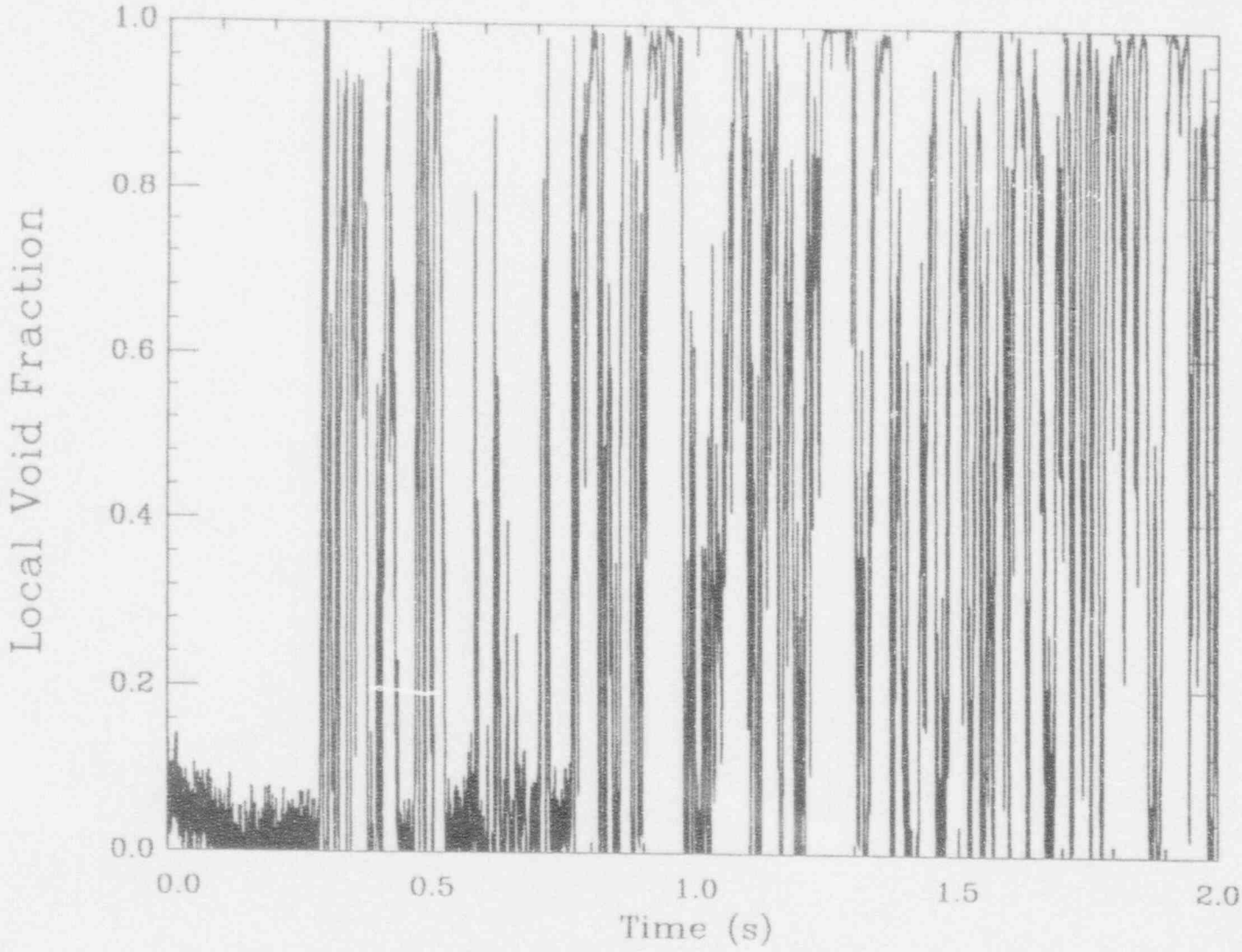

Figure I.C.55. The FLUTE signal for Run #406, position #2 (sampling rate 8 kHz).

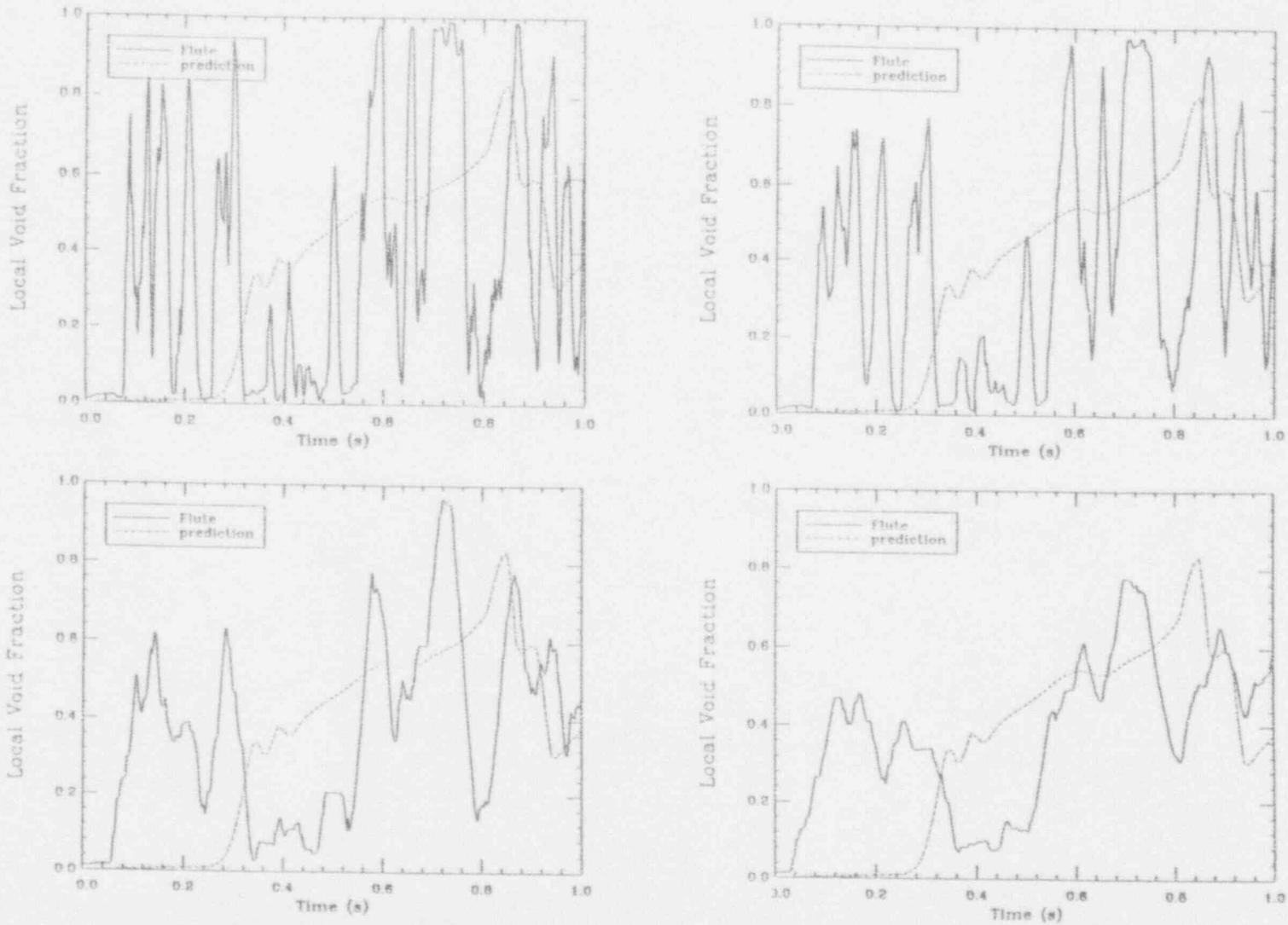

Figure I.C.56. The local void fraction transient for Run #406, position #2 as deduced by 10 (top left) 20 (top right) 50 (bottom left) and 100 (bottom right) millisecond time-averaging of the 8 kHz FLUTE signal.

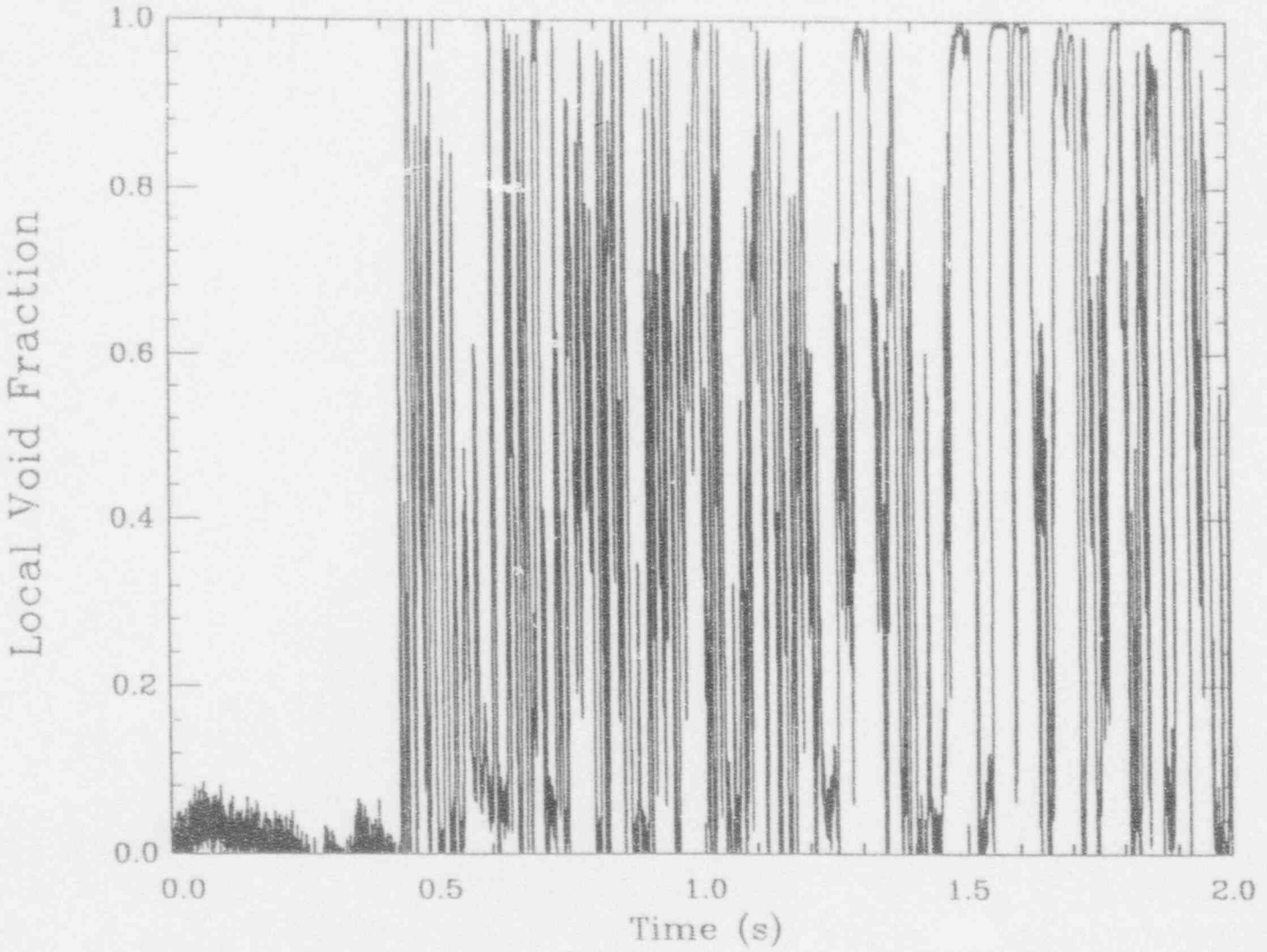

Figure I.C.57. The FLUTE signal for Run #407, position #1 (sampling rate 8 kHz).

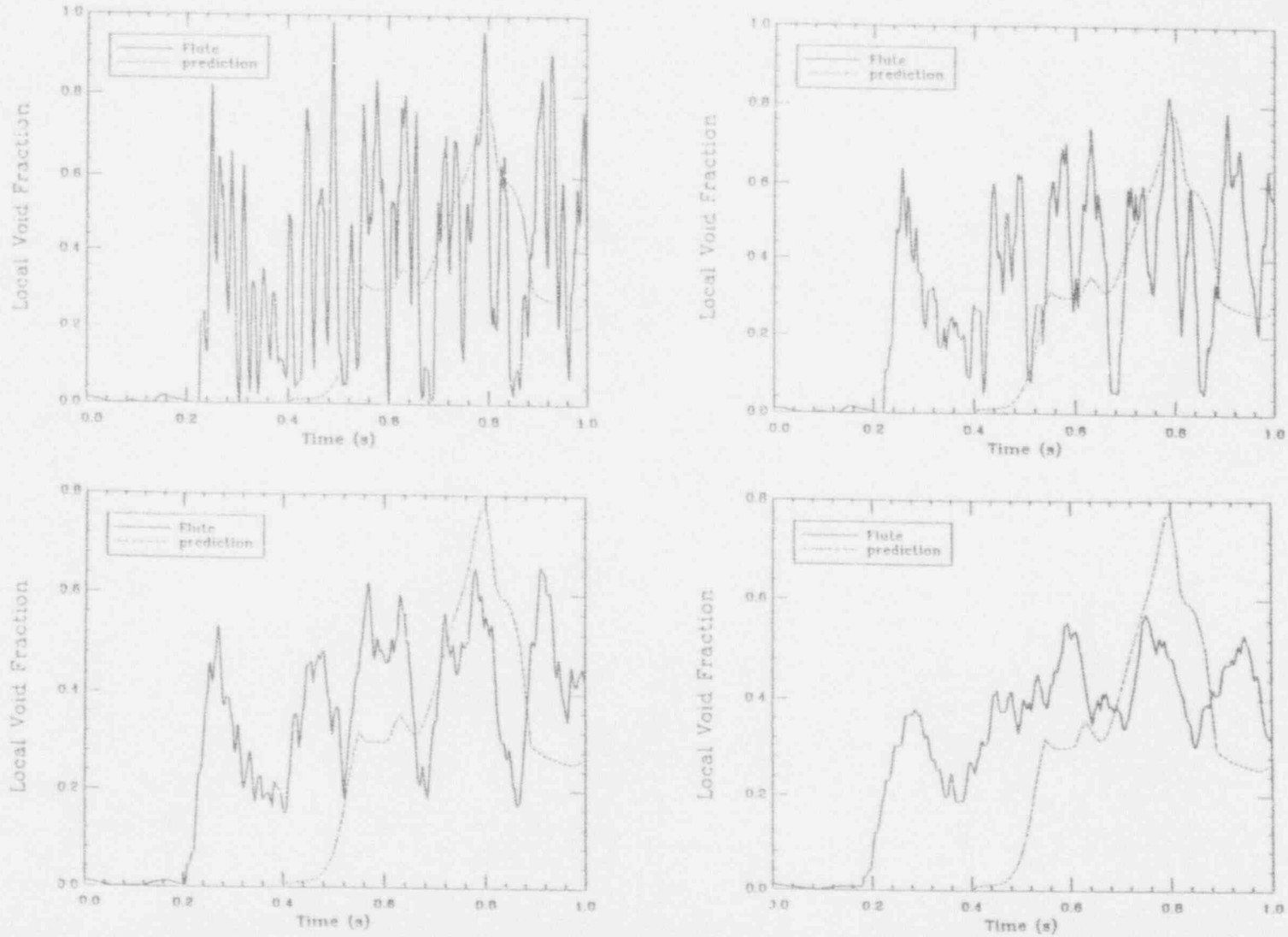

Figure I.C.58. The local void fraction transient for Run #407, position #1 as deduced by 10 (top left) 20 (top right) 50 (bottom left) and 100 (bottom right) millisecond time-averaging of the 8 kHz FLUTE signal.

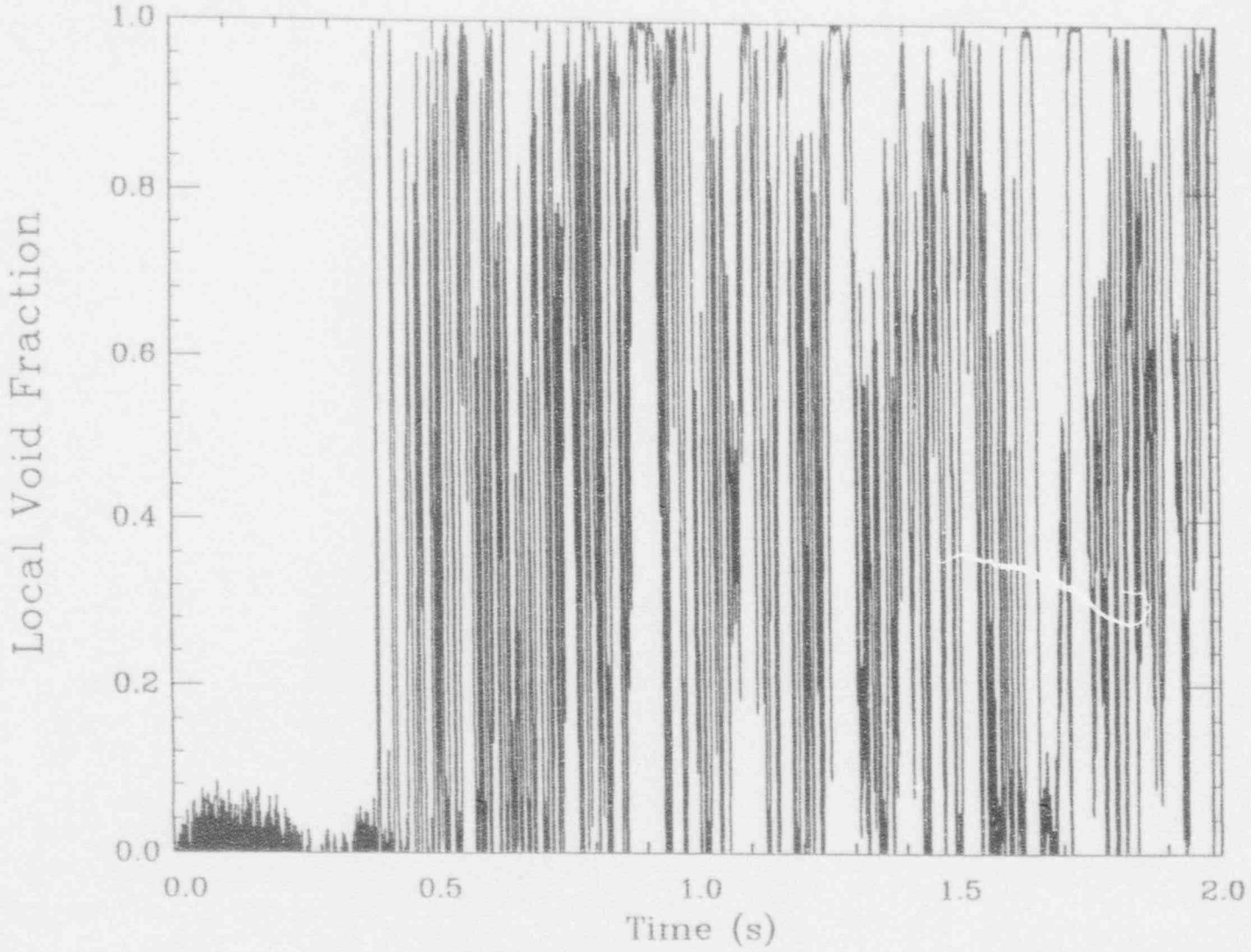

Figure I.C.59. The FLUTE signal for Run #407, position #2 (sampling rate 8 kHz).

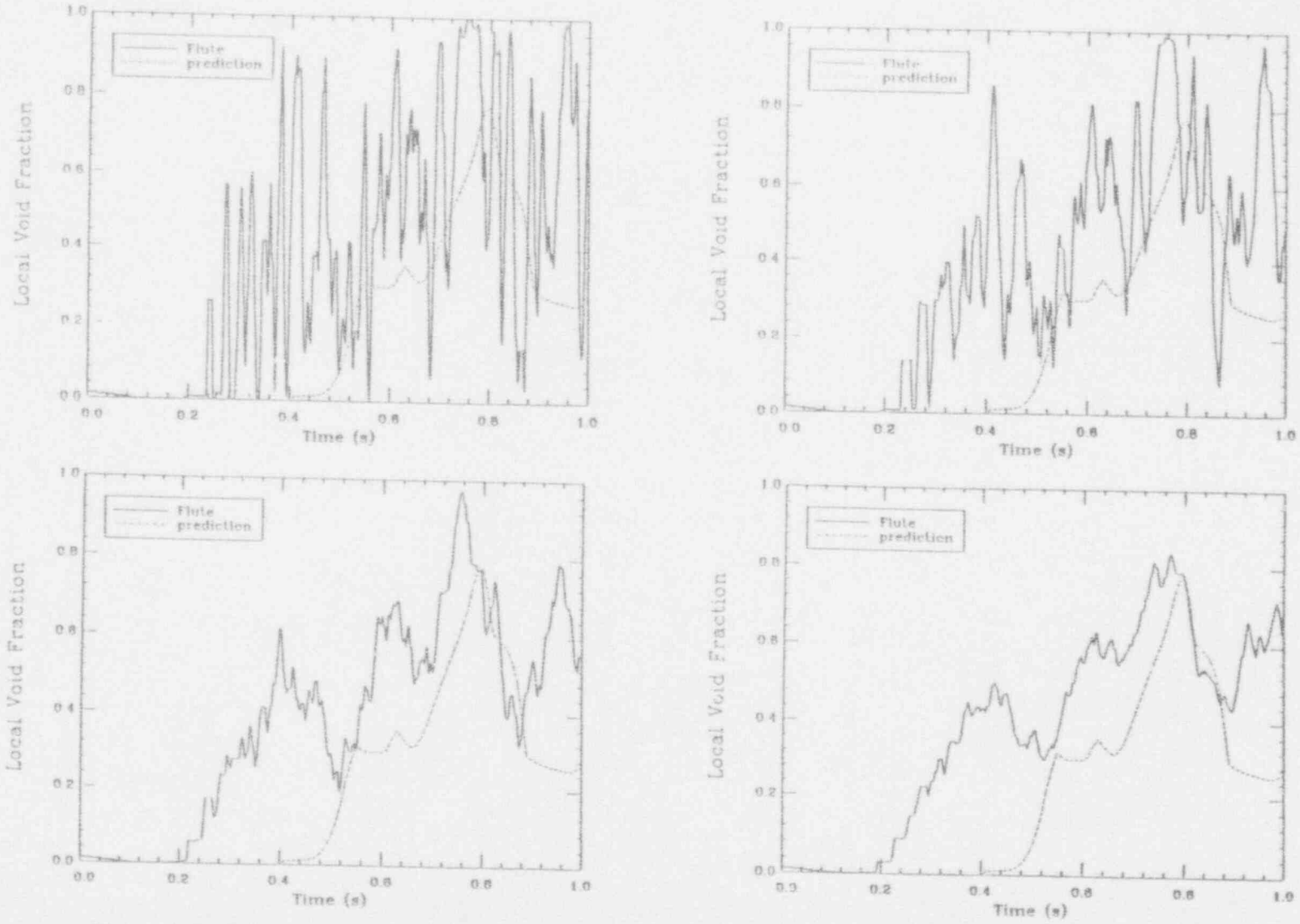

Figure I.C.60. The local void fraction transient for Run #407, position #2 as deduced by 10 (top left) 20 (top right) 50 (bottom left) and 100 (bottom right) millisecond time-averaging of the 8 kHz FLUTE signal.

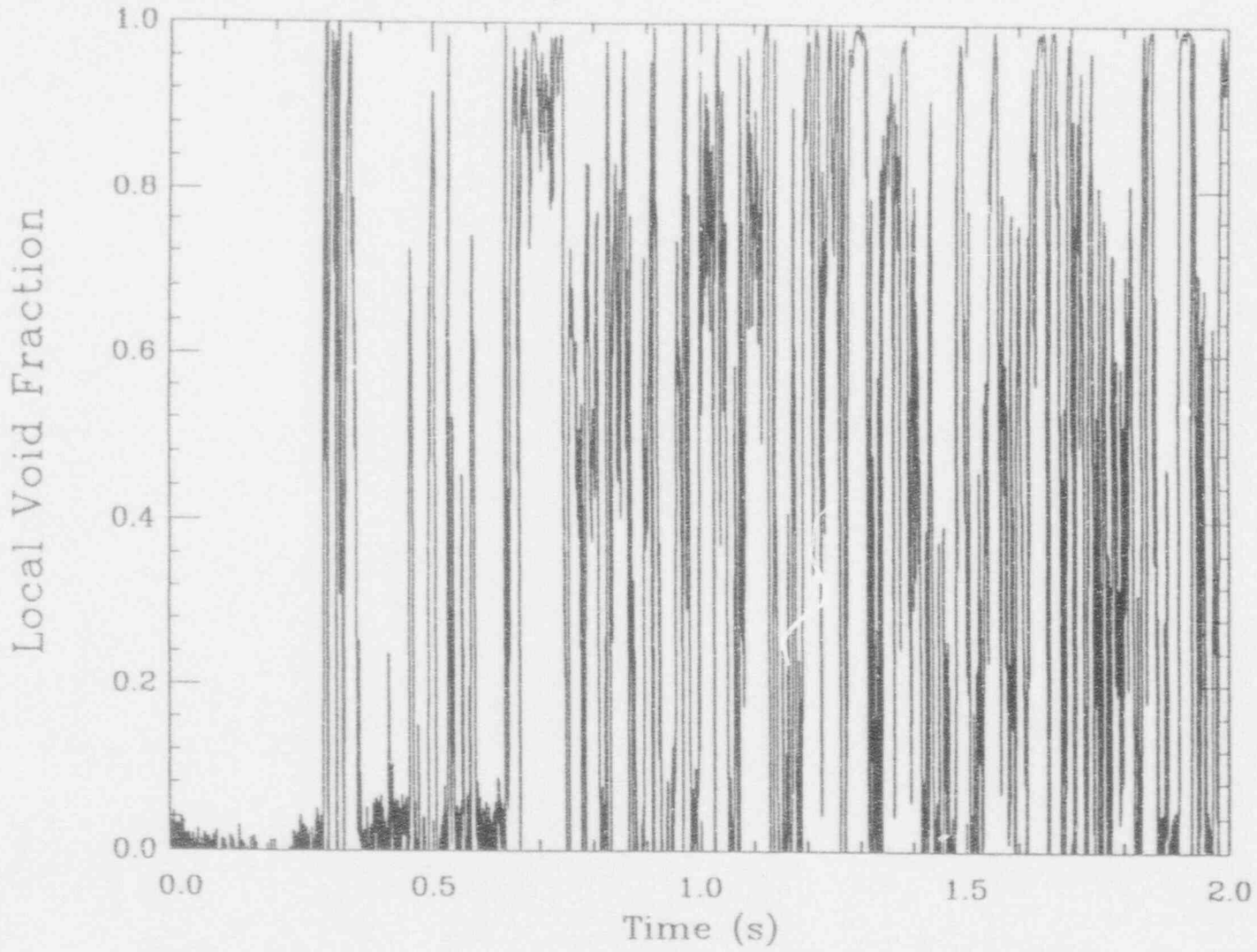

Figure I.C.61. The FLUTE signal for Run #408, position #1 (sampling rate 8 kHz).

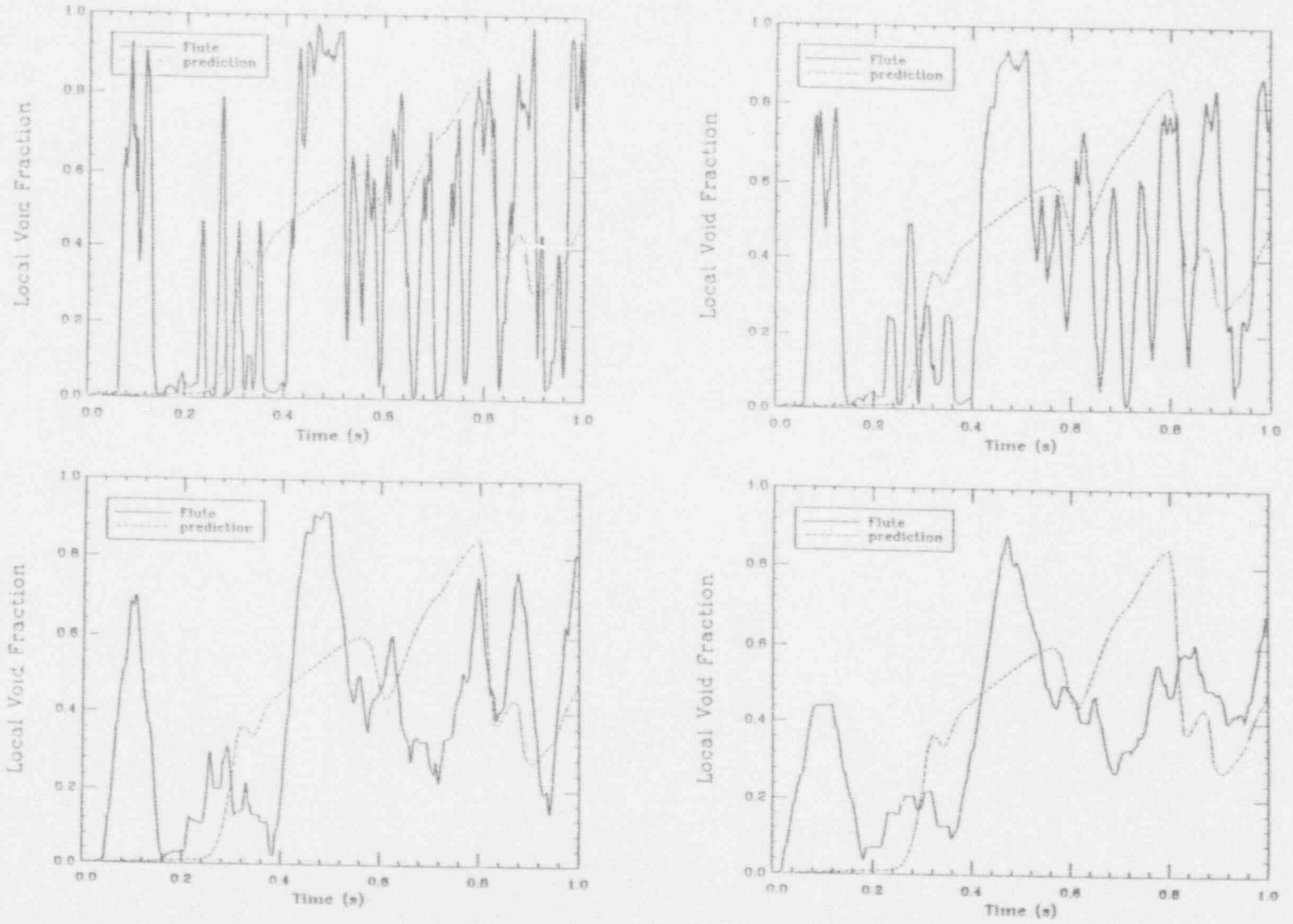

Figure I.C.62. The local void fraction transient for Run #408, position #1 as deduced by 10 (top left) 20 (top right) 50 (bottom left) and 100 (bottom right) millisecond time-averaging of the 8 kHz FLUTE signal.

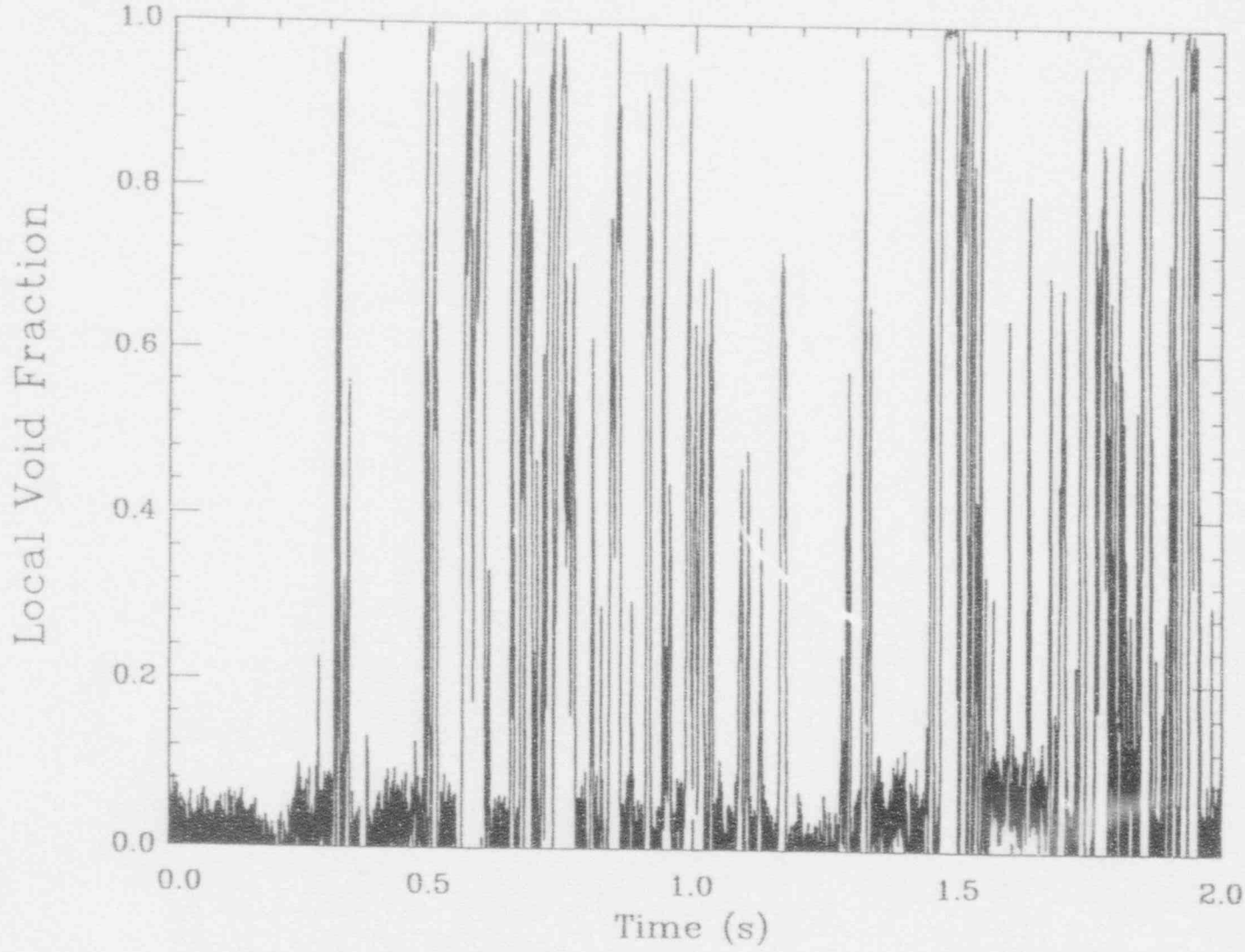

Figure I.C.63. The FLUTE signal for Run #408, position #2 (sampling rate 8 kHz).

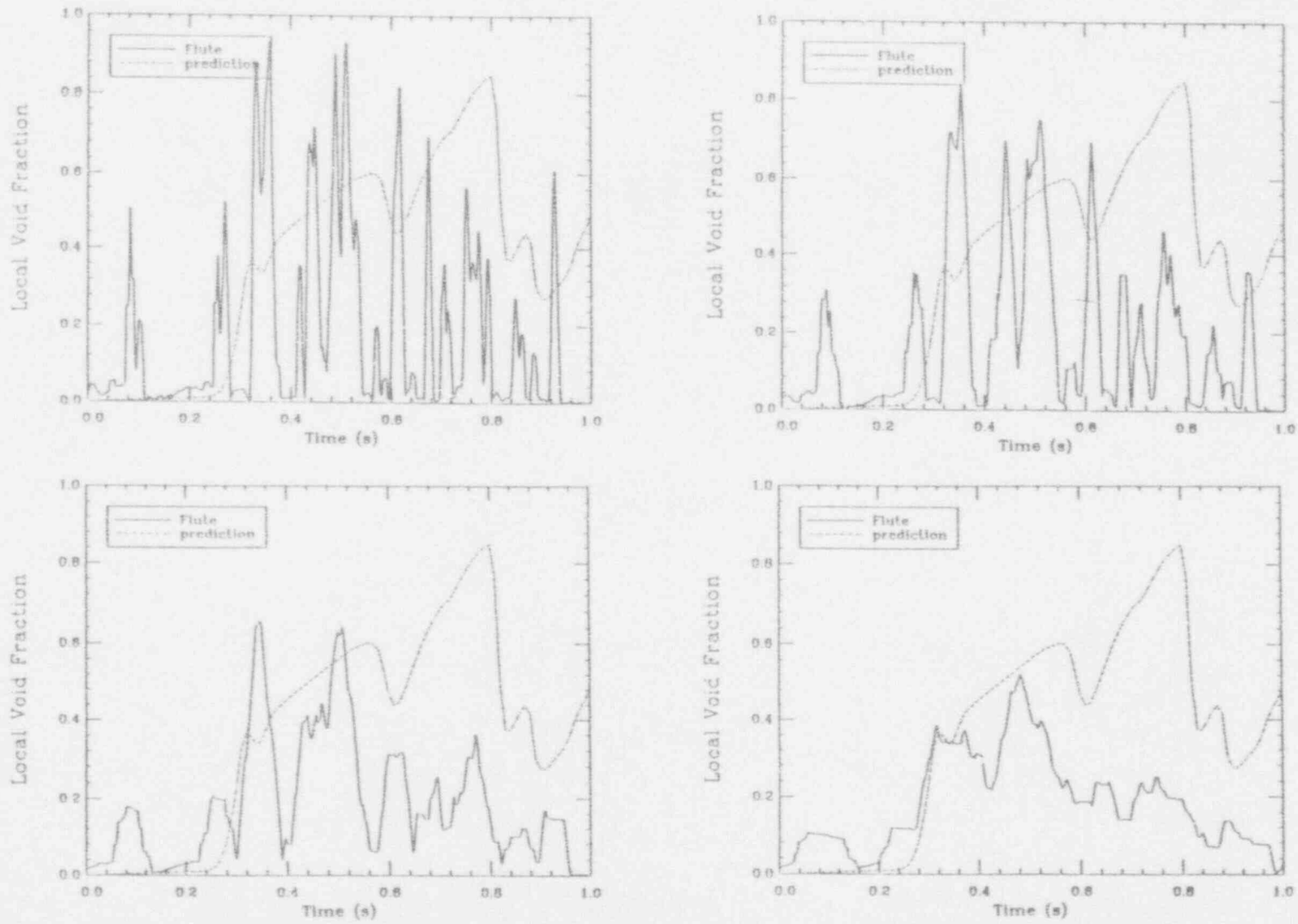

Figure I.C.64. The local void fraction transient for Run #408, position #2 as deduced by 10 (top left) 20 (top right) 50 (bottom left) and 100 (bottom right) millisecond time-averaging of the 8 kHz FLUTE signal.

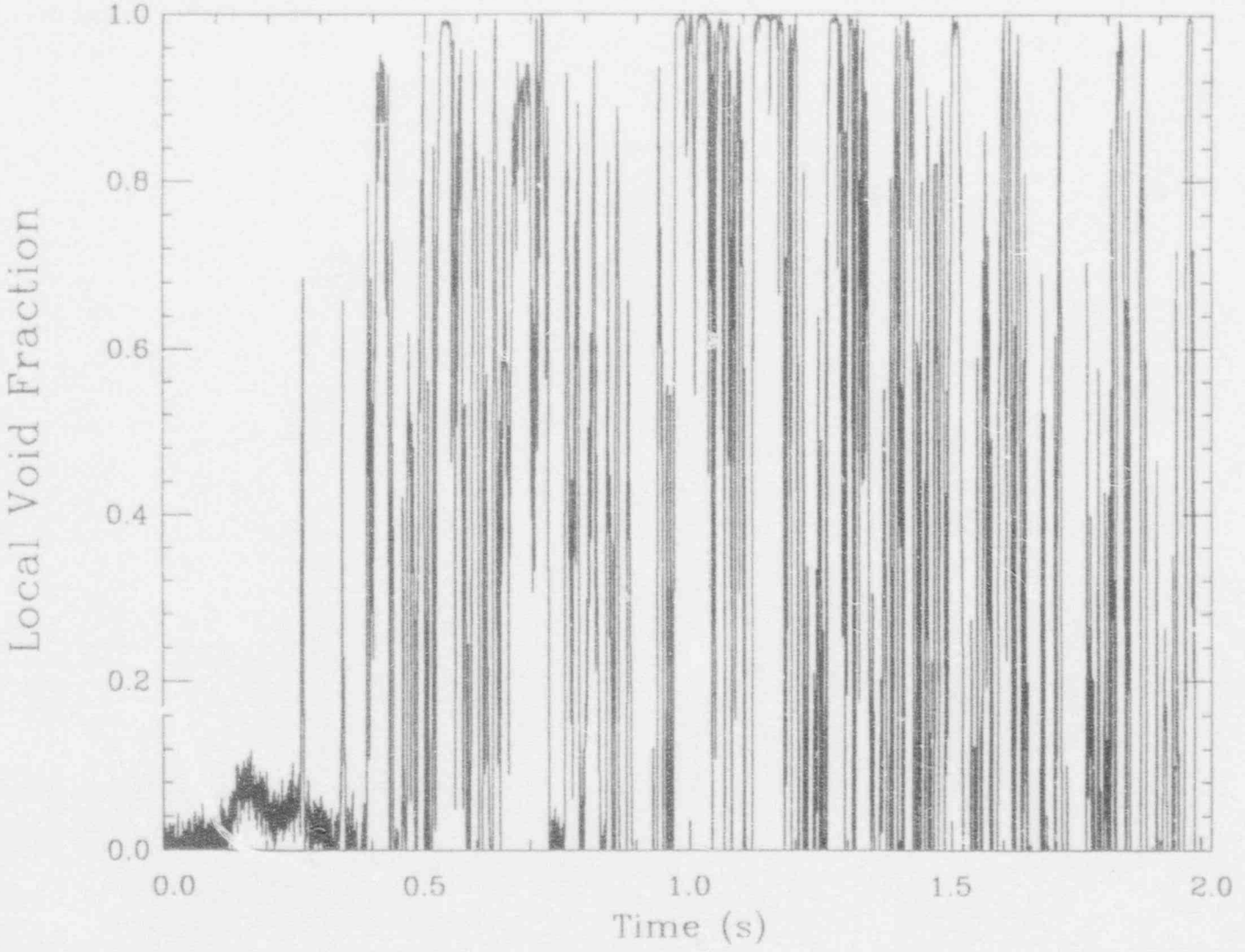

Figure I.C.65. The FLUTE signal for Run #603, position #1 (sampling rate 8 kHz).

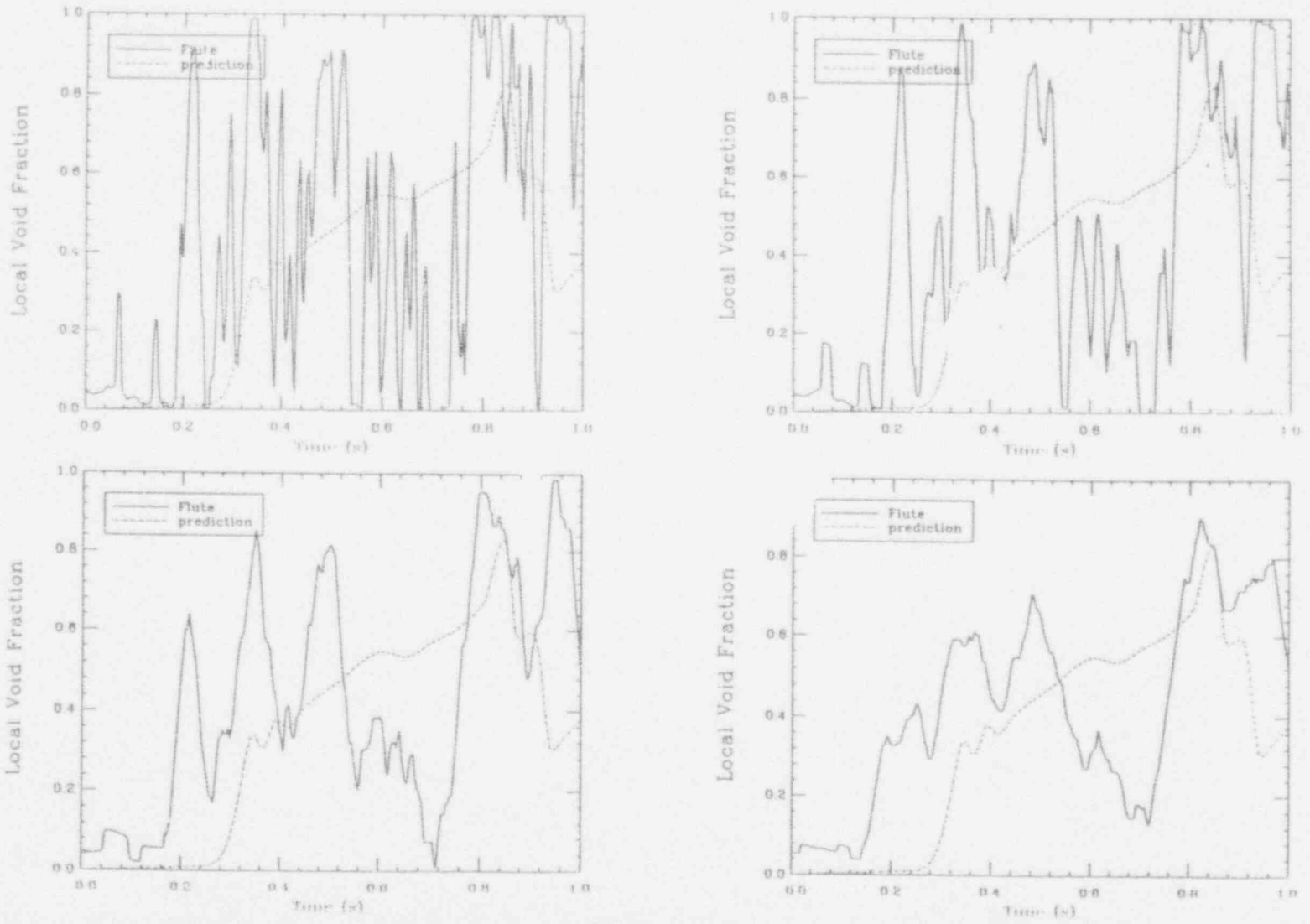

Figure I.C.66. The local void fraction transient for Run #603, position #1 as deduced by 10 (top left) 20 (top right) 50 (bottom left) and 100 (bottom right) millisecond time-averaging of the 8 kHz FLUTE signal.

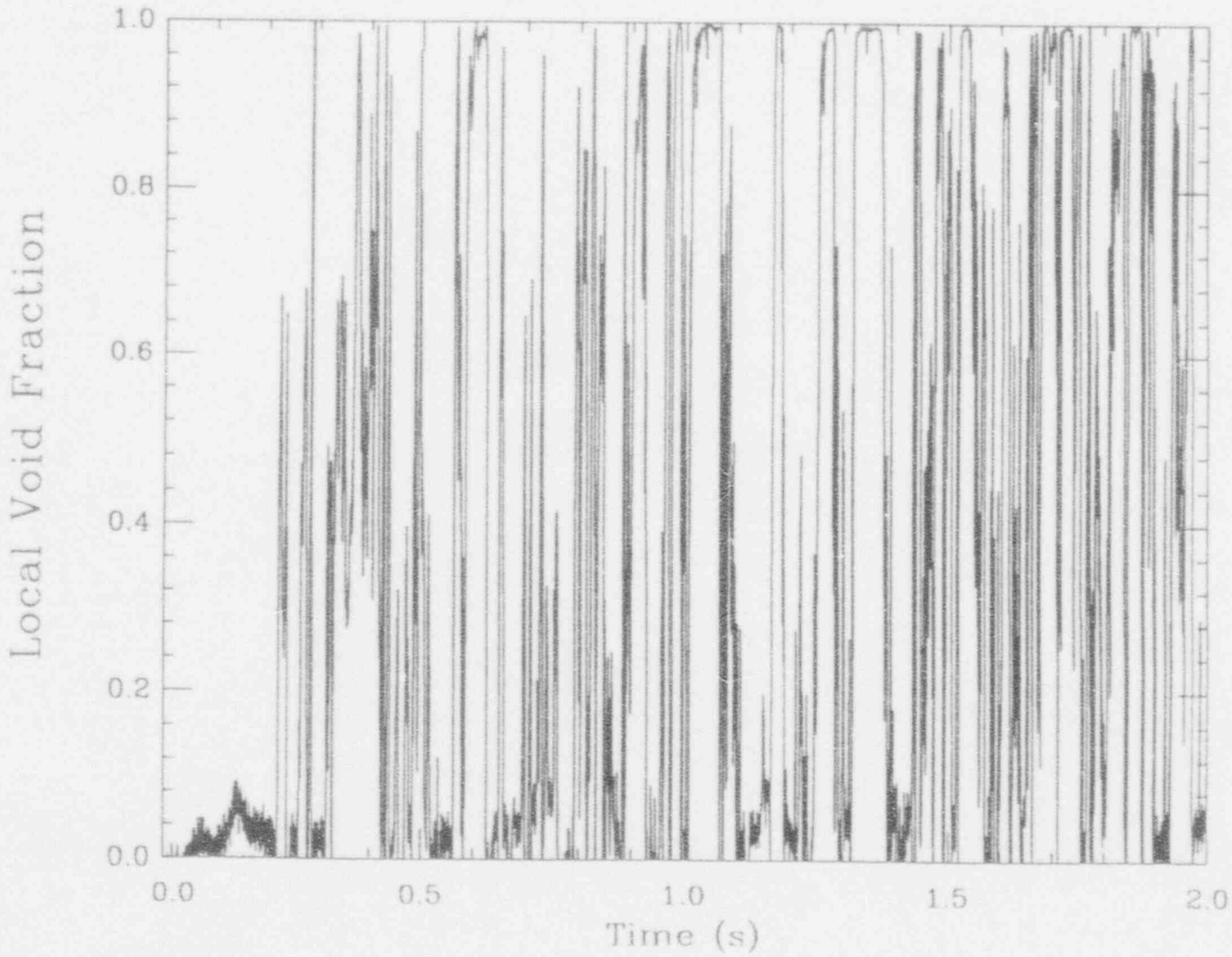

Figure I.C.67. The FLUTE signal for Run #603, position #2 (sampling rate 8 kHz).

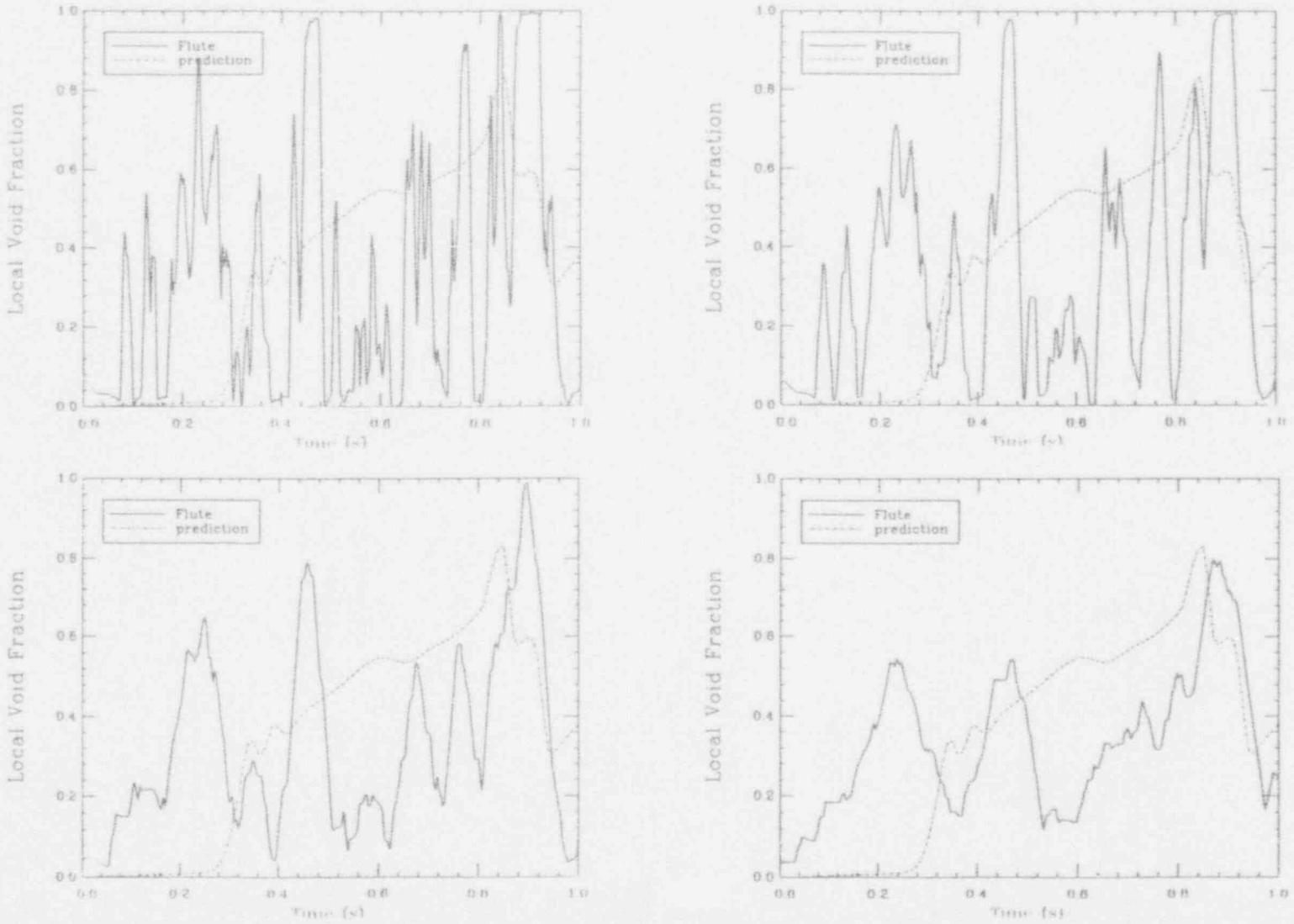

Figure I.C.68. The local void fraction transient for Run #603, position #2 as deduced by 10 (top left) 20 (top right) 50 (bottom left) and 100 (bottom right) millisecond time-averaging of the 8 kHz FLUTE signal.

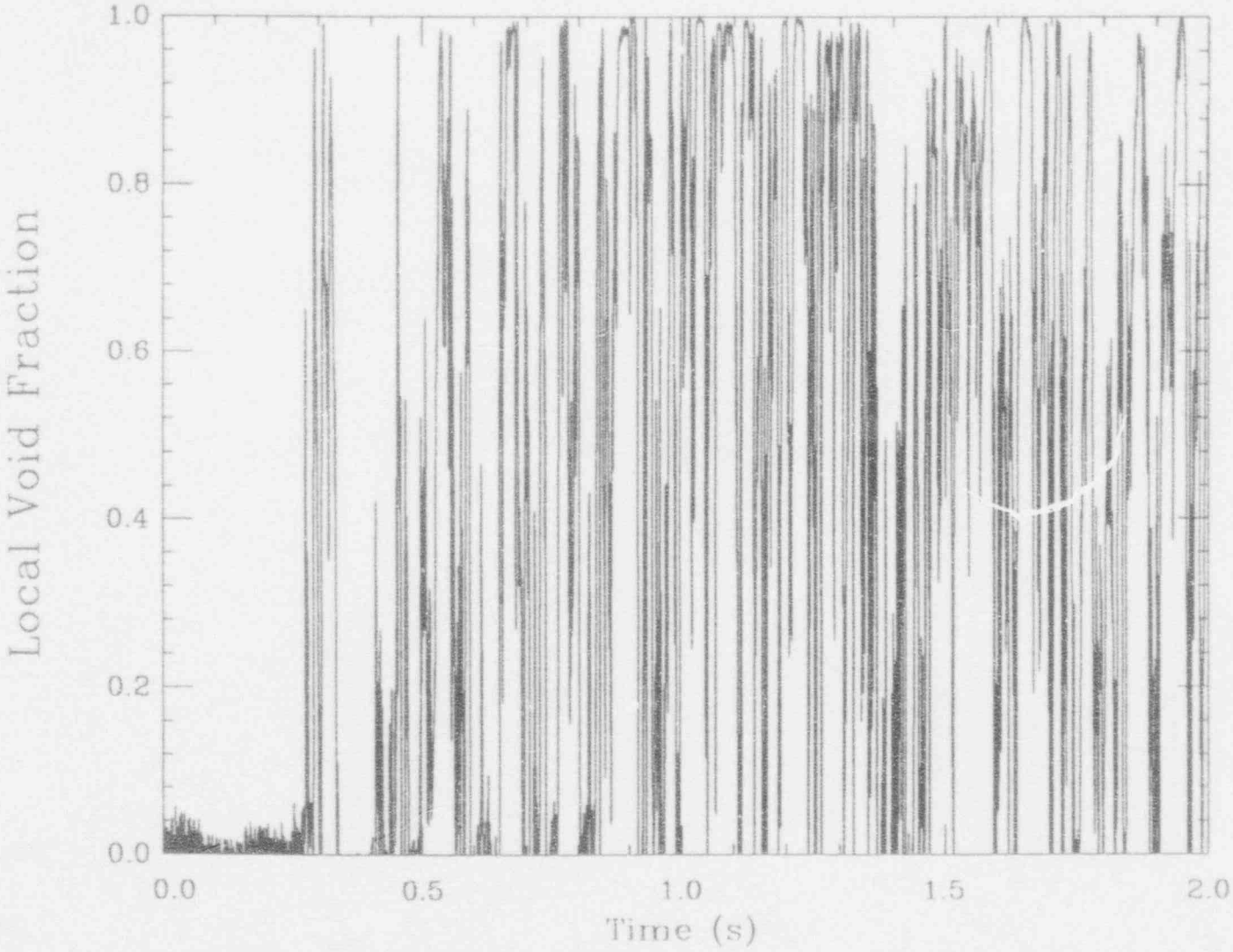

Figure I.C.69. The FLUTE signal for Run #604, position #1 (sampling rate 8 kHz).

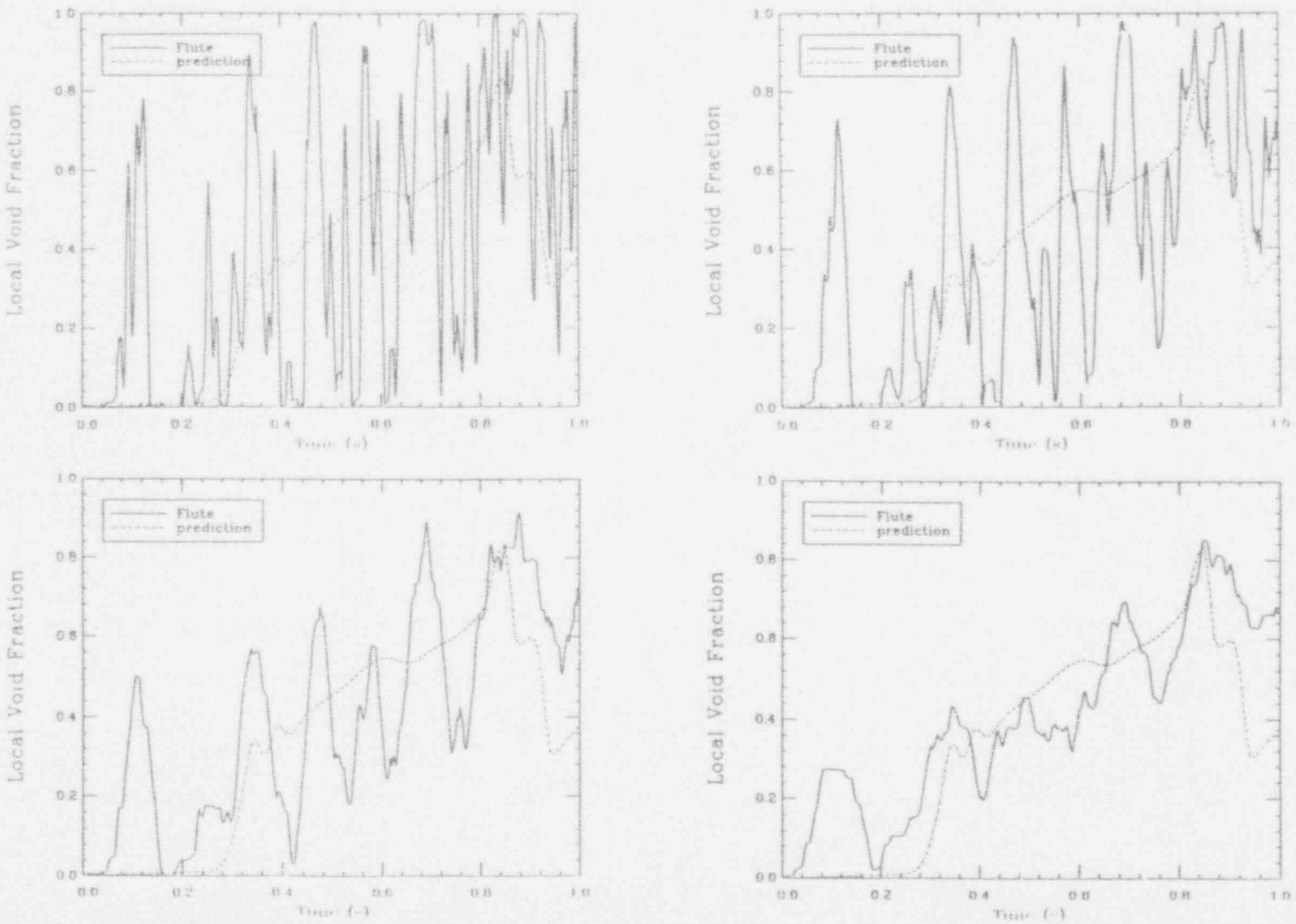

Figure I.C.70. The local void fraction transient for Run #604, position #1 as deduced by 10 (top left) 20 (top right) 50 (bottom left) and 100 (bottom right) millisecond time-averaging of the 8 kHz FLUTE signal.

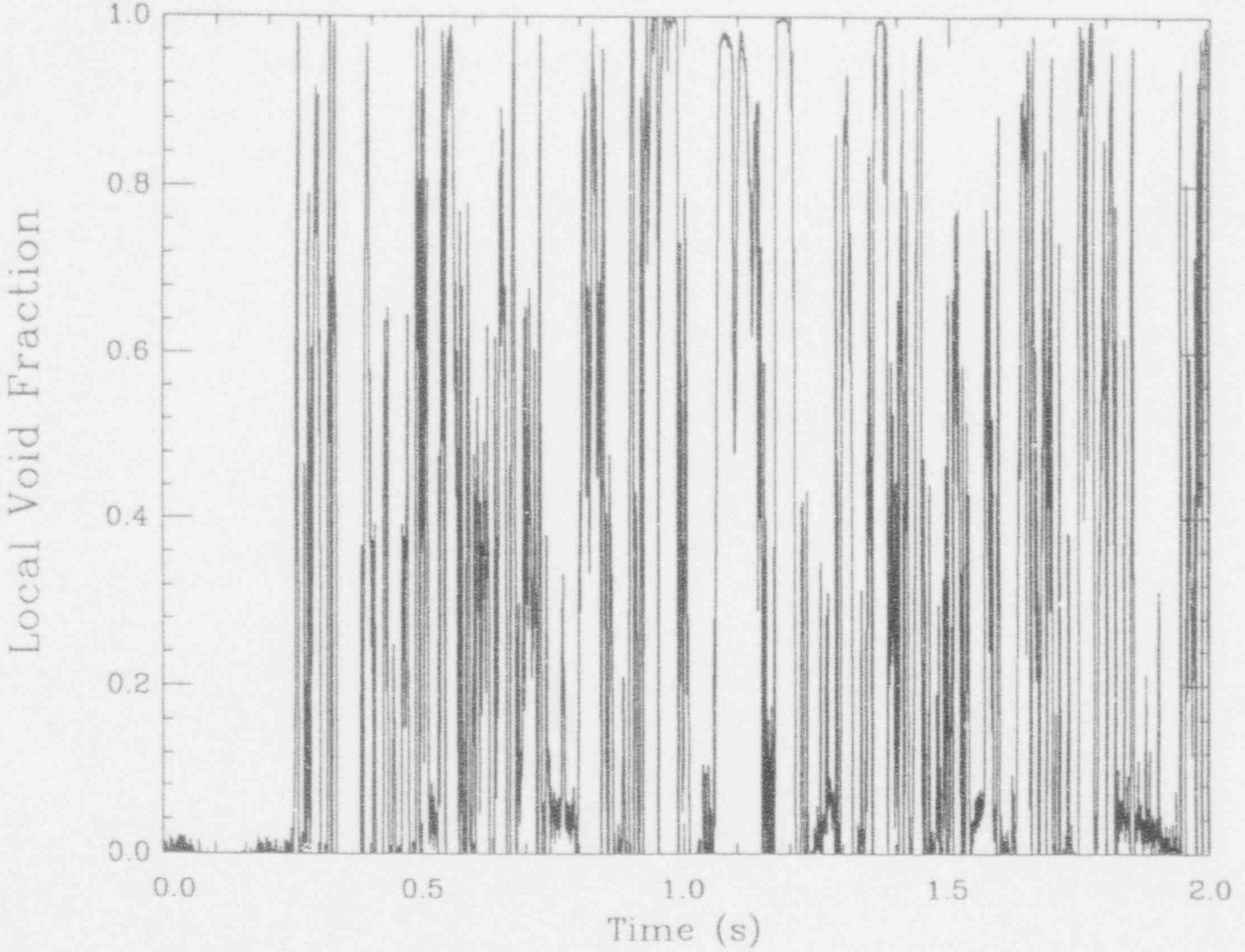

Figure I.C.71. The FLUTE signal for Run #604, position #2 (sampling rate 8 kHz).

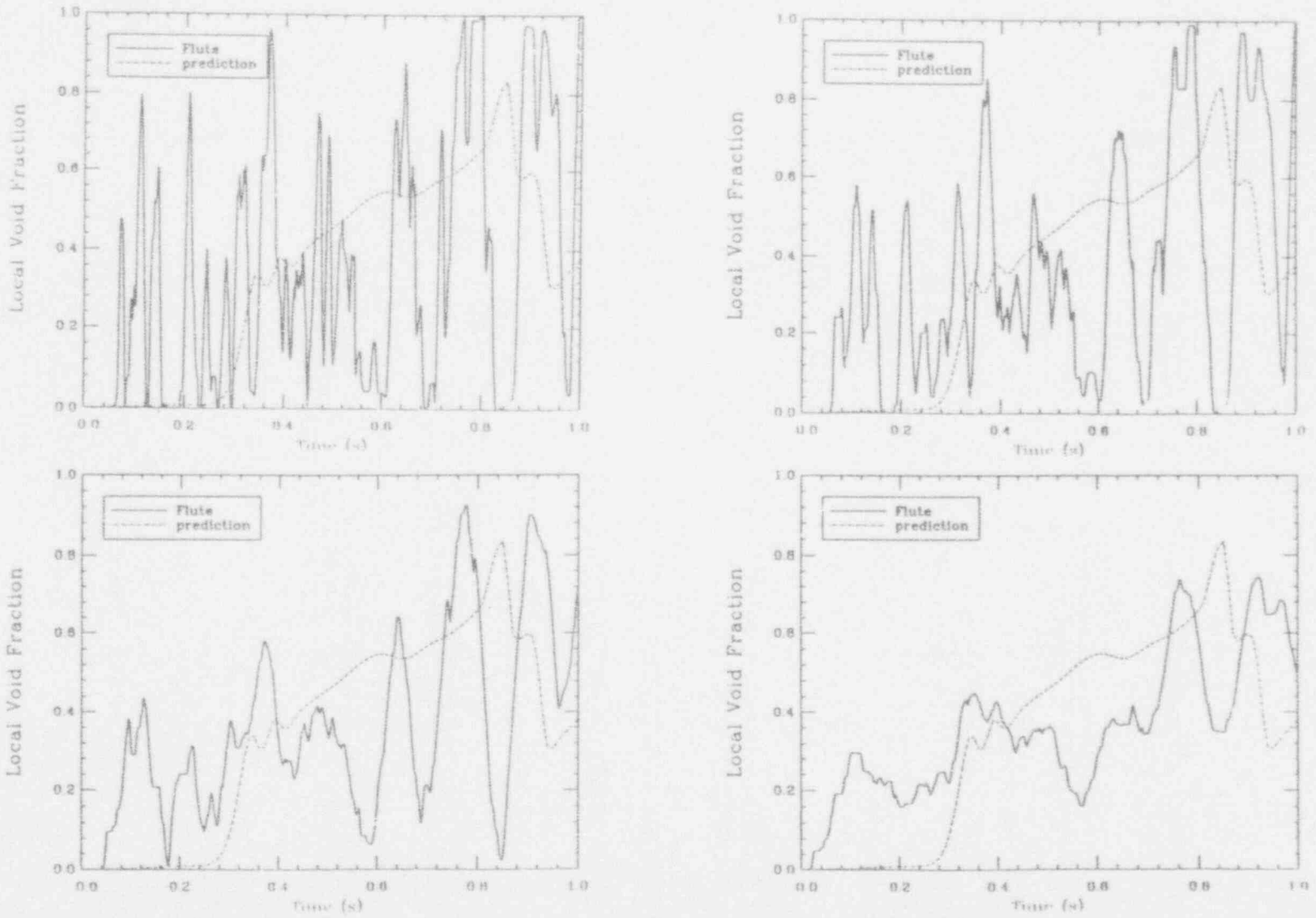

Figure I.C.72. The local void fraction transient for Run #604, position #2 as deduced by 10 (top left) 20 (top right) 50 (bottom left) and 100 (bottom right) millisecond time-averaging of the 8 kHz FLUTE signal.

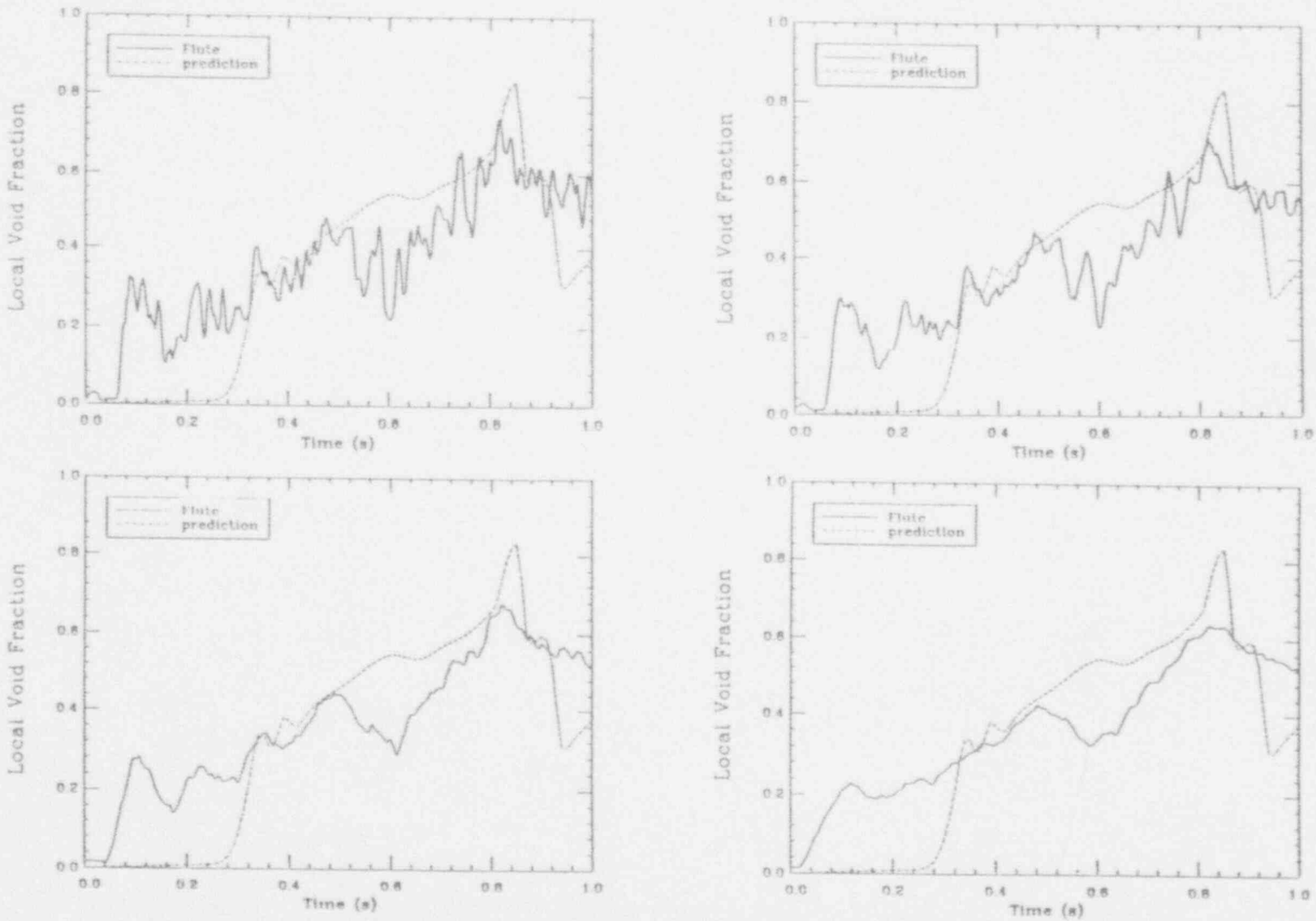

Figure I.C.73. The local void fraction transient obtained by averaging the time-smoothed signals (obtained as in the previous figures) of 9 similar runs.

APPENDIX D

THE DETAILED STRUCTURE OF INTERACTIONS IN MAGICO

Appendix D: The Detailed Structure of Interactions in MAGICO

The premixing transient is a vastly complicated process, which besides the primary quantity of interest, the space-time evolution of the void fraction, has a number of other interesting features. These features relate to the detailed motions and associated interactions, and they are significant in creating the conditions within which the void fraction patterns develop. We study these motions here in terms of the calculated steam and water volume flux patterns for the conditions of MAGICO runs #702 (25-cm pool, 2.4-mm balls, 800 °C) and #905 (50-cm pool, 1.5-mm balls, 800 °C). These runs were chosen for the purpose of explaining the prediction of a "reversal of water volume flux" phenomenon, which we believe relates to, and explains, an experimentally-found sudden increase in steam generation rate under certain conditions during the premixing transient. More specifically, we believe that reversal of water flux causes a strong counter-current melt-water contact and an associated rapid increase in steam generation rates; accordingly, the resulting phenomenon is termed Energetic Transfer of Heat In a Counter-Current Ambient (ETHICCA).

The reversal of water volume flux is illustrated in Figures D.1 and D.2 for runs #702 and #905, respectively. [In these figures, spatial maps are given for only one-half of the flow field—symmetry.] In the initial stages, we can see that the generated steam moves upward and out of the mixing region, while the water is being pushed down and to the sides. This creates a counterclockwise motion in the liquid around the mixing zone. As time goes on, the behavior of the steam remains basically the same, except for being lifted from farther down the pool in a pattern that follows the particle cloud front penetrating the pool. However, the water volume flux undergoes two major changes, one at 0.2 and the other at about 0.5 seconds. At 0.2 s in the interaction, water is seen to begin to move upward within the mixing zone, apparently being "lifted" by the steam flow. The mixing region is therefore becoming depleted of liquid for three reasons: vaporization, water being pushed down and to the sides by the particles, and water being lifted by the steam. The implied internal stagnation region is clearly visible in Figures D.1b and D.2b. The other change occurs around 0.5 s, when the water around the mixing zone reverses sense of "rotation" (note that these are all irrotational motions) and begins to flow into the mixing zone! At about the same time with this flow reversal, the high-speed movies show a relatively violent breakup of the pool surface, as if by a suddenly increased steam generation rate; this is the ETHICCA connection mentioned above. Quantitatively, this sudden change in steaming rate is illustrated in Figures D.3a and D.3b, and in detail is seen to depend on particle size and pool depth, and we expect on particle temperature also. However, we believe that the most important parameter affecting ETHICCA is the pour-to-pool diameter ratio, and in the limit to where this ratio is 1, ETHICCA should vanish; preliminary calculations confirm this expectation. The particular mechanism, in elementary terms, is due to the buildup of gravitational head between the inside (voiding) of the mixing zone and the outside water (hence, absolute value of water pool depth is also important), and is another manifestation of the decisively non-one-dimensional nature of premixing transients.

Apart from the water volume flux evolution, the ETHICCA can be tracked from the evolution of the steam volume fraction in time. This is shown in Figures D.4 and D.5 for runs #702 and #905, respectively. These figures are given in two forms, a synoptic one in D.4i,j and D.5i,j for visualizing the whole transient, and a quantitative one in D.4a-h and D.5a-h with the void fraction contours labelled. From these figures, we can visualize the growth of the mixing zone and the breakup associated with ETHICCA. In addition, they may be seen to be remarkably similar (in shapes) to sample snapshots taken during actual runs and collected in Figures D.6 and D.7. In particular, notice the agreement in the violent breakup of the pool surfaces seen to occur at around 0.4 s in run #905.

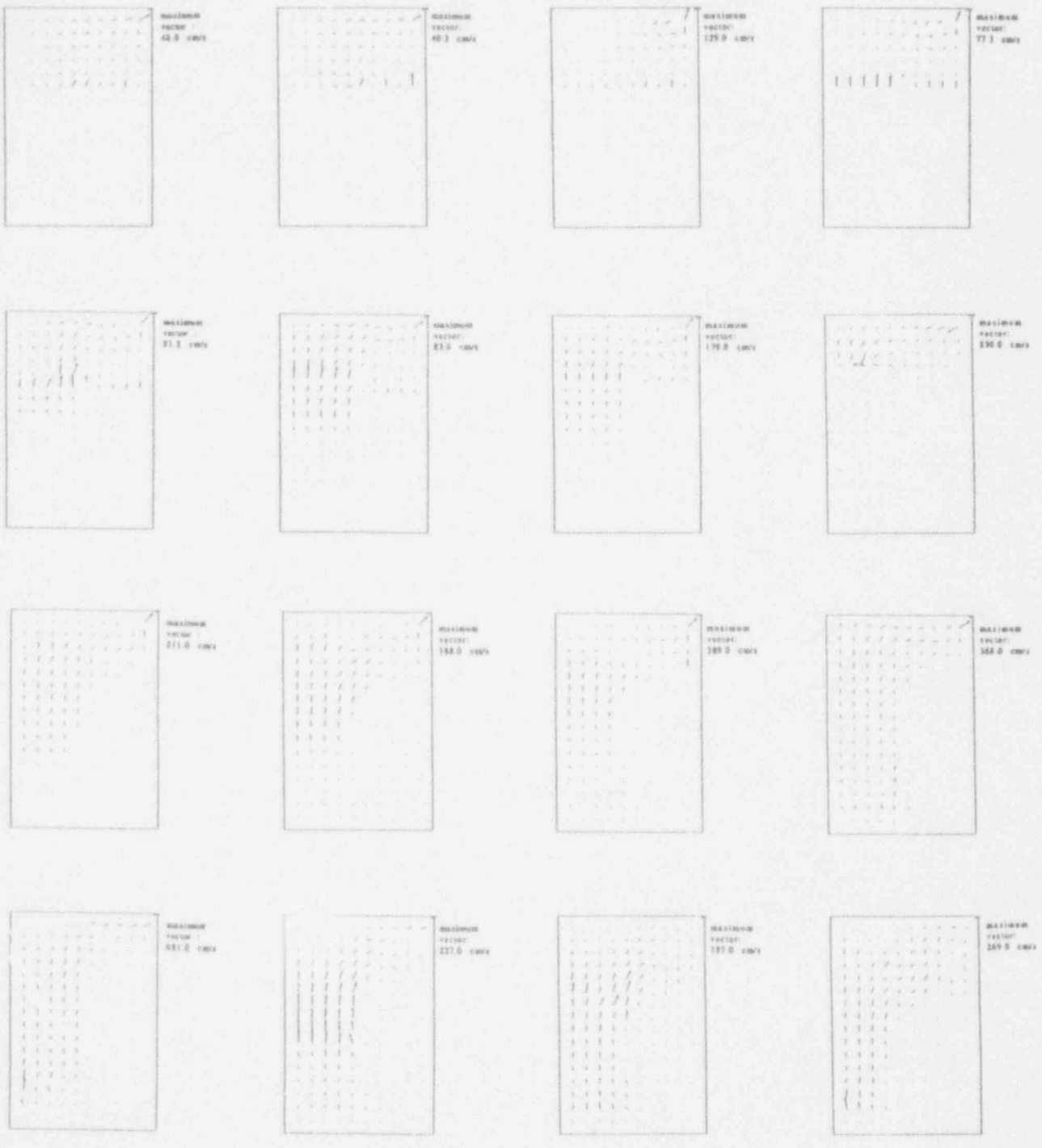

Figure D.1a Evolution of steam volume flux in numerical simulation of Run #702. Upper two rows, times (from impact of balls on the water) are .004 s, .054 s, .104 s, .154 s, .204 s, 254 s, .304 s, .354 s; lower two rows, times (from impact of balls on the water) are .404 s, .454 s, .504 s, .554 s, .604 s, .654 s, .704 s, .754 s.

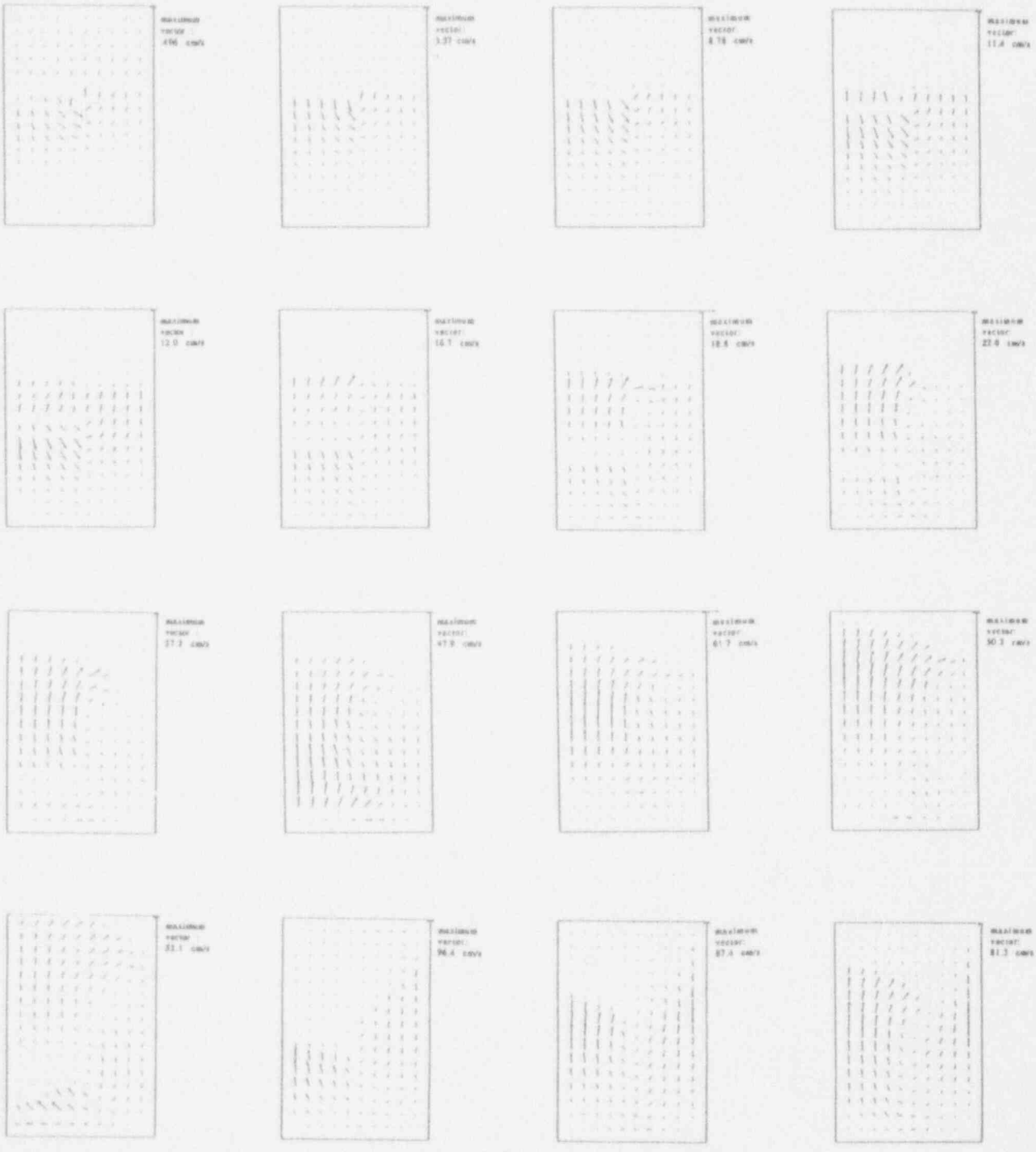

Figure D.1b Evolution of water volume flux in numerical simulation of Run #702. Upper two rows, times (from impact of balls on the water) are .004 s, .054 s, .104 s, .154 s, .204 s, .254 s, .304 s, .354 s; lower two rows, times (from impact of balls on the water) are .404 s, .454 s, .504 s, .554 s, .604 s, .654 s, .704 s, .754 s.

Figure D.2a Evolution of steam volume flux in numerical simulation of Run #905. Upper two rows, times (from impact of balls on the water) are .004 s, .054 s, .104 s, .154 s, .204 s, .254 s, .304 s, .354 s; lower two rows, times (from impact of balls on the water) are .404 s, .454 s, .504 s, .554 s, .604 s, .654 s, .704 s, .754 s.

Figure D.2b Evolution of water volume flux in numerical simulation of Run #905. Upper two rows, times (from impact of balls on the water) are .004 s, .054 s, .104 s, .154 s, .204 s, .254 s, .304 s, .354 s; lower two rows, times (from impact of balls on the water) are .404 s, .454 s, .504 s, .554 s, .604 s, .654 s, .704 s, .754 s.

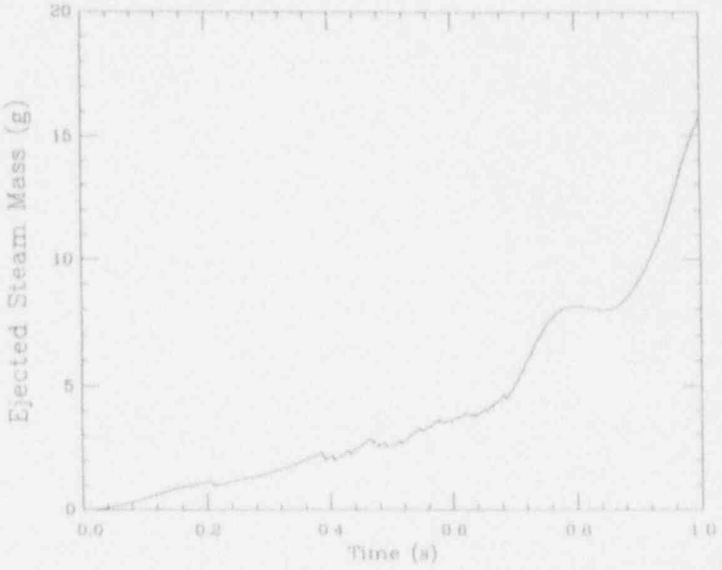

Figure D.3a Mass of steam ejected through venting cell in numerical simulation of Run #702.

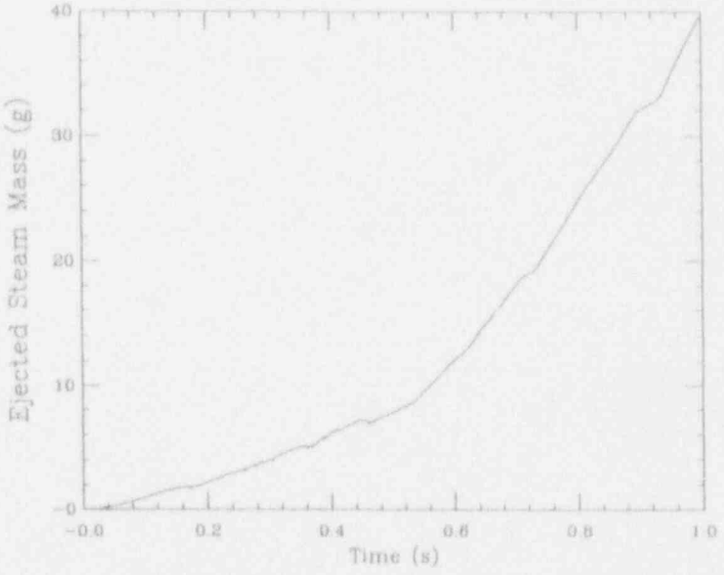

Figure D.3b Mass of steam ejected through venting cell in numerical simulation of Run #905.

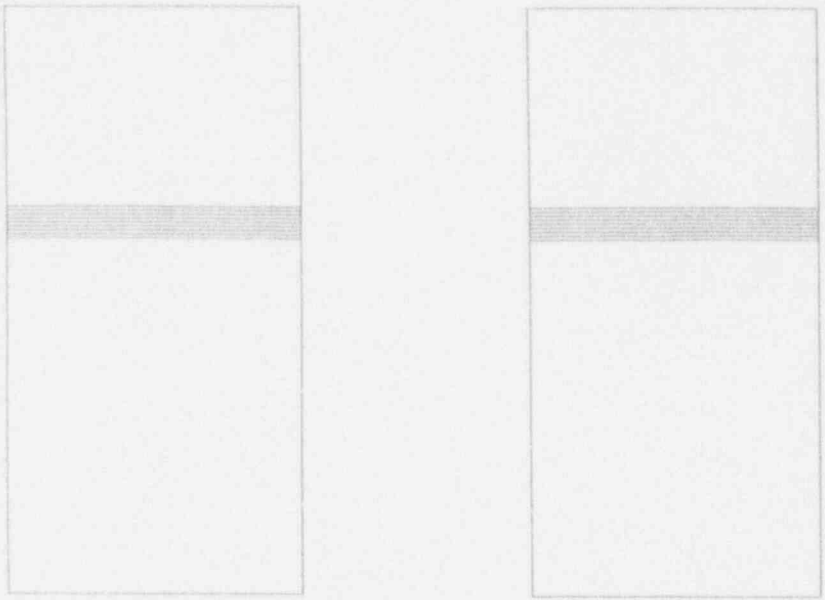

Figure D.4a Evolution of steam volume fraction in numerical simulation of Run #702. Times (from impact of balls on the water) are .004 s, .054 s.

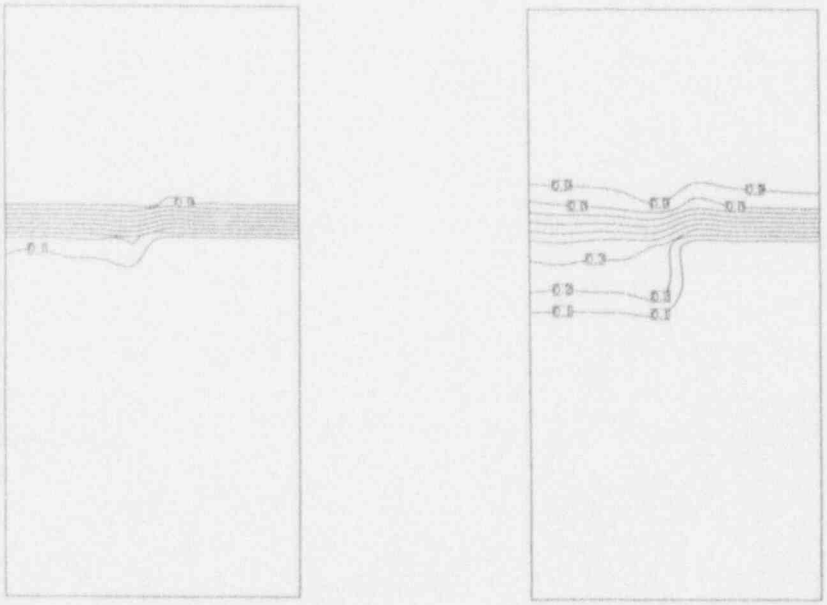

Figure D.4b Evolution of steam volume fraction in numerical simulation of Run #702. Times (from impact of balls on the water) are .104 s, .154 s.

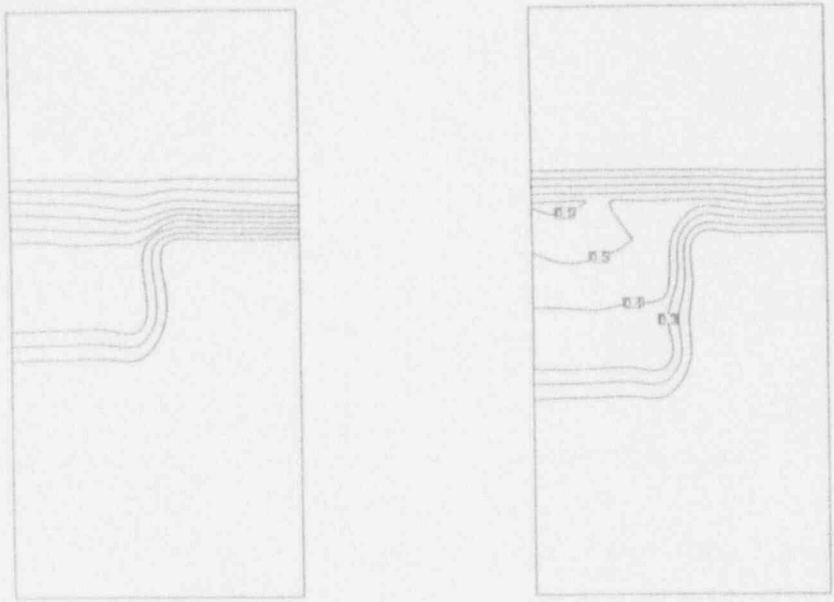

Figure D.4c Evolution of steam volume fraction in numerical simulation of Run #702. Times (from impact of balls on the water) are .204 s, .254 s.

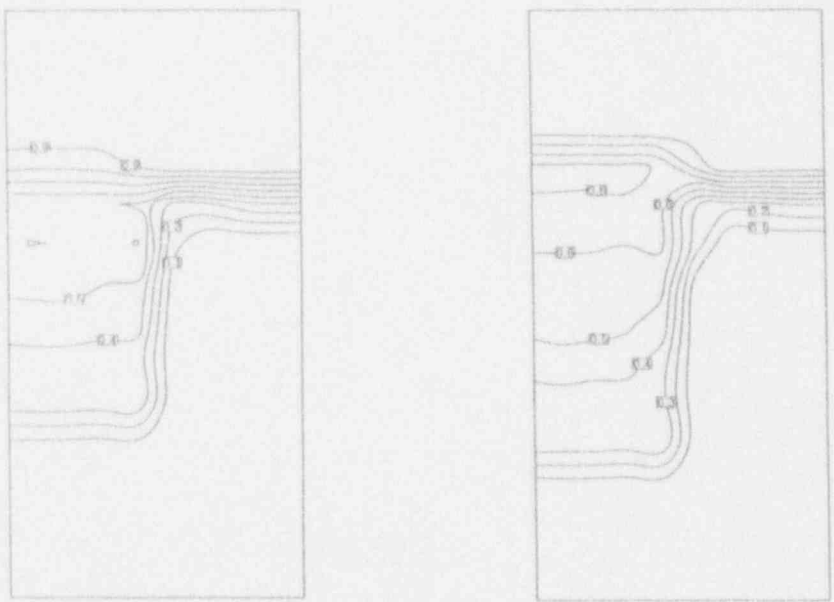

Figure D.4d Evolution of steam volume fraction in numerical simulation of Run #702. Times (from impact of balls on the water) are .304 s, .354 s.

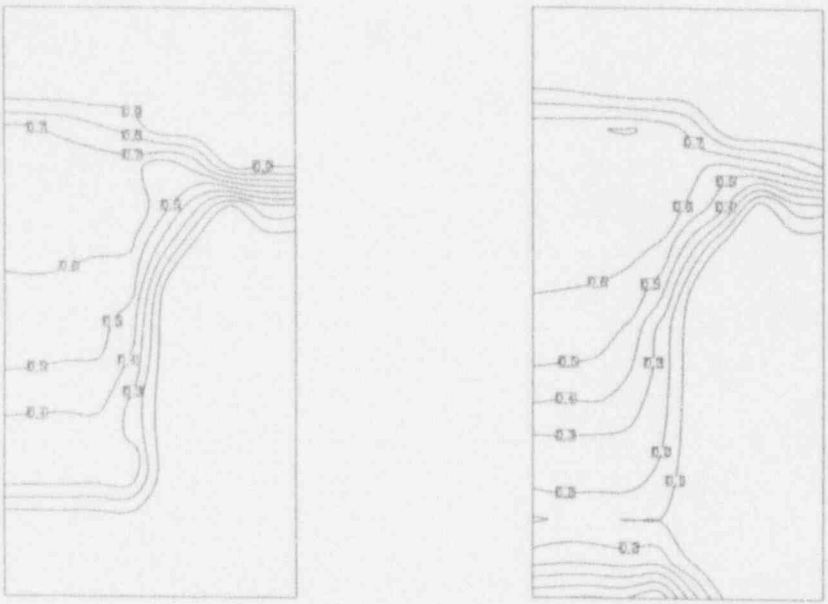

Figure D.4e Evolution of steam volume fraction in numerical simulation of Run #702. Times (from impact of balls on the water) are .404 s, .454 s.

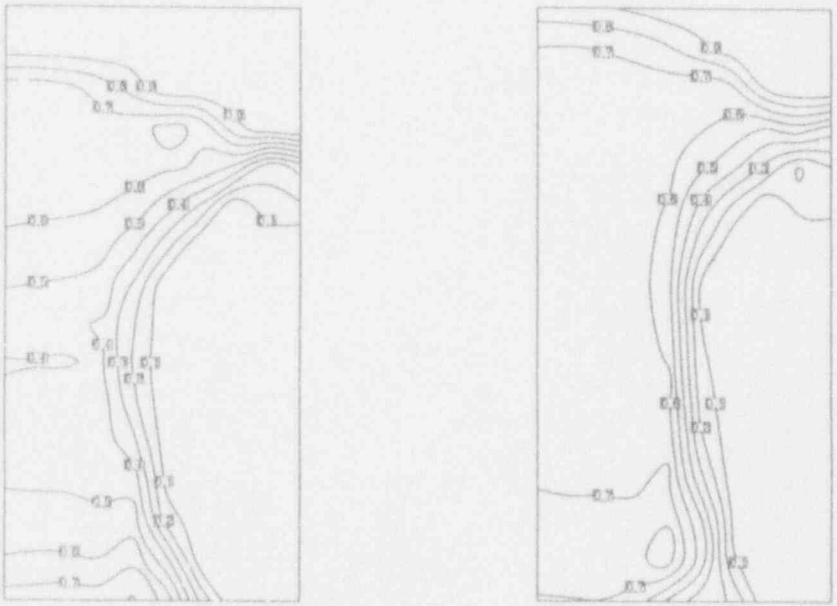

Figure D.4f Evolution of steam volume fraction in numerical simulation of Run #702. Times (from impact of balls on the water) are .504 s, .554 s.

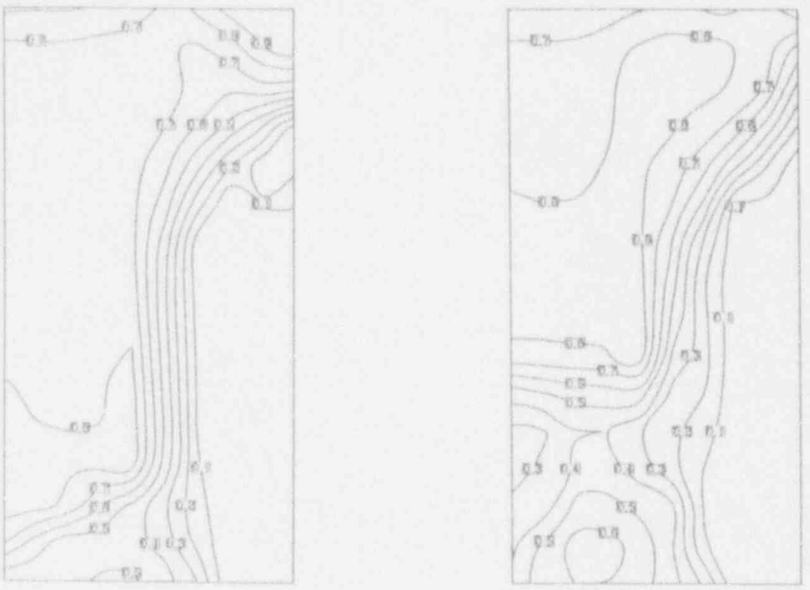

Figure D.4g Evolution of steam volume fraction in numerical simulation of Run #702. Times (from impact of balls on the water) are .604 s, .654 s.

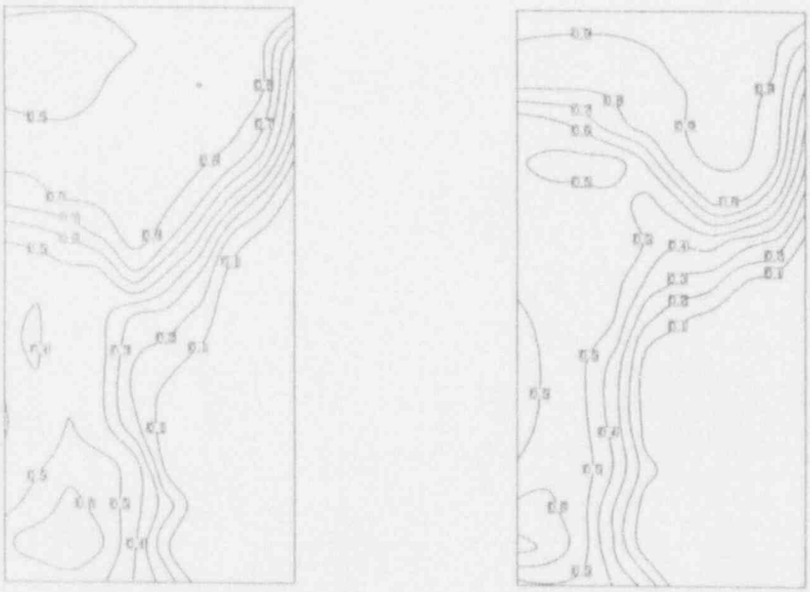

Figure D.4h Evolution of steam volume fraction in numerical simulation of Run #702. Times (from impact of balls on the water) are .704 s, .754 s.

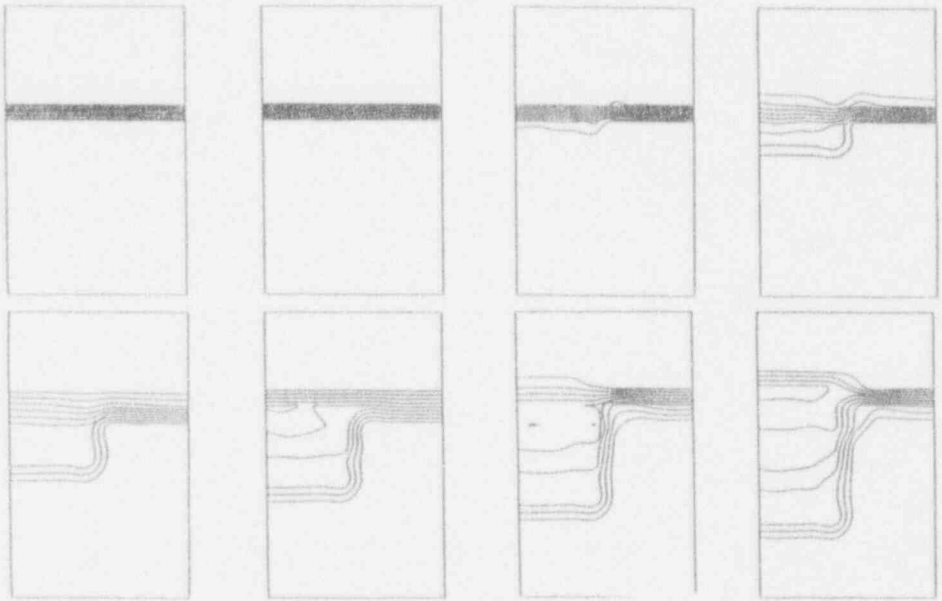

Figure D.4i Evolution of steam volume fraction in numerical simulation of Run #702. Times (from impact of balls on the water) are .004 s, .054 s, .104 s, .154 s, .204 s, .254 s, .304 s, .354 s.

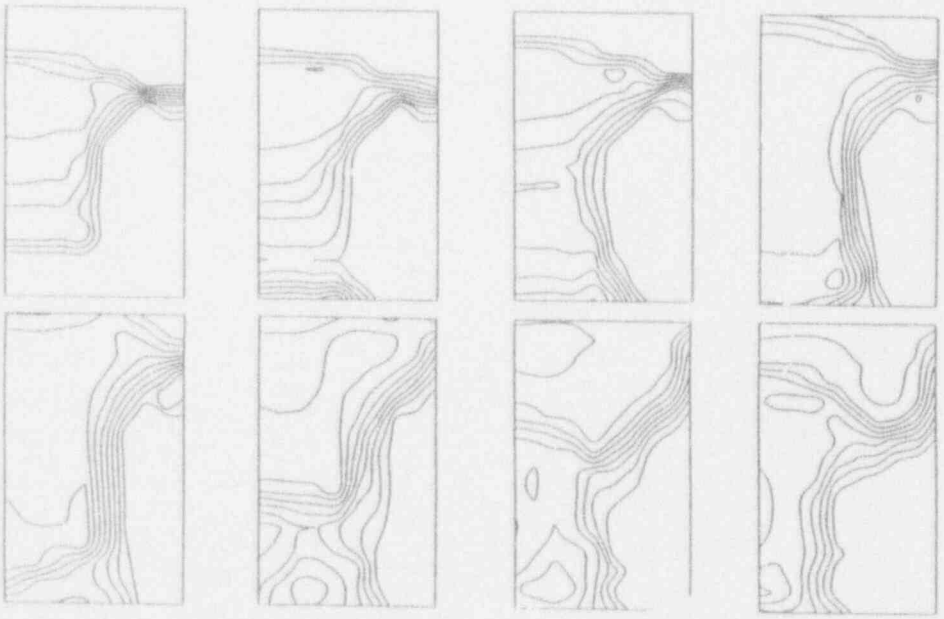

Figure D.4j Evolution of steam volume fraction in numerical simulation of Run #702 Times (from impact of balls on the water) are .404 s, .454 s, .504 s, .554 s, .604 s, .654 s, .704 s, .754 s.

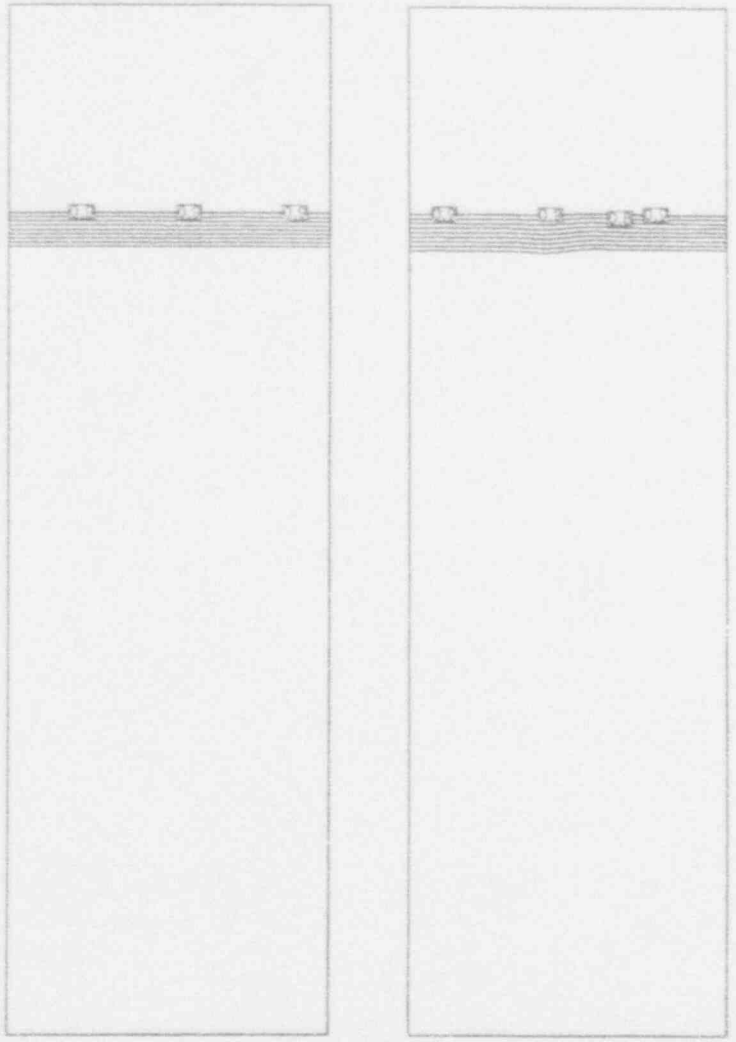

Figure D.5a Evolution of steam volume fraction in numerical simulation of Run #905. Times (from impact of balls on the water) are .004 s, .054 s.

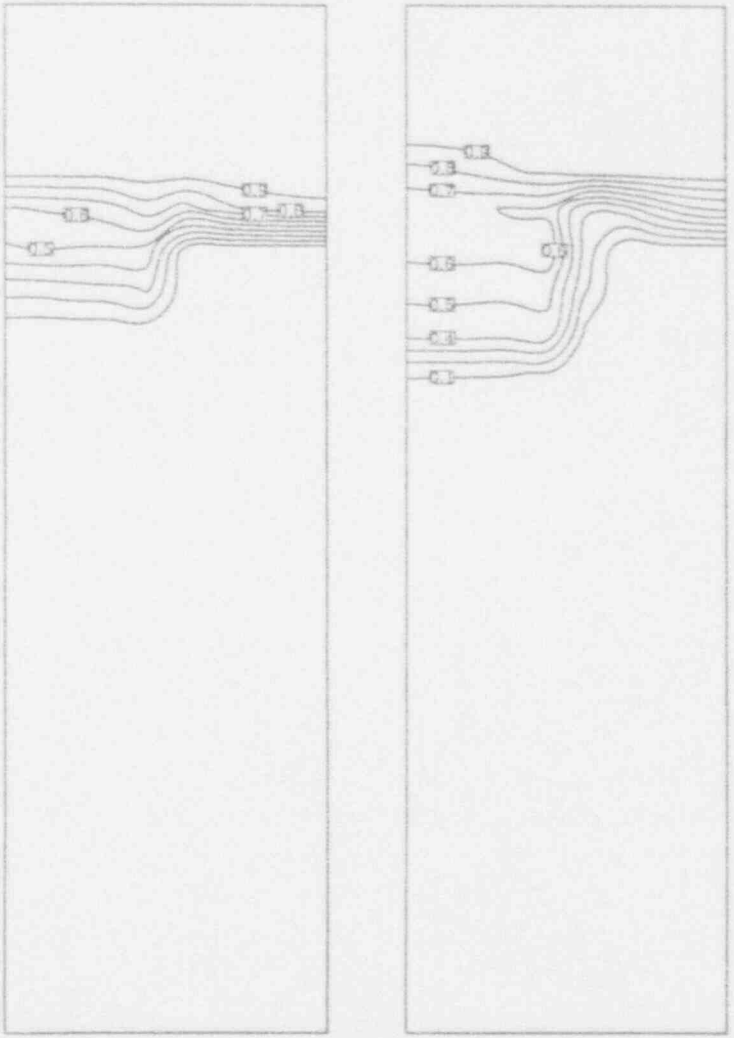

Figure D.5b Evolution of steam volume fraction in numerical simulation of Run #905. Times (from impact of balls on the water) are .104 s, .154 s.

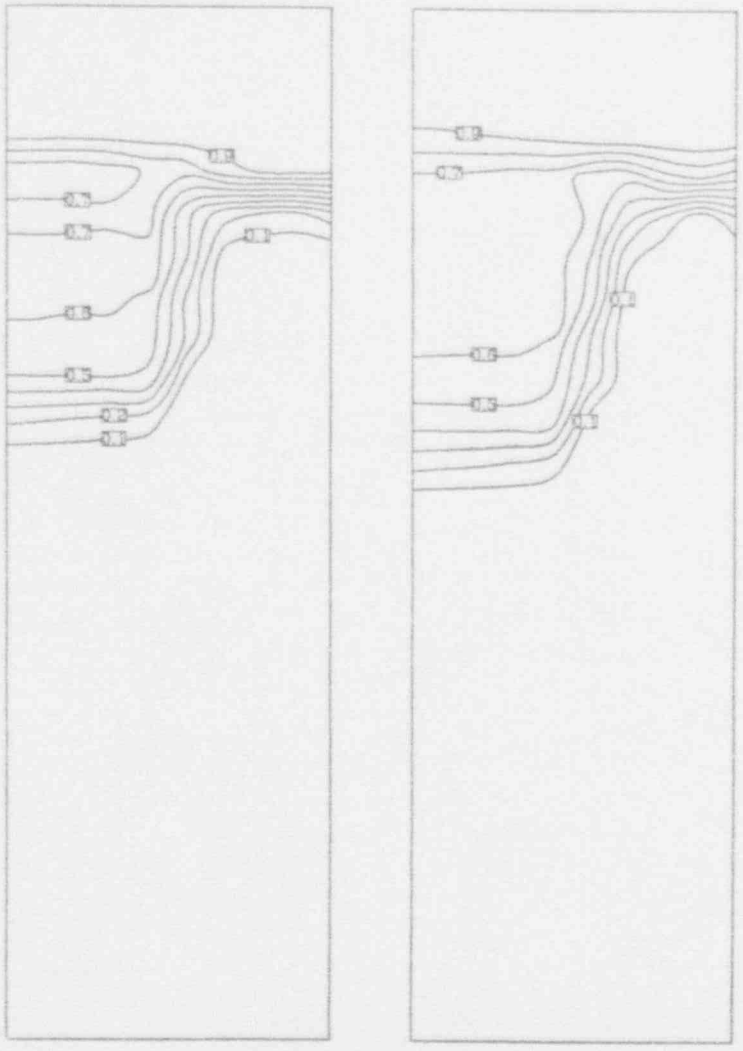

Figure D.5c Evolution of steam volume fraction in numerical simulation of Run #905. Times (from impact of balls on the water) are .204 s, .254 s.

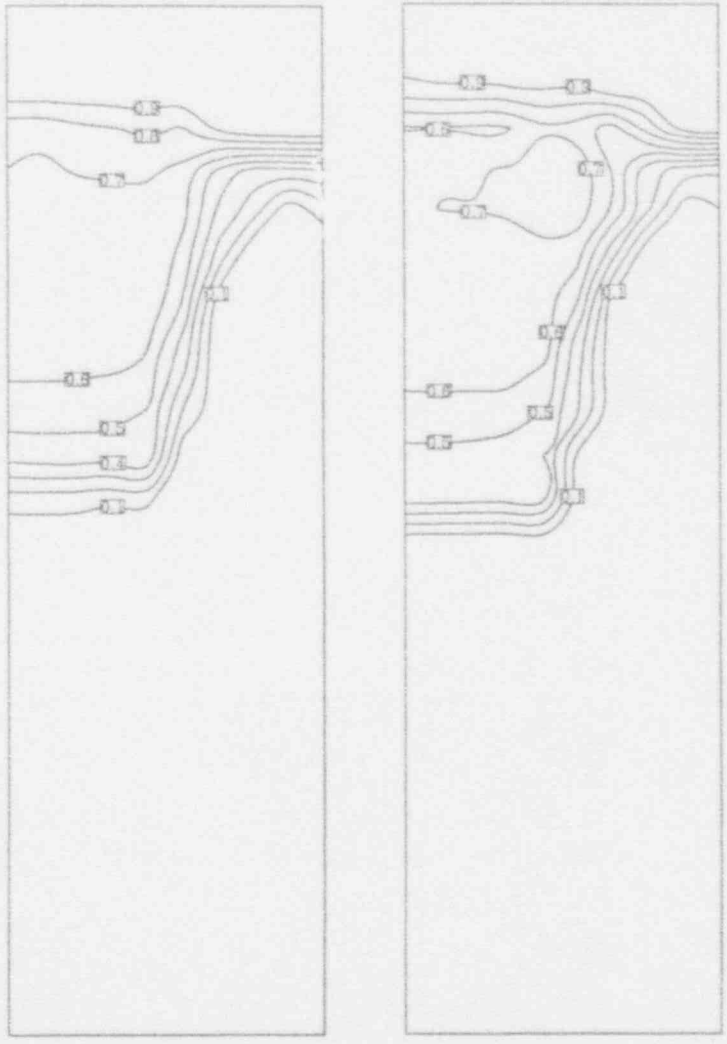

Figure D.5d Evolution of steam volume fraction in numerical simulation of Run #905. Times (from impact of balls on the water) are .304 s, .354 s.

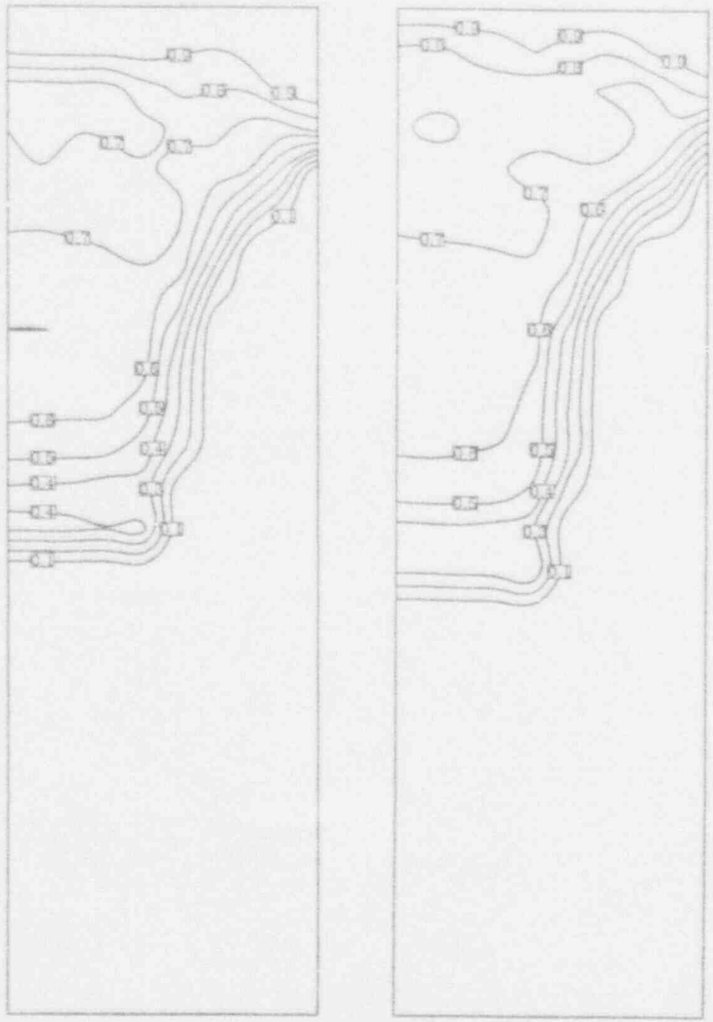

Figure D.5e Evolution of steam volume fraction in numerical simulation of Run #905. Times (from impact of balls on the water) are .404 s, .454 s.

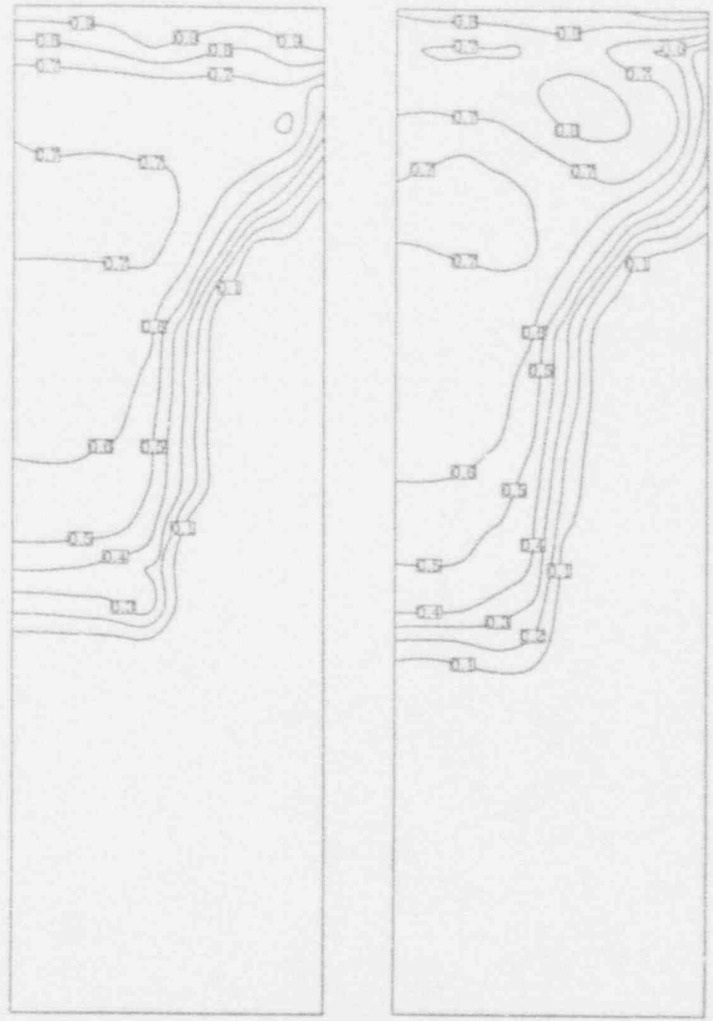

Figure D.5f Evolution of steam volume fraction in numerical simulation of Run #905. Times (from impact of balls on the water) are .504 s, .554 s.

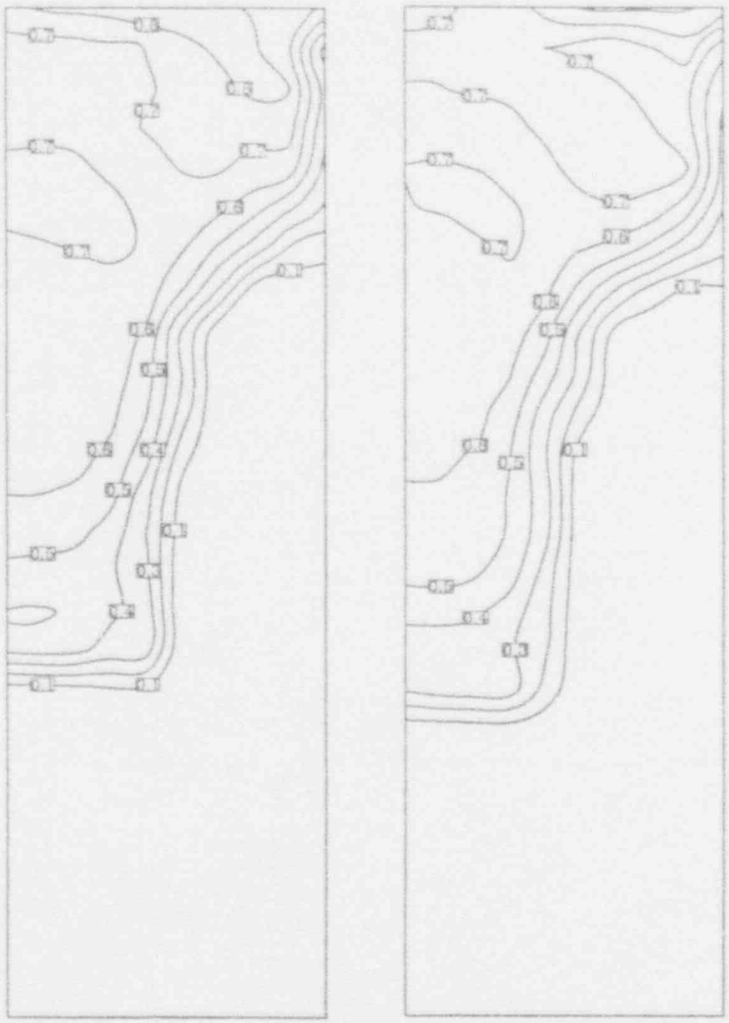

Figure D.5g Evolution of steam volume fraction in numerical simulation of Run #905. Times (from impact of balls on the water) are .604 s, .654 s.

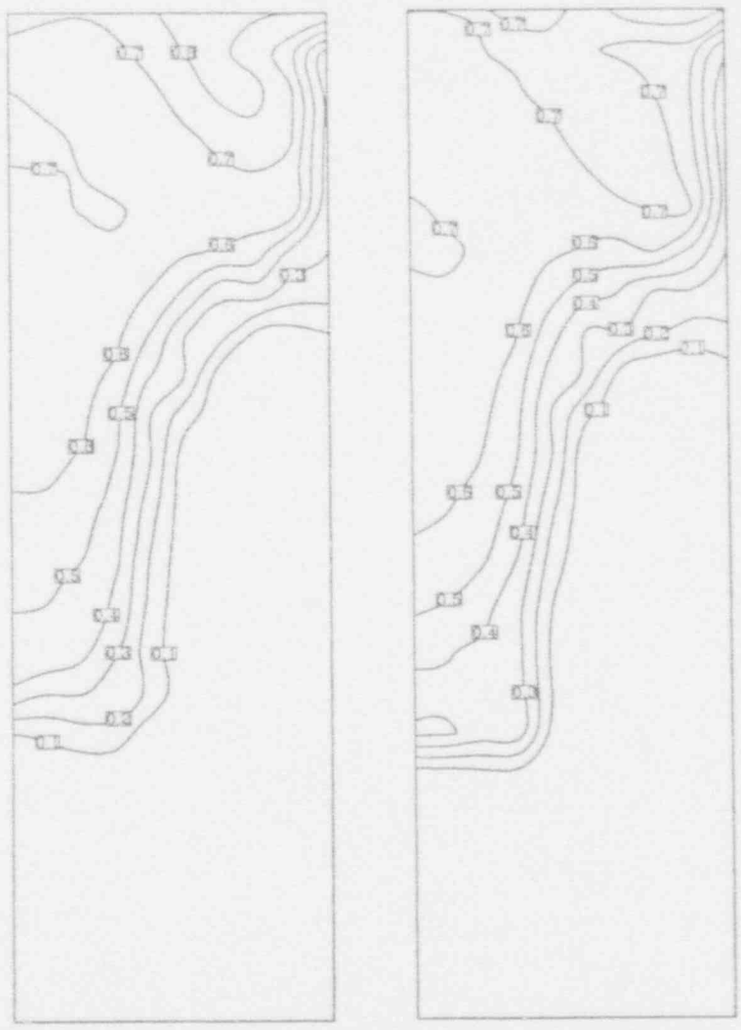

Figure D.5h Evolution of steam volume fraction in numerical simulation of Run #905. Times (from impact of balls on the water) are .704 s, .754 s.

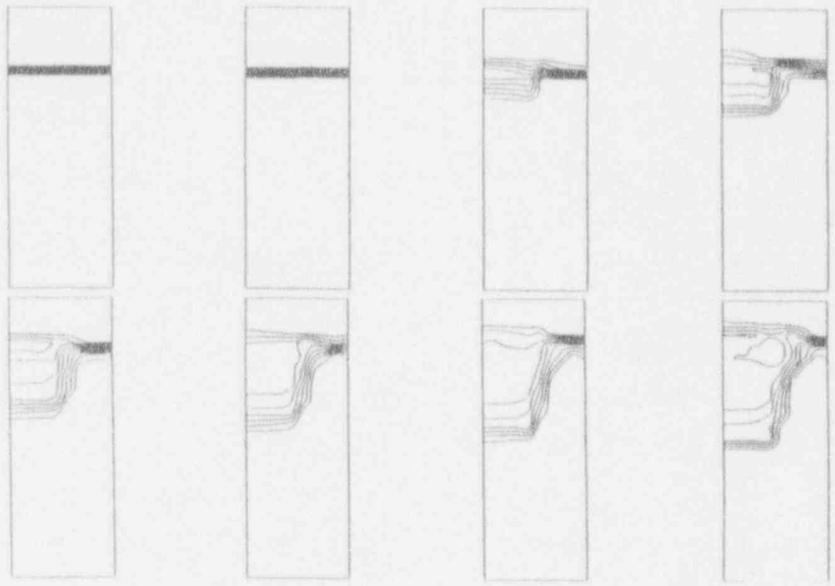

Figure D.5i Evolution of steam volume fraction in numerical simulation of Run #905. Times (from impact of balls on the water) are .004 s, .054 s, .104 s, .154 s, .204 s, .254 s, .304 s, .354 s.

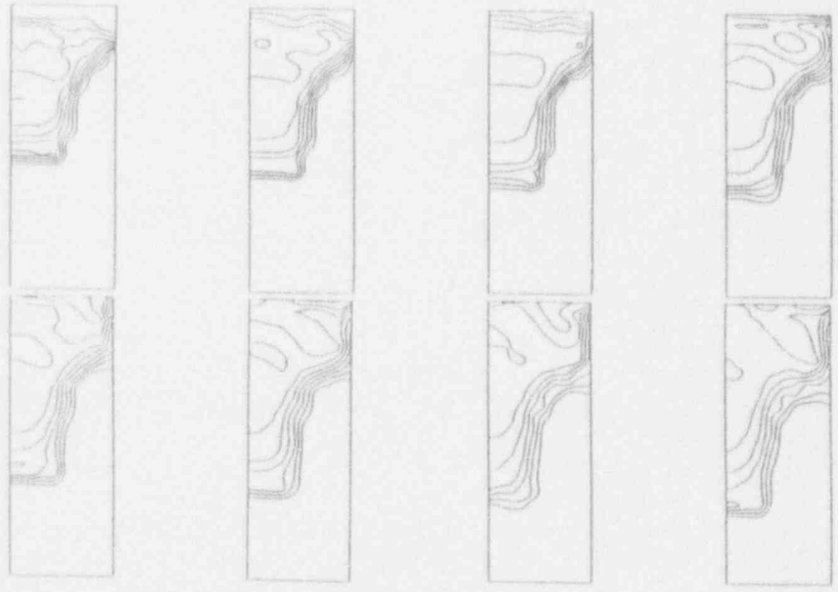

Figure D.5j Evolution of steam volume fraction in numerical simulation of Run #905. Times (from impact of balls on the water) are .404 s, .454 s, .504 s, .554 s, .604 s, .654 s, .704 s, .754 s.

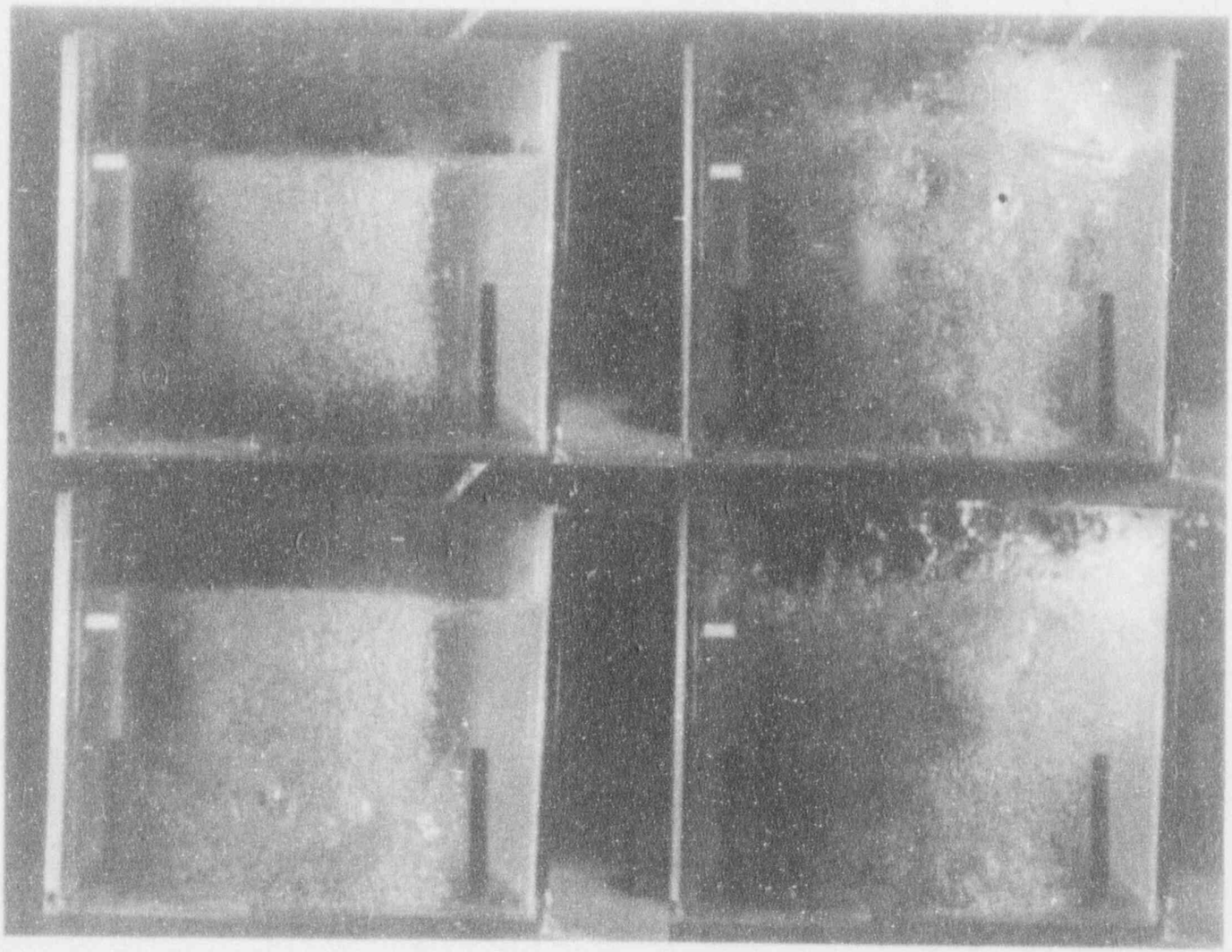

Figure D.6 Snapshots of Run #205 (identical to Run #702). Times (from impact of balls on the water) are .27 s, .57 s, column 1; .87 s and 1.17s, column 2.

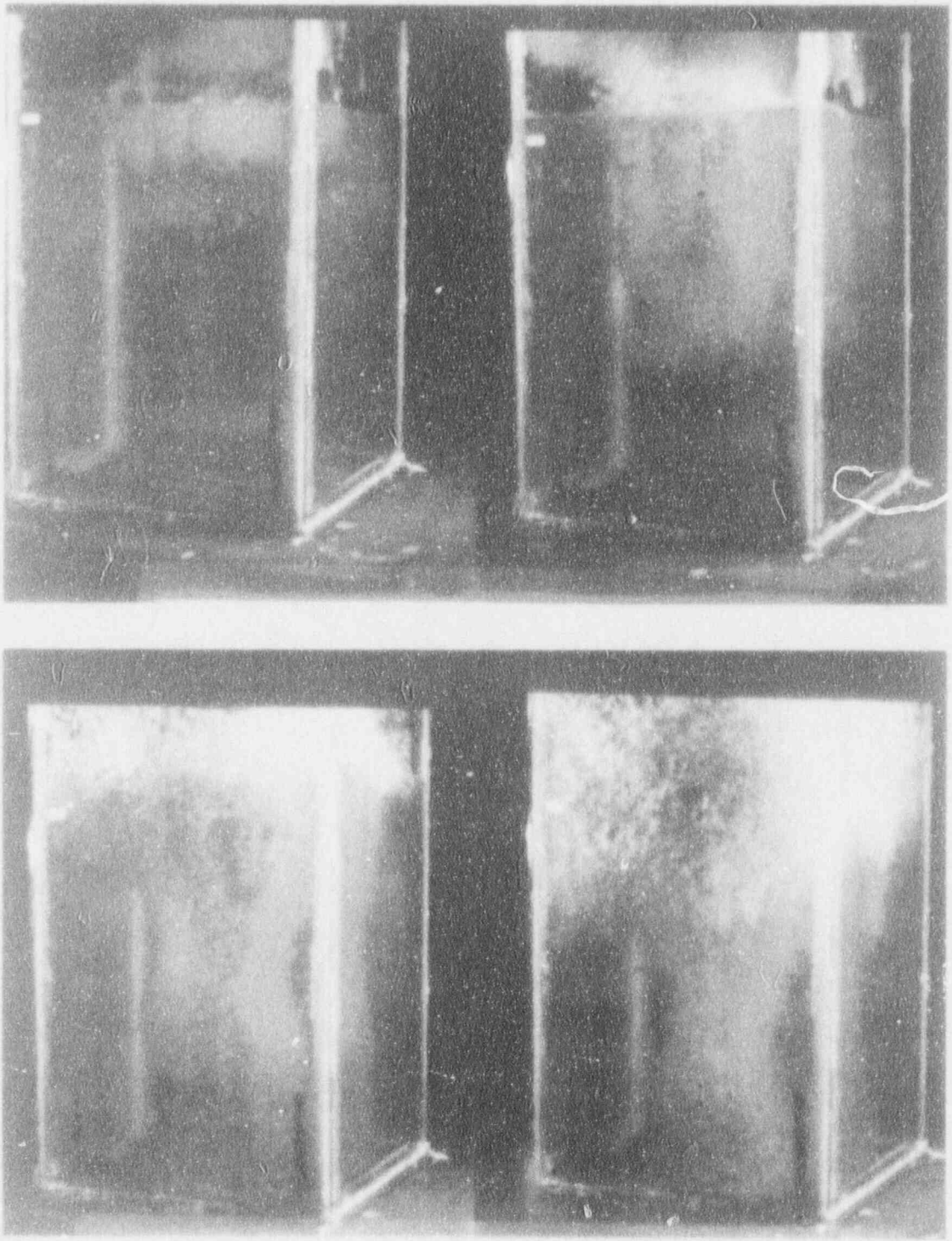

Figure D.7a Snapshots of Run #905. Times (from impact of balls on the water) are .1 s and .4 s., row 1; .7 s and 1.0 s, row 2.

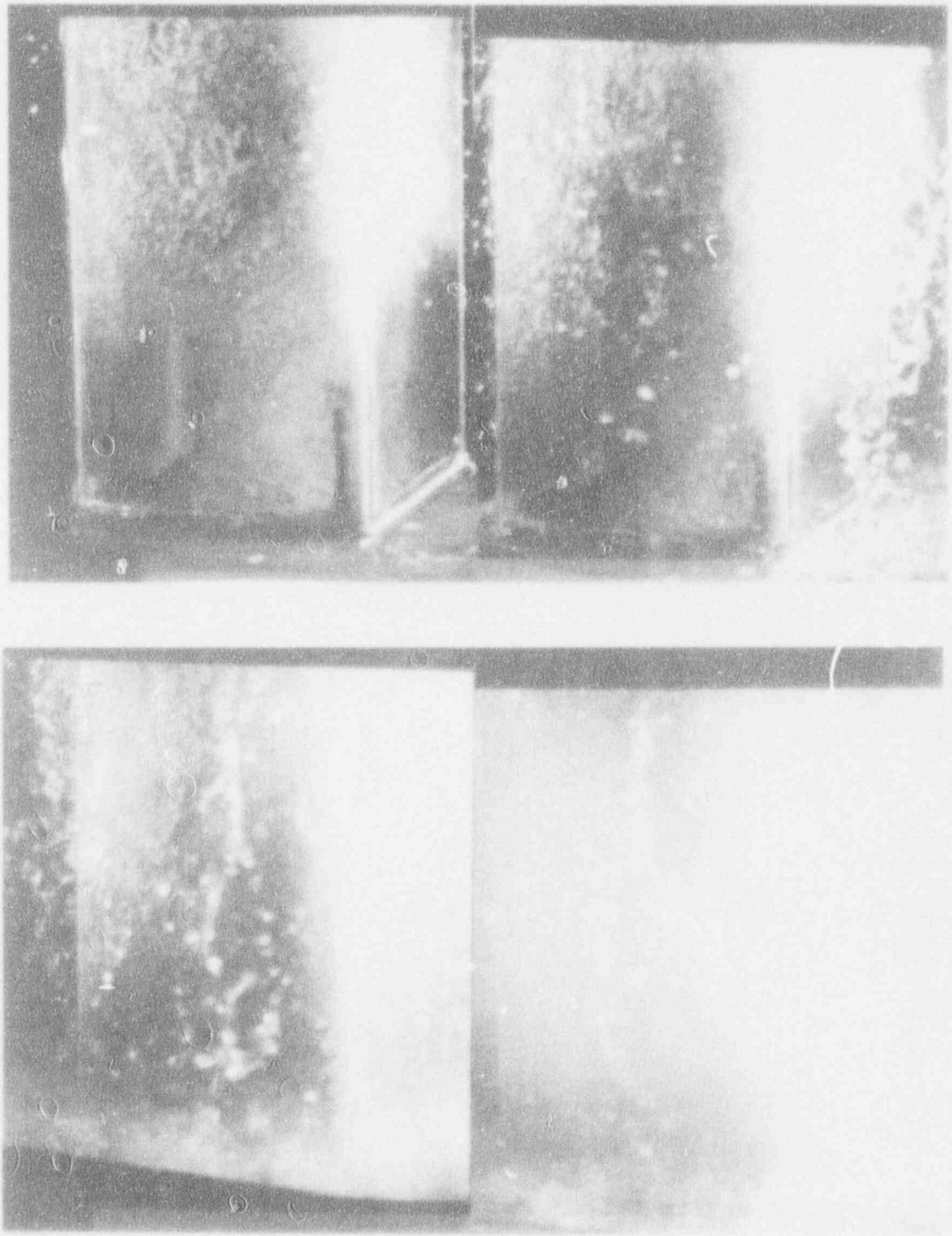

Figure D.7b Snapshots of Run #905. Times (from impact of balls on the water) are 1.3 s and 1.6 s, row 1; 1.9 s and 2.8 s, row 2.

APPENDIX E

FLUTE: FLUORESCENT TECHNIQUE FOR TWO-PHASE-FLOW LIQUID-FRACTION MEASUREMENTS

Appendix E: FLUTE: FLUorescent TEchnique for Two-Phase-Flow Liquid-Fraction Measurements

E.1 Introduction

The phase content is an essential parameter in two-phase flow, so that a whole field of investigation has been devoted to its measurement (Hewitt, 1978; Jones and Delhaye, 1976; Delhaye and Cognet, 1984). The work has been spawned, especially in the 1970's, by the need to understand in detail a very wide spectrum of transient, non-equilibrium, often multi-dimensional two-phase flows as they occur in a postulated Large Break Loss-of-Coolant Accident in a Light Water Reactor (Hon et al., 1980). Early techniques aimed for global measurements (i.e., cross-sectional average), but interest in local measurements began as early as the late sixties and early seventies (i.e., Delhaye et al., 1973). At this time, the available instrumentation is wide ranging in principles employed, and highly sophisticated in technique (e.g., double-sensor resistivity probes that measure not only local void fractions but also local interfacial area concentrations) (Wang and Kocamustafaogullari, 1990; Ishii and Revankar, 1991).

The particular need that led to the investigation and technique reported herein was in measuring the water depletion from the mixing zone prior to a steam explosion. The experiment designed to explore the basic physics of this mixing process involves (Amarasooriya and Theofanous, 1987) a cloud of very hot (hundreds of degrees Celsius) particles poured into a liquid (water) volume, and a complex multiphase interaction as the very high steam production drives water out of the mixing region. The situation is highly transient, the flow patterns strongly two-dimensional, and the range of real interest is where the liquid fraction drops below ~20%, i.e., the measurement is needed from liquid-continuous to a highly dispersed droplet flow. More generally, the technique is uniquely well suited for multi-dimensional, highly dispersed flows for which both radiation attenuation and the local contact probe techniques fail because of the respective attributes; that is, multi-dimensionality requires a local measurement which is not possible by attenuation methods (even tomography is limited by the conflicting requirement of spatial and temporal resolution), and local contact probes are not suitable for highly dispersed flows. For a good perspective on these matters, see Jones and Delhaye (1976).

E.2 The Measurement Principle

The basic idea is to induce and detect narrow band irradiation locally, such that in combination with attenuation principles a linear response, independent of the flow regime, can be obtained. As such, the technique relates to and combines elements of several previously known (not necessarily for two-phase) measurement techniques, including (a) activation methods such as "pulsed neutron activation", "laser raman spectroscopy" (Regnier, 1973), "laser-induced fluorescence", etc., (b) photon attenuation methods such as "γ and X-ray absorption", etc., and (c) optical probe methods (measuring changes of the refractive index of the surrounding medium) such as the "U-shaped fiber optical sensor" of Danel and Delhaye, (1971), etc. In particular, laser-induced fluorescence has been used by McDaniel (1983a, 1983b) to measure velocity, density and pressure in iodine-seeded supersonic gas flows, by Owen (1976) to measure velocity and concentration (i.e., mixing) in a single-phase flow (two confined co-axial liquid jets), and more recently by Lai and Faeth (1987), again for single-phase, gaseous, buoyant wall plumes.

In this development we use Ultraviolet (UV)-induced fluorescence in combination with fiber optics and certain filter/mirror arrangements to achieve:

(a) a good separation between the exciting and emitted radiation and

(b) the proper attenuation behavior for a linear response.

The basic ideas of how these goals can be met are described below. Some details of the instrument in its present configuration (FLUTE.1) are given in the next section.

Fluorescence is a type of luminescence phenomenon created by the emission of energy as a molecule, activated by the absorption of a photon, returns to its ground state. Some of the absorbed energy is dissipated in collisions with neighboring molecules in the brief period prior to emission, thus the emitted radiation will be of lower energy and longer wavelength than the energy absorbed in the excitation (Guilbault, 1973; Udenfriend, 1962). The time for which the molecule stays in the excited state is extremely short (order of 10^{-9} s); for the fluorescein dye utilized in the present work, it is $\sim 5 \times 10^{-9}$ s. The peak excitation occurs at 491 nm and the peak in the fluorescence is at 512 nm. With the fiber optic arrangement of Figure E.1, that is, a well-collimated beam of UV light and an orthogonally-placed detection path, we can create a measuring (or sampling) volume with a characteristic dimension as small as ~1.5 mm. Neglecting beam divergence and attenuation of the fluorescence in the solution (over the path L_2), the power (P) received by the detecting fiber can be expressed as

$$P = I_o A_o \phi e^{-L_1 ac\beta}(1 - e^{-\Delta ac\beta})\mathcal{F} \qquad (E.1)$$

where I_o is the intensity of the UV exiting the emitting fiber, A_o is the cross-sectional area of each fiber, c is the concentration of the fluorescein dye in solution (grams of dye per gram of solution—here 10^{-6} to 10^{-4}), ϕ is the quantum efficiency (defined as the number of quanta emitted for each quantum absorbed; for the dye used here, $\phi = 0.92$), a is the absorption coefficient of the solution for the UV radiation, β is the liquid fraction taken as constant along the short path length, and $\mathcal{F}$ is a factor for the geometric optics involved. The basic idea of the current application is to make $acL_1\beta << 1$, i.e., by appropriate selection of c and L_1, such that $e^{-acL_1\beta} \sim 1 - acL_1\beta \sim 1$ and $e^{-ac\Delta\beta} \sim 1 - ac\Delta\beta$. Thus, Eq. (E.1) can be linearized to

$$P = I_o A_o \phi ac\Delta\beta\mathcal{F} \qquad (E.2)$$

and with all other factors remaining constant the signal received is made proportional to the liquid fraction β.

Note that $\Delta << L_1$ and the conditions for linearity above is achieved by keeping the product $ac\beta L_1$ small. Maximum sensitivity can be obtained by selecting a concentration, c_o, such that, with the liquid fraction at the upper end of the range of interest (for the particular application), say β_{max}, the signal obtained is at the upper end of the linear response. Clearly, as β_{max} increases c_o must decrease proportionally. At the limit of covering the whole liquid fraction range, $\beta_{max} = 1$, c_o has to be quite small; however, with a good UV source, a good signal-to-noise result can be obtained for β's down to a few percent. The advantage of operating at this limit is that the calibration procedure is greatly simplified, i.e., only one reading (with appropriate consideration of background noise, of course) at $\beta = 1$ defines the calibration line.

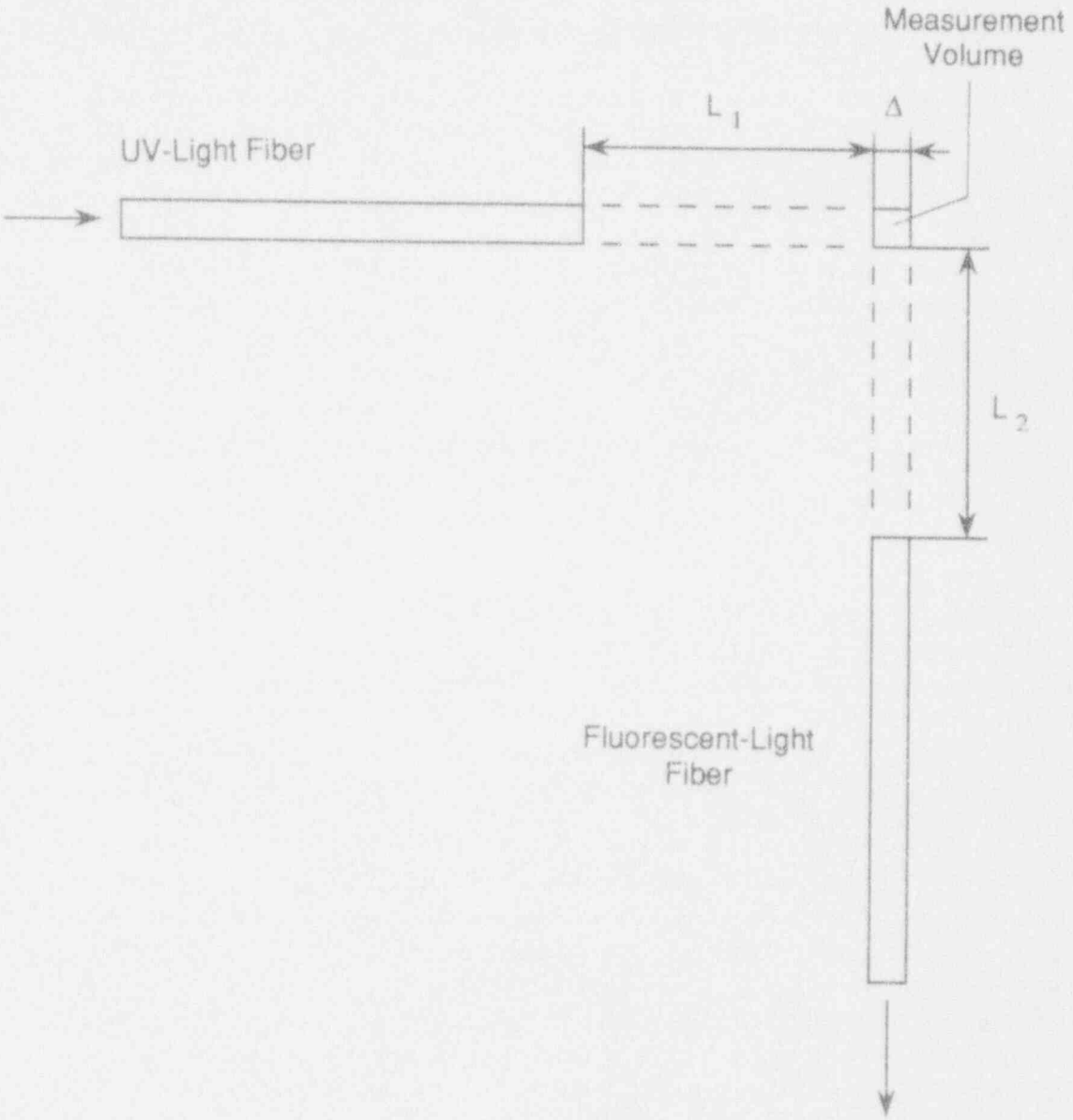

Figure E.1 Schematic of the Arrangement of optical fibers in FLUTE.

For the same concentration then, c_o, the fluorescence can be directly related to liquid fraction through the same calibration line.

Alternatively, assuming that the absorption coefficient does not vary with concentration and that its effective value in two-phase flow is not strongly affected by reflections and refractions (see discussion in Section E.4), Eq. (E.1) can be used directly as providing P as a function of $c\beta$. In this approach a whole calibration curve is obtained by measurements at different values of c, extending well into the non-linear region, in 100% liquid. This is the approach employed in this paper.

E.3 Demonstration of the Technique

In the present experimental set up, the UV source is a 200 W mercury lamp (Oriel Corp. Model 66042). A good separation between excitation and emitted radiations can be obtained by limiting the UV to under 400 nm and measuring the fluorescence in a narrow band around 510 nm. This is accomplished by passing the source light (after collimation) through a dichroic mirror that reflects selectively in the 300–450 nm (and only 10% of the spectrum above), while it transmits and absorbs all other wavelengths. A colored glass filter is used next to eliminate completely the 400 to 700 nm portion of the spectrum (it passes 200–400 nm and above 700 nm) before it enters the transmitting fiber. The collecting fiber leads to a narrow band width interference filter with a peak transmittance at 510 nm and a 50% value in 10 nm around the peak. This filtered signal is read directly into a digital Radiometer/Photometer system (EG&G model 550-1) for steady-state measurements or into a system of photomultiplier tubes, digital voltmeters, and an Hewlett Packard high-speed data acquisition system for transient measurements. Only steady-state measurements are reported here, with the photometer RC time constant set at 400 ms.

The measuring volume can be controlled by adjusting the beam divergence and the distances from the control volume. The best collimation (minimum divergence) can be obtained by placing the input end of the emitting fiber directly into the collimated beam of the UV source. Various degrees of divergence can be obtained by focusing the source beam into the fiber inlet. A corresponding (to the focusing) intensification of the transmitted light can then be obtained. For each application, the selection of these parameters (L_1, L_2, incident beam intensity and divergence) can be made to optimize the results.

We will limit ourselves here to the demonstration of the feasibility of the technique for two-phase dispersed flows in the low liquid fraction range. For this purpose we obtain a basic calibration curve giving the variation of measured signal with dye concentration at 100% liquid, then demonstrate the consistency obtained per Eq. (E.1) by measuring in a dispersed flow of known dye concentration and liquid fraction; that is the same reading for the same $c\beta$. The calibration curve at 100 % liquid was obtained by starting somewhat above the upper end of the linear region (for the spacing of $L_1 = L_2 = 8$ mm utilized) and carrying out successive dilutions, down to a few percent of the original concentration. The known liquid fractions were obtained by using precision-made perforated discs in the manner described below.

The perforated discs were made from acrylic material (~1 cm thick) drilled on a square array covering a circular area of diameter ~23 mm. The center-to-center spacing is called D, and the hole diameter d; a disc is then referred by the particular d/D values in thousandths of an inch as, for example, 30/110 meaning holes of 30 thousandths on a 110 thousandth square array. A steady flow through a disc was created under a constant liquid head h, which could be varied in the range of 30 to 70 cm. Taking into account the acceleration of the flow, under gravity, to a measuring distance z below the disc, the liquid fraction can be simply expressed as

$$\beta = \beta_{ref}\sqrt{\frac{h}{h + z/\alpha_v^2}} \qquad (E.3)$$

where α_v is a loss coefficient for the flow through the hole (measured experimentally) and β_{ref} is the liquid fraction at the disc exit given simply by

$$\beta_{ref} = \frac{\pi}{4}\frac{d^2}{D^2} \qquad (E.4)$$

with d being the actual diameter of the holes. Thus, by varying the liquid head, h, and the measuring distance, z, a range of two-phase flow cross-sections with "known" liquid fraction can be created. Further, some variation of the internal flow characteristics could be obtained by utilizing 5 discs as follows: 29/80, 29/100, 35/80, 35/110, 51/130. The hole diameters specified are nominal values, some variation being present due to "wiggling of the drill". In calculating β_{ref} a rough average value was used within the range obtained from physical inspection of each disc.

The calibration curve obtained at 100% liquid in four separate trials is shown in Figure E.2. Each trial consisted of a series of measurements obtained with liquid samples from a series of standard solutions previously prepared for this purpose, over the time span of 48 hours. The upper end of the linear region appears at a concentration of $\sim 5 \times 10^{-6}$ (relative units, mass of dye to mass of water). Some systematic variation is evident in the non-linear region, whose exact source has not been identified.

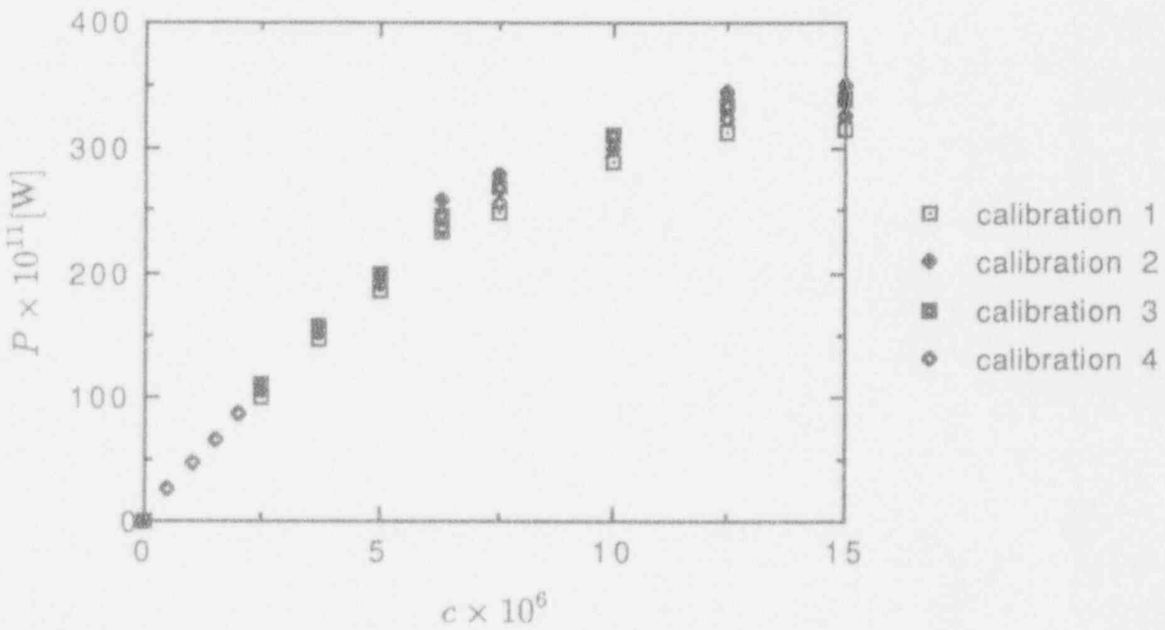

Figure E.2 Four calibrations obtained at 100% liquid, as described in the text. The points in the range $0 < c < 2.5\ 10^{-6}$ were obtained only for calibration 4.

The data obtained with the five discs are shown, in relation to the calibration line, in Figure E.3. In all these runs the same dye concentration of 10^{-5} was utilized. The data were generated with 5 different liquid driving heads, at a fixed measuring distance ($z = 19$ cm) and a fixed

measuring position (center) within the flow. For each disc two independent trials were made—each trial involved a complete reassembly of the experimental set-up. The positioning of the measurement volume was made visually, such that it was well within the flow while avoiding any locally inhomogeneous regions. The difference between these data and the calibration line gives a first idea of the current "accuracy" of the technique, with the following important qualifications:

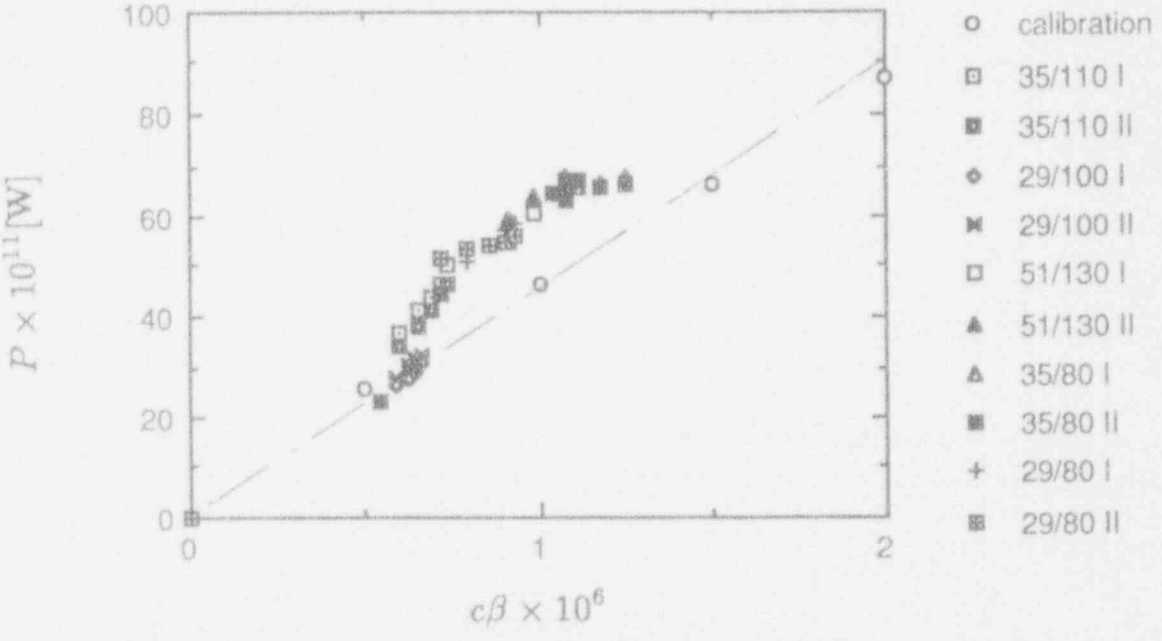

Figure E.3 Fluorescence data as a function of $c\beta$, obtained with five different discs (with a concentration of 10^{-5}) in relation to the calibration line.

(a) Because of small imperfections in hole positioning, size, and alignment there may be a significant variation of *actual local* (in the measuring volume) liquid fraction and the average value calculated from Eqs. (E.3) and (E.4). Thus the measurements could be even better than appear in Figure E.3—disc 29/100 which lies exactly on the calibration line appeared to produce the most uniform flow.

(b) Because of reflections and refractions at the gas/liquid interfaces (see also below) there may be inherent errors in the measurement, depending on the actual frequency and geometry of these interfaces in, and perhaps even around, the measuring volume. In this interpretation, it appears that, at least for the kinds of flows considered here, such errors are limited, and the technique is still rather promising.

(c) The experimental spread in the non-linear portion of the calibration curve (Fig. E.2), and the use of c_o in this range (10^{-5}) for the two-phase measurement, could likewise impact the linear range as in Figure E.3.

E.4 Discussion

The presence of gas/liquid interfaces within the travel paths of the emitted and the detection beams introduce some complications not considered explicitly in the formulation of Eq. (E.1). Several interpretations/approaches are possible, and the purpose of this section is to provide some initial considerations on this topic. In addition, since the high-speed data acquisition system will allow essentially instantaneous "readings" at rates up to 100 kHz, some interesting questions arise on how to optimize the rate in relation to a particular transient under investigation (i.e., time constant of transient, characteristic length scales in the flow, flow speed). Some initial considerations on this topic are presented also in the second part of this discussion.

E.4.1 The Role of Gas/Liquid Interfaces

The refractive index of water in the 400 to 500 nm range of interest is ~1.35 (Hale and Querry, 1973), which implies a normal reflectivity of only 1.7%. As the angle of incidence increases the reflectivity increases also, but it becomes significant only beyond ~70 degrees, thus averaged over all angles the so-called hemispherical reflectivity is still only a few percent (Siegel and Howell, 1981). Clearly, if only a few interfaces are involved the loss due to reflections is negligible. Depending on the two-phase flow regime, i.e., the liquid fraction and the internal length scales, the fiber arrangement can be made such that this condition is met. Note that in addition to fiber distance and beam collimation this "arrangement" can also involve bundles of fibers. The absorptivity in distilled water of both UV and fluorescent radiation is also negligible. Thus refraction remains the only intangible, for now, source of potentially significant error. We believe that it is responsible for a significant fraction, if not all, of the deviation from the ideal behavior (calibration line) observed in Figure E.3. As noted already, it is encouraging that even in the presence of a significant number of drops this error appears to be limited; however, more study is needed to fully characterize this effect, such as to optimize the measurement. On the other hand, a limiting condition can be identified as one with a close enough proximity of the fibers that minimize the refraction error to the required degree. The quantitative consideration of refraction can be found in Appendix I.F

E.4.2 Measurement Statistics

Because of the short response time and the capability of making measurements in a small volume, FLUTE is quite flexible and can be adapted to measure liquid fractions in rapidly varying, in both space and time, two-phase flows. In a specific experiment, the measuring volume and data acquisition rate must be selected to ensure that the correct statistics can be estimated from the "sample" record. To illustrate this point, let us consider an idealized situation as follows: a spherical measuring volume of radius R_o within an infinite regular square array of spherical drops of radius R_ℓ. Depending on the location of the center of the measuring volume, the "measured" liquid fraction will fluctuate between a theoretical maximum and minimum as illustrated in Figure E.4. The number of "measurements" required such that five consecutive "average" liquid fractions (over the total number of "measurements") agrees to within 1% of the true value is shown in Figure E.5. The results shown in Figures E.4 and E.5 provide an initial perspective on the interplay between β, R_o/R_ℓ, the number of measurements required, and the potential error band involved. As expected, the measurement requirements increase as the liquid fraction and the relative (to the drop) size of the measuring volume decrease.

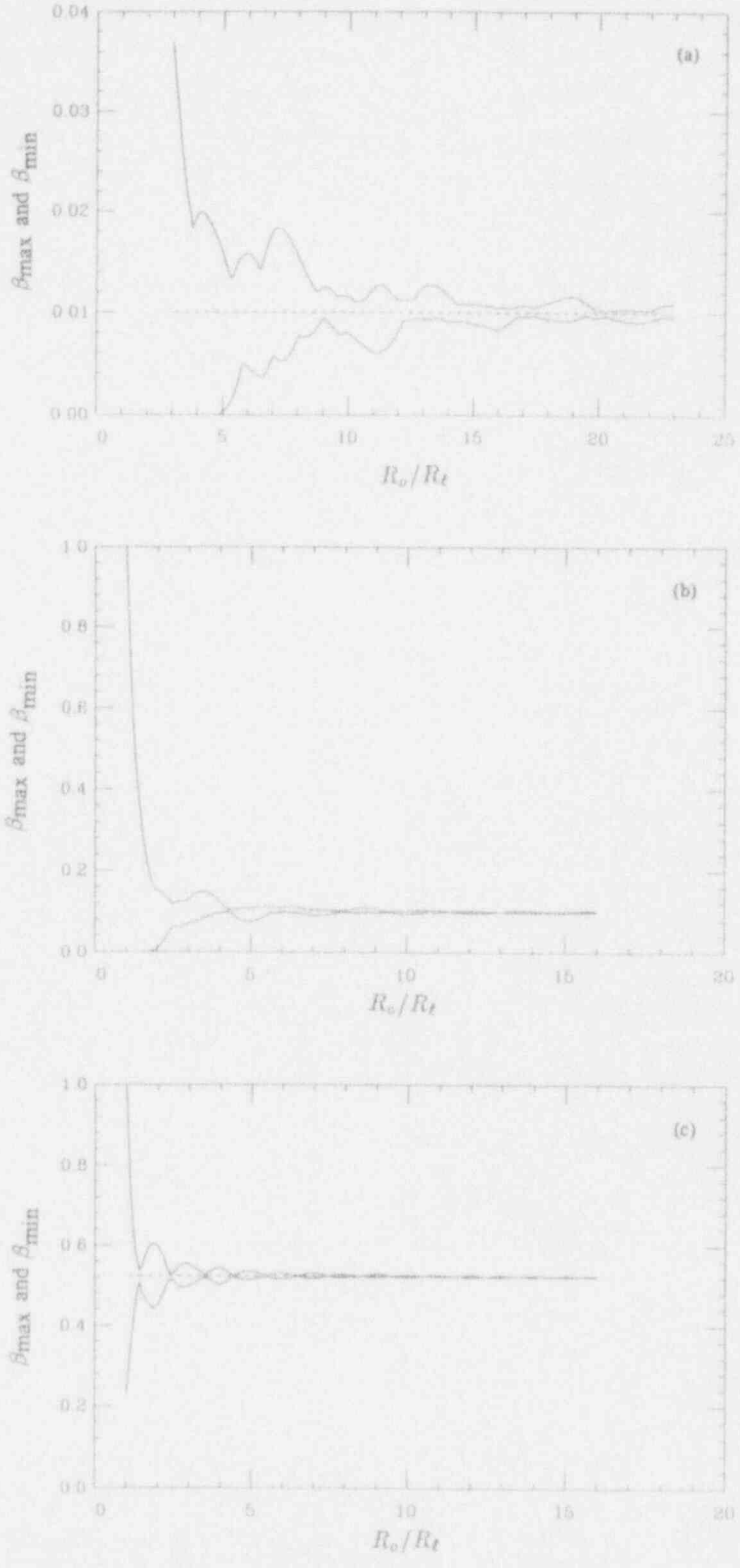

Figure E.4 The dependence of theoretical maximum and minimum values of liquid fractions on the relative size of the measurement volume (to the drop)—see text. (a) $\beta = 0.01$, (b) $\beta = 0.10$ and (c) $\beta = 0.52$.

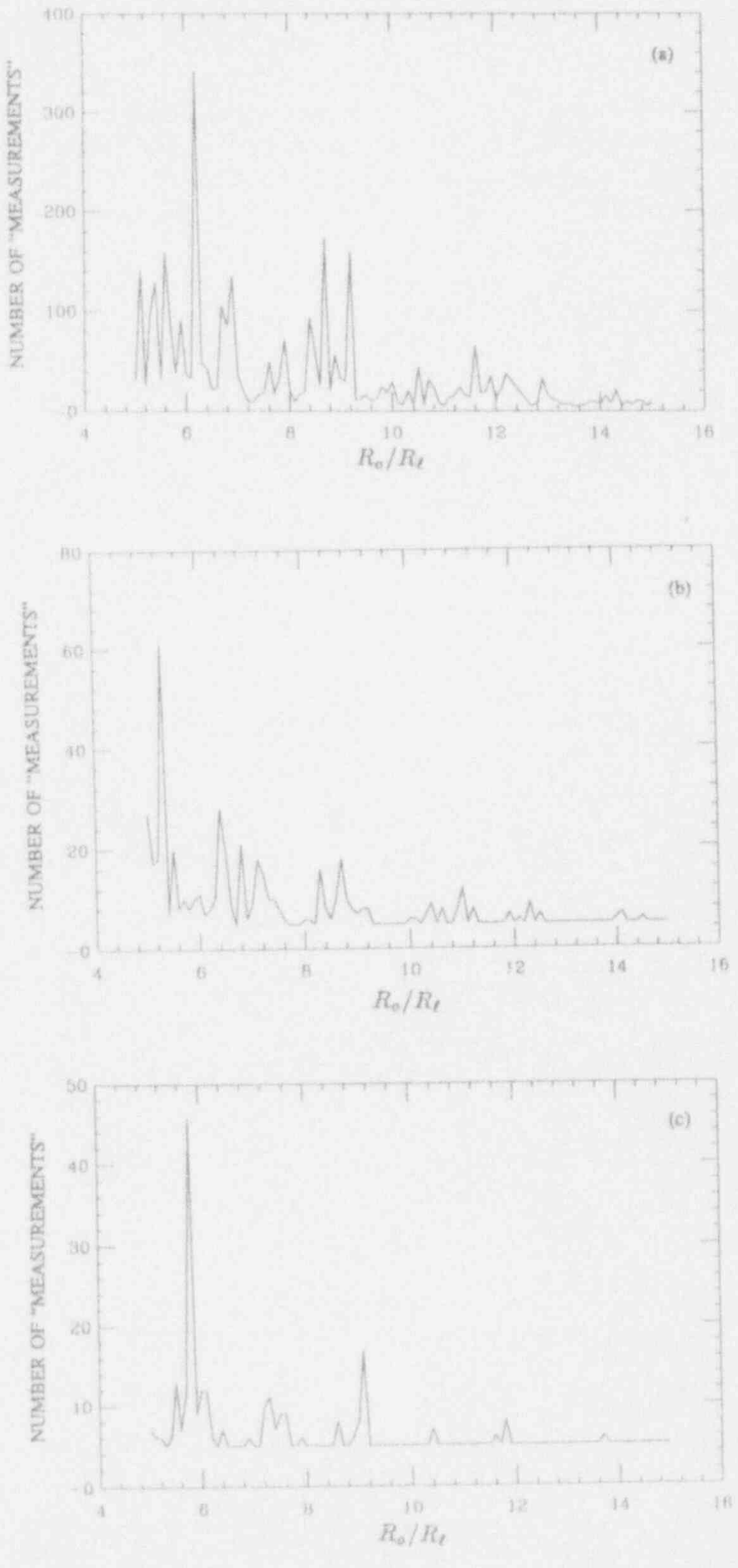

Figure E.5 The required number of "measurements" to converge to the true value of liquid fraction within 1% and remain within the tolerance in 5 consecutive "readings"—see text. (a) $\beta = 0.02$, (b) $\beta = 0.10$ and (c) $\beta = 0.15$.

E.5 Conclusion

The principle and feasibility of a fluorescence-based method for the measurement of liquid fraction in two-phase flow has been demonstrated. The technique appears to be valuable, especially for filling an important need for highly transient, spatially highly non-uniform three-dimensional dispersed flows.

E.6 Nomenclature

A_o	cross-sectional area of fibers
a	absorption coefficient of ultra-violet radiation
c	concentration of solution (grams of dye/grams of solution)
c_o	concentration of solution used in liquid fraction measurement
D	spacing between holes
d	diameter of holes in disc
$\mathcal{F}$	geometric optic factor
h	water level in glass tube
I_0	exciting-light intensity
L_1	distance from end of UV-light carrying fiber to axis of detecting fiber
L_2	distance from end of detecting fiber to axis of UV-light carrying fiber
P	power received by fiber
R_o	radius of detecting volume in numerical simulation
R_ℓ	radius of droplets in numerical simulation
z	distance from disc exit to fiber location

Greek

α_v	loss coefficient in the disc
β	liquid fraction
β_{ref}	reference liquid fraction (disc parameter)
Δ	diameter of fiber
ϕ	quantum yield of dye

E.7 References

1. Amarasooriya, W.H. and T.G. Theofanous (1987) "Scaling Considerations in Steam Explosions," *ANS Proceedings 1987 National Heat Transfer Conference*, Vol. 2, 58–67.

2. Danel, F. and J.M. Delhaye (1971) "Sonde Optique Pour Mesure du Taux de Présence Local en Écoulement Diphasique," *Mesures-Régulation-Automatisme*, Août-Septembre, 1971, 99–101.

3. Delhaye, J.M. and G. Cognet, Eds (1984) "Measuring Techniques in Gas-Liquid Two-Phase Flows," Springer-Verlag.

4. Delhaye, J.M., R. Semeria and J.C. Flamand (1973) "Void Fraction and Vapor and Liquid Temperatures: Local Measurements in Two-Phase Flow Using a Microthermocouple," *J. Heat Trans.*, 365–370.

5. Guilbault, G.G. (1973) *Practical Fluorescence*, Marcel Dekker, Inc., New York.

6. Hale, G.M. and M.R. Querry, M.R. (1973) "Optical Constants of Water in the 200-nm to 200 μm Wavelength Region," *Applied Optics, 12* No. 3, March 1973, 555.

7. Hewitt, G.F. (1978) bf Measurement of Two Phase Flow Parameters, Academic Press, London (1978).

8. Hon, A.L., D. Basdekas, Y.Y. Hsu, N. Kondic and R. Van Houten, ed. (1980) *Review Group Conference on Advanced Instrumentation Research For Reactor Safety*, NUREG/CP-0015.

9. Ishii, M. and S.T. Revankar (1991) "Measurement of Local Interfacial Area and Velocity in Bubbly Flow," *Ans Proceedings 1991 National Heat Transfer Conference*, Vol. 5, 181–189.

10. Jones, O.W. and J.M. Delhaye (1976) "Transient and Statistical Measurement Techniques for Two-Phase Flows: A Critical Review," *Int. J. Multiphase Flow, 3*, 89–116.

11. Lai, M.-C. and G.M. Faeth (1987) "Turbulence Structure of Vertical Adiabatic Wall Plumes," *J. Heat Trans., 109*, 663–670.

12. McDaniel, J.C. (1983) "Quantitative Measurement of Density and Velocity in Compressible Flows Using Laser-Induced Iodine Fluorescence," *AIAA 21st Aerospace Sciences Meeting*, January 10-13, 1983, Reno, Nevada.

13. McDaniel, J.C. (1983) "Nonintrusive Pressure Measurement with Laser-Induced Iodine Fluorescence," *AIAA 18th Thermophysics Conference*, June 1-3, 1983, Montreal, Canada.

14. Owen, R. (1976) "Simultaneous Laser Velocimeter and Laser Induced Fluorescence Measurements of Instantaneous Velocity and Concentration in Complex Mixing Flows," *AIAA 14th Aerospace Sciences Meeting*, January 26-28, 1976, Washington, D.C.

15. Regnier, P. (1973) "Application of Coherent Anti-Stokes Raman Scattering to the Measurement of Gas Concentrations and to Flow Visualization," European Space Agency, Report ESA-TT-200.

16. Siegel, R. and J.R. Howell (1981) *Thermal Radiation Heat Transfer*, second edition, Hemisphere Publishing Co., London.

17. Udenfriend, S. (1962) *Fluorescence Assay in Biology and Medicine*, Academic Press, New York.

18. Wang, Z. and G. Kocamustafaogullari (1990) "Interfacial Characteristic Measurements in a Horizontal Bubbly Two-Phase Flow," *ANS Proceedings, Winter Meeting*, Washington, D.C.

APPENDIX F

THE THEORETICAL BASIS FOR FLUTE

Appendix F: The Theoretical Basis for FLUTE

F.1 Introduction

The particular need that led to the investigation and techi. ique reported herein was in measuring the water depletion from the mixing zone prior to a steam explosion. The experiment designed to explore the basic physics of this mixing process involves (Amarasooriya and Theofanous, 1987) a cloud of very hot (hundreds of degrees Celsius) particles poured into a liquid (water) volume, and a complex multiphase interaction as the very high steam production drives water out of the mixing region. The situation is highly transient, the flow patterns strongly two-dimensional, and the range of real interest is where the liquid fraction drops below ~20%, i.e., the measurement is needed from liquid-continuous to a highly dispersed droplet flow. More generally, the technique is uniquely well suited for multi-dimensional, highly dispersed flows for which both radiation attenuation and the local contact probe techniques fail because of the respective attributes; that is, multi-dimensionality requires a local measurement which is not possible by attenuation methods (even tomography is limited by the conflicting requirement of spatial and temporal resolution), and local contact probes are not suitable for highly dispersed flows. For a good perspective on these matters, see Jones and Delhaye (1976).

The basic idea is to induce (in liquid) and detect narrow band emission locally, such that the signal is uniquely related to the quantity of liquid in the detection volume. As described in the original publication (Angelini et al, 1992), we use ultraviolet (UV)-induced fluorescence in combination with fiber optics (See Figure F.1) and certain filter/mirror arrangements to achieve:

(a) a good separation between the incident and emitted radiation,

(b) a direct relation (not necessary linear) between liquid fraction and measured signal, and

(c) local, internal measurements in highly complex two-phase flows.

In the previous appendix, we gave some initial indication of the feasibility of the technique by showing that the power (q) received by the detecting fiber can be expressed as

$$q = I_0 S_f \xi e^{-L_1 a c \beta} (1 - e^{-L_e a c \beta}) \mathcal{F} \qquad (F.1)$$

and that, for the specific dimensional arrangement as utilized in our experiments, the functional dependence of q on the product $c\beta$ holds well enough that a calibration obtained in 100% liquid ($\beta = 1$), can be applied to highly dispersed droplet flows. That is, the same value of $c\beta$ (with c and β varying independently) gives the same q. In the linear region

$$q = I_0 S_f \xi L_e a \mathcal{F} c \beta \qquad (F.2)$$

and for the same c

$$\frac{q}{q_{\beta=1}} = \beta \qquad (F.3)$$

The particular instrument has been named FLUTE, for FLUorescent TEchnique.

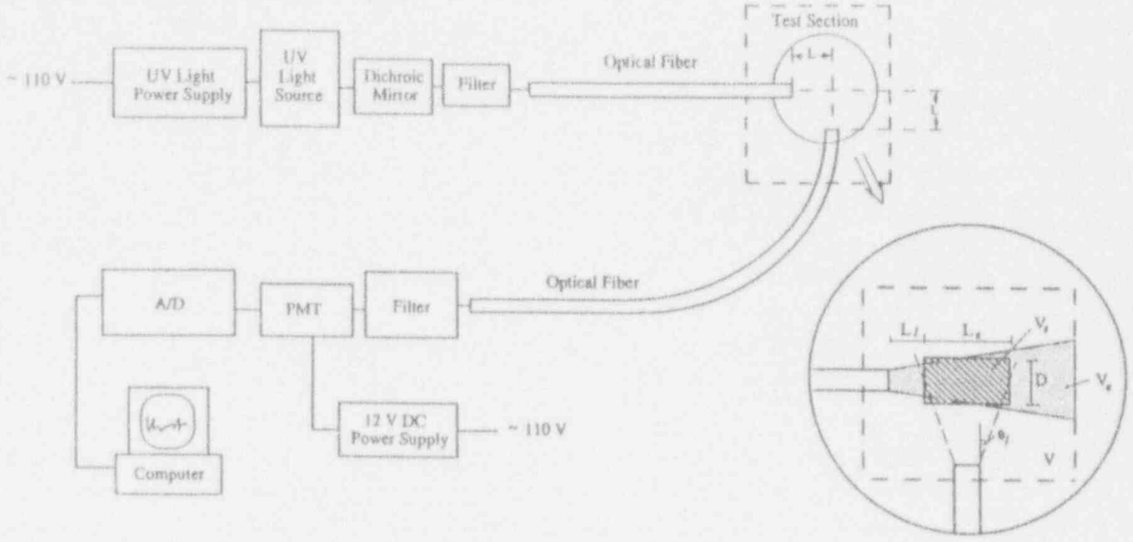

Figure F.1 Illustration of FLUTE arrangement.

In the previous appendix we also discussed some of the potential difficulties arising due to the multiple gas/liquid interfaces within the travel paths of the incident UV and emitted fluorescence beams. Because of the relatively small difference in the index of refraction between water and steam, reflections in this range of wavelength are unimportant, and this issue came down to the potential role of refractions. In addition, since the high speed data acquisition system allows essentially instantaneous "readings" at rates up to 100 kHz, we discussed the need to optimize the rate in relation to the particular transient under investigation. The purpose of this appendix is to pursue further these issues.

Our approach is to conduct numerical experiments of radiation transport, especially accounting for refractions at crossings of interfaces. Random clouds of drops (both positions and sizes) are considered such that with a sufficient number of "realizations," the mean behavior (liquid fraction) can be obtained. More specifically, since the result of each such "realization" corresponds to a FLUTE reading in a physical setting, our effort is to determine (a) whether the average of many such computed "readings" settle to the correct mean value and (b) the number of "readings" required for convergence. Finally, a well-characterized cloud of drops, in an experimental setting, is used to test the predictions of this theory, in a much more precise manner than the feasibility demonstrations provided in the previous appendix.

F.2 Theoretical Development

F.2.1 Geometric Optics of a FLUTE "Reading"

Consider a large cloud of drops. This cloud is characterized by a certain volume-averaged liquid fraction, $\bar{\beta}$, while the local values, β, (defined on any given "sample" volume, V_s) are randomly distributed with a standard deviation σ_β. The spacing between drops is statistically homogeneous and the diameters are normally distributed with a mean $\bar{d}$ and a standard deviation σ_d. Our task is to compute, for a particular cloud arrangement, the radiation received by a fiber tip (defined by its surface area, S_f, and acceptance angle, θ_f) due to emissions (fluorescence)

from drops found inside a "sample" volume[b] positioned directly across from the fiber tip at some distance, L, away from it. Since the emissions are isotropic, and of known total intensity, it is sufficient to determine the fraction of the total emitted radiation that is received by the fiber—as noted above, this corresponds to and will be called a FLUTE "reading." Such a "reading" is computed by discretizing the liquid (emitting) volume and the emitted radiation from each volume element, and following a ray-tracing procedure as illustrated in Figure F.2.

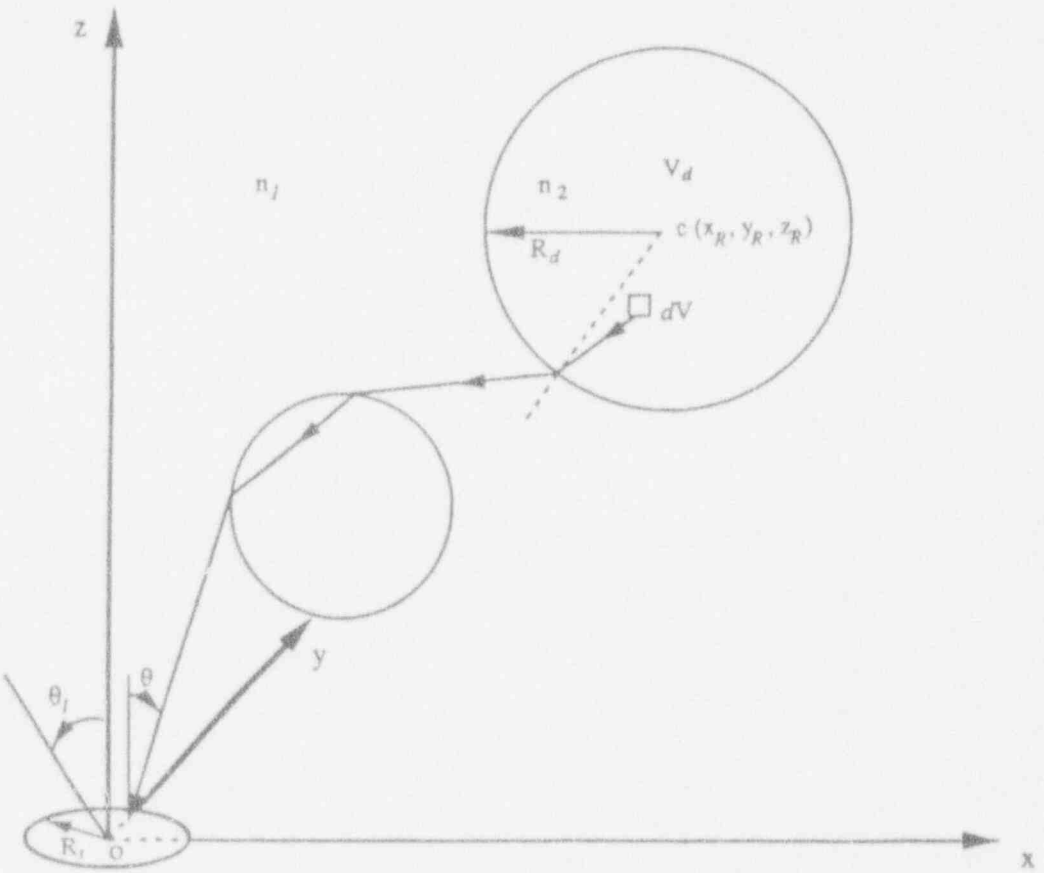

Figure F.2 Illustration of the ray tracing procedure.

Suppose that E is the total radiative power emitted per unit volume of liquid, and dq_{ei} is the emission within the ith solid angle (i.e., 4π discretized to N solid angles, $d\Omega_i$ $i = 1 \ldots N$), then

$$dq_{ei} = E dV \frac{d\Omega_i}{4\pi} \tag{F.4}$$

Now suppose this radiative power is represented by a single ray (within $d\Omega_i$), take all $d\Omega_i$'s of equal size, and further suppose that N_r of these N rays "hit" (are received by) the fiber. A FLUTE "reading" then is:

$$q = N_r dq_{ei} \tag{F.5}$$

[b] Without loss of generality and very little loss of accuracy, we will assume that all drops emit at the same level of intensity, i.e., will ignore attenuation effects.

and if $q_{\beta=1}$ is the same quantity calculated for an all-liquid sample volume, the liquid fraction is

$$\beta = \frac{q}{q_{\beta=1}} \tag{F.6}$$

Clearly, for accurate results the discretization must be very fine ($N \to \infty$, $dV \to 0$), and this is problematic in computing a large number of "readings," in dense multidrop clouds. The numerical procedure devised to make such computations practical is described in subsection F.2.2 that follows. In the remainder of this subsection, we describe the ray tracing procedure.

The key element of the ray-tracing calculation is to find the change in direction of a ray crossing the surface of a drop (see Figure F.3), which can be treated by geometric optics. Let the unit vectors $\vec{r}_i$ and $\vec{r}_r$ represent the incident and refracted direction of the ray respectively. Relative to a fixed coordinate system, these vectors can be written as

$$\vec{r}_i = (\sin\theta_i \cos\phi_i,\ \sin\theta_i \sin\phi_i,\ \cos\theta_i) \tag{F.7}$$

$$\vec{r}_r = (\sin\theta_r \cos\phi_r,\ \sin\theta_r \sin\phi_r,\ \cos\theta_r) \tag{F.8}$$

The unit normal vector at the point of incident at the surface of the drop, $\vec{r}_n$, is given by

$$\vec{r}_n = \left(\frac{x_R - x_i}{R_d}, \frac{y_R - y_i}{R_d}, \frac{z_R - z_i}{R_d}\right) \tag{F.9}$$

The three vectors, $\vec{r}_i$, $\vec{r}_r$ and $\vec{r}_n$ are related by Snell's law

$$\sin\chi_r = \frac{n_1}{n_2} \sin\chi_i \tag{F.10}$$

with

$$\cos\chi_i = \vec{r}_i \cdot \vec{r}_n \tag{F.11}$$

and

$$\cos\chi_r = \vec{r}_r \cdot \vec{r}_n \tag{F.12}$$

n_1 and n_2 are the refractive indexes of gas and liquid, respectively. Noting that $\vec{r}_n$, $\vec{r}_i$ and $\vec{r}_r$ are in the same plane and for a given incident direction (θ_i, ϕ_i) and location on the interface (x_i, y_i, z_i), we can readily express the direction of the refracted ray (θ_r and ϕ_r) as follows:

$$\theta_r = \cos^{-1} c \tag{F.13}$$

$$\phi_r = \begin{cases} \cos^{-1}\frac{a}{\sqrt{a^2+b^2}} & \text{for } b \geq 0; \\ -\cos^{-1}\frac{a}{\sqrt{a^2+b^2}} & \text{for } b < 0. \end{cases} \tag{F.14}$$

where

$$a = A \sin\theta_i \cos\phi_i + B\frac{x_R - x_i}{R_d} \tag{F.15}$$

$$b = A \sin\theta_i \sin\phi_i + B\frac{y_R - y_i}{R_d} \tag{F.16}$$

$$c = A \cos\theta_i + B\frac{z_R - z_i}{R_d} \tag{F.17}$$

with

$$A = \frac{\sin \chi_r}{\sin \chi_i} \tag{F.18}$$

and

$$B = \frac{\sin (\chi_i - \chi_r)}{\sin \chi_i} \tag{F.19}$$

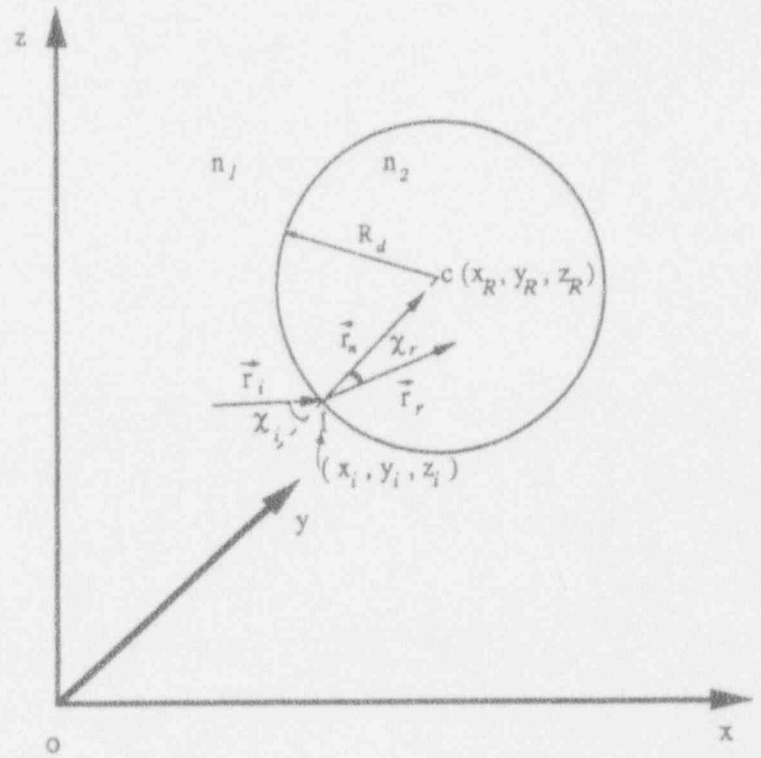

Figure F.3 Nomenclature used in the calculation of a refracted ray.

F.2.2 Computational Procedure

As noted above, for accurate results, we must consider a high enough density of emitted energy rays, and this gives rise to serious constraints of implementation, even for main frame computers. To overcome this difficulty, we developed an adaptive numerical approach that is made to successively focus (or "cluster") the emissions to the region of interest; that is, to the emission solid angle space that produces "hits." This successive focusing proved possible and allowed us to achieve high enough ray densities with reasonable computational effort.

Specifically, the computation starts by first emitting N rays (for each differential volume dV) randomly (but uniformly) over the full solid angle 4π. By mapping the direction of the intercepted (received) energy rays on a (θ, ϕ) plane, the clustering is evident and the first estimate of the region of interest, say $\theta_1 < \theta < \theta_2$, $\phi_1 < \phi < \phi_2$, can be readily generated. A second calculation is then performed by emitting N rays randomly and uniformly *only* within the region

of interest determined in the previous step. The procedure is then repeated until convergence is achieved. To ensure that the first deduction in θ_1, θ_2, ϕ_1 and ϕ_2 is conservative, the hits are computed with a target diameter three times bigger than the one of interest. For $N = 1000$ we have found that only 3 such cycles of computation can produce an adequate focus (on the region of interest). Moreover, we have shown that the choice of 1000 rays over the region of interest produces a fine enough discretization for convergence in the "reading" itself. Specific illustrations of this technique are provided in the next section.

F.3 Numerical Experiments

To illustrate the numerical procedure as outlined in the previous section, energy emitted by a single drop in a cloud of 100 uniformly-sized drops is first considered. The cloud of 100 drops was formed by randomly positioning the centers in the cube $-8 < x < 8$, $-8 < y < 8$ and $0 < z < 16$; all dimensions in mm. The drops have a diameter of 2.64 mm and the average liquid fraction is 15%. The emitting drop, same size, is positioned at (0, 0, 13.7). The calculations are carried out by discretizing the emitting drop into 64 small volumes and considering 1000 rays emitted from each volume, in each cycle. The results of three successive cycles are summarized in Table F.I. Results generated ignoring the effect of refraction are shown in the same table. Note that for the case without refraction, the exact value of q/E can be determined analytically and it is 3.15 x 10^{-12} m^3. The computational procedure is clearly both accurate and efficient. To generate the same accuracy as cycle 3, for example, a "straight" calculation with uniform emission over 4π would require 10^6 rays per volume element, dV—as opposed to 3,000 rays used to arrive at the Table F.1 result. The drop positions projected on the x–y plane are shown in Figure F.4. Figures F.5 to F.10 correspond to each computational run of Table F.1 and show the clustering (in $\theta - \phi$ space) of the emitted rays that hit the target. They also show the process of "focussing-down" of $\Delta\Omega$ to the proper region of interest—this focussing is done automatically by the computer. With reference to these figures, and Table F.1, the following points can be made.

Table F.1 Results of Sample Calculations

Cycle No.*	Solid Angle $\Delta\Omega$				Size of Target (mm)	$(q/E) \times 10^{12}$ (m^3)
	θ_1	θ_2	ϕ_1	ϕ_2		
1 w/o R	0	π	0	2π	1.5	25.83
w R	0	π	0	2π	1.5	14.79
2 w/o R	2.95	π	0	2π	.5	3.113
w R	2.90	π	0	2π	.5	3.644
3 w/o R	3.02	π	0	2π	.5	3.148
w R	3.02	π	0	2π	.5	3.298

* w R and w/o R means "with" and "without" consideration of refractions.

1. The clustering is rather sharp and allows an unambiguous choice of the area to focus on the next cycle.
2. No significant clustering is observed in the ϕ dimension, because of the symmetric position of the drop right in front of the target; off-the-side positions would create ϕ-clustering also (see below).

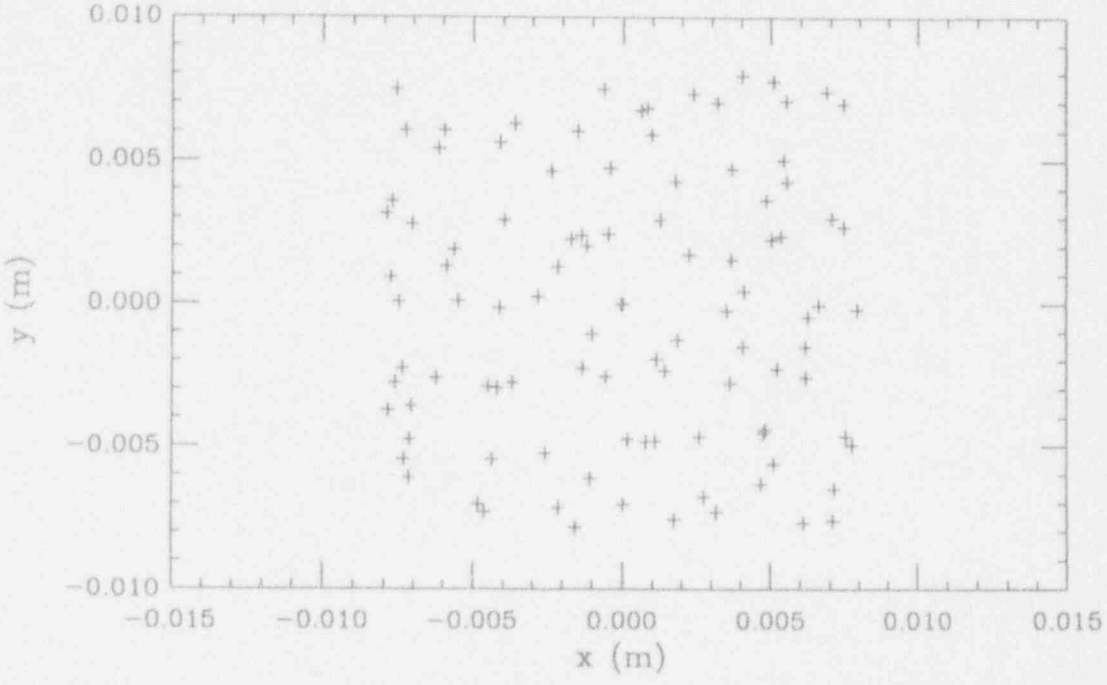

Figure F.4 Drop positions projected on the x-y plane.

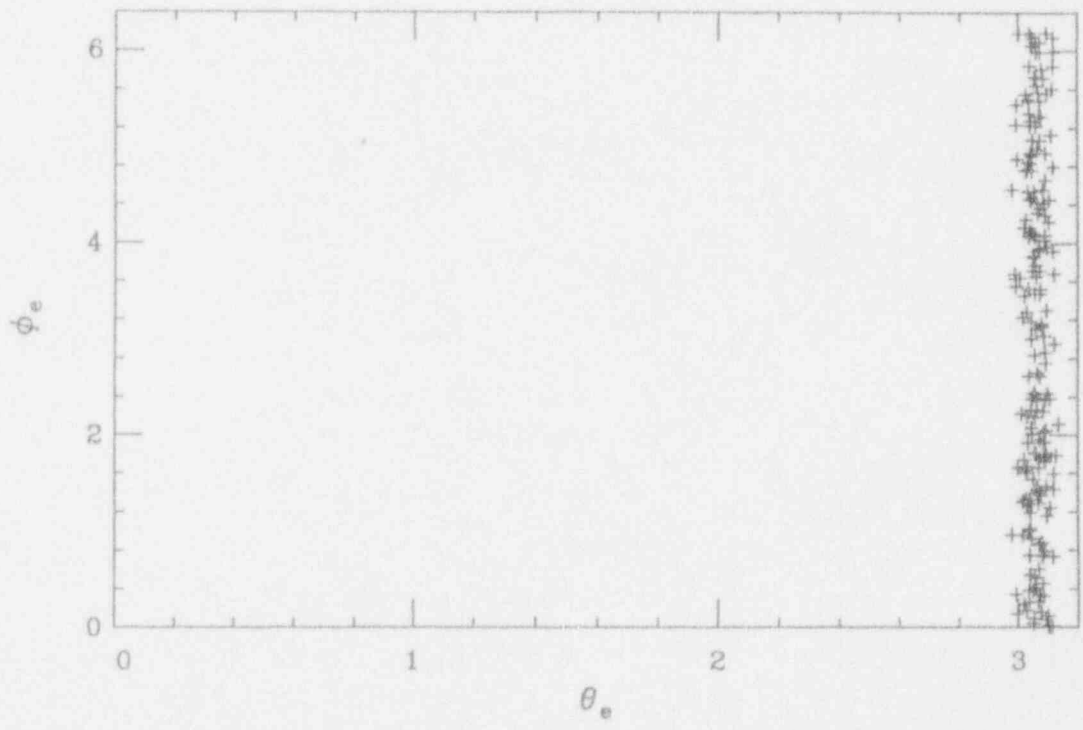

Figure F.5 Clustering in $\theta - \phi$ space for cycle No. 1 w/o R.

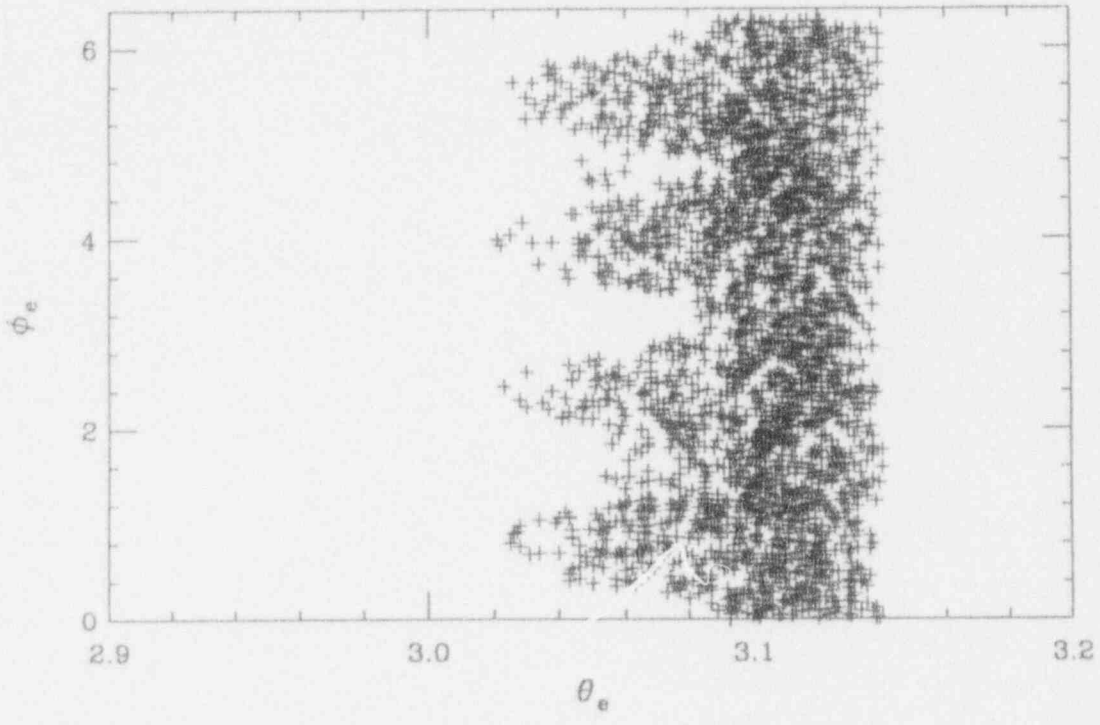

Figure F.6 Clustering in $\theta - \phi$ space for cycle No. 2 w/o R.

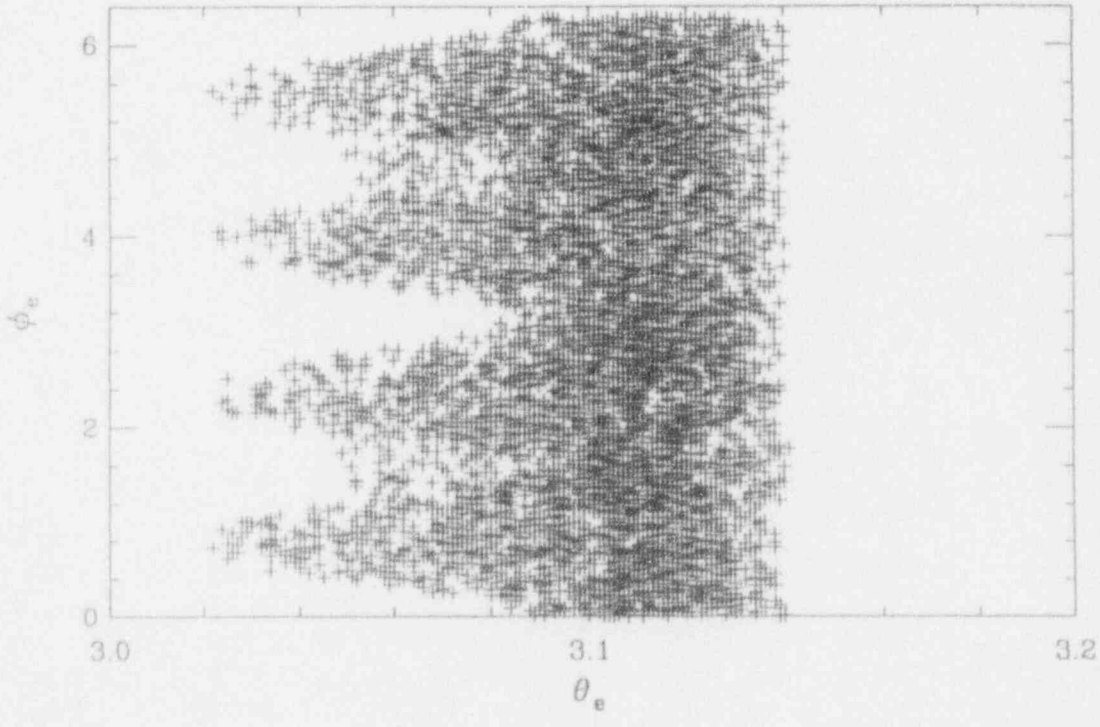

Figure F.7 Clustering in $\theta - \phi$ space for cycle No. 3 w/o R.

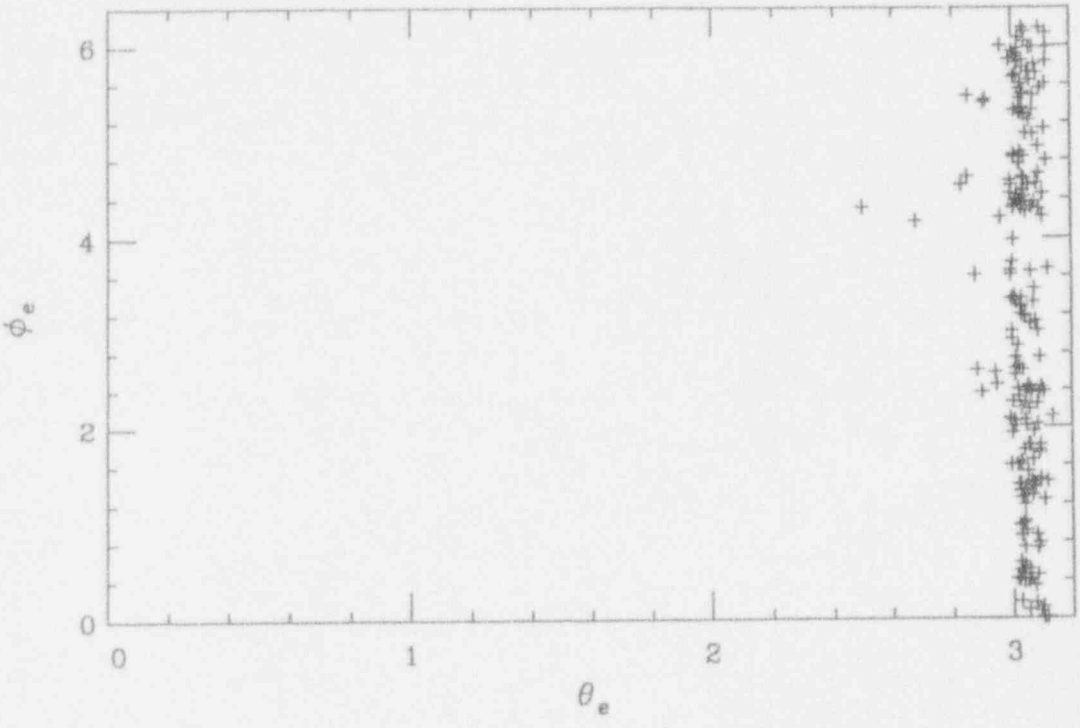

Figure F.8 Clustering in $\theta - \phi$ space for cycle No. 1 w R.

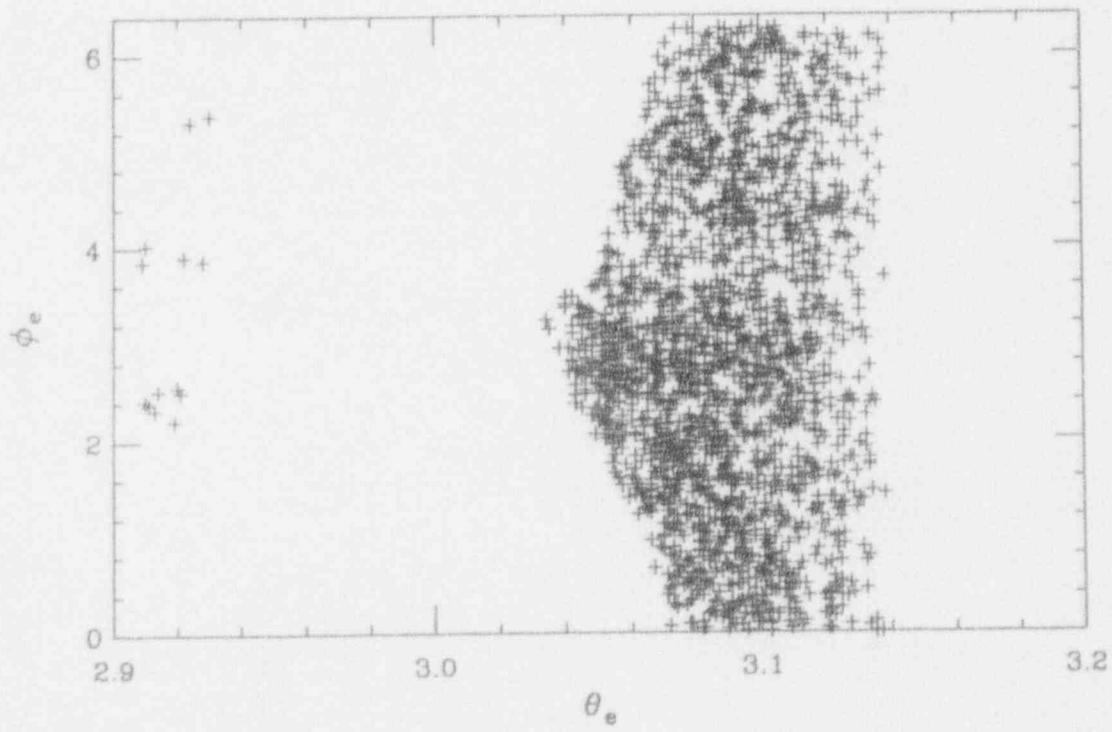

Figure F.9 Clustering in $\theta - \phi$ space for cycle No. 2 w R.

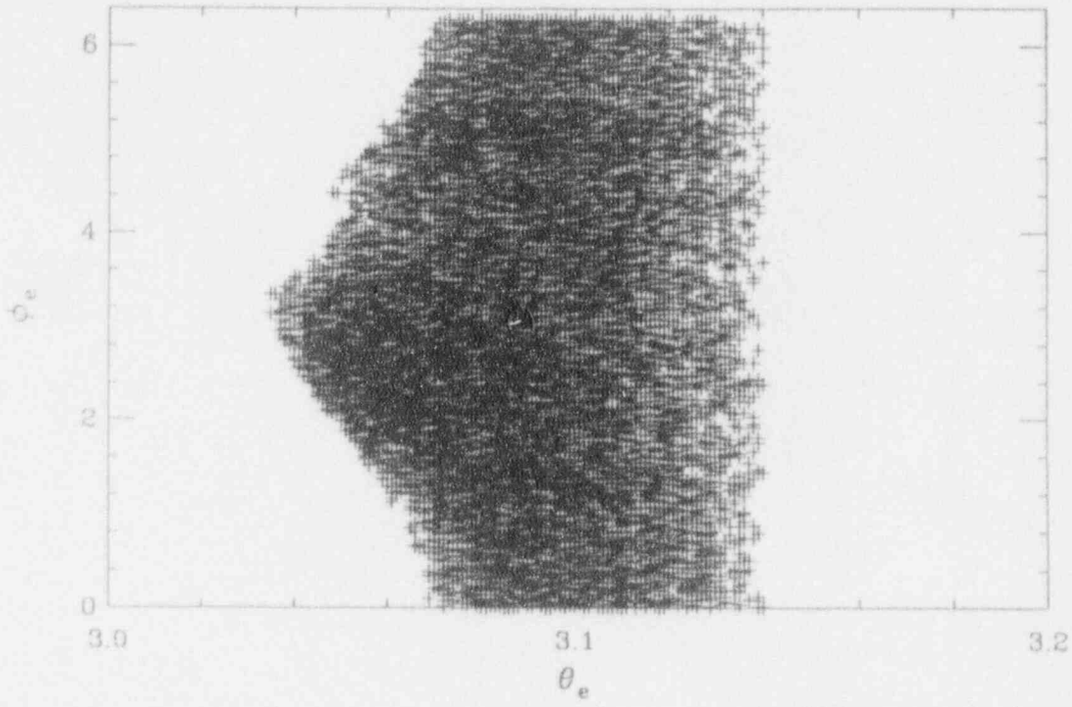

Figure F.10 Clustering in $\theta - \phi$ space for cycle No. 3 w R.

3. The regular "hit" pattern in Figures F.7 and F.9 is probably due to the symmetry of discretizing the emitting drop (4 x 4 x 4) which in the absence of refractions shows through. Additional studies are required to understand the physical significance of this pattern. As seen in Figures F.8 and F.10 refractions "randomize" the behavior sufficiently to destroy this pattern.

4. For this particular realization the effect of refractions is to increase the "reading" by less than 5%.

Turning next to the general problem, the key parameters to consider are:

$\bar{\beta}$: the true liquid fraction in a cloud of volume V.
σ_β: the true standard deviation of liquid fraction for a sample volume V_s.
$\bar{d}$, σ_d: mean and standard deviation of droplet size distribution.
S_f, θ_f: area and maximum admitting angle of fiber tip.
V_s, L: sample volume and distance of emitting drops from target.

Using numerical experiments of the type illustrated above, our purpose here is to predict and optimize the performance of FLUTE in terms of appropriate ranges of these parameters. In particular, we wish to establish any limitations due to the refractions (the issue raised in the introduction) and/or due to the particular geometry of the "emitting" volume, V_e. This latter point requires some further elaboration. The relation of the "emitting" and "sample" volumes in FLUTE is illustrated in Figure F.1—the issue is whether there is an apparent increase of sample volume, due to refractions, from emissions outside it, or whether in some average sense such a gain is cancelled by an equivalent loss (again by refractions) of the emitted radiation within. A particular choice of V_s and L implies an equivalent diameter, D, of a pencil of UV radiation.

This then is the diameter of the emitting volume which can be parametrized by one more variable, the effective length of it, L_e. We will show shortly that any increases of L_e beyond the value determined from the geometric intersection of receiving fiber with the UV pencil, produce a negligible effect. Thus we chose and fixed $L = 10$ mm, $L_e = 8$ mm, $\theta_\ell = 22°$, and $R_f = 0.5$ mm, thus focusing this study on β, $\bar{d}$, and σ_d. The matrix of variations considered is shown in Table F.2. Each run involved 10 successive "readings," each "reading" or computation carried for a new, randomly arranged cloud, with the parameters as specified. For each cloud two computations were run—one with and the other without considering refractions.

Table F.2 The Matrix of Parameters in the Numerical Experiments
In all runs $L = 10$ mm, $L_e = 8$ mm, $\theta_\ell = 22°$

Run #	β (%)	$\bar{d}$ (mm)	σ_d (mm)
1	3.0	1.2	0.3
2	5.5	1.2	0.3
3	5.5	2.4	0.3
4	14.0	2.4	0.3

The results are summarized in Figures F.11 to F.14. The figures show the successive readings and the "current" average (i.e. the average of all previous readings). The correct values, based on the known liquid fraction, and taken as the same fraction of the "reading" at 100% liquid, are also shown. There are two main observations: (a) The fluctuations are significant, but the average reading quickly converges to the correct value, and (b) the effect of refractions is negligible. To illustrate the role of the effective length L_e, the first "reading" of Run#1, the second "reading" of Run #3 and the last "reading" of Run #4 were repeated with with L_e taken as 12 and 16 mm and results are shown in Figure F.15. We see that the effect of increasing L_e (symmetrically around the geometrically determined minimum value) has no significant consequence on the results.

F.4 Laboratory Experiments

The approach here is similar to that employed in the original publication (Angelini et al, 1992). That is, to create a well-controlled, uniform cloud of particles of known liquid fractions, and to test the $q - c\beta$ relation of Eq. (F.1). The cloud is created by letting water flow through a perforated disc under a constant driving head. In the previous study we found some non-uniformities (in the flow) developing with distance along the free-fall due to small imperfections, in hole pattern, etc. For the present work, we chose the best disc, visually, and from close-up photographs we determined the position where the jets first disintegrated into drops. This is an ideal position for a local measurement with a known liquid fraction. The fiber positioning was set at L = 10 mm and the FLUTE sampling rate at 200 Hz.

The experimental signal from a series of calibration runs (varying the concentration of the dye), and the resulting calibration curve are shown in Figures F.16 and F.17, respectively. Figure F.17 clearly shows the linear region of Eq. (F.1). The signals obtained in the droplet flow described above, at liquid fractions of 7% and 8.5% are shown in Figures F.18 and F.19, respectively. The average values obtained from these signals (and several others obtained in the same range of liquid fractions), normalized by the signals in 100% liquid (also shown in Figures F.18 and F.19), are shown in Figure F.20, plotted against the respective (known) liquid fractions.

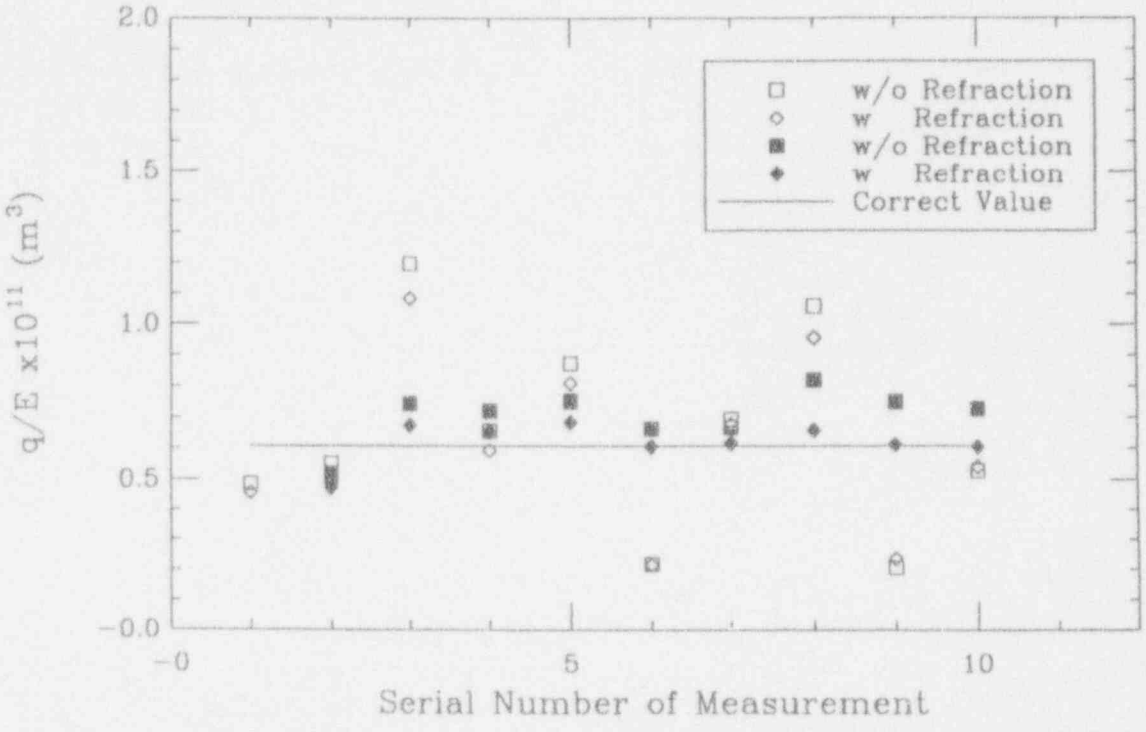

Figure F.11 Results of Run #1. ■ and ◆ are the averages of all previous readings.

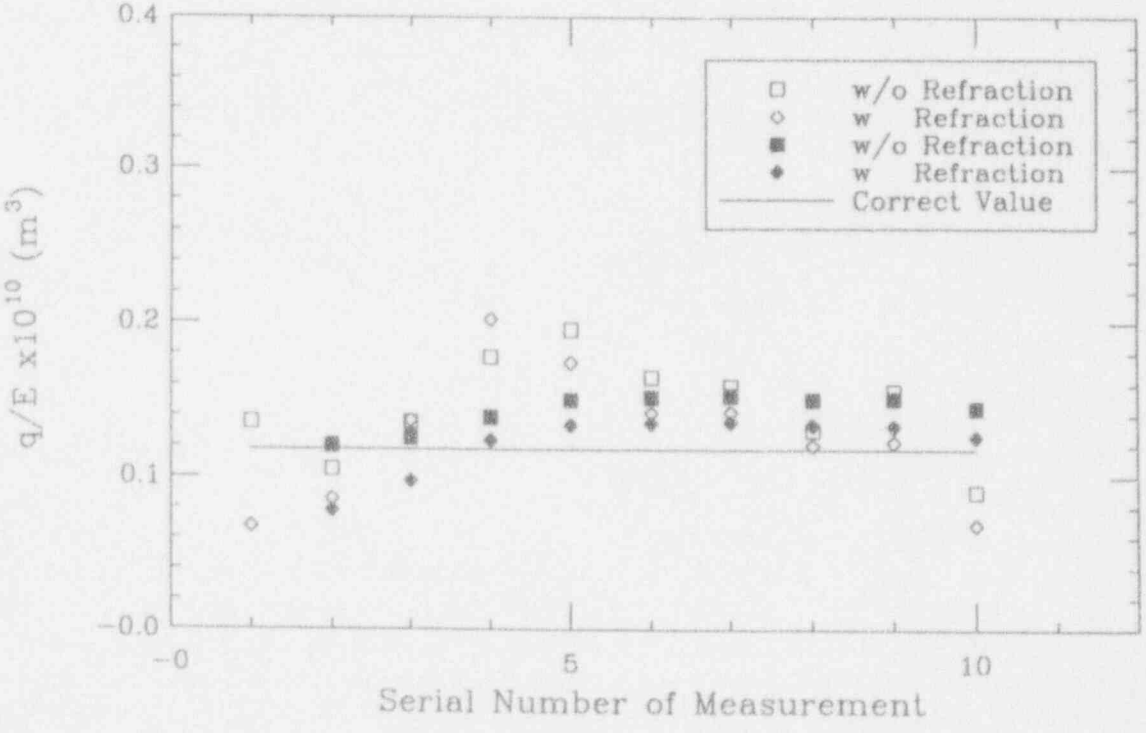

Figure F.12 Results of Run #2. ■ and ◆ are the averages of all previous readings.

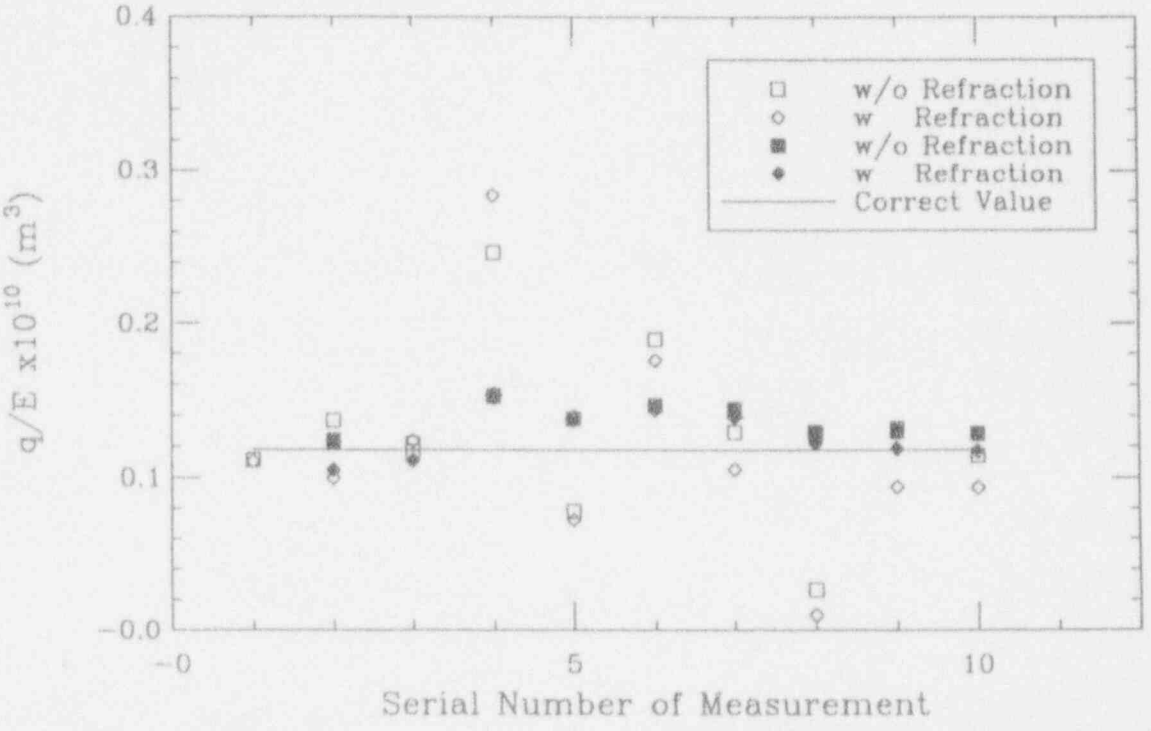

Figure F.13 Results of Run #3. ■ and ◆ are the averages of all previous readings.

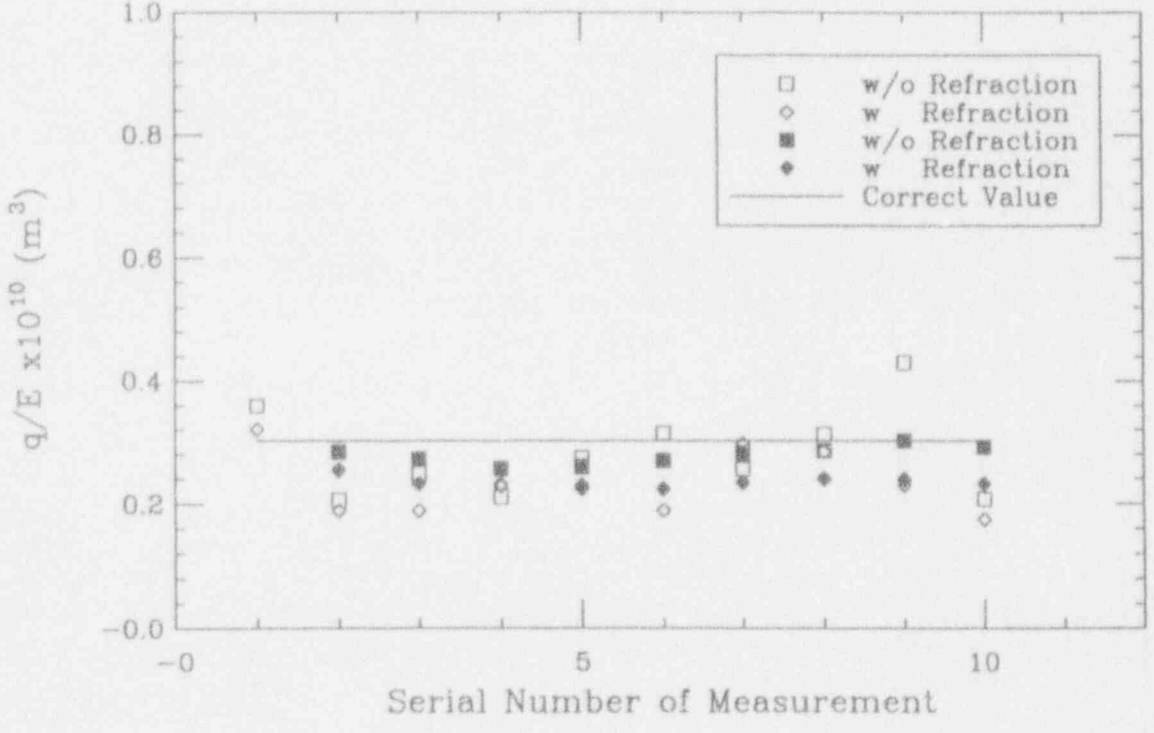

Figure F.14 Results of Run #4. ■ and ◆ are the averages of all previous readings.

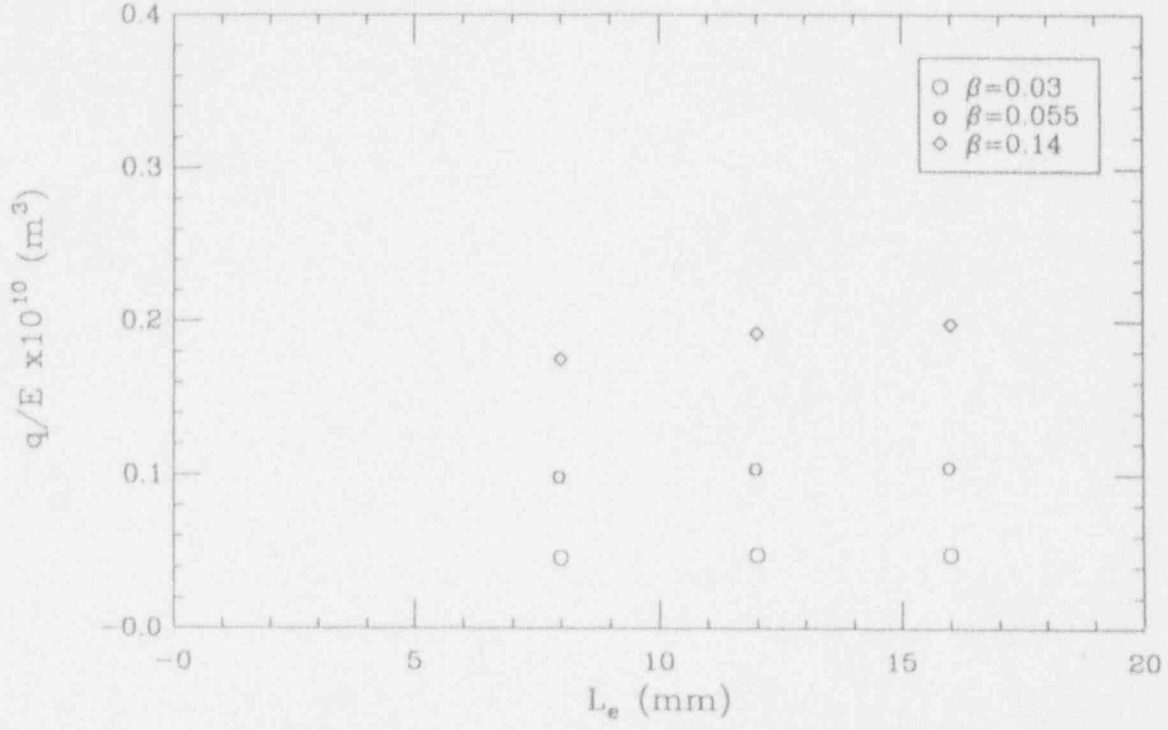

Figure F.15 Effect of L_e on "readings" with refraction consideration.

The "numerical" data on this figure are those obtained in the numerical simulations discussed above. The solid line expresses an ideally linear relation, i.e., $q \sim \beta$, as deduced from the linear region of Eq. (F.1). We see that at the high end of the liquid fraction considered refractions are predicted to introduce non-negligible errors; however, the performance is excellent at the low end, and it is predicted to be in excellent agreement with the measurements. [Note that the non-linearity exhibited by the numerical experiments is not the same as that of Eq. (F.1)—the latter is due to attenuation.] Further experimental work and numerical simulations are needed to fully explore the range of validity of FLUTE at liquid fractions higher than 10%; however, it should also be noted that the dispersivity in this range is expected to diminish (by drop coalescence) such that flow regime considerations are also essential in establishing the range of FLUTE applications to real two-phase flows.

F.5 Conclusions

In this appendix we provide the theoretical foundation of FLUTE, and basically an explanation of why it "works." In particular, we have shown that for $\beta < 0.1$ the role of refractions on the reliability of the signal is negligible, and that random clouds of drops (of distributed size) can be characterized by the average of only a few measurements. This means the technique is applicable also to highly transient flows, with varying liquid content.

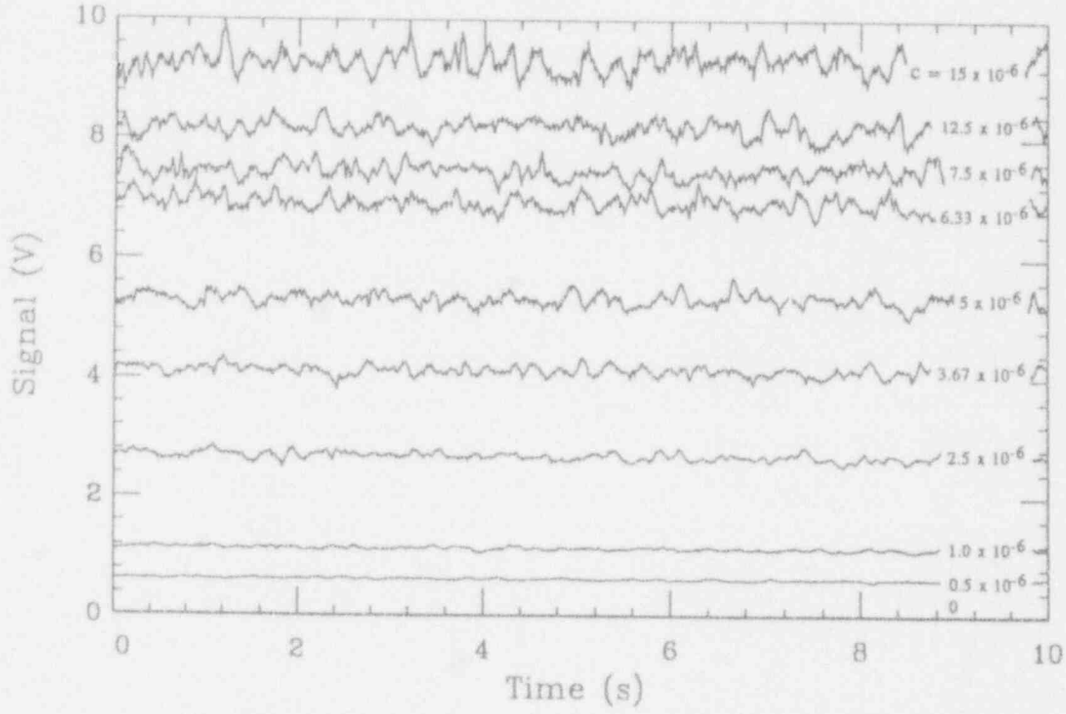

Figure F.16 Experimental signals for varying mass fraction in 100% water.

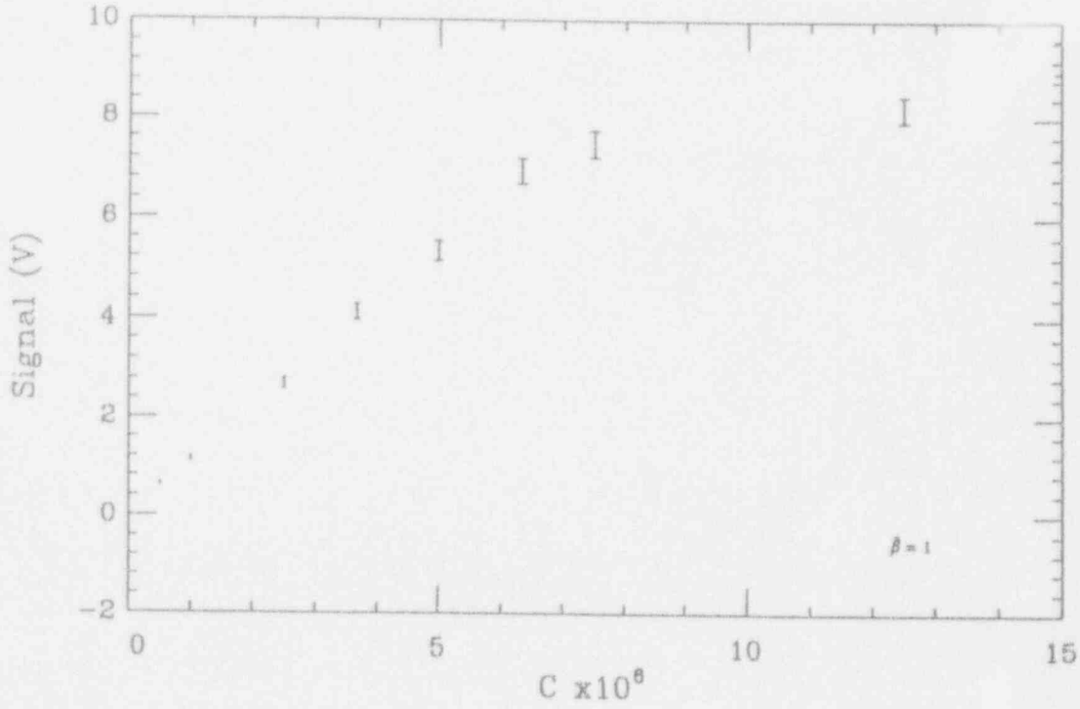

Figure F.17 FLUTE signal in 100% water as function of the dye mass fraction content.

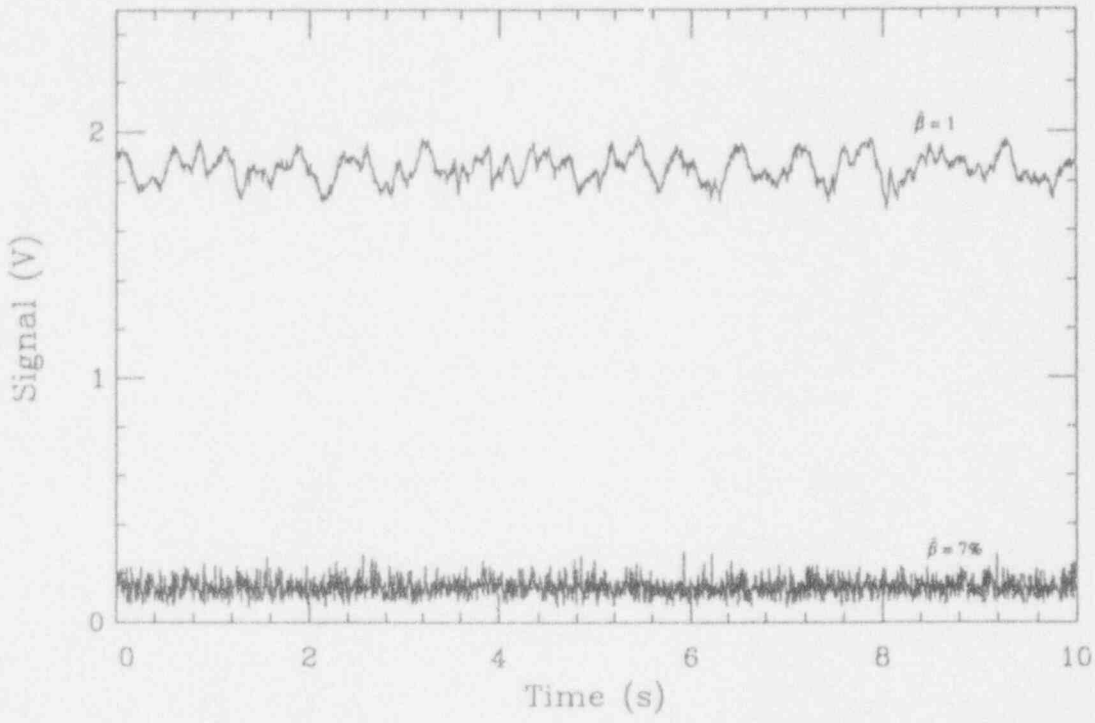

Figure F.18 FLUTE signals obtained in droplet flow (with $\bar{\beta} = 0.07$) and in all liquid ($\bar{\beta} = 1.0$).

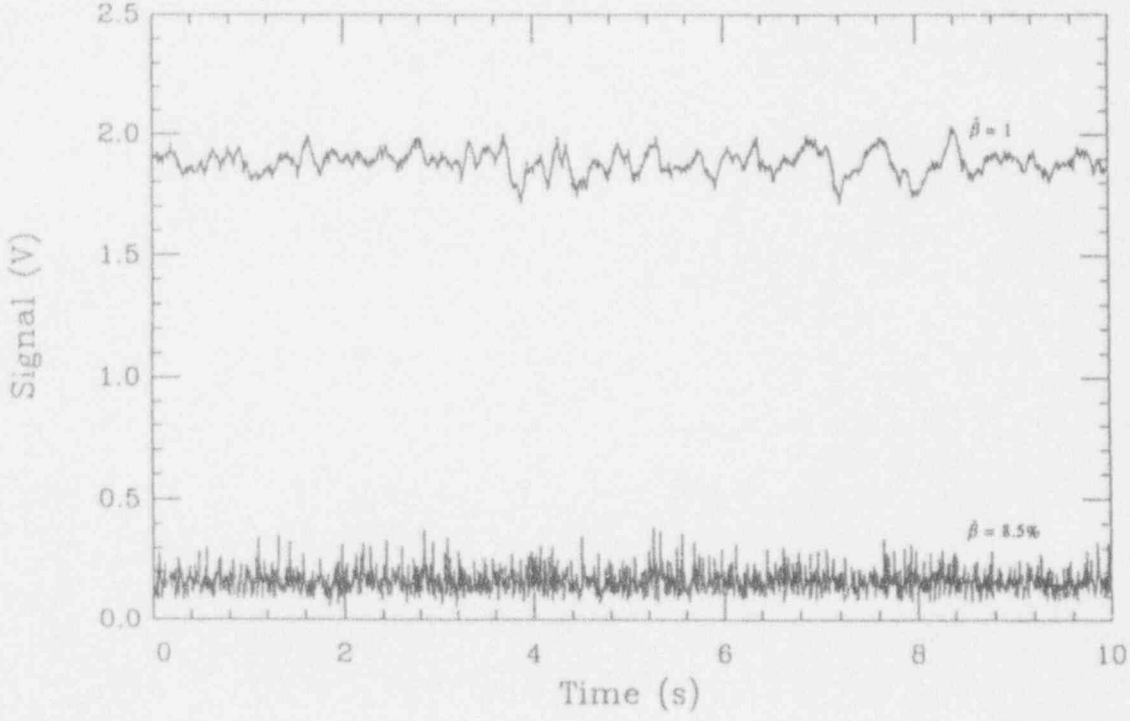

Figure F.19 FLUTE signals obtained in droplet flow (with $\bar{\beta} = 0.085$) and in all liquid ($\bar{\beta} = 1.0$).

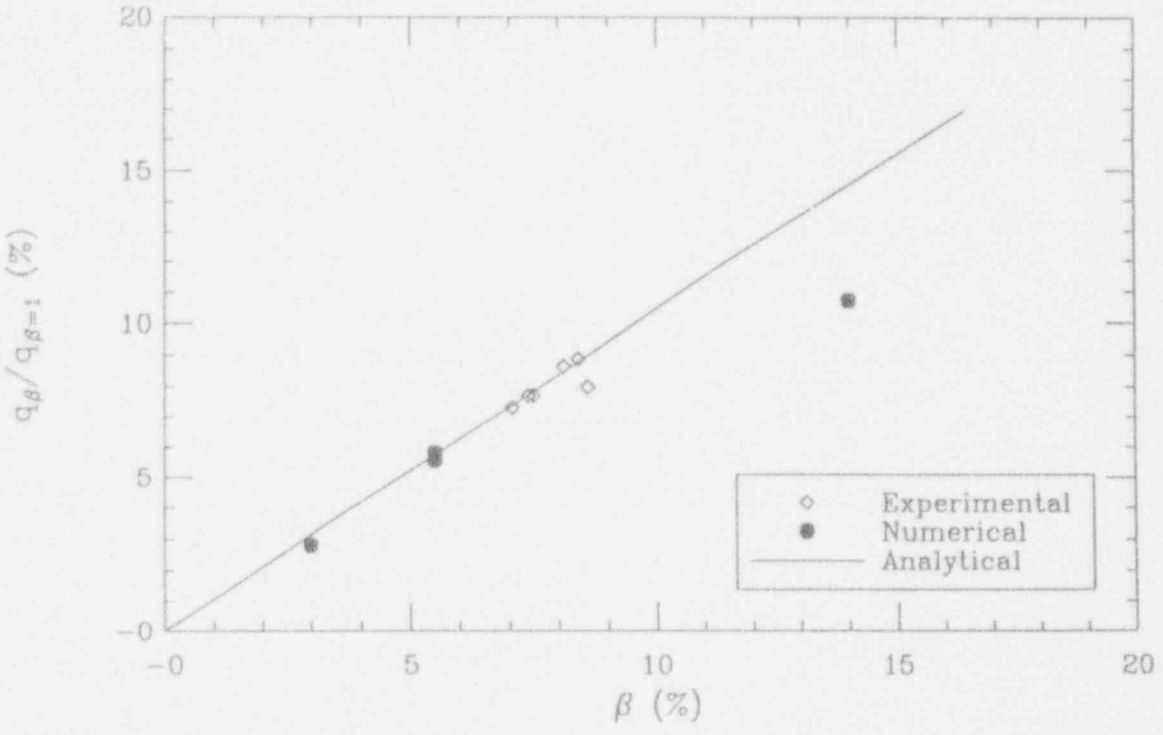

Figure F.20 Comparison between experimental results and numerical simulations. The solid line (analytical) reflects linearity as in Eq. (F.3).

F.6 Nomenclature

a	absorption coefficient of ultra-violet radiation
c	concentration of solution (grams of dye/grams of solution)
$\bar{d}$	mean drop diameter
D	diameter of emitting volume
E	radiant power emitted per unit volume
$\mathcal{F}$	geometric optic factor
I_0	exciting-light intensity
L	distance of center of sample volume from target
L_e	effective length of emitting volume
L_1	distance from end of UV-light carrying fiber to axis of detecting fiber
n_i	index of refraction of medium i
N	number of emitting rays
N_r	number of rays received by target
q	total radiant power received by target
r, θ, ϕ	spherical coordinates
$\vec{r}$	unit vector
R_d	drop radius
R_t	radius of target (fiber)
R_ϕ, R_θ	random numbers in (0,1)

S_f surface area of target (fiber)
V volume of droplet cloud
V_d volume of a droplet
V_e emitting volume
V_s sample volume of emitting drops in a cloud
x, y, z cartesian coordinates

Greek

β liquid fraction
$\bar{\beta}$ true liquid fraction in a drop cloud
Ω solid angle considered in the ray-tracing calculation
θ_ℓ limiting acceptance angle in target or maximum admitting angle by target (fiber)
σ_β true standard deviation of liquid fraction for V_s
σ_d standard deviation of drop diameter distribution
ξ quantum yield of dye
χ angle between normal and incident or refracted directions

Subscripts

e emitting volume or experiment value from a lab experiment
i incident
m "measurement" value in a numerical experiment
n normal
r refracted
R position of a drop center
1 lower bond of clustering in $\theta - \phi$ space
2 upper bond of clustering in $\theta - \phi$ space

F.7 References

1. Amarasooriya, W.H. and T.G. Theofanous (1987) "Scaling Considerations in Steam Explosions," *ANS Proceedings 1987 National Heat Transfer Conference*, Vol. 2, 58-67.

2. Angelini, S., W.M. Quam, W.W. Yuen and T.G. Theofanous (1992) "FLUTE: **FLU**orescent **TE**chnique for Two-Phase-Flow Liquid-Fraction Measurements," *Chemical Engineering Communications* **118**, 237–249.

3. Jones, O.W. and J.M. Delhaye (1976) "Transient and Statistical Measurement Techniques for Two-Phase Flows: A Critical Review," *Int. J. Multiphase Flow* **3**, 89-116.

APPENDIX G

SCALING CONSIDERATIONS IN THE DESIGN OF MAGICO

Appendix G: Scaling Considerations in the Disign of MAGICO

If the water depletion phenomenon was the primary focus of the investigations with MAGICO, it was important to ensure, in the design, that the relevant regimes actually could be achieved. In particular, it was not immediately obvious what particle pouring densities and volume fluxes could be obtained, and what particle sizes and temperatures would be required at the small scales (and short contact times) feasible experimentally to obtain the significant water depletion predicted for premixing in the reactor conditions of interest (large pours into the lower plenum). We reached the important decisions with the help of PM-ALPHA, as described below. In other words, we used PM-ALPHA as the scaling tool (to scale down!), with the understanding that justification was pending verification of this analysis tool by the experiments themselves.

An illustration of the reactor conditions of interest is provided in Figure G.1. Note the rather uniform melt volume fraction distribution, the steep void fraction gradients in the outer regions of the premixing zone, and the high void fractions on the inside. After some scoping analyses, for the small scale, we zeroed in on a saturated water pool of 50 cm depth, a pour diameter of 20 cm, and a particle diameter of 2 mm and a velocity of 1 m/s, and carried out a series of calculations investigating the effect of melt temperature, particle inlet volume fraction, and particle density. The key to the various cases considered is given in Table G.1, and the results can be found in the remaining figures of this appendix in terms of this key.

Table G.1 The Key to Parametric Calculations for Scoping the Water Depletion Phenomenon at Small Scale (The table gives the particle temperature, density and inlet volume fraction.)

Case #	Temperature (°C)	Inlet Volume Fraction %	Density (g/cm^3)
R1	1000	2	7.9
R2	2000	2	7.9
R3	1000	2	2.0
R4	2000	2	2.0
R5	1000	20	7.9
R6	2000	20	7.9
R7	1000	20	2.0
R8	2000	20	2.0

The most important observation is that even at 1000 °C and with dilute clouds (2%) of heavy particles (7.9 g/cm^3)—that is, all three conditions most adverse (among those considered) to water depletion as in Case R1—the general pattern is similar to that discussed above for the reactor. Increasing the temperature to 2000°(as in Case R2) produces an even more extensive voiding, but even so, the impact on the melt volume fraction distribution is seen to be minimal. The low density particles (Cases R3, R4, R7 and R8) are distinctly different in exhibiting less penetration, radial spreading to occupy essentially the whole available cross section, and a correspondingly concentrated voiding. Finally, from Cases R5 and R6, we see the impact of a

high inlet melt volume fraction. Again, the voiding is much more extensive than in Case R1, and in fact to such an extent that it impacts the melt volume fraction distribution.

Now, regarding the MAGICO design, it would take very special efforts to create high inlet melt volume fractions (higher than a few percent), or to achieve temperatures significantly higher than 1000 °C, while Case R1 appeared to reproduce the key features adequately enough. More importantly, since this was the first experimental demonstration of water depletion, we judged that it should be made under not particularly optimistic conditions (i.e., maximum voiding). Thus we chose nominally the R1 conditions and designed and ran MAGICO accordingly. The results, and related PM-ALPHA comparisons, allow us now to conclude that water depletion has been experimentally demonstrated and analytically verified (Angelini et al., 1993)

References

1. Angelini, S., W.W. Yuen and T.G. Theofanous (1993) "Premixing-Related Behavior of Steam Explosions," CSNI Specialists Meeting on Fuel-Coolant Interactions, Santa Barbara, CA, January 5-8, 1993.

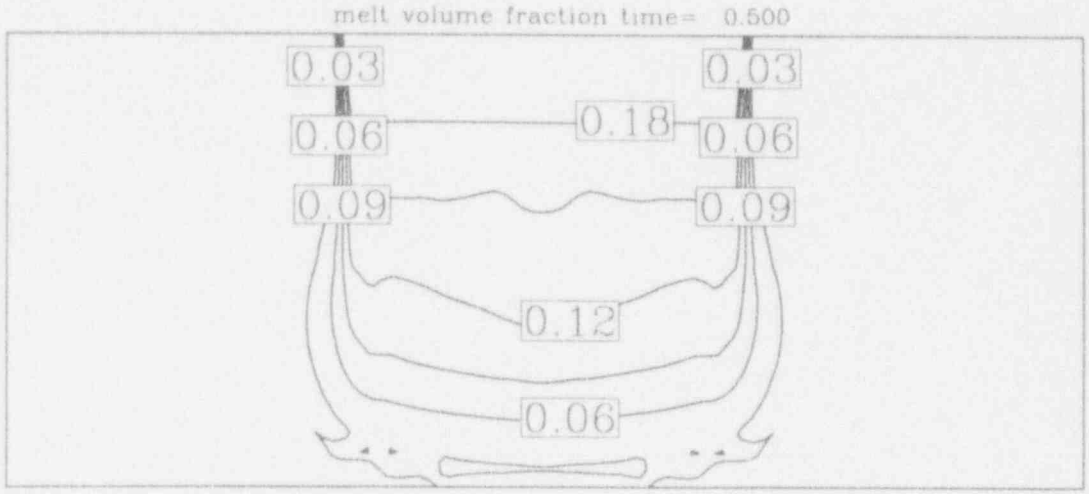

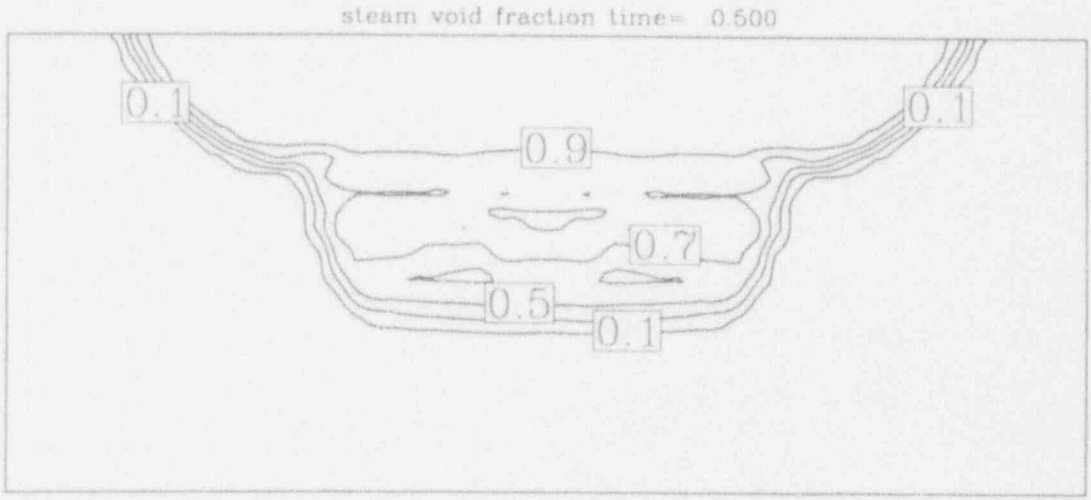

Figure G.1 Illustration of water depletion during premixing at reactor conditions. See Appendix III.A for details.

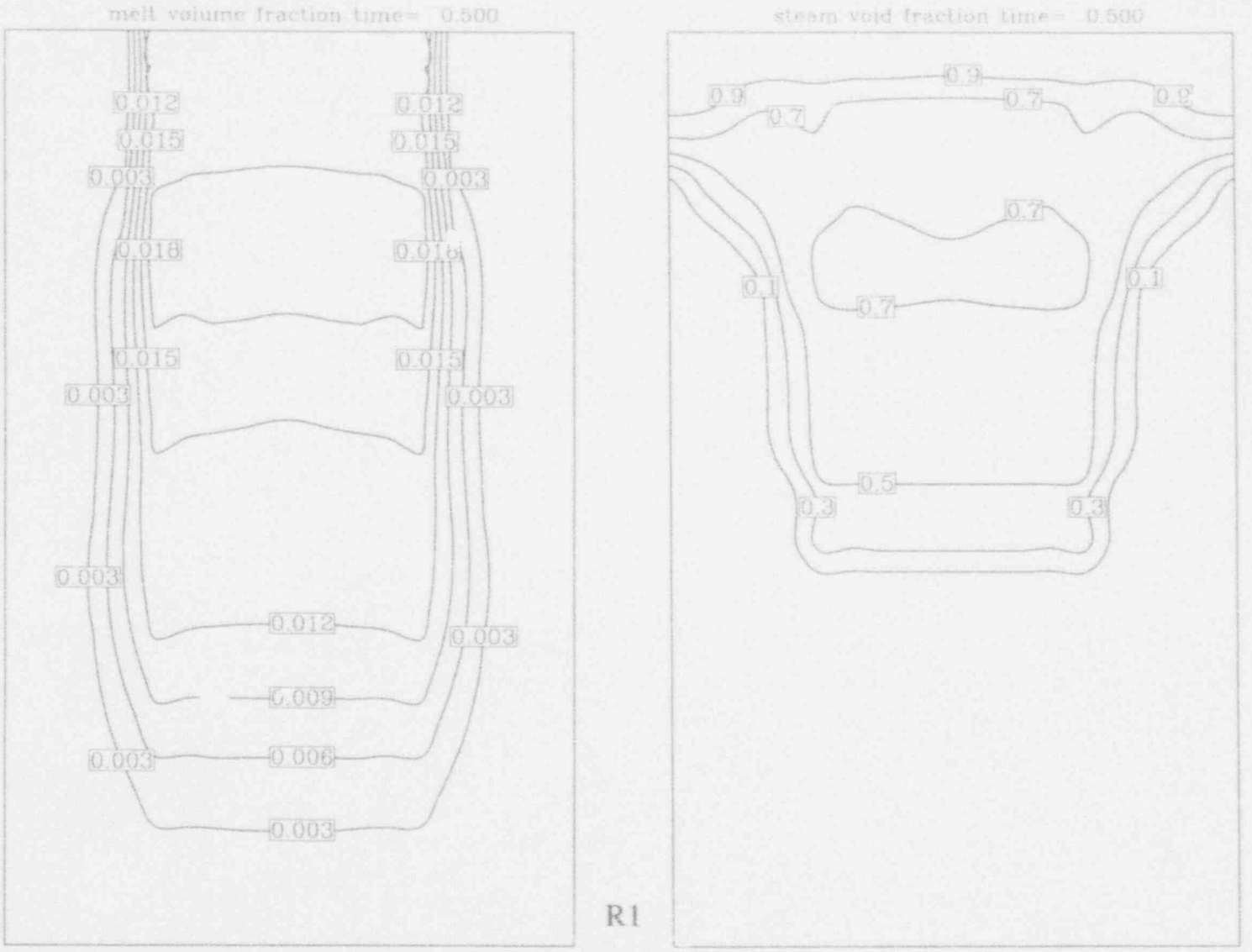

Figure G.2 Calculated melt and steam volume fractions at 0.5 s during premixing under the conditions keyed to the R-numbers in Table G.1. [Figure continues]

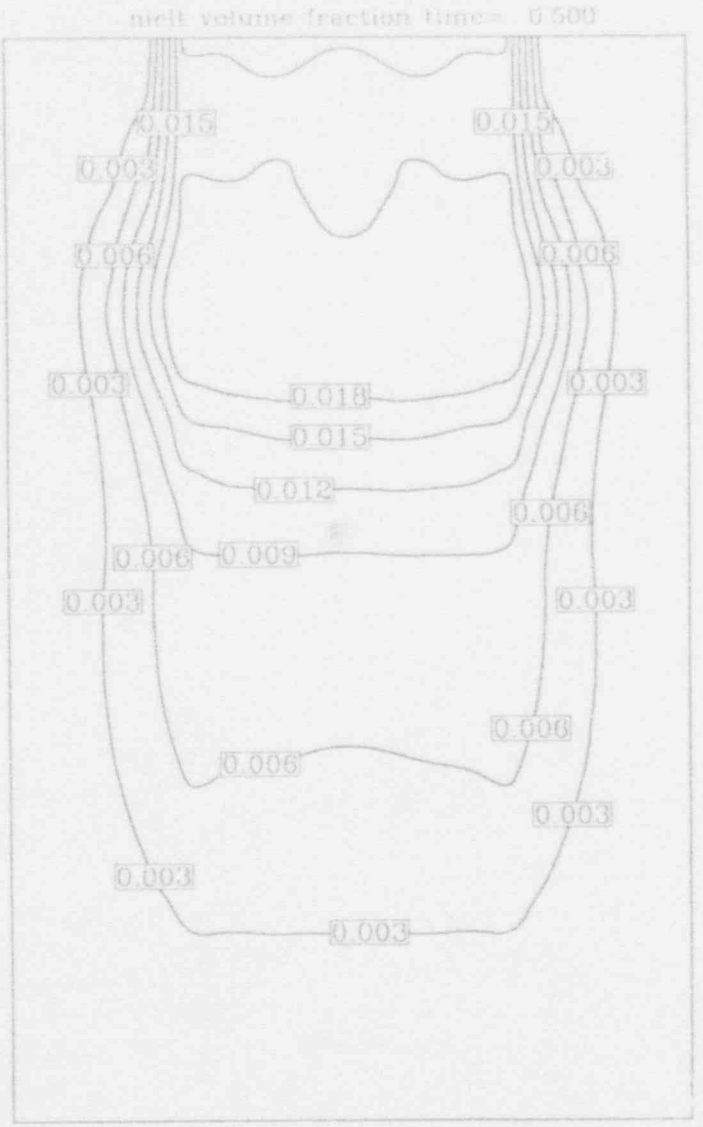
melt volume fraction time= 0.500
0.015
0.015
0.003
0.003
0.006
0.006
0.003
0.018
0.003
0.015
0.012
0.006
0.006
0.009
0.003
0.003
0.006
0.006
0.003
0.003
0.003

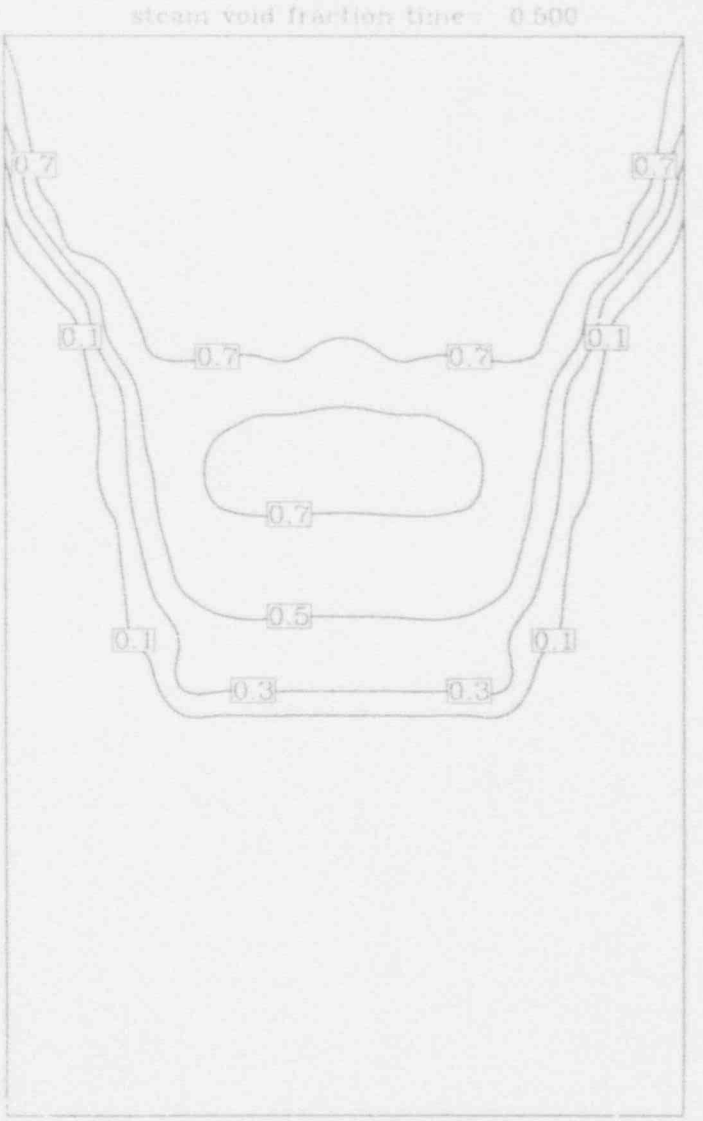
steam void fraction time= 0.500
0.7
0.7
0.1
0.7
0.7
0.1
0.7
0.5
0.1
0.1
0.3
0.3

R2

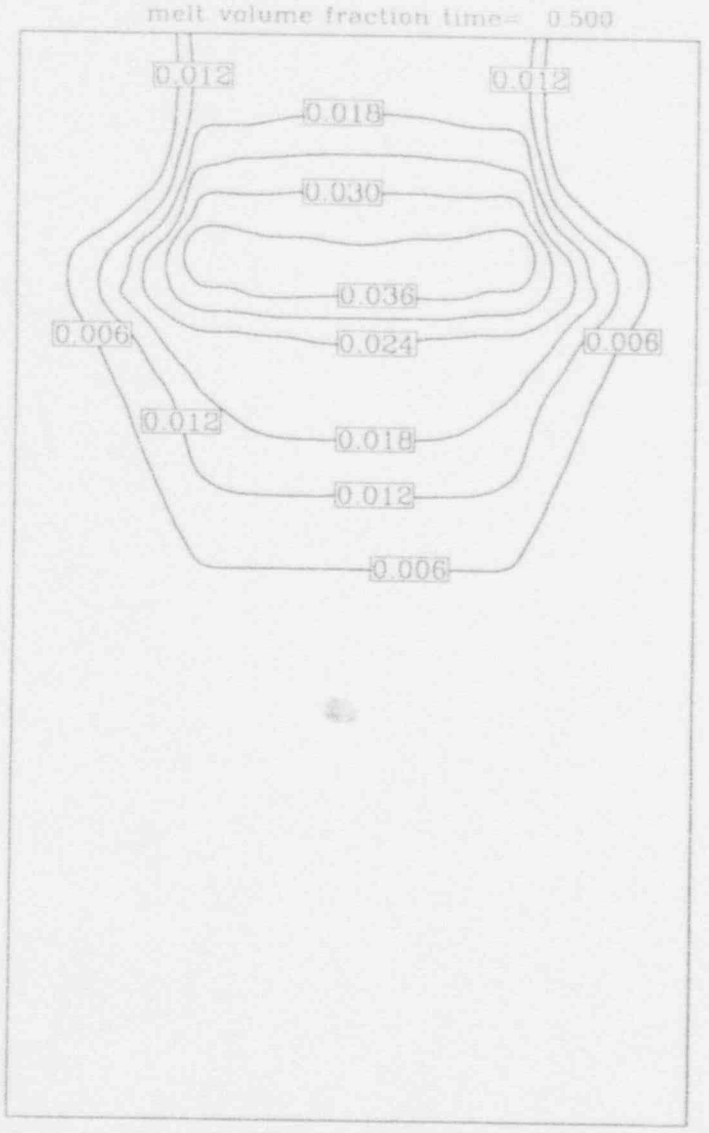
melt volume fraction time= 0.500
0.012
0.012
0.018
0.030
0.036
0.006
0.024
0.006
0.012
0.018
0.012
0.006

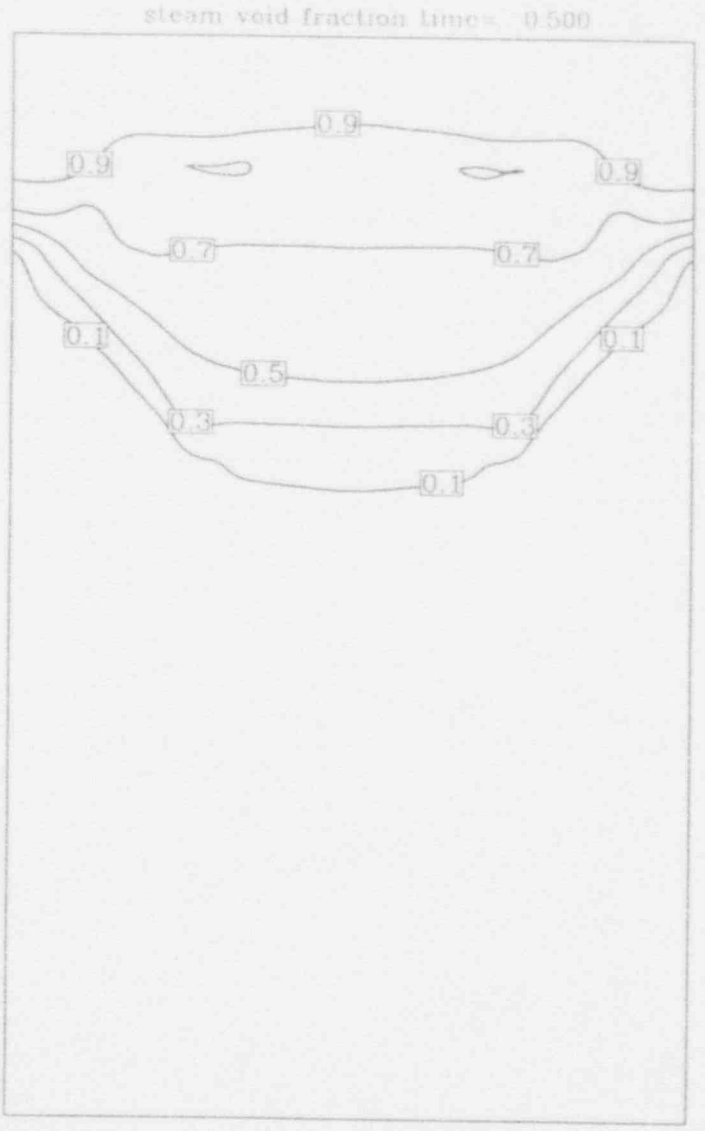
steam void fraction time= 0.500
0.9
0.9
0.9
0.7
0.7
0.1
0.1
0.5
0.3
0.3
0.1

R3

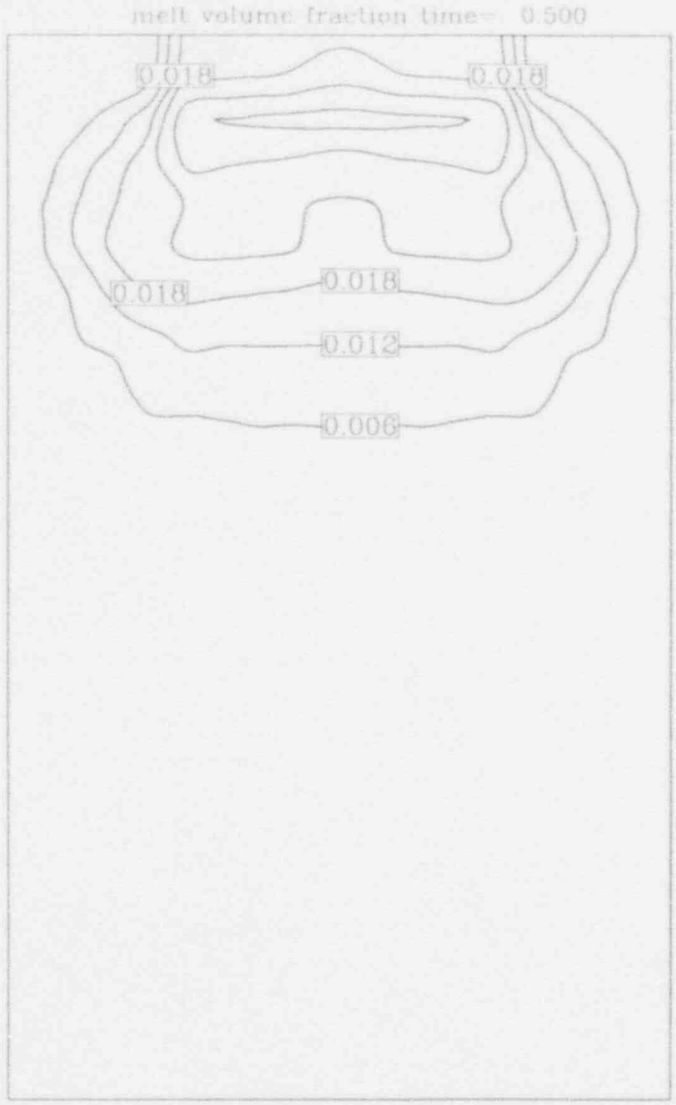
melt volume fraction time= 0.500
0.018
0.018
0.018
0.018
0.012
0.006

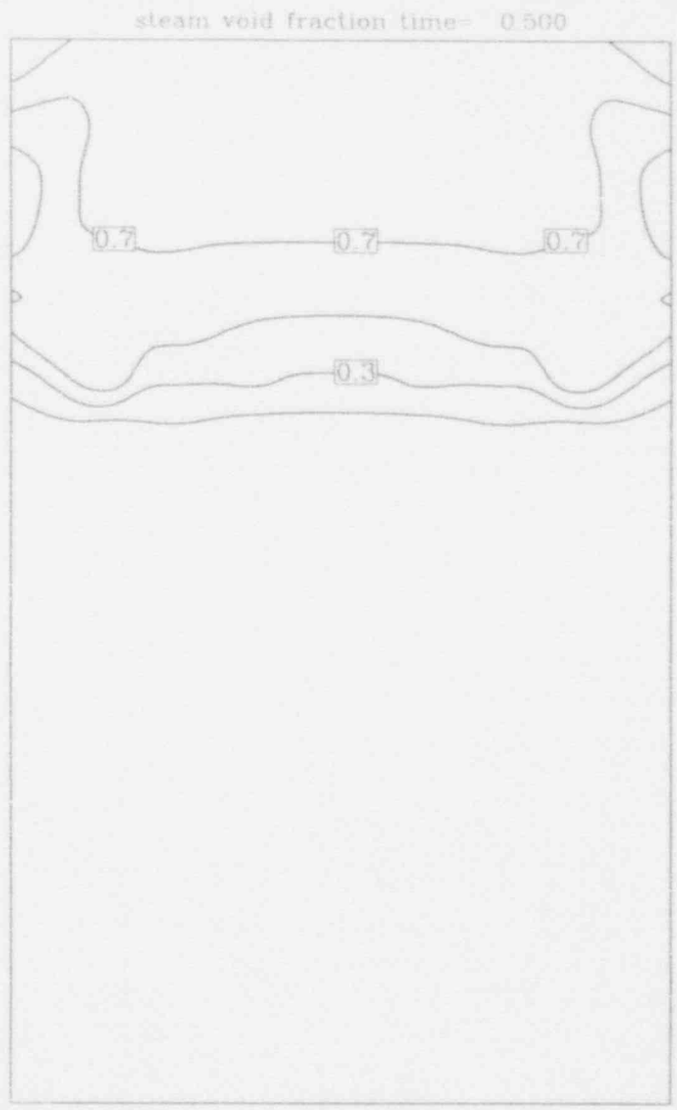
steam void fraction time= 0.500
0.7
0.7
0.7
0.3

R4

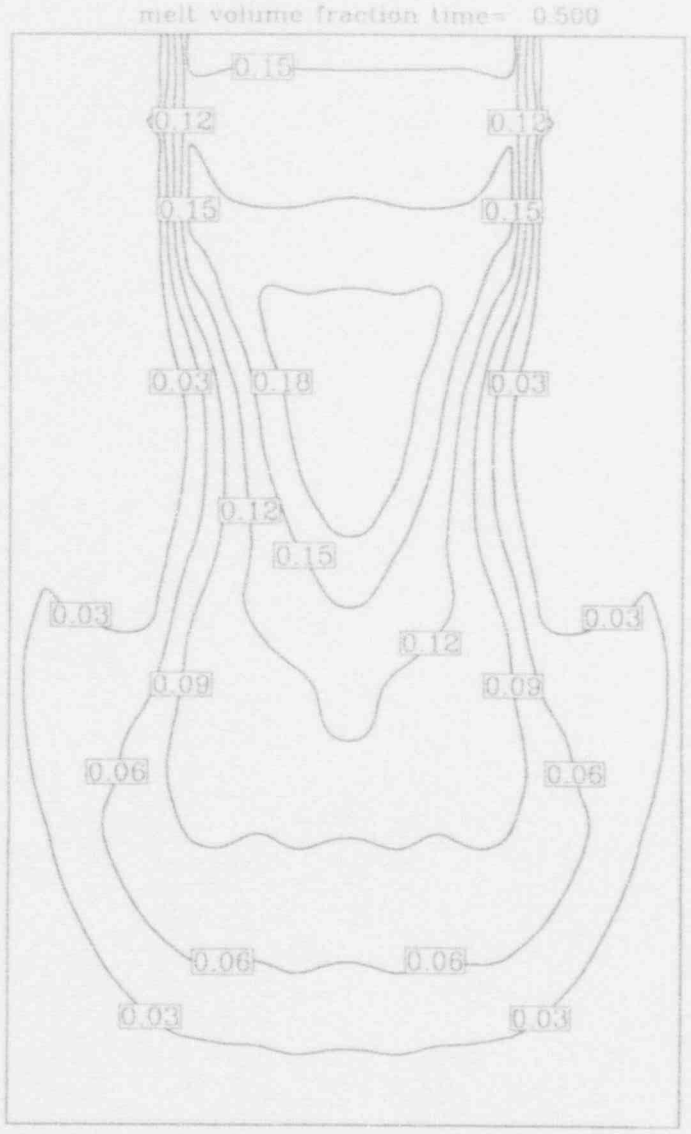
melt volume fraction time= 0.500
0.15
0.12
0.12
0.15
0.15
0.03
0.18
0.03
0.12
0.15
0.03
0.03
0.12
0.09
0.09
0.06
0.06
0.06
0.06
0.03
0.03

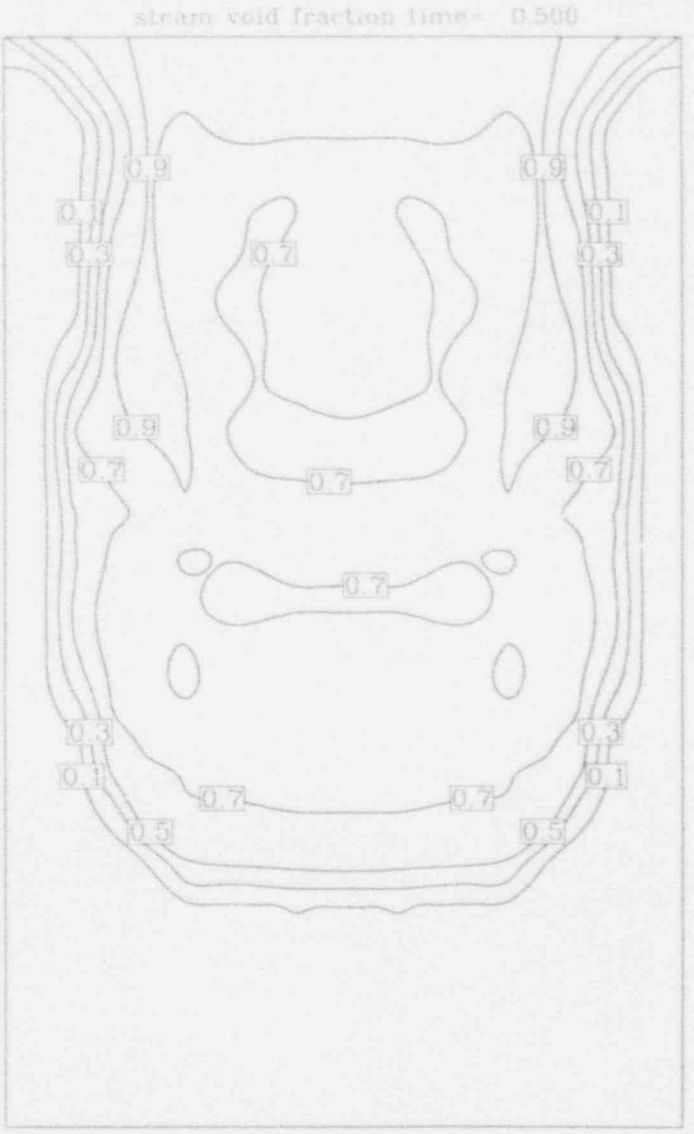
steam void fraction time= 0.500
0.9
0.9
0.1
0.3
0.7
0.3
0.9
0.9
0.7
0.7
0.7
0.7
0.3
0.3
0.1
0.7
0.7
0.1
0.5
0.5

R5

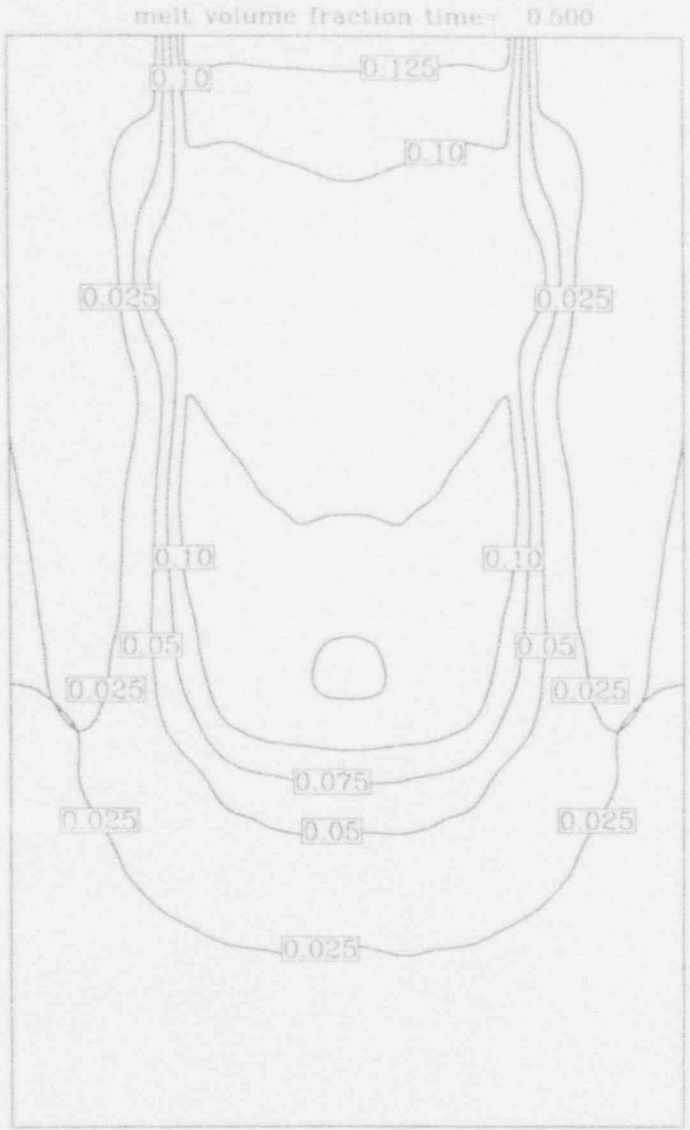
melt volume fraction time= 0.500
0.10
0.125
0.10
0.025
0.025
0.10
0.10
0.05
0.05
0.025
0.025
0.075
0.025
0.05
0.025
0.025

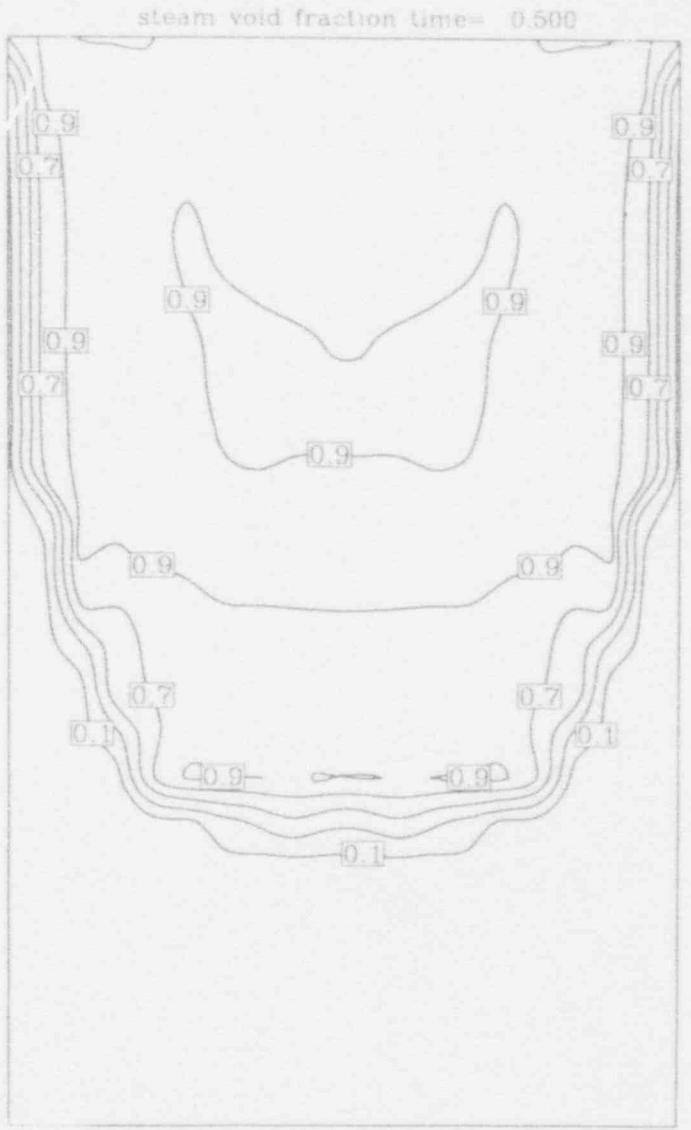
steam void fraction time= 0.500
0.9
0.9
0.7
0.7
0.9
0.9
0.9
0.9
0.7
0.7
0.9
0.9
0.9
0.7
0.7
0.1
0.9
0.9
0.1

R6

I.G-11

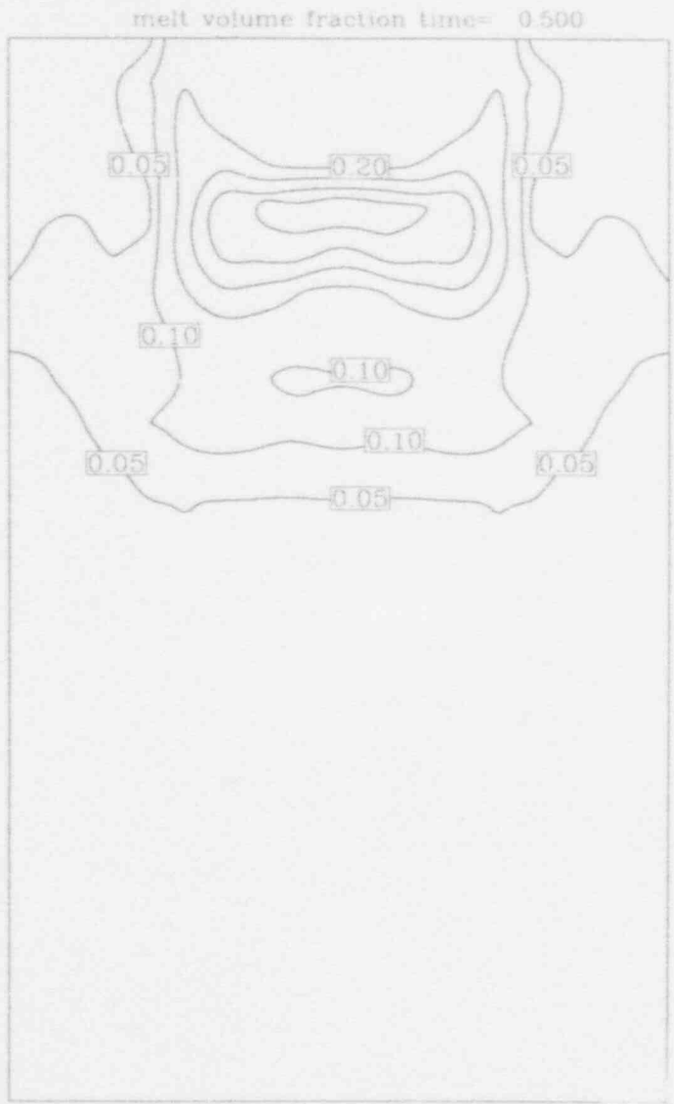
melt volume fraction time= 0.500
0.05
0.20
0.05
0.10
0.10
0.10
0.05
0.05
0.05

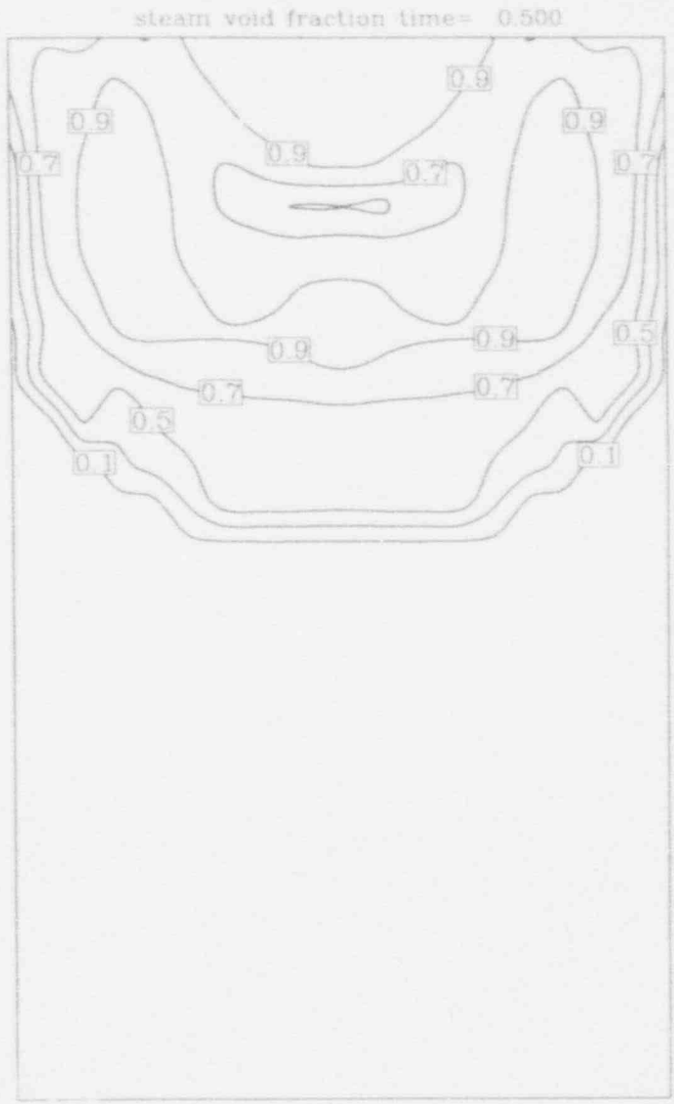
steam void fraction time= 0.500
0.9
0.9
0.9
0.9
0.7
0.7
0.7
0.9
0.9
0.5
0.7
0.7
0.5
0.1
0.1

R7

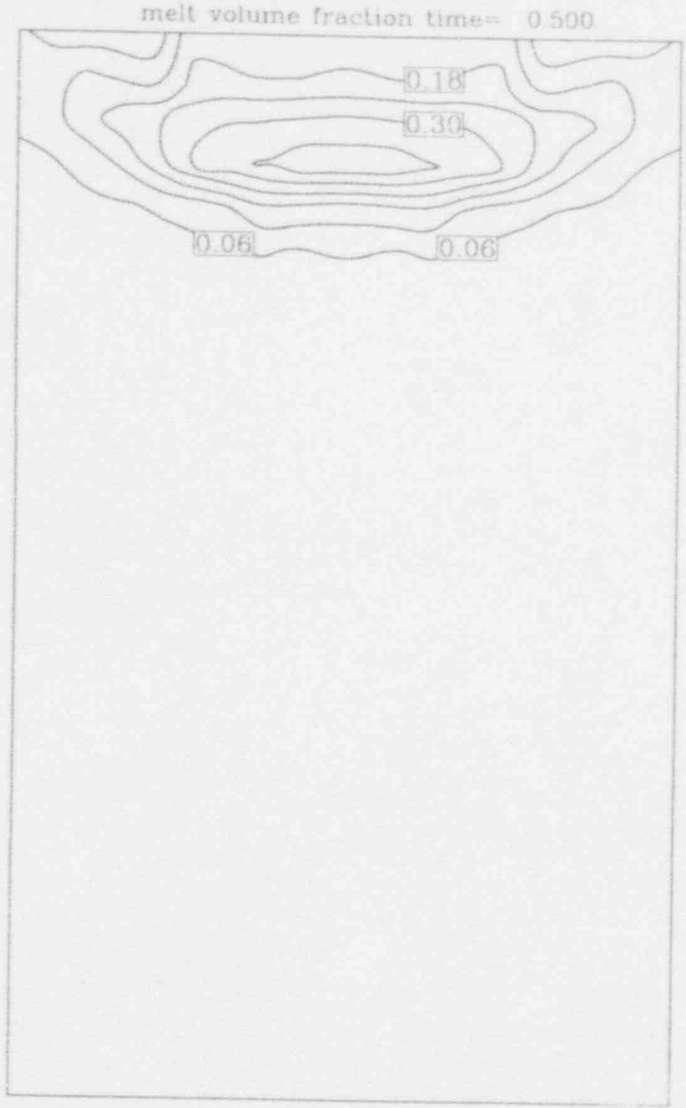
melt volume fraction time= 0.500
0.18
0.30
0.06
0.06

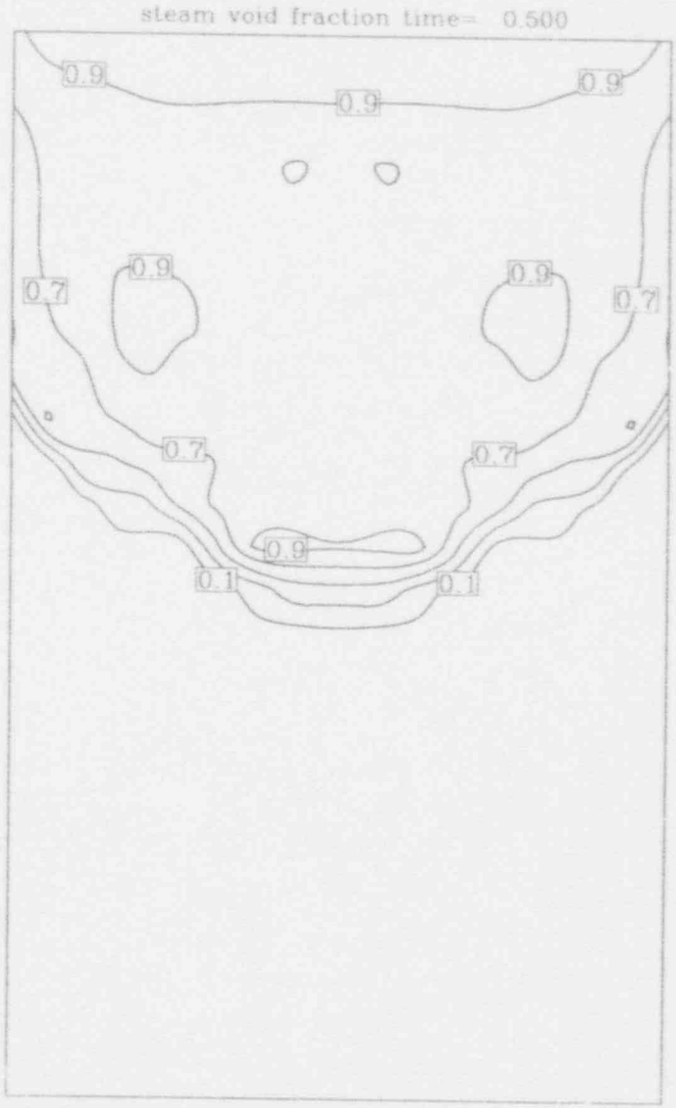
steam void fraction time= 0.500
0.9
0.9
0.9
0.7
0.9
0.9
0.7
0.7
0.7
0.9
0.1
0.1

R8

PART II. THE FUNDAMENTAL MICROINTERACTIONS THAT SUPPORT THE PROPAGATION OF STEAM EXPLOSIONS

Table of Contents

Figures

II.1 Introduction

It is known that under certain conditions "hot" liquid drops can violently interact ("explode") after coming in contact with a surrounding "cold" and volatile liquid (the "coolant"). These thermal interactions are the consequence of rapid and fine fragmentation (of the drop) and the accompanying mixing with the surrounding coolant. Such interactions are known to be initiated by the contact of the two liquids; such contact can be observed either spontaneously (for appropriate combinations of temperatures) or it can be caused by forcing the collapse of the intervening vapor blanket, as for example, by a sharp pressure pulse. It is also known that droplet fragmentation can result from purely hydrodynamic causes (i.e. in isothermal systems) in an induced rapid acceleration environment, as the one that accompanies a large pressure wave. In the detonation wave of a steam explosion clearly both mechanisms are present, yet their relative role, and hence the actual kinetics that control the various stages of escalation from the initiating trigger event to a "full-strength" detonation, has not been elucidated in the past.

More specifically, while the very initial stages of a spontaneously triggered explosion will be dominated by thermally-induced fragmentation, and while at the other extreme of a fully developed detonation into the supercritical pressure region only hydrodynamic breakup is relevant, nothing is known about the intermediate, escalation, regime. *This regime is crucial in that it determines whether the premixture conditions can support an escalation into a highly developed detonation, and perhaps more importantly, whether this escalation is possible within the physical constraints of the practical system under investigation.*

This then is the main theme of this work, with some more specific considerations including: the details of micromixing environment around each drop as it fragments, the dynamic aspects of the pressure and velocity fields behind the shock front (especially in the so-called reaction zone), and the fundamentally non-one-dimensional character of the process. Our experimental approach is based on the detailed observation of droplets forced to interact with the coolant in a simulated steam explosion environment—especially with regard to *sustained* pressure waves that characterize the reaction zone. This is accomplished in a hydrodynamic shock tube. All analytical interpretations are carried out with our computer code, ESPROSE. The initial formulation of ESPROSE was documented by Medhekar et al. (1989, 1991). The complete model is summarized in Appendix II.A.

Previous related work can be briefly summarized as follows:

Thermally-Induced Fragmentation. Most of the work in this area has been aimed to delineate and interpret the so-called temperature interaction zone. No fragmentation rate data exist, but inferences on fragmentation (and interaction) rates have been made from comparisons of calculations with Nelson's (Nelson and Duda, 1981) data on the growth and collapse cycles of vapor bubbles from triggered single-drop melt-water interactions. Such interpretations have been offered by Kim and Corradini (1988) and by Inoue et al. (1989) among others. In particular, the Kim-Corradini model is intended to be predictive; in it the fragmentation time is obtained from the penetration of the drop by liquid coolant jets arising from the "spikes" of Taylor waves at the interface upon collapse and rebound of the vapor blanket. In a simple interpretation* of this model the jet velocity is obtained from

---

* M. Corradini, Personal Communication (1991).

$$U_j = \left\{ \frac{\Delta P}{\rho_c (1 + \rho_d/\rho_c)^{1/2}} \right\}^{1/2} \qquad (II.1)$$

which yields a fragmentation time t_b of

$$R_d/U_j < t_b < D_d/U_j \qquad (II.2)$$

In the above, ΔP is the pressure rise across the shock front. Note that this model makes no distinction for the duration of the pressure pulse or of the droplet temperature, and it does not explain how these microscopic jets can survive the intense heating environment, but rather are taken to penetrate the droplet all the way through. For example, for a corium melt drop 10 mm in diameter, and a shock pressure rise of 200 bar, the above yields a fragmentation time of 50 to 100 μs. Note that this is short compared to the residence time in the reaction zone, and too long regarding the microjet's potential response to the intense heating.

Hydrodynamically-Induced Fragmentation. Experimental work in this area, for the relevant liquid-liquid system, is scarce and not well documented; worse, it appears to be contradictory. On the one hand Baines et al. (1979) and Kim et al. (1983) working with mercury and gallium drops in water have reported (visual determination) fragmentation times consistent with old results obtained in gas-liquid systems; namely, the boundary layer stripping mechanisms and a dimensionless fragmentation time, t_b^*, of

$$t_b^* \equiv \frac{t_b U_r}{D_d} \left(\frac{\rho_c}{\rho_d} \right)^{1/2} \sim 4 \text{ to } 5 \qquad (II.3)$$

On the other hand, Theofanous, Saito and Efthimiadis (1979), using flash X-ray diagnostics reported, for a mercury-water system, significantly lower breakup times. These results were correlated in terms of a $\mathrm{Bo}^{1/4}$ dependence, motivated by a Taylor instability mechanism, as

$$t_b^* = 10.3 \ \mathrm{Bo}_o^{-1/4} \qquad (II.4)$$

For example, for a Bond number of 10^4 this yields a dimensionless breakup time of $\sim$1, or four to five times faster than boundary layer stripping. For a Bond number of 10^3 the result is $\sim$2 and still more than a factor of 2 faster. Both the X-ray photos and the quantitative analysis of them has been documented by Theofanous et al.(1983).

Fragmentation in Detonation Models. Not surprisingly, the formulation of fragmentation in detonation modelling has been widely varied. To start with, the formulation in the original, steady-state, detonation model of Board and Hall (1974) made use of Eq. (II.4), with a coefficient of 22, known at the time from experiments with gas-liquid systems. Modern transient detonation models have also made use of hydrodynamic fragmentation; Fletcher and Thyagaraja (1989) use the stripping correlation of Carachalios et al.; Medhekar et al. (1989, 1991) used the Reinecke-Waldman fragmentation rate correlation (Reinecke and Waldman, 1970) (developed also from gas–liquid work) with a dimensionless fragmentation time of 1 [motivated from Eq. (II.4)]. It should be noted that all these (gas–liquid) data were obtained with steady flow conditions (by imposing an instantaneous acceleration and thus a fixed free-stream velocity behind

the shock) while for liquid–liquid systems the relative velocity changes during the fragmentation time is very significant. In a detonation calculation this is further aggravated by the highly variable pressure and velocity field histories behind an escalating shock front. Finally, besides the fragmentation kinetics, another equally important aspect in detonation modelling is to properly reflect the micromixing between the finely fragmented debris and the coolant available to mix in the immediate proximity. This is particularly important in fuel–dilute premixtures (as is commonly the case) and also in interpreting experiments that may not be truly one-dimensional. As experienced by Bürger et al. (1982), one-dimensional simulations lead to considerable inconsistencies. With the exception of ESPROSE, all other published detonation models are restricted to one dimension.

The presentation in this report is made in three parts. The first is concerned with the recasting of Eq. (II.4) in differential form; that is, expressing the fragmentation rate in terms of the instantaneous Bond number. This is done with the help of ESPROSE, made to simulate the single-drop response as observed in the shock-tube experiments that formed the basis for Eq. (II.4). In the second part we present new experimental data, obtained in the same shock-tube facility but with molten tin drops superheated by different amounts and subjected to pressure waves of various magnitudes, such as to span the potential range of thermal vs hydrodynamically controlled mechanisms. A rough interpretation of these data (hydrodynamic vs. thermal fragmentation mechanisms) is also provided with the help of ESPROSE and the instantaneous Bond number formulation derived in the first part. Finally, in the third part these fragmentation kinetics results are supplemented with a non-equilibrium treatment introduced in ESPROSE to "simulate" and discuss certain detonations observed in the KROTOS facility at the European Joint Research Center in ISPRA (Italy). These examples also illustrates the importance of two-dimensionality even for apparently one-dimensional situations.

II.2 The Instantaneous Bond Number Formulation

The operation of the hydrodynamic shock tube (the SIGMA facility) was simulated with ESPROSE by introducing a small enough mercury mass in one computational shell to correspond to the one drop used in the experiments. The facility and experimental technique have been described previously (Patel and Theofanous, 1981). Briefly, a prescored diaphragm is ruptured, to suddenly release the pressure from the 1.2 m long driver section into the water-filled 3 m long expansion section. The tube is designed for pressures up to 1000 bar. In the particular experiments considered here (isothermal at room temperature) the mercury drops were initially stationary (resting on a thin teflon piece) and the fragmentation states were determined from flash X-ray radiographs obtained for different delay times after the arrival of the shock. The fragmentated mass on these X-ray films was determined (Theofanous et al., 1983) from the mass found in the "particle cloud" by quantitative image analysis. (This method is demonstrated for tin drops in the next section). The driver pressures in this set of experiments were set at 200, 333 or 466 bar. We could match the data well with an instantaneous fragmentation rate given by

$$\frac{dM_d}{dt} = -\frac{\pi D_d^2(t)|U_d(t) - U_c(t)|}{6t_b^*}(\rho_c\rho_d)^{1/2} \qquad (II.5)$$

with a dimensionless breakup time given in terms of the instantaneous Bond number by

$$t_b^* = 13.7\ \mathrm{Bo}_i^{-1/4} \qquad (II.6)$$

Note that in the implementation of Eqs. (II.5) and (II.6), all fluid properties and flow velocities are evaluated at their instantaneous values. The results are shown against the experimental data in Figure II.1.

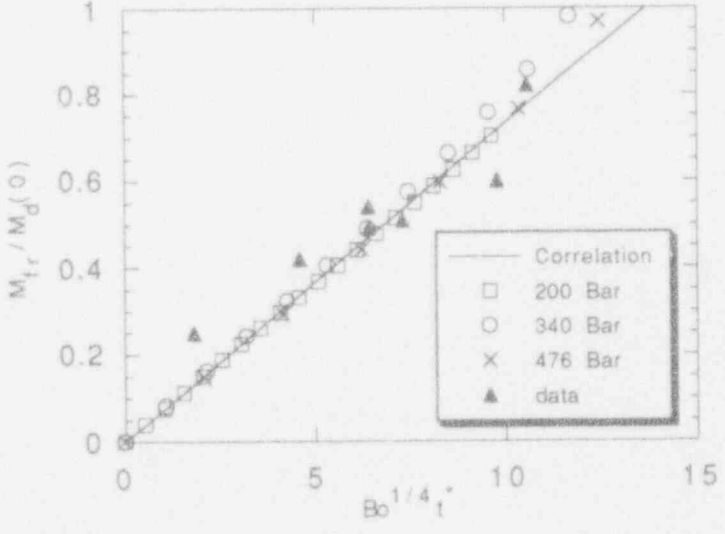

Figure II.1 Computed fragmented mass (○, □, ×) in comparison to experimental data in the mercury/water system (isothermal).

The detailed results from the 200 bar simulation are summarized in Figure II.2 In particular, we can observe the changes in relative velocity, particle diameter, and the resulting variation of the Bond number. The evolution of the debris volume fraction distributions is also shown—this is of significance in gaining some perspective on local mixing obtained and resulting pressure feedback effects responsible for sustaining a propagation. The computed liquid and droplet velocities are in good agreement with the data. The computed shock front exhibits minimal numerical diffusion, and its speed is also in excellent agreement with the data. The node size in this computation was 1 cm and the time step, 0.01 ms.

Similar calculations were carried out for the boundary layer stripping and the Reinecke–Waldman correlations discussed above. In these calculations the correlations were used in their differentiated form and with the instantaneous flow/drop parameters during the transient. The results for different combinations of pressures and fragmentation time are collected in Figure II.3. We observe that

(a) the Reinecke–Waldman formulation cannot be made to agree for any choice of t_b^*, and

(b) for the boundary layer stripping formulation, the value of t_b^* needed to produce reasonable agreement changes with shock pressure.

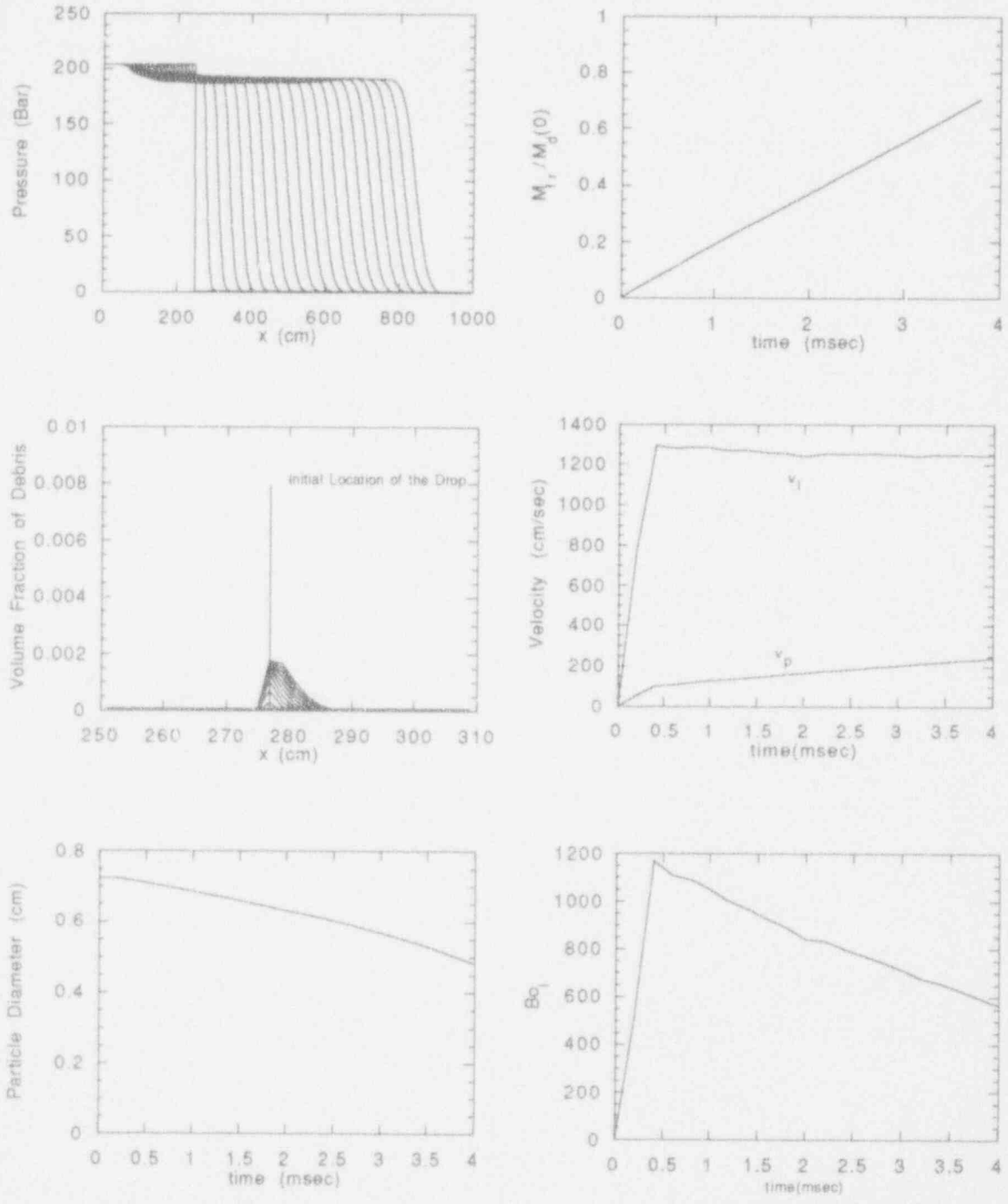

Figure II.2 Detailed results from an ESPROSE simulation of a mercury drop subjected to a 200 bar shock in water. The distance x is along the length of the shock tube starting at the top of the driver section. The position of the diaphragm is at $x = 250$ cm (in this simulation a longer tube, than in the experimental one, was chosen to allow a longer evolution of the transient before reflected waves arrive back at the drop). The pressure front is given in time increments of 0.2 ms. In the debris volume fraction plot, the time increment is 0.4 ms. In the time plots, the origin is at the shock arrival time to the droplet position.

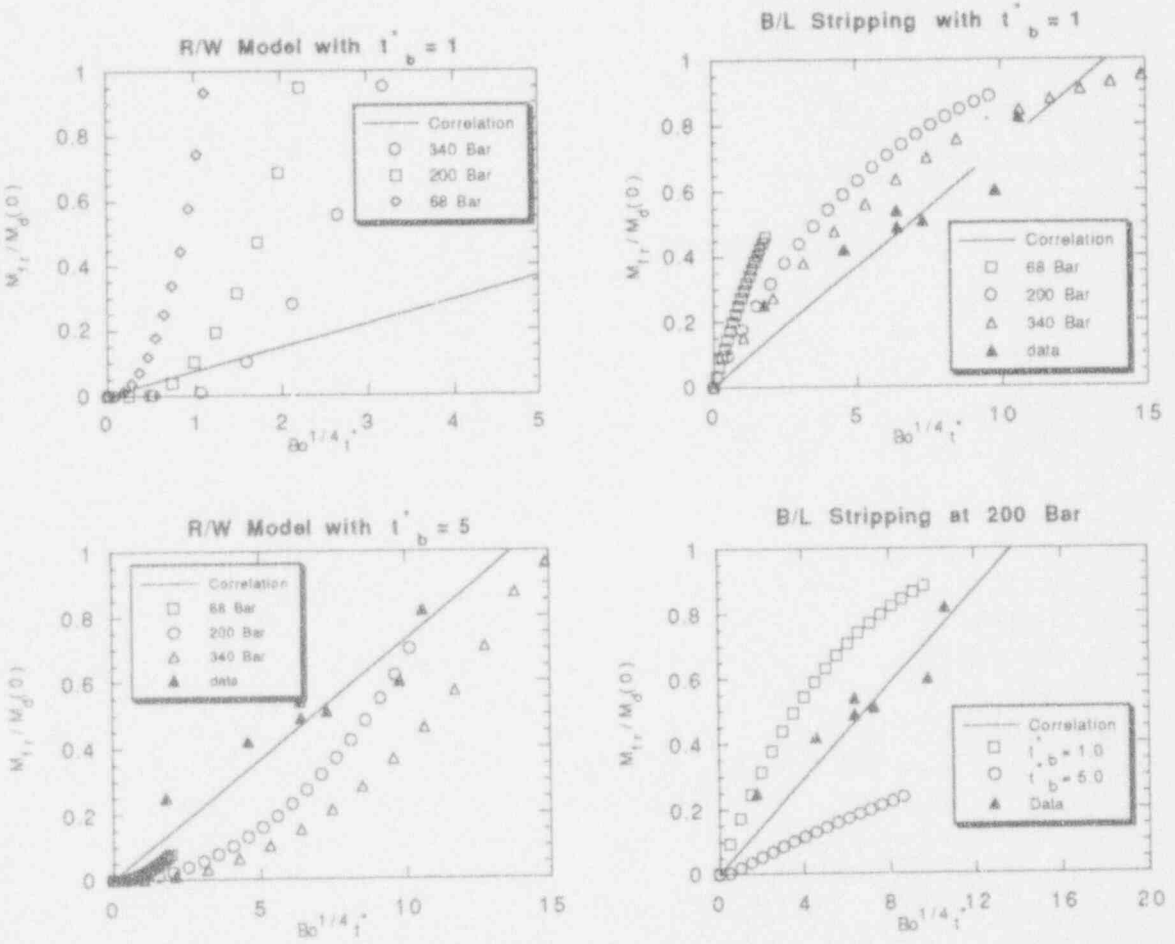

Figure II.3 Comparison of the Boundary Layer Stripping and the Reinecke–Waldman correlations (for various choices of t_b^*) with the experimental data in a mercury/water system.

II.3 Fragmentation of Molten Tin Drops

For these experiments the SIGMA facility was equipped with a melt generator, a device that could produce and release a single (occasionally split into two equal parts) drop of molten tin at required temperatures of up to 1000 °C. Data were obtained at low (360 °C), intermediate (670 °C), and high (1000 °C) temperatures, and at two shock (pressure) levels, 66 and 200 bar. The drop temperature (quoted at the time of shock impact) was reproducible with ±20 °C. In all experiments the drop mass was fixed at 1 g and the water pressure and temperature at 1 bar and 85 °C (to prevent spontaneous interactions), respectively. The shock was timed to hit the drop while it is within view of the shock tube window. This timing could be adjusted so that the drop remained in view for times up to 2 ms following impact. In the present configuration, the pressure/flow conditions of the water in the viscinity of the droplet remain unchanged for up to 2.5 milliseconds, at which time the reflected shock travelling back from the bottom of the tube arrives. As noted already, however, by appropriate modifications in the driver section a wide range of pressure pulse shapes can be obtained. Also, a two-phase flow environment around the drop can be generated by means of steam injection at the bottom of the tube.

As in the mercury/water experiments discussed above, data were obtained from single flash X-ray exposures at different times along the fragmentation process. Since all conditions are highly reproducible, these data provide the time-wise evolution of a "representative" drop as well. In these older experiments, the unfragmented portion of the drop could not be adequately penetrated, even with hard X-rays. Thus, only the fragmented mass (debris cloud) could be quantified. In the present experiments with tin, the whole drop can be penetrated, even with soft X-rays, and the whole image, including the unfragmented part, could be quantified. The procedure involved the use of a calibration curve obtained from exposing a tin stepwedge and two (later three) "witness" pieces to allow for variability in the exposure (small) and film development (quite significant). The X-ray image was digitized by a scanner creating a two-dimensional array of light intensities. These data were then processed by the computer using the calibration curve (with appropriate normalizations, based on the witness pieces) to obtain a two-dimensional array representing the spatial distribution of tin mass. A test of the accuracy of the procedure is the extent to which these calculated masses add up to the known total drop mass (1 g, or 0.5 g for the case of split drops). From the results obtained so far (discussed below) this test was met beyond our expectations. Because of the non-linearities involved, visual inspection of such films can be quite misleading, and such quantitative results are essential to understanding the fragmentation process.

Additional information about the extent and intensity of the interaction, in an overall sense, is available from the debris which is collected with an especially constructed plastic "pan" located some 10 cm below the interacting drop. These data are typically composed of two groups of masses—one highly fragmented at micron-size round spheres and the other highly porous, but macroscopic in dimension, particles. In the 1000 °C runs this macroscopically fragmented mass amounted to 50% and 40% of the drop mass for the 66 and 200 bar runs, respectively. Thus, as a first indirect measure it appears that at 1000 °C about one-half of the drop is finely fragmented, with a bias for more fragmentation at the higher shock pressures.

All the X-ray results obtained so far can be found in Figures II.4 through II.7. The 100-series runs in Figure II.4 were obtained with shock pressures of 66 bar (1000 psi), while the

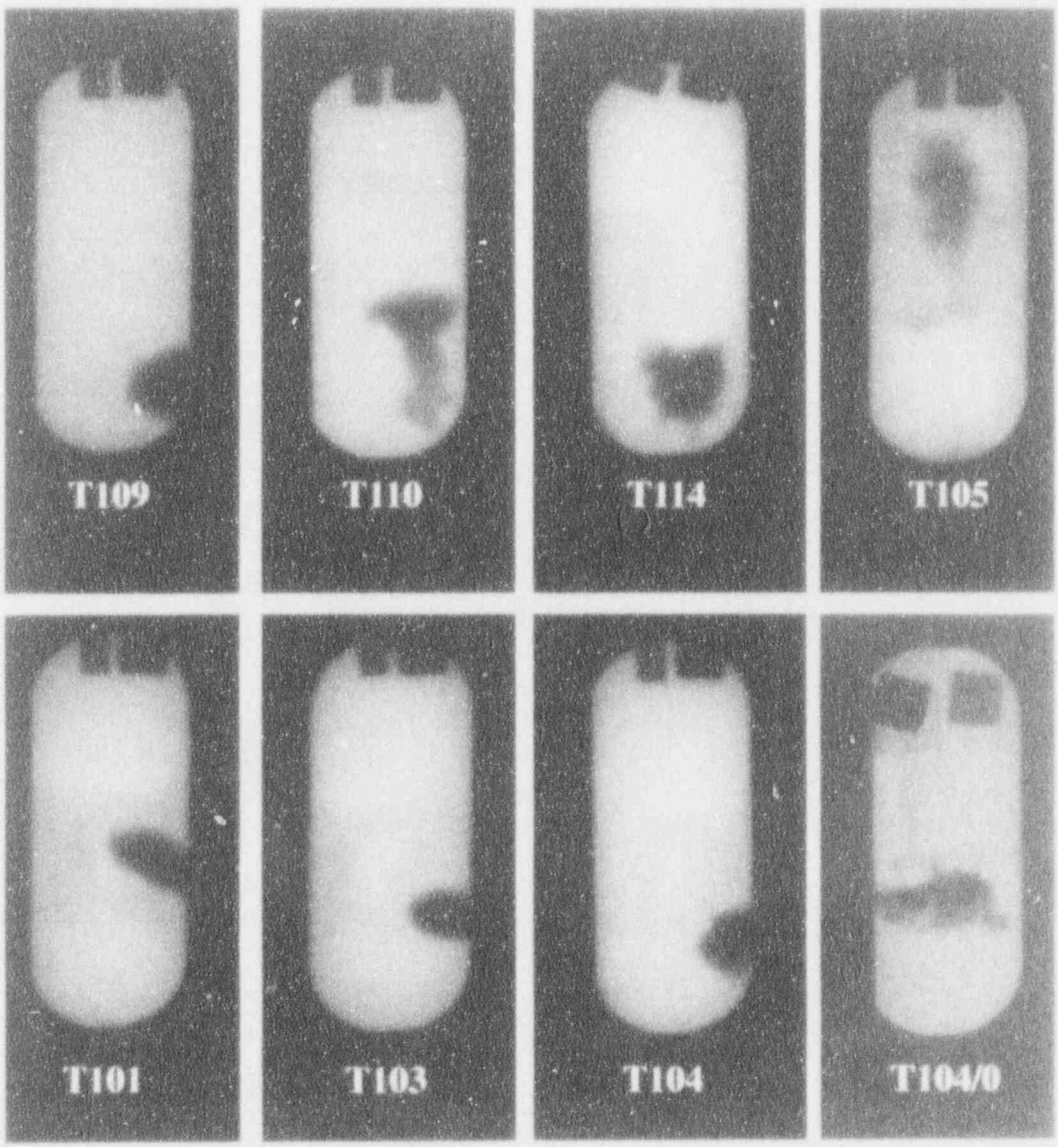

Figure II.4 X-ray snapshots from the runs with 66 bar shocks. Tin temperatures of 1000 °C and 670 °C for the top and bottom rows, respectively. Times (in ms) following shock arrival: T109–1, T110–1.5, T114–1.5, T105–2, T101–0.5, T103–1, T104–2, T104/0–2.

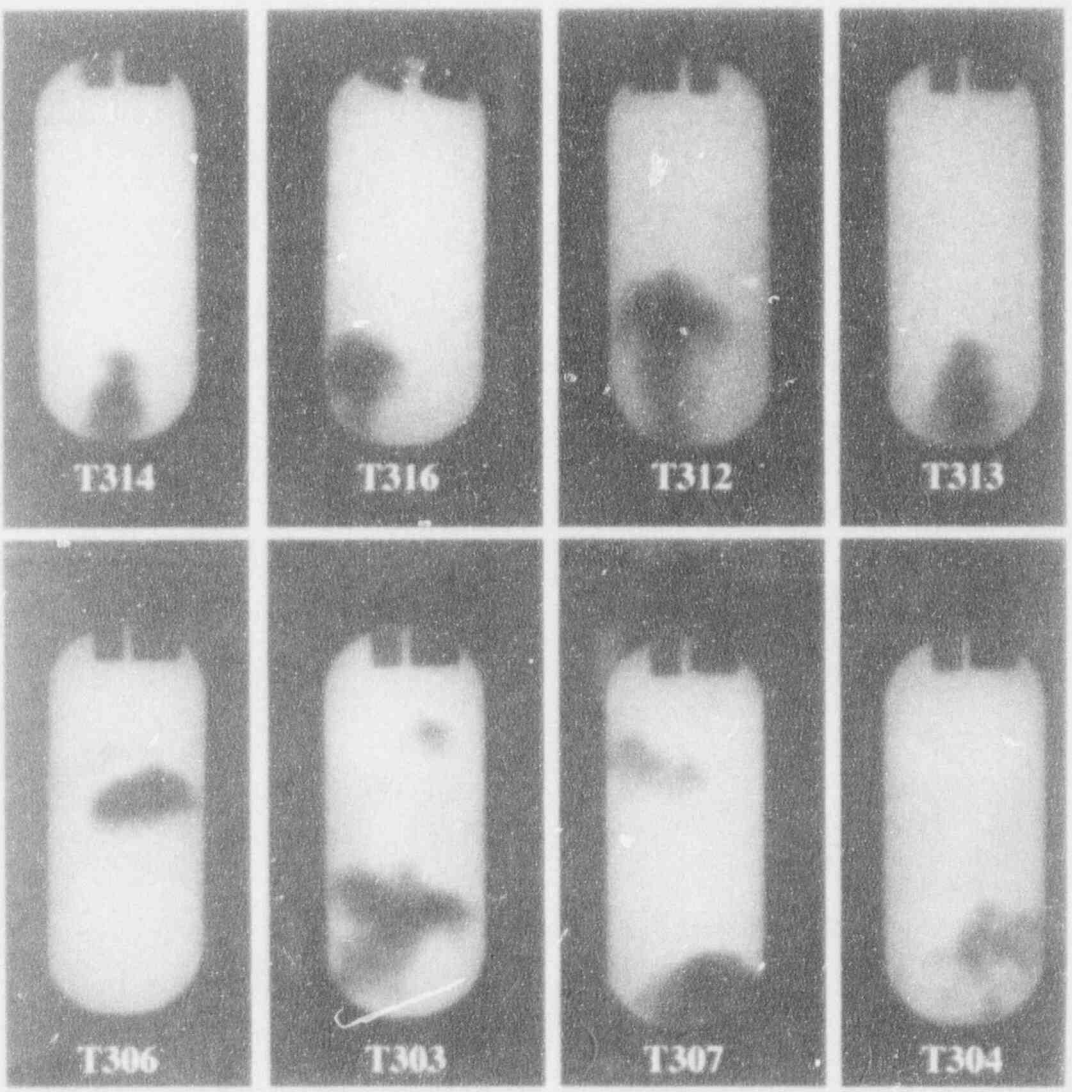

Figure II.5 X-ray snapshots from the runs with 200 bar shocks. Tin temperatures of 1000 °C and 670 °C for the top and bottom rows, respectively. Times (in ms) following shock arrival: T314–0.75, T316–0.85, T312–1, T313–1.5, T306–0.75, T303–1, T307–1.5, T304–2.

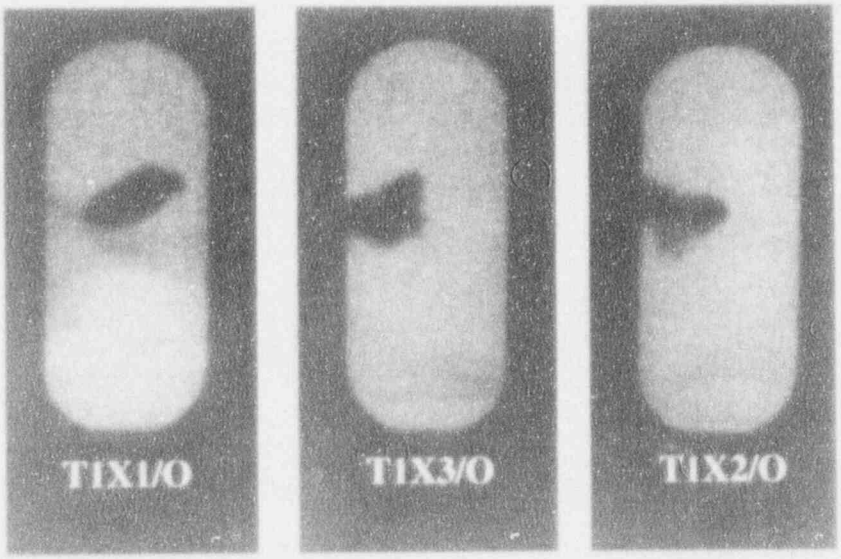

Figure II.6 X-ray snapshots from the low temperature (360 °C) runs with 66 bar shocks. Times (in ms) following shock arrival: T1X1/0–0.25, T1X2/0–1.5, T1X3/0–2.

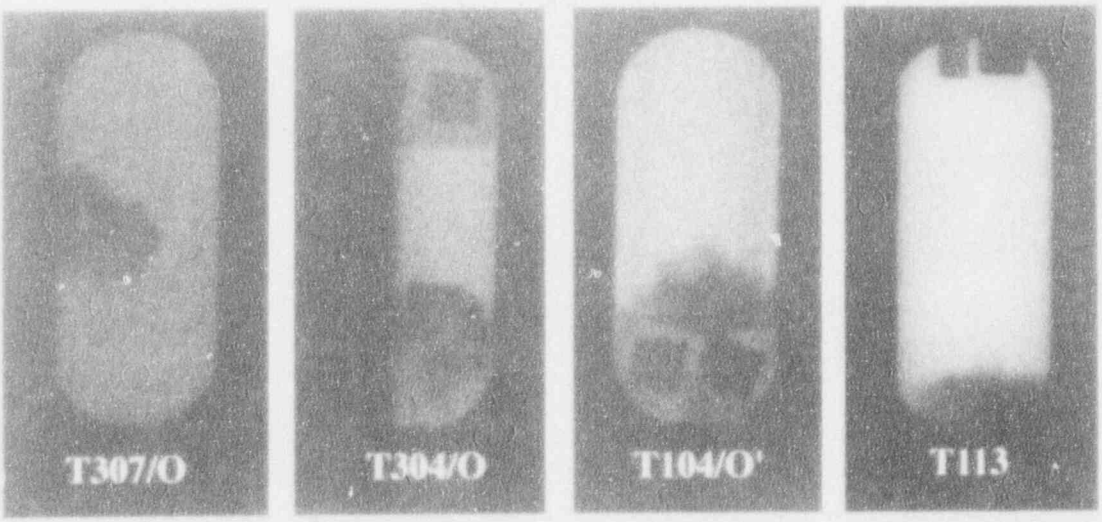

Figure II.7 Snapshots from miscellaneous runs. Shock pressures of 66 and 209 bar for the 100- and 300-series, respectively. Tin temperature 1000 °C for T113 and 670 °C for all others. Times (in ms) following shock arrival: T307/0–1.5, T304/0–2, T104/o'—2, T113–1.5.

300-series results obtained with shock pressures of 200 bar (3000 psi) are in Figure II.5. In these figures the top line is for tin drop temperatures of 1000 °C while the bottom line for 670 °C. In Figures II.6 and II.7 we have collected certain "older" experimental data obtained during the development of the experimental techniques. As such, the tin temperatures for these "old" data are not very reliable, but they are included here because of certain interesting features in the fragmentation morphology they exhibit. Before discussing these data, it is useful to have in mind Figure II.8, which shows in real time the expected fragmentation of a tin drop according to the hydrodynamic fragmentation model (the instantaneous Bond number formulation discussed in the previous section). Also, it is useful to consider the digital X-ray "reconstructions" (i.e., mass distribution) for runs T109, T312 and T313 as shown in Figure II.9. The total mass computed for T109 and T312 was 0.98 g and 0.89 g, respectively, while for runs T113, which was apparently a split drop, the mass adds up to 0.49 g.

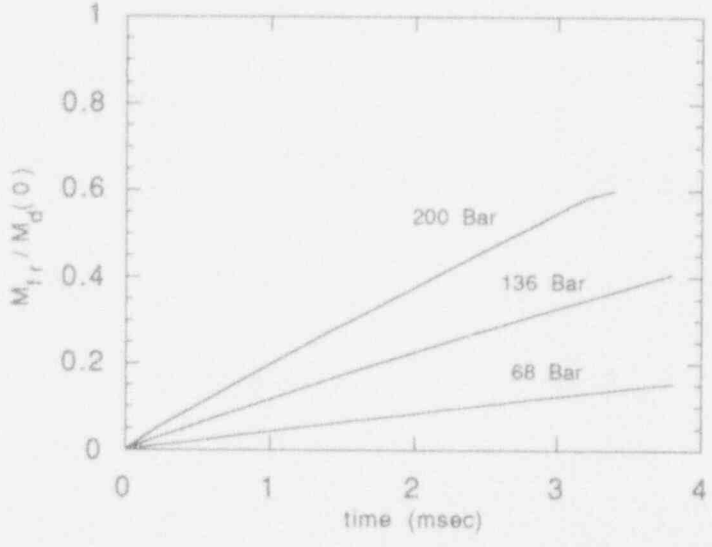

Figure II.8 Hydrodynamic fragmentation in tin/water system. ESPROSE with the instantaneous Bond number formulation.

The following observations can now be made:

(a) At low tin temperatures (360 °C), even at 2 ms, the fragmentation observed under a 66 bar shock is negligible. This is consistent with Figure II.8.

(b) At intermediate tin temperatures (670 °C) fragmentation is again negligible (up to 2 ms) under a 66 bar shock, but a catastrophic breakup is seen to occur at just before 1 ms under a 200 bar shock. This is clearly thermally driven as it is far faster than that expected from the hydrodynamic mechanism (see Figure II.8) and is also suggested by the morphology (see Figure II.5). As seen by the result of T304, by 2 ms "there is nothing left."

(c) At high tin temperatures (1000 °C) thermally driven fragmentation seems to set in already at 66 bar (it is essentially complete by ~1.5 ms) but, again, it is faster at 200 bar (see T312 in Figures II.5 and II.9).

(d) In both T101 and T109, both taken at 1 ms, it appear that something is already beginning at the interface—see also T109 in Figure II.9. However, it is also clear that there is a significant delay time before thermal fragmentation can be seen to be clearly in progress. This delay time seems to be decreasing as shock pressure and/or tin temperature increase.

(e) Finally, attention is directed to the interesting *and varying* morphologies seen in tests T114 and T303 (seeming to have caught the very early stages of a fully developing event) and in tests T105 and T304 (showing the final, highly dispersed stage). Also very interesting is test T104/0′ showing an upward-directed fragmentation event with quite a lot of detail on the interfacial structure.

It is clear from these results that neither Eq. (II.1) nor Eq. (II.6) capture the essential physics involved in the thermal or combined thermal-hydrodynamic regimes of fragmentation. Moreover, the various interdependencies on shock pressures and melt temperatures seem to be rather complex. Based on this, it can be expected that even the pressure pulse duration (in fact shape) will play an important role in the process.

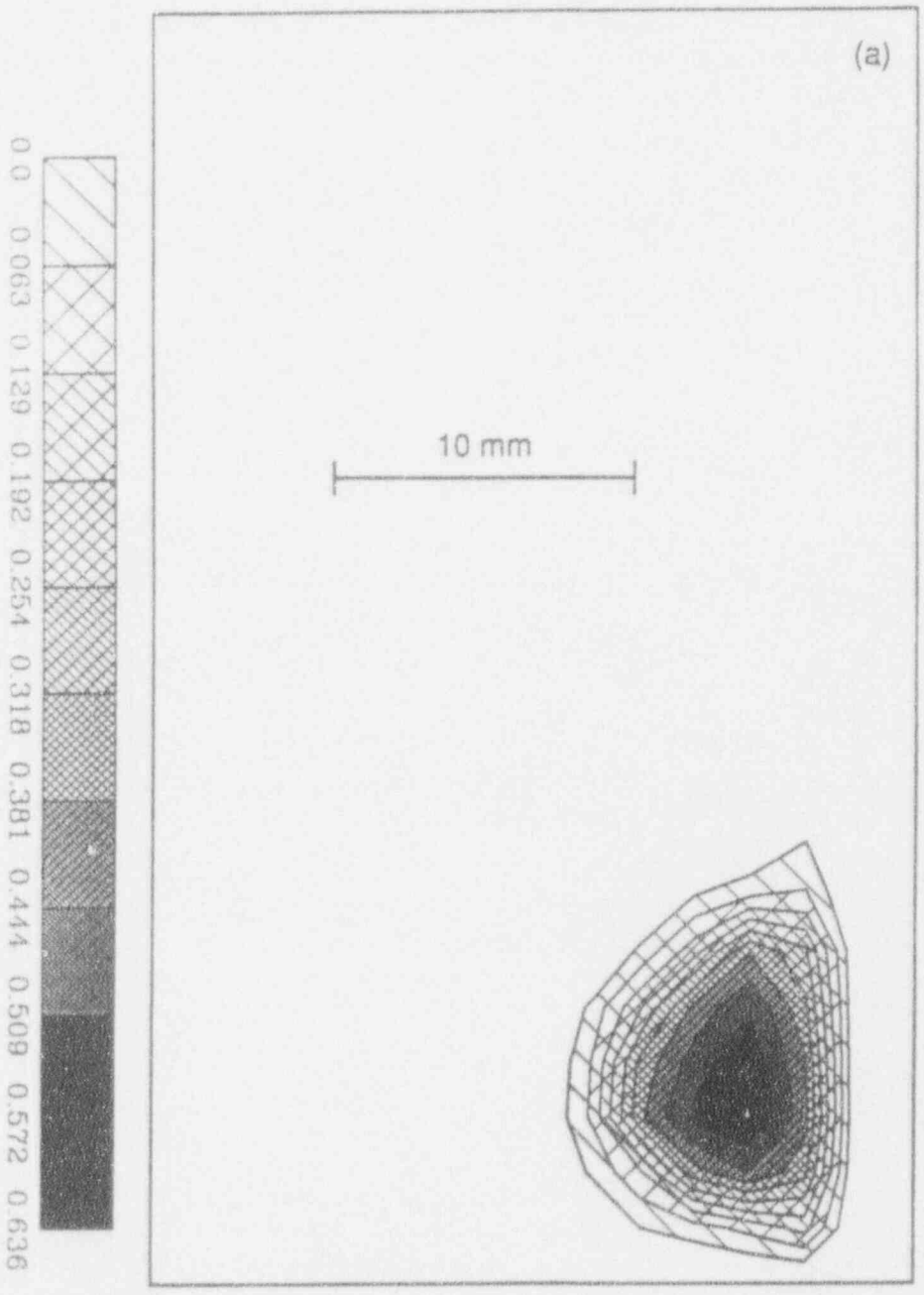

Figure II.9 Digital reproductions of the X-ray films for runs T109 (a), T312 (b) and T313 (c). The numbers in the shade-scale are in cm. Note that the diameter of a 1 g spherical tin drop is 0.66 cm.

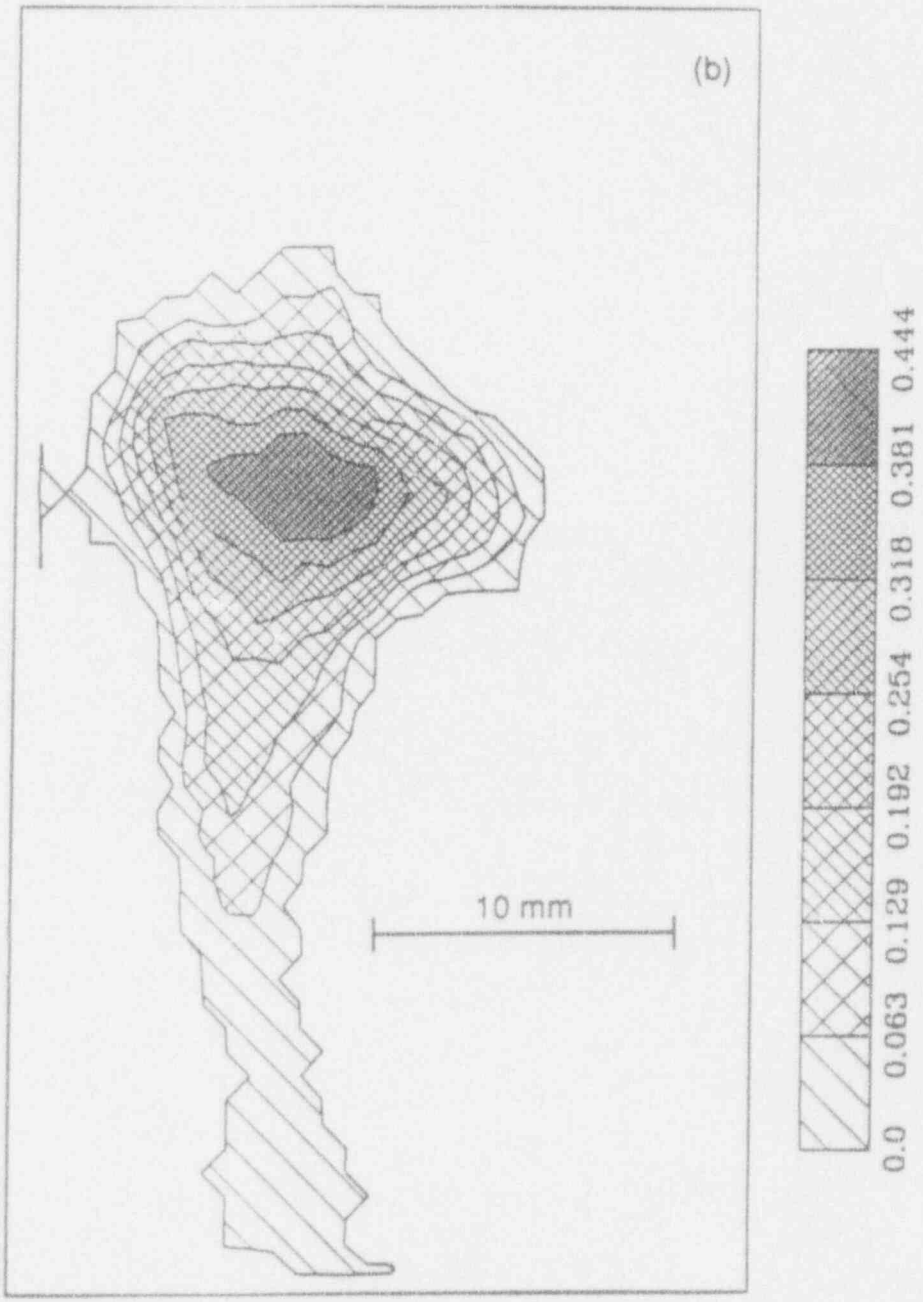

Figure II.9 Continued.

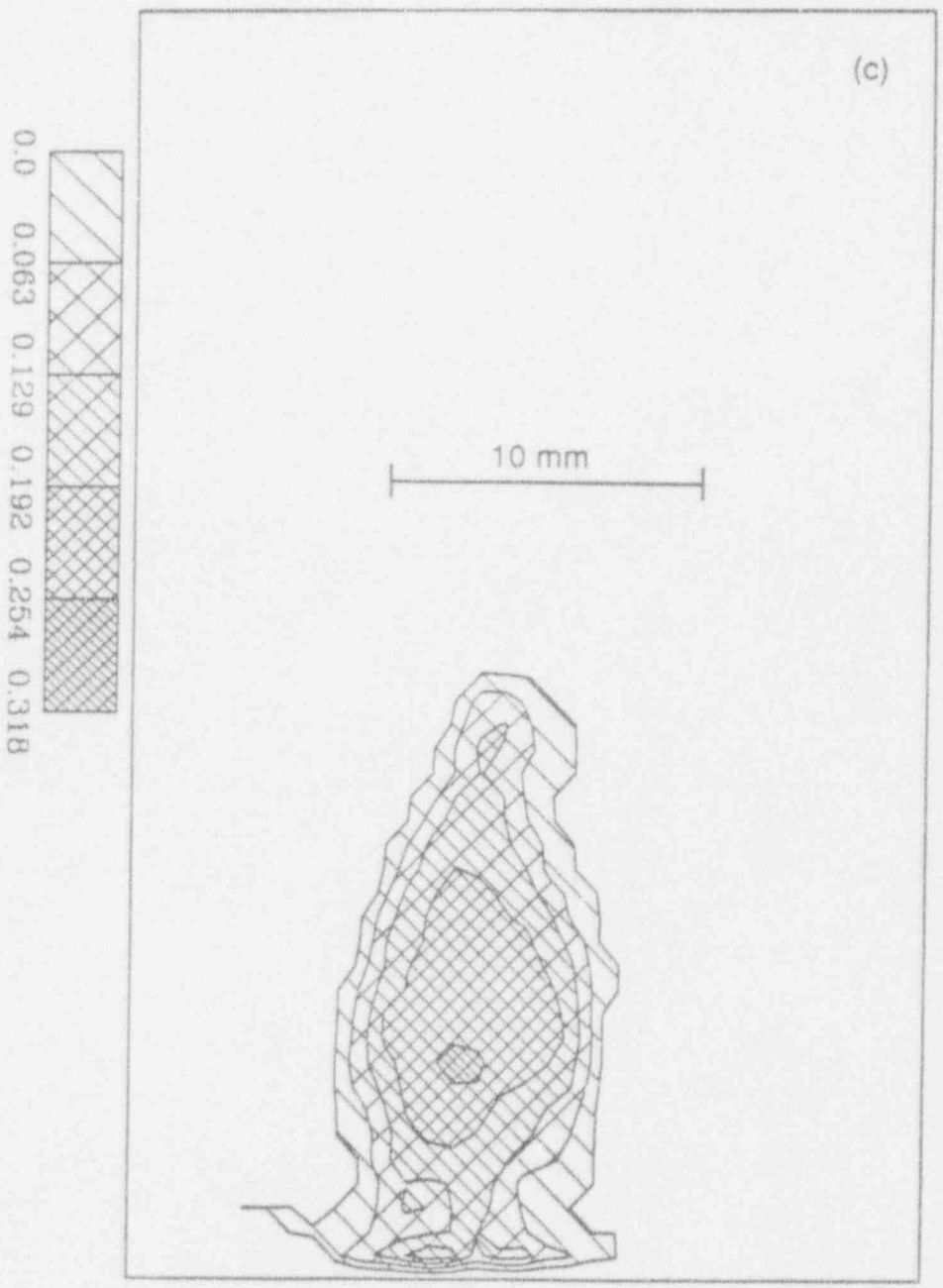

Figure II.9 Continued.

II.4 Quasi-One-Dimensional Explosions in the KROTOS Facility

Integral type explosion experiments are currently carried out in the KROTOS facility at the European Joint Research Center in ISPRA (Hohmann et al., 1993). These experiments involve the pouring of tin or aluminum oxide melts into a tube filled with water, the sudden release of a compressed gas volume at the bottom of the tube, and the measurement of the pressure transients of the resulting explosions along the length of the tube. The tube is 10 cm in diameter and it can contain water up to a level of 1.25 m, thus the geometry is essentially one dimensional. The trigger is well-characterized by the expansion of the known volume and initial pressure of some compressed gas at the bottom of the tube. The melt is released in a controlled fashion from a well-known initial temperature, and the water temperature is uniform and known. Because of all these features, these experiments are very attractive for testing explosion concepts/models. This is especially so because the most recent KROTOS-28 test using aluminum oxide melts produced very energetic explosions and very high (supercritical) pressures. The main shortcomings currently are on the quantitative aspects of data-"prediction" comparisons, in that the local melt and steam volume fractions along the tube are not measured directly, and in that the range of the pressure transducers was exceeded in the latest and most interesting explosions. Even so, these are the best characterized experiments so far and are worth pursuing their detailed understanding with diligence.

Here we consider three KROTOS tests. The one, KROTOS-21, was run with ~7 kg of tin at 1075 °C, and the other two, KROTOS-26 and KROTOS-28, were run with ~1.4 kg of aluminum oxide at 2300 °C. The water depth in the tube was ~1 m in all three tests. The trigger was the same also (15 cc of compressed nitrogen at 120 bar) applied roughly when the melt arrived at the tube bottom, except for KROTOS-26, which triggered prematurely. The explosions were recorded by 6 pressure transducers mounted along the tube.

The calculations were carried out with ESPROSE, as summarized in Appendix II.A. This formulation includes the following changes to the previously published version (Medhekar et al., 1991).

(a) The original phase change model, formulated to drive the coolant to local thermodynamic equilibrium, was replaced by a full non-equilibrium treatment. In it, the phase change is computed by the difference in heat transport, through each phase to the vapor-liquid interface. The constitutive laws for these fluxes are in the PM-ALPHA code (see Part I).

(b) A certain specified fraction (f_v) of the fragmenting fuel (the debris) energy is taken to go directly to vapor production. The rest is taken to equilibrate with the liquid coolant.

(c) The fragmentation kinetics formulation is based on the instantaneous Bond number formulation, as described in Section II.2. A multiplicative factor, f_f, is used to approximately accound for thermally-induced fragmentation effects, as discussed in Section II.3.

Moreover, we made use of the 2D capability of ESPROSE to simulate the fact that in the experiment, as the fuel fragments during the escalation/propagation process, it can only mix with a relative small fraction of the water contained in the tube. The limitations of a one-dimensional treatment can be appreciated by recognizing that distributing the melt volume (~0.2 ℓt) uniformly in the 1-m-long water column would produce a melt volume fraction of only ~3%. In a coherent jet configuration the resulting diameter would be ~2 cm, which is to be compared

to the 10 cm diameter of the tube. To approximate this limited contact, we made use of two radial nodes; the inner one, of a radius 2.37 cm, was assumed to contain the melt. Since the void was not measured approximate local values were deduced from the observed shock propagation speeds.

In KROTOS-21 the water temperature was about 100 °C, and the initial distributions of melt and void volume fractions are shown in Figure II.10. The calculations were carried out with $f_f = 1$ and $f_v = 0.025$ or $f_v = 0$. The calculated pressure transients are shown in Figure II.11, and in comparison with the experimental data in Figure II.12. The total fragmented mass in the 3.75 ms of the calculation was only 354 g (out of a total of 6.5 kg), which means a certainly very weak explosion. Alternatively, this experiment, and calculation, make it quite evident that strong triggers can be sustained and propagate with a very small amount of fuel participating in the interaction. With no direct vaporization ($f_v = 0$), the trigger pressure pulse fizzled out.

In KROTOS-26 the water temperature was 60 °C and as already mentioned the trigger occurred prematurely, allowing only a partial melt penetration into the water column. This penetration was estimated to be about 30 cm. On this basis, and because of the high subcooling, the void fraction was taken to be essentially zero; the initial conditions for ESPROSE were specified as in Figure II.13. The calculations were carried out with $f_f = 5$ and $f_v = 0.05$. The calculated pressure transients at the six transducer locations are shown together with the experimentally measured traces in Figure II.14. The structure of these pressure transients is seen to consist of three main components: the propagation of the trigger pulse, a mild escalation event at 0.8 ms around transducer K4, and a stronger explosion at ~1 ms around transducer K5. We note that the trigger pulse propagates with relatively small attenuation after position K1, that the mild escalation event at K4 builds up significantly by the time it reaches K5, and that this buildup leads to a downward (toward the bottom of the tube) propagating pulse. All of these features are well represented by the calculation. In addition, the calculation shows also that the mild event at K4 leads to a downward propagating pulse, which is not present in the experimental data; however, this is more of a detailed feature that depends on the roughly estimated initial fuel distribution. On the other hand, the main discrepancy is observed at position K4, where the data, in view of what has been measured at positions K3 and K5, must be considered suspect.

While KROTOS-26 gave a prliminary glimpse of a rapidly escalating explosion, KROTOS-28 actually produced one. This is, therefore, the only truly interesting KROTOS result so far. In this experiment the water temperature was 80 °C, and the melt had reached the bottom at the time the trigger fired. The ESPROSE calculation was carried out with the initial conditions shown in Figure II.15 and with $f_f = 5$ and $f_v = 0.05$, as in the case of KROTOS-26, just discussed. The calculated pressure transients are compared to the experiment in Figure II.16. The experiment shows rapid escalation by K1 and "topping off" the pressure transducers (500 bar maximum range) at all higher positions. The calculated results indicate a similar trend, except considerably lower amplitudes. This is not for lack of adequate fragmentation; by the end of the calculation 1 kg of the fuel had been fragmented, and this compares well with the amount of debris found in the experiment. Rather, the difficulty is due to the inadequacy of even the 2D treatment to represent the proper fuel-coolant mixing during fragmentation, as demonstrated by followup work using the ESPROSE.m code (Yuen and Theofanous, 1993).

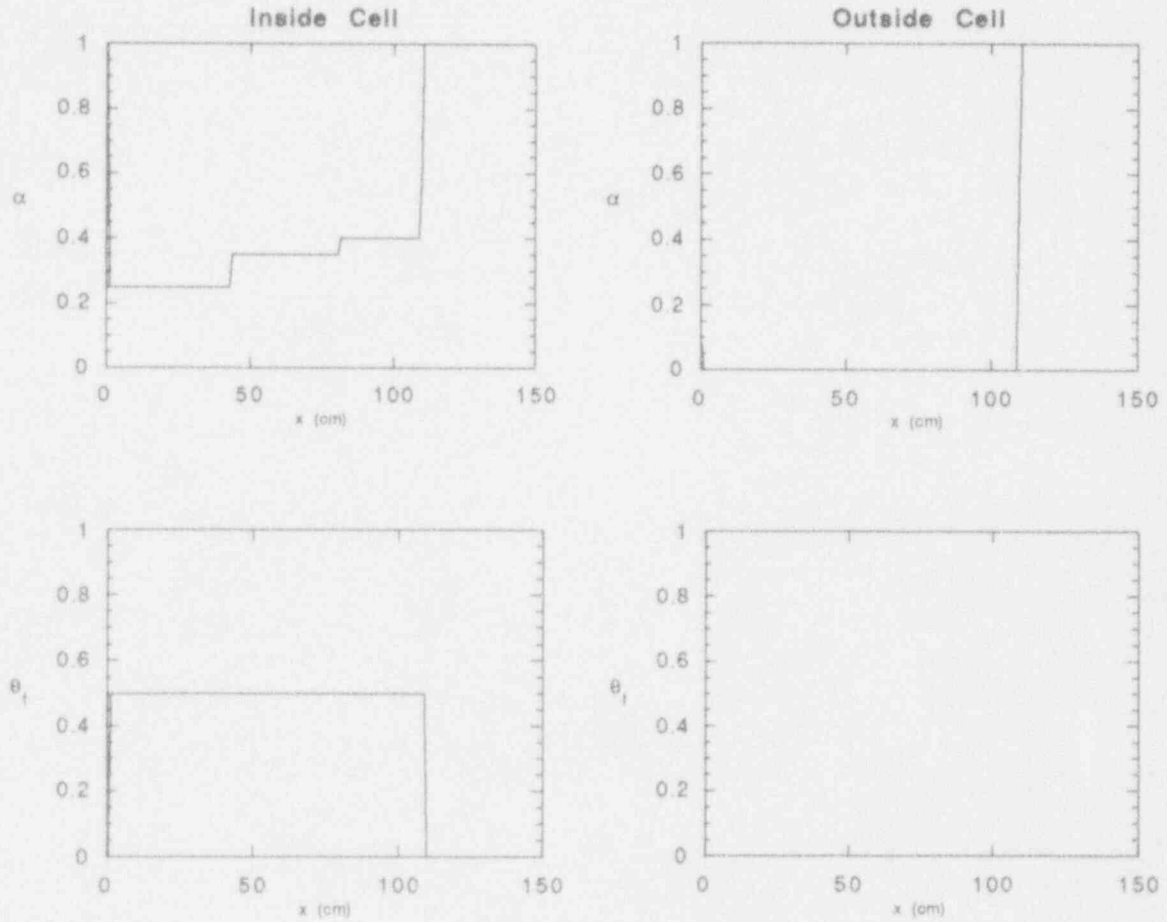

Figure II.10 Initial conditions used in the ESPROSE calculations for KROTOS-21.

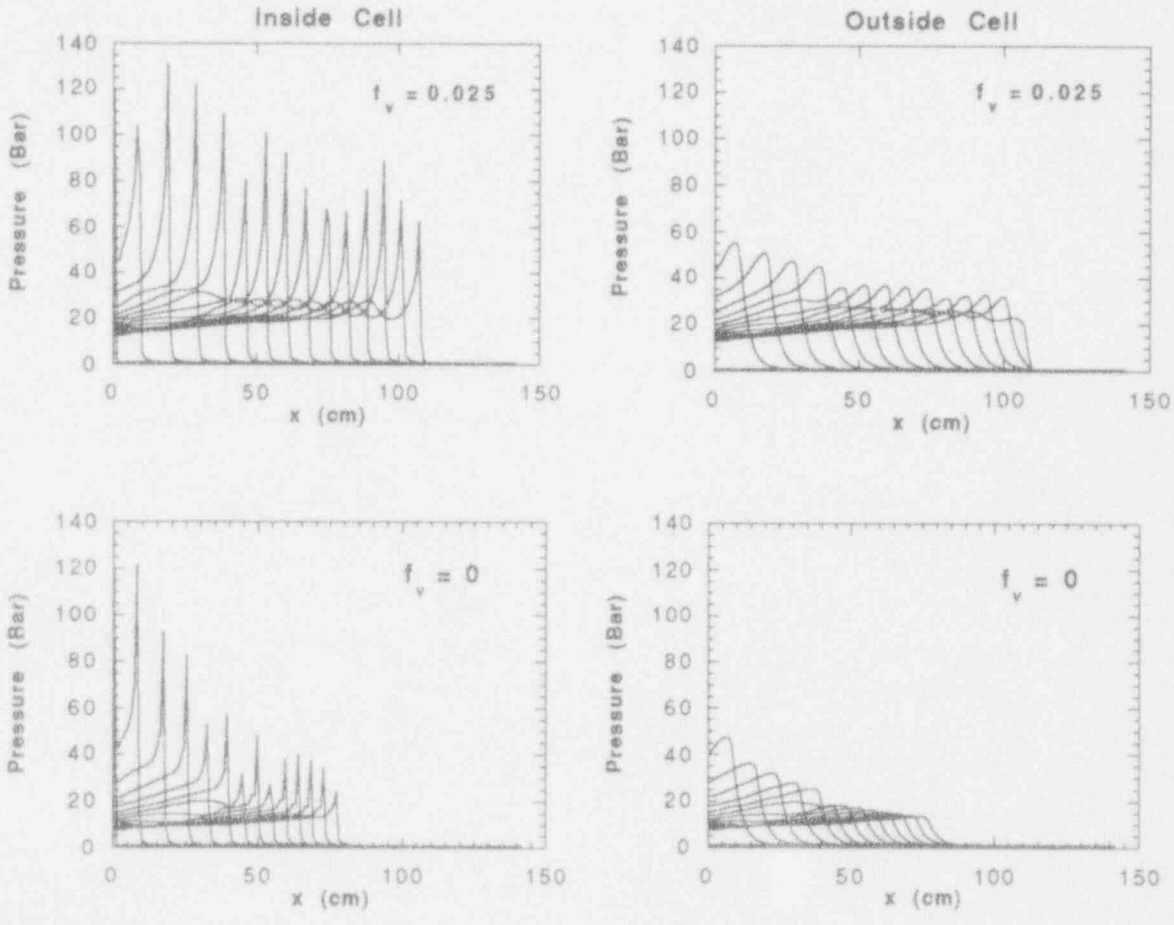

Figure II.11 ESPROSE simulations of the KROTOS test with (top) and without (bottom) direct vaporization from the debris-coolant interaction. Print interval 0.25 ms.

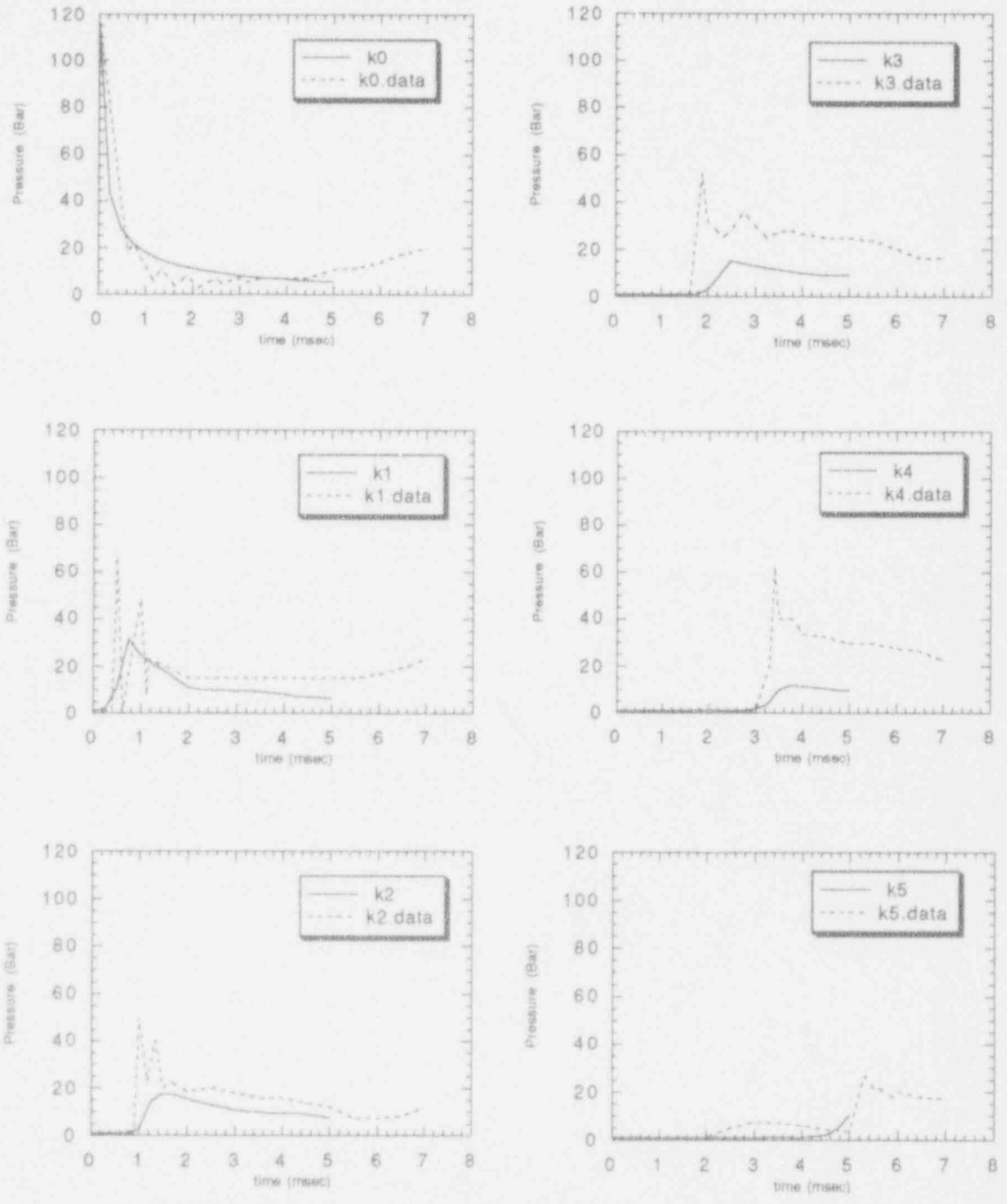

Figure II.12a Comparison of the pressure traces taken in the KROTOS test with ESPROSE results (outer radial cell)—"without" direct vaporization (corresponding to the heat from 2.5% of the fragmenting debris).

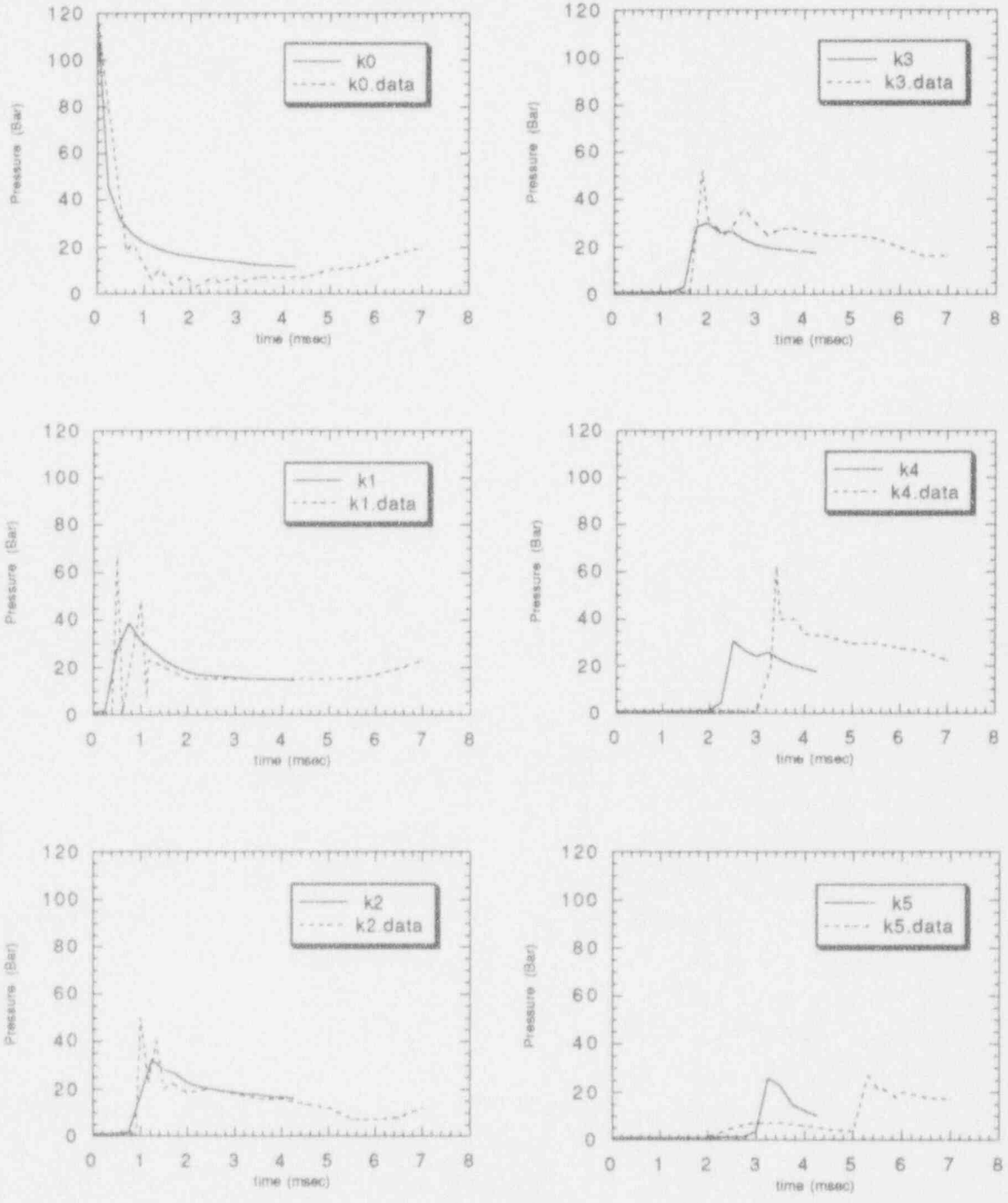

Figure II.12b Comparison of the pressure traces taken in the KROTOS test with ESPROSE results (outer radial cell)—"with" direct vaporization (corresponding to the heat from 2.5% of the fragmenting debris).

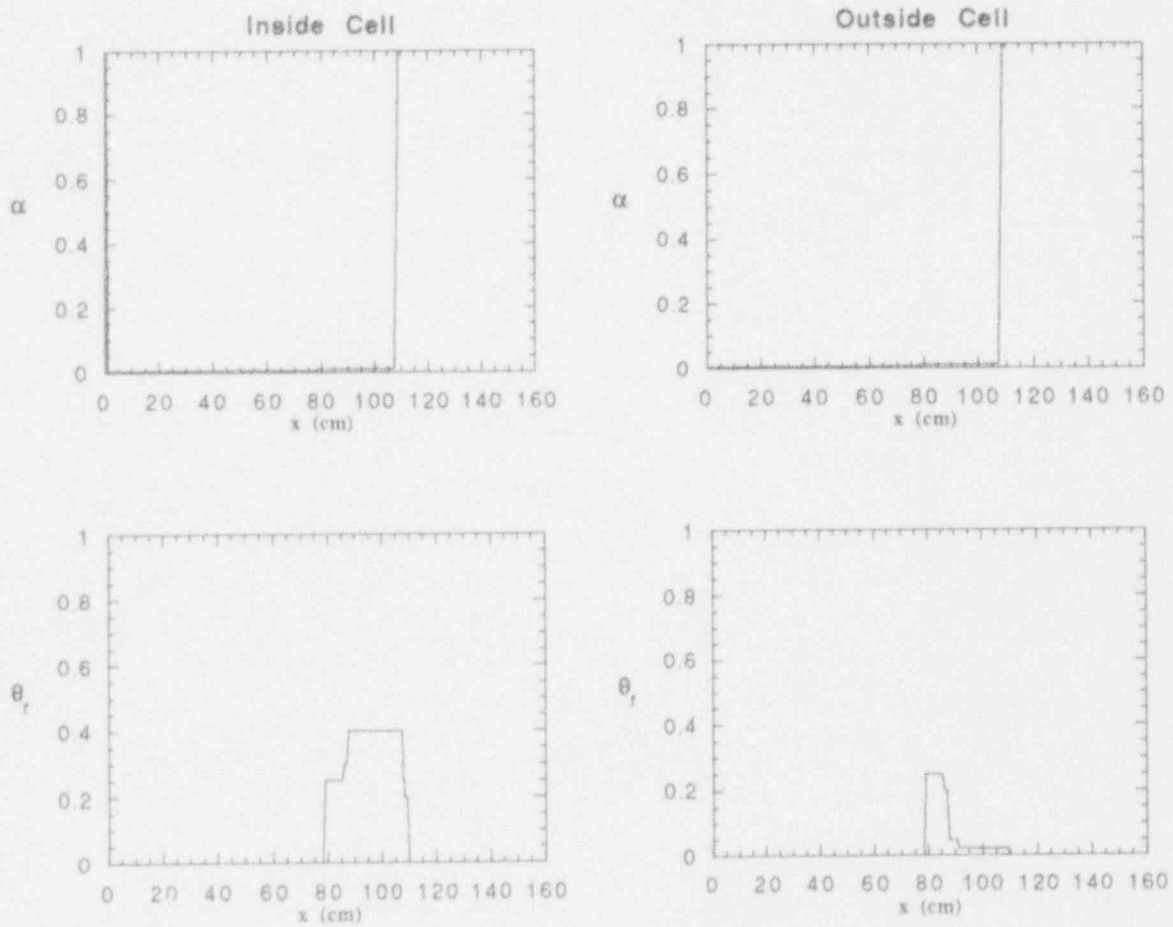

Figure II.13 Initial conditions for the KROTOS-26 ESPROSE calculation.

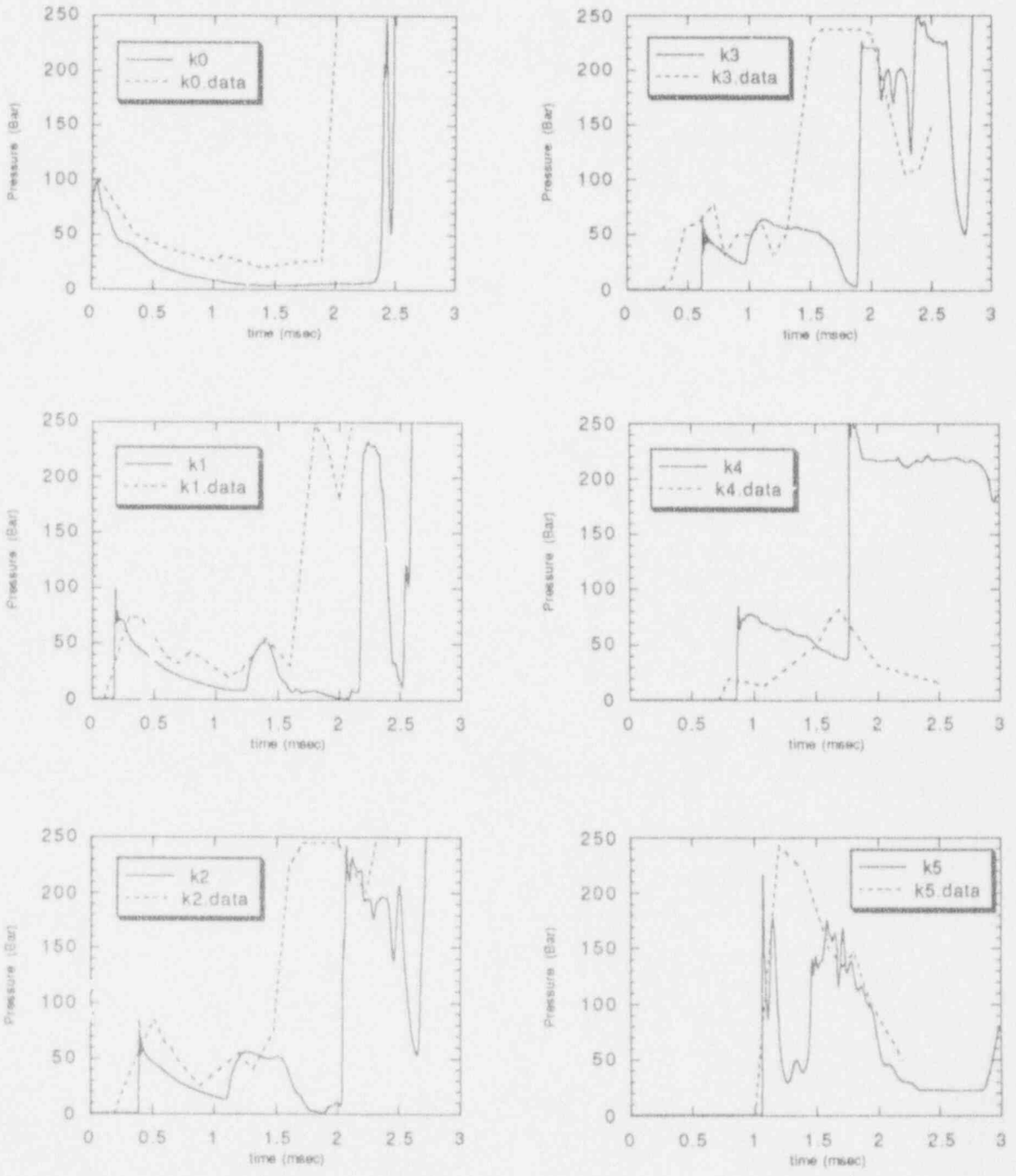

Figure II.14 Comparison of an ESPROSE.a calculation of KROTOS-26 test with experimental data of pressure measured along the tube length.

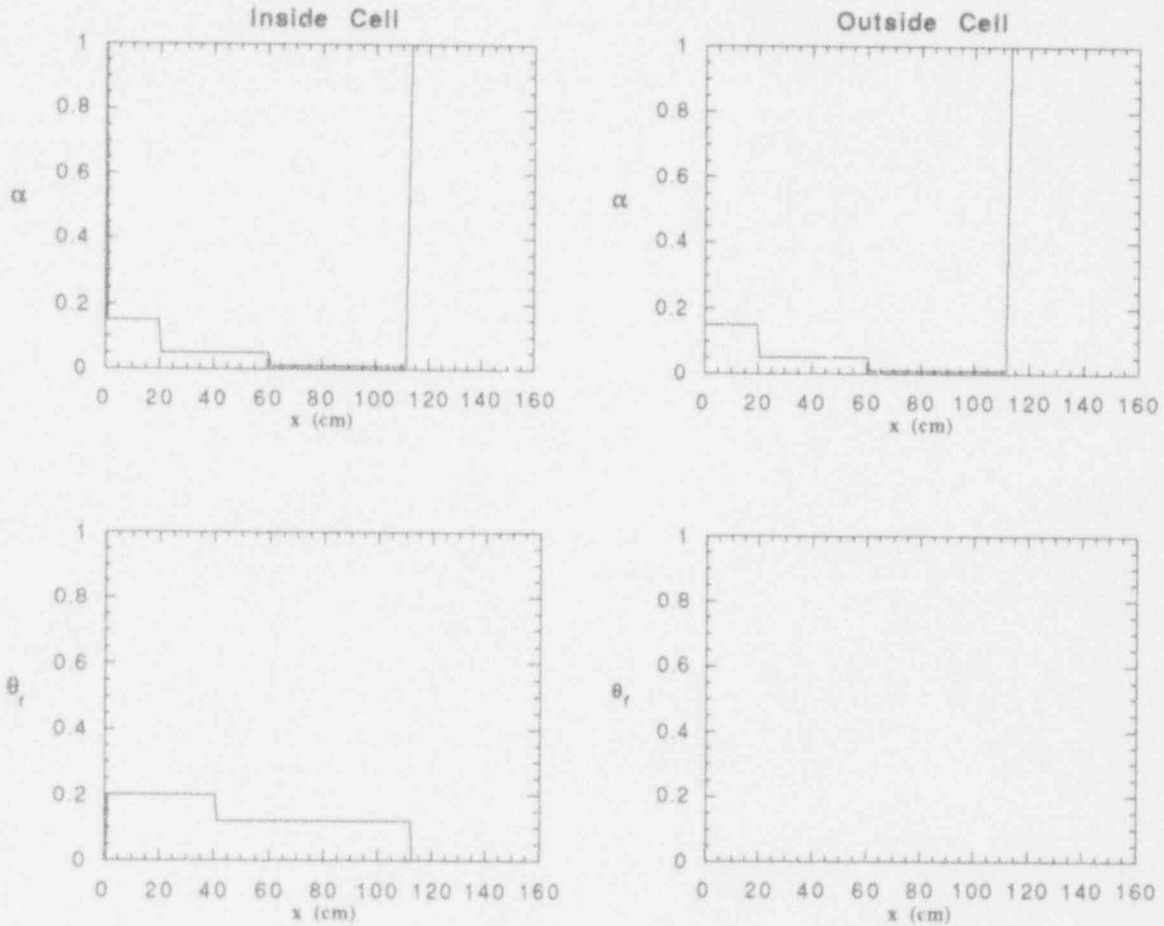

Figure II.15 Initial conditions for the KROTOS-28 ESPROSE calculation.

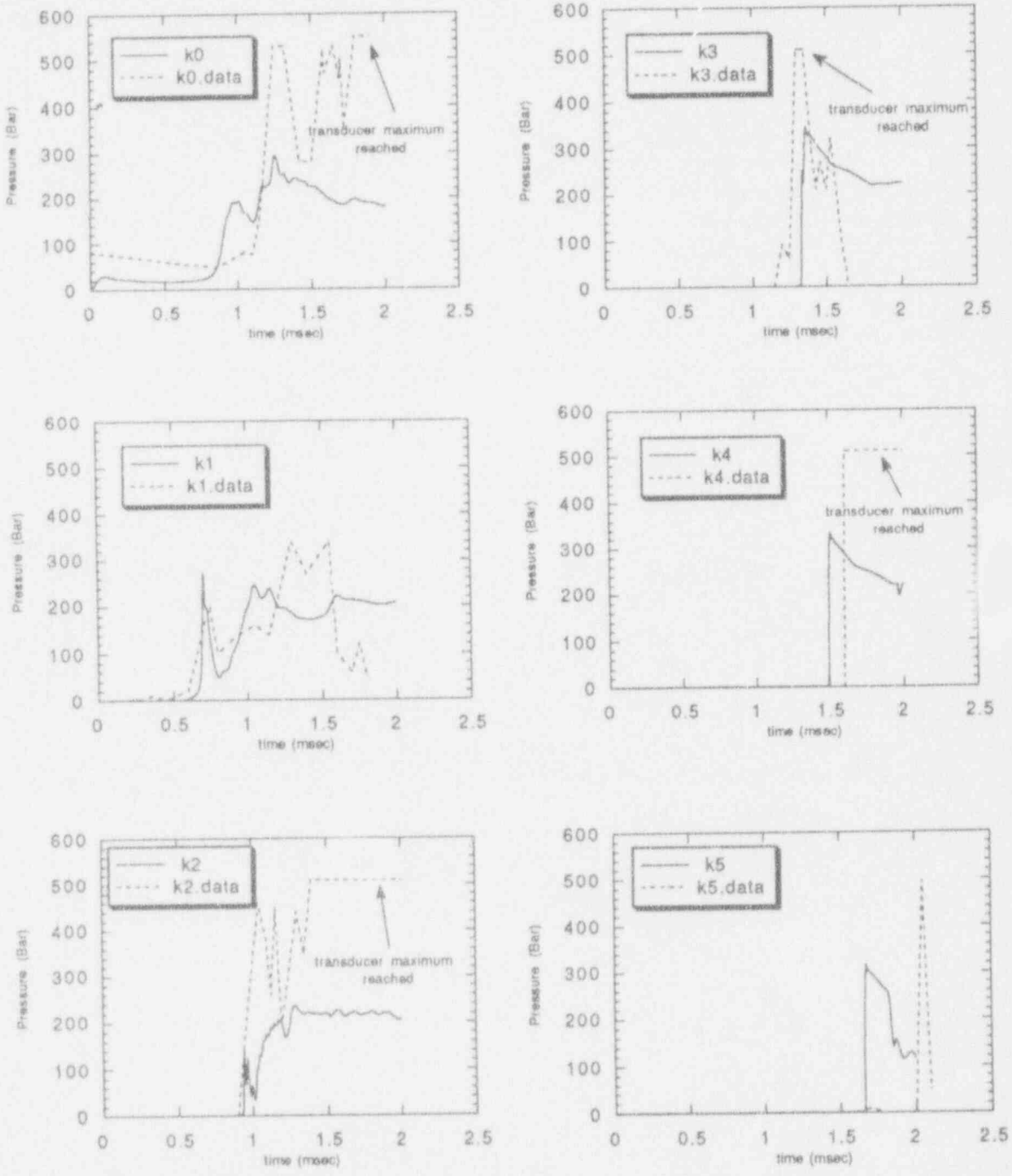

Figure II.16 Comparison of an ESPROSE.a calculation of KROTOS-28 with experimental data of pressure measured along the tube length.

II.5 Concluding Remarks

This study makes available the first experimental data on exploding drops in an environment that simulates that of a propagating steam explosion. It also shows that fragmentation kinetics, and the micromixing behavior with the surrounding coolant, can be quantitatively derived by an X-ray imaging technique. The results show very interesting interplay(s) between thermal and hydrodynamic in origin fragmentation mechanisms.

Further examination of hydrodynamic fragmentation kinetics supports the quantification proposed earlier by Theofanous et al. (1979). Using this correlation, with an enhancement factor to roughly account for thermal effects, and a non-equilibrium phase change treatment in the ESPROSE code, interpretations of KROTOS tests –21 (tin) and –26, –28 (aluminum oxide) have been attempted. We conclude that in low void fractions systems strong triggers can be sustained by relatively weak fragmentation rates, and that to properly simulate rapidly escalating explosions besides the fragmentation kinetics a realistic treatment of the local fuel-coolant mixing is required. This is the "microinteractions" concept that led to the ESPROSE.m code and reasonable interpretations of these KROTOS tests (Yuen and Theofanous, 1993).

II.6 References

1. Baines, M. and N.E. Buttery (1979) "Differential Velocity Fragmentation in Liquid-Liquid System," Berkeley Nuclear Labs, RD/B/N 4643.
2. Board, S.J. and R.W. Hall (1974) "Propagation of Thermal Expansions Part 2: A Theoretical Model," Berkeley Nuclear Labs, RD/B/N 3249.
3. Bürger, M. W. Schawalbe and H. Unger (1982) "Application of Hydrodynamic and Thermal Fragmentation Models and a Steady State Thermal Detonation Model for Molten Salt-Water Vapor Explosions," Int. Meeting on Thermal Nuclear Reactor Safety, Chicago, Illinois.
4. Fletcher, D.F. and A. Thayagaraja (1989) "A Mathematical Model of Melt/Water Detonations," *Applied Mathematical Modelling*, **13**, 339–347.
5. Inoue, A., M. Aritomi and Y. Tomita (1989) "An Analytical Model on Vapor Explosion of a High Temperature Molten Metal Droplet With Water Induced by a Pressure Pulse," Proceedings Fourth International Topical Meeting on Nuclear Reactor Thermal-Hydraulics, Karlsruhe, FRG, Oct. 10-13, Vol. 1, 274-281.
6. Kim, D.S., M. Bürger, G. Fröhlich and H. Unger (1983) "Experimental Investigation of Hydrodynamic Fragmentation of Gallium Drops in Water Flows," Proceedings International Meeting on Light Water Reactor Severe Accident Evaluation, Cambridge, MA, Aug. 28-Sept. 1, 1983, Vol. 1, 6.4-1.
7. Kim, H.J. and M. L. Corradini (1988) "Modelling of Small Scale Single Droplet Fuel Coolant Interactions," *Nuclear Science and Engineering* **98**.
8. Medhekar, S., W.H. Amarasooriya and T.G. Theofanous (1989) "Integrated Analysis of Steam Explosions," Proceedings Fourth International Topical Meeting on Nuclear Reactor Thermal-Hydraulics, Karlsruhe, FRG, Oct. 10-13, 1989, Vol. 1, 319-326.
9. Medhekar, S., M. Abolfadl and T.G. Theofanous (1991) "Triggering and Propagation of Steam Explosions," *Nuclear Engineering and Design* **126**, 41-49.
10. Nelson, L.S. and P.M. Duda (1981) "Steam Explosion Experiments with Single Drops of Iron Oxide Melted with a CO_2 Laser," NUREG/CR-2295, September, 1981.
11. Patel, P.D. and T.G. Theofanous (1981) "Hydrodynamics Fragmentation of Drops," *J. Fluid Mech.* **103**, 207-223.
12. Reinecke, W.G. and G.D. Waldman (1970) "Investigation of Water Drop Disintegration in a Region Behind Strong Shock Waves," Third Int. Conf. on Rain Erosion and Related Phenomena, Hampshire, UK.
13. Theofanous, T.G., M. Saito and T. Efthimiadis (1979) "The Role of Hydrodynamic Fragmentation in Fuel Coolant Interactions," Fourth CSNI Specialist Meeting on Fuel-Coolant Interactions in Nuclear Reactor Safety, Bournemouth, England, April 2-5, 1979, CSNI Report No. 37, Vol. 1, 112, Paper #FC14/P5.
14. Theofanous, T.G. et al. (1983) "LWR and HTGR Coolant Dynamics: The Containment of Severe Accidents," NUREG/CR-3306, July 1983.
15. Yuen, W.W. and T.G. Theofanous (1993) "The Prediction of 2D Thermal Detonations and Resulting Damage Potential," CSNI Specialists Meeting on Fuel-Coolant Interactions, Santa Barbara, CA, January 5-8, 1993.

APPENDIX A

FORMULATION OF THE ESPROSE MODEL

Appendix A: Formulation of the ESPROSE Model

A.1 Conservation Equations

There are four separate phases; namely, liquid coolant, coolant vapor, fuel (melt) drops, and the fragmented fuel (melt) debris. They will be referred to as liquid, gas, fuel, and debris, respectively. The liquid, the gas, and the fuel are modelled as three separate phases (three-fluid approach) with their own mass, momentum, and energy equations. The debris is assumed to give most of its energy to the coolant instantaneously (i.e., very fine fragmentation) and then to flow with the liquid field. A small fraction, f_v, of the debries energy is assumed to go to direct vaporizaion. Only one, the mass continuity, equation is required for the debris phase. In the usual manner, the fields are allowed to exchange energy and momentum with each other. With the definition of the macroscopic density of phase i,

$$\rho_i' = \theta_i \rho_i \qquad \text{for} \quad i = g,\ \ell,\ f,\ \text{and}\ db, \tag{A.1}$$

and the compatibility condition,

$$\theta_g + \theta_\ell + \theta_f + \theta_{db} = 1, \tag{A.2}$$

these equations can be interpreted rather directly (Ishii, 1975).

• Continuity Equations.

Gas:

$$\frac{\partial \rho_g'}{\partial t} + \nabla \cdot (\rho_g' \mathbf{u}_g) = J \tag{A.3}$$

Liquid:

$$\frac{\partial \rho_\ell'}{\partial t} + \nabla \cdot (\rho_\ell' \mathbf{u}_\ell) = -J \tag{A.4}$$

Fuel:

$$\frac{\partial \rho_f'}{\partial t} + \nabla \cdot (\rho_f' \mathbf{u}_\mathbf{f}) = -F_r \tag{A.5}$$

Debris:

$$\frac{\partial \rho_{db}'}{\partial t} + \nabla \cdot (\rho_{db}' \mathbf{u}_\ell) = F_r \tag{A.6}$$

• Momentum Equations.

Gas:

$$\begin{aligned}\frac{\partial}{\partial t}(\rho_g' \mathbf{u}_g) + \nabla \cdot (\rho_g' \mathbf{u}_g \mathbf{u}_g) = &- \theta_g \nabla p - F_{g\ell}(\mathbf{u}_g - \mathbf{u}_\ell) - F_{gf}(\mathbf{u}_g - \mathbf{u}_f) \\ &+ J(H[J]\mathbf{u}_\ell + H[-J]\mathbf{u}_g) + \rho_g' \mathbf{g}\end{aligned} \tag{A.7}$$

Liquid:

$$\frac{\partial}{\partial t}((\rho'_\ell + \rho'_{db})\mathbf{u}_\ell) + \nabla \cdot ((\rho'_\ell + \rho'_{db})\mathbf{u}_\ell \mathbf{u}_\ell) =$$
$$-(\theta_\ell + \theta_{db})\nabla p + F_{g\ell}(\mathbf{u_g} - \mathbf{u}_\ell) - F_{\ell f}(\mathbf{u}_\ell - \mathbf{u_f})$$
$$- J(H[J]\mathbf{u}_\ell + H[-J]\mathbf{u_g}) + (\rho'_\ell + \rho'_{db})\mathbf{g} + F_r \mathbf{u}_\ell \qquad (A.8)$$

Fuel:

$$\frac{\partial}{\partial t}(\rho'_f \mathbf{u_f}) + \nabla \cdot (\rho'_f \mathbf{u_f} \mathbf{u_f}) = -\theta_f \nabla p + F_{gf}(\mathbf{u_g} - \mathbf{u_f}) +$$
$$F_{\ell f}(\mathbf{u}_\ell - \mathbf{u_f}) + \rho'_f \mathbf{g} - F_r \mathbf{u_f} \qquad (A.9)$$

• Energy Equations.

Gas:

$$\frac{\partial}{\partial t}(\rho'_g I_g) + \nabla \cdot (\rho'_g I_g \mathbf{u}_g) = -p\left[\frac{\partial \theta_g}{\partial t} + \nabla \cdot (\theta_g \mathbf{u}_g)\right] + J(H[J]h_\ell + H[-J]h_g) - R_{gs}(T_g - T_s) + \dot{Q}_{fg} \qquad (A.10)$$

Liquid:

$$\frac{\partial}{\partial t}(\rho'_\ell I_\ell + \rho'_{db} I_{db}(T_\ell)) + \nabla \cdot [(\rho'_\ell I_\ell \mathbf{u}_\ell + \rho'_{db} I_{db}(T_\ell))\mathbf{u}_\ell] =$$
$$- p\left[\frac{\partial}{\partial t}(\theta_\ell) + \nabla \cdot (\theta_\ell \mathbf{u}_\ell)\right]$$
$$- J(H[J]h_l + H[-J]h_g) - R_{\ell s}(T_\ell - T_s) + \dot{Q}_{f\ell} \qquad (A.11)$$

Fuel:

$$\frac{\partial}{\partial t}(\rho'_f I_f) + \nabla \cdot (\rho'_f I_f \mathbf{u}_f) = -\dot{Q}_{fg} - \dot{Q}_{f\ell} \qquad (A.12)$$

The heat transfer due to fragmentation is incorporated in the $\dot{Q}_{f\ell}$ or $\dot{Q}_{fg}$ terms. In the above equations $H[J]$ is the Heavyside step function that becomes unity for positive values of the argument and zero otherwise, and J is given by

$$J = \frac{1}{h_g - h_\ell}[R_{\ell s}(T_\ell - T_s) + R_{gs}(T_g - T_s) + f_v F_r(I_f - I_{db}(T_\ell))]$$

where f_v is the fraction of fragmentation debris energy which is allowed to go directly to vapor production.

It should be pointed out that diffusive transport **within** each field (shear stresses and conduction) has been ignored in the above formulation. Indeed, resolution of the shear layers would impose quite more extensive demands on the computation in both nodalization and the physics of turbulence processes responsible for such transport. Although this is certainly an area for further improvement, we doubt that it will materially change the results for the particular process quantified here.

A.2 The Exchange Laws

The interfacial exchanges of mass, momentum and energy are clearly regime dependent, and uncertainties remain even for two-phase flows. For now, our approach aims to incorporate first-order physics that account for the major flow and heat transfer regimes as identified by simple criteria of fuel volume fraction, θ_f, and gas void fraction, α, i.e., $\alpha = \theta_g/(\theta_g + \theta_\ell)$. The flow regimes are shown in Figure A.1. For $\theta_f < 0.3$ we consider the fuel particles immersed in a two-phase gas-liquid flow, whose own flow regimes are defined by the value of the void fraction: $\alpha \leq 0.3$ (Bubbly), $0.3 < \alpha < 0.7$ (Churn-Turbulent), and $\alpha \geq 0.7$ (Droplet). For $\theta_f \geq 0.3$, as the fuel particles are densely packed, we considered a flow of gas and liquid through a porous bed of fuel particles.

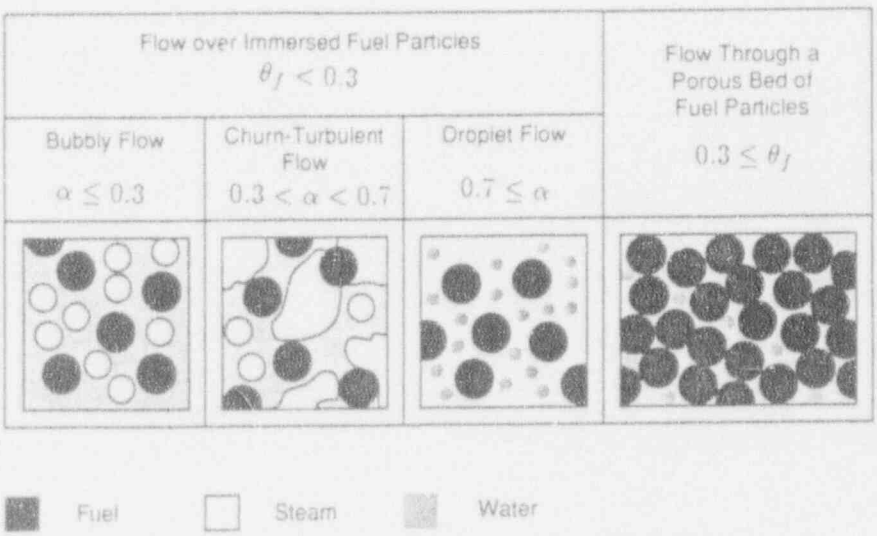

Figure A.1. Schematic diagram of flow regimes considered in characterizing interface transfers.

We use the exchange laws available for two-phase systems after making suitable modifications to account for, as a first approximation, the effect of a third phase. In calculating interfacial momentum exchange, one needs to know the projected area concentration of the dispersed phase. Also, in calculating interfacial heat exchange, one needs to know the interfacial area concentration. In a two-phase system, these area concentrations can be estimated from the length scale and the volume fraction of the dispersed phase. However, the presence of a third phase reduces the area concentration as the third phase must also share the same area. Therefore, we modify the area concentration, by a factor, ϕ_{ij}; ϕ_{ij} representing the effect of the phase k on the area

concentration of phase i for its interaction with phase j. This is calculated from the respective volume fractions as

$$\phi_{ij} = \frac{\theta_j}{\theta_j + \theta_k}. \tag{A.13}$$

Note that with this definition ϕ_{ij} lies between 0 and 1.

A.2.1 Interfacial Momentum Coupling

The interfacial momentum coupling is primarily due to drag. For the bubbly flow regime ($\alpha < 0.3$) we have also included the added mass effect as given by Wallis (1969)

$$F_a = \frac{\theta_g}{3 - \theta_g} \rho_\ell \frac{1}{\mid \mathbf{u}_g - \mathbf{u}_\ell \mid} \mid \frac{\partial}{\partial t}(\mathbf{u}_g - \mathbf{u}_\ell) \mid \tag{A.14}$$

For $\theta_f < 0.3$ the drag force is based on Ishii and Zuber (1979). Specifically,

$$F_{ij} = \frac{3}{4} \theta_i \phi_{ij} \rho_j \frac{C_{Dij}}{\ell_i} \mid \mathbf{u}_i - \mathbf{u}_j \mid \tag{A.15}$$

where suffices i and j refer to dispersed and continuous phases, respectively. The drag coefficient for churn flow ($0.3 < \alpha < 0.7$) is defined by:

$$i = g,\ j = \ell,\ C_{Dij} = \frac{8}{3}(1 - \alpha)^2 \text{ and } \ell_i = 4 \left\{ \frac{g \Delta \rho}{\gamma} \right\}^{-1/2} \tag{A.16}$$

For dispersed flow we have:

$$C_{Dij} = \frac{2}{3} \ell_i \left\{ \frac{g \Delta \rho}{\gamma} \right\}^{1/2} \left\{ \frac{1 + 17.67 (f(\alpha_i))^{6/7}}{18.67 f(\alpha_i)} \right\}^2 \tag{A.17}$$

where

$$i = g, \quad j = \ell, \quad \alpha \leq 0.3 \qquad f(\alpha_i) = (1 - \alpha)^{1.5} \tag{A.18}$$

$$i = \ell, \quad j = g, \quad \alpha > 0.7 \qquad f(\alpha_i) = \alpha^3 \tag{A.19}$$

$$i = f, \quad j = g, \ell, \quad f(\alpha_i) = (1 - \theta_f)^{1.5} \tag{A.20}$$

and ℓ_i is obtained from

$$\frac{\rho_j \mid \mathbf{u}_\ell - \mathbf{u}_g \mid^2 \ell_i}{\gamma} = \text{We}_{cr} \begin{cases} 8 & \text{for } i = g \\ 12 & \text{for } i = \ell \end{cases} \tag{A.21}$$

For the "dense fuel regime" ($\theta_f > 0.3$) we use laminar and turbulent permeabilities (Sissom and Pitts, 1972).

$$F_{if} = F_{if}^{\ell} + F_{if}^{t} \qquad i = g, \ell \tag{A.22}$$

where

$$F_{if}^{\ell} = \begin{cases} 150 \frac{\theta_i \theta_f^2}{(1-\theta_f)^3} \frac{\mu_i}{\ell_f^2} & \text{for } \mathrm{Re}_i' < 1000 \\ 0 & \text{for } \mathrm{Re}_i' \geq 1000 \end{cases} \tag{A.23}$$

and

$$F_{if}^{t} = \begin{cases} 1.75 \frac{\theta_i \theta_f}{(1-\theta_f)^3} \frac{\rho_i' | \mathbf{u}_i - \mathbf{u}_f |}{\ell_f} & \text{for } \mathrm{Re}_i' > 10 \\ 0 & \text{for } \mathrm{Re}_i' \leq 10, \end{cases} \tag{A.24}$$

$$\mathrm{Re}_i' = \theta_f \frac{\rho_i' \ell_f \mid \mathbf{u}_i - \mathbf{u}_f \mid}{\mu_i} \tag{A.25}$$

It is noted, however, that this regime is of very limited relevance to computations of practical interest.

A.2.2 Interfacial Heat Transfer and Phase Change

The distinction of the fuel-to-coolant heat transfer mechanisms is made again on the basis of the flow regimes. The key distinction is whether or not there is sufficient water in the coolant phase to completely engulf the fuel particles, thus a gas void fraction criterion is used.

For $\alpha < 0.7$, heat transfer to liquid is estimated by superposition of radiation, film boiling heat fluxes and the addition of debris energy due to fragmentation. That is,

$$\dot{Q}_{f\ell} = n_f (h_r + h_c) \pi \ell_f^2 \phi_{f\ell} (T_f - T_\ell) + f_v F_r I_{db}(T_\ell) + (1 - f_v) I_f F \tag{A.26}$$

where

$$n_f = \frac{6\theta_f}{\pi \ell_f^3}, \qquad h_r = \sigma E_f \frac{T_f^4 - T_\ell^4}{T_f - T_\ell} \tag{A.27, A.28}$$

and (Witte, 1968; Liu et al., 1992)

$$h_c = 2.98 \left\{ \frac{\rho_g k_g [h_{fg} + 0.68 c_{pg} (T_f - T_\ell)]}{\ell_f (T_f - T_\ell)} \mid \mathbf{u}_f - \mathbf{u}_\ell \mid \right\}^{\frac{1}{2}} \tag{A.29}$$

The emissivity value $E_f = 0.7$ is selected for the calculations of typical interest. Heat transfer from fuel to gas in this regime need not be accounted for separately.

For $\alpha > 0.7$, we assume a vapor-continuous regime in which heat is transferred to liquid drops by irradiation and to the gas by convection. The gas is allowed to superheat and convect heat to the liquid drops which boil at saturation. Thus:

$$\dot{Q}_{f\ell} = \min\left(n_\ell \pi \ell_\ell^2, n_f \pi \ell_f^2\right)\sigma E_f E_\ell (T_f^4 - T_\ell^4) + (1 - f_v)F_r\{(1-\alpha)I_f + \alpha I_f(T_\ell)\} + f_v F_r I_{db}(T_\ell) \quad (A.30)$$

and

$$\dot{Q}_{fg} = n_f \phi_{fg} \pi \ell_f^2 h_c'(T_f - T_g) \quad (A.31)$$

where $n_\ell = 6\theta_\ell/\pi\ell_\ell^3$ and h_c' is given by Bird et al. (1960):

for $\theta_f < 0.3$

$$h_c' = \frac{k_g}{\ell_f}\left\{2 + 0.6\mathrm{Re}_g^{1/2}\mathrm{Pr}_g^{1/3}\right\} \quad (A.32)$$

where

$$\mathrm{Re}_g = \frac{\rho_g \mid \mathbf{u}_g - \mathbf{u}_f \mid \ell_f}{\mu_g} \quad (A.33)$$

and for $\theta_f \geq 0.3$

$$h_c' = 0.91 c_{pf}\rho_g' \mid \mathbf{u}_g - \mathbf{u}_f \mid \mathrm{Re}_g''^{-0.51}\mathrm{Pr}_g^{-2/3} \text{ for } \mathrm{Re}_g'' \leq 50 \quad (A.34)$$

$$h_c' = 0.61 c_{pf}\rho_g' \mid \mathbf{u}_g - \mathbf{u}_f \mid \mathrm{Re}_g''^{-0.41}\mathrm{Pr}_g^{-2/3} \text{ for } \mathrm{Re}_g'' > 50 \quad (A.35)$$

where

$$\mathrm{Re}_g'' = \frac{\rho_g' \ell_f \mid \mathbf{u}_g - \mathbf{u}_f \mid}{6\theta_f \mu_g} \quad (A.36)$$

The factor E_ℓ in Eq. (A.30) was introduced to empirically degrade the radiation heat transfer to liquid by the portion that could not be absorbed. For reactor calculations we typically use $E_\ell = 0.3$ to conservatively bias the predictions.

Similarly, for vapor-to-liquid heat transfer we have:

For $\alpha < 0.7$, with vapor as the dispersed phase

$$R_{\ell s} = c_\ell n \phi_{g\ell} \pi \ell_g^2 \frac{k_\ell}{g_g} \left\{ 2 + 0.6 \ \mathrm{Re}^{1/2} \mathrm{Pr}_\ell^{1/3} \right\} \tag{A.37}$$

$$R_{gs} = 2 n_g \phi_{g\ell} \pi \ell_g^2 \frac{k_g}{\ell_g}$$

while for $\alpha > 0.7$, with liquid (drops) as the dispersed phase

$$R_{gs} = n_\ell \phi_{\ell g} \pi \ell_\ell^2 \frac{k_g}{\ell_\ell} \left\{ 2 + 0.6 \ \mathrm{Re}^{1/2} \mathrm{Pr}_g^{1/3} \right\} \tag{A.38}$$

$$R_{\ell s} = 2 c_\ell \eta_\ell \phi_{\ell g} \pi \ell_\ell^2 \frac{k_\ell}{\ell_\ell}$$

In the above the coefficient c_ℓ was introduced as a way to control the liquid superheat in cases where these simplified formulations for heat transfer coefficients are not deemed adequate.

A.2.3 Fragmentation Kinetics

The constitutive law for the fragmentation rate is given by

$$F_r = \frac{6 \theta_f}{\pi \ell_f^3} \frac{dM}{dt} \tag{A.39}$$

where

$$\frac{dM}{dt} = f_f \frac{\pi \ell_f^2 \mid \vec{\mathbf{u}}_\ell - \vec{\mathbf{u}}_f \mid}{6 t_b^*} (\rho_f \rho_\ell)^{1/2} \tag{A.40}$$

The "enhancement" factor, f_f, is introduced to account for the possible thermal effect on fragmentation rate. The "fragmentation time", t_b^*, is a function of the instantaneous Bond number and they are given by

$$t_b^* = 13.7 \ \mathrm{Bo}_i^{-1/4} \quad \text{and} \quad \mathrm{Bo}_i = \frac{3}{8} \frac{C_D \rho_\ell}{\sigma} \mid \mathbf{u}_\ell - \mathbf{u}_f \mid^2 \frac{\ell_f}{2} \tag{A.41}$$

This fragmentaion formulation was shown to be consistent with experimental data (from the SIGMA facility) where fragmentation is dominated by hydrodynamic instabilities (Yuen et al., 1992).

A.3 Nomenclature

Bo	Bond number
C_D	drag coefficient
c_ℓ	control coefficient
c_p	specific heat at constant pressure
E_f	emissivity of fuel particles
E_ℓ	absorptivity of water droplets
f_f	enhancement factor for the fragmentation rate
f_v	fraction of debris energy which goes to direct vaporization
F_r	fragmentation rate
g	acceleration of gravity
H	Heaviside step function
h	heat transfer coefficient; specific enthalpy
h_{fg}	enthalpy of evaporation
I	specific internal energy
J	phase change rate per unit volume
k	thermal conductivity
ℓ	length scale
n	number of particles (or drops) per unit volume
Pr	Prandtl number
p	pressure
$\dot{Q}$	rate of heat transfer per unit volume
R	heat transfer coefficient between the phase (liquid or vapor) and interface
Re	Reynolds number
T	temperature
t	time
t_b^*	charcteristic fragmentation time
u	velocity vector
We_{cr}	critical Weber number for bubble/drop breakup

Greek

α	void fraction of vapor (per unit volume of coolant)
γ	surface tension between vapor and liquid; specific heat ratio
θ	volume fraction (per unit volume of total mixture)
μ	viscosity
ρ	microscopic density
ρ'	macroscopic density
σ	Stefan–Boltzmann coefficient, surface tension
ϕ_{ij}	area concentration factor, defined in eq. (A.12)

Subscripts

a	added-mass effect
c	convection
db	debris
f	fuel
g	gas (steam)
ℓ	liquid (water)
r	radiation
s	saturation

Superscripts

ℓ	laminar flow
t	turbulent flow

A.4 References

1. Bird, R.B., W.E. Stewart and E.N. Lightfoot (1960) *Transport Phenomena*, Wiley, New York.

2. Ishii, M. (1975) "Thermo-Fluid Dynamic Theory of Two-Phase Flow," Eyrolles.

3. Ishii, M. and N. Zuber (1979) "Drag Coefficient and Relative Velocity in Bubbly, Droplet or Particulate Flows," *AIChE J.* **5**, 843.

4. Sissom, L.E. and D.R. Pitts (1972) *Elements of Transport Phenomena*, McGraw-Hill, New York.

5. Wallis, G.B. (1969) *One-dimensional Two-phase Flow*, McGraw-Hill, Inc., New York.

6. Witte, L.C. (1968) *Ind. Eng. Chem. Fundamentals* **7**, 517.

7. Yuen, W. W., X. Chen and T. G. Theofanous (1992) "On the Fundamental Microinteractions that Support the Propagation of Steam Explosion," *ANS Proceedings NURETH-5, Salt Lake City, UT., September 21-24, 1992* **2**, 627.

APPENDIX B

DETAILED RESULTS OF SIGMA SIMULATIONS WITH ESPROSE

Appendix B: Detailed Results of SIGMA Simulations with ESPROSE

The purpose of this appendix is to provide the details of the calculated behavior in the ESPROSE simulations of SIGMA experiments with mercury or tin drops. For fragmentation we made use of the instantaneous Bond number formulations as described in Section II.2, and calculations were carried out for shock pressure levels ranging from 200 to 476 bar for mercury and from 68 to 300 bar for tin, to correspond to the experimental conditions of intrest. The results, in the form of Figure II.2, are shown in Figures B.1 through B.5.

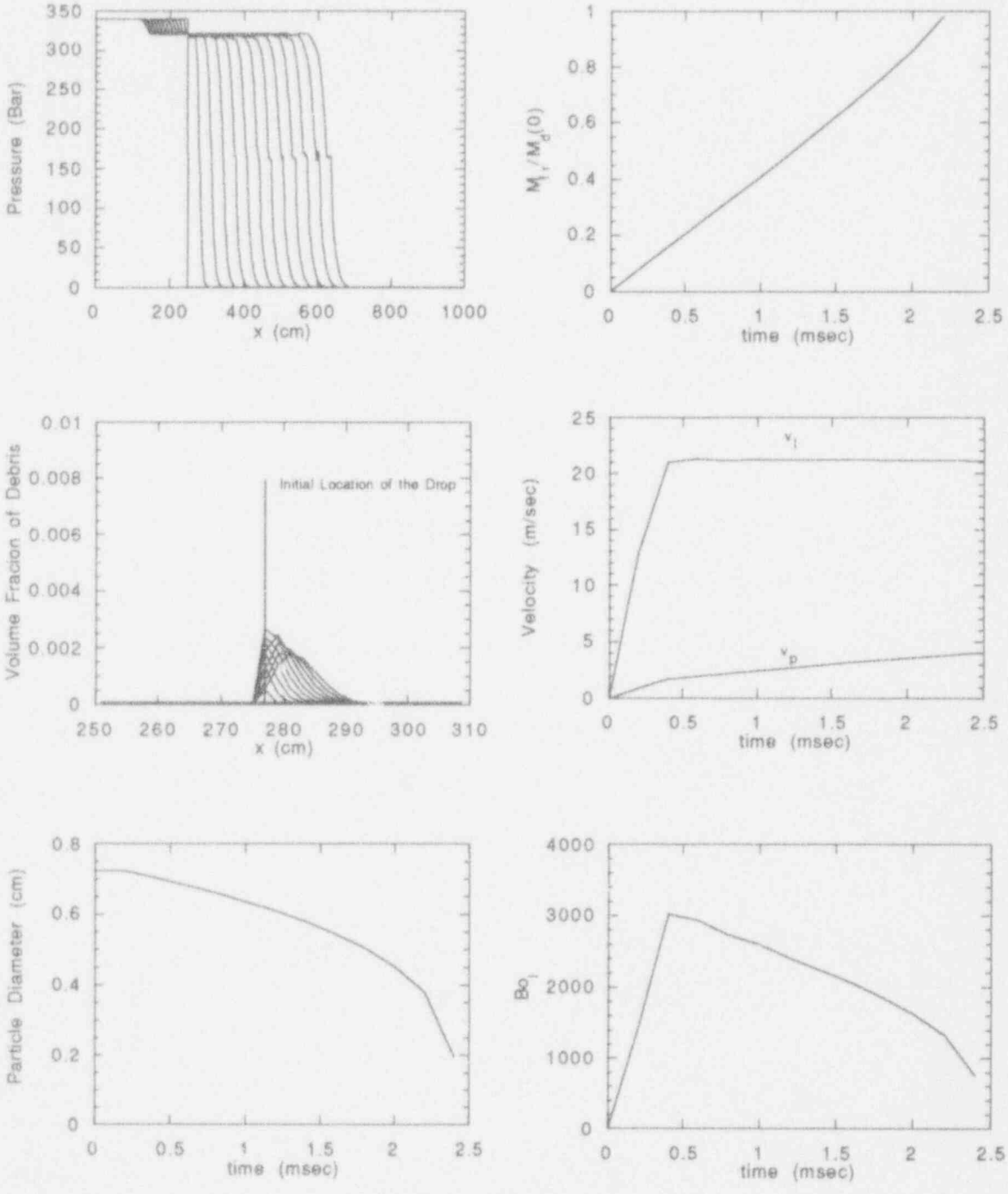

Figure B.1 Details of a mercury drop fragmentation process in the SIGMA geometry under a shock pressure of 340 bar.

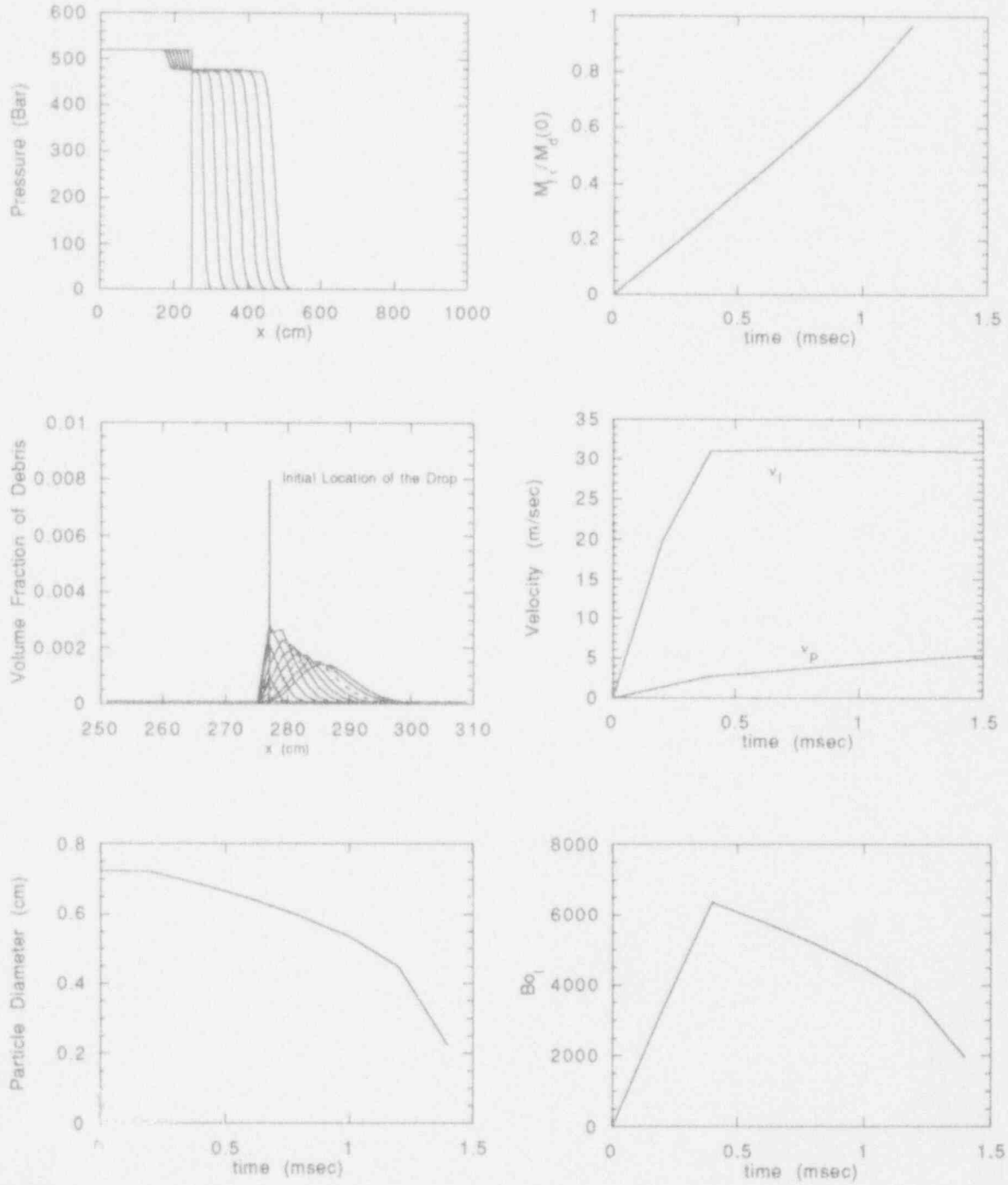

Figure B.2 Details of a mercury drop fragmentation process in the SIGMA geometry under a shock pressure of 476 bar.

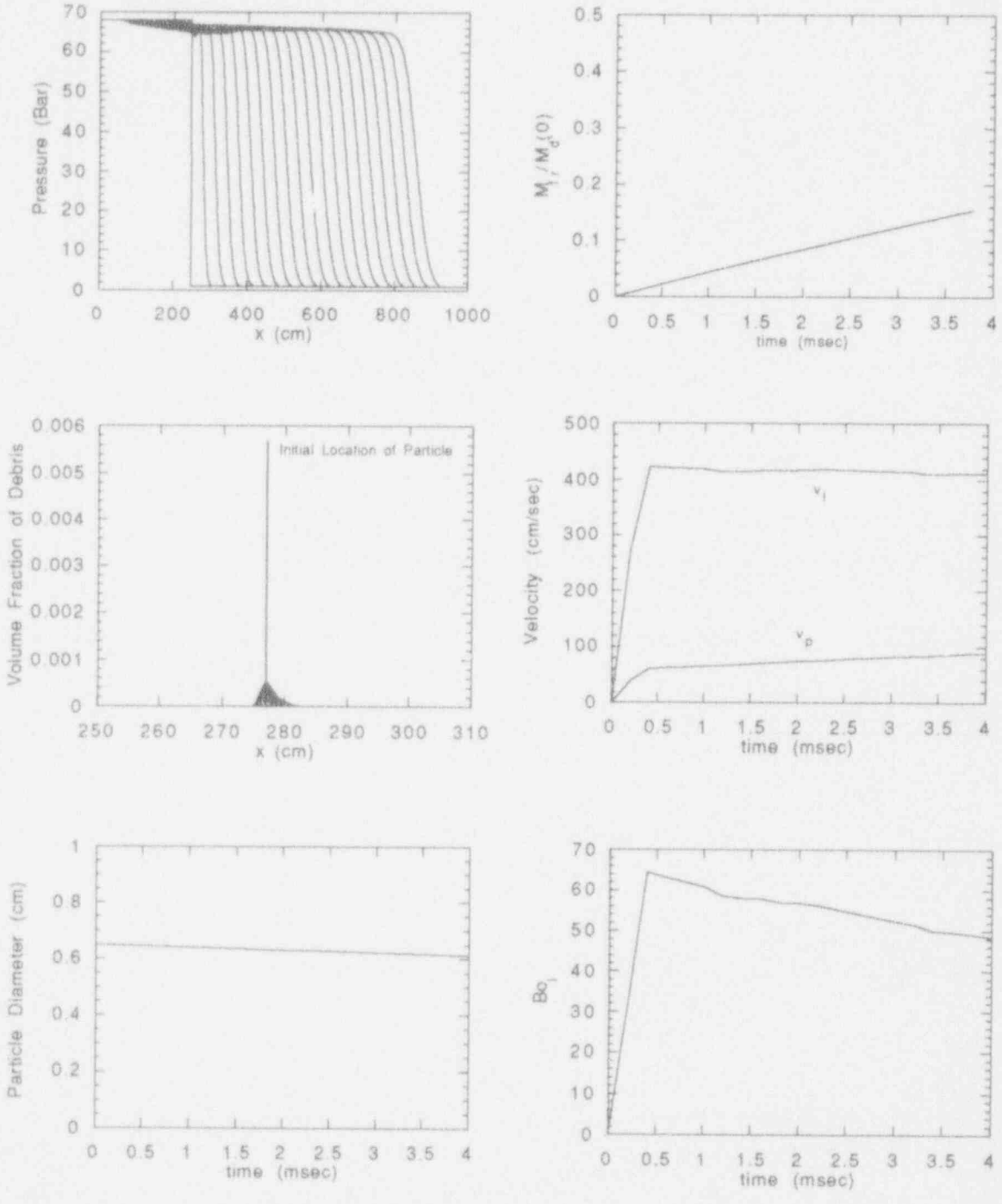

Figure B.3 Details of a tin drop fragmentation process in the SIGMA geometry under a shock pressure of 68 bar.

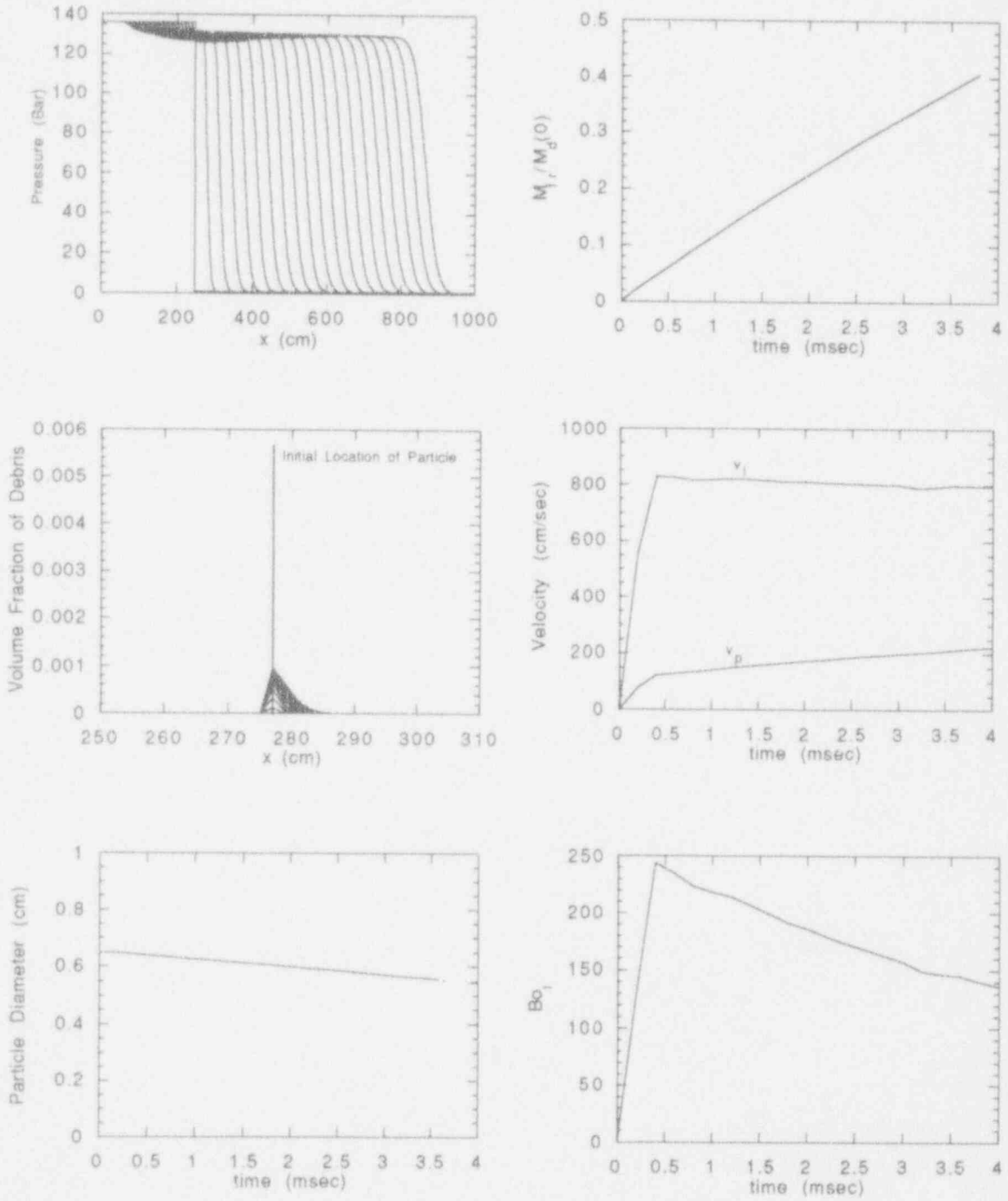

Figure B.4 Details of a tin drop fragmentation process in the SIGMA geometry under a shock pressure of 136 bar.

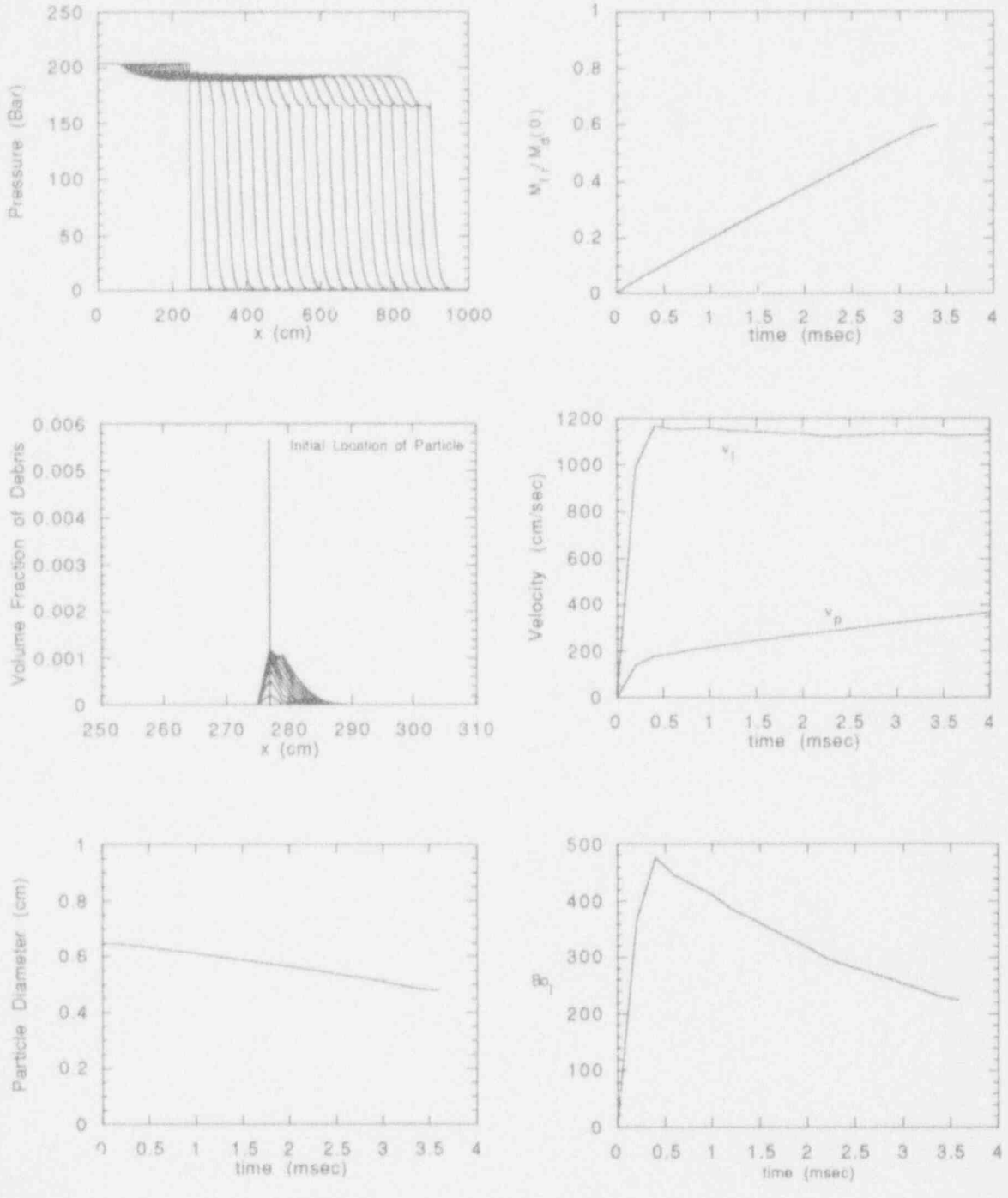

Figure B.5 Details of a tin drop fragmentation process in the SIGMA geometry under a shock pressure of 300 bar.

PART III. REACTOR APPLICATIONS

Table of Contents

Figures

III.1 Assessment of In-Vessel Energetics

Because of the densely-packed control rod guide tubes in the lower plenum BWRs are not subject to in-vessel steam explosion energetics concerns. For PWRs a comprehensive assessment was offered by Theofanous et al. (1987) under an initial implementation of the Risk oriented Accident Analysis Methodology (ROAAM). Publication of this study created an unusual, and strong, reaction from the readers as manifested in several letters-to-the-editor published a few months later (Berman, 1988; Marshall, 1988; Corradini, 1988a) and a second round still a few months later (Hopenfeld, 1989; Fletcher & Thyagaraja, 1989; Corradini, 1989b; Young, 1989). As already acknowledged in the original study, the quantification offered, especially the causal relation describing the quantity of melt available to participate in a coherent explosion (i.e., the quantity premixed) as a function of pour area was only a first, analytical result, that needed careful scrutiny and experimental verification. Not surprisingly, this happened to be the central point of the controversy. In the intervening 4 to 5 years the following key developments have taken place.

a. In the UK an assessment of in-vessel energetics for Sizewell was completed as a part of the licensing activities. This study will become available shortly; at this point we have learned that it adopted the probabilistic framework of the 1987 study mentioned above, with certain improvements, and that the results (of assessed α-failure probabilities) are quite acceptable.

b. The quantification of premixing given in the 1987 study (it was based on a 2-fluid model) was confirmed by using a 3-fluid model, which became known as the PM-ALPHA code (Amarasooriya & Theofanous, 1991). This is the code used to interpret the premixing experiments in Part I of this report.

c. A detailed comparison of premixing predictions between PM-ALPHA and the CHYMES code used in the UK study was recently published (Fletcher, 1992).

During the finishing stages of this document we explored further these PM-ALPHA, CHYMES comparisons, and the results are presented in Appendix III.A. We conclude that consideration of water subcooling is essential, even for initially saturated water, if the premixing occcurs in confined geometries such as in a lower plenum. Moreover, we draw from these comparisons further confidence on the numerical and multifield treatment of PM-ALPHA. Finally, we offer an updated quantification of premixing and on this basis we re-affirm that α-failure is physically unreasonable.

Appendix III.A also provides the first results of direct dynamic loading of the lower head from a calculated (ESPROSE) steam explosion with a realistic (water-depleted) premixture. These results indicate the importance of two-dimensionality, and of dynamically coupling the explosion zone to the voided, highly compressible "inner" premixture region, as well as to the highly incompressible water medium that surrounds the explosion zone and transmits the loads to the structures.

III.2 Assessment of Ex-Vessel Energetics

A previous evaluation of the impulsive loads from ex-vessel steam explosions, as a containment failure mechanism has been made in NUREG-1150. The reference plants in this study include 2 PWRs (Zion and Surry) with large dry containments, 1 PWR with an ice condenser (Sequoyah), and 2 BWRs with Mark I and Mark III containments (Peach Bottom and Grand Gulf). To a large extent these plant configurations, ex-vessel contact modes, loading mechanisms, and structural capabilities span the range of possible interest, and they will be used, therefore, in the present assessment also. For completeness we will include a BWR with a Mark II containment also (Limerick).

For the Zion and Surry plants no containment failure mechanisms could be identified in NUREG-1150, and we concur with this result. More generally, for PWRs, with large dry containments, the following considerations can be offered:

(a) The reactor cavities are usually buried well into ground; thus, they are not susceptible to mechanical failures.

(b) Quite often curbs prevent containment water from draining into the cavity; thus only condensation levels are relevant. Even in the absence of curbs rather modest water accumulations are thought to exist. This preliminary impression evolved from recent work on Direct Containment Heating; however, no systematic examination of all plants and relevant scenarios is yet available. Such examination is clearly outside the scope of the present effort, but it is strongly recommended for future work with the Individual Plant Examinations (IPEs).

(c) Because of cavity geometries, sizes, and water depths dynamic coupling to the containment pressure boundary or sensitive equipment inside it is highly inefficient.

On this basis the subject is not pursued any further here.

For the Sequoyah two containment failure mechanisms were identified, and both pertain only to deeply flooded cases—reactor vessel submerged up to the hot leg nozzles. The one involves consideration of the dynamic impulse traveling (through water) up the keyway, impacting on and failing a 2.5 ft. concrete wall in the room below the seal table, and the resulting fragments impacting on the containment shell. The other mechanism involves accelerating the whole reactor vessel upwards. In both cases the failure probability (conditional) was assessed as 10^{-2}, which is adequately low for this failure mode to be judged negligible. For the first mechanism it was noted that a steam explosion involving 10 tons of corium would be required to produce the 100 kPa-s impulse needed for failure of the concrete, and that it would be difficult to involve that much debris in a coherent explosion in a deeply-flooded cavity. In addition, we note that the simple correlations used to estimate the propagation of impulses was found to be conservative, by more than a factor of 7, when compared to a few numerical calculations using the CSQ code. For the second mechanism it was noted that more than 3 tons of corium would need to explode coherently in order to produce failure of the pipe restraints. Besides this being judged very unlikely for a fully-flooded cavity, a number of other losses exist that make significant upward acceleration of the reactor vessel highly unlikely and, indeed, according to recent findings even reactor vessel failure may be prevented altogether (under such deep-flooded conditions). We concur with both of these assessments, and the subject is not pursued further here.

For the Peach Bottom, two potential containment failure modes were also identified. With the explosion somewhere inside the pedestal the one involves propagation of the impulse, through

the pedestal wall to the liner, while the other is the dynamic loading on the pedestal itself. It was recognized that the shallow water pool (limited by the downcomer inlet elevation to only 0.7 m) does not allow efficient dynamic coupling, and the failure probability was assessed as "zero." We concur with this assessment. In addition, we note that stratified explosions in the immediate vicinity of the liner (as the melt is spread on the drywell floor) are not possible because of the intense corium-concrete interactions that accompany such spreading. [This topic is discussed in more detail in a recent study on the thermal attack of the Mark I liner (Theofanous et al., 1993).] Accordingly, this subject is not pursued further here.

The Limerick has a Mark II containment, and the primary concerns would be with the integrity of the drywell-to-wetwell paths, i.e., the downcomers. Such failure would allow bypass of the suppression pool, and it is highly undesirable because besides causing an earlier venting it would also defeat the suppression pool scrubbing action. Starting with the structural capability, we could find no previous studies that give a perspective on the relevant (for failure) level of energetics. We note, however, that these downcomers are very substantial pieces that have to be heavily braced for seismic and condensation (LOCA) loads considerations. Regarding the conditions leading to steam explosions and potential magnitude of the resulting loads the following comments can be made.

(a) **Rates and Compositions of Melt Release.** In NUREG/CR-5423 (Theofanous et al., 1991) two melt release scenarios were considered to bound the conditions of thermal attack on a Mark I liner. In a follow-up study Podowski and Cho (1993) confirmed the releases for "slow" Scenario II, but could not find evidence for the "fast" Scenario I. Limiting, therefore attention to Scenario II, we find an initial metallic release (mainly steel) at peak rates lower than 0.7 m^3/min for a total release of ~20 m^3 and rather low superheats. The superheat would be quickly lost as the melt spreads on the concrete floor and we would expect that the downcomer protrusions above the floor will survive. For Limerick these protrusions extend up to 45 cm above the floor and by making use of another NUREG/CR-5423 follow-up study (Sienicki et al., 1993) addressing corium spreading phenomena we can conclude that expected corium levels will be less than those needed to overflow into the downcomers. Indeed, with peak releases of 15 m^3 at 0.7 m^3/min following a slower release of 15 m^3 at 0.1 m^3/min the drywell melt levels were found to be below 20 cm. This calculation was done with water on the drywell floor. In another calculation, with a dry floor, a 30 m^3 release at 0.15 m^3/min produced a level of 42 cm, i.e., still below the downcomer inlets. The releases become gradually oxidic much later in time while the rates of melt release are reduced to decay–heat–limited levels of ~0.1 m^3/s. Such low releases are of no concern for the conditions of interest here.

(b) **Premixing.** As discussed above, conditions favorable for significant quantities of melt pouring coherently into the downcomers cannot be expected. In addition, we note that the one-dimensional geometry (~0.6 m in diameter, ~4 m deep) would promote strong water-melt interactions, steaming, and fluidization. Moreover, the process of melt inflow would be limited (or periodically halted) by the high steam rates resulting from these mild interactions.

(c) **Propagation.** On top of the unlikelihood of melt availability, and of good premixing, we note here that any steam explosion would be rather weak (low temperature melt, and high void fractions) and one dimensional. This means that it would be easily contained within

the downcomer and could not produce the significant asymmetric (lateral) loads needed to violate the strong supports.

On the basis of the above considerations we conclude that there is no significant technical issue for the Mark II case either.

Turning, finally, to the Grand Gulf, with a Mark III geometry, we find a situation not quite as straightforward as those discussed for the other plant geometries. This is because the pedestal area is deep-flooded (2 to 7 meters). The failure mechanism identified in NUREG-1150 is impulsive loading of the pedestal wall, and according to rough structural evaluations made there failure may be expected at impulses in the range of 25 to 125 kPa-s. Gross failure of the pedestal would topple the reactor vessel and fail the drywell by either direct impact, or more likely by dragging along major lines (i.e., main steam line, etc.). A CSQ calculation with 10% of the core in a 7 m-deep water pool produced an impulse of 125 kPa-s, i.e., failure. On this basis it was judged that such failures cannot be excluded and the failure probability was assessed at 0.5. Clearly this was left, in NUREG-1150, as an open issue, and we focus on it for the remainder of this section. In the CSQ calculations mentioned above the thermal energy (from 2500 to 1500 K) of 10% of the core (or 6 GJ) was released into a volume of water of 1 m in diameter and 7 m high, in 1 millisecond. [In another case using 10 milliseconds instead, no observable impulse was obtained.]

As discussed above, only Scenario II events are relevant; accordingly, consider a metallic release, mainly steel at ~1500 °C exiting a penetration (or drain plug) failure at a peak rate of 0.7 m^3/min. In falling through 7 meters of water such a release would breakup and slow down to a velocity of ~2 m/s (according to PM-ALPHA calculations presented below); thus, it would take about 3.5 seconds to reach the pool bottom. An explosion could occur at any time during this freefall, but rather clearly the quantity of melt found **at any** time in contact with water cannot be more than 0.04 m^3 (or ~325 kg), which is negligible in comparison to the 25 tons used in the CSQ calculation. Moreover, such a debris would be expected to be solidified, and unable to explode after traversing 2 to 3 meters of subcooled water (Sienicki et al., 1993). Thus the appropriate, but still conservative, geometry to consider is one involving only 0.015 m^3 (or ~100 kg) of melt in the top 2.5 meters of the water pool. On this basis and using a melt volume fraction of a few percent (see calculations below) we can estimate the premixing zone cross-section area as 0.2 m^2 (or 50 cm in diameter). Such an explosion clearly cannot be of concern to the 1.7 meter-thick reinforced concrete pedestal wall. This is also clear from the CSQ calculation performed for the Peach Bottom in NUREG-1150. In it, 25 tons of high temperature melt (2500 K) in a pool depth of 0.7 m gave only 4 kPa-s on the pedestal wall.

Some additional perspectives on the effects of pool depth can be obtained from some integral PM-ALPHA/ESPROSE calculations presented by Yuen and Theofanous (1993). It is emphasized, however, that the material (oxide corium) and pour rates were selected for illustration purposes only and they are very conservative compared to the realistic conditions discussed above.

The melt pouring conditions are very much system and scenario specific, thus we make no attempt to represent anything in particular here—for illustration purposes only, we assume a pour of 0.6 meters in diameter with velocities of 9.7 and 7.1 m/s at 0.2 and 0.4 m above the water surface ("inlet" to the computational flow field) for the 1 and 3 meter pool cases, respectively. In both cases the melt (UO_2 properties) volume fraction at the inlet was taken as 0.05, and the particle size was fixed as 1 cm. The premixing transient was calculated with PM-ALPHA and

the explosions were triggered at the time the fuel reached the pool bottom, by suddenly releasing the pressure of saturated steam at 120 bar from one of the computational cells. The calculation was carried out using ESPROSE (with $f_f = 1$ and $f_v = 0.05$).

The initial conditions for the explosion in the 1-meter pool are depicted in Figure III.1. The calculated pressure pulses along the side boundary are shown in Figure III.2, and the dynamics of the explosion zone interacting with the surrounding fluid and the free surface can be surmised from Figure III.3. For the 3-meter pool case the corresponding type of information is found in Figures III.4, III.5 and III.6, respectively. The venting processes are quite evident in both cases from Figures III.3 and III.6, and they manifest themselves in Figures III.2 and III.5, by the relatively low pressure at the wall as compared to that in the explosion zone. It is also clear that this venting is more pronounced in the 1-meter case, as expected.

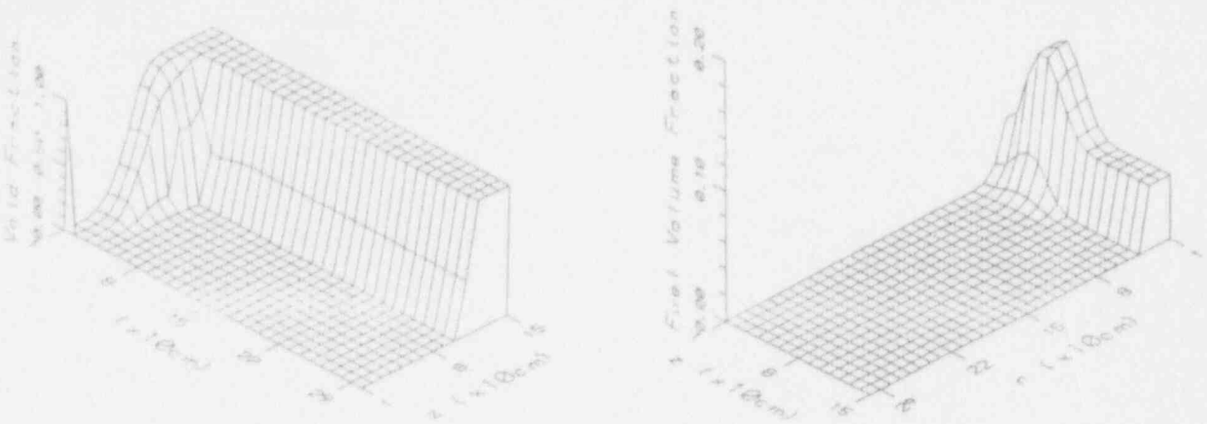

Figure III.1 Initial conditions for the ex-vessel, 1-m deep pool, ESPROSE.a calculation.

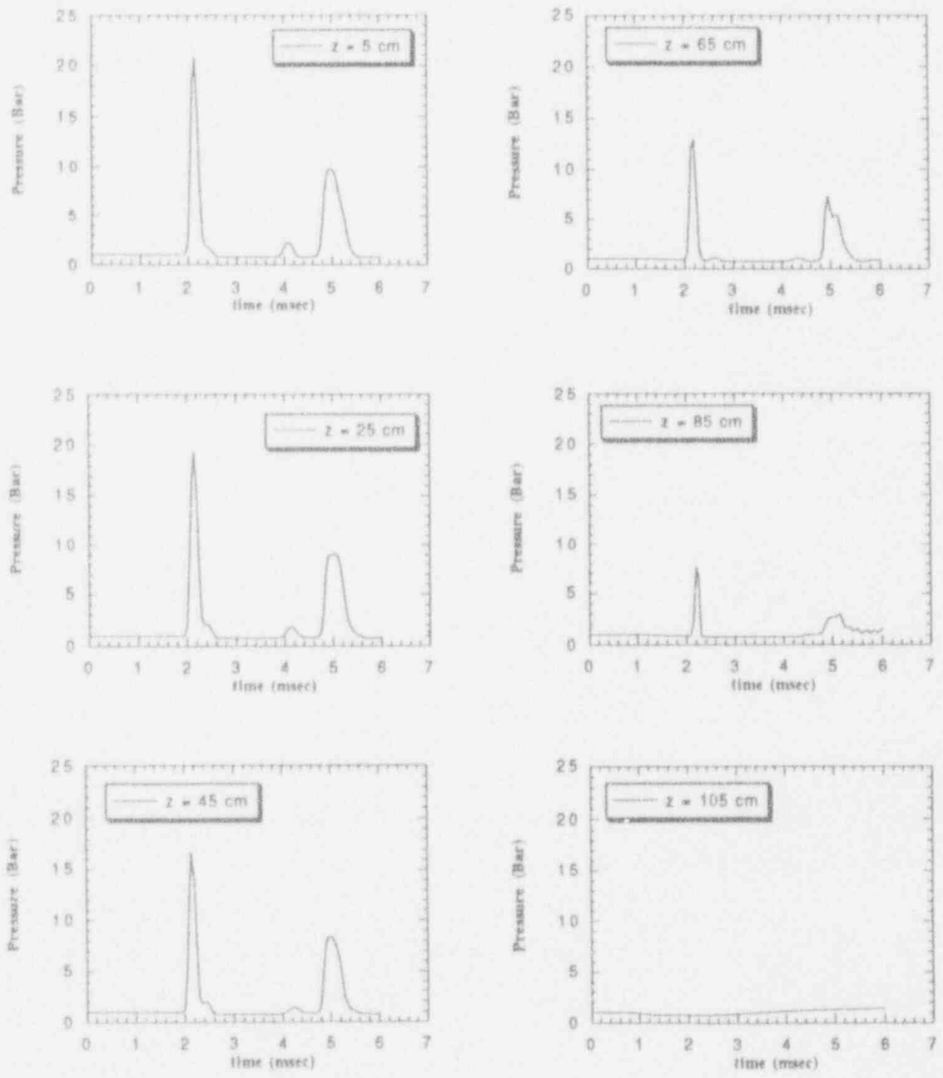

Figure III.2 Calculated loadings on lateral pool boundary for a 1-m deep pool. ESPROSE.a with $f_f = 1$ and $f_v = 0.05$.

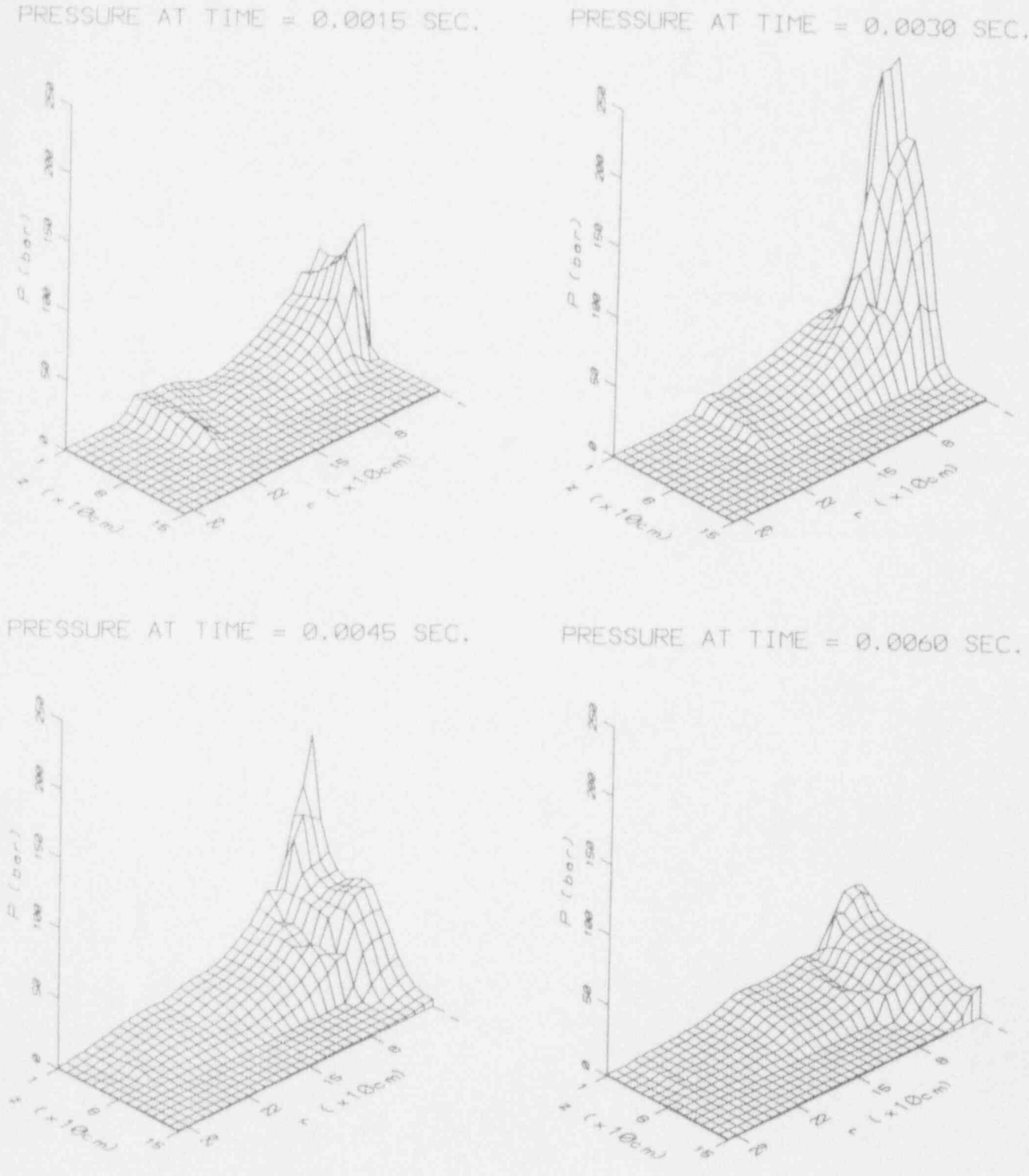

Figure III.3 Calculated transient pressure distribution of an ex-vessel explosion for a 1-m deep pool using ESPROSE.a.

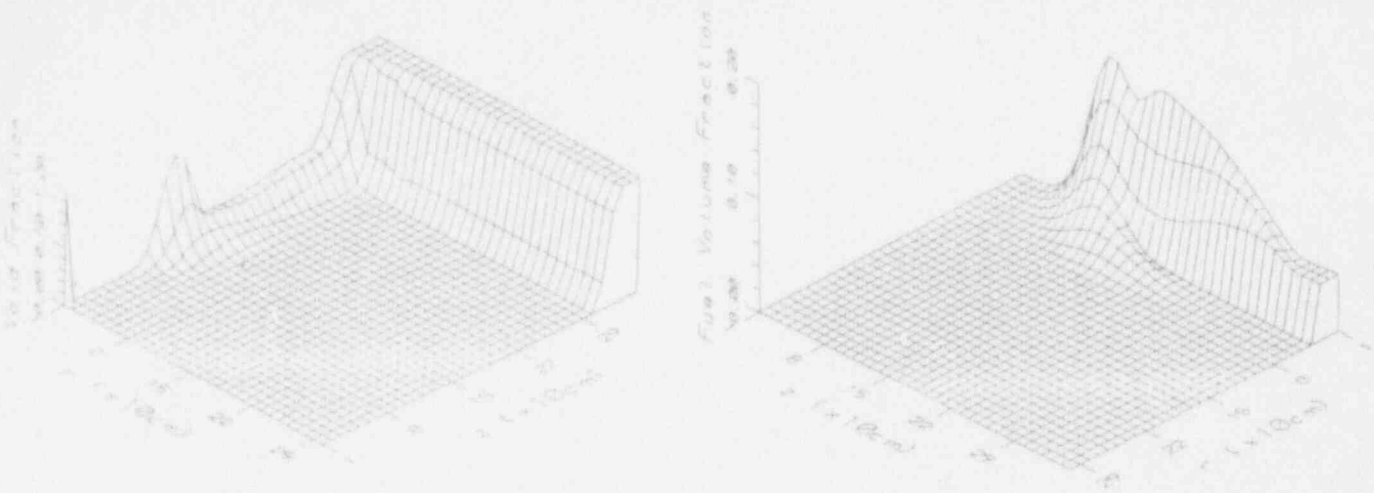

Figure III.4 Initial conditions for the ex-vessel, 3-m deep pool, ESPROSE.a calculation.

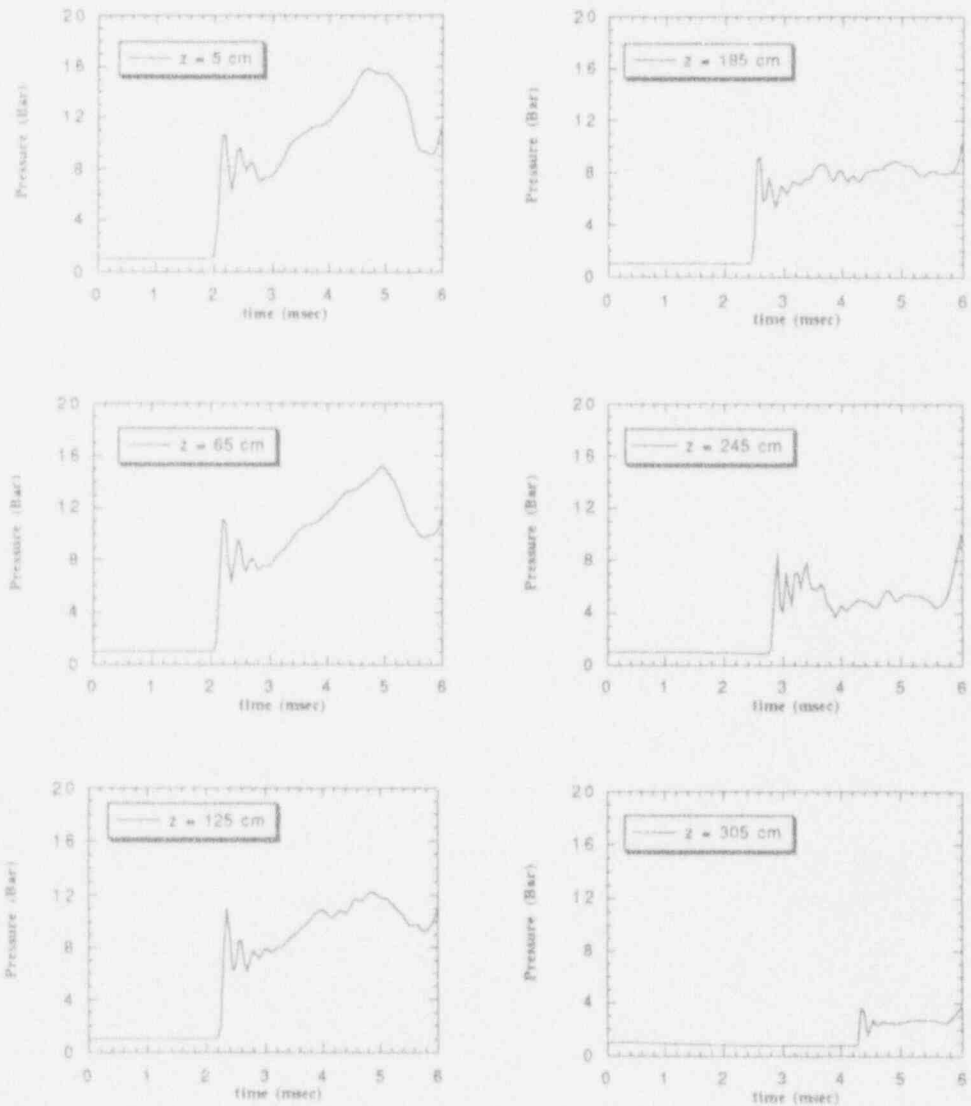

Figure III.5 Calculated loadings on lateral pool boundary for a 3-m deep pool, ESPROSE.a with $f_f = 1$ and $f_v = 0.05$.

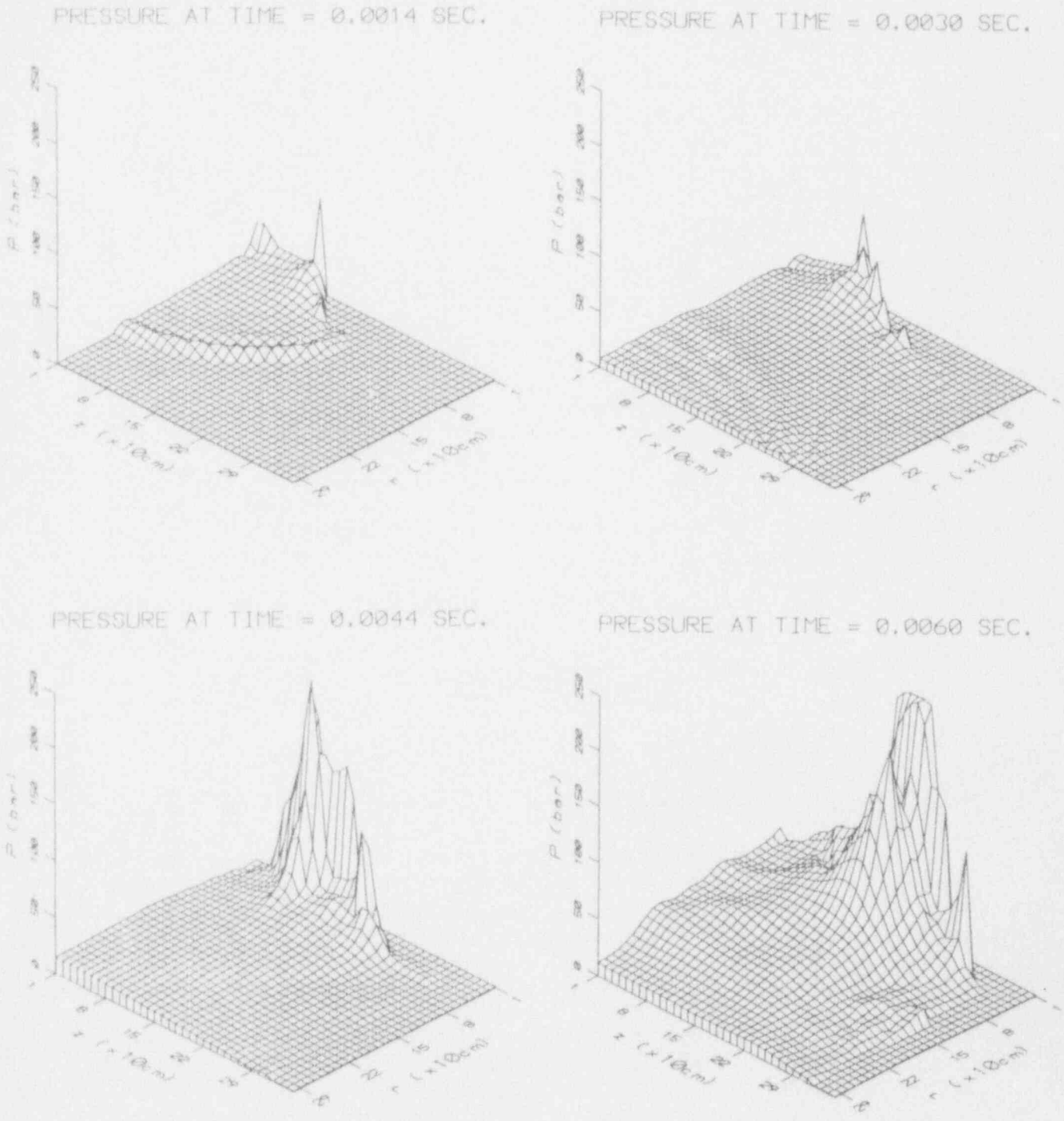

Figure III.6 Calculated transient pressure distribution of an ex-vessel explosion for a 3-m deep pool using ESPROSE.a.

III.3 Conclusions

For in-vessel explosions (PWRs only) we can conclude that the water depletion phenomenon is now confirmed experimentally, and that it is predictable quantitatively. We believe that PM-ALPHA predicts premixing conservatively, and besides the comparisons with experiments, the comparisons with the code CHYMES provides an additional mutually beneficial reinforcement for reactor-specific applications. Besides limiting the magnitude of the interacting masses, this water depletion phenomenon is seen to significantly mitigate the escalation of a triggered explosion. Based on these results we conclude that the 1987 assessment of α failure (Theofanous et al., 1987) is robust and conservative. The about-to-be-released α-failure study for Sizewell will provide further depth and insight to this conclusion.

For ex-vessel explosions we find no vulnerabilities in any of the existing (in the US) plant geometries. This is consistent with the NUREG-1150 result except for the deeply flooded case of a Mark III containment, where (in NUREG-1150) the issue of failure was left open. With the present understanding of core meltdown scenarios, and vessel failure, for BWRs, we also conclude that this case cannot be energetically significant (i.e., to fail the pedestal walls). Much larger release rates than those presently considered physically possible and deep penetration into the water pool would be required to obtain significant impulses on the walls, as illustrated by sample calculations.

In summary, at this point we see no outstanding issues from energetic steam explosions in any of the existing plant geometries. However, the fundamental aspects of both premixing and fragmentation kinetics are scientifically interesting and sufficiently fertile to warrant continuing attention.

III.4 References

1. Amarasooriya, W.H. and T.G. Theofanous (1991) "Premixing of Steam Explosions: A Three-Fluid Model," *Nuclear Engineering & Design*, **126**, 23-39.
2. Berman, M. (1988) Letters to the Editor, *Nuclear Science and Engineering*, **100**, 149-162.
3. Corradini, M.L. (1988) Letters to the Editor, *Nuclear Science and Engineering*, **100**, 171-174.
4. Corradini, M.L. (1989) Letters to the Editor, *Nuclear Science and Engineering*, **103**, 103-104.
5. Fletcher, D.F. and A. Thyagaraja (1989) Letters to the Editor, *Nuclear Science and Engineering*, **103**, 101-102.
6. Fletcher, D.F. (1992) "A Comparison of Coarse Mixing Predictions Obtained from the CHYMES and PM-ALPHA Models," Technical Note, *Nuclear Engineering and Design*, **135**, 419-425.
7. Hopenfeld, J. (1989) Letters to the Editor, *Nuclear Science and Engineering*, **103**, 100.
8. Marshall, B.W., Jr. (1988) Letters to the Editor, *Nuclear Science and Engineering*, **100**, 165-170.
9. Podowski, M.Z. and C.S. Cho (1993) Part II of NUREG/CR-6025 (see Ref. 13).
10. Sienicki, J.J., C.C. Chu and B.W. Spencer (1993) Part IV of NUREG/CR-6025 (see Ref. 13).
11. Theofanous, T.G., M. Abolfadl, W. H. Amarasooriya, G.E. Lucas B. Najafi and E. Rumble (1987) "An Assessment of Steam-Explosion-Induced Containment Failure. Parts I–IV," *Nuclear Science and Engineering*, **97**, 259-326 (1987).
12. Theofanous, T.G., W.H. Amarasooriya, H. Yan and U. Ratnam (1991) "The Probability of Liner Failure in a Mark-I Containment," NUREG/CR-5423, August 1991.
13. Theofanous, T.G. et al. (1993) "The Probability of Mark-I Containment Failure by Melt-Attack of the Liner," NUREG/CR-6025, September 1993.
14. Young, M.F. (1989) Letters to the Editor, *Nuclear Science and Engineering*, **100**, 106-107.
15. Yuen, W.W. and T.G. Theofanous (1993) "The Prediction of 2D Thermal Detonations and Resulting Damage Potential," CSNI Specialists Meeting on Fuel-Coolant Interactions, Santa Barbara, CA, January 5-8, 1993.

APPENDIX A

THE PROBABILITY OF ALPHA-MODE CONTAINMENT FAILURE UPDATED

THE PROBABILITY OF ALPHA-MODE CONTAINMENT FAILURE UPDATED

T.G. Theofanous and W.W. Yuen
Center for Risk Studies and Safety
University of California, Santa Barbara, CA 93106
Tel. (805) 893-4900 — Fax (805) 893-4927

ABSTRACT

Since the original quantification of the likelihood of α failure in NUREG/CR-5030, major experimental and analytical developments have taken place. By taking advantage of these developments, we believe it is possible to reduce the substantial conservatisms in the original quantification, and to thus conclude that even vessel failure by steam explosions may be regarded as physically unreasonable. We have illustrated how this can be done within the original framework, as well as in a complementary framework that takes advantage of current integral analysis capabilities. On this basis, the α-failure issue is now ripe for final resolution; what is needed is a complete set of calculations supporting a revised quantification of CR1 and CR3 and a final review step in the ROAAM process.

INTRODUCTION

Since its definition and initial quantification in WASH-1400, the α-mode containment failure has maintained a unique place in risk analyses of nuclear reactors and related safety research. It involves an energetic fuel-coolant interaction that takes place in the lower plenum of a pressurized water reactor (PWR): the generation of an internal missile that loads the upper head of the reactor vessel to failure, the generation of an external missile, and containment boundary (upper dome) impact. The energetic interaction presupposes a massive pour of molten corium from a crucible-held geometry into the lower plenum; the energetics of the internal missile depend on a number of dissipative phenomena associated with the momentum and structural interactions leading up to and including upper head loading and failure; and the external missile (the detached vessel head or portion of it) must destroy or "sweep-away" the missile shield before it can begin to rise toward impacting the containment. The problem is significant because it gives rise to the possibility of "early" containment failure, and it has become an "issue" because the complex phenomenology has been addressed variably and on occasion with conflicting results.

In interesting contrast to most other major containment integrity "issues" (in severe accidents), the α failure has evolved as a rather benign one, that is, more as a matter of omission rather than one of commission. In other words, more as a result of failure to deliver a definitive (generally agreeable) closure rather than as a result of explicitly specified and generally accepted active concerns on it. This is quite evident in the first systematic evaluation of it by an *ad hoc* panel of experts, the Steam Explosions Review Group (SERG, 1985), some eight years ago, as well as in the latest quantification of it as a part of the NUREG-1150 study two years ago. Specifically, in SERG, we find panel member assessments that, with only a few exceptions, agree that α failure is of adequately low likelihood not to pose serious containment integrity concerns, while the NUREG-1150 expert panel on this issue agreed that these SERG assessments were appropriate and made use of an aggregate (based on arithmetic averaging) of them in the quantification. The NUREG-1150 results indicate that the probability of α failure (conditional on core melt) is under 1%, with an upper bound (95^{th} percentile) estimate of "a few" percent. The reasons for further attention on this issue can be listed as follows:

1. *Quality and Robustness of Assessments.* Individual assessments in SERG were based on widely variable reasoning and to a great extent on judgment.

2. *Treatment of Outliers.* Individual SERG assessments of probability varied over many orders of magnitude, including some extremely small as well as some rather large (the few exceptions noted above) values.

3. *Interpretation of Results.* The SERG-aggregate mean value of 0.8% and the above-quoted NUREG-1150 result (under 1%) may mean different things to different people, and not necessarily always a negligible concern.

It is worth noting that these specific, quantitative, concerns were framed in the context of the scenario described above; it can be expected that their resolution will provide the impetus and help address explicitly other less tangible aspects of this issue, including multiple explosions and other (than pouring) modes of contact, especially as they arise in consideration of accident management actions (Theofanous, 1991).

An initial step toward resolving the concerns listed above was made five years ago (Theofanous et al., 1987, to be referred to as NUREG/CR-5030) under an approach formalized later as the Risk-Oriented Accident Analysis Methodology (ROAAM) — Theofanous and Yan (1991). Meanwhile, the methodology has been employed to the

resolution of two other major issues—Mark-I Liner Attack (Theofanous et al., 1991) and Direct Containment Heating (Pilch et al., 1992)—while new data and calculations anticipated by, and relevant to, the original quantification have recently become available. Guided by the methodological insights from these further applications of ROAAM, our purpose here is to re-examine the NUREG/CR-5030 quantification, in light of these new data and calculations, with an eye toward an ultimate resolution.

OVERVIEW OF THE ORIGINAL QUANTIFICATION AND THE NEW DEVELOPMENTS

The probabilistic framework employed in NUREG/CR-5030 is shown (in current notation and with the practically unimportant limit of molten core available omitted) in Figure 1, and it can be understood in terms of the explosion scenario described in the early part of the introduction section, with the help of Figures 2 and 3. Of critical importance to the quantification, is the "upper-central" portion of this framework including, in particular, the quantification of premixtures (CR1) and of the energy partition associated with lower head failure (CR3). Indeed, these also happened to be the focus of the criticism received in the review process, as documented in NUREG/CR-5030, and accordingly, these will be the focus of the present reexamination here. In passing, we note that the overall framework and, in general, the approach, has been well received; moreover, a similar approach has been taken in addressing this issue within the licensing proceedings of the Sizewell plant in the UK. The details of this study are to be made openly available soon (Turland et al., 1993), but it is our understanding that the results indicate an adequately low likelihood (of containment failure) for licensing purposes. This can be taken as generally reinforcing of the NUREG/CR-5030 conclusion that such failures are "physically unreasonable," but the extent of actual synergism obtained can only be understood after a detailed comparative study of the two quantifications.

Premixing, in NUREG/CR-5030, was quantified strictly on the basis of computations. In particular, a two-fluid model was used to compute the transient penetration of fuel particles in a locally homogeneous steam-water mixture, allowing for two-dimensional motions and to thus demonstrate the water-depletion phenomenon envisioned by Henry and Fauske (1981). Assuming that fuel surrounded by highly voided coolant (say, 50 to 70%) cannot effectively participate in an explosion, limits to the quantities of fuel premixed (and thus able to explode) could be obtained for arbitrarily large pours. The resulting quantification, allowing for highly generous margins above the quantities deduced from such computations to judgementally cover uncertainties, is shown in Figure 4. Important subsequent developments include: a new and more general three-fluid formulation and computer code, the PM-ALPHA, that confirms the conservative nature of the original quantification (Amarasooriya and Theofanous, 1991); a comparative study of reactor-scale premixing calculations between PM-ALPHA and the independently developed CHYMES code (Fletcher, 1992); and the MAGICO (Angelini et al, 1992) and MIXA (Denham et al., 1992) experiments designed specifically for comparisons with the PM-ALPHA and CHYMES codes predictions, respectively. At a much larger scale, the FARO Quenching Test series is now also beginning to produce the first results. We will argue that these developments provide the firm basis needed to drastically reduce the conservatism built in the quantification of Figure 4.

Energy partition, during the early yield phase of the explosion, in NUREG/CR-5030, was based on what was thought to be a conservative treatment of explosion energetics in combination with the structural response of the lower head. The simple idea was that an explosion energetic enough to produce an upper-head-threatening missile should be able to fail the lower head that contained it in the first place; such failure provides downward relief and thus significant mitigation of energy in the upward-directed missile. The quantification is reproduced in Figure 5. The "break" in slug energy due to lower head failure is seen to occur at ~1 GJ of total mechanical energy release, and this is consistent with other independent studies. Still, the mechanism depends on the time scale of the energy release, and it can, therefore, be (it has been) questioned in a quantification based on equilibrium thermodynamics that bypasses the dynamic aspects of the interaction. It is now possible to account for these dynamic aspects and thus address this question directly. Several developments have contributed to this new capability, including: experience with several independent one-dimensional detonation codes (Medhekar et al., 1991; Fletcher and Thyagaraja, 1991; Bürger et al., 1993), single-drop fragmentation data under conditions relevant to an established detonation wave (Yuen et al., 1992), the first quantified experimental demonstration of a strong detonation with $A\ell_2O_3$ melts (Hohmann et al., 1993) as compared to mild ones obtained with tin melts in previous works, and an experimentally-tested analysis tool, the ESPROSE code, that when interfaced with PM-ALPHA can follow the triggering and escalation of an explosion in two dimensions from realistic premixtures and in relevant reactor geometries (Yuen and Theofanous, 1993). We will argue that these developments provide a firm basis for the consideration of lower head integrity, and the related energy partition question, under physically meaningful explosions in the lower plenum.

With this integral capability at hand, from a methodological standpoint, the question arises as to whether the lower-central portion of the framework affected should be condensed into one single operation, as illustrated in Figure 6. This structure is attractive because it captures in a consistent manner the "size" of the explosion in terms of premixture characteristics and respective level of energetics. In the original quantification, this could be done only in a preliminary way, by making the conversion ratio a function of the energy stored in the premixture (CR2). Also, this approach continues to capture the main variable characterizing the "massiveness" of the melt pour. In particular, we note that this is adequate to reflect "side" versus "bottom" pours as well as other variables in accident characteristics such as system pressure or lower plenum subcooling by defining an appropriate set of splinter scenarios (Theofanous and Yan, 1991). An important disadvantage of such a condensation, on the other hand, is that it could detract

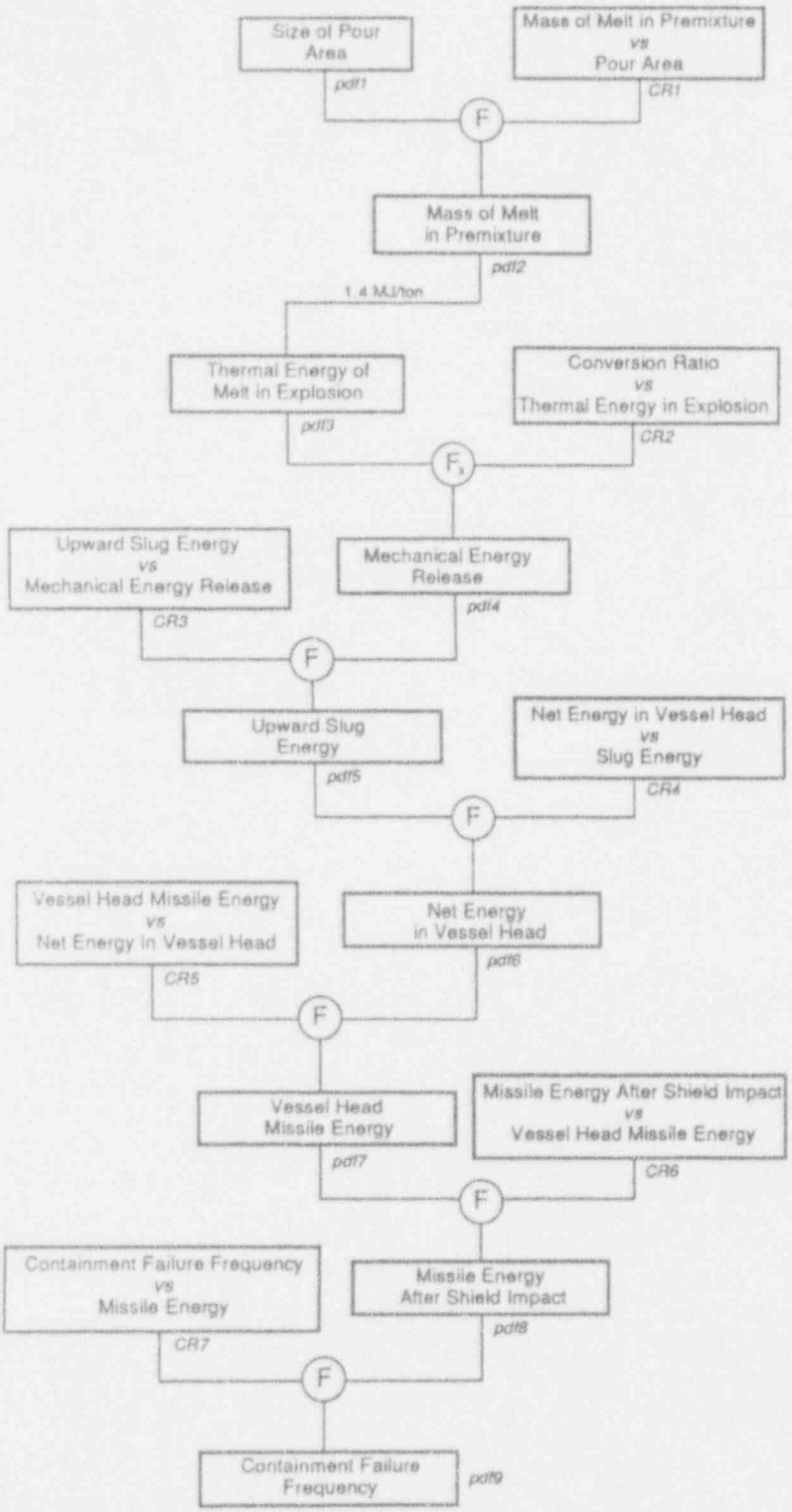

Figure 1. Probabilistic framework for the assessment of α failure as proposed in NUREG/CR-5030. pdf and CR refer to "probability density function" and "causal relation" in the ROAAM terminology.

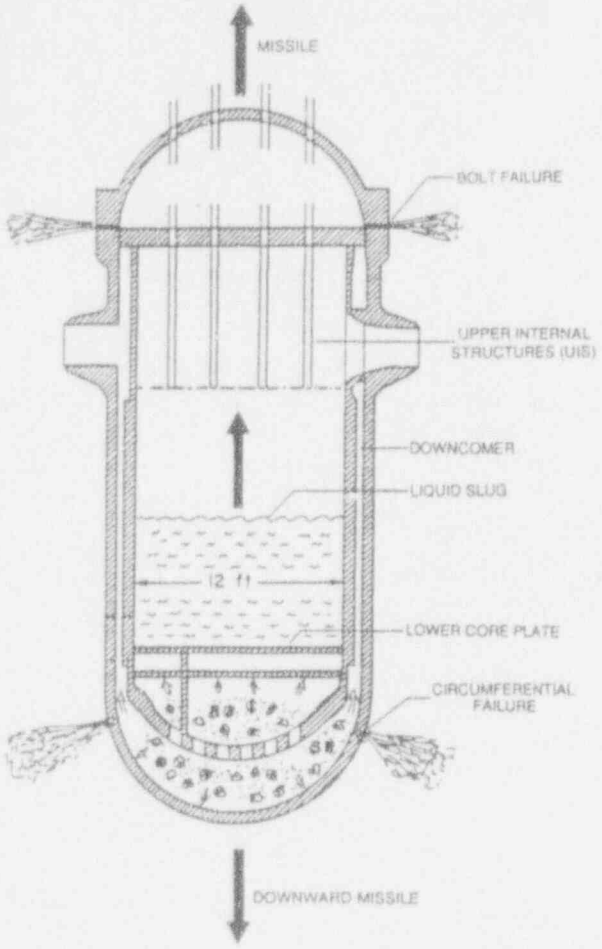

Figure 2. Key mechanisms and terminology for a steam explosion event (in-vessel portion).

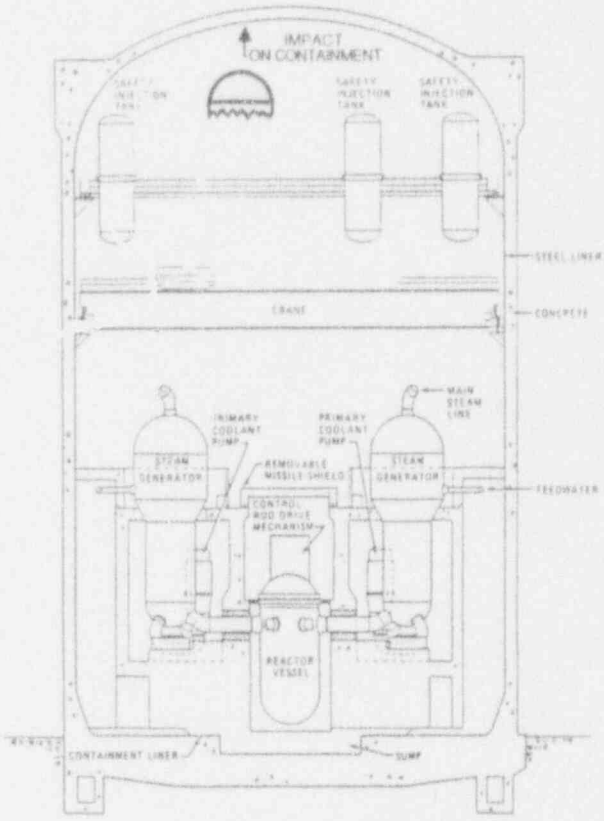

Figure 3. Geometry relevant to the ex-vessel portion of a steam explosion event in a large dry containment.

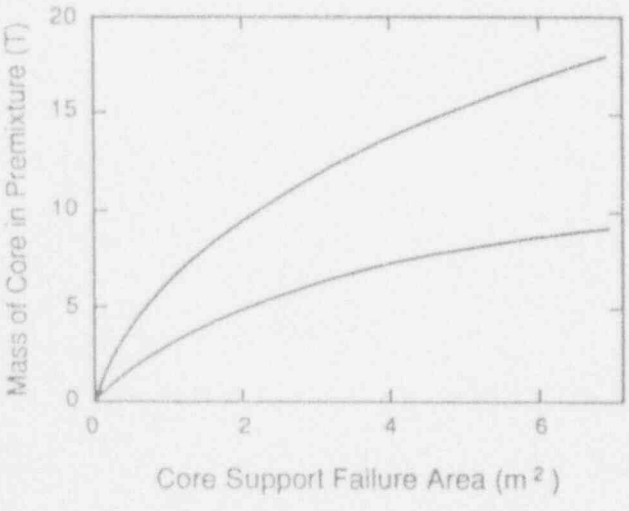

Figure 4. CR1 according to NUREG/CR-5030. A flat distribution was assumed between the 5 and 95% limit lines shown. The point refers to a calculation presented later on in this paper.

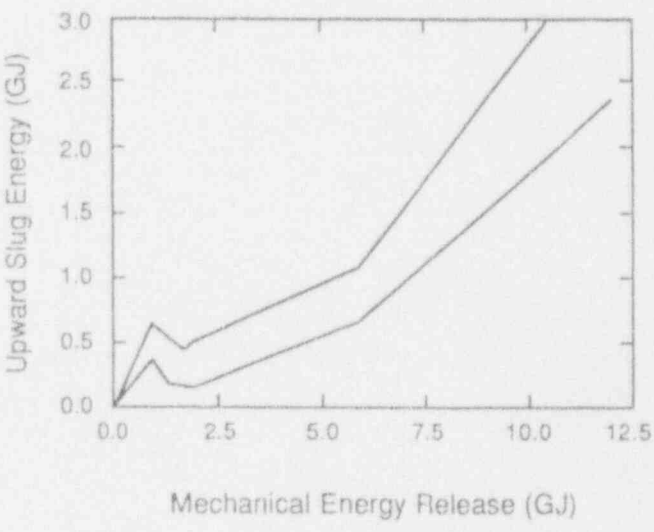

Figure 5. CR3 according to NUREG/CR-5030. A normal distribution is assumed between the 5 and 95% limit lines shown.

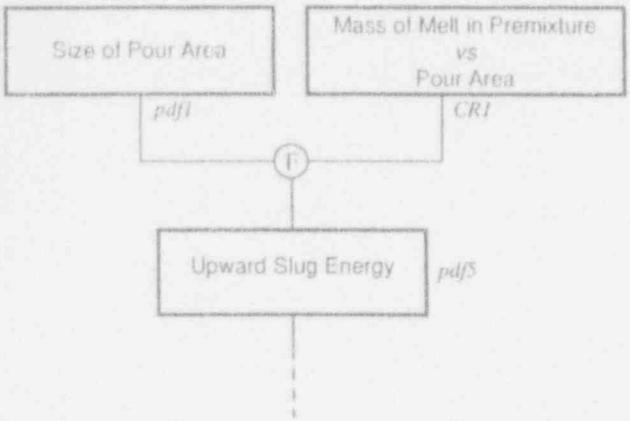

Figure 6. A condensed version of the upper-central portion of the probabilistic framework in NUREG/CR-5030, making use of currently available integral analysis capability.

from one of the key aims of ROAAM; that is, allowing for as many independent quantifications of each component of the framework as possible. For example, an independent contribution to the quantification of premixing could not be made to the condensed framework. Conversely, the breakdown of the results from integral analyses, for the purposes of the original framework, should always be possible while still retaining the essential features of consistency (or dependencies). For these reasons, we propose the condensed framework as a complement to rather than as a substitute for the original one.

QUANTIFICATION OF PREMIXING

The fundamental parameter in quantifying a premixture is the void fraction. From a bounding equilibrium thermodynamics standpoint (i.e., Hicks–Menzies), the implied working-fluid depletion drastically reduces the thermal-to-mechanical energy conversion (Amarasooriya and Theofanous, 1987), while from an explosion dynamics standpoint, it interferes with both the triggering and the escalation processes. This interference is further augmented by two-dimensionality (Medhekar et al., 1989; Yuen and Theofanous, 1993), and vice versa, two-dimensionality is essential to the prediction of void fraction distributions (Angelini et al., 1993). Accordingly, this discussion and a related experimental program are focused on void fractions.[a] The analysis tool is PM-ALPHA, and its performance against these experiments has been presented in a companion paper (Angelini et al., 1993). The only other comparable analysis tool available at this time is CHYMES, and the first comparisons of its predictions, with those made previously by PM-ALPHA for reactor-scale premixing calculations, have just been published (Fletcher, 1992). Melt volume fraction distributions were very consistent, and even premixed-mass transients up to the melt contact time with the lower head were found to be in excellent agreement; however, disturbingly large discrepancies on the spatial evolution of the steam volume fractions were also noted. The author attributed these discrepancies to differences in the drag laws employed in these two codes but offered no specific recommendations for resolution. To us, these discrepancies became a significant cause of concern, especially in light of our opinion of the importance of void fractions, as detailed above, and the prior use of PM-ALPHA to quantify premixing for the actual assessment of α failure.

In fact, the cause could be traced to an organic difference between the two codes: CHYMES cannot allow for the presence of subcooling, while PM-ALPHA does. More specifically, in CHYMES, the local rate of boiling is taken as a local latent heat requirement; i.e., in CHYMES's notation (Fletcher and Thyagaraja, 1991),

$$\dot{m}_s = 6\alpha_m\alpha_w h(T_m - T_{sat})/(L_m h_{fg}) \qquad (1)$$

where the α's are the melt and water volume fractions, h is the heat transfer coefficient, h_{fg} is the latent heat of vaporization, and L_m is a melt length scale used to estimate the heat transfer area. By contrast, in PM-ALPHA, boiling occurs at the rates necessary to bring the water locally to saturation. In practical terms, this means that the water cannot sustain any significant amount of superheat, which is, of course, the physically meaningful behavior. Moreover, CHYMES cannot allow for condensation, while in PM-ALPHA, steam is allowed to condense, as it should, if it happened to flow through a subcooled water region. [The complete constitutive package can be found in Angelini et al., 1993.] The importance of subcooling is not limited to scenarios with an initially "cold" pool of water; gravitational head in deep pools (as the one in the lower head) implies a non-negligible subcooling even in "saturated" cases, but more importantly, even modest increases in pressure due to the limited venting area from the lower plenum (the area leading into the downcomer) can produce, through the induced subcooling, a most significant feedback effect on boiling. In the absence of this feedback, as in CHYMES, the calculation in a sense "runs away," since any large quantities of steam are taken to escape, not accounting for the higher and higher pressure increases required to actually deliver this escape. To demonstrate this as the root-cause of the discrepancy under investigation, we ran PM-ALPHA with only the one change needed to make it mimic the CHYMES phase-change formulation; namely, we used Eq. (1) for boiling and set the condensation rate identically to zero. The current comparison with CHYMES is shown, side-by-side with the comparison produced by Fletcher (1992), in Figure 7. Note the remarkable agreement even at the "microscopic" level, i.e., the shape of the 0.7 contours. The pressure field responsible for these important differences is shown in Figure 8. In a vice-versa comparison, we ran PM-ALPHA with CHYMES's drag laws; as shown in Figure 9, the differences are rather minor. Clearly, CHYMES's "run-away" boiling rates pushed the calculation

[a] Note: "void fraction" refers the "steam content" to the "coolant volume," while "steam volume fraction" refers the "steam content" to the total (three-phase) mixture volume.

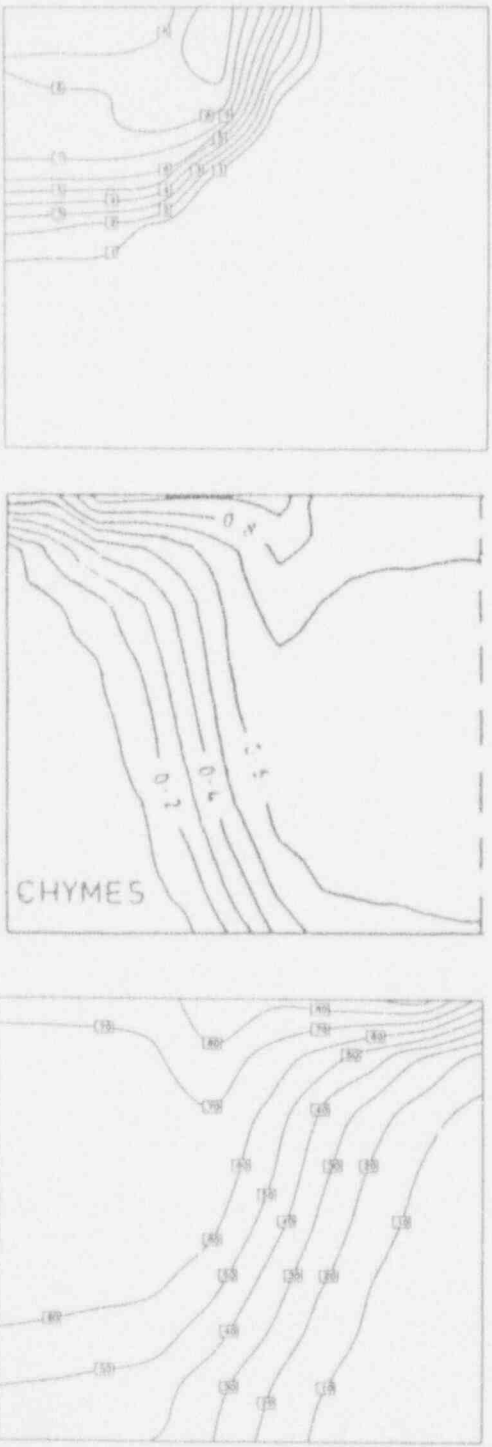

Figure 7. A side-by-side comparison of calculated steam volume fraction distributions at 0.5 s, for the premixing problem of Amarasooriya and Theofanous (1991), predicted by PM-ALPHA (a), CHYMES (b), and PM-ALPHA modified to mimic CHYMES' boiling model (c).

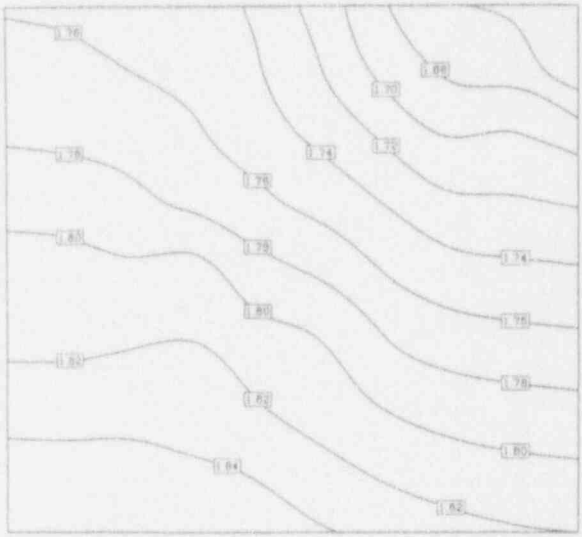

Figure 8. The calculated pressure field at 0.5 s into the premixing transient.

into a regime that accentuated these drag-related differences in Fletcher's comparisons.

Further insights into "what is important" were obtained from a series of related calculations made within the same context. In particular, we investigated fuel emissivity, gravitationally-induced subcooling, and condensation. The results are summarized in Table 1 and the figures indicated on this table. We conclude that only the treatment of subcooling is the essential difference regarding the practical aspects of application to reactor conditions, while in every other aspect, CHYMES provides indirect support to PM-ALPHA for both the numerics as well as the formulation of premixing of steam explosions.

With the numerical and physical aspects of the three-fluid formulation in PM-ALPHA well scrutinized, we are prepared to take the next major step in the quantification of premixing. In this, we persist in the fixed-particle size treatment; we expect that the real behavior can be captured/bounded by appropriate parametric variations of particle sizes, and this is all that is possible until a reasonably defensible approach to accounting for melt breakup behavior becomes available. For the particular calculation reported here, we chose the case considered above (fuel pour diameter 1.60 m, inlet velocity 1 m/s, inlet void melt fraction 0.5, melt temperature 2500 °C, and pressure 0.1 MPa), except for modifying the shape of the liquid pool boundary into the hemispherical shape of the lower head (same maximum depth). To better resolve the curved portion of the boundary, the grid size was reduced by a factor of 3 (a 30 by 27 mesh). Otherwise, aspects of accuracy and convergence (time step, spatial discretization, convergence criteria in the numerical iteration) are well at hand and need not be elaborated here. A sample of the main results, including a couple of snapshots (at times of mid- and full-penetration of the water pool by the melt front) of melt and steam volume fraction distributions and the premixed-mass transient,

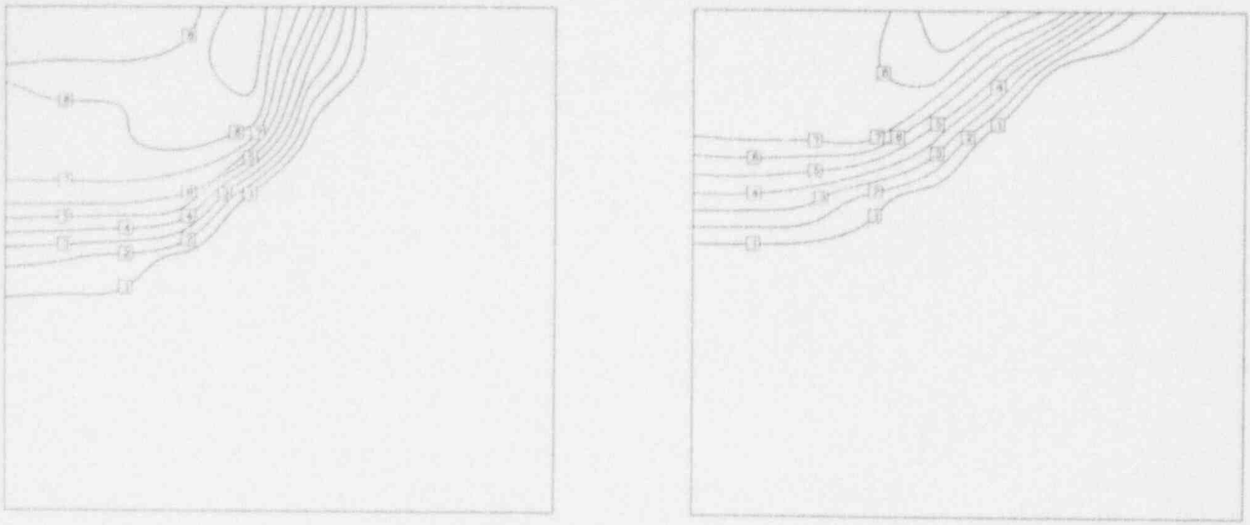

Figure 9. The effect of drag laws in the calculation of premixing. (a) PM-ALPHA, (b) PM-ALPHA with CHYMES' drag laws.

Table I

Sensitivity to Various Treatments in the CHYMES and PM-ALPHA Formulations, Deduced by Making the Change Indicated to the PM-ALPHA Code

CASE	PARAMETER OF PROCESS	PM-ALPHA BASE VALUE	CHYMES VALUE FOR SENSITIVITY	COMMENTS
I	Fuel Emissivity	0.7	0.85	Slight Effect See Figure 10
II	Condensation	Allowed	Set to Zero in Addition to Case I Change	Moderate Effect: Spreading of the Void Near Top See Figure 11
III	Gravitational Subcooling	Allowed	Set to Zero in Addition to Case I, II Changes	Negligible Effect

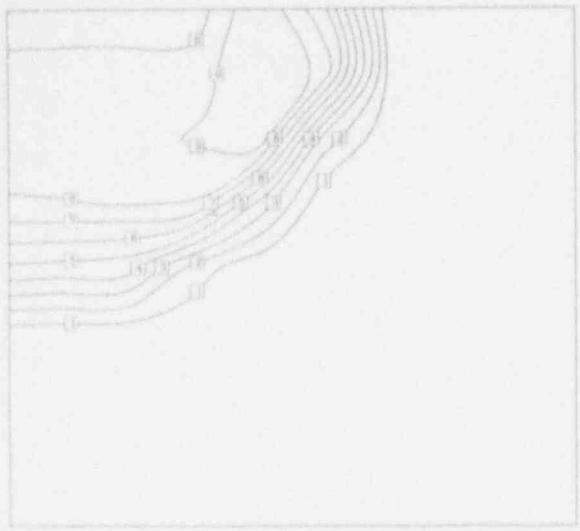

Figure 10. The calculated steam volume fraction for the premixing problem of Amarasooriya and Theofanous (1991), with increased particle emissivity.

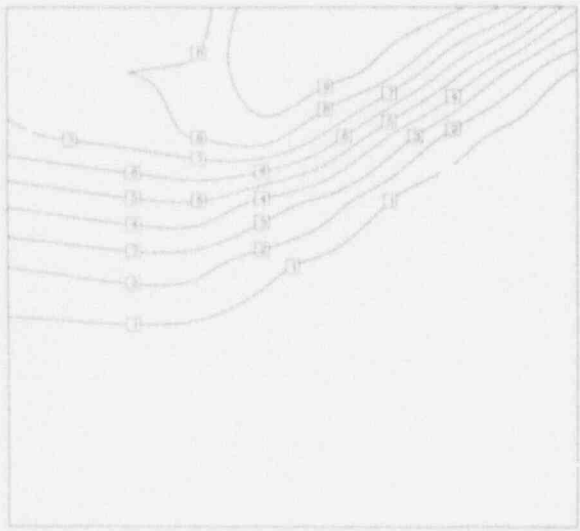

Figure 11. The calculated steam volume fraction for the premixing problem of Amarasooriya and Theofanous (1991), with increased particle emissivity and zero condensation

are shown in Figures 12 through 14. Again, we notice the familiar fuel spreading and mixing zone voiding patterns. The premixed mass is seen to depart early enough from the total quantity of melt poured to reach a peak value of ~2.5 tons at about the time that the melt front touches the lower head (~1 s). Shown in Figure 4, this calculation provides an indication of the very large degree of conservatism embodied in the NUREG/CR-5030 quantification. A systematic set of calculations for the complete requantification of premixing are currently in progress, but we expect both 5 and 95% bounds to be reduced by at least a factor of 2. Within the context of the original quantification, the impact of such a reduction is in revealing further significant margins, as discussed in Section 4, and thus to further confirm the NUREG/CR-5030 conclusion that α failure is "physically unreasonable."

QUANTIFICATION OF ENERGY YIELD

With 1.3 GJ/ton and a conservatively bounding conversion ratio of 20%, the 2.5-ton premixture found in the particular PM-ALPHA calculation of Section 3 implies a mechanical energy release of 0.65 GJ, that is, a value way too small to threaten the lower head. Conversely, for an energy yield of 1.5 GJ, we would need a mass of ~6 tons which, based on the discussion of Section 3, cannot be anticipated to be physically possible under any circumstances relevant to reactor accidents. Clearly, only a small portion (the one under 1.5 GJ) of the CR3 quantification in Figure 5 is relevant, and by reference to the NUREG/CR-5030 quantification of CR4 reproduced here as Figure 15, it is rather clear that the upper head is not threatened either.

In fact, based on our experience of the effects of water depletion and two-dimensionality, we expect that the above estimates are highly conservative and that the real margins to vessel failure are even larger. This is illustrated below by an integral calculation that accounts for the dynamics of the energy conversion process, along the lines of the alternative framework of Figure 6. [A systematic set of calculations along these lines needed to quantify pdf7 in this framework are underway.]

Using ESPROSE.a, the premixture of Figures 12 and 13 was triggered by means of suddenly releasing the contents of a computational cell pressurized (by steam) to 12 MPa. The timing of the trigger corresponds to melt arrival and contact of the lower head; its location is taken at the bottom of the axis of symmetry; and its magnitude is chosen to ensure a strong initial escalation (based on experience with the KROTOS Al_2O_3 calculations discussed by Yuen and Theofanous, 1993). In this calculation, we chose the fragmentation (f_f) and vaporization (f_v) parameters (see reference above) as 1.0 and 0.05, respectively, and the calculation was run with all flow paths, in or out of the lower plenum, sealed, and all boundaries rigid. This maximizes the loads on the lower head and, in particular, it provides an upper bound estimate of the impulse that could be delivered if the explosion was constrained from above by a hydrodynamic mass (i.e., a slug of material) instead. The results are summarized in Figures 16 and 17.

Figure 12. Calculated melt volume fraction distribution at different times into the transient.

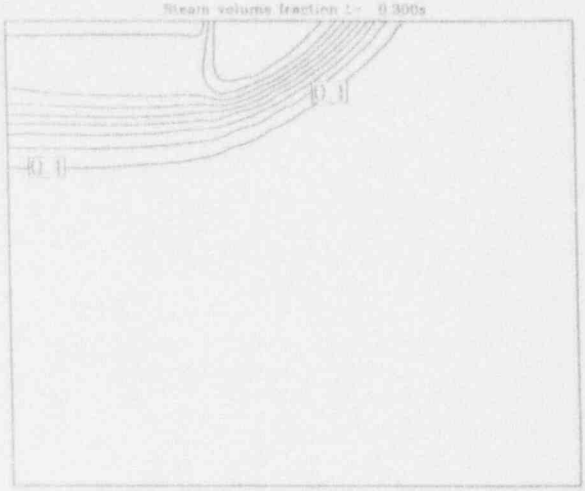

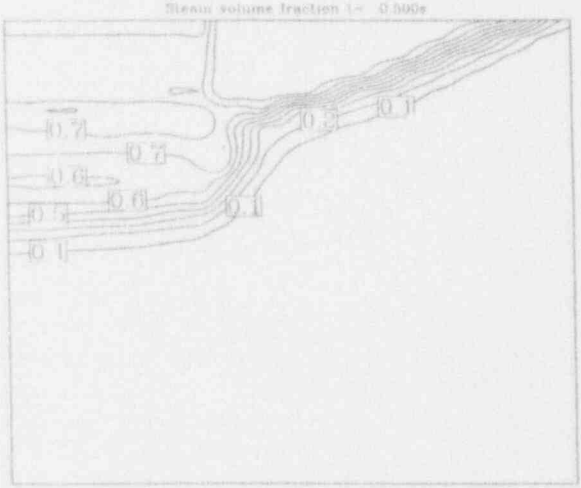

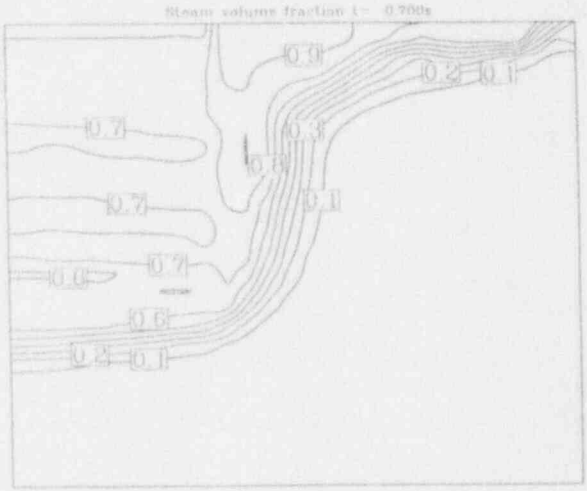

Figure 13. Calculated steam volume fraction distribution at different times into the transient.

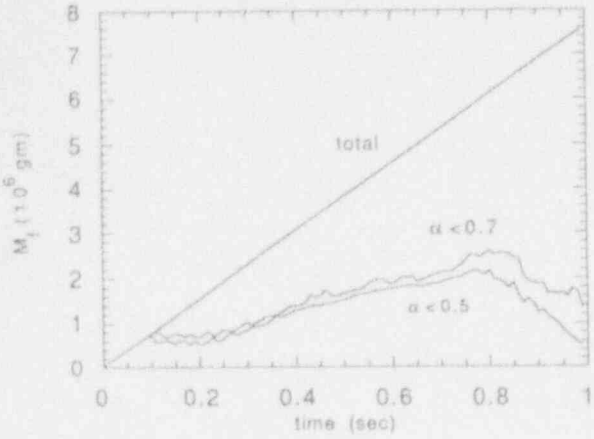

Figure 14. Premixed mass transient compared to the total quantity of melt poured.

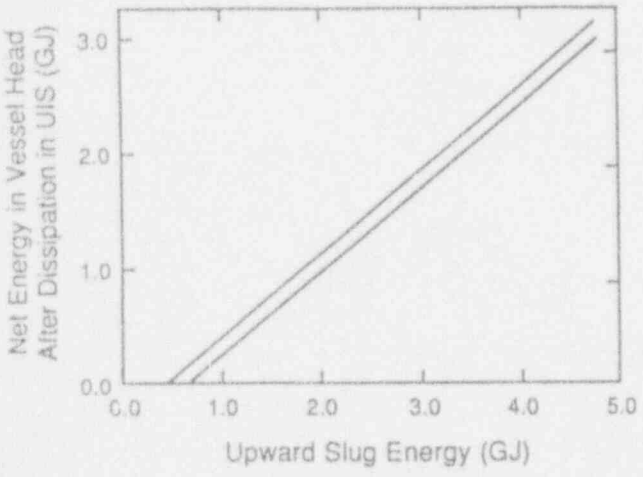

Figure 15. CR4 according to NUREG/CR-5030.

The basic results of this calculation, i.e., the evolution of the pressure field, are summarized in Figure 16. Some particular results, the pressure transients at five points along the lower head, are shown in Figure 17. We note the generically benign character of this calculated explosion; an initial trend to escalate seems to die out rather quickly as the wave encounters the highly voided mixing zone, while a larger amplitude wave is seen to propagate *around* the periphery of the mixing zone where there is fuel but the void is low. Further, we see that this wave is reinforced by reflections off the curved boundary of the lower head in a complicated wave interaction pattern that exhibits the effect of void in the mixing zone. A sample of wall pressure pulses is provided in Figure 17. Again, we note that the pressure pulses are rather low and clearly of no consequence to lower head integrity. These results are presently tested against a new model, ESPROSE.m (Yuen and Theofanous, 1993), that effects unique opportunities for representing the basic physics of the steam explosion phenomenon.

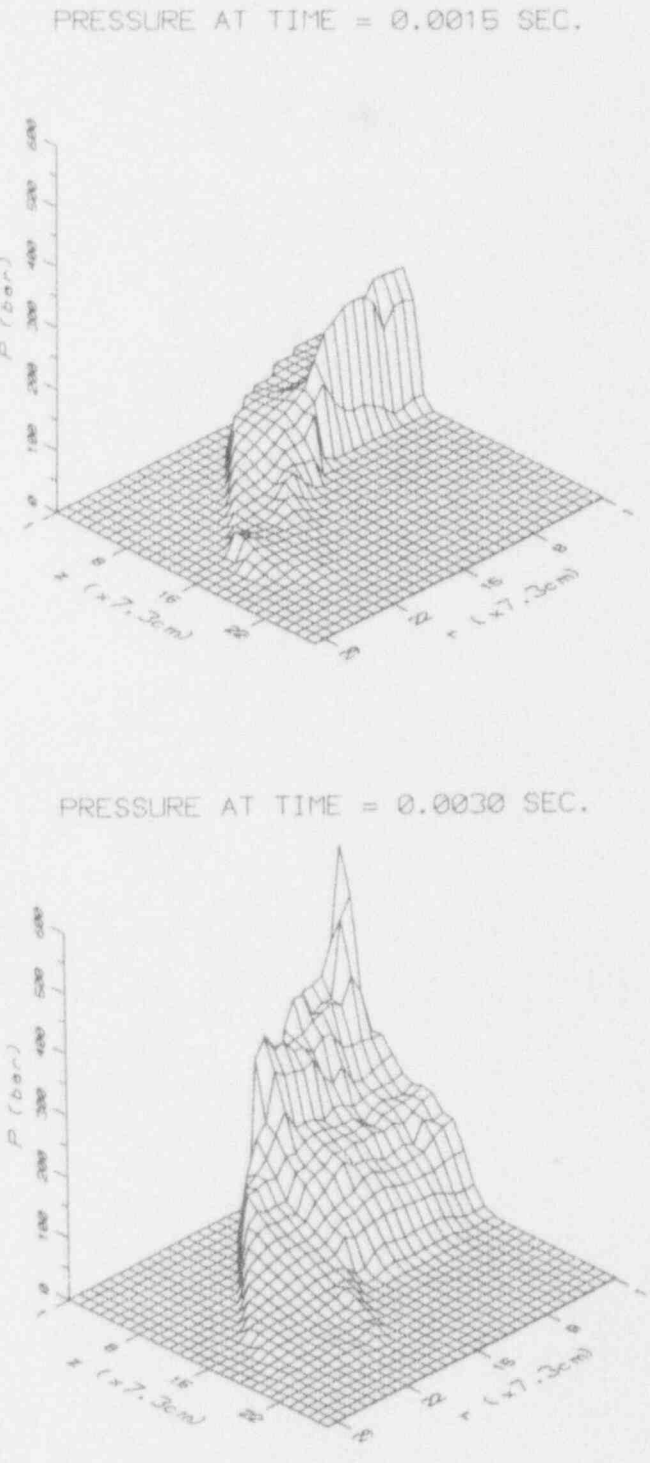

Figure 16. Evolution of an explosion in the lower head under total confinement.

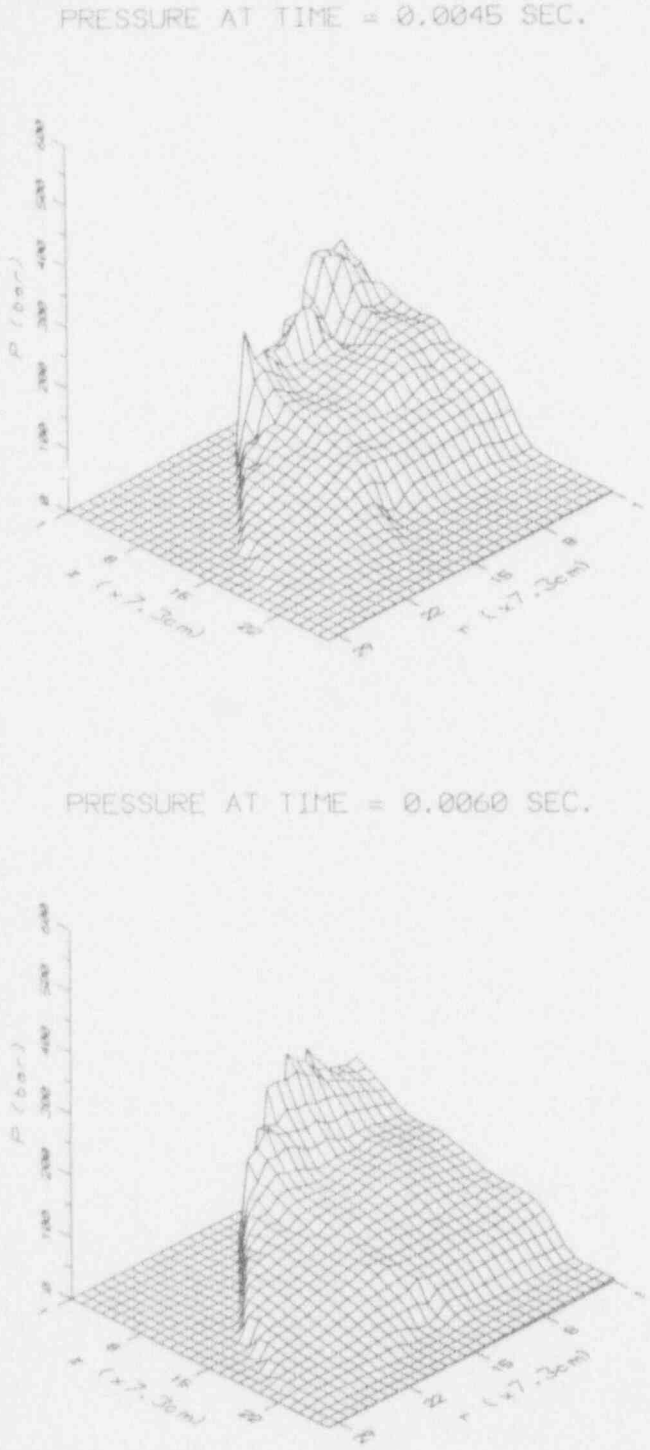

Figure 16. Cont.

CONCLUSIONS

Since the original quantification of the likelihood of α failure in NUREG/CR-5030, major experimental and analytical developments have taken place. By taking advantage of these developments, we believe it is possible to reduce the substantial conservatisms in the original quantification, and to thus conclude that even vessel failure by steam explosions may be regarded as physically unreasonable. We have illustrated how this can be done within the original framework, as well as in a complementary framework that takes advantage of current integral analysis capabilities. On this basis, the α-failure issue is now ripe for final resolution; what is needed is a complete set of calculations supporting a revised quantification of CR1 and CR3 and a final review step in the ROAAM process.

ACKNOWLEDGMENTS

The ESPROSE.a code is an advanced, developmental version of the ESPROSE code, which together with PM-ALPHA and related premixing calculations reported here were supported by the U.S. Nuclear Regulatory Commission under contract number 04-89-082.

REFERENCES

1. Amarasooriya, W.H. and T.G. Theofanous (1991) "Premixing of Steam Explosions: A Three-Fluid Model," *Nuclear Engineering & Design* **126**, 23-39.
2. Amarasooriya, W.H. and T.G. Theofanous (1987) "An Assessment of Steam-Explosion-Induced Containment Failure. Part III: Expansion and Energy Partition," *Nuclear Science and Engineering*, **97**, 296-315.
3. Angelini, S., W.W. Yuen and T.G. Theofanous (1993) "Premixing-Related Behavior of Steam Explosions," CSNI Specialists Meeting on Fuel-Coolant Interactions, Santa Barbara, CA, January 5-8, 1993.
4. Angelini, S., E. Takara, W.W. Yuen and T.G. Theofanous (1992) "Multiphase Transients in the Premixing of Steam Explosions," Proceedings NURETH-5, Salt Lake City, UT, September 21-24, 1992, Vol. II, 471–478.
5. Bürger, M., M. Buck, K. Müller and A. Schatz (1993) "Stepwise Verification of Thermal Detonation Models: Examination by Means of the KROTOS Experiments," CSNI Specialists Meeting on Fuel-Coolant Interactions, Santa Barbara, CA, January 5-8, 1993.
6. Denham, M.K., A.P. Tyler and D.F. Fletcher (1992) "Experiments on the Mixing of Molten Uranium Dioxide with Water and Initial Comparisons with CHYMES Code Calculations," ANS Proceedings NURETH-5, Salt Lake City, UT, September 21-24, 1992, Vol. VI, 1667-1675.
7. Fletcher, D.F. (1992) "A Comparison of Coarse Mixing Predictions Obtained from the CHYMES and PM-ALPHA Models," *Nuclear Engineering and Design*, **135**, 419-425.
8. Fletcher, D.F. and A. Thyagaraja (1991) "The CHYMES Coarse Mixing Model," *Progress in Nuclear Energy*, **26** No. 1, 31-61.

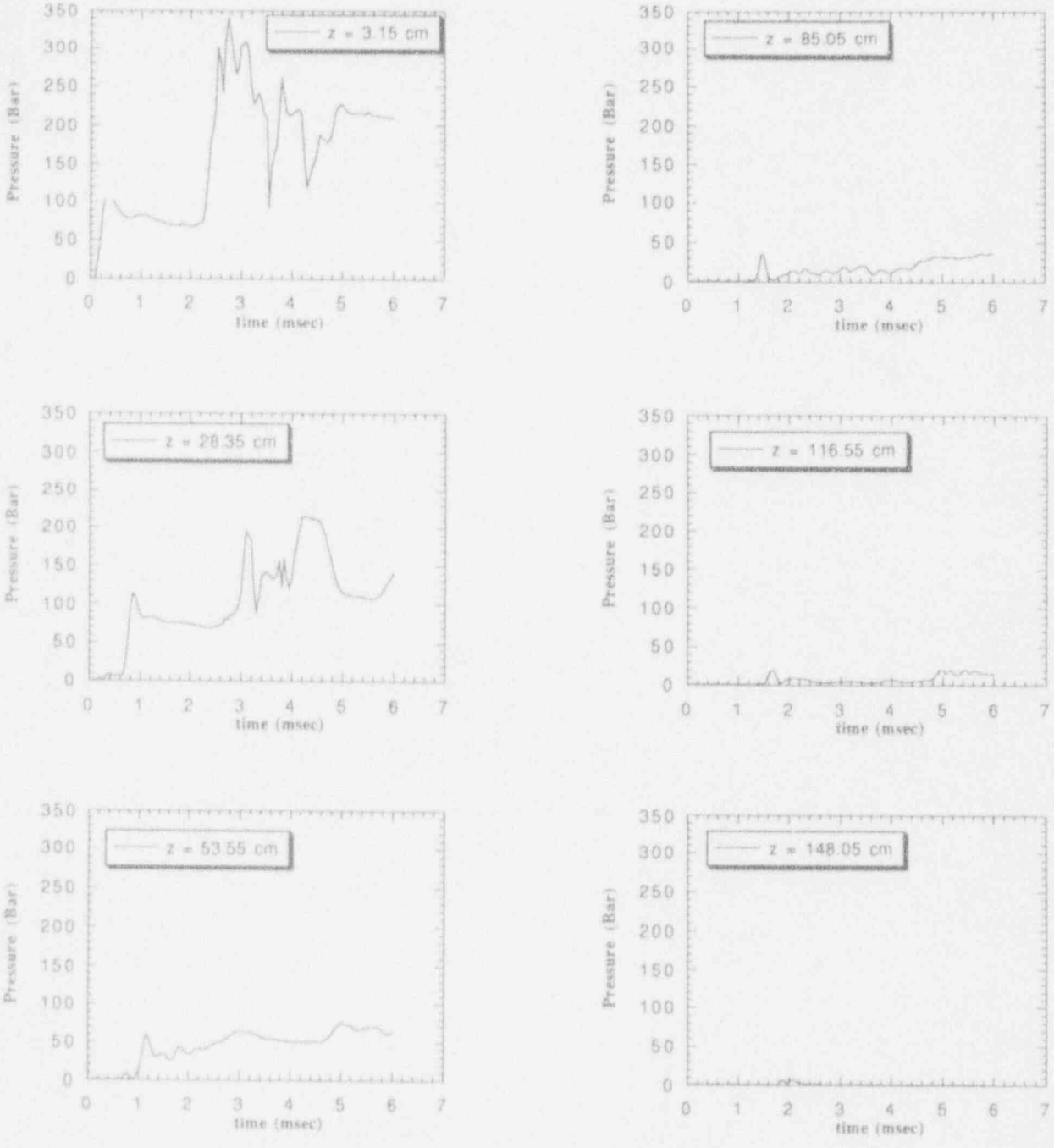

Figure 17. Transient loadings at various positions along the containing boundaries of the explosion in Figure 16.

9. Henry, R.E. and H.K. Fauske (1981) "Required Initial Conditions for Energetic Steam Explosions," *Fuel-Coolant Interactions, HTD-V19*, American Society of Mechanical Engineers.

10. Hohmann, H., D. Magallon, H. Schins and A. Yerkess (1993) "FCI Experiments in the Aluminumoxide/Water System," CSNI Specialists Meeting on Fuel-Coolant Interactions, Santa Barbara, CA, January 5-8, 1993.

11. Medhekar, S., M. Abolfadl and T.G. Theofanous (1991) "Triggering and Propagation of Steam Explosions," *Nuclear Engineering & Design* **126**, 41-49.

12. Medhekar, S., W.H. Amarasooriya and T.G. Theofanous (1989) "Integrated Analysis of Steam Explosions," Proceedings Fourth International Topical Meeting on Nuclear Reactor Thermal-Hydraulics, Karlsruhe, FRG, Oct. 10-13, 1989, Vol. 1, 319–326.

13. Pilch, M., H. Yan, M. Allen and T.G. Theofanous (1993) "The Probability of Containment Failure by Direct Containment Heating," SAND93-1535.

14. Steam Explosion Review Group (1985) "A Review of Current Understanding of the Potential for Containment Failure Arising from In-Vessel Steam Explosions," NUREG-1116, U.S. Nuclear Regulatory Commission.

15. Theofanous, T.G. (1991) "The Role of Fuel-Coolant Interactions in Severe Accident Management," Appendix A in NUREG/CR-5682, U.S. Nuclear Regulatory Commission.

16. Theofanous, T.G., W.H. Amarasooriya, H. Yan and U. Ratnam (1991) Failure in a Mark-I Containment," NUREG/CR-5423, U.S. Nuclear Regulatory Commission.

17. Theofanous, T.G., B. Najafi and E. Rumble (1987) "An Assessment of Steam-Explosion-Induced Containment Failure. Part I: Probabilistic Aspects," *Nuclear Science and Engineering*, **97**, 259-281. (Also, including peer review comments, in NUREG/CR-5030, 1989.)

18. Theofanous, T.G. and H. Yan (1991) "ROAAM: A Risk-Oriented Accident Analysis Methodology," Proceedings, International Conference on Probabilistic Safety Assessment and Management (PSAM), Beverly Hills, CA, February 4-7, 1991, Vol. 2, 1179–1185.

19. Turland, B., D.F. Fletcher, K.I. Hodges and G.J. Attwood (1993) "Quantificaton of the Probability of Containment Failure Caused by an In-Vessel Steam Explosion for the Sizewell B PWR," CSNI Specialists Meeting on Fuel-Coolant Interactions, Santa Barbara, CA, January 5-8, 1993.

20. Yuen, W.W., X. Chen and T.G. Theofanous (1992) "On the Fundamental Microinteractions That Support the Propagation of Steam Explosions," ANS Proceedings NURETH-5, Salt Lake City, UT. September 21-24, 1992, Vol. II, 627–636.

21. Yuen, W.W. and T.G. Theofanous (1993) "The Prediction of Two-Dimensional Detonations and Resulting Damage Potential," CSNI Specialists Meeting on Fuel-Coolant Interactions, Santa Barbara, CA, January 5-8, 1993.

NRC FORM 335 (2-89) NRCM 1102, 3201, 3202

U.S. NUCLEAR REGULATORY COMMISSION

BIBLIOGRAPHIC DATA SHEET

(See instructions on the reverse)

1. REPORT NUMBER (Assigned by NRC, Add Vol., Supp., Rev., and Addendum Numbers, if any.)

NUREG/CR-5960

2. TITLE AND SUBTITLE

Steam Explosions: Fundamentals and Energetic Behavior

3. DATE REPORT PUBLISHED

MONTH	YEAR
January	1994

4. FIN OR GRANT NUMBER

L1173

5. AUTHOR(S)

T. G. Theofanous, W. W. Yuen, S. Angelini, X. Chen, W. H. Amarasooriya, S. Medhekar

6. TYPE OF REPORT

Technical

7. PERIOD COVERED (Inclusive Dates)

8. PERFORMING ORGANIZATION - NAME AND ADDRESS (If NRC, provide Division, Office or Region, U.S. Nuclear Regulatory Commission, and mailing address; if contractor, provide name and mailing address.)

Department of Chemical and Nuclear Engineering
Center for Risk Studies and Safety
University of California
Santa Barbara, CA 93106

9. SPONSORING ORGANIZATION - NAME AND ADDRESS (If NRC, type "Same as above"; if contractor, provide NRC Division, Office or Region, U.S. Nuclear Regulatory Commission, and mailing address.)

Division of Systems Research
Office of Nuclear Regulatory Research
U.S. Nuclear Regulatory Commission
Washington, DC 20555-0001

10. SUPPLEMENTARY NOTES

11. ABSTRACT (200 words or less)

This report presents the results of a multifaceted research effort in the field of steam explosions. The scope ranges from the fundamentals to assessing the energetics in applications relevant to Severe Accidents in Light Water Reactors. The consideration of fundamentals is built around two key ideas: the water depletion phenomenon during premixing and the microinteractions, including fragmentation kinetics, during propagation. The application to reactor conditions includes consideration of in-vessel steam explosions in PWRs and ex-vessel explosions in all five containment designs in current plants (in the USA). The report is structured in three parts, dealing with premixing, propagation, and energetics, respectively.

12. KEY WORDS/DESCRIPTORS (List words or phrases that will assist researchers in locating the report.)

Steam Explosions, Vapor Explosions, Thermal Detonations, Premixing Propagation, Fragmentation, Shock Waves, PM-ALPHA, ESPROSE

13. AVAILABILITY STATEMENT

Unlimited

14. SECURITY CLASSIFICATION

(This Page)

Unclassified

(This Report)

Unclassified

15. NUMBER OF PAGES

16. PRICE

Federal Recycling Program

UNITED STATES
NUCLEAR REGULATORY COMMISSION
WASHINGTON, D.C. 20555-0001

OFFICIAL BUSINESS
PENALTY FOR PRIVATE USE, $300

SPECIAL FOURTH-CLASS RATE
POSTAGE AND FEES PAID
USNRC
PERMIT NO. G-37